

UNCLASSIFIED

AD NUMBER

AD819188

LIMITATION CHANGES

TO:

Approved for public release; distribution is unlimited.

FROM:

Distribution authorized to U.S. Gov't. agencies and their contractors;
Administrative/Operational Use; JUL 1967. Other requests shall be referred to HQ, Air Weather Service, Scott AFB, IL.

AUTHORITY

MAC ltr 20 Oct 1988

THIS PAGE IS UNCLASSIFIED

UNCLASSIFIED

Security Classification

DOCUMENT CONTROL DATA - R & D

(Security classification of title, body of abstract and indexing annotation must be entered when the overall report is classified)

| | | | |
|--|--|--|--------------------------|
| 1. ORIGINATING ACTIVITY (Corporate author) Hqs, Air weather Service | | 2a. REPORT SECURITY CLASSIFICATION UNCLASSIFIED | |
| | | 2b. GROUP - | |
| 3. REPORT TITLE Proceedings of the Technical Exchange Conference 4-7 April 1967. | | | |
| 4. DESCRIPTIVE NOTES (Type of report and inclusive dates) Final | | | |
| 5. AUTHOR(S) (First name, middle initial, last name) (See Table of Contents, 47 authors). | | | |
| 6. REPORT DATE 20 July 1967 | | 7a. TOTAL NO. OF PAGES 302 | 7b. NO. OF REFS - |
| 8a. CONTRACT OR GRANT NO. - | | 9a. ORIGINATOR'S REPORT NUMBER(S) Technical Report 196 | |
| b. PROJECT NO. - | | | |
| c. - | | 9b. OTHER REPORT NO(S) (Any other numbers that may be assigned this report) | |
| d. - | | | |
| 10. DISTRIBUTION STATEMENT This document is subject to special export controls and each transmittal to foreign governments or foreign nationals may be made only with approval of Hqs, Air Weather Service. | | | |
| 11. SUPPLEMENTARY NOTES Contains 47 separate articles by different authors from various military and civilian agencies, given at meeting in Monterey, Calif., 4-7 April 1967 | | 12. SPONSORING MILITARY ACTIVITY Results reported were supported by agencies with which the authors are affiliated. | |
| 13. ABSTRACT Full length report or summaries are given of 47 presentations made at the AWS Technical Exchange Conference, Monterey, 4-7 April 1967. Authors represented Air Force Army, and Navy activities and their contractors, Environmental Science Services Administration, and several universities. Subject fields covered were: - Interpretation and use of meteorological satellite data, solar and upper atmospheric phenomena, Dynamic models (of the atmosphere), Tropical meteorology, Surface weather and boundary-layer phenomena, and Data handling and prediction techniques. | | | |

DD FORM 1473
1 NOV 65UNCLASSIFIED
Security Classification

UNCLASSIFIED

Security Classification

| 14 KEY WORDS | LINK A | | LINK B | | LINK C | |
|---|--------|----|--------|----|--------|----|
| | ROLE | WT | ROLE | WT | ROLE | WT |
| Meteorology Meteorological Satellite Data Cloud Cover Photo Interpretation Numerical Weather Analysis Numerical Weather Prediction Solar Flares Sudden Ionospheric Disturbances Neutron Monitors Solar Protons Sunspots Convection, Atmospheric Correlation Tropical Meteorology Models Cyclones Cosmic Rays, Solar Ionosphere, Tilts Topside sounders Atmospheric density SPADATS Atmospheric General Circulation Meteorological Networks Fronts Energetic Particles Radio, millimeter waves F2 layer Ionospheric propagation Geomagnetic indexes Magnetic storms Hurricanes Southeast Asia Rainfall Infrared Vegetative canopy Momentum flux Micrometeorology Snow and Ice Missile impact prediction Statistical methods Ballistic meteorology Atmospheric Turbulence. | | | | | | |

UNCLASSIFIED

Security Classification

AWS Technical Report 196

APT Retain

#41



PROCEEDINGS OF THE TECHNICAL EXCHANGE CONFERENCE 4-7 APRIL 1967

This Document is Subject to Special Export Controls
and Each Transmittal to Foreign Governments or
Foreign Nationals May Be Made Only With Approval
of Hq Air Weather Service

PUBLISHED BY
AIR WEATHER SERVICE (MAC)
UNITED STATES AIR FORCE
JULY 1967

FOREWORD

In 1964 the Air Weather Service prepared its first Techniques Development Plan. The objective was to insure timely development of required analysis and forecasting techniques. This was to be done through efficient use of expensive computer equipment and of limited resources in the form of talented, highly trained yet operationally motivated, atmospheric scientists. It succeeded in minimizing duplication within AWS and resulted in a well-coordinated effort among its development centers.

Although several internal conferences preceded completion of the plan, the first Techniques Development Conference to involve people from outside AWS was held in 1965. The 35 participants included representatives from the Navy and Army as well as two civilian agencies. In 1966 at the second Conference the representation included still more agencies and was attended by 90 people, resulting in further streamlining of the AWS technique-development program.

The expansion of the AWS mission to include support to operations within the total aerospace environment led us to incorporate in this year's conference discussions on the environment beyond the classical atmosphere of the meteorologist. Thus we shall obtain invaluable assistance in the refinement of the support now rendered by the Solar Forecast Center in Colorado Springs. The Conference program which originally dealt only with techniques requiring computers, has been broadened also to include methodologies involving the man-machine mix and even purely manual approaches. Hence the title has been changed to the "Technical Exchange Conference" to symbolize its more comprehensive nature.

This year the conference was further enhanced and strengthened in that the U. S. Naval Weather Service was co-sponsor with AWS and the host at the Naval Postgraduate School in Monterey, California. The NWS has been a leader in operational applications of theory and experience involving the air-sea interface. It is especially appropriate that the conference was held at the NWS' major operational computer center in view of the ever broadening operational aspects of the geophysical sciences.

The U. S. Army has offered to co-host the 1968 conference with AWS at a site to be announced. Thus the value of the conference will be increased through more emphasis on the environment of Army operations.

A selection of presentations at the 1966 meeting was reproduced in Air Weather Service Technical Report 188. This year we are reproducing herewith all presentations for which manuscripts (full length or summary) were submitted to us. Because the papers provide a good cross-section of development now in progress, we believe that the entire developmental community in aerospace sciences will find this report useful in reference to their existing and planned programs. We thank the speakers for their trouble in submitting their manuscripts "ready to print." All but a few papers or summaries are included--the omissions are mainly presentations which the authors felt were too preliminary for publication. Several papers scheduled on the agenda were not presented because the speakers were unable to attend; and some of these are omitted from the report.

AWS is highly appreciative of the cooperation extended by other agencies participating in the 1967 conference. Among the great number of individuals who wholeheartedly joined with us, I feel that it is appropriate to acknowledge specifically the outstanding cooperation of Capt Paul Wolf, Officer in Charge of the Fleet Numerical Weather Facility at Monterey and acting in behalf of Naval Weather Service to co-host the meeting; Col Donald E. Martin, Deputy Director of Aerospace Sciences, AWS, and architect of the entire series of conferences; Mr. Stanley E. Pearce, AWS, program organizer; and Lt Cdrs William Groscup and Glen Hamilton, of FNWF, who saw to it that the 1967 conference of over 150 participants ran with complete smoothness and efficiency.

DR. ROBERT D. FLETCHER
Director, Aerospace Sciences
Hq Air Weather Service

Distribution; X (Continued on page vi)

31 May 1967

TABLE OF CONTENTS

(In Order of Agenda for the Conference)

| <u>Presentation</u> | <u>Page</u> |
|---|-------------|
| * <u>Session I. - Interpretation and Use of Meteorological Satellite Data</u> (Chairman - Major John Perry, vice Robert D. Fletcher, Hq AWS) | |
| ✕ Some Solutions to Weather Analysis Problems through the Use of Satellite Data - Edward Ferguson, ESSA/NESC | 1 |
| ✕ Application of Satellite-Picture Interpretation Principles to Analysis in Sparse Data Regions - Major Golden R. Farr, 6 Wea Wg/ ETAC | 11 |
| ✕ A Satellite Cloud Photo-Interpretation Key - Roy Lee and Charles I. Taggart, Meteorological Service of Canada/Toronto | 33 |
| Recent Results and Current Activities in Satellite Meteorology at AFCRL - Thomas J. Keegan, AFCRL (Paper not received) | |
| Quantitative Cloud Motion and Growth Information from Earth- Synchronous Satellite-Picture Pairs - Charles L. Bristol, ESSA/ NESC (Abstract) | 38 |
| <u>Session II. - Interpretation and Use of Meteorological Satellite Data</u> (Cont'd) (Chairman - E. Paul McClain, ESSA) | |
| APT Use at Fuchu AF Weather Central - Capt Lee G. Dickinson, 1 Wea Wg/Fuchu | 39 |
| Recent Research on the Application of Meteorological Satellite Data to Numerical Weather Analysis - E. Paul McClain and Harold J. Brodrick, ESSA/NESC | 42 |
| Utilization of Meteorological-Satellite Cloud Data in a Numerical Analysis and Prediction System - Roland Nagle, Meteorology International, Inc. (Abstract) | 51 |
| Use of Data in FNWF Products as Derived from Meteorological Satellites - Project FAMOS/USN (Presentation not given) | |
| Applications of Satellite Observations of Extratropical Cloud Vortices - William K. Widger, Jr., C. W. C. Rogers, and Paul E. Sherr, Aracon Geophysics Co. | 52 |
| A Correlation Study of a TIROS-IV MRIR-Data Case with Synoptic Meteorological Variables - F. L. Martin, USN Postgraduate School (Paper not received) | |
| <u>Session IIA. - Solar and Upper-Atmospheric Phenomena</u> (Chairman - Frederick Ward, AFCRL) | |
| The Need for Objective Observing and Reporting of Solar Flares - Capt Hans Fischer, 6 Wea Wg/Hanscom | 83 |
| A Solar-Flare Videometer - Paul Tallant, AFCRL/Sacramento Peak Observatory | 92 |

| | <u>Page</u> |
|---|-------------|
| Early Automatic Recognition of Sudden Ionospheric Disturbances - J. R. Winkelman and J. A. Koch, ESSA/ITSA (Paper not received) | |
| Use of Ground-Level Neutron Monitors in a Real-Time Solar-Proton Monitoring Network - M. A. Shea, AFCRL | 110 |
| The Effect of Physical Foreshortening on Sunspot Area Measurements - Capt Ronald T. Podsiadlo, 6 Wea Wg/Hanscom (Summary) | 119 |
| <u>Session III. - Dynamic Models</u> (Chairman - George J. Haltiner, USN Postgraduate School) | |
| Numerical Modeling of Convection - Francis W. Murray, Rand Corporation | 121 |
| Fields by Correlation Assembly - Maurice Danard, Manfred Holl, and James R. Clark, Meteorology International, Inc. (Abstract) | 126 |
| Current New Operations in Numerical Weather Prediction Including the Tropical Program and PE Model with Emphasis on PE Outputs and Future Plans - F. W. Burnett, ESSA/WB (Paper not received, to be published in Journal of Applied Meteorology) | |
| On the Application of Scaling Theory and Energetics to the AWS Six-Level Model - Maj Harold Hart, 3 Wea Wg | 127 |
| A Diabatic Multi-Level Primitive-Equation Prediction Model and an Illustration of a Wave Cyclone Development - T. N. Krishnamurti, U. S. N. Postgraduate School (Outline) | 133 |
| Diabatic Heating and its Significance to Dynamic Prediction - Earl C. Kindle, Research Triangle Inst. (Presentation not given) | |
| <u>Session IIIA. - Solar and Upper Atmospheric Phenomena (Cont'd)</u> (Chairman - Robert Knecht, ESSA) | |
| Monitoring Solar Cosmic-Ray Events - G. W. Adams, ESSA/ITSA (Summary) | 136 |
| Computer Ray-Tracing Techniques to Determine the Effects of Ionospheric Tilts to MUFs. - Alfred F. Barghausen and James W. Finney, ESSA/ITSA | 138 |
| Observation and Mapping of MUFs and Large Horizontal Variations of the Ionosphere - L. A. Berry, R. D. Hunsucker, and L. H. Tveten, ESSA/ITSA (Abstract) | 144 |
| Morphology of Topside Polar Ionosphere - Capt C. F. Power, Hq AWS, and Charles M. Rush, University of California | 146 |
| The Computation of Atmospheric Densities Using SPADATS Data - Capt R. E. de Michaels, 4 Wea Wg | 156 |
| An Investigation of Atmospheric Density Between 180 km and 300 km. - Lt Col L. L. DeVries, Hq AWS (Presentation not given, but summary received) | 160 |

| | <u>Page</u> |
|---|-------------|
| <u>Session IV. - Dynamic Models (Cont'd)</u> | |
| (Chairman - Col Donald E. Martin, Hq AWS) | |
| Results from the Two-Level Version of the NCAR General Circulation Model - Warren M. Washington and Akira Kasahara, NCAR | 162 |
| Grid Telescoping in Numerical Weather Prediction - Goeffrey D. Hill, AFCLRL | 172 |
| Preliminary Results of Numerical Experiments to Determine Optimum Hemispheric Meteorological Networks - F. Lewis, J. D. Stackpole, and M. A. Alaka, ESSA/WB (Paper not received) | |
| Objective Improvements of Numerical Prognoses - H. B. Wobus and P. R. Lowe, NWRP (Abstract) | 178 |
| The Application of Numerical Analysis of Baroclinicity to the Objective Location of Frontal Zones - Robert J. Renard, USN Postgraduate School. | 179 |
| Numerical Modeling Efforts of 3 Weather Wing - Lt Col Herbert Edson, 3 Wea Wg | 200 |
| <u>Session IVA - Solar and Upper-Atmospheric Phenomena (Cont'd)</u> | |
| (Chairman - Capt C. F. Power, vice Lt Col Leonard DeVries, Hq AWS) | |
| Techniques for Prediction of Solar Flares and Energetic-Particle Events - Maj Donald T. Sherry, 4 Wea Wg/SFF | 202 |
| The Application of Millimeter-Wave Radio Mapping to Flare Prediction - Maj William O. Banks, 4 Wea Wg/ElSegundo | 207 |
| Short-Term Prediction of F2-Layer Maximum Usable Frequencies for Local Magnetic Activity - Robert M. Savis, Jr., ESSA/ITSA | 209 |
| Short-Term Forecasting of Ionospheric Propagation for DCA Trunks in S. E. Asia - R. J. Slutz, T. N. Gautier, and M. Leftin, ESSA/ITSA (Abstract) | 212 |
| Real-Time Specification of the Planetary Geomagnetic Index a_p - Capt William F. Johnson, Hq AWS (Summary) | 213 |
| Preliminary Report of Micro-Wave Burst Characteristics and Related HF Propagation Characteristics During Ensuing Magnetic-Storm Periods - Verne Hildebrand, Naval Ordnance Lab./Corona (Paper not received) | |
| <u>Session V - Tropical Meteorology</u> | |
| (Chairman - R. Cecil Gentry, ESSA/NHRL) | |
| Prediction of Hurricane Movement - Banner I. Miller and R. Cecil Gentry, ESSA/NHRL | 215 |
| The Onset of Widespread Rain During the Southeast Asia Summer Monsoon - Marvin Lowenthal, USAECOM/Ft Monmouth (Presented by W. C. Conover) (Summary) | 224 |
| Annual Versus Daily Rainfall: Southeast Asia - Ruth L. Wexler, USA Natck Labs | 226 |

Page

| | |
|---|-----|
| The Tropical-Analysis and Forecasting Model Running Operationally at FWC Pearl Harbor - Capt John G. Joern, 1 Wea Wg/Pearl Harbor | 243 |
| Diurnal Variation in Cloud Cover Over a Tropical Island Region as Shown by TIROS-VII Infrared Data - Earl S. Merritt, Aracon Geophisics Co. | 245 |

Session VI. - Surface Weather and Boundary-Layer Phenomena
(Chairman - Kenneth M. Barnett, USAECOM)

| | |
|---|-----|
| Short-Range Subsynoptic Surface-Weather Prediction - Harry R. Glahn and Dale A. Lowry, ESSA/WB | 254 |
| A Mathematical Model for Air Flow in a Vegetative Canopy - Ronald M. Cionco, USAECOM/Ft Huachuca (Summary) | 260 |
| Momentum Flux Studies over a Horizontally Homogeneous Site - Duane A. Haugen and J. Chandran Kaimal, AFCRL, (Paper not received) | |
| An Empirical Study of Low-Level Sounding Prediction - Carl W. Kreitzberg, AFCRL | 262 |
| A Low-Level Circulation Model for Diagnostic and Prognostic Applications. Maj R. A. Derrickson and Capt Paul Janota, 3 Wea Wg (Summary) | 276 |
| An Objective Precipitation and Moisture-Forecast Model - Leo C. Clarke FNWF (Abstract) | 277 |

Session VII. - Data-Handling and Prediction Techniques
(Chairman - Carl W. Kreitzberg, AFCRL)

| | |
|--|-----|
| Systematic Approach to Weather Presentation - Clement J. Todd and Steven H. Cohen, NWRP | 278 |
| Teleplot - J. W. Nickerson, NWRP | 280 |
| Surface Observations of Snow and Ice for Correlation with Remotely Collected Data - Michael A. Bilello, USA/CRREL | 285 |
| Real-Time Pre-Launch Missile-Impact Prediction Techniques - Louis D. Duncan, USAECOM/White Sands (Paper not received) | |
| Some Considerations on the Problems of Developing Forecasting Techniques by Statistical Methods - C. F. Roberts, ESSA/WB (Presentation not given) | |
| Ballistic Meteorology Variation in Mountainous Areas - Anthony Barichivich, USAECOM/Ft Monmouth (Presentation not given) | |
| Application of Radio and Optical Path-Length Measurements to Studies of Low-Level Turbulence - B. R. Bean and C. B. Emmanuel, ESSA/ITSA (Summary) | 294 |
| Determination of the 500-mb Circulation over North Hemispheric Oceans for Satellite and Conventional Surface Measurements - William E. Shenk, GCA Corporation (Presentation not given) | |

Index of Authors

| <u>Name</u> | <u>Page</u> | <u>Name</u> | <u>Page</u> |
|--------------------|-------------|---------------------|-------------|
| ADAMS, G. W. | 136 | JOERN, J. G. | 243 |
| BANKS, W. O. | 207 | JOHNSON, W. F. | 213 |
| BARGHAUSEN, A. F. | 138 | KASAHARA, AKIRA | 162 |
| BEAN, B. R. | 294 | KREITZBERG, C. W. | 262 |
| BERRY, L. A. | 144 | KRISHNAMURTI, T. N. | 133 |
| BILELLO, M. A. | 285 | LEE, R. | 33 |
| BRISTOR, C. L. | 38 | LEFTIN, M. | 212 |
| BRODRICK, H. J. | 42 | LOWE, P. R. | 178 |
| CIONCO, R. M. | 260 | LOWENTHAL, M. | 224 |
| CLARK, J. R. | 126 | LOWRY, D. A. | 254 |
| CLARKE, L. C. | 277 | MCCLAIN, E. P. | 42 |
| COHEN, S. H. | 278 | MERRITT, E. S. | 245 |
| CONOVER, W. C. | 224 | MILLER, B. I. | 215 |
| DANARD, M. | 126 | MURRAY, F. W. | 121 |
| DAVIS, R. M. | 209 | NAGLE, R. | 51 |
| DEMICHAEELS, R. E. | 156 | NICKERSON, J. W. | 280 |
| DERRICKSON, R. A. | 276 | PODSIADLO, R. T. | 119 |
| DEVRIES, L. L. | 160 | POWER, C. F. | 146 |
| DICKINSON, L. G. | 39 | RENARD, R. J. | 179 |
| EDSON, H. | 200 | ROGERS, C. W. C. | 52 |
| EMMANUEL, C. B. | 294 | RUSH, C. M. | 146 |
| FARR, G. R. | 11 | SHEA, M. A. | 110 |
| FERGUSON, E. | 1 | SHERR, P. E. | 52 |
| FINNEY, J. W. | 138 | SHERRY, D. T. | 202 |
| FISCHER, H. | 83 | SLUTZ, R. J. | 212 |
| GAUTIER, T. N. | 212 | TAGGART, C. I. | 33 |
| GENTRY, C. | 215 | TALLANT, P. | 92 |
| GLAHN, H. R. | 254 | TODD, C. J. | 278 |
| HART, H. | 127 | TVETEN, L. H. | 144 |
| HILL, G. E. | 172 | WASHINGTON, W. M. | 162 |
| HOLL, M. | 126 | WEXLER, R. L. | 226 |
| HUNSUCKER, R. D. | 144 | WIDGER, W. K. JR. | 52 |
| JANOTA, P. | 276 | WOBUS, H. B. | 178 |

Distribution; X (Continued)

AWS.....112
 Wings..... 5
 Except 7 Wea Wg 17
 ETAC..... 25
 Squadrons..... 2
 Forecasting Dets..... 1
 Special

Some Solutions to Weather Analysis
Problems Through the Use of Satellite Data

by Edward W. Ferguson

ABSTRACT

Large scale cloud patterns and cloud distribution as observed in satellite data identify the positions of vortices, fronts, jet streams, upper level troughs and ridges, surface ridges and centers of mid-tropospheric cyclonic vorticity. Cloud types and cloud line orientation provide information concerning the stability and thermal structure of the atmosphere.

Examples of these cloud patterns are shown and related to synoptic analyses, atmospheric motions, and temperature structure. Then examples are shown on how information derived from satellite data can be applied to weather analyses and forecasts.

Soon after the launch of the first TIROS weather satellite in the spring of 1960, meteorologists using the satellite pictures were able to identify correctly in them synoptic features such as cold fronts, vortices and tropical storms. Since this first satellite was launched, fifteen more weather satellites have been in operation.

The research with data from these satellites has materially increased our knowledge of how to use the specialized kind of information provided by these observation platforms in space. Interpretation of the data has become much more sophisticated and now, by interpretation of the cloud pictures, we can locate jet streams, upper level troughs



Figure 1.--ESSA 3 photo montage. March 23, 1967.

and ridges, centers of mid-tropospheric positive vorticity and can assign finite values to the intensity of tropical storms. With the launch of TIROS IX early in 1965 we were able, for the first time, to view the entire sunlit portion of the earth once daily. Prior to this time, our data sampling had been rather meager and, because the satellite data were sparse, much speculation and guesswork went into the meteorological interpretation of satellite pictures. At present, the TOS series of satellites (ESSA 1, 2, 3, and 4) provide complete daily coverage of much improved quality. Because of these improvements, it is now possible to identify many cloud patterns and features which prior to this time had little meaning. Through satellite viewing and correct interpretation of cloud types and cloud distributions, one can make certain inferences as to the synoptic flow patterns associated with these cloud features. In data-sparse areas this capability is invaluable. In addition, cloud alignment and striations in overcast cloud masses give information which can be related to thermal properties of the atmosphere.

The area photographed by the ESSA 3 satellite during a 24-hour period on March 23, 1967, is shown in figure 1. Large cloud features such as fronts and vortices can be seen at higher latitudes, the clouds associated with the ITCZ are visible near the equator in the Pacific and Atlantic Oceans, and convective activity appears over South America.

A closer view of how a vortex appears in satellite pictures is shown in figure 2. A cold frontal cloud band extends north-eastward from the lower left portion of the picture and spirals into a center of circulation near 40°N-155°E. The effect of dry air being brought into the center of circulation is apparent by the decrease in cloud

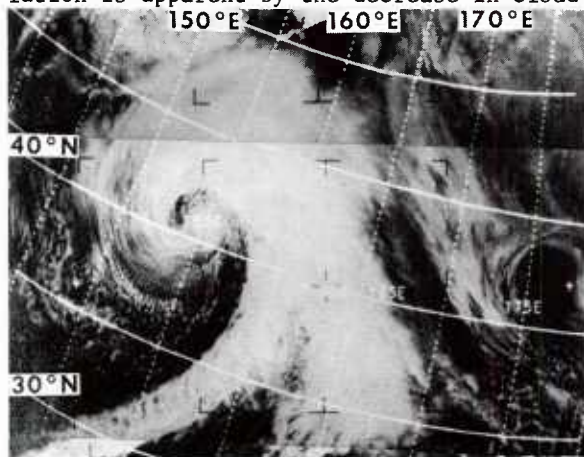


Figure 2.--Occluded low pressure system over the North Pacific Ocean. ESSA 3, March 19, 1967.

amount in the arc which spirals cyclonically from 40°N-157°E. There is some evidence of warm frontal cloudiness near 35°N-165°E. To the rear of cold fronts over water, that is on the cold air side, it is common to observe huge areas of cumulus arranged in patterns of cells with open centers. These are clouds which form as a result of instability due to heating from below. Research has shown that polygonal open-cell patterns of this type closely approximate regions of precipitation--especially when the cells are large and bright and located well to the rear of a cold front (1). A good example of this cloud type appears in figure 3. In this case, some of the clouds near 42°N-133°W have reached a stage in development where cirrus is being produced and blown from the tops of the individual convective cloud masses.

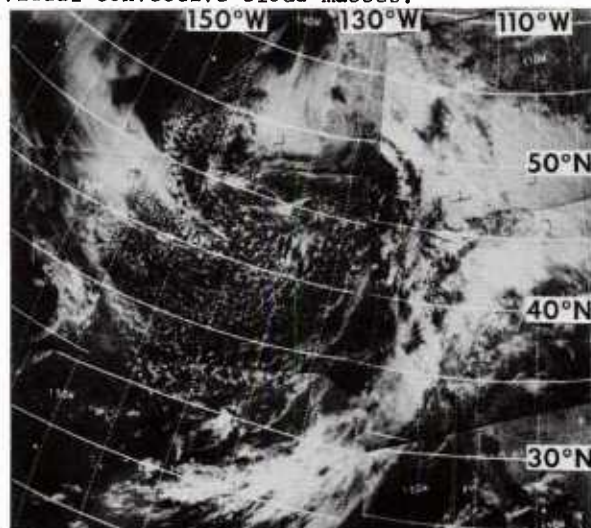


Figure 3.--Open cellular cumulus to rear of cold front. ESSA 3, March 16, 1967.

It is common to observe over water areas frontal bands that are 3,000 to 4,000 miles in length. One such example is shown in figure 4. These pictures were acquired after a cold polar outbreak had moved into the north Pacific. The uniform width and curvature of the frontal band permits the conclusion that there is no wave development on the front at this time. Of significance is the small, bright cloud mass which forms a comma-shaped pattern through points at 35°N-152°E, 39°N-155°E and 37°N-152°E. This kind of cloud pattern is commonly seen in areas where there is a secondary center of positive vorticity to the rear of a cold front. The clouds are produced in the region of positive vorticity advection and normally appear as a comma-shaped mass. The identification of this feature, in my opinion, is one of the greatest contributions that has been made to the analysis program. In the past, the presence of a second band of clouds and precipitation to the rear of a front were

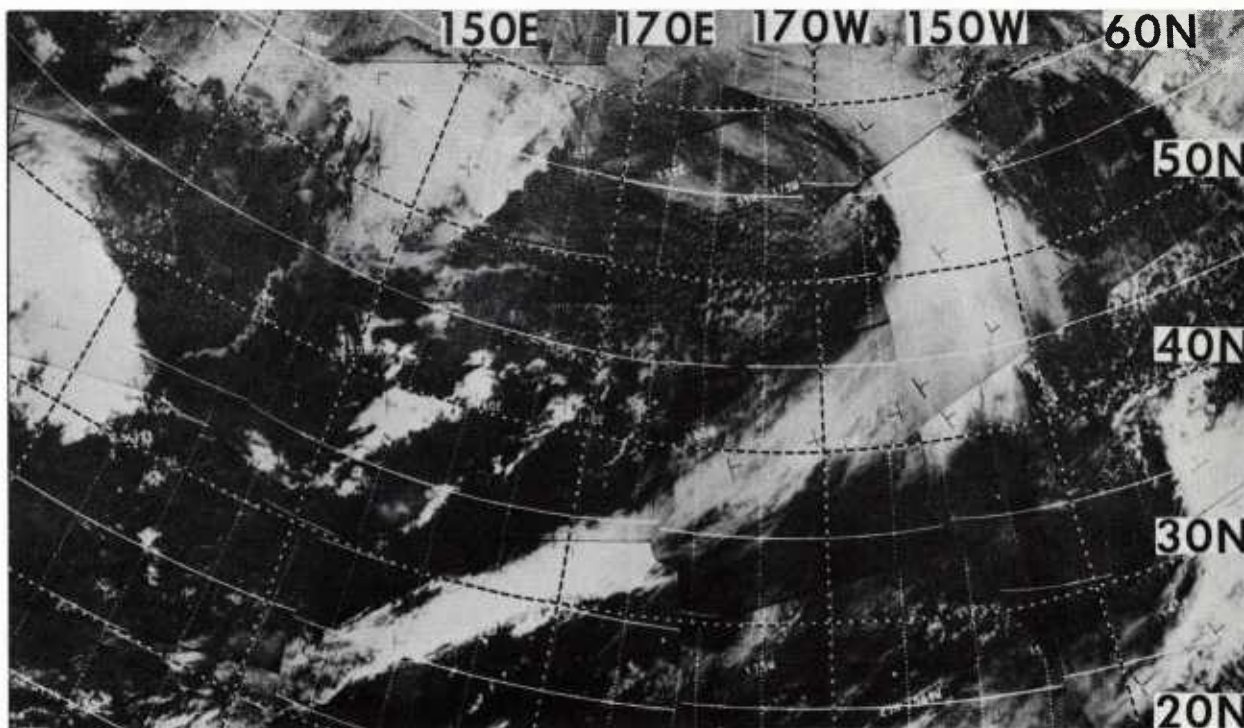


Figure 4.--Frontal cloud band and clouds associated with secondary positive vorticity center. ESSA 3, March 25, 1967

attributed to a secondary cold front or a bent-back occlusion. The satellite photographs show that the clouds associated with these secondary vorticity centers are completely separate from the primary center of vorticity rather than being attached as would be the case with a secondary cold front or bent-back occlusion. In figure 4 the occluded system is centered at 55°N - 170°W . The white, filmy cirriform clouds along the east side of the secondary vorticity center suggest considerable vertical motion in the region of positive vorticity advection. The most useful aspect in the detection of centers of positive vorticity lies in the possibility of predicting the result of the downstream advection of this vorticity. Pettersson (2), Oliver (3), Anderson (4) and others have said the most common cause of wave development is the advection of positive vorticity into a baroclinic zone. In satellite pictures it is common to observe the evolution of wave development as a result of secondary vorticity centers interacting with a frontal zone. As a vorticity center begins to interact with a frontal zone the clouds along the front begin to bulge back toward the cold air, and the front, which curved cyclonic earlier, begins to bend anti-cyclonically along the cold air side. There is also an increase in high level clouds in advance of the wave at this time. At this stage of development, the upper level jet stream assumes a slight anticyclonic deformation over the wave so that the jet stream

location can often be detected in the cirriform cloud formation.

The ESSA 3 mosaic in figure 5 shows the Pacific area as it appeared twenty-four hours after the picture in figure 4. The comma-shaped cloud mass which is associated with the secondary vorticity center is now located through points 32°N - 166°E , 39°N - 169°E , 39°N - 165°E and 37°N - 166°E and shows an increase in cloud amount. As a result of the interaction of the vorticity center with the front near 34°N - 173°E an open wave has developed and is apparent by the large area of multilayered cloud northeast of that point. The back and leading edges of the clouds associated with the wave are sharply anti-cyclonic. The pattern shown is typical of the clouds associated with an open wave. If a wave of this type is not cut-off from the westerlies by a blocking ridge, it is common for it to move northeastward and occlude. The resulting cloud pattern would be similar to that shown in figure 2.

The positions of upper level troughs and ridges are detectable in satellite data. At the point where an upper level trough intersects a frontal zone there is a distinct change in the appearance of the frontal clouds. The clouds tend to dissipate; the front appears much more ragged and full of holes west of the trough line in the region of subsidence where air is sinking. East of the upper level trough the clouds are much

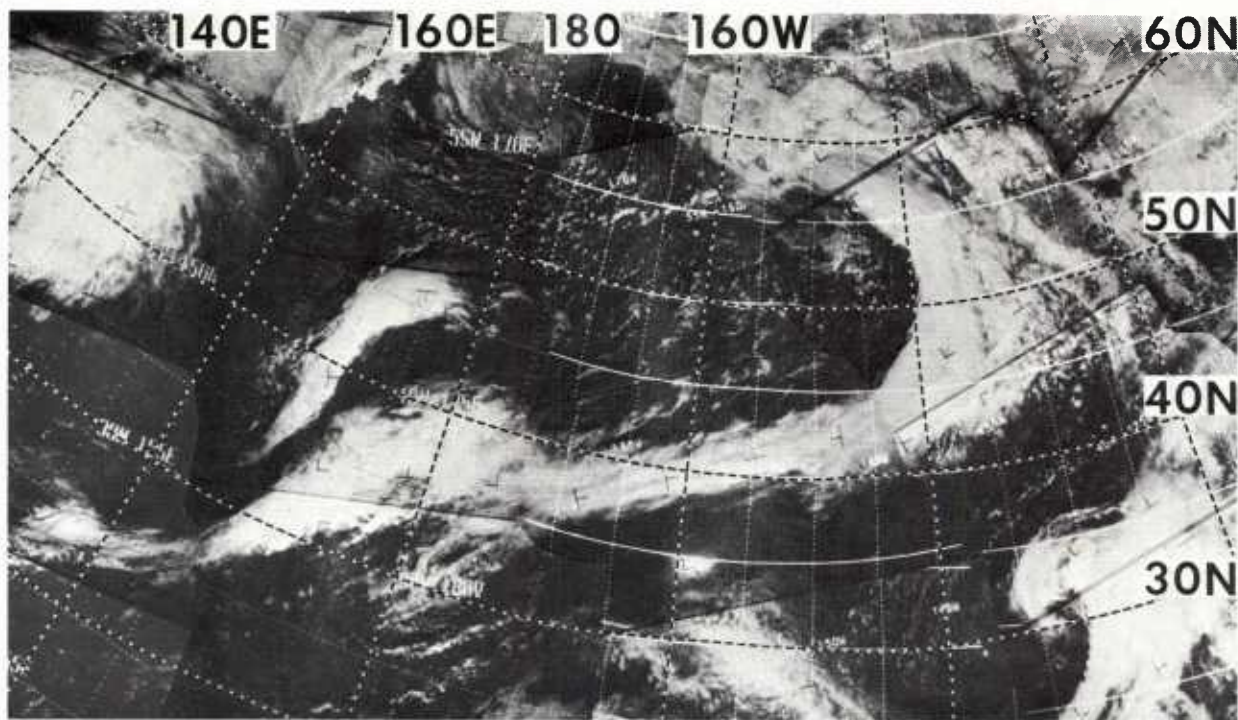


Figure 5.--Wave development on cold front. ESSA 3, March 26, 1967

brighter, the frontal zone is broader, and the amount of high level clouds is considerably greater due to upward motion in the southwesterly flow. These characteristics are quite apparent in the satellite photographs of figure 6. The 500 mb trough line is indicated by a dashed line. Note the change in the cloud band where the trough intersects the front (indicated by arrow).

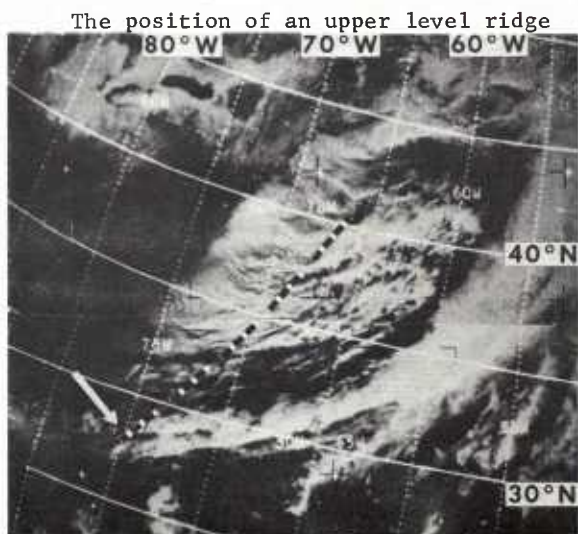


Figure 6.--Change in appearance of a frontal cloud band where an upper level trough line crosses the front (500 mb trough indicated by dashed line). ESSA 3, March 1, 1967.

line can usually be determined from cloud data with an accuracy of two or three degrees of longitude. The multilayered clouds tend to dissipate rapidly east of the point where the upper level flow has its maximum anticyclonic curvature. In figure 7, subsidence has caused the clouds to end abruptly east of the 500 mb ridge line (dashed). The accuracy with which upper level ridges can be positioned from cloud data is dependent on the

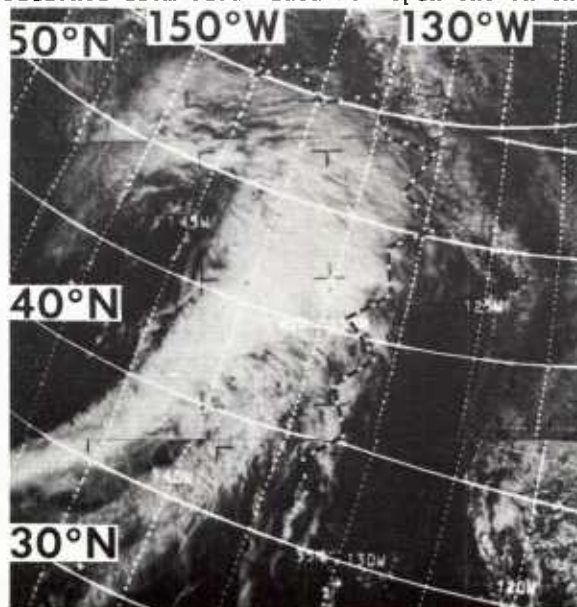


Figure 7.--Cloud pattern indicating the position of an upper level ridge. ESSA 3, February 25, 1967

wind-speed and the amplitude of the ridge. When the upper level ridge is quite broad and only slightly anticyclonic its position is quite difficult or even impossible to pin-point. If the wind is very strong over a ridge line, the multilayered clouds are advected some distance to the east of the ridge thus making it difficult to determine the exact position of the ridge. In the later two cases, the multilayered clouds do not end so abruptly and are more diffuse in appearance along the eastern side of a cloud mass, but if the ridge has large amplitude and sharp anticyclonic curvature, it is normally well defined in the satellite data.

Many studies made by research meteorologists of the National Environmental Satellite Center and by others relate certain features seen in satellite data to the position of upper level jet streams. Paul Kadlec of Eastern Airlines made some 400 flights from Boston to Miami and observed changes in cloud amount and type in the region of the jet core. He found that high level cirriform cloudiness tends to be restricted to the tropical side of a polar jet. Using this idea as a hypothesis, many satellite pictures were examined to see if

this postulate could be confirmed. Results of these studies show that the upper level jet can be accurately located about eight out of ten times when well defined cloud characteristics are observed in satellite pictures (5). The evidence of a jet stream is made apparent by shadows which high level clouds cast on lower underlying surfaces and by bands in the higher clouds which are oriented normal to the jet stream. Calculations made using sun angle, satellite attitude, variations in the heights of two layers of clouds, show that it is theoretically possible for a high level cloud deck to cast a shadow as wide as about 20 miles on the upper surface of a lower deck of clouds (6). The ESSA satellite picture in figure 8 shows a long, dark shadow extending from central Mexico (25°N-105°W) to off the east coast of the U.S. (36°N-66°W). The upper level jet stream is located about sixty miles poleward of and parallel to the shadow. Over data sparse regions this ability to determine correctly the position of the upper level jet is valuable to analysts and forecasters.

Because temperature is a parameter used in most numerical models, the Applications Group of NESG has done considerable work to

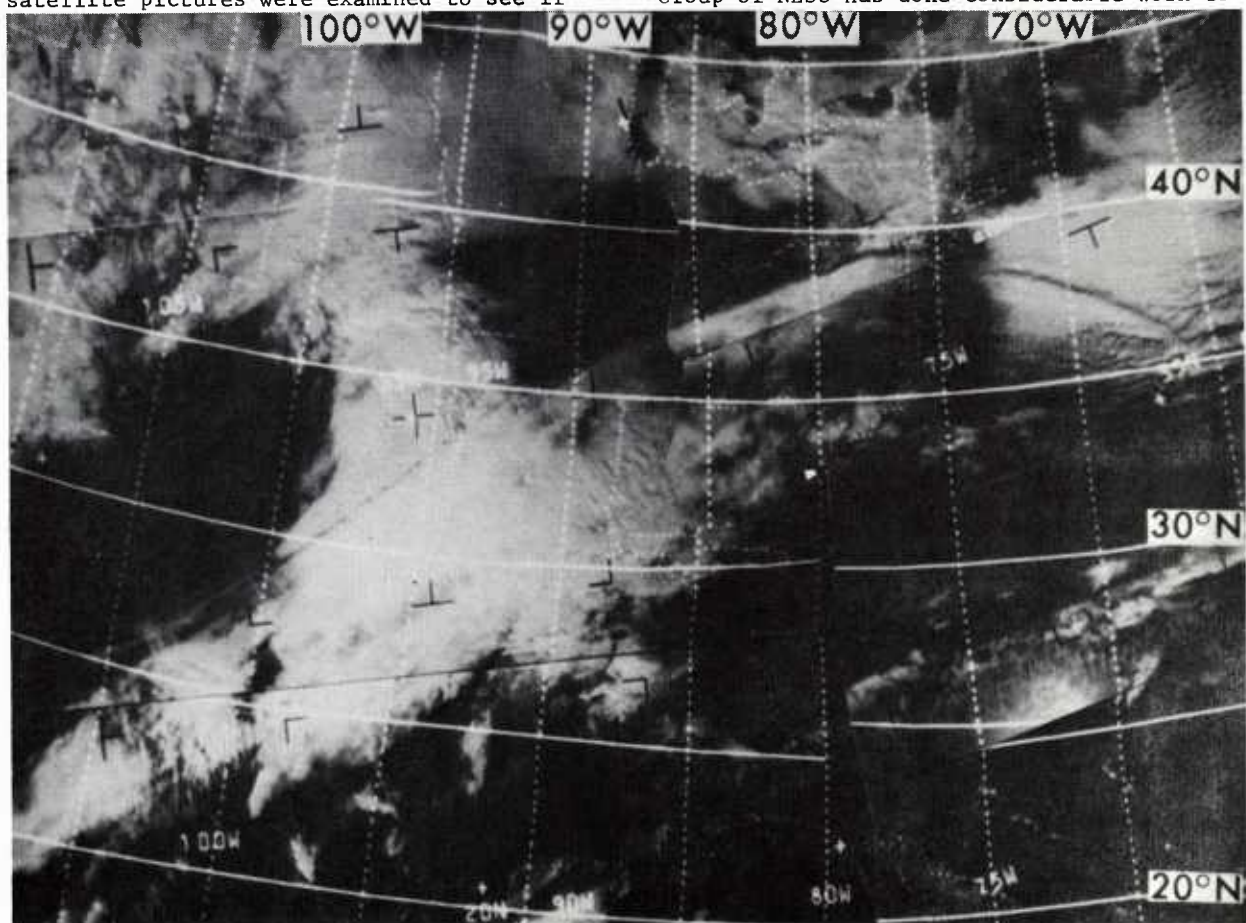


Figure 8.--Shadow along jet associated cirrus cloud edge. ESSA 3, December 30, 1966

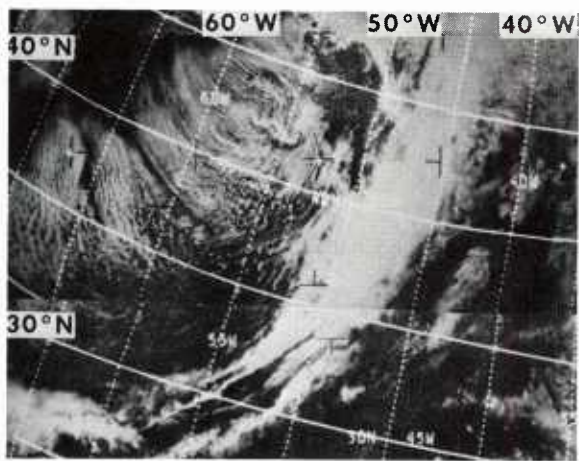


Figure 9.--Cumulus cloud lines in a region of cold air advection. ESSA 3, March 2, 1967.

determine what patterns can be detected in satellite data which might be related to thermal properties of the atmosphere. The cloud lines extending southeastward from 42°N-65°W in the satellite picture of figure 9 are of the type which are oriented parallel to the thickness field in the 1000 mb-500 mb layer. It is common to observe this pattern in regions of cold air advection after a front has passed off the coast of a continent and the air to the rear of a front is being heated rapidly from below. Striations in upper level clouds, such as those shown in figure 10 (indicated by arrows), are also found to be parallel to the thermal winds. The striations are due to the combined effects of thinner spots in the clouds beneath the high level clouds and shadows being cast by high level clouds onto a lower surface.

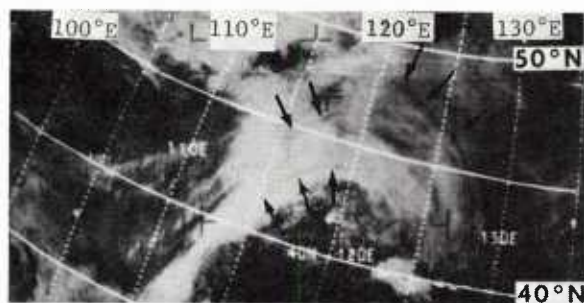


Figure 10.--Striations in high level clouds (arrows point to striations). ESSA 3, March 2, 1967.

An example of one of the digital products now prepared at the National Environmental Satellite Center is shown in figure 11. This represents the total data received from the ESSA 3 satellite in one twenty-four hour period. Portions of this product are transmitted to Kennedy Airport in New York City to aid in analysis and transoceanic flight briefings. A similar product is prepared on a 1:15 million scale mercator projection for the area between 40°N and 40°S latitude. The analog picture signal received from the satellite at Wallops Island, Virginia or Fairbanks, Alaska, is relayed to Suitland, Maryland where it is digitized, rectified, gridded, and made into a mosaic. It first appears in the form of 35mm negatives from which the product shown in figure 11 is produced. The Atlantic portion of the mercator projection which covers the equatorial region is transmitted to the Tropical Analysis Center in Miami once daily and there is incorporated with the analyses

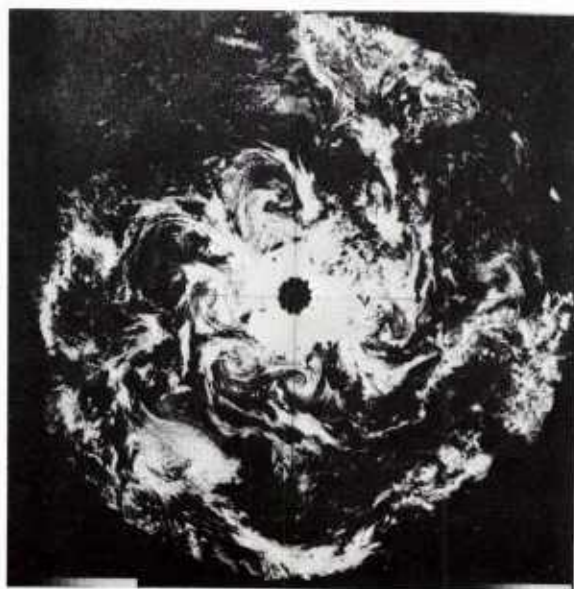
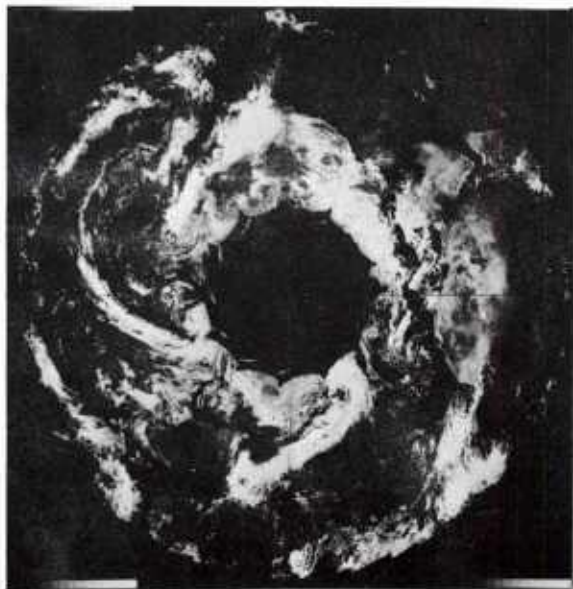


Figure 11.--ESSA 3 digital mosaics. March 23, 1967

prepared at the Center. The analysts there have been trained in the interpretation of satellite data and use this facsimile product to produce a more accurate analysis over data-sparse areas.

A more recent effort by the Applications Group of the Satellite Center deals with the application of the satellite data to numerical upper air analyses. The satellite data are examined daily for areas of cirrus clouds. Based on the appearance and orientation of cirrus shields and cirrus plumes, information is derived which can be related to the direction and speed of the upper level winds. About 100 points of data are taken from the satellite pictures daily and incorporated with the conventional data available at the time of the particular chart being prepared. A typical example of cirrus extending from convective activity is shown in figure 12. The cloud mass north of 28°S-122°W has a sharp western edge while the east side shows long streamers of cirrus extending toward the southeast. This would be interpreted to be flow toward the south-east.



Figure 12.--Cirrus plumes from convective activity. ESSA 3, March 18, 1967

cal 200 mb flow pattern for 1200 GMT March 14. Satellite data based on information from the pictures are indicated by the large dots at the end of the windshaft. Analyses of this type cover the area from 48°N to 48°S and are transmitted twice daily to Miami and Honolulu. Figure 14 shows the numerical 200 mb analysis (solid lines) which was computed using only the conventional data. The dashed lines indicate the reanalysis made after the satellite data was incorporated

Figure 13 shows a portion of a numeri-

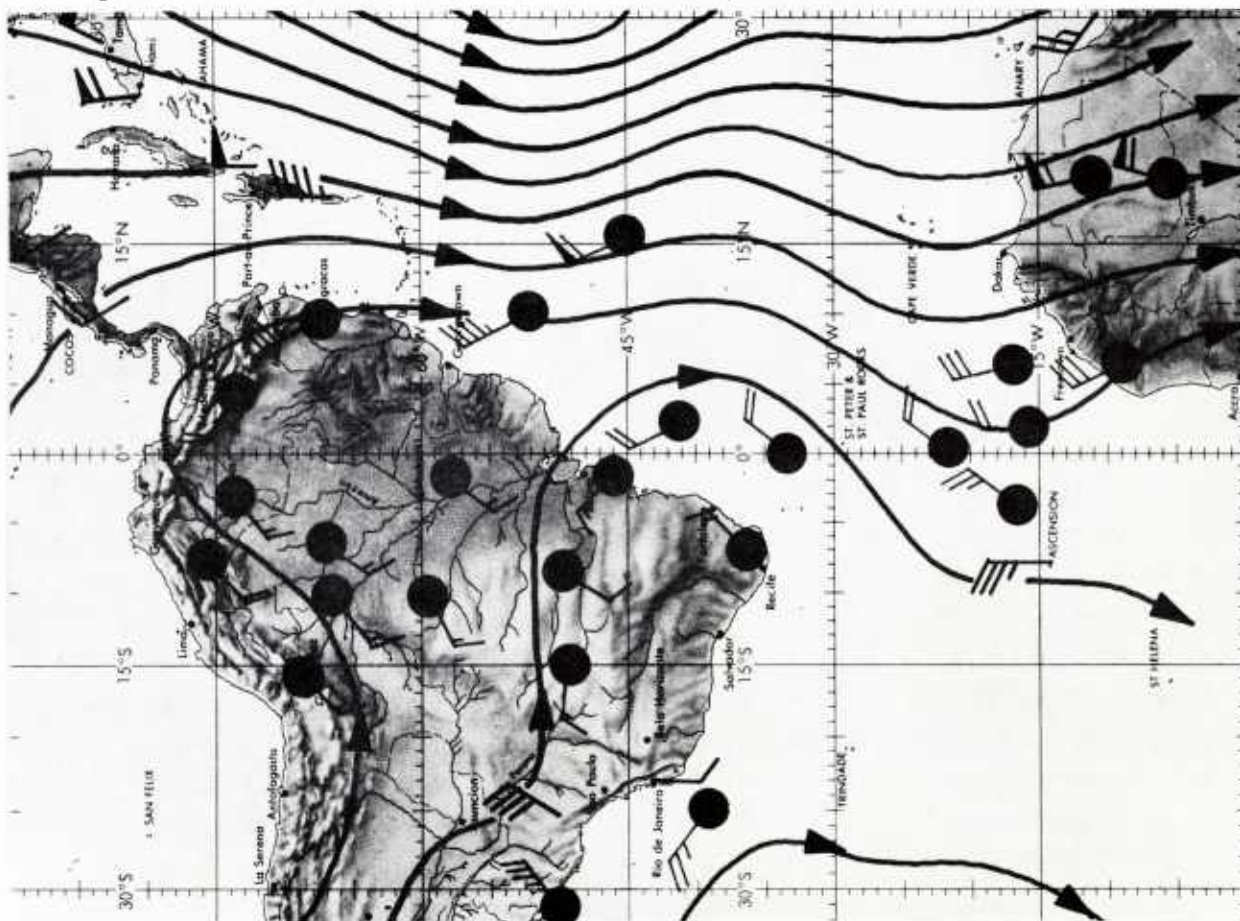
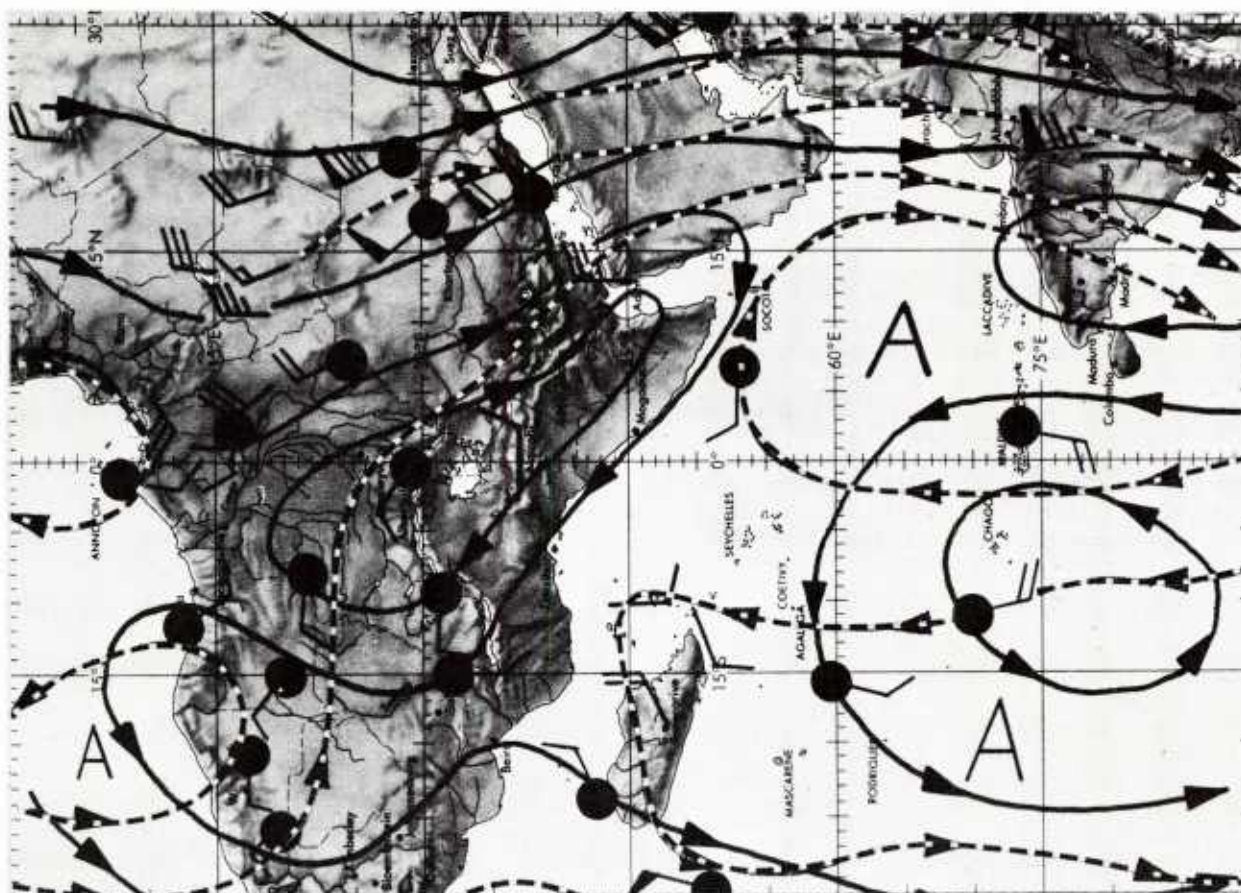


Figure 13.--Numerical 200 mb flow pattern. Satellite data indicated by dots at the end of wind shafts. 1200 GMT March 14, 1967.



with the conventional data. Several changes are quite apparent. One of the biggest changes can be seen over an area south of India where the large anticyclone has been reanalyzed as two centers of circulation--one in the Indian Ocean and another east of Madagascar. Another major change in the flow pattern can be seen east of the Somalia Peninsula. Where the initial analysis showed a northeasterly flow, the satellite data suggested a southerly flow in that area.

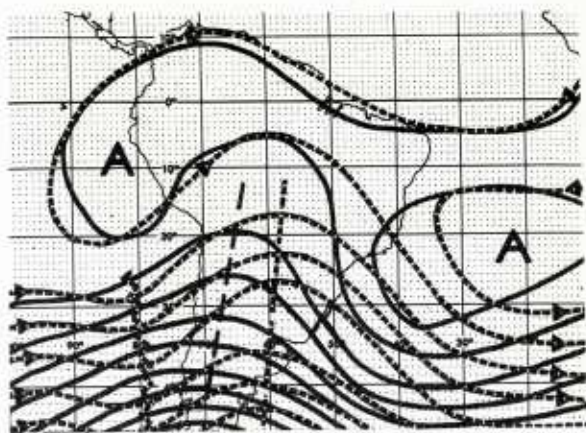


Figure 16.--Initial 500 mb analysis (solid lines). Dashed lines represent the revised analysis based on the suggested height changes shown in figure 15. 0000 GMT, February 15, 1967.

satellite is positioned above the equator in the middle of the Pacific Ocean and produces pictures of a major portion of the North and South Pacific Oceans. Work is now in progress to determine cloud motion and cloud growth from the ATS pictures. An example of how the area over the Pacific Ocean appeared on January 7, 1967 is shown in figure 17.

In conclusion it can be said that meteorologists now have at their disposal in the form of satellite data a new and powerful means for more accurate analysis of the position of jet streams, upper level troughs and ridges, fronts, vortices and areas of convective activity. The forecaster now can better forecast the probability of wave development due to the early detection of centers of secondary positive vorticity by means of satellite data. Great strides have been made in improving the quality and increasing the quantity of satellite data. Six years ago we were receiving data which



Figure 17.--ATS-1 photograph. West coast of North America appears at upper right. January 7, 1967.

covered between 20 and 30 percent of the earth each day. We now view the entire sunlit portion of the earth's surface daily. At the present, each ESSA satellite has only one type camera on board. In 1969, a new satellite, the improved TOS, will be launched. Each satellite will carry redundant AVCS camera systems, APT systems, and high resolution radiometers to provide both nighttime and daytime coverage thus allowing meteorologists to view every portion of the earth once every twelve hours. As newer types of satellite data are made available, research will be done to insure that it is used to its fullest extent. The interpretation of satellite data hopefully will result in weather analyses and forecasts greatly improved through the application of this new and powerful observing tool.

REFERENCES

1. Blackmer, R. H., Jr. and Serebreny, S. M., 1967: "The Relationship Between Maritime Precipitation Radar Echoes and Cloud Cover Viewed by Satellites in Polar Orbits," Final Report, Vol.1, Contract Cwb 11091, Stanford Research Institute, Menlo Park, California, 84pp.
2. Petterssen, S., 1956: Weather Analysis and Forecasting, Vol.1, McGraw-Hill, p.303.
3. Oliver, V.J. and Ferguson, E.W., 1966: "The Use of Satellite Data in Weather Analysis," Proceedings of a workshop held in Boulder, Colorado, August, 1965. NCAR-TN-11 pp.85-101.
4. Anderson, R.K., Ferguson, E.W. and Oliver, V.J., 1966: "The Use of Satellite Pictures in Weather Analysis and Forecasting," WMO Technical Note No. 75, World Meteorological Organization, Geneva, Switzerland, 184pp.
5. Whitney, L.F., Jr., Timchalk, A. and Gray, T.I., Jr., 1966: "On Locating Jet Streams from TIROS photographs," Monthly Weather Review, Vol.94, pp.127-138.
6. Oliver, V.J., Anderson, R.K. and Ferguson, E.W., 1964: "Some Examples of the Detection of Jet Streams from TIROS Photographs," Monthly Weather Review, Vol.92, pp.441-448.

APPLICATION OF SATELLITE PICTURE INTERPRETATION
PRINCIPLES TO ANALYSIS IN SPARSE DATA REGIONS

Major G. R. Farr
Environmental Technical Applications Center, USAF
Washington, D. C.

ABSTRACT

Analyses for surface and upper air charts were made using only features seen in the satellite cloud pictures. Rules of interpretation in use at the National Environmental Satellite Center and streamline analysis procedures were used to derive rather detailed charts for the surface, 500 mb, thickness (approximately 1000 to 500 mb), and 200 mb. It is shown that useful surface and upper air analyses for data sparse regions can be derived from the satellite cloud pictures, and that conventional analyses can be refined and improved.

Interpretation of the satellite cloud pictures has developed to a point at the National Environmental Satellite Center (NESC), where it is possible to derive useful analyses for both surface and upper air charts. These analyses are especially valuable for data sparse areas. The surface and upper air analyses were made for two cases, using only features seen in the satellite cloud pictures. Some of the rules and ideas used were presented earlier in Edward W. Ferguson's paper. Other rules used at NESC were combined with streamline analysis procedures to produce the analyses.

The first case, in the northern Pacific Ocean, shows analyses for the surface, 500 mb, and surface to mid-tropospheric thickness (approximately 1000 to 500 mb). Two satellite cloud picture presentations were used. The first was a computer rectified product, reproduced in polar stereographic presentation, 1:20,000,000, Figure 1. The second, Figure 2, was from the same satellite pictures, non-rectified, but computer gridded and montaged. Both were produced from the ESSA 3 weather satellite. The computer rectified product has the advantages of improved perspective with no duplication or overlap in cloud features, while the montage shows better cloud detail, especially noted in cirrus clouds, striations, and small scale features. Comparisons of Figures 1 and 2 will show the advantages of each.

Figure 3 is an analysis made by interpretation of the cloud features. The frontal positions follow our models except for the wave at 180°W. This is not a classical occluded front with the vortex to the west. It is a large secondary area of a maximum positive vorticity advection (PVA) which is joining up with the developing wave on the front. Twenty-four hours earlier, the PVA maximum was located several degrees north of

the front and a small wave near 30N 157E was forming on the front. However, in this case, previous cloud pictures were not necessary to identify this PVA. The cloud finger extending southward into the frontal clouds with the clear area east of it, plus thinner clouds where the frontal clouds join the secondary maximum are all indications that the PVA is joining the front and the wave has not yet occluded. Yet, it is interesting to note that the cloud structure is similar to the classical occlusion model, and in a few hours no difference will be seen.

A streamline analysis is presented, with dashed and solid lines. The solid lines represent wind directions as seen in the clouds. The dashed lines are entered where the actual wind direction is not seen, but where indications of curvature, either cyclonic or anticyclonic, can be found. For instance, the solid lines seen in the northwestern section of the satellite picture show that the wind direction is parallel to the cloud banding in the cumulus. As the cold continental air flows over warmer water, cumulus cloud lines form, and while the clouds have little vertical development, the cloud lines or bands form parallel to the low level flow. It has been noted that in the northwesterly flow behind the polar front open cellular clouds are found in regions of low level cyclonic flow and closed cellular clouds are found in regions of low level anticyclonic flow. The flow around vortices, thru frontal zones, over ridges and troughs, and around high pressure cells fits our meteorological models.

In addition to the large PVA associated with the wave on the front, there are three other PVA, each designated with the comma symbol. For the Pacific case, they were drawn in the streamline analysis as closed, although it was recognized that there may

only be a trough or increased cyclonic curvature under these mid-tropospheric cloud patterns. Two cold lows are seen, one off the west coast of Canada and the second, east of Kamchatka. An old weakening cut off low is centered near 27N 175W. The absence of middle and high clouds indicates that it is weakening.

Vincent Oliver has developed three rules for finding points on the surface ridge lines. These rules will generally place a point on the ridge within one degree.

The first rule briefly states that there are often cloud fingers tied in a continuous fashion to the leading edge of a frontal band, generally extending in a more southerly direction than the frontal band. A point chosen on the extreme end of this continuous cloud finger will lie on the surface subtropical ridge line. Using this rule the surface subtropical ridge was entered from 37N 178W southwestward to the long extended finger at 18N 165E.

A second rule states that when a sharp surface polar ridge is wedged between two cyclones, the ridge line can be located where the cumulus in the northerly flow begins and the high level stratified cloudiness ends (the high clouds sometimes overlap). The ridge between 40 to 50N near 147W is of this type. The cumulus clouds are hard to see on the rectified product, but are more visible on the montage.

The third rule notes that on the western side of subtropical high cells a change in the character of the clouds from cumulus globs to a more stratified nature occurs where the winds change direction from southeasterly or easterly to southwesterly or southerly. A point on the surface ridge is positioned where the greatest distinction occurs in the cloud character. An example of this can be seen at 50W in the Atlantic case.

A fourth rule, pointed out by Vern Dvorak, NESG, points out that on the northeastern side of subtropical high cells off the western coast of continents in the Northern Hemisphere, a point on the surface ridge can be located on the northeastern edge of the stratocumulus clouds south of the clear or almost clear region. A point on this ridge is seen off the coast of California and the ridge is extended westward into the clearing ahead of the front. A solid ridge line was drawn where the rules indicate an accuracy close to one degree latitude. A broken ridge line was entered where ridging is indicated, but the one degree accuracy could not be assumed.

It would require a long, detailed explanation to define the reasoning at all points; however, after placing the lows, highs, troughs, ridges, fronts, and the known areas of flow direction and curvature, then analysis principles guide the analyst in completing the surface chart.

Figures 4 and 5 are surface analyses from NMC for times corresponding with the satellite cloud pictures. Figure 4 at 0000Z should be compared with the eastern part of the Pacific from the coast of North America to about 170W and Figure 5 for 0600Z should be compared with the western part from about 170W to Japan and Kamchatka.

The surface lows and PVA maxima are well positioned, except that the PVA off the coast of California is reflected in the shear instead of a closed low at the surface. The surface ridges are well chosen, but the second high center south of the front near 140W is not there. The second center existed twelve hours previously on NMC's analysis. Placing the center of the high cell is difficult and although the ridge was placed correctly where the surface flow changes direction from northwesterly to northeasterly, only one center actually existed, and that is to the rear of the front, close to where one was analyzed.

The subtropical ridge line which extends from 37N 178W southwest to 18N 165E is substantiated by the ship near 19N 167E. On the 0000Z NMC surface analysis the wind at the ship is southeast and on the 0600Z analysis, it has shifted to southwest. This places the ridge close to the top of the cloud finger.

The north-south cloud band, which extends into the ITCZ, between 160 and 170W was analyzed as a disturbance or wave in the low level easterly flow. The 0000Z chart shows cyclonically curved flow in that region and the 0600Z chart gives indications of a wave in the easterly flow.

Both analyses show the front near 180° to be occluded; however, as stated before, the wave has not yet occluded. The two PVA maxima to the west are substantiated in the data at the surface.

Figure 6 has a 500 mb and a thickness analysis superimposed on the cloud picture. The wide lines represent thickness features seen in the clouds and all other lines refer to the 500 mb information. The 500 mb wind directions are generally not readily available from the cloud pictures, but by placing the troughs, ridges and pressure centers,

the general flow pattern can be depicted. Some idea of whether a ridge is narrow or broad and whether it is sharp or flat can often be deduced from the associated clouds. Using all of these features, a 500 mb pattern was derived.

There is one 500 mb wind direction which can be picked out in the mountain wave clouds over California. The transverse waves in the middle clouds should lie perpendicular to the flow from the mountain tops through the middle troposphere. Any large directional shear with height would break down the mountain wave; therefore, we have a wind direction indicated in this area.

The 500 mb short wave ridge line is often observed in the cloud formations associated with frontal systems. Poleward of the position where the jet stream crosses the frontal band, the middle clouds are more easily seen. (The ridge can often be found whether the jet stream crosses the occluded front or not.) The forward edge of the middle clouds is nearly coincident with the 500 mb ridge line. Further equatorward, the middle and high clouds may extend somewhat east of the ridge line. The ridge near 150W is placed along the eastern edge of the middle clouds where the clouds dissipate. A ridge was also entered near 157W, where the middle clouds dissipate along the east side of the north-south cloud band which extends into the tropics.

Troughs at 500 mb which cross frontal bands are indicated by dissipation of middle and high clouds behind the trough. In this case, troughs cross the front at three places, first from the cold low off Canada south to the PVA maximum, second from the vortex in the Bering Sea southward across the front near 165W, and third from the large PVA maximum south and crossing the front near 170E. In each case, the middle and high frontal clouds thin out or dissipate behind the trough. The north-south cloud bands extending into the tropics are generally found in the southwesterly flow at 500 mb, and in this case southwesterly flow was entered in the 500 mb cloud analysis.

Comparison of the cloud analysis with NMC's 500 mb analysis for 0000Z, Figure 7, shows that the major features were depicted in the cloud pictures. The ridge along 150W fits very well. Farther south the ridge along 157W appears to be too far west, but it is possible that more data in this area might show the cloud pictures to be more exact. The troughs from the Aleutian low and the large PVA maximum are well placed and the low east of Kamchatka is represented in the bulge in the contours. NMC's analysis east of Japan does not show the troughs and PVA maxi-

ma very well. Use of the satellite pictures might have added more detail in that area.

The thickness lines in Figure 6 show up in the cloud pictures as striations in middle clouds or as banding in cumuliiform fields. The striations, most often seen in front and vortex cloud patterns, have been found to be oriented parallel to the vertical shear vector or thermal wind of the layer. The banding in the cumuliiform clouds has been found to parallel the vertical shear vector through the layer of clouds. In both cases, they give an indication of the orientation of thickness lines. Here, several thickness lines may be drawn fairly close together but this does not imply packing, only orientation.

Several interesting striations are seen over the occluded front south of Alaska and in the associated vortex. One is entered over the front and a second long striation is seen north of the Aleutian chain. Compare these with the NMC thickness analysis for 0000Z, Figure 8. An excellent orientation is portrayed. The orientation of the bands east and north of Hawaii is good and banding around the cut off low agrees with NMC's analysis. The most interesting detail in the clouds is seen around the PVA maxima east of Japan. The cloud banding appears to show the cold air south of the clouds (aligned east-west between the two maxima) and a slight warm tongue in the east-west cloud band. This detail was not shown in the NMC analysis. It is possible that more detailed analysis is available from cloud pictures than previously supposed.

The second case in the Atlantic will be a summary of most of the interpretation rules presented in the Pacific case. The exception will be the addition of a 200 mb wind direction analysis derived from cirrus patterns.

Figure 9 is the ESSA 3 montage for 10 February 1967, with the easternmost pass starting at 1305Z and the pass near the east coast of the United States starting at 1848Z. For comparisons against the 1200Z surface chart, use analyses east of 40W and compare the 1800Z surface chart with the cloud analysis west of 40W.

The cloud pictures show a wave on the front near 56N 24W with another wave forming ahead of a comma shaped PVA maximum near 45N. The front then extends south and west to an open wave near 37N 41W and from there west to the occluded front and on southwest toward Cuba. Two indications of PVA maxima are seen, one at 46N 33W just west of the wave and a second near 50N 37W. A vortex is

seen to the north of the latter, but the analysis was not completed in that area. A cut off low is located off the west coast of Africa at 15W. Figure 10 is a surface analysis interpretation of these points.

The surface ridges were drawn from several cloud indicators. Where the ridge line is shown continuous, there were points on the subtropical ridge line which were chosen using previously stated rules. The north-west-southeast ridge line which crosses 45N is of the type which is wedged between two cyclones. The discontinuous ridge lines are drawn for cloud indicators not fitting the four stated rules and whose accuracy has not been determined. The subtropical ridge line west of 40W appears to be about 2° latitude south of the surface position in Figure 12. The surface winds through this area are light and it is possible that the actual ridge line and the position shown by the cloud indicators are still within the one degree accuracy. Compare Figures 11 and 12 to the interpreted cloud picture analysis in Figure 10.

The 500 mb and thickness patterns from the montage are depicted in Figure 13. Figures 14 and 15 are the NMC analyses for 1200Z on the same date. The thickness lines have been extended where no banding or striations are seen. The dashed thickness lines denote the extensions, and some semblance of packing was entered. However, where the thickness lines are solid, they only represent the striations and banding seen in the clouds. An interesting banding pattern is seen around the two PVA maxima, which shows considerable more detail than usually depicted in thickness patterns. Otherwise, the thickness pattern is similar to NMC's analysis.

The trough from south of Greenland toward the southeast was indicated in the satellite pictures from the PVA maxima. The upper air ridge is seen along the forward edge of the frontal cloudiness and extends into the cloudiness north of the occlusion. The middle clouds end along the ridge line, but the cirrus clouds, at greater altitudes extend farther east. The trough analyzed with the vortex off the east coast of the United States is placed five degrees ahead of the 1200Z NMC analysis along 71-72W. The satellite picture for that time was taken at almost 1900Z and should be ahead of the 1200Z position. The next 500 mb analysis at 0000Z moved the trough ahead to 61-62W at 40N and so the position seen in the satellite picture would be close to the actual position at 1900Z.

The 200 mb analysis was made from the

wind directions seen in the cloud pictures as cirrus blow-offs or plumes from cumulonimbus, cirrus shields associated with the jet stream, transverse bands in the cirrus patterns and other cirrus clouds. It has been found in studies at NESG that shear in the cirrus layer and shear between the cumulonimbus movement and the upper wind direction do not appear to cause large deviations between the actual flow and winds derived from cirrus patterns. Comparison of the winds derived from the cirrus to the reported wind data shows that the difference is nearly always less than 30 degrees, and a large percent of the satellite winds fall within 10 to 20 degrees of reported winds.

The solid arrows on the 200 mb cloud analysis chart, Figure 16, are wind directions taken from the cirrus clouds. A cirrus cloud shield associated with the jet stream is seen north of the front from 75W to about 65W. Close inspection also reveals the transverse bands in the cirrus, which are generally seen when the wind speed is greater than 80 knots. The jet stream cirrus shield is also seen crossing the frontal clouds.

Many more wind directions could have been derived from the cloud pictures, especially in the western regions of the montage, but they would not show more detail. Note that the ridge and trough lines can be quite accurately placed in this case. A comparison with the NMC 200 mb analysis, Figure 17, shows good correlation. The jet stream in the cloud pictures is associated with the southern jet coming from the Gulf of Mexico. The NMC 200 mb analysis 12 hours later showed this southern jet moving to 33N 65W and turning southward. Use of the satellite picture would provide a better analysis.

A great amount of valuable information can be derived from the satellite cloud pictures and used in analysis. It is valuable not only as an aid to analysis of conventional data but can be used alone to produce useful charts. For this presentation, conventional data was not used, but if actual data from a few stations had been entered, more detail could have been available on the charts.

Although isotach values were not analyzed, it should be noted that estimates on wind speed can be made in many cases for the surface, 500 mb and 200 mb levels. Wind speed information is still somewhat limited, but comparison with climatology, actual data and use of some of the studies of wind and satellite cloud patterns, make it possible to enter some data at the surface and 500 mb. The 200 mb wind speed picture can be quite

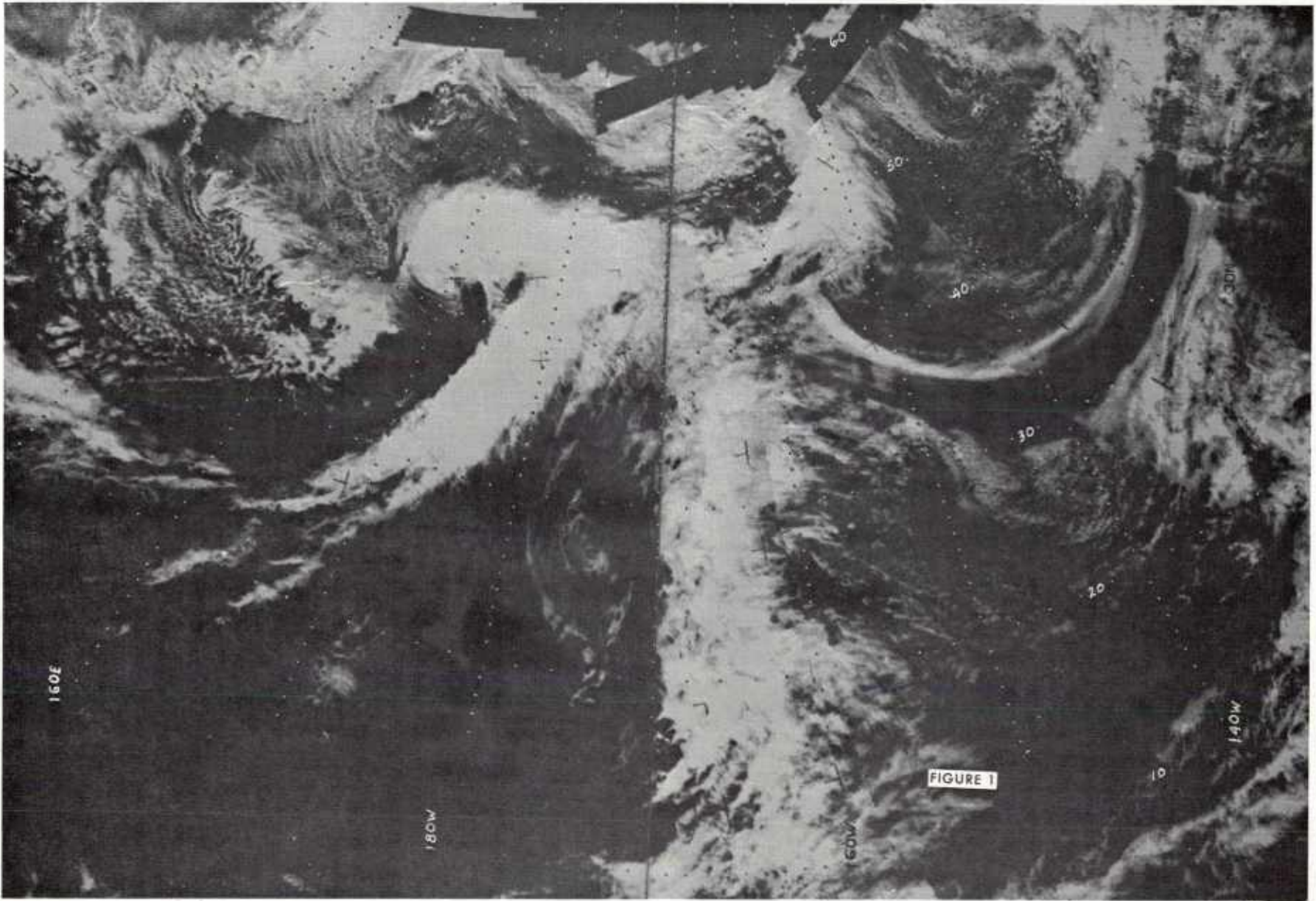
fully estimated using experience, climatology, actual data and indications in the clouds.

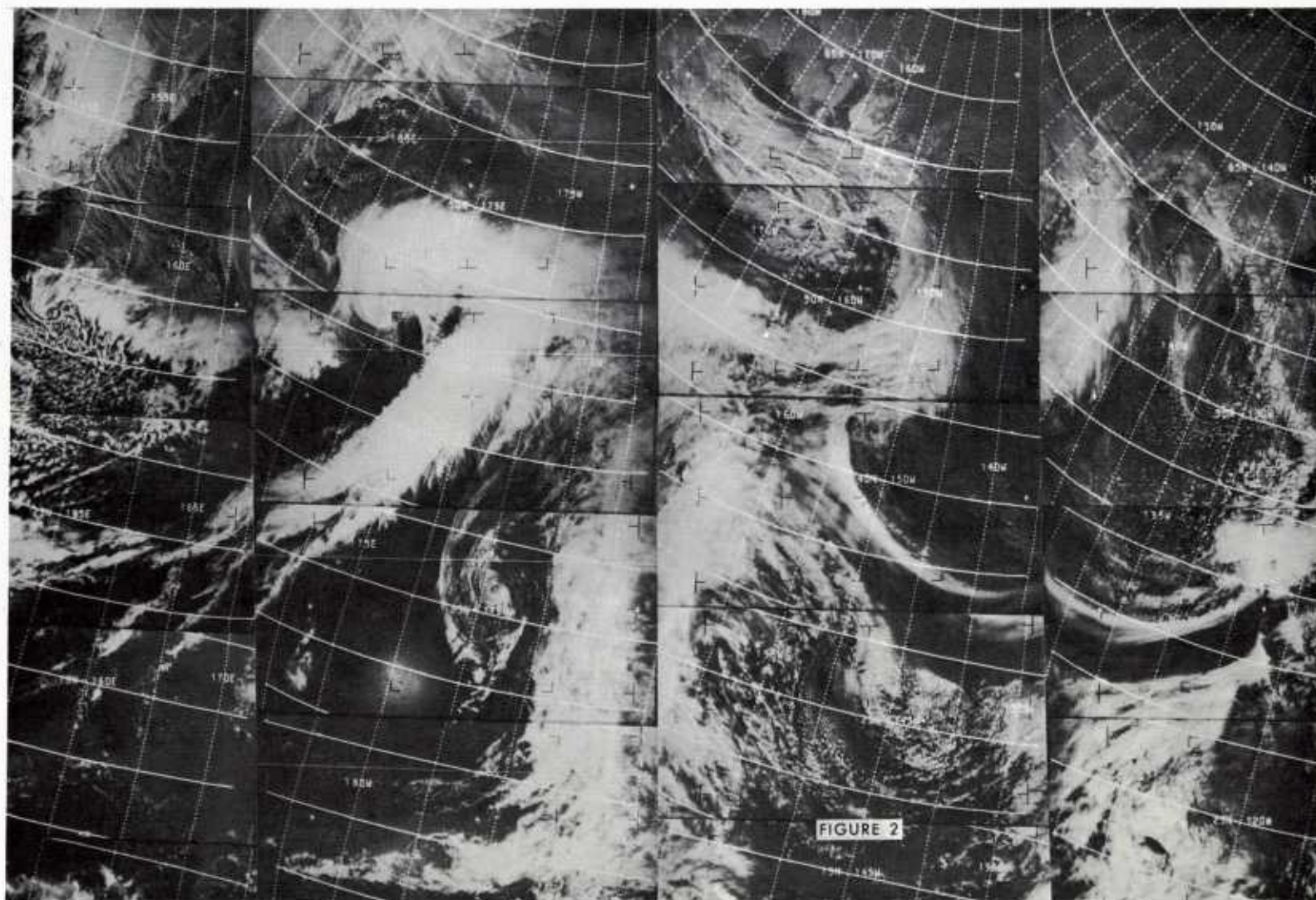
In conclusion, it can be stated that useful surface and upper air analyses for sparse data regions can be derived from satellite cloud pictures, and that existing analyses in other areas can be refined and improved.

Bibliography

Anderson, R. K., Ferguson, E. W., and Oliver, V. J.: "The Use of Satellite Pictures in Weather Analysis and Forecasting," World Meteorological Organization Technical Note No. 75, 184 pp., 1966.

Follensbee, W., Jager, G., and Johnson, H.: Unpublished notes on Winds Derived from Cirrus Satellite Photographs, 1967.





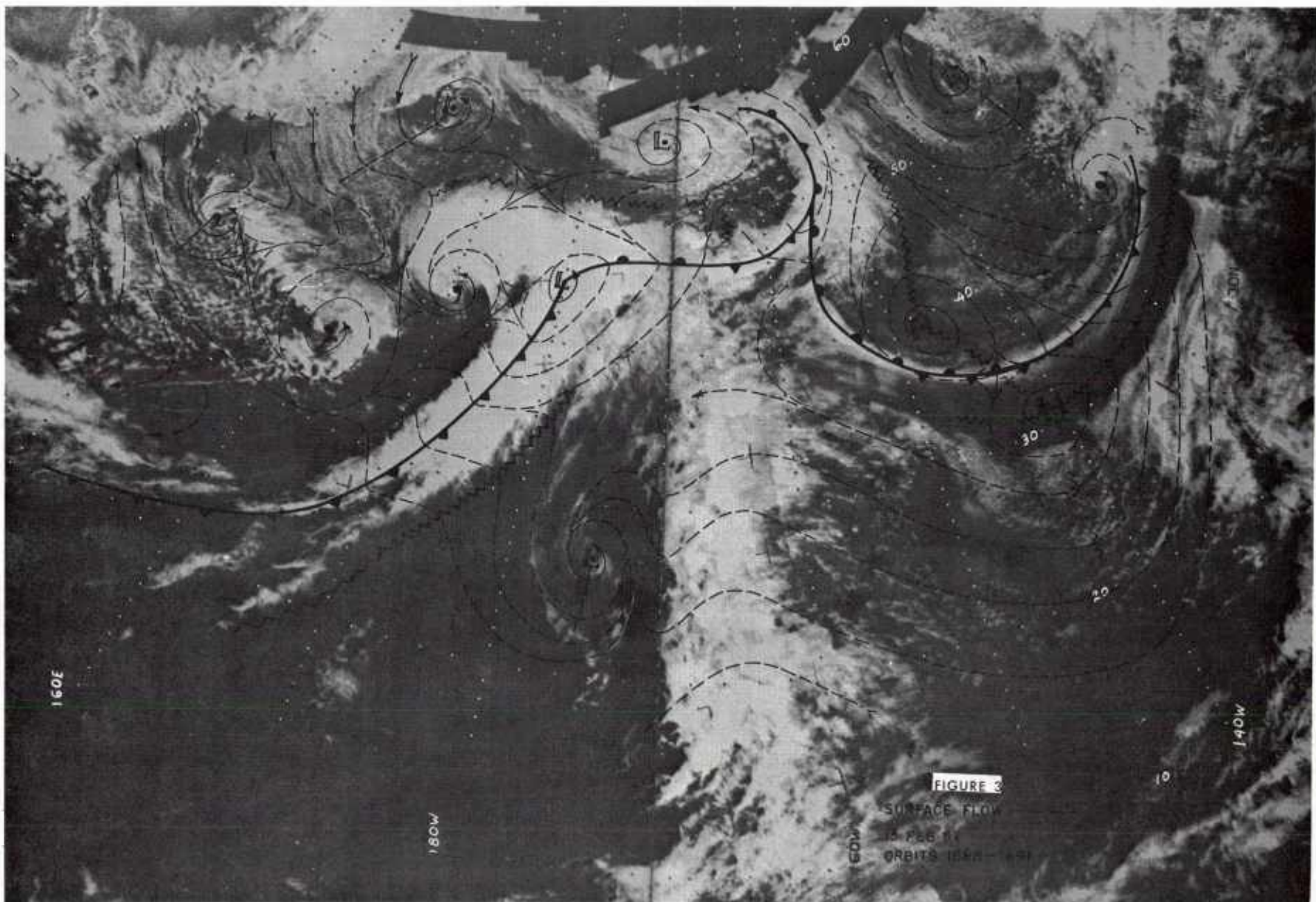


FIGURE 4

PACIFIC AREA
SURFACE ANALYSIS NMC
0000 Z
14 FEB 67

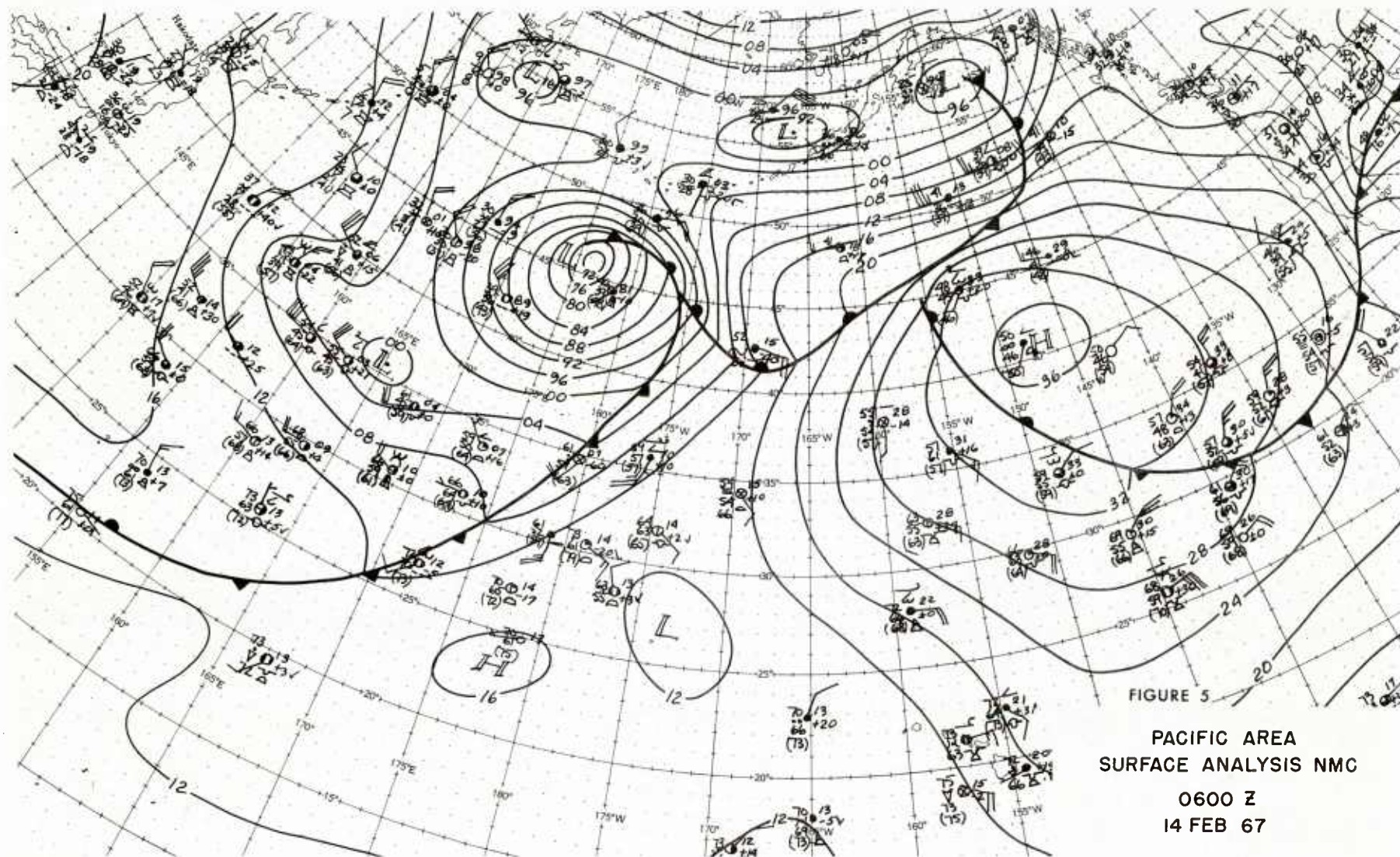


FIGURE 5
PACIFIC AREA
SURFACE ANALYSIS NMC

0600 Z
14 FEB 67

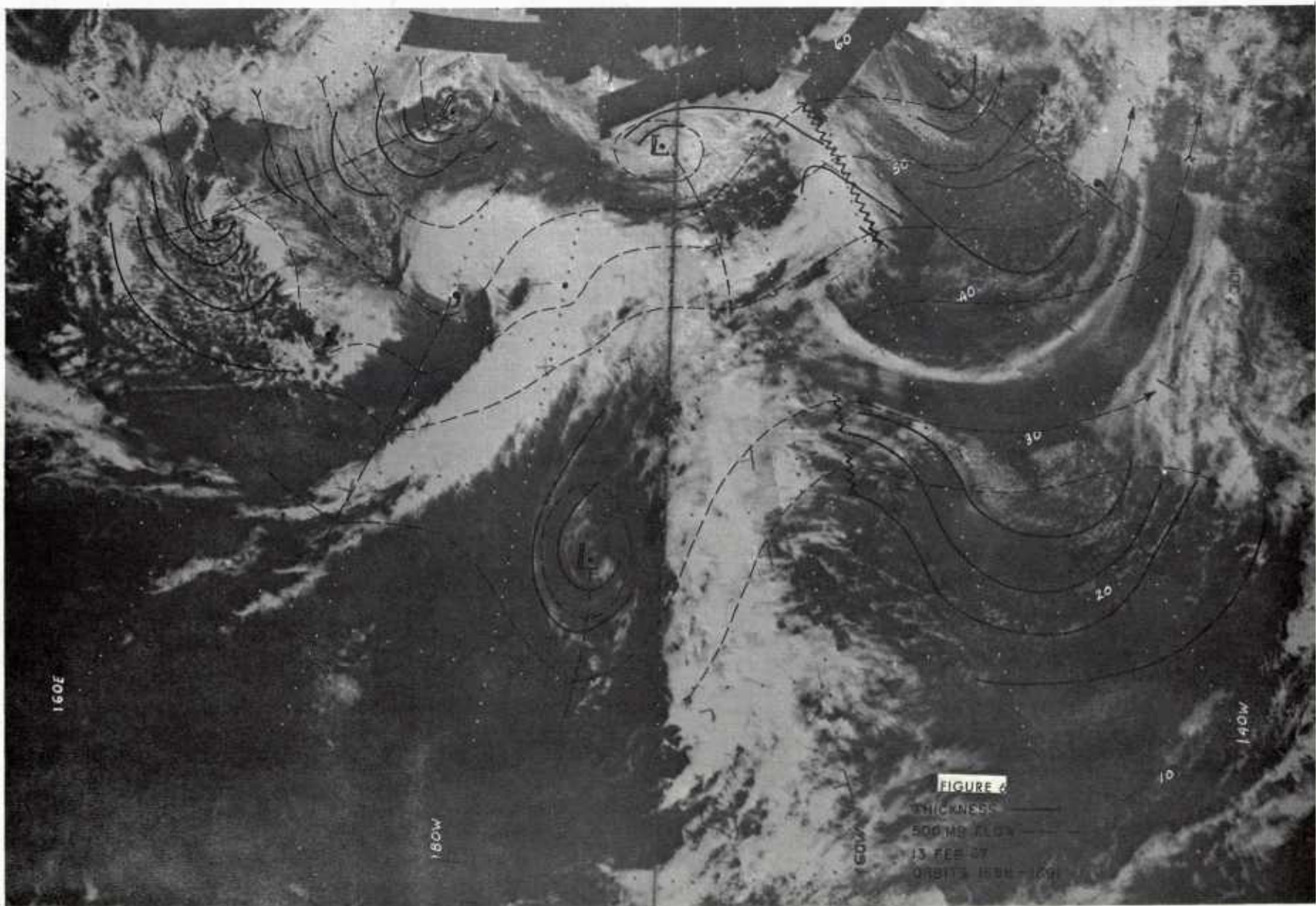
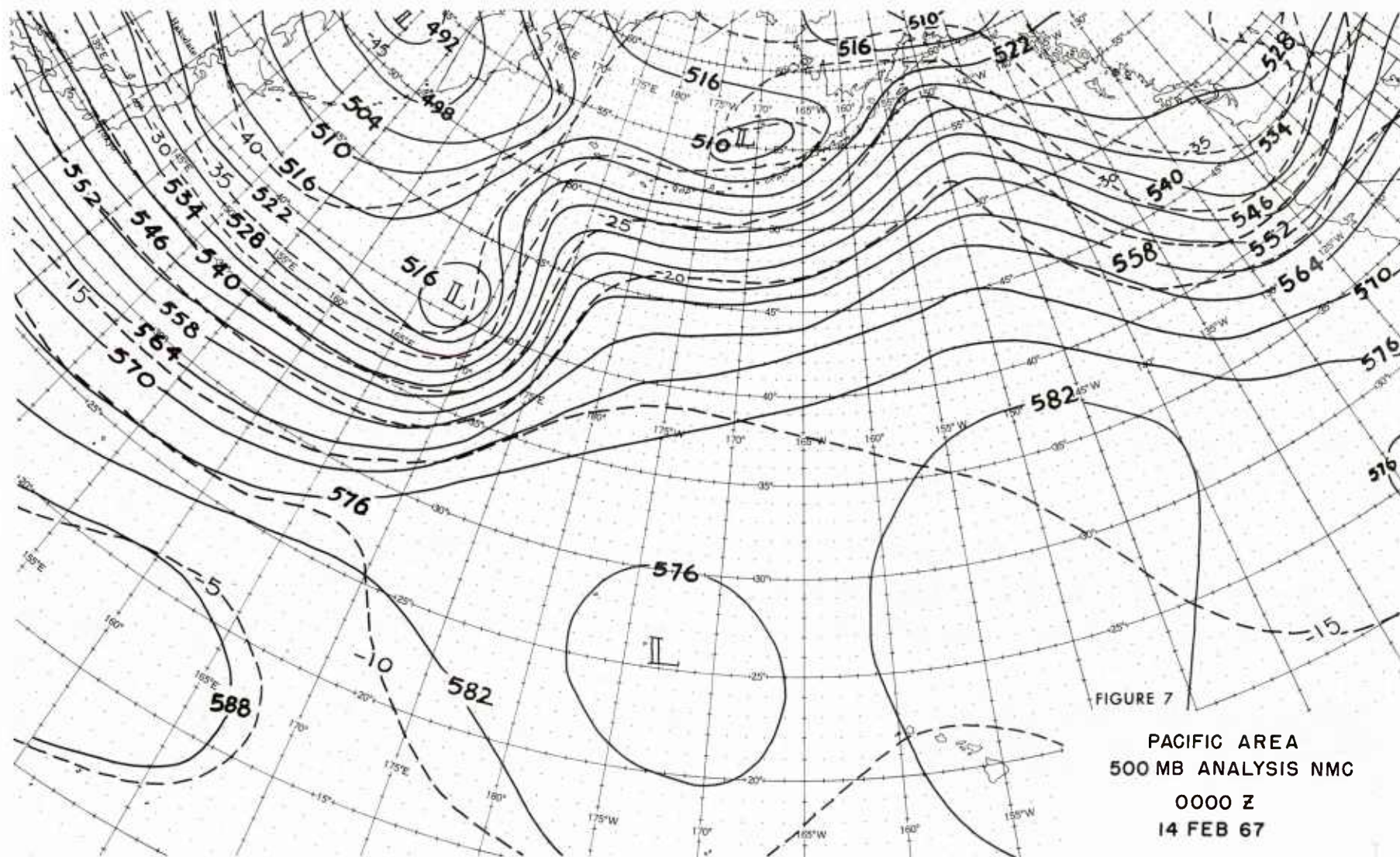
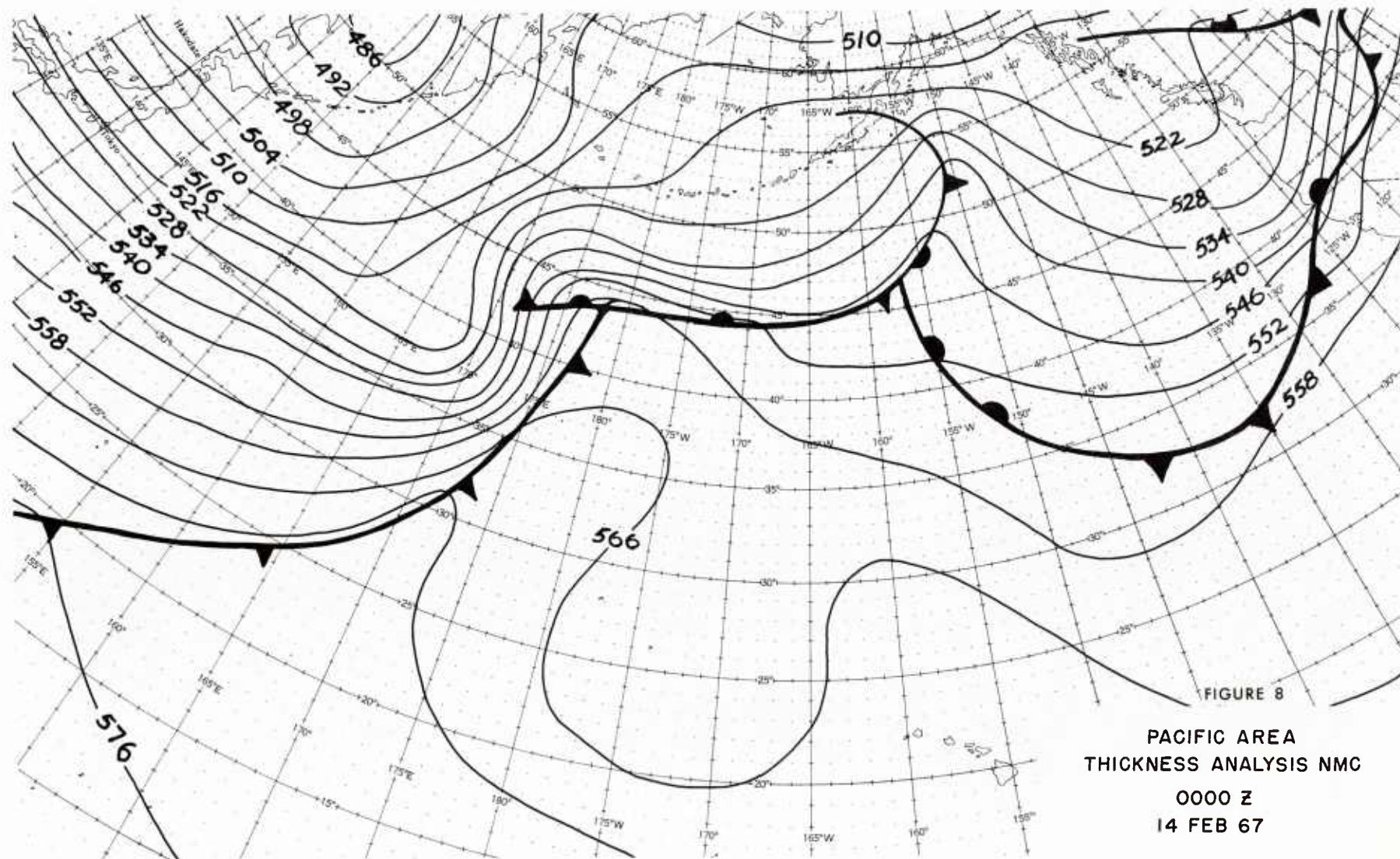
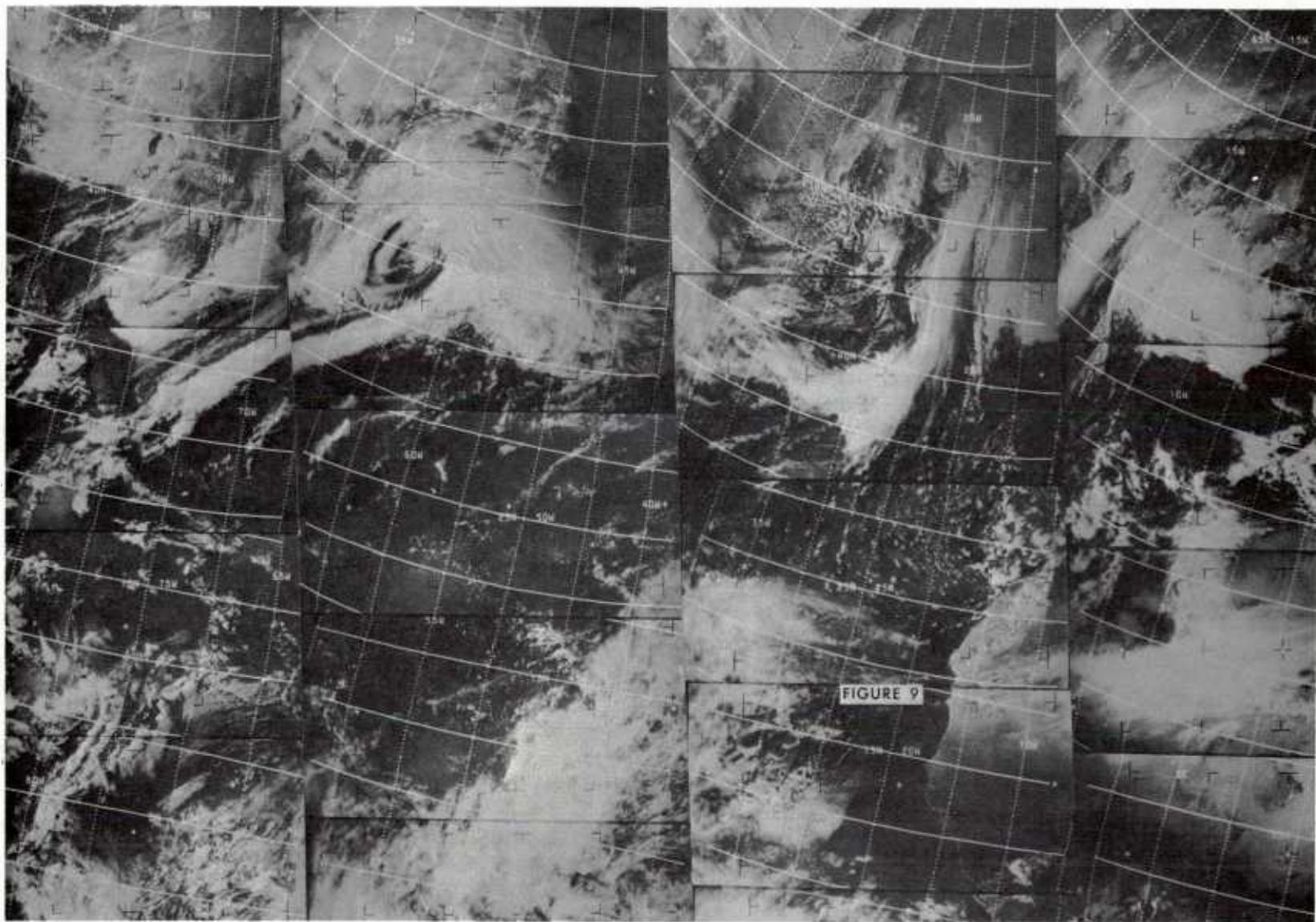


FIGURE 6

THICKNESS
500 MB XLOW
13 FEB 27
ORBIT 1500-1600







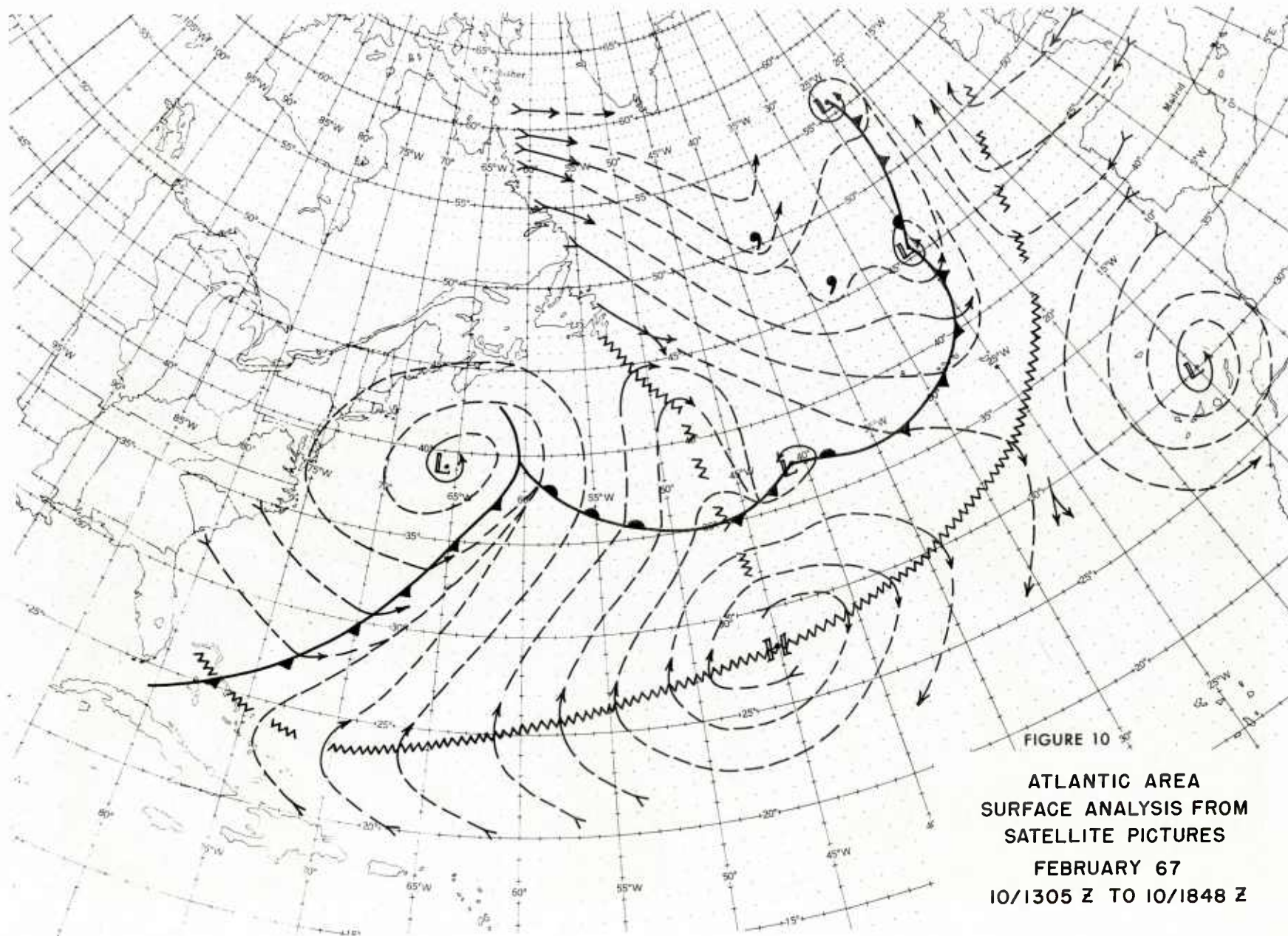


FIGURE 10

ATLANTIC AREA
SURFACE ANALYSIS FROM
SATELLITE PICTURES

FEBRUARY 67
10/1305 Z TO 10/1848 Z

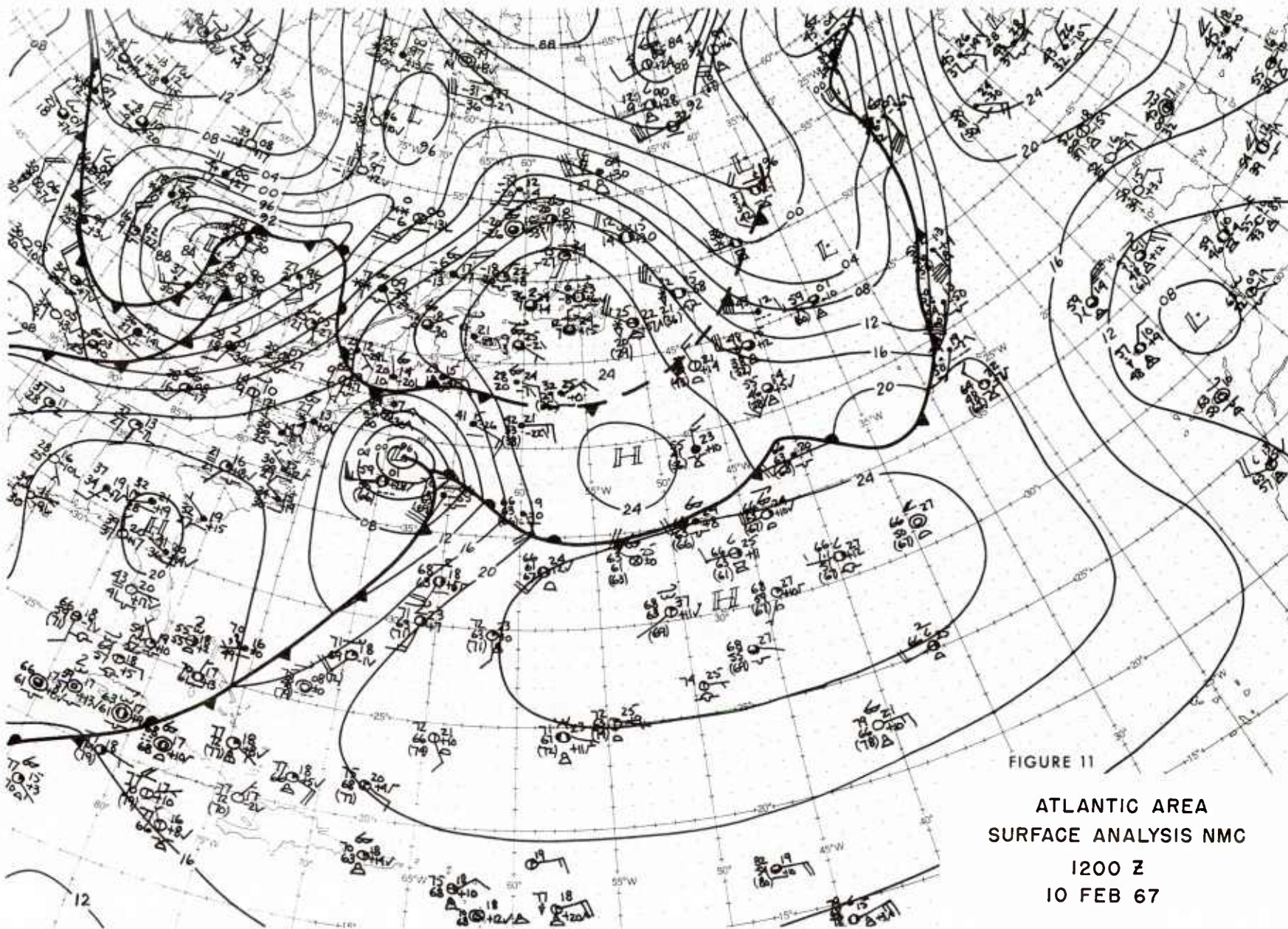
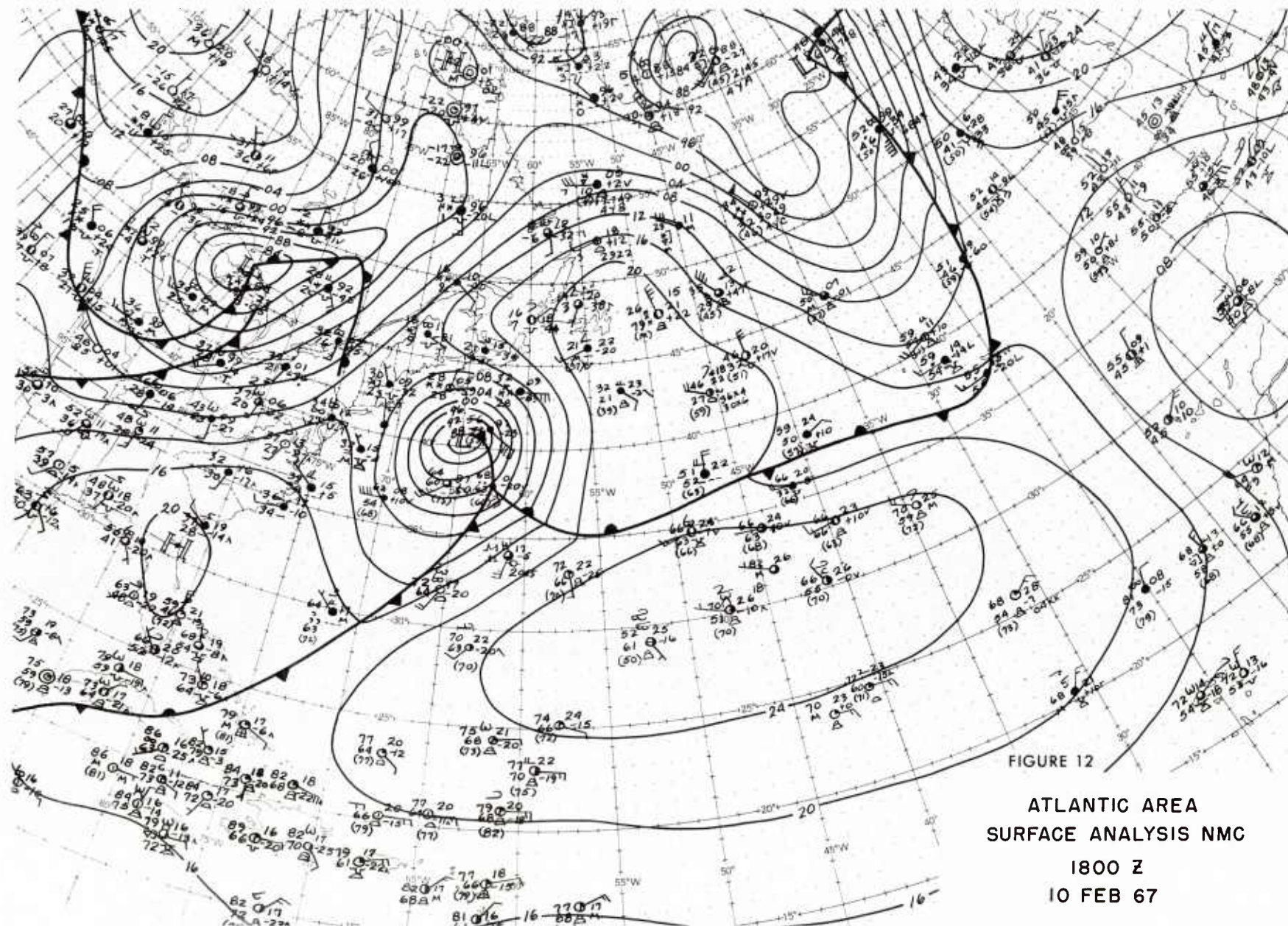
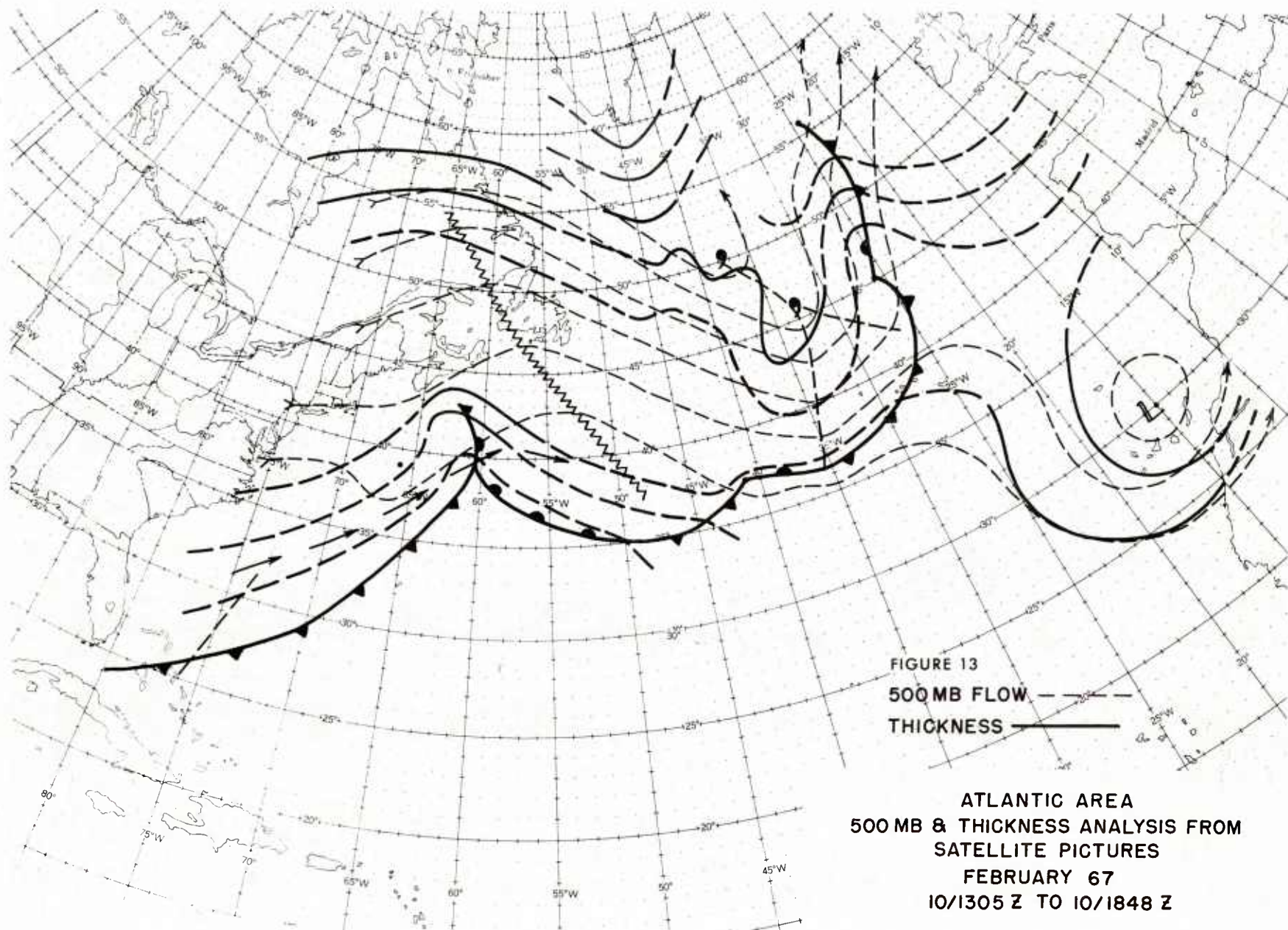


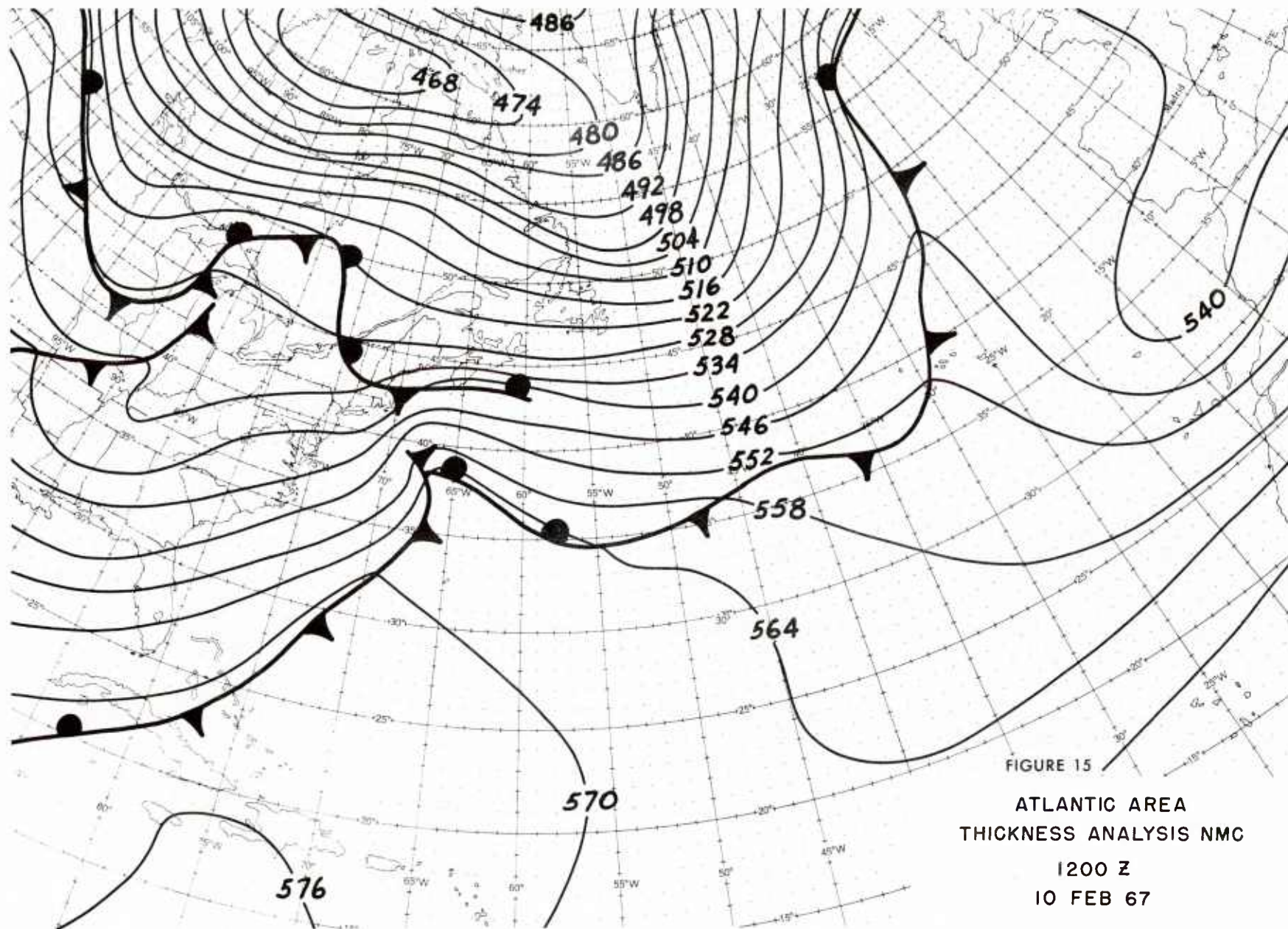
FIGURE 11

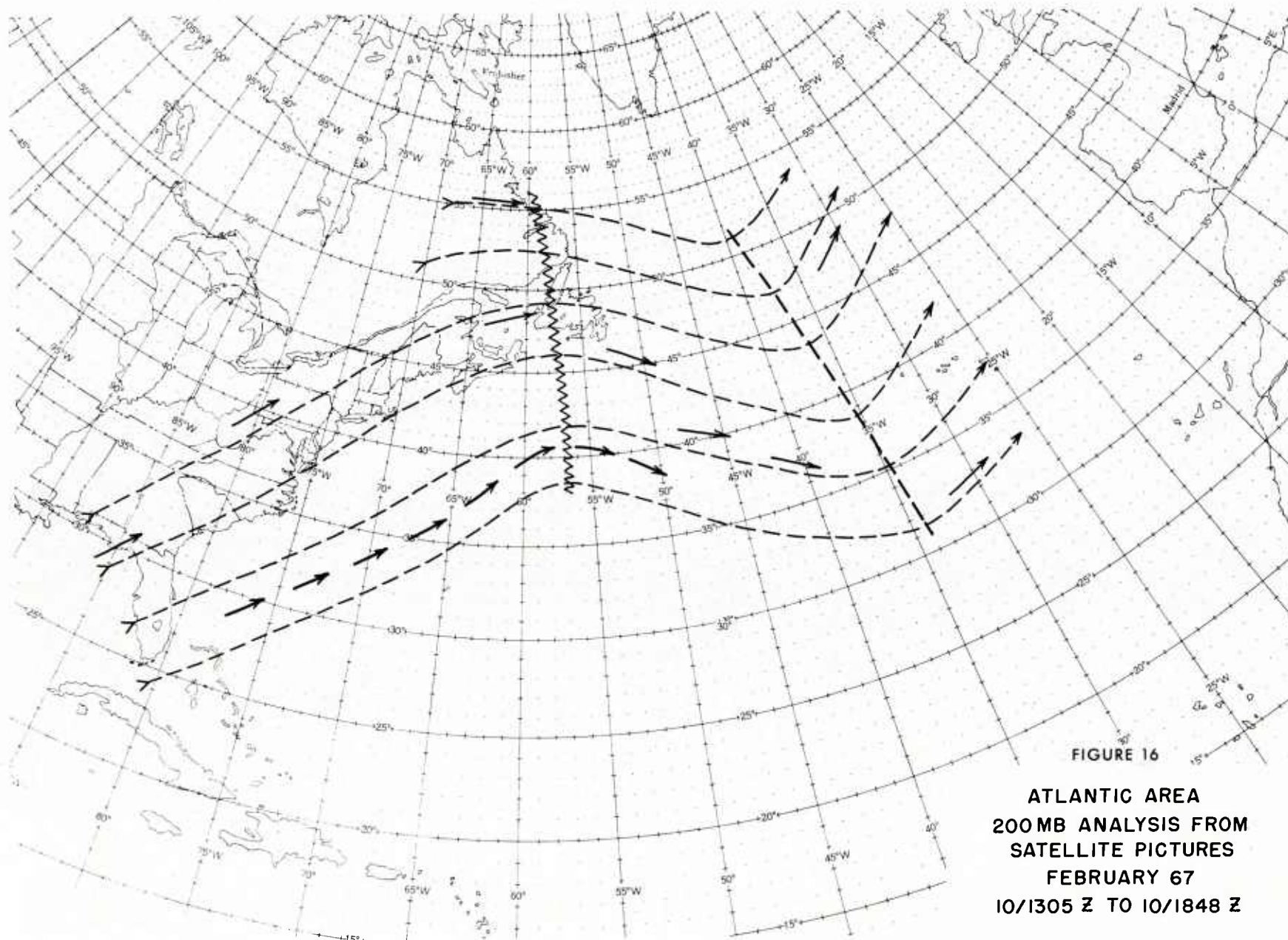
ATLANTIC AREA
SURFACE ANALYSIS NMC
1200 Z
10 FEB 67





ATLANTIC AREA
500 MB ANALYSIS NMC
1200 Z
10 FEB 67





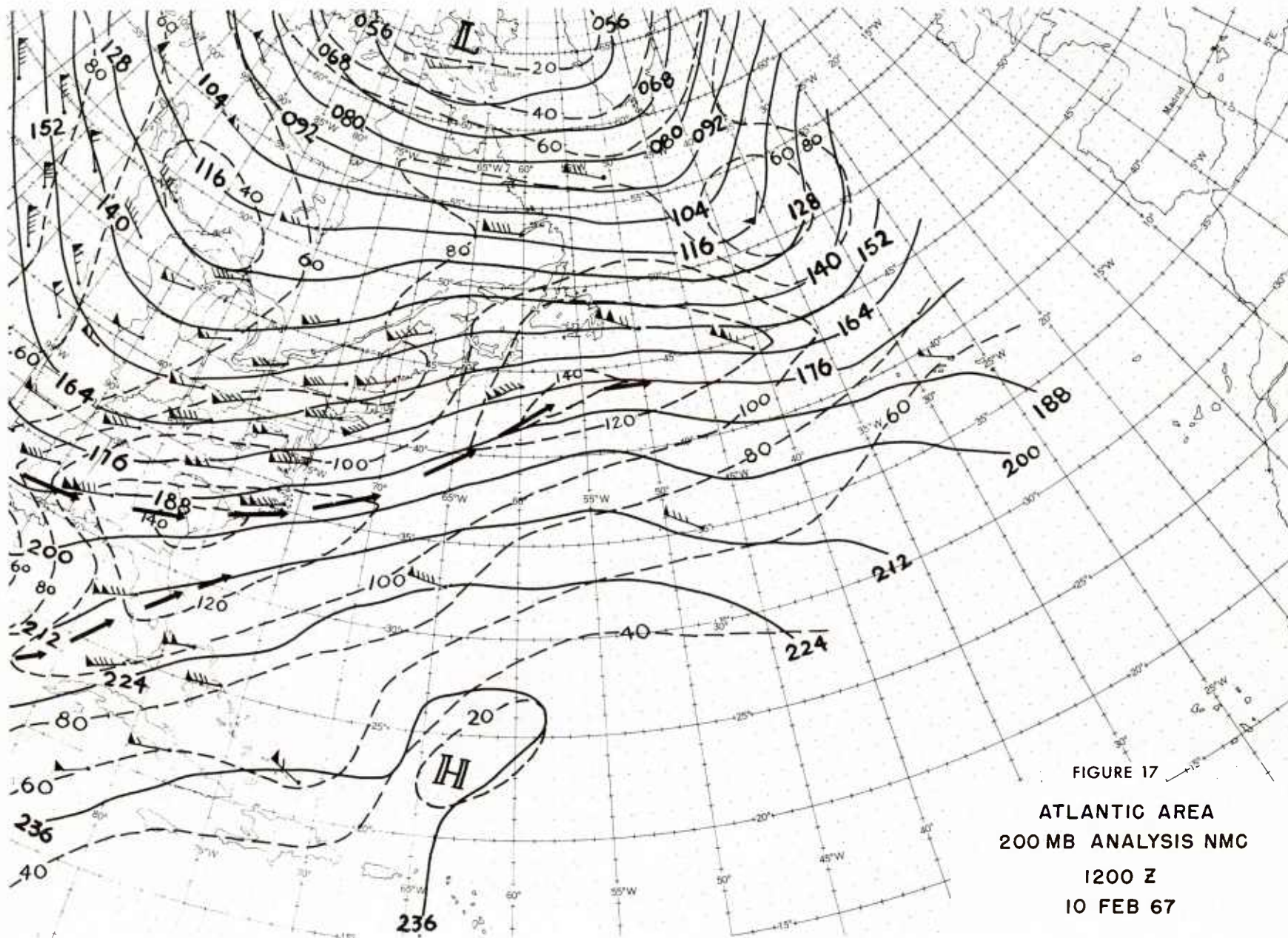


FIGURE 17

ATLANTIC AREA
200 MB ANALYSIS NMC
1200 Z
10 FEB 67

A SATELLITE PHOTO INTERPRETATION KEY

by

Roy Lee and Charles I. Taggart
Meteorological Service of Canada, Toronto

ABSTRACT

The problem of using satellite pictures at a regional office interested only in a limited portion of the atmosphere is discussed. A solution involves three factors, (a) adjustment and familiarity to a new point of view, (b) acquiring knowledge and experience in recognizing cloud forms from satellite altitudes, and, (c) adopting the systematic approach of the professional photo-interpreter to satellite pictures, namely, the principle of convergence of evidence. Two charts summarizing the appearance of clouds from satellite altitudes together with a systematic approach to satellite photo interpretation are presented. These are part of a satellite cloud catalogue in preparation in Canada.

INTRODUCTION

The perfection of the operational weather satellite stands out as one of the many outstanding scientific achievements of your country in recent years. Its influence is being felt abroad, particularly on operational practice and on the quality of weather service. However, we surmise that its potentialities are not fully appreciated at the moment and that they still lie ahead of us. The Meteorological Service of Canada is also participating in the development of a prototype APT Station. This paper will describe our approach to the use of satellite APT data in Canada.

Perhaps the most valuable property of the weather satellite lies in the nature of the observation. Apart from its ability to provide global coverage, it gives a continuous distribution of information in contrast to the discrete point value type of data obtained by other conventional weather observing systems. The only other sensing instrument with this property is the weather radar. The second important property of satellite information is that the information is real as opposed to symbolic, which characterizes all of the other types of weather information available to the forecaster. In the hands of a skilled interpreter, the

satellite picture can provide more firsthand knowledge of cloud types, extent, boundaries and physical processes than he can possibly infer from conventional maps alone.

The particular use of satellite pictures depends greatly on the scope of the related operational problem. For example, for global analysis, one requires extensive satellite coverage, for which computer processing is a virtual necessity. One can then obtain the broad scale cloud patterns, vortices, and so on, for use in the analysis program. On the other hand, there is the regional type of problem, in which only knowledge of the detailed local cloud patterns are of importance to the forecaster. It is toward the local type of problem that we are directing our attention in Canada.

Assuming that satellite pictures, located geographically, are available to the forecaster, how is he going to use it in his day-to-day work? In short, what is the problem of using satellite pictures from the forecaster's viewpoint? It is generally agreed that the main problem is one of interpretation.

In this connection, the first adjustment that a forecaster using satellite pictures must make is to change his point of view. For persons accustomed to looking at clouds from below or from the side at distances of up to twenty-five miles, a view from eight hundred miles looking down can be initially quite strange. For instance, one can easily imagine the difficulties in seeing cloud detail at Chicago, if he was as far away as Boston, but straight up.

Secondly, the forecaster requires skill in meteorological interpretation - to take the composite picture of the earth's surface and identify the meteorological phenomena from the non-meteorological - to infer the nature and extent of cloud forms, and what is happening. He must then relate this picture to the other observations and charts available to him to obtain a coherent picture of the

portions of the atmosphere of direct concern to him.

The solution to this problem we are adopting in Canada is not new. We have relied greatly on the pioneer work of Conover, Fujita, Oliver, Hubert, Widger and others who are too numerous to name here. We have incorporated ideas from their many valuable research papers and reports. We regard it as much a problem of forecaster training as one of technique development. Consequently, our answer is to provide a satellite cloud catalogue for use by forecasters which will serve as an introductory guide to cloud photo-interpretation. This projected catalogue is to include selected ESSA and NIMBUS pictures received at the APT station in Toronto which are of the type he will be seeing daily. The pictures are selected to illustrate the typical appearance of the main cloud types as seen from satellite altitudes, for example, cirrus, middle cloud, wave clouds, convective clouds, fog, etc. These pictures are accompanied by a brief description of the appearance of clouds as seen from 800 miles up in terms of the well-known characteristics of photographic images - size, shape, shadow, tone, texture and pattern, as shown in Figure 1.

The catalogue proper will contain selected pictures mounted on a base map of approximately the same scale. The pictures are annotated. Corresponding surface maps, upper level charts, stability index charts, etc. are included as appropriate and we hope to make it convenient for the forecaster to superimpose the standard charts as overlays on the photographs to study their interrelationships.

The second part of our solution is to encourage the forecaster to adopt the well-established approach used in the photo interpretation field to satellite pictures, namely, convergence of evidence. This approach can be thought of as consisting of three parts.

1. Tentative cloud identification by photo interpretation techniques.
2. Direct evidence to confirm tentative interpretation.

3. Indirect supporting evidence.

First of all, one can approach the problem of cloud identification by standard photo-interpretation techniques, that is, by appeal to our knowledge and experience in recognizing clouds from their size, shape, shadow, tone, texture and pattern. With experience, one can be fairly certain of what there is most of the time, since the atmosphere tends to reproduce similar cloud patterns under similar circumstances. However, the type of cloud form cannot always be uniquely resolved by this method, because different cloud types may often appear alike. Because of this, it is often necessary to examine other evidence to arrive at the most probable answer, which leads to the second part.

If one is fortunate enough to have available other types of meteorological observations such as surface, aircraft or radar reports, one can use them to resolve interpretation problems by inter-comparison. For example, one can refer to surface observations to distinguish between stratus and fog, or between stratocumulus and altocumulus. Historical continuity is also a valuable guide.

When conventional observations are not available, a situation which occurs over about seventy percent of the earth's surface, we may still be able to obtain indirect evidence to confirm or reject a tentative interpretation. This evidence is largely obtained from flow patterns and parameters which may be derived from them.

To cite an example, a large area of overcast stratocumulus cloud in sun glint will often have an appearance similar to that of an altostratus layer. In this case, a comparison of the cloud feature with the 700 mb contour or isotherm field may help one to decide which is the more likely. This conclusion would be based on the well-known relationship between organized middle cloud layers with 700 mb troughs and ridges.

The foregoing is summarized in Figure 2. The cloud forms are listed in the left hand column. A brief summary of

the photo-interpretation characteristics of each cloud type is listed in the second column. In the next column is listed the type of direct observations which one may have for direct comparison. Finally, the right column shows a selection of factors which would generally support the tentative interpretation.

It is well known why a systematic approach to photo-interpretation of satellite pictures is necessary, i.e., because of the limited resolution of the camera and transmission system. This has been convincingly demonstrated by Oliver on many occasions, who showed that a satellite picture of the present quality has an appearance similar to

a good photograph that is slightly out of focus.

To conclude, it would be worthwhile to add a few remarks on the type of APT equipment in use in Canada at the time of writing. The Department of Transport operates two research and development sets at Toronto and Halifax. There is one at the National Research Council in Ottawa and others in industry. At Toronto, the APT pictures are simultaneously reproduced on polaroid film, paper facsimile and automatic photo-facsimile. The picture is also recorded on magnetic tape which enables reproduction of pictures with different contrast as well as archiving.

Fig. 1. APPEARANCE OF CLOUDS FROM SATELLITE ALTITUDES

| CLOUD TYPE | SIZE | SHAPE (ORGANIZATION) | SHADOW | TOPE (BRIGHTNESS) | TEXTURE |
|---|---|--|---|---|---|
| CIRRUS CIRROSTRATUS | TYPICAL LENGTHS OF ORGANIZED BANDS HUNDREDS OF MILES; WIDTHS OF SINGLE BANDS MAY BE 25-50 MILES; EXTENSIVE LAYERS OF CIRROSTRATUS MAY ALSO COVER LARGE AREAS. | LONG BANDS, PARALLEL TO UPPER TROPOSPHERIC WINDS, OFTEN HAVING SHARPLY DEFINED LEFT BOUNDARY, RELATIVE TO AN OBSERVER FACING DOWNWARD, RIGHT BOUNDARY SOMETIMES WELL-DEFINED, BUT IS MORE FREQUENTLY INDISTINGUISHED WHEN IT APPEARS OVER A MIDDLE CLOUD LAYER. | NORMALLY PRESENT AS A DARK LINE ALONG ONE EDGE; MOST NOTICEABLE WHEN SHADOW IS CAST ON A LOWER CLOUD LAYER OR A SMOOTH SURFACE WITH HIGH REFLECTIVITY. | TYPICALLY LIGHT GREY, BUT TONE IS DEPENDENT ON SUN ANGLE; TRANSLUCENT; LOWER CLOUDS AND GEOGRAPHICAL FEATURES ARE USUALLY ONLY PARTLY OCCURRED BY CIRROFORM CLOUD. | CIRROSTRATUS NORMALLY HAS A UNIFORM TEXTURE, WHILE CIRRUS TENDS TO BE MORE FIBROUS; CLOUD BANDS PERPENDICULAR TO THE WIND INDICATES WAVE STRUCTURE. |
| ANVIL CIRRUS (DETACHED FROM CUMULONIMBUS) | MAY BE QUITE EXTENSIVE, COVERING AREAS AROUND FIVE HUNDRED MILES OR MORE IN LENGTH AND WIDTH | CHAOTIC APPEARANCE WITH ALIGNMENT OF CLOUD STREAKS PARALLEL TO UPPER TROPOSPHERIC WINDS; DIFFUSE OR POORLY-DEFINED EDGES. | ONLY DETECTABLE WHEN CLOUD LAYERS ARE SUFFICIENTLY THICK AND SHADOW FALLS ON AN ILLUMINATED LOWER CLOUD LAYER OR BRIGHTLY REFLECTIVE LAND OR WATER SURFACE. | LIGHT GREY OR WHITE, DEPENDING ON CLOUD THICKNESS AND SUN ANGLE. | FIBROUS WITH NUMEROUS STREAKS, OR MORE UNIFORM TEXTURE WHEN DENSE CIRRUS LAYERS ARE CONCENTRATED WITHIN A SMALL AREA. |
| ALTOSTRATUS ALTOCUMULUS | EXTENSIVE SHEETS OR BANDS COVERING AREAS AS TENS TO HUNDREDS OF THOUSANDS OF SQUARE MILES; BANDS MAY BE TWO OR THREE HUNDRED MILES ACROSS. | ORGANIZED INTO VORTICES, BANDS, LINES OR LARGE COMMA-SHAPED AREAS ASSOCIATED WITH CYCLONES AND FRONTS; CHARACTERIZED BY PERSISTENCE IN FORM OVER PERIODS OF 12-24 HOURS OR MORE, SINCE CLOUD IS ASSOCIATED WITH SYNOPTIC SCALE MOTION SYSTEMS, USUALLY WELL-DEFINED BOUNDARIES. | OFTEN PRESENT ALONG ONE EDGE, SHADOW ENHANCED IF IT APPEARS ON A LAYER OF LOWER CLOUD. | VERY WHITE, ONE OF THE TWO BRIGHTEST CLOUD FORMS, THE OTHER BEING CUMULONIMBUS - DUE TO GREAT VERTICAL DEPTH OF CLOUD WHITEST CLOUD LAYERS ARE OFTEN ASSOCIATED WITH NIMBOSTRATUS AND PRECIPITATION AT THE GROUND. | STRATIFORM CLOUD WITH UNIFORM TOP SURFACE HAS UNIFORM TEXTURE; IF CONVECTIVE CLOUDS ARE PRESENT OR THE MIDDLE CLOUD IS NOT SOLID VARIATIONS IN TEXTURE WILL APPEAR AS A RESULT OF SHADOWS, BREAKS, OR THICKNESS VARIATIONS. |
| WAVE CLOUDS CIRRUS ALTOCUMULUS STRATOCUMULUS | NARROW PARALLEL BANDS OF THE ORDER OF TEN TO A HUNDRED MILES IN LENGTH; UNIFORM SPACING OF CLOUD BANDS IS CHARACTERISTIC OF THESE CLOUD FORMS. | UNIFORMLY SPACED; PARALLEL BANDS, MORE OR LESS PERPENDICULAR TO THE WIND DIRECTION AT CLOUD LEVEL, MOST OFTEN FOUND TO BE OF HILLS AND MOUNTAINS, NOTABLE EXAMPLES APPEAR OVER THE ROCKIES, APPALACHIANS, LABRADOR, AND OTHER RANGES. | NOT USUALLY DISCERNIBLE. | GREY, OCCASIONALLY WHITE, DEPENDING ON SUN ANGLE AND VERTICAL THICKNESS OF CLOUD. | CONTINUOUS OR BROKEN PARALLEL BANDS, MAY BE VERMICULATED. |
| CUMULUS TOWERING CUMULUS | INDIVIDUAL CUMULUS CLOUD CELLS ARE NORMALLY TOO SMALL TO BE DISCERNIBLE AT 800 MILES, RATHER WHAT APPEARS SIMILAR TO INDIVIDUAL CUMULI AS SEEN FROM THE GROUND ARE GROUPS OF CLOUDS HAVING A REGULAR ORGANIZATION OR PATTERN NOT NORMALLY DETECTABLE FROM SURFACE OBSERVATIONS; DIMENSIONS OF CLOUD GROUPS 3 TO 10 MILES. | WITH LIGHT WINDS, CLOUD GROUPS PRESENT A UNIFORM CELLULAR PATTERN OR MAY BE ORGANIZED IN SINGLE OR PARALLEL STREETS, STRAIGHT OR GENTLY CURVED, GENERALLY PARALLEL TO THE WINDS. OCCASIONALLY HOLLOW POLYGONAL CELLS, CRESCENTS OR SOLID CELLS WILL APPEAR IN THE OVERALL PATTERN, USUALLY LUMPY APPEARANCE. | USUALLY PRESENT WITH TOWERING CUMULUS; DESTRUCTIVE SHADOWS OR DOWN SUN SIDE; SHADOWS NOT SO EVIDENT WITH SMALLER CLOUDS OR CLOUD GROUPS. | BROKEN DARK GREY, GREY OR WHITE DEPENDING ON DIMENSIONS AND THICKNESS OF CLOUD GROUPS AS SEEN FROM SATELLITE ALTITUDES; SMALLER CLOUD GROUPS ARE DARKER IN TONE, WHILE CUMULUS CELLS SMALLER THAN THE THRESHOLD RESOLUTION OF THE CAMERA (2 MILES) WILL NOT BE VISIBLE IF SEPARATION IS GREATER THAN 2 MILES. AREAS OF SMALL CUMULUS WILL APPEAR IN BROKEN GREY TONE. | NON-UNIFORM, ALTERNATING PATTERN OF WHITE, GREY AND DARK GREY, OFTEN HAVING GREAT REGULARITY, DUE TO CONTAINED SHADOWS; HOLLOW CENTERS MAY BE PRESENT IN A RING OF CELLS. |
| CUMULONIMBUS | INDIVIDUAL ISOLATED CUMULONIMBUS CLOUDS ARE OF THE ORDER OF TENS OF MILES IN DIAMETER, COMBINED CLUSTERS OF SUCH CLOUDS MAY PRESENT A PATTERN AS LARGE AS A HUNDRED MILES ACROSS DUE TO MERGING OF CIRRUS ANVILS. | ISOLATED CELLS HAVE SHARPLY DEFINED EDGES ON ONE SIDE WITH CIRRUS ANVIL SPREADING OUT ON THE OPPOSITE SIDE IN THE PRESENCE OF PRONOUNCED WIND SHEAR, OTHERWISE THEY APPEAR AS ISOLATED, WHITE, NEARLY CIRCULAR CELLS. | SHADOWS USUALLY PRESENT AND WELL-DEFINED WITH CUMULONIMBUS. | VERY WHITE, PARTICULARLY TOPS HAVE CHARACTERISTIC BRIGHTNESS. | UNIFORM TEXTURE, SHARPLY DEFINED EDGES, ALTHOUGH CIRRUS PLUMES ARE OFTEN QUITE DIFFUSE BEYOND MAIN CELLS. |
| STRATOCUMULUS | APPARENT SIZE OF CELLS 2-10 MILES ALTHOUGH LAYERS WILL HAVE NO DISTINCTIVE SIZE. | STREETS OR BANDS ALIGNED WITH THE BOUNDARY LAYER WINDS, OR EXTENSIVE AREAS WITH WELL-DEFINED BOUNDARIES. | SHADOWS MAY SHOW STRIATIONS ALONG THE WIND. | SMALL CLOUD GROUPS ARE MOSTLY GREY OVER LAND, THICK OVERCAST STRATOCUMULUS LAYERS OVER OCEANS OFTEN APPEAR WHITE DUE TO CONTRAST IN REFLECTIVITY. | OVERCAST STRATOCUMULUS CLOUD LAYERS OFTEN SHOWS HOLLOW WITH DIFFUSE CENTERS. |
| STRATUS | VARIABLE. | VARIABLE, EXCEPT WHEN STRATUS CLOUD IS LOWER THAN SURROUNDING TERRAIN, IN WHICH CASE IT ASSUMES THE SHAPE OF A VALLEY MOUNTAIN, OR COAST LINE, ETC. BOUNDARY WELL-DEFINED BUT MAY HAVE A RAGGED EDGE. | NORMALLY NOT DISCERNIBLE, BUT PRESENCE IS DEPENDENT ON HEIGHT OF STRATUS LAYER ABOVE GROUND. | WHITE OR GREY, DEPENDING ON VERTICAL CLOUD THICKNESS AND SUN ANGLE. | UNIFORM. |
| FOG | VARIABLE | VARIABLE, IRREGULAR, BUT IN THE CASE OF FOG OVER BODIES OF WATER, SHAPE CONFORMS TO THAT OF SURROUNDING LAND; BOUNDARIES SHARPLY-DEFINED AND MAY BE THE ONLY DISTINGUISHING CHARACTERISTIC FROM STRATUS. | NORMALLY NOT DISCERNIBLE. | WHITE OR GREY, DEPENDING ON THICKNESS OF FOG LAYER AND SUN ANGLE; NORMALLY IF DEPTH OF FOG LAYER EXCEEDS 1000 FT IT APPEARS WHITE. | VERY UNIFORM. |

Fig. 2. A PROCEDURE FOR SATELLITE CLOUD PHOTO INTERPRETATION

| CLOUD TYPE | TENTATIVE CLOUD IDENTIFICATION BY PHOTO INTERPRETATION TECHNIQUES | DIRECT EVIDENCE TO CONFIRM TENTATIVE INTERPRETATION | INDIRECT SUPPORTING EVIDENCE |
|---|---|--|--|
| CIRRUS CIRROSTRATUS | CIRRUS CAN ALMOST ALWAYS BE POSITIVELY IDENTIFIED BY PHOTO INTERPRETATION TECHNIQUES CIRROSTRATUS MAY BE DISTINGUISHED FROM STRATUS AND FOG BY ITS CHARACTERISTIC TRANSLUCENCE | 1 SURFACE OBSERVATIONS. 2 AIRCRAFT OBSERVATIONS. | 1 ORIENTATION OF CLOUD STREAKS GENERALLY PARALLEL TO 300 MB WINDS. 2 OCCURRENCE OF JET STREAM CORE PARALLEL AND TO THE LEFT OF CLOUD EDGE, RELATIVE TO DOWNWIND DIRECTION. 3 POSITIVE VORTICITY ADVECTION AT 300 MB WHERE CLOUD OCCURS, ALTHOUGH THIS IS NOT NECESSARILY CONCLUSIVE EVIDENCE SINCE ONLY 85 PERCENT OF CIRIFORM CLOUDS OCCURS IN AREAS OF POSITIVE VORTICITY ADVECTION AT 300 MB. |
| ANVIL CIRRUS (DETACHED FROM CUMULONIMBUS) | CAN BE POSITIVELY IDENTIFIED BY PHOTO INTERPRETATION TECHNIQUES | 1 SURFACE OBSERVATIONS. 2 AIRCRAFT OBSERVATIONS. | 1 ORIENTATION OF CLOUD STREAKS GENERALLY PARALLEL TO 300 MB WINDS. 2 SHOW WETTER STABILITY INDICES LESS THAN +2 WITHIN OR UPSTREAM FROM CLOUD AREA |
| ALTOSTRATUS ALTOCUMULUS | CAN USUALLY BE IDENTIFIED BY ITS SIZE, SHAPE, VERY BRIGHT TONE AND UNIFORM TEXTURE ALTHOUGH OVERCAST LAYERS OF STRATOCUMULUS IN AREAS OF HIGH REFLECTIVITY MAY HAVE A SIMILAR APPEARANCE, OTHER EVIDENCE WILL HELP TO DISTINGUISH THE TWO, WHEN IT OCCURS OVER AN EXTENSIVE ICE SHEET, THERE ARE GENERALLY PRONOUNCED SHADOWS | 1 SURFACE OBSERVATIONS WITH IN OR NEAR OUTER BOUNDARY OF MIDDLE CLOUD LAYER 2 AIRCRAFT OBSERVATIONS 3 RADAR OBSERVATIONS OF PRECIPITATION OVER EXTENSIVE AREA. | 1 OCCURRENCE OF EXTENSIVE PRECIPITATION WITHIN AREA OF CLOUD. 2 CLOUD COINCIDES WITH MAIN ISOTHERM RIBBONS AT 850MB AND 700 MB. 3 CLOUD COINCIDENT WITH AREAS OF LARGE SCALE ASCENT ON VERTICAL MOTION CHARTS 4 CLOUD PATTERN OCCURS BETWEEN TROUGH LINE AND DOWNSTREAM RIDGE LINE AT 700 MB OR 500 MB 5 COINCIDENCE OF CLOUD AND POSITIVE VORTICITY ADVECTION AT 300 MB 6 DEW POINT DEPRESSIONS LESS THAN 2°C IN LAYER 850 MB TO 600 MB 7 CLOUD AREA OCCURS BETWEEN 850MB AND 600MB FRONTAL CONTOURS ON FRONTAL CONTOUR CHART. 8 COINCIDENCE OF CLOUD WITH ASCENDING MOTION INFERRED FROM WIND SHEAR INDICATORS. |
| WAVE CLOUDS CIRRUS ALTOCUMULUS STRATOCUMULUS | WAVE CLOUDS AS A CLASS ARE CONCLUSIVELY IDENTIFIED BY APPEARANCE AND ORGANIZATION, HOWEVER, CLOUD GENERALLY CAN ONLY BE DISTINGUISHED BY APPEAL TO DIRECT OBSERVATIONS OR INDIRECT SUPPORTING EVIDENCE | 1 SURFACE OBSERVATIONS 2 AIRCRAFT OBSERVATIONS | 1 OCCURRENCE OF WAVE CLOUDS OVER OR DOWNWIND FROM MOUNTAIN RANGE, OR OTHER HIGH TERRAIN FEATURES 2 CIRRUS WAVE CLOUDS WILL BE FOUND TO BE TRANSVERSE TO THE 300MB WIND DIRECTION 3 ALTOCUMULUS WAVE CLOUDS WILL BE TRANSVERSE TO THE 700MB WIND DIRECTION 4 STRATOCUMULUS WAVE CLOUDS ARE DISTINGUISHED BY CLOUD BANDS TRANSVERSE TO THE BOUNDARY LAYER WIND 5 LIFTING CONDENSATION LEVEL OF SURFACE AIR LIKELY OCCURRING WITHIN LAYER OF TURBULENT MIXING WILL CONFIRM STRATOCUMULUS TYPE. |
| CUMULUS TOWERING CUMULUS | THESE CONVECTIVE CLOUD FORMS CAN NORMALLY BE IDENTIFIED DIRECTLY BY SIZE, SHAPE, SHADOW, TONE, TEXTURE AND PATTERN | 1 SURFACE OBSERVATIONS. 2 AIRCRAFT OBSERVATIONS. | 1 OCCURRENCE OF INSTABILITY IN LOWER TROPOSPHERE AS DEDUCED FROM TEPHROGRAMS 2 INFERRD INSTABILITY FROM INTERPOLATED SURFACE, 850MB AND 700 MB TEMPERATURES IN CLOUD AREA 3 LIKELY OCCURRENCE OF STRONG SURFACE RADIATIONAL HEATING OR HEATING OVER RELATIVELY WARM B AND OR WATER SURFACE, NOTABLY OVER THE GULF STREAM |
| CUMULONIMBUS | POSITIVE IDENTIFICATION OF CUMULONIMBUS CLOUDS IS NORMALLY POSSIBLE BECAUSE OF THEIR CHARACTERISTIC SIZE, SHAPE, PRONOUNCED SHADOW, VERY BRIGHT TONE AND TEXTURE, HOWEVER, OTHER CLOUD AREAS OF SIMILAR DIMENSIONS AND PATTERN OR EVEN SMALL LAKES IN SUN GLINT MAY BE MISINTERPRETED AS CUMULONIMBUS BECAUSE OF ENHANCED BRIGHTNESS. | 1 SURFACE OBSERVATIONS 2 RADAR OBSERVATIONS 3 AIRCRAFT OBSERVATIONS. | 1 CLOUDS APPEAR IN UNSTABLE AREAS ON STABILITY INDEX CHARTS 2 UNSTABLE AIR MASS CHARACTERISTICS, AS INFERRED BY TEPHROGRAM ANALYSIS IN CLOUD AREA. 3 ALIGNMENT OF CLOUDS WITH SURFACE OR UPPER LEVEL FRONTS 4 CYCLONIC CURVATURE OF MEAN SEA LEVEL ISOBARS IN CLOUD AREA. 5 OCCURRENCE OF CLOUDS IN FORWARD PART OF UPPER WAVE TROUGH 6 EVIDENCE OF STRONG SURFACE HEATING 7 EVIDENCE OF DIFFERENTIAL ADVECTIONAL COOLING, OR DIFFERENTIAL MOISTURE ADVECTION PATTERNS FAVOURABLE TO CUMULONIMBUS DEVELOPMENTS. |
| STRATOCUMULUS | CAN USUALLY BE IDENTIFIED BY TONE ORGANIZATION AND TEXTURE, HOWEVER EXTENSIVE LAYERS OF OVERCAST STRATOCUMULUS CLOUDS OVER OCEANS MAY APPEAR SIMILAR TO MIDDLE CLOUD, HENCE THEIR DIFFERENTIATION MAY ONLY BE POSSIBLE BY REFERRING TO OTHER EVIDENCE | 1 SURFACE OBSERVATIONS. 2 AIRCRAFT OBSERVATIONS. | 1 ALIGNMENT OF CLOUD STREETS IN GENERAL DIRECTION OF THE BOUNDARY LAYER WINDS 2 SURFACE WIND SPEEDS GREATER THAN 10 TO 15 MILES PER HOUR TOGETHER WITH LOW LIFTING CONDENSATION LEVEL IN CLOUD AREA. 3 OCCURRENCE OF A LOW LEVEL TURBULENCE INVERSION IN CLOUD AREA 4 CLOUDS OCCUR IN COLD AIR MASS TO REAR OF SURFACE COLD FRONT WITH CLOUD STREETS BEARING AN APPRECIABLE ANGLE TO THE ALIGNMENT OF FRONTAL CLOUD |
| STRATUS | CANNOT BE NORMALLY DISTINGUISHED FROM FOG BY APPEARANCE ALONE, ALTHOUGH PICTURES HAVING GOOD DEFINITION AND TONAL RANGE SHOW BOUNDARIES OF STRATUS LAYERS TO BE MORE DIFFUSE THAN FOG BOUNDARIES; CLOUD SHADOW ALSO A DISTINGUISHING CHARACTERISTIC MAY CONFORM TO TERRAIN FEATURES. | 1 SURFACE OBSERVATIONS. 2 AIRCRAFT OBSERVATIONS | 1 SURFACE WINDS IN 5-12 MPH RANGE WITH LOW LIFTING CONDENSATION LEVEL. 2 OCCURRENCE OF A LOW LEVEL TURBULENCE INVERSION IN CLOUD AREA. 3 EVIDENCE OF SURFACE COOLING BY RADIATION, MOTION OVER COLDER SURFACE OR UPSLOPE MOTION 4 ABSENCE OF MIDDLE CLOUD; i.e., LOW MOISTURE CONTENT IN MIDDLE LEVELS OR DESCENDING MOTION |
| FOG | CANNOT NORMALLY BE DISTINGUISHED FROM STRATUS BY APPEARANCE ALONE, ALTHOUGH SHARP BOUNDARIES AND, ABSENCE OF SHADOW ARE USEFUL CHARACTERISTICS TO LOOK FOR USUALLY CONFORMS TO SHAPE OF TERRAIN | 1 SURFACE OBSERVATIONS. 2 AIRCRAFT OBSERVATIONS. | 1 SURFACE TEMPERATURE AND DEW POINT EQUAL IN CLOUD AREA 2 SURFACE WINDS LESS THAN 5MPH IN CLOUD AREA, AND EVIDENCE OF RADIATIONAL COOLING IN CASE OF RADIATIONAL FOG. 3 SURFACE AIR MOTION CONDUCTIVE TO ADVECTIONAL COOLING OVER COLDER LAND, WATER OR SNOW SURFACE. 4 PRONOUNCED UPSLOPE MOTION WITH LIGHT OR EVEN MODERATE WINDS IN CASE OF UPSLOPE FOG. 5 IN CASE OF ARCTIC SEA SMOKE, EVIDENCE OF SURFACE AIR TEMPERATURES APPRECIABLY LOWER THAN WATER TEMPS. WITH OFFSHORE FLOW 6 IN CASE OF LOW TEMPERATURE FOG, OCCURRENCE OF FOG NEAR UNINHABITED AREA WITH SURFACE TEMPERATURES BELOW -30 DEGREES F |

QUANTITATIVE CLOUD MOTION AND GROWTH INFORMATION FROM EARTH
SYNCHRONOUS SATELLITE PICTURE PAIRS

C. L. Bristor, Chief
Data Processing & Analysis Division
National Environmental Satellite Center
Environmental Science Services Administration

Abstract

Current computer efforts are described whereby pairs of spin-scan camera images from the ATS1 satellite are digitized and conditioned so as to automatically evaluate time changes. A pattern manipulating technique is employed whereby both image brightness topographies are reduced to skeletal "event" fields. Comparisons of the "erosion" required for this reduction provides growth information. Trial displacements of selected skeletal field sectors of one image upon the other provides opportunity for a "best fit" displacement determination. The work is presently at a preliminary stage and considerable effort must be expended in satellite attitude determination and image positioning before image pair comparisons can be made automatically. Some speculative remarks are offered in connection with the possible application of such evaluations as measures of the three dimensional wind field.

APT USE AT FUCHU AF WEATHER CENTRAL*

Captain Lee G. Dickinson
Detachment 1, 20 Weather Squadron

ABSTRACT

APT use is described with particular emphasis on its value to a weather central whose area of responsibility includes large oceanic and potentially data-silent areas. The technique Fuchu developed for preparing APT pictures for facsimile transmission is outlined. Fuchu's participation in the WEFAX experiment and Japanese uses of APT are reviewed.

1. Uses of APT Pictures.

Fuchu was one of the world's first APT satellite tracking stations. In early 1964 Fuchu tracked the experimental TIROS-VIII, the first APT equipped satellite. Very little use could be made from those early pictures due to the low altitude orbit, nonearth-oriented picture, and magnetic (venetian blind) effect on the picture quality.

During Sep 1964 APT pictures were received from Nimbus-I. Limited use was derived from those pictures as the satellite's highly elliptical orbit made accurate gridding quite difficult. Another limiting factor was the satellite's short lifetime of less than one month. Definite improvements over TIROS-VIII were noted because Nimbus-I was earth-oriented and also picture quality was much improved.

On 3 March 1966 the Western Pacific entered the operational APT age when Fuchu received its first picture from ESSA-2. Since that time we have received over 8000 APT pictures from ESSA-2, ESSA-4, and Nimbus-II. These pictures cover an area extending 40 latitude degrees in all directions from Fuchu. Maximum acquisition includes the northern half of New Guinea, Vietnam, Himalayan Mountains, Ob River, North Pole, Kodiak Island, Johnston Island, and back to New Guinea. The northern portion of our satellite acquisition area is controlled by available sunlight so we get much more extensive picture coverage during summer than in winter.

Every possible use is made from APT pictures. Our surface analysis incorporates APT data in locating fronts, trough lines, vortexes, vorticity centers, frontal waves, and surface ridge lines. Upper air chart analyses are improved by locating vortexes, trough lines, vorticity centers, ridge lines, and jet stream associated cirrus.

A Japan-Korea area severe weather advisory function is aided by observing APT indicated jet stream cirrus, mountain wave clouds, and thunderstorms.

Iwo Jima and Tokyo area forecasts are greatly assisted by APT. The major weather producing phenomena for these areas are wave developments emerging from China. APT spots their movement and indicates how extensive their cloud areas are. This is particularly important for Iwo Jima as there are no nearby weather reporting stations. APT views of typhoons also help in the preparation of forecasts for these areas.

A nephanalysis is made from each day's pictures. This is used by our forecasters in the preparation of Horizontal Weather Depiction (HWD) forecasts. These forecasts as well as all our surface and upper air analyses are transmitted via facsimile to USAF and USN weather stations in the Far East.

Daily weather briefings are given to the Commander and staff, US Forces Japan/Fifth Air Force. Diazo chrome copies of current APT pictures are used in the briefings.

Our Southeast Asia Support Section has a vital interest in the weather affecting Vietnam and South China. APT plays a large supporting role in the analysis and forecast function for that important part of the world.

Fuchu functions as the Alternate Joint Typhoon Warning Center. We are responsible for assuming the typhoon forecasting function of the Joint Typhoon Warning Center at Guam in the event of Guam's incapacitation. APT is an extremely useful tool for observing typhoons, tropical storms, tropical depressions, and suspect areas. We locate and estimate wind speeds of typhoons using APT pictures on a routine basis to develop and maintain interpretative skills for APT tropical analysis.

* Renamed Asiatic Weather Central on 1 May 1967.

APT has had many additional uses at Fuchu: the advance and ebb of snow fields in Russia, the extent of ice in the Sea of Okhotsk and Arctic Ocean, differentiation between the layered clouds and the stratus/fog which dominate the Bering Sea and North Pacific Ocean during spring and summer, the breakup of ice on several Russian lakes and rivers, orographic effects on clouds in South and West China, the change in the Asiatic monsoon from southwest to northeast and vice versa.

During the month of January we noticed that when a cloud shield moved eastward from the China mainland wave development would occur shortly afterwards. Once the clouds moved east of Okinawa a wave would form within 24 to 36 hours near the China coast close to the southern edge of the clouds.

We have been fortunate to receive several APT pictures which played important roles in Japan. The first was a picture received only two to three hours prior to the crash of a BOAC Boeing 707 jetliner onto the slopes of Mount Fuji. Over 100 passengers were killed in Japan's largest airplane accident and one of the world's worst single aircraft disasters. Mountain wave turbulence was suspected as one of the major causes of the accident and the picture showed several mountain wave clouds just to the south of the Mount Fuji area. Our picture was shown on Japanese national television the evening of the crash, 5 Feb 1966, to millions of interested viewers. A week later the Japanese crash investigation team requested copies of the picture for use in determining the cause of accident.

In April the Gemini-8 spacecraft made an emergency splashdown into an alternate recovery area near Iwo Jima. The area was nearly devoid of weather reports, and due to a weak cold front in the area there was some question on the validity of the official recovery area forecast. The APT picture verified the favorable recovery area forecast and normal recovery operations ensued. To aid recovery units this picture was transmitted via facsimile to them. As far as we know this was a first for an operational APT picture.

APT again proved its worth during the typhoon season. When a typhoon threatens bases in the Fifth Air Force area, and particularly the Tokyo area, our weather central is flooded by people seeking weather

information. APT pictures of the typhoons were shown the visitors and used as supporting evidence for our forecasts. The result was that people were convinced of the accuracy of the forecasts in minimum time thus easing our workload. APT pictures provided credibility.

2. Preparation of APT Pictures for Facsimile Transmission.

The first APT pictures transmitted via facsimile were accomplished by fastening an original picture to a piece of white pasteboard cut to fit the transmitter's revolving drum. This proved unwieldy and it also deprived the forecasters of the use of pictures for analysis work while they were being transmitted. Next we experimented with transmitting combinations of original pictures and ozalid copies of them at the same time. The resulting reception of these picture combinations showed us that most of the picture clarity and resolution loss experienced by facsimile receiving stations was due to the facsimile process, and that nearly equal quality pictures were received whether those transmitted were originals or ozalid copies.

By 1 May 1966 we settled on a six ozalid copy picture format. It measures 18x32 inches. The pictures are lined up in orbital sequence with the grid lines in dark areas accentuated with white grease pencil. Key grid lines are labeled with felt-tip pen (for readability). An interpretation of each picture's content is written with felt-tip pen both on the white cloud areas in the pictures and below each picture. This chart is transmitted daily at 0330Z. Special transmission of satellite pictures received after the 0330Z facsimile time showing significant meteorological features are transmitted at 0515Z. The specials usually consist of two pictures.

We have experimented with transmitting several hand-drawn nephanalyses of our picture content. Preparation time was excessive, so we found the nephanalysis technique less practical than a transmission of ozalid copies of the original pictures.

3. WEFAX.

We are one of three Air Force APT stations designated to participate in the NASA/ESSA WEFAX experiment. From our position in the western Pacific we view the ATS-1 satellite with an elevation angle of eight degrees and azimuth angle of 103

degrees. This means that our antenna is directed across the Tokyo metropolis. Radio noise interference is a continuing problem that has been partially solved by having one transmitting station's frequency changed. We also raised our antenna's elevation angle to near 25 degrees. At 25 degrees the acquisition cone for the antenna apparently is raised above most of Tokyo's radio noise, and yet still intersects ATS-1.

We have little need for most of the WEFAX-relayed charts. WEFAX relayed ATS-1 Spin Scan Cloud Camera pictures are useful provided they are timely. Our most profitable use of WEFAX is derived from the relay of ESSA-3 AVCS pictures showing the Indian Ocean and Vietnam area.

The ESSA-3 WEFAX relay is a rather interesting process. ESSA-3's tape recorders are interrogated by the Command Data Acquisition (CDA) station at Gilmore Creek or Wallops Island. From either of those stations the signal is fed to the National Environmental Satellite Center at Suitland, Maryland. After computer digitalization and gridding the pictures are transmitted to the Mojave tracking station in California. From there they are transmitted to ATS-1 via WEFAX which in turn relays the pictures to us. The entire process can take as little as two hours, and is usually accomplished in less than five hours. We consider the WEFAX relay of ESSA-3 pictures to be a vital real-time operational use of the ATS-1 spacecraft. WEFAX is providing us with important and timely picture information unavailable from any other source.

4. Japanese Uses of APT.

There are two principle users of APT among the Japanese. One is the Weather Central Service Squadron of the Japan Air Self Defense Force (JASDF), and the other is the Meteorological Research Institute (MRI) of the Japan Meteorological Agency (JMA).

JASDF has no APT tracking equipment of their own but they have free access to our APT pictures at Fuchu. The JASDF Weather Central is colocated with Fuchu AF Weather Central. Several of their forecasters have been trained in picture gridding and interpretation. They have used APT pictures in support of gunnery exercises, joint Japan/US air defense exercises, forecaster training,

instruction at their military academy, and typhoon research in conjunction with the University of Kyoto. Daily they transmit over the JASDF facsimile network a neph-analysis of pictures showing the Japan-Korea area.

The Meteorological Research Institute has its own APT tracking equipment constructed by the Nippon Electric Company. Pictures are approximately $6\frac{1}{2}$ inches square. (MRI is located near the Koenji train station which is nearly midway between Fuchu and downtown Tokyo). They grid no individual pictures, but make mosaics of each day's pictures and use an overlay grid for the entire mosaic. This mosaic is microfilmed and used in conjunction with typhoon and radar research under the direction of Mr. Kazuo Watanabe. Copies of MRI pictures are sent by messenger to JMA's map analysis section and maritime agency for use in analysis, forecasting, and ice alerts. Unfortunately most of the pictures are several hours old by the time they are delivered. Later another APT station will be constructed to provide real-time use of APT pictures for JMA's analyses and forecasts.

Last summer MRI had their APT equipment modified so that they could receive Direct Readout Infrared (DRIR) pictures from Nimbus-II. Recently the equipment was modified so that WEFAX could be received.

Between MRI, JASDF, and Fuchu Air Force Weather Central there is a free exchange of pictures, techniques, and research work. Thus there is mutual help and understanding in the advancement and use of APT in the Far East.

RECENT RESEARCH ON THE APPLICATION OF METEOROLOGICAL
SATELLITE DATA TO NUMERICAL WEATHER ANALYSIS

E. Paul McClain and Harold J. Brodrick

National Environmental Satellite Center
Environmental Science Services Administration
Washington, D. C.

ABSTRACT

Major cloud systems and the mass structure of the atmosphere are linked through the time-integrated three-dimensional air motions. One approach to the general problem of inferring the state of the atmosphere in sparse data regions from satellite information is that of synoptic/dynamic modeling. A model of the stages in the evolution of deep stratiform cloud systems associated with major extratropical cyclones has been developed in terms of the evolving vorticity and thermal structure of these systems. The four stages of development are illustrated schematically and by means of TIROS and ESSA pictures from two cases.

A. INTRODUCTION

The complete coverage of the sunlit portion of Earth by operational ESSA meteorological satellites has made available valuable cloud observations for improving weather analyses in the areas of the world where conventional ground-based and balloon observations are sparse or lacking altogether. Although direct, or nearly direct, use of the satellite-gathered cloud data for inferring weather conditions and for the detection and tracking of major storm systems is now routine, the input of satellite data to numerical analysis and prediction of the stream field or pressure field has been quite limited to date. The chief reason for this is the great difficulty of inferring quantitative information about the stream field from qualitative information about the cloud field. This seems to be true in spite of the fact that much qualitative, or semi-quantitative, information about aspects of the stream field can already be deduced from the cloud patterns [1]. The authors' earlier experiments in this area [2] were based on several simplifying assumptions about the relation of the vertical motion field to the cloud field on the one hand, and about the relation of the stream field to the vertical motion field on the other. The work reported here represents an extension of these earlier investigations, and its purpose is to provide a firmer basis for future experiments in providing satellite input to numerical analysis and prediction.

B. BASIC CONSIDERATIONS

The well-ordered and recurring large-scale cloud patterns so graphically portrayed in satellite pictures contain much information about the kinematical and dynamical processes that produce them. Studies such as those by Brodrick [3], Nagle, Clark & Holl [4], and Barr, Lawrence & Sanders [5] have demonstrated the connection between large-scale horizontal and vertical displacements of air and the evolution of deep and extensive layer-type cloudiness. Even instantaneous vertical motions are closely related to this type of cloudiness in certain portions of the cloud pattern. The typically deep, large-scale vertical motion associated with major extratropical cyclones can be partitioned principally between two major forcing functions: the vertical variation of vorticity advection and the Laplacian of thickness advection [5, 6]. The characteristic spiral configuration that nearly always develops with major storm systems, however, is only partially accounted for by vertical excursions of air. Important also is the principally horizontal motion of the air relative to the moving cyclone center in the lower troposphere.

Boucher and Newcomb [7] presented a preliminary cyclone model that related large-scale cloud patterns viewed in early TIROS pictures to the stages of development depicted in the classical Norwegian frontal cyclone model. This work was extended and broadened somewhat by Sherr and Rogers [8, 9], who made use of satellite infrared radiation measurements in addition to the picture data. They developed a hypothesis specifying the relative roles of vertical cloud patterns associated with developing, low-level baroclinic cyclones.

In an attempt to investigate more systematically and more comprehensively the relation between the vorticity and thermal structure of major cyclonic systems and their associated cloud patterns, a classification scheme based on cloud pattern models and on dynamic quantities important to cyclone development [10] and vertical motion generation (viz. vorticity advection and thickness advection) has been developed. This categorization recognizes two principal kinds of cyclones: progressive vorticity maxima (PVM) and quasi-stationary vorticity maxima (QVM). The most common, and most important, of the PVM is called Type A. This type is associated with developing, baroclinic cyclones in the lower troposphere, and it is the only type of vorticity maxima considered in this paper.

C. STAGES IN EVOLUTION OF TYPE A PROGRESSIVE VORTICITY MAXIMA

Type A PVM are generally analyzed on sea-level weather charts as occluding, polar front, wave cyclones, although a few appear to develop in the absence of a frontal zone and almost always within the cold air mass. They are typified at the 500 mb level by progressive short-wave troughs having wavelengths of the order of 20-50 deg. longitude and with amplitudes generally in the range of 10-20 deg. latitude. The vorticity and thermal structure of these systems, as well as the associated cloud patterns, tend to vary systematically with the stage of development. The evolution of Type A PVM may be divided into four stages: initial development, rapid development, maximum intensity, and dissipation. These stages are illustrated schematically in Fig. 1 and by actual cases in Figs. 2 and 3. Figure 2 consists of four TIROS IX frames taken approximately 24 hours apart. The sections of Fig. 3 are also about a day apart in time, but they are taken from digitized, rectified, ESSA 3 mosaics (see Bristor, Callicott & Bradford [11]). The process used to derive these mosaics results in a narrower gray scale and poorer resolution than in the conventional satellite pictures such as those in Fig. 2

1. Stage 1: Initial Development

a. Early Phase: This phase is characterized in the cloud pattern by a broadening of the frontal band in the form of a convex bulge poleward (see Fig. 2, upper left) or by an irregular mass of cloud, almost always within the cold air, whose area approximates that of a circle some 3-7 deg. latitude in diameter (Fig. 1, upper left). Some substantial portion of the total cloud system, in either case, should have the rather solid, bright appearance that is typical of deep, solid or multi-layered, and predominantly stratiform cloud masses when viewed in satellite cloud photographs. This portion of the cloud system, whatever the stage, is indicated by the heaviest stippling in Fig. 1. The successively lighter stippling indicates that these portions of the cloud system are accordingly less reflective, less solid, or less defined. The early phase of Stage 1 is typified at sea-level by a weak pressure minimum, either on the front or within the cold air, and no increase in low-level vorticity is yet in evidence. Although the vorticity and vorticity advection of the associated upper-level trough may already be appreciable in strength, the trough is still far enough west of the low-level circulation center at this time such that only weak cyclonic vorticity advection is present over it. The northwestern part of the main cloud mass is best accounted for by cyclonic vorticity advection aloft, whereas the remainder is attributable to warm advection, mostly at middle and upper levels, and by low-level convergence into the sea-level pressure trough. Both the latter factors are rather weak at this time, however.

b. Late Phase: In the late phase of Stage 1 the curvature of the poleward bulge on the frontal band is more pronounced, but the "open" tongue that characterizes subsequent stages has not appeared (see Fig. 3, upper left). As for the non-frontal cloud mass, it has become better defined by the late phase of Stage 1. The downstream edge tends to develop convex curvature, the upstream edge concave curvature (Fig. 1, upper left). Low-level cyclogenesis is underway by this phase, but vorticity is not yet increasing rapidly. Cyclonic vorticity advection aloft is increasing over and to the west of the surface center as the upper trough

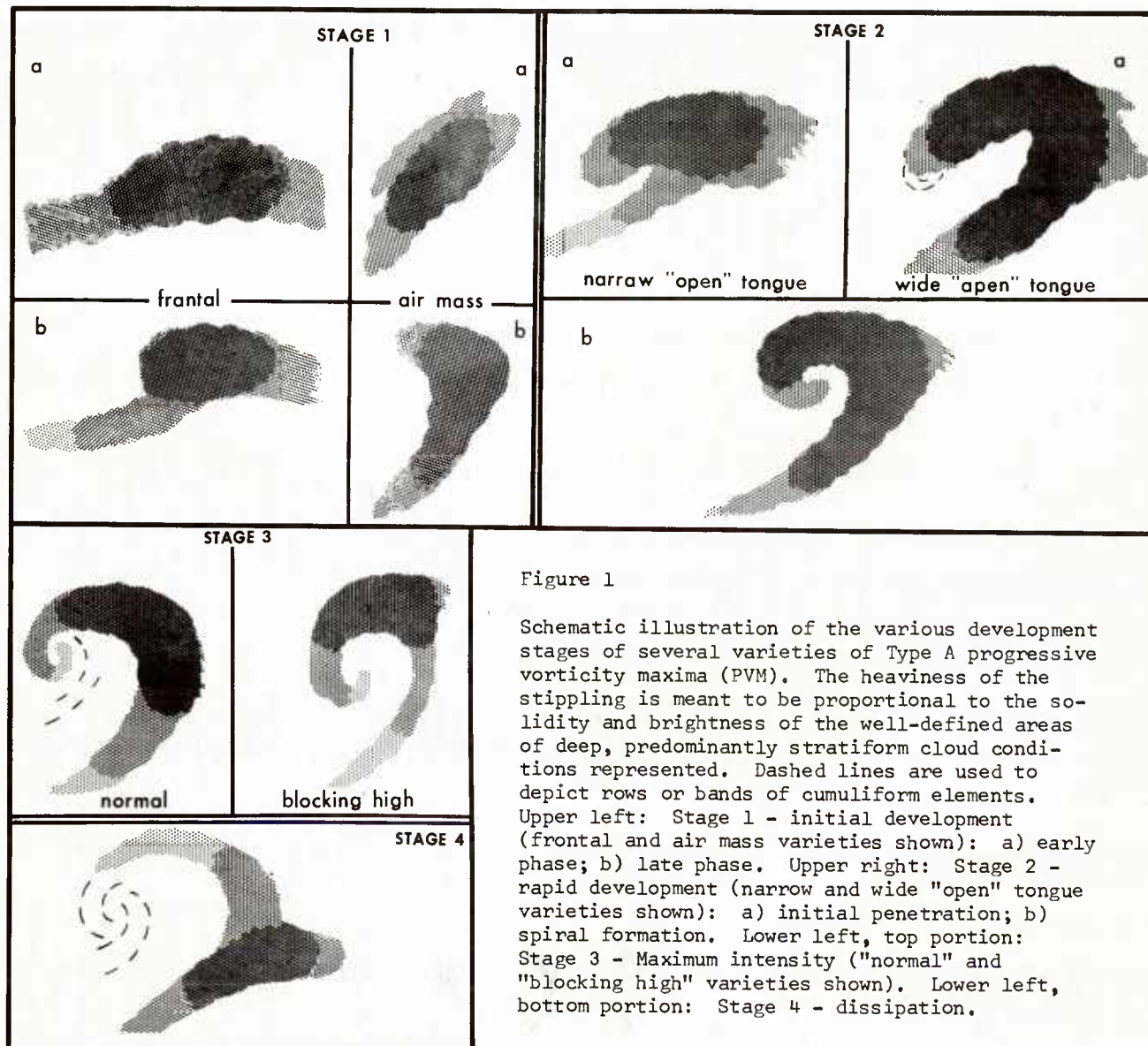
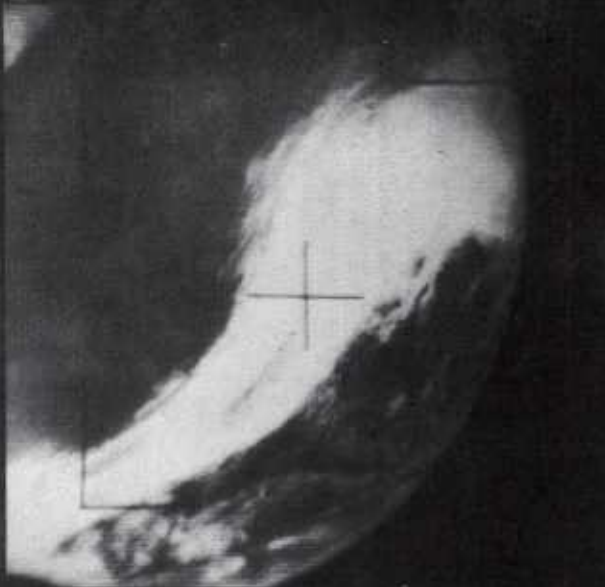


Figure 1

Schematic illustration of the various development stages of several varieties of Type A progressive vorticity maxima (PVM). The heaviness of the stippling is meant to be proportional to the solidity and brightness of the well-defined areas of deep, predominantly stratiform cloud conditions represented. Dashed lines are used to depict rows or bands of cumuliiform elements.

Upper left: Stage 1 - initial development (frontal and air mass varieties shown): a) early phase; b) late phase. Upper right: Stage 2 - rapid development (narrow and wide "open" tongue varieties shown): a) initial penetration; b) spiral formation. Lower left, top portion: Stage 3 - Maximum intensity ("normal" and "blocking high" varieties shown). Lower left, bottom portion: Stage 4 - dissipation.

FEB. 14, 1965



FEB. 15, 1965



FEB. 16, 1965

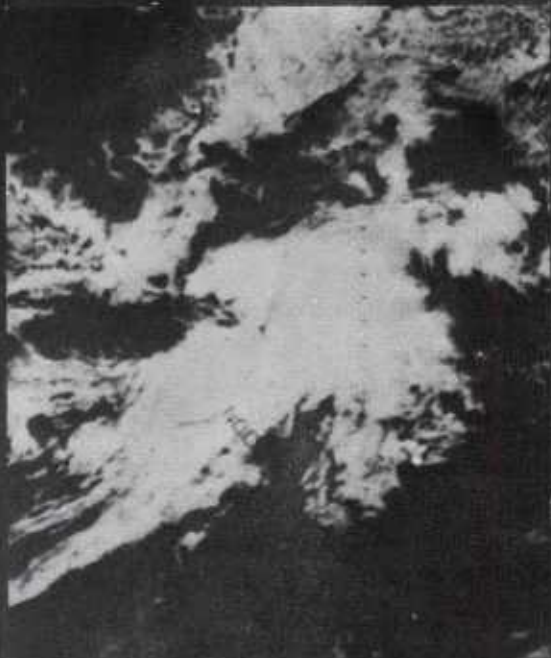


FEB. 17, 1965



Figure 2. Developmental stages of a Type A progressive vorticity maximum in the North Atlantic. Upper left: Stage 1a. Upper right: Stage 2a. Lower left: transitional from Stage 2b to early Stage 3. Lower right: transitional from late Stage 3 to early Stage 4.

FEB 15, 1967



FEB 16, 1967



FEB 17, 1967



FEB 18, 1967

Figure 3. Developmental stages of a Type A progressive vorticity maximum in the North Pacific. Upper left: Stage 1b. Upper right: Stage 2a. Lower left: Stage 3. Lower right: early Stage 4.

begins to overtake it (this frequent type of cyclone development has been described in detail by Petterssen [10]). Warm advection, especially just east of the cyclone center and in the lower troposphere, has increased, as has low-level frontal convergence.

2. Stage 2: Rapid Development

a. Initial Penetration of Open Tongue: In this first phase of Stage 2, initial penetration of the "open" tongue into the main mass of solid, bright, stratiform cloud has taken place, but the tongue has no appreciable curvature (Fig. 1, upper right). Thus the beginning of a spiral character to the system is evident in the cloudy air but not in the "open" tongue (see Figs. 2 and 3, upper right). The sea-level cyclone has now begun to intensify rapidly as the overtaking upper trough results in significant cyclonic vorticity advection directly over the low-level circulation center. Increasing circulation in the lower troposphere results in strong, generally localized maxima of thickness advection. Warm advection is centered just in advance of the cyclone center and cold advection just to the rear. The main mass of deep stratiform cloud may be accounted for by sustained and increasing ascent of air associated with strong warm advection, especially in the lower troposphere, in advance of the cyclone. The cloud is extended over and just to the north and northwest of the center by ascent associated with substantial cyclonic vorticity advection reaching maximum values in the middle and upper troposphere. Increasingly dry and cloudfree air is created farther to the west or southwest of the low center by strong cold advection, particularly at the lower levels, and by anticyclonic vorticity advection increasing in intensity upwards. Circulation of descent-dried air in the lower troposphere relative to the moving cyclone center is just beginning to result in the initial penetration of the cloud mass by the characteristic "open" tongue.

b. Spiral Formation: By this phase of Stage 2 the "open" tongue spirals cyclonically into the deep stratiform cloud mass (Fig. 1, upper right). Maximum rate of organization of the "open" and cloudy arms is underway, although the cloudy arm exhibits the greater amount of spiral turning (Fig. 2, lower left). This phase of spiral organization often evolves from the previous phase in 24 hours or less, and it appears to be attributable chiefly to the influence of the relative circulation mentioned above. This circulation serves to carry cloudy air farther westward, and thence southward, from the region of main ascent than can be accounted for purely from instantaneous upward motions. Similarly, it carries the relatively cloud-free air forming the "open" tongue farther eastward, and thence northward, from the region of main descent than would be expected from instantaneous downward motions. Incidentally, the "open" tongue over the oceans is frequently occupied by much cellular cloudiness, a condition that has been attributed to the addition of heat and moisture to cold air streaming over a warmer water surface [12]. The cyclonic system as a whole is developing at its maximum rate during this phase of Stage 2. The main forcing functions with respect to a Petterssen-type development, as well as with respect to large-scale vertical motion, are acting essentially as described in the first phase of this stage, but they are now rapidly approaching their peak values.

3. Stage 3. Maximum Intensity: By this stage the main mass of brightest, most solid-appearing cloudiness is no longer part of the spiral configuration, instead it is found some distance east of the apparent spiral center (Fig. 1, lower left). The entire cloud system has expanded in area, with the south-to-north portion of the "open" tongue generally having greatly broadened. The center, which is now chiefly defined by the spiral character of the "open" tongue, is connected to the main cloud mass by a less reflective and/or less solid stratiform cloud band (see Fig. 2, lower right; and Fig. 3, lower left). The maximum low-level and upper-level cyclonic vorticity, both in magnitude and area, has now been attained. The axis of the system is either vertical or tilts only slightly westward with height. High-level vorticity advection has significantly lessened, and the maximum values are usually situated east or southeast of the sea-level cyclone center rather than over it. Thickness advection has remained strong, the maximum values tending to become localized northeast (warm) and southwest (cold) of the cyclone center.

4. Stage 4: Dissipation: By this final stage the remains of the spiral center consist chiefly of cumuliform elements or detached inner portions of the original spiral cloud band (Fig. 1, lower left). The center is often completely detached from the main mass of deep stratiform cloud far to the east, although a dull and/or ragged stratiform cloud band occasionally still exists as a connection (see Fig. 3, lower right). The vorticity maximum

at both lower and upper levels is diminishing, although generally at a slower rate than it increased during the rapid development stage. Vorticity advection aloft decreases to low values as the upper low center tends to become circular and situated vertically over the sea-level low center. Thickness advection becomes weaker also, the maximum warm advection becoming situated north-northeast or north of the cyclone center, the maximum cold advection south-southwest or south of the center. By this final stage, however, the general picture often has become complicated by one of several possible situations: wave development has begun to the west along the trailing portion of the cold front; new development has begun to the southeast or east at the triple-point of the occlusion; or a new system moves in from the west or begins to develop in the cold air to the west of the old center. It would appear best to treat these as separate cloud systems rather than attempt to incorporate them with this stage.

D. MAGNITUDE OF MAXIMUM VORTICITY VERSUS STAGE OF DEVELOPMENT

As discussed in the preceding section, the cloud system of a developing cyclone evolves in stages. The cloud pattern in any given stage is determined in part by the circulation relative to the moving cyclone center. The deeper and more intense is the cyclone, the stronger is its circulation. Therefore, it seems reasonable to expect that the maximum vorticity of a cyclone, which is a measure of its circulation, is related to the stage of development as defined by the cloud pattern.

Absolute vorticity distributions were computed at the 1000 mb and 500 mb levels for some 30 Type A PVM that had been classed independently as to their stage of development. The 1000 mb and 500 mb vorticities were averaged to derive layer-mean vorticity charts also. The apparent centers of circulation in the satellite-viewed cloud patterns correlated better with the vorticity maxima in the layer mean charts than they did with the maxima either in the 1000 mb charts or in the 500 mb charts. The heavy lines in Figure 4, which is a graph of maximum layer-mean vorticity versus stage of development, specify the envelope that includes more than 95% of the sample cases. Note the rapid increase in vorticity during Stage 2 and the more gradual decline in Stage 4. The graph in Figure 4 represents the preliminary results of a relatively small sample. If confirmed by additional cases, it would be a means of obtaining quantitative estimates of the vorticity field in the lower half of the troposphere from the satellite picture data.

Although the stage classification requires a subjective interpretation of the pictures, the stages are distinctive enough so that, with adequate training, sufficiently close agreement between independent classifiers could be made for the scheme to be a useful one. The subjectivity of the classification could be reduced yet further by the use of cloud brightness values [11] or by knowing something about the cloud top temperature distribution from satellite radiation measurements in the water vapor "window" [8]. Research toward this end has recently been initiated.

E. SUMMARY REMARKS

A classification scheme based on the vorticity/thermal structure of cloud systems has been developed in order to systematize attempts to infer quantitative information about the mass/motion structure of the atmosphere from satellite picture data. Developmental stages of one of these systems, namely Type A progressive vorticity maxima, have been described, and they have also been illustrated by schematic drawings and by satellite pictures. The main areas of deep stratiform cloud, as well as those extensive regions not containing such cloud conditions, were accounted for partly in terms of the principal forcing functions in the omega equation and partly in terms of the horizontal air motion relative to the moving cyclone system. The maximum mean vorticity in the lower half of the troposphere was shown to vary systematically with the stage of development of the cloud system.

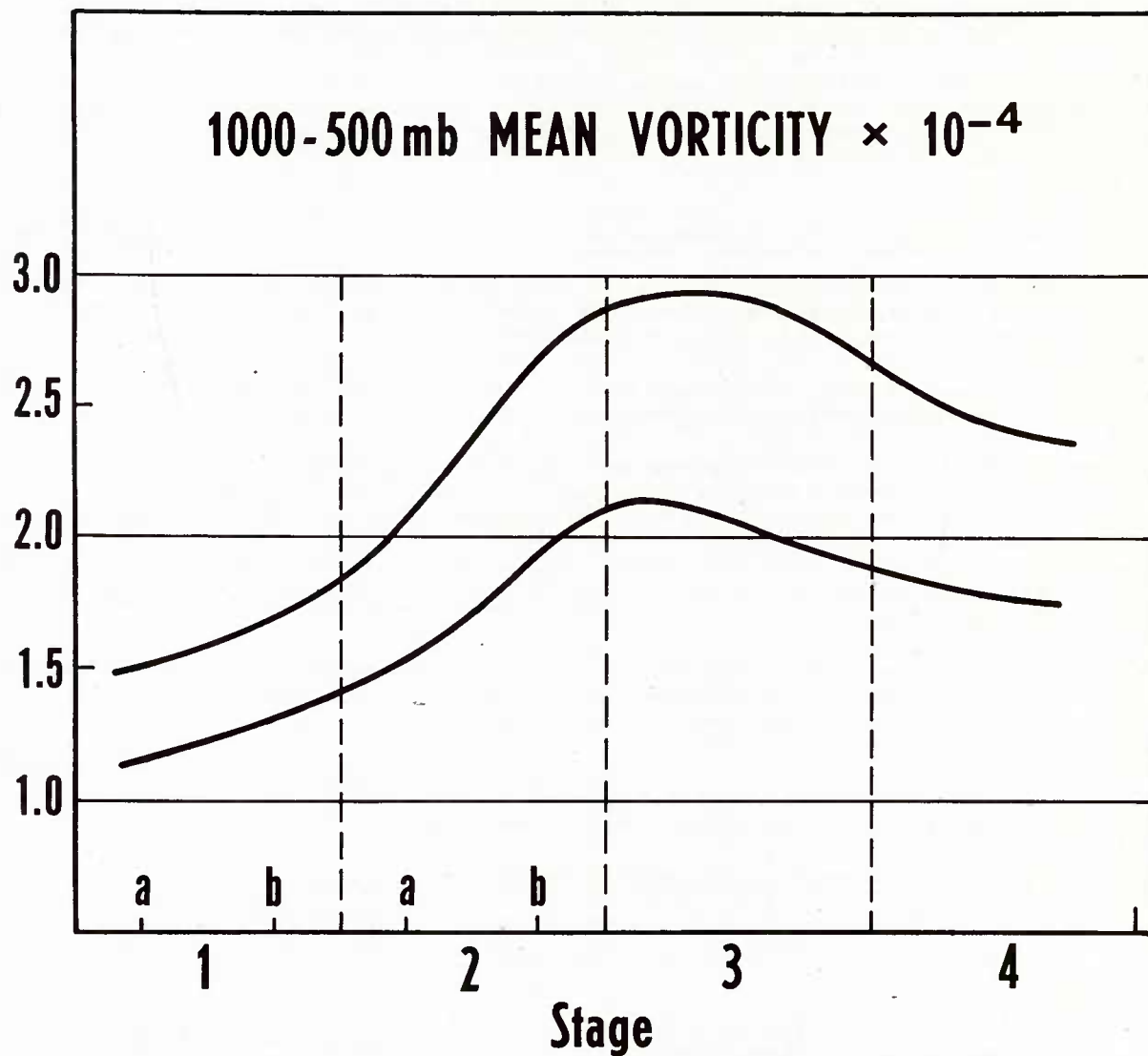


Figure 4. Variation of maximum, layer-mean, vorticity (absolute) with stages in the development of Type A progressive vorticity maxima. The heavy lines define the envelope that includes $<95\%$ of the sample.

REFERENCES

1. Anderson, R. K., E. W. Ferguson, and V. J. Oliver, The Use of Satellite Pictures in Weather Analysis and Forecasting. WMO Tech. Note 75, No. 190, TP. 96, 184 pp., 1966.
2. McClain, E. P., M. A. Ruzecki, and H. J. Brodrick: "Experimental Use of Satellite Pictures in Numerical Prediction," Monthly Weather Review, vol. 93, p. 445-452, 1965.
3. Brodrick, H. J.: TIROS Cloud Pattern Morphology of Some Midlatitude Systems. Meteorological Satellite Laboratory Report No. 24, 31 pp., U. S. Weather Bureau, 1963.
4. Nagle, R. E., J. R. Clark, and M. M. Holl: Evaluation of the Diagnostic-Cycle Routine in the Interpretation of Layer-Cloud Evolutions. Final Report, U. S. Weather Bureau (NWSC) Contr. No. Cwb-10884, 87 pp., Meteorology International, 1965.
5. Barr, S., M. B. Lawrence, and F. Sanders: "TIROS Vortices and Large-Scale Vertical Motion," Monthly Weather Review, vol. 94, p. 675-696, 1966.
6. Krishnamurti, T. N.: On the Partitioning of the Baroclinic Vertical Motions in a Developing Wave Cyclone. Sci. Rep. No. 1, U. S. Air Force Contract No. AF 19(628)4777, 33pp., Dept. of Meteorology, Univ. of Cal. at Los Angeles, 1966.
7. Boncher, R. J. and R. J. Newcomb: "Synoptic Interpretation of Some TIROS Vortex Patterns: A Preliminary Cyclone Model," Journal of Applied Meteorology, vol. 1, p. 127-136, 1962.
8. Sherr, P. E. & C. W. Rogers: The Identification and Interpretation of Cloud Vortices Using TIROS Infrared Observation. Final Report, U. S. Weather Bureau (NWSC) Contr. No. Cwb-10812, 98 pp., Aracon Geophysics Co., 1965.
9. Rogers, C. W. and P. E. Sherr: Toward the Dynamical Interpretation of Satellite Observed Extratropical Vortical Cloud Patterns. Final Report, ESSA (NESC) Contr. No. Cwb-11123, 125 pp., Allied Research Associates, 1966.
10. Petterssen, S.: Weather Analysis and Forecasting (2nd Ed.), Vol. I, p. 320-339, 1956.
11. Bristol, C. L., W. M. Callicott, and R. E. Bradford: "Operational Processing of Satellite Cloud Pictures by Computer," Monthly Weather Review, vol. 94, p. 515-527, 1966.
12. Hubert, L. F.: Mesoscale Cellular Convection. Meteorological Satellite Laboratory Report No. 37, 68 pp., 1966.

UTILIZATION OF METEOROLOGICAL SATELLITE INFORMATION IN A NUMERICAL WEATHER ANALYSIS AND PREDICTION SYSTEM

by

Roland E. Nagle

Abstract

This report presents the results of an exploratory investigation of relationships between cloud patterns and features of mass/motion distributions. The underlying motif was a consideration of indigenous scale relationships between characteristics of satellite observed cloud patterns and entities of numerically-produced weather analyses.

The problem of using mass/motion information inferred from satellite cloud observations in a numerical weather analysis system is discussed. A synopsis of Holl's Inherent-Scale Separation Technique is presented. To illustrate the relationships between layer-cloudiness patterns and indigenous scale-components of the 500 mb height field, a case study covering an eight-day period is presented. The successive stages-of-development of a spiral cloud system are shown in selected TIROS IX videographs, along with the corresponding 500 mb height fields, the 500 mb short-wavelength disturbance component fields and the 500 mb large-scale disturbance fields.

The results of a statistical study of the relationship between the 500 mb short-wavelength, disturbance-component extremals and the centers of spiral cloud patterns are presented and discussed. The results of a statistical study of the relationship between the magnitude of the short-wavelength, disturbance-component extremals and the long-wavelength component, height field is presented.

The Omega Equation is transformed into a form in which the short-wavelength, disturbance-component of the 500 mb height field can be used in the computation of a gross vertical motion parameter. Vertical motion fields computed under this formulation are compared with selected nephanalyses of synoptically-significant cloud patterns. On the basis of the results of these comparisons, a simplified quasi-empirical method for modifying the 500 mb height field on the basis of information inferred from satellite observed cloud patterns is suggested. Two alternative methods are outlined for integrating these data into an operational numerical weather analysis system.

Extracted from Nagle, R. E., et al., Objective Assembly of Meteorological Satellite Information, Final Report, Contract No. N62306-1775, Meteorology International Incorporated, Monterey, California. Copies of this report may be obtained by writing to the author at the following address:

Meteorology International Incorporated
P. O. Box 1364
Monterey, California

APPLICATIONS OF SATELLITE OBSERVATIONS OF EXTRATROPICAL CLOUD VORTICES

William K. Widger, Jr., C. William Rogers

and

Paul E. Sherr

Allied Research Associates, Inc.
Concord, Massachusetts

Abstract

The combined use of satellite television and infrared observations has provided an improved understanding of the three-dimensional cloud patterns associated with extratropical cyclones, and of the typical sequence of development of these patterns. It appears that dynamically induced vertical motions are of particular significance during the early stages of system development, and remain significant in the eastern portions of a system through at least the mature stage. Horizontal advection of existing cloud covered and clear areas becomes paramount in the western portions of these systems.

These findings are now being confirmed and extended by further analyses which include concurrent, multiple level, vertical motion computations. The existing findings, however, already provide an operationally applicable basis for estimating the probable stage of storm development, especially in areas deficient in conventional data.

It would appear that the horizontally advected cloud cover to the west of a mature cyclonic center may be a factor in accelerating dissipation, and may ultimately need to be taken into account as diabatic effects are included in numerical prediction models.

Some speculations as to the processes occurring during the initial stages of cyclogenesis are also included.

I - Introduction

Extratropical cyclones have been the subject of intense and essentially continuous study for more than a century [1]. Contributing to our present knowledge has been the work of Franklin, Dove, LeVerrier, Fitz Roy, Buys Ballot, and others far too numerous to cite. General thinking on this topic as it stood as the satellite data became available was particularly influenced by the studies of Bjerknes and Solberg [2], Bjerknes and Holmboe [3], Sutcliffe [4], and Petterssen [5].

Why then, it may be asked, do extratropical cyclones still continue to be such a central problem in meteorology? There are at least three reasons:

1. They are accompanied by areas with far more than their share of operationally adverse weather.
2. It is in these areas that operational forecasts are most likely to be in significant error.
3. From the scientific viewpoint, these cyclones are associated with the maximum latitudinal exchanges of heat and moisture and so contribute significantly to the general circulation. In contrast, anticyclones seem to serve far more the functions of reservoirs and exhausts. They tend to operate at slower rates and in somewhat more predictable fashions. As in any engine system, the energy conversion processes probably deserve more attention than the fuel tanks.

II - Conditions Apparently Necessary for Active Cyclogenesis

As Petterssen [5] suggested, active cyclogenesis occurs when a local vorticity maximum, usually in the form of a mid-tropospheric short wave trough, moves into the vicinity of a lower tropospheric temperature gradient or baroclinic zone. Two initial conditions for the low-level baroclinic zone are recognized. The first is a pre-existing zone, usually in the form of a stationary front extending to the south and west of a mature or decaying cyclone. From the satellite viewpoint, this front is marked by a cloud band trailing



Figure 1 Stable Frontal Wave (Atlas' 11c picture)

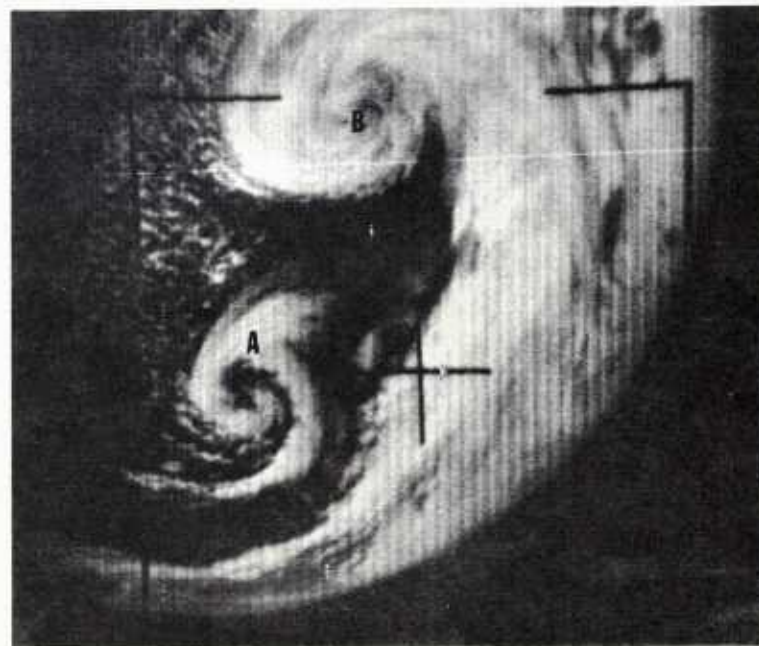


Figure 2 A Well Defined Comma-Shaped Cloudmass, A, Behind a Frontal System in an Area of Positive Vorticity Advection. The Major Storm Center Can be Seen at B.

behind the old cyclone. The second is a low-level baroclinic zone which develops or intensifies as the upper level vorticity maximum approaches. Such zones are particularly frequent, during the winter season, along the boundary between a cold continent and an adjacent warmer ocean surface to its east. Any cloud associated with this zone is usually hidden from the satellite beneath the cloud shield associated with the short wave trough.

1. Cyclogenesis Associated with Pre-existing Cloudy Baroclinic Zones

Both conventional and satellite data indicate that weak wave disturbances may form and move along quasi-stationary fronts. In the satellite data, these disturbances are revealed by bulges on the poleward side of the cloud band (Fig. 1). Experience has also shown that these disturbances seldom develop into significant storms in the absence of upper level support. In the case of an actively developing wave, however, the satellite data frequently show the concurrent existence of a vorticity maximum in the northwest flow around the old cyclone. The associated cloud pattern is comma-shaped, and frequently composed of clouds originally produced by lower level convection. Identification of these cloud patterns allows the vorticity centers to be tracked as they approach the low-level baroclinic zone. Figure 2, taken from Oliver and Ferguson [6], is only one of the many examples of these cloud patterns as noted in the TIROS and ESSA satellite data.

It would appear that systems like those shown in Figure 2 have, in the past, been often erroneously analyzed as secondary cold fronts, bent-back occlusions, upper level fronts, or similar apocryphal features.

The satellite data have clearly re-emphasized the importance of these mid-tropospheric vorticity maxima, even when they are of sub-synoptic scale. There are many indications that they are often directly associated with different types of operationally significant conditions which may range, depending on other factors, from (a) meso- or subsynoptic variations in local cloudiness, to (b) localized areas of moderate to severe convective activity (e.g. analogous to the 10,000 foot level microtrough frequently used in World War II thunderstorm forecasting practice), to (c) the initial stage of extratropical cyclogenesis and/or the areas of the most active weather within mature extratropical cyclones. Certain of these conditions are discussed in later sections.

2. Cyclogenesis Associated with Developing Baroclinic Zones

Both conventional and satellite data indicate that mid-tropospheric vorticity maxima, frequently in the form of short wave troughs, can move along for some time in the basically zonal planetary flow (as opposed to those in northwest flow) with little or no development. Satellite observations show that a comma-shaped pattern, composed of middle and high cloud, is most frequently associated with these disturbances (Fig. 3). Development occurs when a modification of the low level flow, induced by the mid-tropospheric vorticity maximum, is able to establish the necessary thermal gradient and thermal advection field. It is generally thought that rapid cyclogenesis, both in this case and that of a frontal wave, can begin only when significant low level thermal advection becomes established.

III - A Model of Cyclogenesis as Suggested by the Integration of Satellite Data and Conventional Data.

The earliest stages of cyclogenesis, prior to the development of low level thermal advection, are still largely unexplained. We shall speculate on a possible sequence of initial development for the frontal wave case in a later section.

Synoptic data and calculations clearly show, however, that, early in the developing cyclone, low level thermal advection is created and leads to a region of low level upward vertical motion ahead of the system.[†] Accordingly, to the east of the upper level vorticity maximum, a deep layer of upward vertical motion then exists. This in contrast with the previous condition, when significant upward vertical motion existed principally at mid-tropospheric levels (due to vorticity advection associated with the mid-tropospheric trough).

Accompanying these changes of the distribution of upward vertical motion should be a lowering of the level of non-divergence. Petterssen [5] observed that a low height of the level of non-divergence occurs when temperature advection becomes predominant, and implied that a low height of the level of non-divergence accompanies development. He also derived an equation for the change of particle vorticity, at 1000 mb, which, for the case of increasing cyclonic vorticity, requires positive vorticity advection below the level of

[†] (See Reiter [24]).

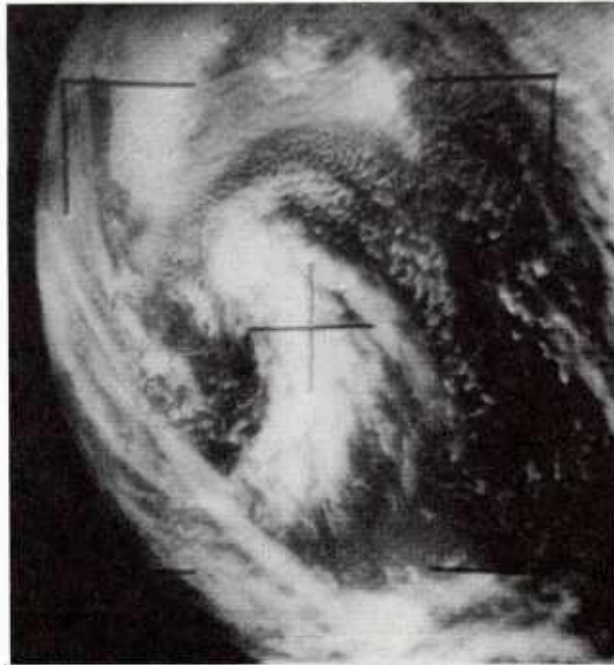


Figure 3 Comma-Shaped Cloud Mass Associated with Short Wave Trough

non-divergence and/or a positive maximum in the temperature advection field. (This situation was the basis for his empirical rule for the forecasting of cyclone development.) In a related case study, Petterssen, et al [12] showed that, when the level of non-divergence is high, synoptic situations are typically either non-developing or in an initial stage of development.

These relationships seem intuitively reasonable since (1) deepening and development (increasing cyclonic vorticity) are typically well correlated; and (2) if it is assumed that the absolute magnitudes of the divergence are of about the same order of magnitude at individual levels, a deep layer of divergence above a shallower layer of convergence will lead to deepening and to associated intensified cyclogenesis.

Of course, the patterns of vertical motions, advections, divergences, etc., will be reversed to the rear of the system, leading to pressure rises there. The rates of deepening and system motion will depend on the absolute and relative strengths of the effects ahead of and behind the system. The subsidence in the cold air and the rising of the warm air is, of course, in the proper direction for the conversion of eddy potential energy to kinetic energy.

As the circulation about the system intensifies, thermal advection will, for a time, increase at low levels, and will propagate into and then increase at progressively higher levels. Thus, the storm will continue to intensify until the resulting circulations have (1) acted to reduce or destroy the gradients and advections, and (2) cut-off the system from significant additional inflows of contrasting air masses. The system can then only dissipate the previously generated kinetic energy, and must soon die out. Another process which may also influence the rate of final decay of the system will be considered later.

IV - The Typical Sequence of Cyclonic Development as Observed in the Satellite Data

Our present thinking regarding the observed sequences of satellite-observed vortical cloud patterns is in many respects an evolution from the initial Boucher-Newcomb model [13]. Also contributing were such subsequent studies as those of Widger [14] (and especially some of the earlier thinking of Rogers as reported therein); Nagle, Clark and Holl [15]; and Barr, Lawrence and Sanders [16].

The reader may note many similarities between the cloud pattern sequence model described below and ones developed more or less concurrently by others. In part, this represents the close coordination of the studies of most of those working on this problem. From the viewpoint of the operational forecaster, these similarities are fortunate, since he would be in an untenable position if research workers looking at basically the same data presented the operational meteorologist with drastically different interpretations.

Since most aspects of the model to be presented here have already been described in previous papers and reports [17, 18, 19], some aspects will only be summarized.

Our ability to develop this model derived very largely from the availability and use [17] of the TIROS 8-12 μ (Channel 2) atmospheric window infrared data, which permitted the unambiguous differentiation between clouds with significantly different cloud top heights when this would not have been possible from the satellite television picture data alone. For example, consider the two successive TIROS pictures, in Figure 4, taken on a single pass. In the left picture, the major cloud mass appears uniformly bright, although the superimposed infrared blackbody temperature isotherms clearly indicate a sharp gradient of cloud top height over the left portion of the cloud mass. In the right picture, taken from a slightly different sun-cloud-satellite angle, this difference in cloud top heights does show up in the brightness differences between the lower-left and the remaining portions of the cloud mass.

Cases such as that in Figure 4 clearly demonstrate the need for operational satellites, such as those of the ESSA or TOS series, to provide operationally available atmospheric window infrared data with resolutions of 50 miles or better, in addition to the presently available television pictures.

In brief, our model, as discussed in more detail below, shows that during the earlier stages of storm development, the observed cloud patterns result principally from the characteristic patterns of vertical motion associated with the mid-tropospheric short wave troughs, either singularly or in association with a frontal wave. In later stages, as closed circulations develop first at the lower levels and then at progressively higher levels, both the

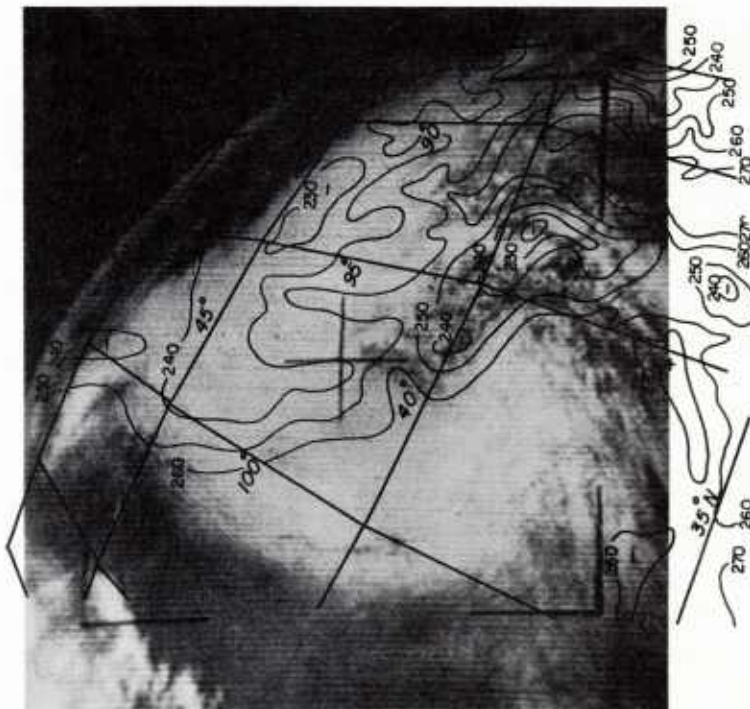
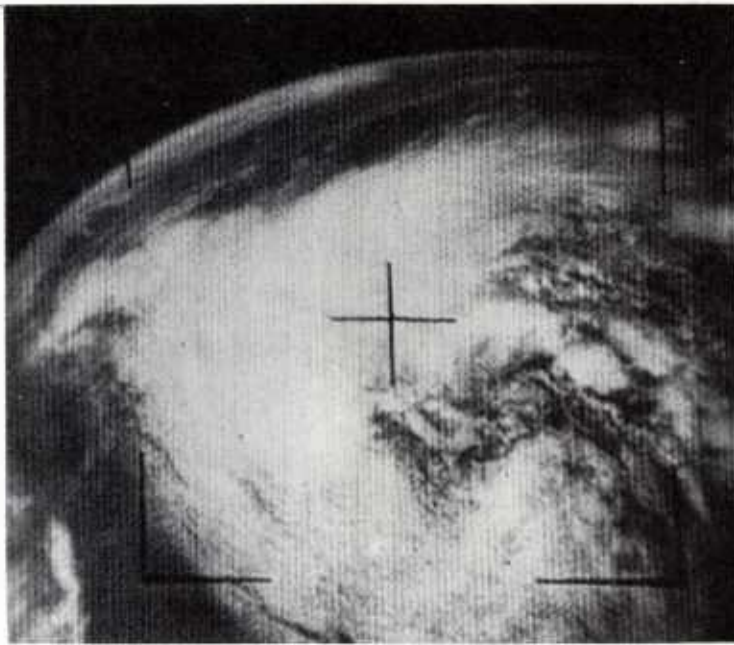


Figure 4 An Example of the Ambiguity in Cloud Brightness, and the Requirement for Infrared Data, for Determining Cloud Top Heights.

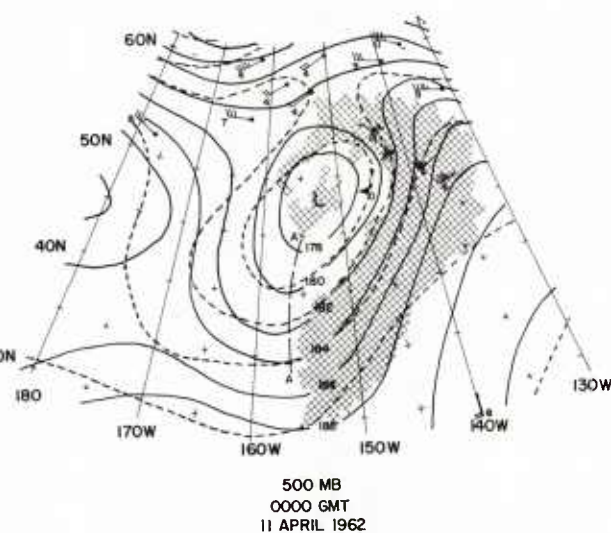
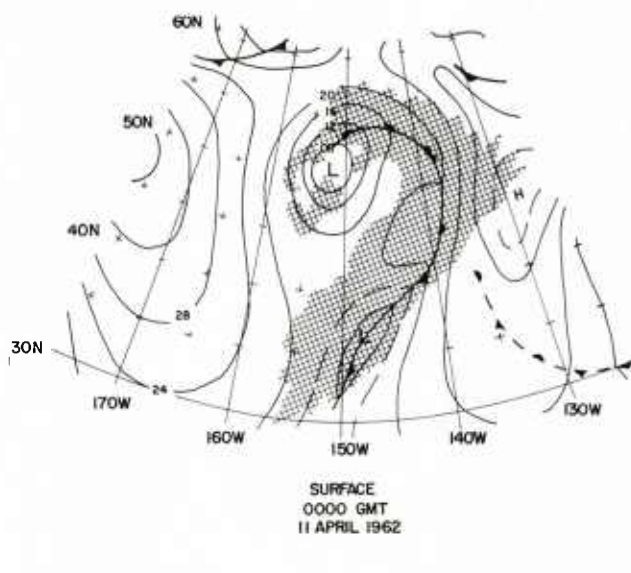
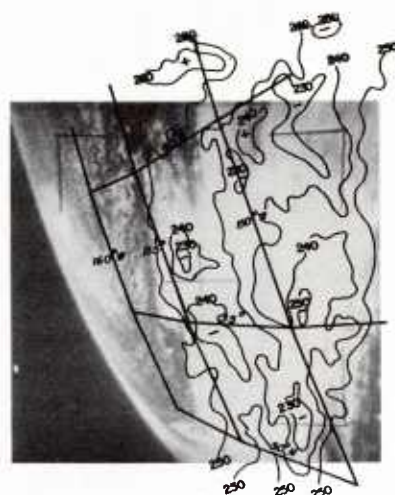


Figure 5 Example of TIROS Picture of Frontal Wave, with and without Superimposed Channel 2 Blackbody Isotherms, and Concurrent Conventional Analyses.

thermal advection components of the vertical motions and the horizontal advection of the previously formed cloud masses become progressively more important in shaping the cloud field. The cloud patterns in the eastern and northern portions of the system continue, at least through the stage of maturity, to derive principally from the combined effects of the vorticity advection and thermal advection forced vertical motions, while the western and central portions of the cloud patterns are largely advectively derived.

The satellite data have revealed, however, that several different cloud fields may exist during the very initial stages of low level baroclinic cyclogenesis. Four such cloud fields which have been observed are listed below. These differences probably depend on the relative saturation deficit in the lower levels (in association with the baroclinic zone) as compared to that at mid-tropospheric levels (in association with the short wave trough).

1. Bulging of the frontal band, with no evidence in the satellite data of an approaching vorticity maximum. (see Fig. 5).
2. A bulging of the frontal band plus a clearly marked approaching vorticity maximum (see Fig. 2).
3. A middle tropospheric vorticity maximum with no apparent low-level baroclinic zone (i. e., no frontal cloud band visible in the satellite data). (see Fig. 3).
4. No evidence of clouds associated with either the upper level vorticity maximum or a low level baroclinic zone, until they come in juxtaposition, and clouds then appear.

Satellite television and infrared observations of the initial stages of (1) and (3) have been studied in some detail and are discussed below. Satellite television observations suggest that the initial stages of (2) are similar to those of (1).

1. Frontal Wave on a Pre-existing Cloudy Baroclinic Zone

Initial Stage

With a pre-existing frontal cloud band, and no cloud associated with the approaching vorticity maximum, a wave-like poleward bulging of this cloud band is the first indication of cyclonic storm development (Fig. 5). In the case where cloud is also associated with the vorticity maximum, both this cloud pattern and the bulge on the frontal cloud band, indicative of development, are visible (see Fig. 2). The extent of the bulge, prior to the appearance of the hook-shaped pattern (to be discussed next) is indicative of the degree of development during this phase of the life cycle.

Rapidly Developing Stage

The initial stage of development described above typically exists only for a short time, and is soon succeeded by a stage of rapid development and deepening. A hook-shaped pattern (Fig. 6) is typical of this stage of development for cases when the initial stage was characterized by no cloud associated with the mid-tropospheric vorticity maximum. Comparison of Figures 5 and 6 shows that the area of high cloud tops (typically enclosed by the 230°K isopleth) has increased and the Channel 2 isotherm field is more organized. To our knowledge, no detailed vertical motion computations for this stage have been published. However, one set of computations is available for the initial stage [16]. Reasoning from these data, the following situation seems plausible. The upward vertical motion ahead of the mid-tropospheric trough has tapped the moisture in the frontal zone, and the resulting cloud field reflects this organized, large scale field of upward motion.

The cloud pattern for this stage, in the case where clouds are associated with both the lower baroclinic zone and the upper trough, is not yet known. It seems likely that it is also some form of hooked-shaped pattern, formed by the complex merging of the two pre-existing cloud patterns. This conjecture is supported by the fact that a hook-shaped pattern is also produced in the case of a developing baroclinic zone (to be discussed below).

Since the hooked-shaped pattern seems in all cases to be associated with the stage of rapid development, discussion of conditions typically associated with it will be postponed until we reach it again in the other sequence.

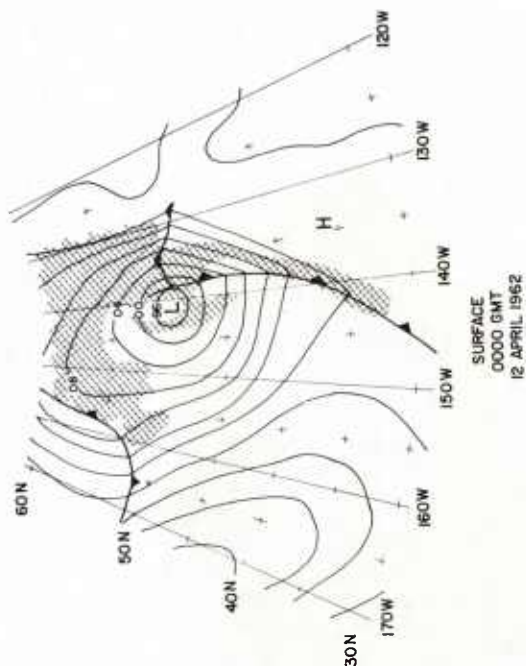
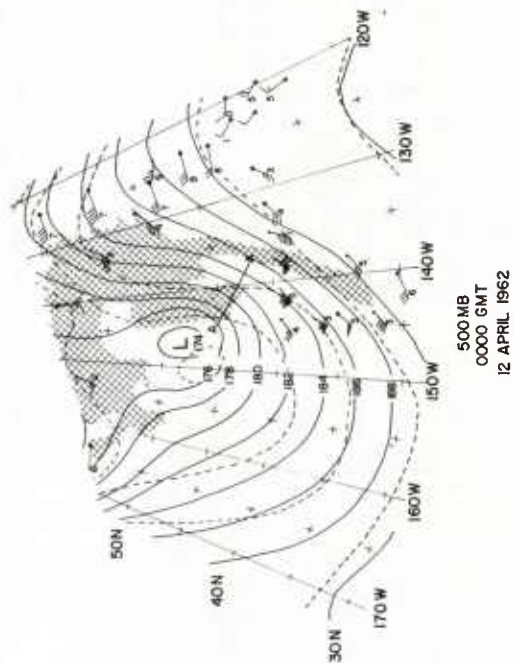
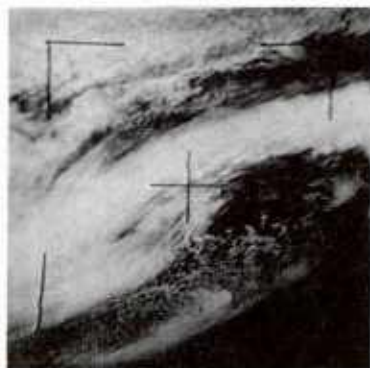
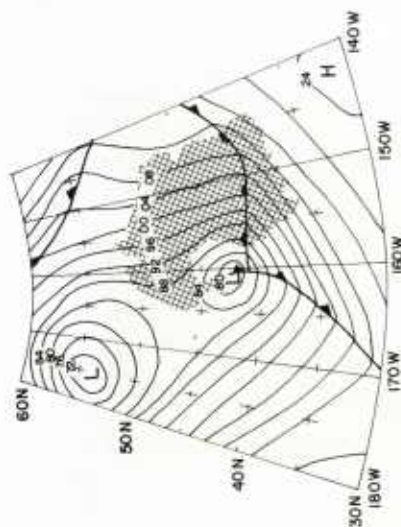
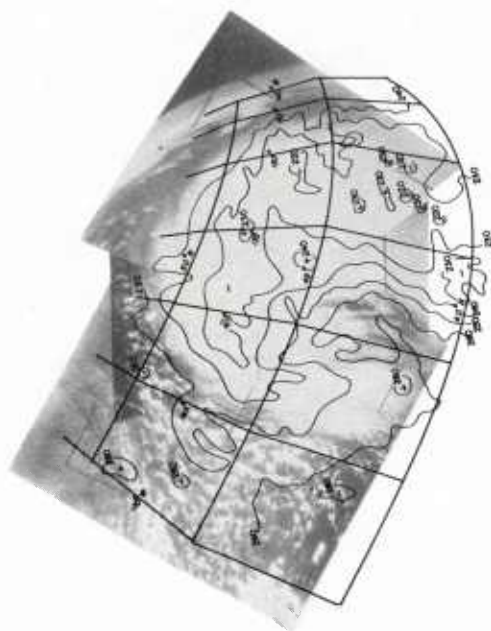
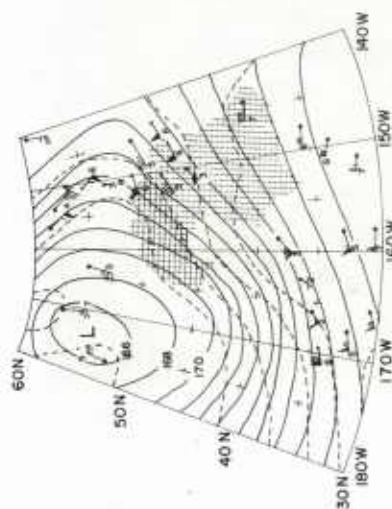


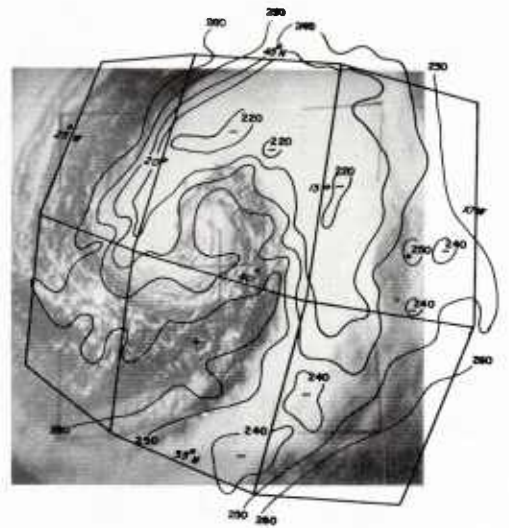
Figure 6 Example of Hook-Shaped Cloud Pattern Associated with Frontal-Wave Initial Stage.



SURFACE
0000 GMT
2 APRIL 1962



500 MB
0000 GMT
2 APRIL 1962



2. Cyclogenesis in a Developing Baroclinic Zone

Initial Stage

The initial satellite observed cloud pattern is often the comma-shaped cloud mass associated with and just to the east of the mid-tropospheric vorticity maximum (Fig. 3). As development becomes significant, the cloud mass takes on a more crescent-shaped appearance (Fig. 7).

At this and subsequent stages, it may be possible to see lower level cumuliform cloud to the southwest of the concave edge of the predominant pattern formed by the middle and higher cloud overcast. When visible, the pattern of these cumulus may define the low-level circulation. Infrared data are, of course, desirable to permit clearly distinguishing between upper and lower level cloudiness.

It is to be noted that the satellite data, of course, provide no specific information on the cloud distributions under the highest layer of opaque cloudiness. Deductions in these regards must await further case studies using concurrent satellite, aircraft and conventional data, and on models developed from such studies. While there is at present no high probability of ultimate direct satellite observations of such multiple-layer cloudiness, future developments in the microwave radiometer field may possibly contribute to satisfying this requirement.

Both the comma and crescent cloud patterns owe their shape to the pattern of upward vertical motions (principally those due to vorticity advection) ahead of the short wave trough. Accordingly, the western edge of these patterns signifies a wind across itself with a velocity component in excess of the displacement of the cloud pattern and the trough with which it is associated. Because an air parcel crossing the trough line must usually rise some significant distance before condensation occurs, the western edge of the comma is typically some 200 miles downstream from the trough line. The concave shape of this western edge derives from the fact that the air passing through the equatorward portion of the trough undergoes the greatest descent and drying while in the region to the west of the trough line. The eastern edge of the comma or crescent shaped cloud lies approximately along or slightly to the east of the 500 mb ridge line, where the air passing through the cloud-covered area has again entered a region of sufficient descent and drying for the cloud particles to re-evaporate.

Stage of Rapid Intensification

As in the case with a frontal cloud band, a cloud pattern with a distinct hooked shape (Fig. 8) approximately coincides with closing off the circulation at the 500 mb level (which may or may not coincide with the first closed 500 mb contour), and with the stage of most rapid intensification and deepening. The comma or even the crescent shape pattern and its associated short wave may progress along the mid-tropospheric flow for a few days without significant development (as might be expected from the earlier discussions) before finally either dissipating or intensifying. The appearance of the hook-shaped stage, however, usually signifies a high probability of the development of a major storm, which will complete the full cyclone cycle.

In the hook-stage, the advection of previously formed cloudiness first forms a significant part of the pattern, that in the equatorward portion of the western part of the hook. Here, the winds in the middle troposphere can be deduced as blowing from cloud to clear at the end of the hook, and along any striations that may be visible in this area. The remainder of the middle and upper level cloud is due to upward vertical motion. Patterns of low level cumuliform clouds are most likely to be evident at this stage.

Both this development sequence and that starting with the frontal wave produce (in the terms used in our morphological description) hook-shaped patterns (Figs. 8 and 6). In both cases the associated cyclone is in a stage of rapid development and will proceed to a mature stage. However, the meager infrared data processed so far indicate the hook-shaped patterns (from the two different development modes) differ in size and in the location of the high cloud top area, i. e. that with blackbody temperatures of 230°K or less. Comparison of Figures 8 and 6 shows the frontal wave case has a smaller area enclosed by the 230°K isotherm, and lacks the tapered southern extensions evident in the other situation. This difference probably results from different initial cloud conditions and vertical motion patterns.

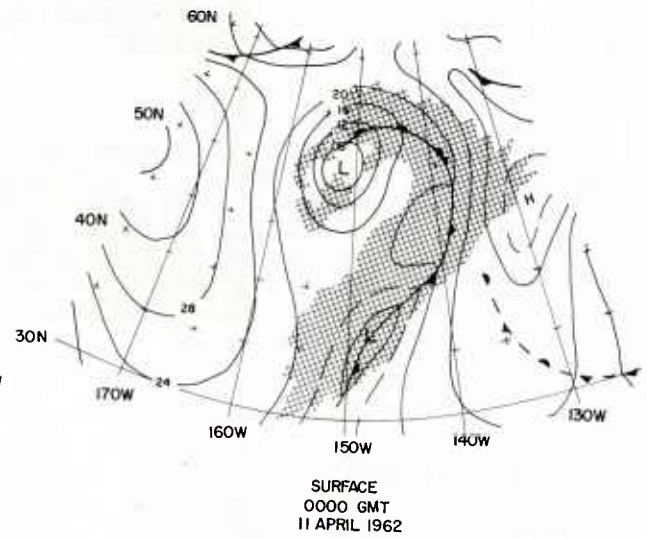
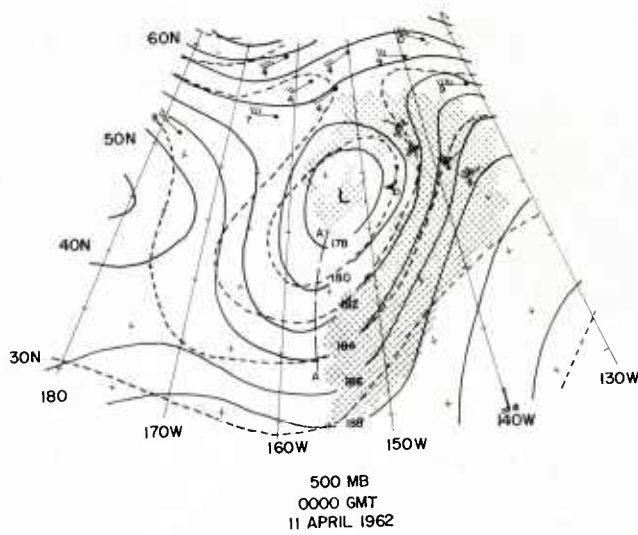
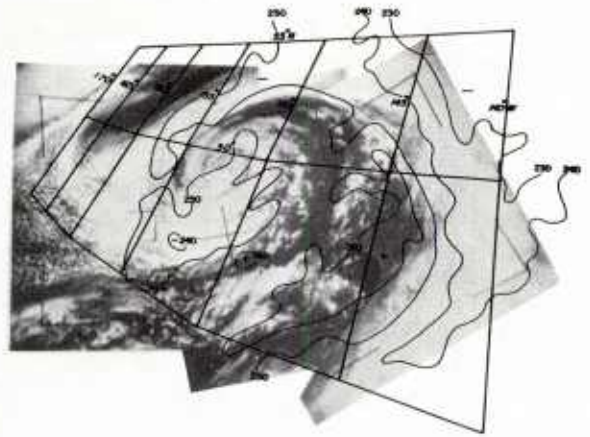


Figure 9 Example of Mature Extratropical Cyclone.



Figure 10 Nimbus I High Resolution Infrared Observation of a Mature Cyclone Near Kamchatka. White Areas are Cold (high clouds); Grey Areas Cool (low to middle clouds); Black Areas Warm (clear or low clouds).

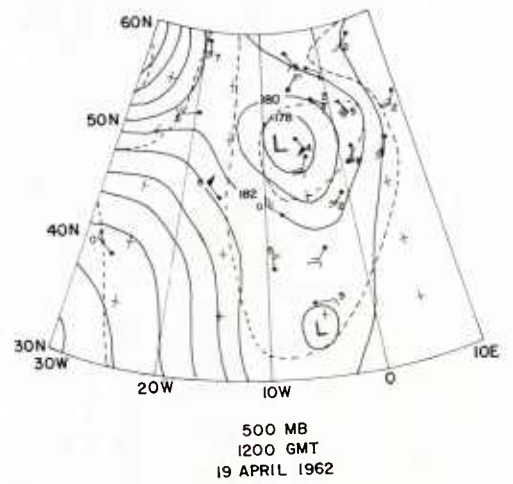
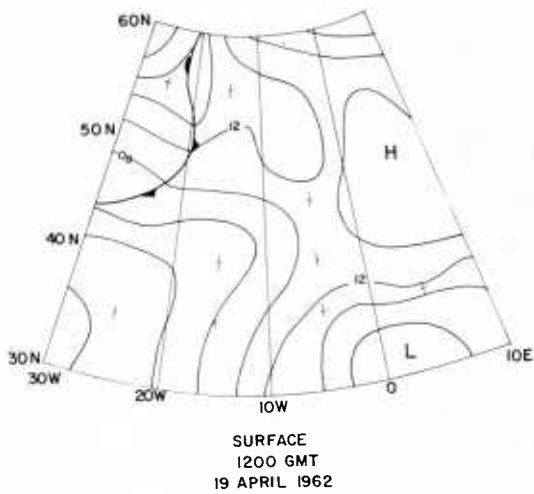
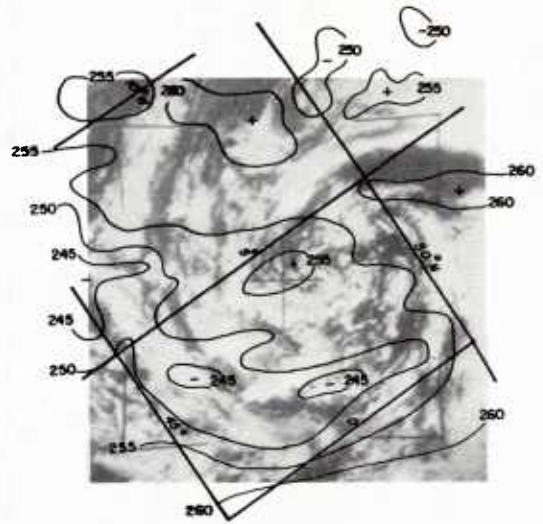
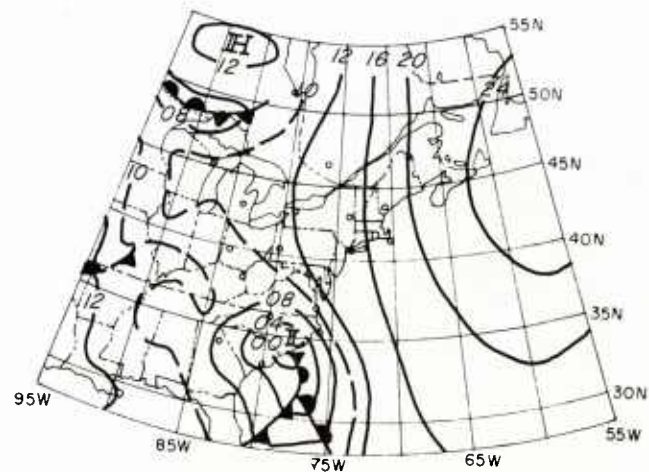
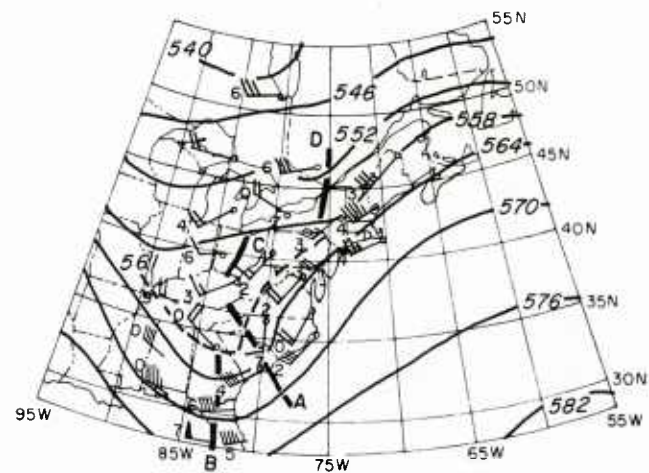
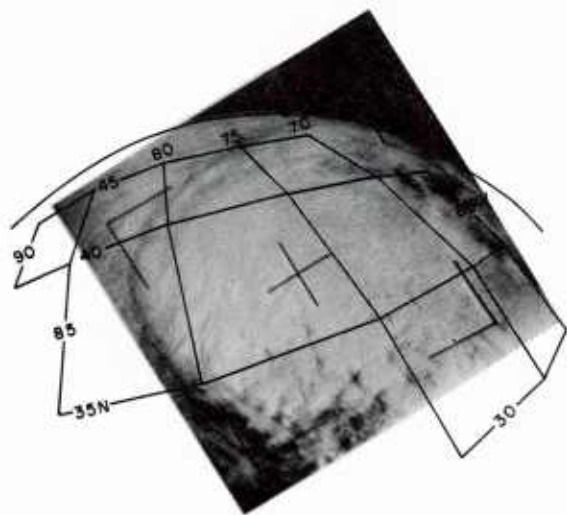


Figure 11 Example of a Decaying Cyclone.



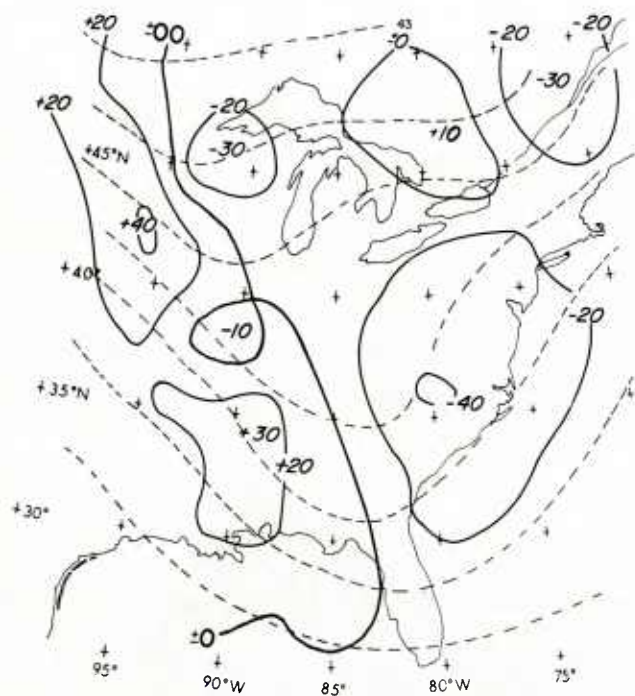


Figure 12b Quasi-geostrophic 500 mb Vertical Motions in Units of 10^{-4} mb sec^{-1} (solid lines), and 500 mb Contours at 60 meter Intervals (dashed lines) for 1200 GMT, 6 November 1963.

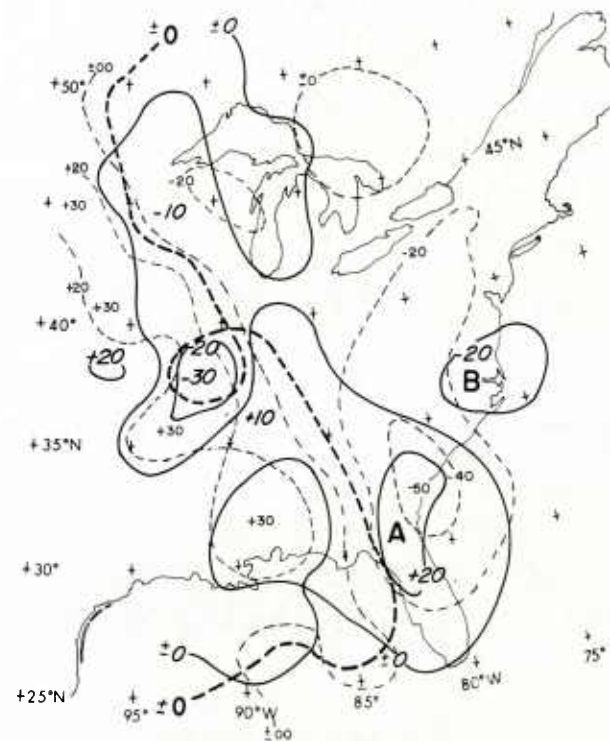


Figure 12c 500 mb ω_T (solid lines) and ω_V (dashed lines) in Units of 10^{-4} mb sec^{-1} for 1200 GMT, 6 November 1963. Heavy Dashed Line is ± 00 ω -Isopleth from Figure 12b.

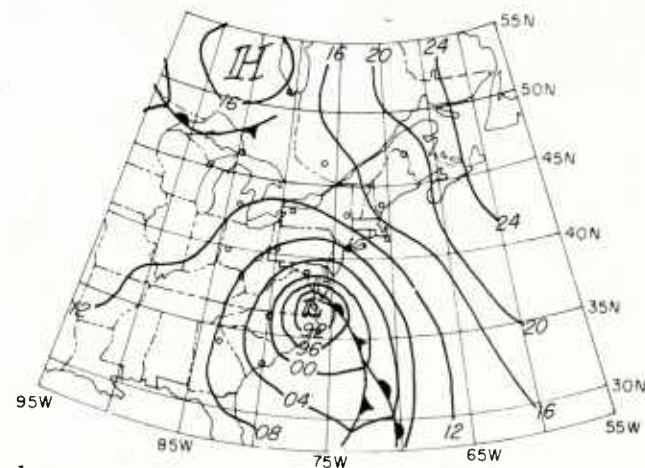
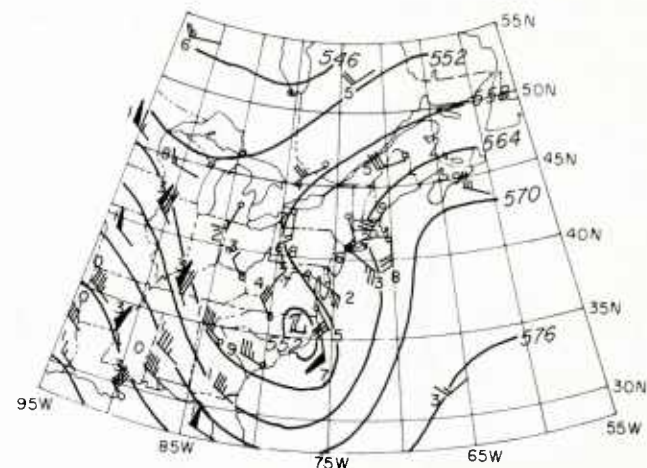
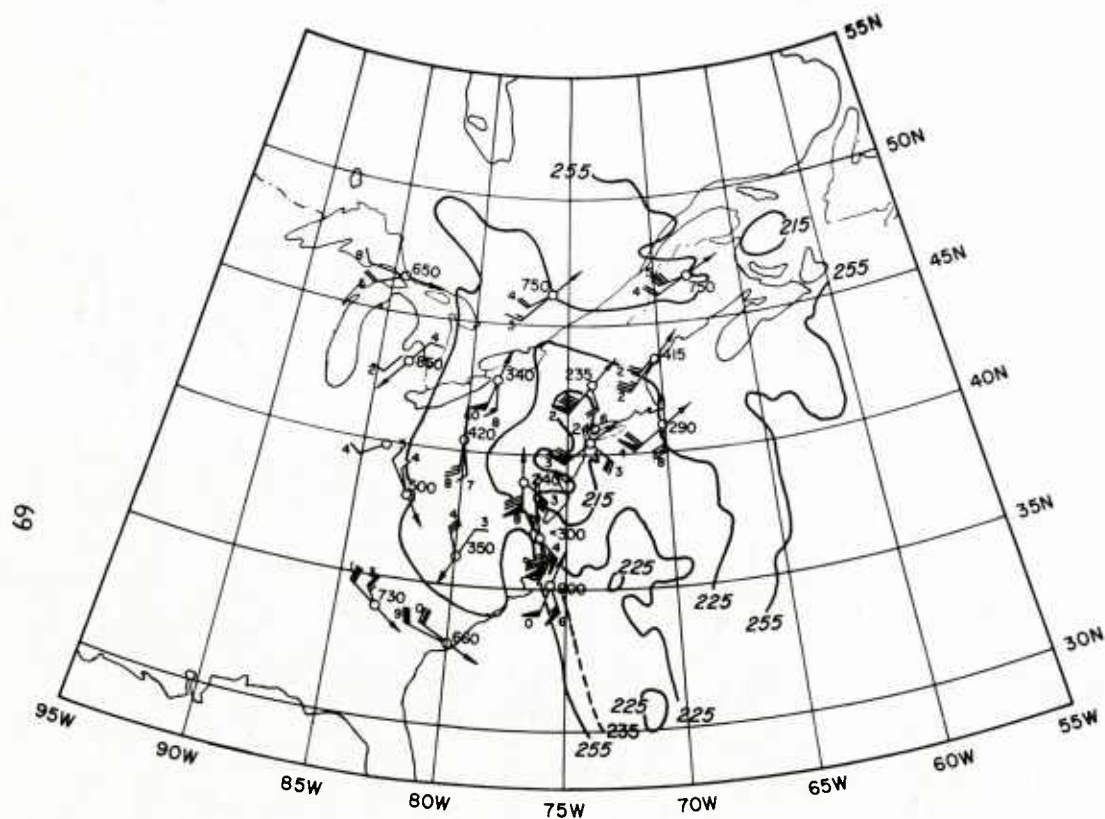


Figure 13a Satellite Infrared Data for 2037 and 2219 GMT, 6 November 1963, and Conventional Data for 00 GMT, 7 November 1963. IR Data Consist of Isopleths for Selected, Uncorrected Black-body Temperatures for 8-12 μ Radiometer Channel of TIROS VII for Orbits 2077 and 2078 (hook stage).

In the frontal wave case, little cloud exists in the dry air at these high levels in the initial stage (Fig. 5). As the mid-tropospheric short wave interacts with the frontal zone area, the associated upward vertical motion ahead of the trough is only able to produce a small area of cloud at these high levels. In the cloud-identified mid-tropospheric short wave case, initially there is a large area of high cloud, since the vertical motion area has been operating on relatively moist air for some time (Fig. 7). This large cloud area is modified into the hook-shape as the vertical and horizontal motion fields evolve [19].

In both cases, the cyclone associated with the hook-shaped pattern is in a stage of rapid development and leads to a mature stage whose cloud pattern is common to the two types of development sequences. Because the time interval between the hooked-pattern and mature stage is short (of the order of 12 hours), little satellite and/or conventional evidence is available as to the details of the respective evolutions of the two hook-shaped patterns to the mature stage. Therefore, the next stage in our model is the mature stage.

3. Mature Stage

The most vivid and aesthetically interesting spiral patterns (Fig. 9) coincide with the mature or most intense stage of the cyclone, and often for some period thereafter. The equatorward, western portion of the outermost major spiral band is principally due to advected, previously formed, cloudiness. The inner spiral bands are due either also to advection, or to lower level cloudiness. Again, infrared data are required to unambiguously distinguish the cloud levels, although an experienced interpreter can usually draw reasonably reliable inferences.

The clear spiral shaped areas, between the spiral bands, are due to strong, thermal advection-related, subsidence; or to very dry air with a previous history of strong and long subsidence.

The basic spiral pattern may be modulated by local areas that appear particularly bright in the television pictures, and/or are very cold (high cloud tops) in the infrared data (Fig. 10). Such areas are often those of more intense cloud cover and precipitation. They seem to be associated with two conditions: (a) short wave troughs within the system, which may be remnants of the original short wave, or additional short waves that moved into the system; and (b) poleward moving portions of the internal spiral bands.

4. Decaying Stage

As the system dissipates, the cloud patterns become more random and cumuliform (Fig. 11). They are principally the results of the advection of previously formed clouds. The patterns are at times still relatively spiral in appearance, and to the inexperienced analyst may suggest a more intense circulation than actually exists.

V - Preliminary Results of Calculations of the Vertical Motions

Recently calculations have been made of the vertical motions associated with a satellite-observed extratropical cyclone which moved along the eastern coast of the United States. The Philips [11] - Sanders [9] 10-level model was used for these calculations, permitting separate determinations of the vorticity and thermal advection components. The vertical motions are provided in terms of $\omega = dp/dt$.

Since only partial results are yet available, only the 500 mb level values for two stages (comma and hook) will be discussed. Figure 12 shows a TIROS picture and neph-analysis of the cloud pattern at the comma stage of development, and the associated patterns of the ω values at 500 mb. Figure 13 shows the hook stage, about 12 hours later, as depicted by the TIROS Channel 2 data, and the related vertical motion patterns.

In both cases, it can be seen that the cloud and total vertical motion patterns are well correlated. In the comma stage, the $\omega = 0$ isopleth, like the trough line, is slightly upstream of the western cloud edge. In the hook stage, an area of total downward ω is located near the southern end of the concave clear area or "slot."

When the vertical motions are presented in terms of their components, it is seen that ω_V (the vorticity advection component, that associated with the mid-tropospheric trough) predominates at the comma stage. There is also some ω_T (thermal advection component), although much less than the ω_V . It is to be noted that ω_T is downward not only west of the

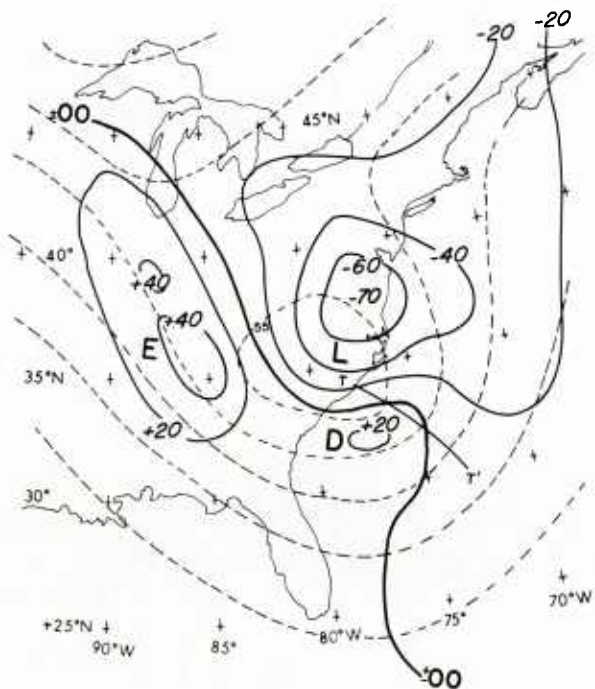


Figure 13b Quasi-geostrophic 500 mb Vertical Motions in Units of 10^{-4} mb sec $^{-1}$ (solid lines), and 500 mb Contours at 60 Meter Intervals (dashed lines) for 0000 GMT, 7 November 1963.

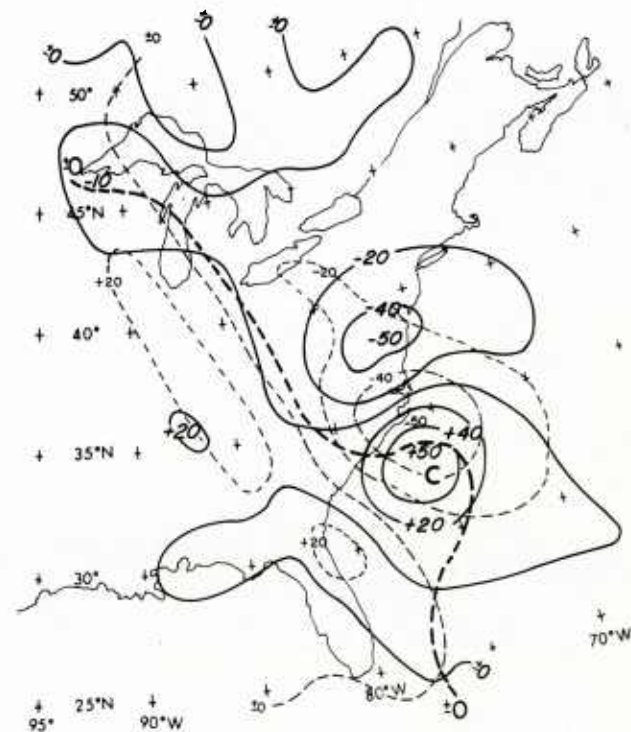


Figure 13c 500 mb ω_T (solid lines) and ω_V (dashed lines) in Units of 10^{-4} mb sec $^{-1}$ for 0000 GMT, 7 November 1963. Heavy Dashed Line is ± 00 ω -Isopleth from Figure 13b.

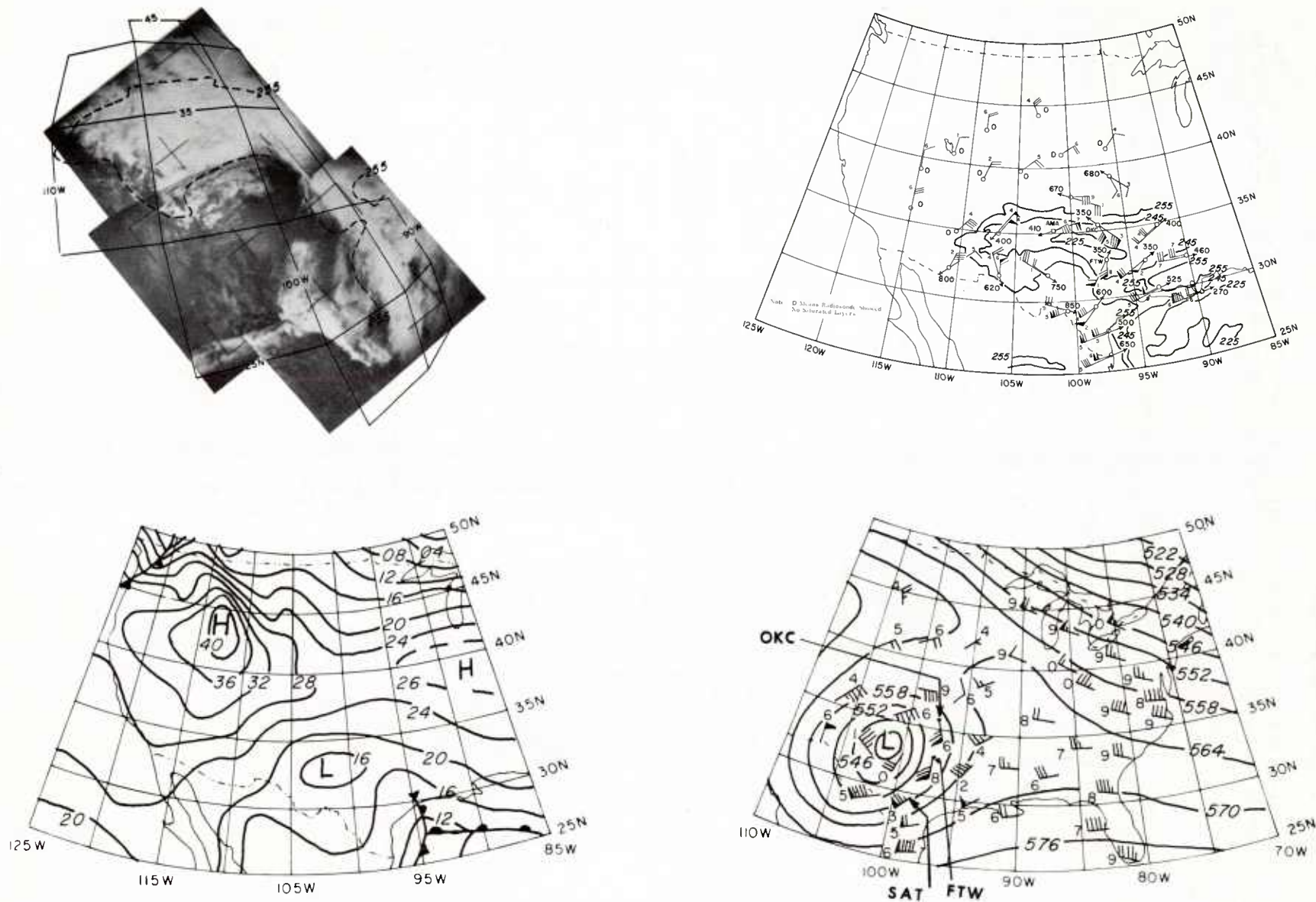


Figure 14 TIROS Picture, Channel 2 Analysis, and Surface and 500 mb Charts, for an Upper Level Cyclonic System.

500 mb trough (where ω_V is also downward), but also in an area east of the 500 mb trough and southwest of the position of the surface low (an area where ω_V is upward, as it is in all areas east of the 500 mb trough).

At the hook stage, it is apparent that the situation has already changed. ω_T now predominates over ω_V ; and in particular produces the downward total ω area south of the clear "slot."

VI - Upper-Level Cyclones

A study by Sherr [18] has shown that the cloud patterns associated with upper level extratropical cyclones (Fig. 14) derive from the same basic principles of clouds formed by vertical motion and subsequently advected. Upper level cyclones can often be identified as such from the satellite data by their narrower cloud bands and the lack of low level cumulus in organized patterns.

Sherr's studies of these cyclones also showed that, when a cloud top col can be identified in the satellite data, the wind near the cloud tops can be deduced to be blowing along the valley axis of the col.

VII - Operational Applications of the Above Concepts and Model

Studies and operational experience with satellite observations associated with extratropical cyclones show they can be usefully applied in operational practice for:

1. Short wave trough identification and tracking
2. Trough and ridge line analysis and placement, as discussed above
3. Storm stage deductions and qualitative prognosis
4. Cloud distribution determinations, both present and prognostic (especially by considering the probable areas of cloud formation and advection)
5. Determinations of the most likely areas of more intense precipitation (the brighter or higher cloud areas, associated with short waves within the system)
6. Determinations of approximate wind directions at levels near the cloud tops
 - (a) Across the western edges of vertical motion produced cloud pattern areas
 - (b) Parallel to advectively produced portions of cloud pattern
 - (c) Parallel to the valley axes of cloud top cols.

Still other operational applications of the satellite data which have been known for some time, including those associated with vortices, are discussed in Reference 20.

VIII - Speculations as to the Role of Upper-Level Vorticity Maxima in the Very Early Stages of Frontal Wave Development

A major matter of concern must be how the upper level vorticity maxima and the lower level baroclinic zones interact to produce cyclonic development. Since the associated vertical motions are critical in such developments, calculations suggest that the mid-tropospheric disturbance and its vorticity advection are the more critical aspects in setting off development. The lower and middle level baroclinic conditions, and the associated thermal advection, subsequently become predominant. They continue and accelerate the development, supplying the energy necessary to allow a cyclonic system to proceed through the typically observed sequence (also see Reiter [24]).

Before speculating on the possible role of the mid-tropospheric disturbances in cyclogenesis, we should examine some of the physical processes associated with the vertical motion fields.

Sanders [9, 10], following Phillips [11], has stated the omega equation in the form:

$$\left[\nabla^2 + \frac{f_o^2}{\sigma} \frac{\partial^2}{\partial p^2} \right] \omega = - \frac{f_o}{\sigma} \frac{\partial}{\partial p} \left(- \bar{\mathbf{V}} \cdot \nabla \eta \right) - \frac{R}{p\sigma} \nabla^2 \left(- \bar{\mathbf{V}} \cdot \nabla T \right) - \frac{1}{\sigma} \nabla^2 H$$

where

$$\sigma \equiv (\partial \phi / \partial p)(\partial \ln \theta / \partial p),$$

$$\omega \equiv dp/dt, \text{ is the measure of vertical motion}$$

and

$$f_o = \text{a constant value of the Coriolis parameter}$$

$$p = \text{pressure}$$

$$\bar{\mathbf{V}} = \text{wind velocity}$$

$$\eta = \text{absolute vorticity}$$

$$R = \text{the Gas Constant}$$

$$T = \text{temperature}$$

$$H = \text{the effect of diabatic heating}$$

$$\phi = \text{geopotential}$$

$$\theta = \text{potential temperature}$$

$$t = \text{time}$$

Inspection of this equation shows that the first term on the right, the vorticity advection forcing function, is principally kinematic in nature. That is, it includes no significant energy conversion processes; it merely states how the vertical motions will proceed as a result of the kinetic energy that is already available in the system. Development in the sense of increased total kinetic energy, or significant conversion of thermal energy, is dependent on the thermal advection and diabatic heating forcing functions (the second and third terms on the right).

Synoptic experience suggests, and calculations confirm, that the mid-tropospheric subsynoptic waves are largely barotropic in nature, and that the associated vertical motions derive principally from the vorticity advection forcing function. (This is doubtless not completely true, but the departures from these conditions appear to be only of the order of those necessary to compensate for the frictional losses of these systems.) Accordingly, and as is observed, we would seldom expect to see significant development of these wave systems unless they are in a position to interact with conditions favorable to energy conversion.

What then, is the likely role of these waves in leading to cases of cyclogenetic development. It would appear that it is principally of the nature of creating an environment more favorable to development than had previously existed. The required energy for development must come from elsewhere. (Presumably this is also the role of these waves in areas of augmented convection, as we will consider briefly later.)

The satellite data, of which the case in Figure 2 is reasonably typical, often clearly show a disturbance in the lower level baroclinic zone (along the frontal zone, as shown by the beginning of a bulging of the cloud band into the cold air) well before the mid-tropospheric trough has come to a position where it intersects the low level trough. Thus, the initial process is, at least typically, not the direct hydrostatic creation of a surface low center. If it was, one might suggest that the transformation of the surface trough to a surface low center led to a rearrangement of the low level flow (in a manner perhaps analogous to the Brunt-Douglas isallobaric winds) such that thermal advection could begin to play its role.

GENERATION OF EDDY AVAILABLE POTENTIAL ENERGY

Significant

Negligible

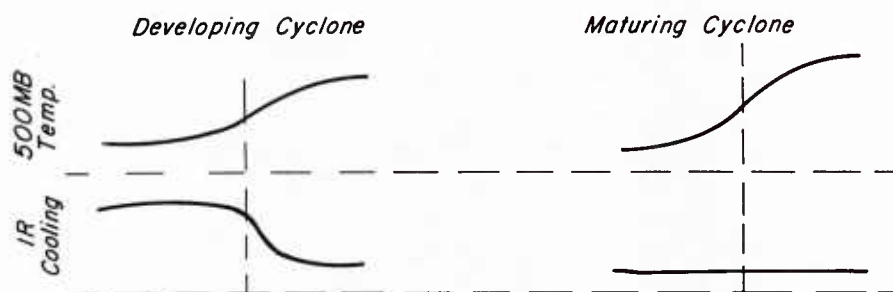
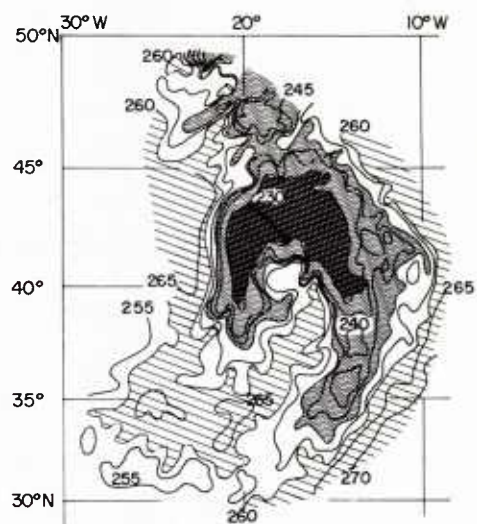
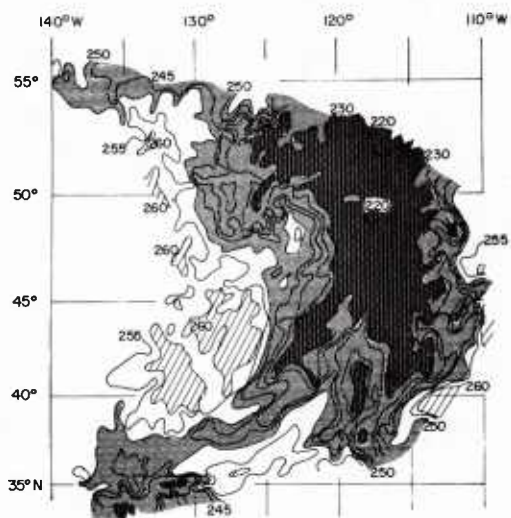


Figure 15

The satellite data show, however, a sharp eastern edge to the cloud mass associated with the mid-tropospheric trough, presumably indicative of a subsynoptic ridge ahead of the trough. Furthermore, the earliest developments along the lower level frontal cloud band are typically in evidence while there is still a clear region between the eastern edge of the clouds associated with the mid-tropospheric trough and the western edge of the frontal cloud band. Presumably, this denotes a subsynoptic region of anticyclonic flow, with a polar component, in the mid-troposphere.

Principally as a basis for further investigation, one can speculate as to the following possible model of the processes occurring at these early stages of the development:

1. The subsynoptic mid-tropospheric ridge might first operate hydrostatically to create a surface micro-ridge just to the west of where the surface low center will come into existence. This hypothesis is strengthened by common synoptic experience; the first signs of a developing wave on the surface chart are often the transformation of a small portion of a pre-existing stationary front into a distinct cold front, and the associated backing of the surface winds on the cold air side of the front.

2. This model creates the question, however, as to why such a subsynoptic surface ridge would not just move along with the upper ridge, essentially wiping out successively more easterly portions of the surface trough. At this point, we can only speculate that:

- (a) the reorganization of the low level flow, due to the creation of the subsynoptic ridge, might somehow lead to the formation, just to its east, of a micro-low with cyclonic flow (as is observed in synoptic practice) (Reiter [24] also discusses this problem)

- (b) the southerly flow isobarically induced to the east of such a newly formed low could lead to positive thermal advection and upward vertical motion at low levels.

- (c) as the mid-tropospheric ridge moves across such a new surface low, it might act as a warm ridge, and the associated upper level divergence be adequate to maintain the low and its associated region of upward vertical motion, until

- (d) the region of mid-tropospheric, vorticity advection induced, upward vertical motion (east of the upper trough) could move over the newly developed area of low level, thermal advection forced, upward vertical motion.

From this point on, the development proceeds as outlined in Section III.

IX - A Suggested Role of the Distribution of Clouds in Mature and Decaying Extratropical Cyclones

Another topic deserving of study is the possibility that cloud patterns formed during the life cycle of a typical extratropical cyclone may turn out to be a significant factor influencing its rate of dissipation.

Various studies, such as those of Suomi and Shen [21] and of Corcoran and Horn [22] have shown that the distribution of outgoing infrared radiation in the vicinity of troughs and cyclones tends to generate eddy available potential energy. (Eddy available potential energy is used here in the sense defined by Lorenz [23].) This results from the tendency towards more high cloudiness to the east, than the west, of the center of the cyclonic systems.

Corcoran and Horn noted, however, that the rate of generation was inversely correlated with the wave length of the cyclonic systems. It would seem reasonable to associate this finding with the observed sequence of cloud patterns described earlier. As noted then, as a cyclonic system develops beyond the point of a closed 500 mb circulation, the area covered by the system enlarges and middle or high cloud cover is advected, progressively, further into the western and southwestern parts of the system. This increasing symmetry of cloud cover must lead to an increasing symmetry of radiative cooling (Fig. 15). This in turn leads to a decrease in the generation of eddy available potential energy, since the generation of eddy available potential energy is given by the integration, over the volume of interest, of the product of the temperature and the rate of cooling.

Based on these associations, it would appear that the circulations established during cyclonic development re-distribute the cloud cover in such a way that the radiative generation of eddy available potential energy is reduced. Obviously this is only one of the processes acting. Nevertheless, it must certainly play somewhat the role of a "governor" in controlling the rate and extent of cyclonic development during the later stages of the life cycle of

cyclones, and ultimately in their decay. Perhaps the most significant question is the relative magnitude of the radiative effects compared to those of the other processes that are acting concurrently.

Let us consider the various factors of concern in somewhat more detail. Although the details of the energy conversion processes are not entirely clear, it is generally accepted that the kinetic energy of a cyclone is largely derived from eddy available potential energy. Such energy is created when cold air to the north and/or west of the system comes in juxtaposition with warm air to the south and/or east. Prior to significant closing-off of the circulation, there is little to impede the inflows of air that can replenish the eddy available potential energy. Furthermore, in these early stages of the system, the cloud and associated infrared radiative patterns are such as to further generate eddy available potential energy. This has been shown in the above referenced discussions of Suomi and Shen [21], and of Corcoran and Horn [22].

As a cyclone develops, there is typically a period of rather rapid intensification. This period is concurrent with the significant closing-off of the circulation and with the early stages of a vertical and horizontal expansion of the closed circulation. About the same time, horizontal advection begins to bring cloud into and around the western side of the system, leading to an increasing symmetry of the cloud covered areas.

Following this typically short period of rapid development, both the rate and extent of further development is minimal. The mature storm may persist without significant change for some period of time. Eventually the storm weakens and dissipates, except in the case of new disturbances entering it.

These latter stages of the life cycle appear to be due to a number of factors:

1. Due to the closed circulation, the contrasting air masses, which are a source of eddy available potential energy, are detoured around the storm. Accordingly, they can no longer feed energy to its central region. Most new or associated developments now form and intensify to the south and/or east of the region of closed circulation. In these peripheral regions the contrasting air masses can come into juxtaposition and create a new, localized region with significant eddy available potential energy.
2. Although some additional eddy available potential energy may be generated within the closed circulation area, due to cross-isobar convergent flow in the lower layers, the rate cannot be large. Furthermore, as the area of closed circulation expands, geometrical factors cause the size of the area of the closed circulation (which is a factor in energy dissipation) to increase as the square of the radius of closed circulation. On the other hand, the circumference, which influences the amount of inflow, increases only proportional to the radius. Thus, the area (and so the dissipative potential) increases more rapidly than the circumference (and so the energy producing inflows).
3. The increasing symmetry of the cloud cover first decreases, and eventually stops, radiative generation of eddy available potential energy.

All of these three factors, plus surface friction, operate together to prevent an unlimited expansion of the size and kinetic energy of the system, and thus act as a governor.

The principal source of energy dissipation is, at least ultimately, surface friction. It will thus be appropriate to consider the relative rates of:

1. Surface frictional dissipation
2. Energy generation due to cross-isobaric convergence
3. Actual energy generation due to radiative factors
4. Probable radiative generation in the hypothetical case of no horizontal cloud advection and the consequent persistence of a highly asymmetrical cloud pattern.

Surface friction is presumably the primary dissipative process, and the rate of dissipation increases with surface wind velocity. It is thus interesting to note that, after a cyclone reaches maturity, the surface wind velocities often drop off while the circulation aloft persists at a more significant intensity. This produces a low level buffer against strong frictional dissipation. Accordingly, the generation of even limited amounts of eddy available potential energy might well be sufficient to maintain the upper air circulations for a rather extended period of time.

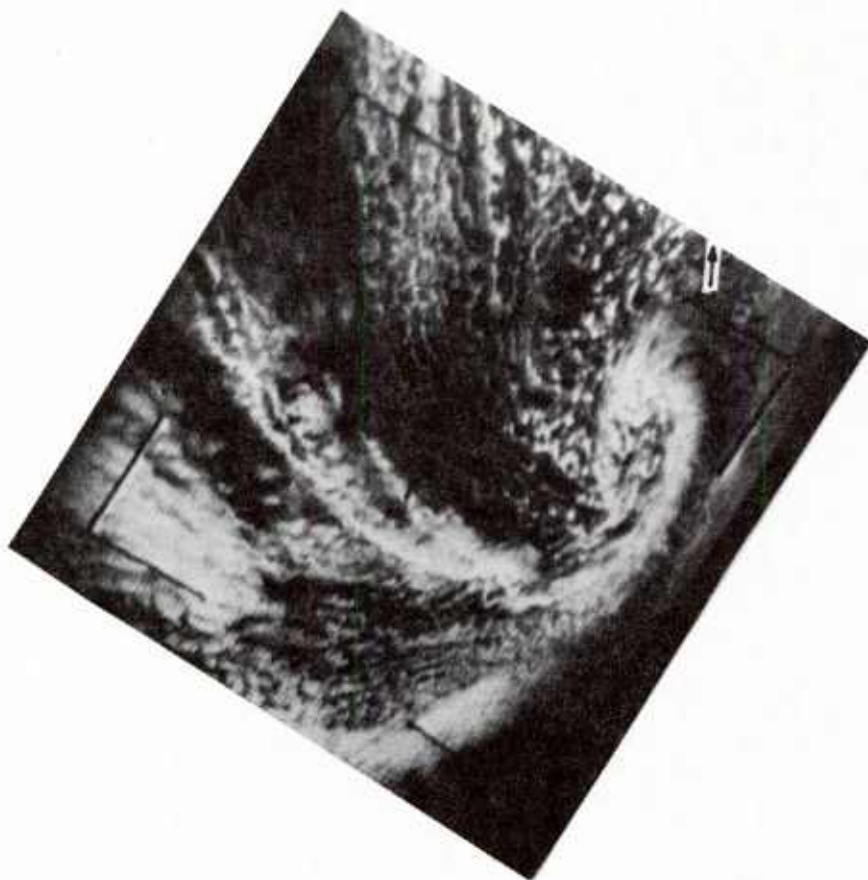


Figure 16 Spiral Cumuliform Pattern Associated with
A Short Wave Trough in Northwesterly Flow.

Suomi and Shen [21] state (based on some frictional dissipation estimates which they admit are rather gross) that:

"The available potential energy produced (by infrared radiative effects on certain dates) is close to that removed by friction" over the area 30-50N, 40-180W.

They later conclude:

"The average value of generation by infrared cooling for the cases studied in this paper is less than the estimated value of dissipation by friction but equal to or greater than the estimates of eddy generation from other sources. More cases must be studied to determine whether this mode of generation of eddy available potential energy is an important meteorological phenomenon or merely a straw added to a bonfire."

Based on the above discussion, we suggest the following hypothesis, which it would appear desirable to test:

"The relatively symmetrical cloud patterns established, by horizontal advection, about a mature cyclone prevent the generation of eddy available potential energy by differential rates of radiative cooling. This energy generation would otherwise be sufficient, when combined with any other sources of generation such as cross-isobar convergence, to significantly prolong the life of the cyclone beyond that observed in nature."

If this hypothesis proves correct, it would indicate that, in diabatic numerical models of the general circulation, provision must be made for cloud cover in areas other than just those of significant upward vertical motion. The subsequent horizontal advection of cloud cover, until the three-dimensional flows cause dissipation, must also be incorporated.

X - Other Considerations Needing Further Study

1. Subsynoptic Scale Perturbations

More attention needs to be focused on the sources and effects of subsynoptic scale perturbations in the planetary flow. Likely source possibilities include (a) areas of dynamics (or inertial) instability at the crests of sharp mid-tropospheric ridges, or where there is excessive anticyclonic shear; in this case, the trajectory cusp [7] which frequently is found downstream is a manifestation of the instability; (b) air flow over significant topographical barriers, or traveling waves propagating out of standing lee waves; and (c) the remnants of dissipated cyclonic systems. There is also a need to give more attention to means of locating, analyzing, following, and predicting the future positions of these disturbances than is now common in operational practice. Unfortunately, the scale of these waves is such that they are usually smoothed out by the operational numerical weather prediction procedures and analyses. An encouraging sign is provided by the grid telescoping procedures being studied by Hill [8]. One would hope that ultimately significant developments within the telescoped area would be used to modify the grosser mesh grid, as well as Hill's present use of the grosser grid to update the boundary conditions of the smaller area.

The satellite data can serve a vital role in identifying and following these subsynoptic wave disturbances. One of the basic problems in operationally identifying them is that frequently no single type of data is adequate for non-ambiguous identification. Although these waves are often accompanied by clouds, certainly no one is prepared to accept every anomalous patch of cloudiness as evidence of a subsynoptic wave disturbance. On the other hand, the primary evidence of these disturbances in conventional data is often only a cyclonic wind shift of the order of $10-20^\circ$. This is of the same order as the uncertainty between two conventional wind measurements. Another condition is an equivalent singularity in the wind speed or shear (Saucier once showed that the conditions associated with a small wind shift in the lower troposphere are analogous to those associated with a localized speed maximum at nearer jet stream levels). Inspection of an upper level map to detect each such wind shift or shear is tedious and time consuming, and even those that are found leave the question as to whether they are real or only a result of observational system limitations.

Anomalous cloudy areas, frequently composed of enhanced convective cloudiness, are easily identified in the satellite data, however, and immediately flag the areas deserving of such a search, especially if the clouds form a comma-shaped or spiral pattern (Fig. 16). If

even a small cyclonic wind shift or shear exists just upwind of such a cloud mass, the combined evidence suggests a subsynoptic wave. The persistence of these cloud and/or wind indicators on successive charts makes the case even more convincing.

As discussed in Section VIII, one role of these mid-tropospheric vorticity disturbances is to produce a more favorable environment for cyclogenesis. In other cases, their role is to produce a more favorable environment for convection. This environment presumably results from a decrease in mid-tropospheric stability due to either or both (a) vertical stretching, due to the upward vertical motion area just ahead of the wave, and (b) the small area of somewhat lower mid-tropospheric temperatures that will exist near the trough (to the degree these waves are quasi-geostrophic). But the wave can only create a more favorable environment; the required energy for creating the augmented convection must come from elsewhere (for example, from surface heating of the air due to either solar radiation or cold advection).

In the region of equatorward flow to the west of a planetary trough, the degree to which subsynoptic waves are associated with cloudiness and/or the initial stages of cyclonic development depends on the relative strengths of (a) the small scale area of upward vertical motion just ahead of the wave, (b) the large scale subsidence associated with the region between the upstream planetary ridge and the downstream planetary trough, and (c) the low level cold advection relative to the surface sources of heating.

2. Development of Mid- and Upper-Tropospheric Closed Circulations in Baroclinic Cyclones

The actual processes leading to the formation of the upper level closed low, and the closing off of the circulation and contours at levels well above the surface, are still not understood. There are some indications that this may be more associated with an upward propagation of the initial surface level closed low than with the mid-tropospheric trough. There are suggestions that at least the equatorward portion of the initial, mid-tropospheric short wave trough may remain a separate, identifiable entity which continues to move around the storm center, and to serve as a focus of an area of more intense weather.

3. Developments Due to Short Wave Troughs Within the Storm

These include:

1. Any effects of the three alternate sources: (a) original; (b) new waves that propagate in; and (c) those that form within storm
2. The differentiation between:
 - (a) Those that will move out of the system to the east, often with secondary formation and relatively rapid dissipation of the original cyclone
 - (b) Those that will remain and circulate within the original system, maintaining or re-intensifying (see Figs. 1e and 1f, and p. 313 of Reference 19) it, or producing local areas of more intense weather.

4. Continental-Oceanic Differences

The differences, if any, between cyclogenesis over the continents and over the oceans are still open to question. The cloud patterns associated with oceanic cyclogenesis at times appear to be more distinct. If this reflects a real and basic difference, deductions drawn from the continental cases (where better conventional data networks aid the analyses) may not be universally applicable.

XI - Acknowledgements

The studies whose results, in part, have been reported here were made possible only by the support provided, at various stages, by the National Environmental Satellite Center of the Environmental Science Services Administration; the Goddard Space Flight Center of the National Aeronautics and Space Administration; and the Air Force Cambridge Research Laboratories.

References

1. Shaw, N.: Manual of Meteorology, Volume I, Meteorology in History, Cambridge University Press, 343 pp., 1942.
2. Bjerknes, J., and H. Solberg: "Life Cycle of Cyclones and Polar Front Theory of Atmospheric Circulation," Geophysics Publication, 3(1), 1922.
3. Bjerknes, J., and J. Holmboe: "On the Theory of Cyclogenesis," Journal of Meteorology, 1, pp. 1-22, 1944.
4. Sutcliffe, R. C.: "A Contribution to the Problem of Development," Quarterly Journal of the Royal Meteorological Society, 73, pp. 370-383, 1947.
5. Petterssen, S.: "A General Survey of Factors Influencing Development at Sea Level," Journal of Meteorology, 12, pp. 36-42, 1955.
6. Oliver, V. J., and E. W. Ferguson: "The Use of Satellite Data in Weather Analysis," Satellite Data in Meteorological Research, Technical Note No. 11, National Center for Atmospheric Research, pp. 85-101, 1966.
7. Angell, J. K.: "Use of Constant Level Balloons in Meteorology," Advances in Geophysics, 8, pp. 137-219, Academic Press, New York, 1961.
8. Hill, G.: "Grid Telescoping in Numerical Weather Prediction," paper presented at Joint Technical Exchange Conference, NWS-AWS, Monterey, Calif., 1967.
9. Sanders, F.: Further Research Directed Toward the Study of Relations of Atmospheric Flow to Weather, Final Report, Contract No. AF 19(604)-8373, Massachusetts Institute of Technology, 1963.
10. Sanders, F.: Large-Scale Vertical Motion and Satellite Cloud Photographs, Final Report, Contract No. Cwb-10843, Massachusetts Institute of Technology, 1965.
11. Phillips, N. A.: See Sanders, F., A. J. Wagner, and T. N. Carlson: Specification of Cloudiness and Precipitation by Multi-Level Dynamical Models, Scientific Report No. 1, Contract No. AF 19(604)-5491, Massachusetts Institute of Technology, 1960.
12. Petterssen, S., G. Dunn, and L. L. Means: "Report of an Experiment in Forecasting of Cyclone Development," Journal of Meteorology, 12, pp. 58-67, 1955.
13. Boucher, R. J., and R. J. Newcomb: "Synoptic Interpretation of Some TIROS Vortex Patterns: A Preliminary Cyclone Model," Journal of Applied Meteorology, 1(2), pp. 127-136, 1962.
14. Widger, W. K., Jr.: "A Synthesis of Interpretations of Extratropical Vortex Patterns as Seen by TIROS," Monthly Weather Review, 92(6), pp. 263-282, 1964.
15. Nagle, R. E., J. R. Clark, and M. M. Holl: "Tests of the Diagnostic-Cycle Routine in the Interpretation of Layer-Cloud Evolutions," Monthly Weather Review, 94(2), pp. 55-66, 1966.
16. Barr, S., M. B. Lawrence, and F. Sanders: "TIROS Vortices and Large-Scale Vertical Motion," Monthly Weather Review, 94(12), pp. 675-696, 1966.
17. Sherr, P. E., and C. W. C. Rogers: The Identification and Interpretation of Cloud Vortices Using TIROS Infrared Observations, Final Report, Contract No. Cwb-10812, ARACON Geophysics Company, Allied Research Associates, Inc., 1965.
18. Rogers, C. W., and P. E. Sherr: Toward the Dynamical Interpretation of Satellite-Observed Extratropical Vortical Cloud Patterns, Final Report, Contract No. Cwb-11123, ARACON Geophysics Division, Allied Research Associates, Inc., 1966.
19. Widger, W. K., Jr., C. W. C. Rogers, and P. E. Sherr: "Looking Down on Spirals in the Sky," American Scientist, 54(3), pp. 288-314, 1966.

References (cont)

20. Widger, W.K., Jr., P E. Sherr, and C.W.C. Rogers: Practical Interpretation of Meteorological Satellite Data, Air Weather Service Technical Report No. 185, 1965.
21. Suomi, V.E , and W.C. Shen: "Horizontal Variation of Infrared Cooling and the Generation of Eddy Available Potential Energy," Journal of the Atmospheric Sciences, 20(1), pp. 62-65, 1963.
22. Corcoran, J. L, and L.H. Horn: "The Role of Synoptic Scale Variations of Infrared Radiation in the Generation of Available Potential Energy," Journal of Geophysical Research, 70(18), pp. 4521-4527, 1965.
23. Lorenz, E.N.: "Available Potential Energy and the Maintenance of the General Circulation," Tellus, 7(2), pp. 157-167, 1955.
24. Reiter, E.R.: Jet-Stream Meteorology, The University of Chicago Press, 515 pp., 1961.

THE NEED FOR OBJECTIVE OBSERVING AND REPORTING OF SOLAR FLARES

by

Captain Hans J. E. Fischer
Detachment 54, 6th Weather Wing

ABSTRACT

The paper discusses errors and their sources in the historical solar flare records covering the period from 1955 to 1964. The major sources of error are: (1) Inconsistent and frequently changed reporting formats submitted by individual observatories to world data centers, (2) a variety of different units of measure, (3) redundant information in flare reports, and (4) the present practice requiring observers to perform unnecessary computations on raw data. A flare report format is suggested to minimize errors stemming from handling of the data before it is published.

I. INTRODUCTION

An investigation by Fischer et al [1] of flares that were reported by 62 observatories during the period from 1955 to 1964, uncovered systematic errors and random mistakes in observing and reporting. This paper discusses the general disposition of the flare data and the areas where improvements in observing and reporting are urgently needed if data of this type is to be used in routine operational forecasting of solar events. It is not the intent of this paper to discuss the inhomogeneities in flare observations resulting from differences in instrumentation at the various observatories, but rather, to stress systematic errors and mistakes due to a lack of standardization of observing and reporting procedures. The topic will be covered under two general areas: (1) The reporting habits and the flare report formats, and (2) superfluous manipulations of the flare data by observers. Subsections under these main areas will amplify the varying format arrangement among observatories, the use and misuse of units of measure, redundant information in the report, and the present practices which requires observers to perform other computations. A flare report format is suggested summarizing proposed improvements in the reporting of flare observations. It is hoped that this paper will make users aware of the deficiencies in the historical records of flare observations, and that it will serve as a guide in formulating observing and reporting procedures for observatories belonging to the Solar Observing and Forecasting Network (SOFNET) of the Air Weather Service.

Fischer et al found an error of 12.5% in flare reports published by ITSA* (in the CRPL-F, Part B Series) and an error of 11.2% in flare reports published by the IAU** (in the Quarterly Bulletin) on basis of consistency checks and comparison of identical reports in both sources. Figure 1 summarizes their results in terms of the number of discrepancies which were accredited to errors either in the CRPL series or in the Quarterly Bulletin (QB). The CRPL list is only a tentative working list of the re-checked and edited compilation of the same reports in the QB. Therefore Fischer et al accepted the version of the reports in the QB whenever related information in correcting discrepancies was unavailable. For this reason, the number of discrepancies in the CRPL series is much higher than that in the QB, particularly when discrepant flare areas are not counted. (Discrepancies in the flare areas will be discussed in the following section). The actual number of discrepancies in flare position are nearly ten times greater than shown in Figure 1, because Fischer et al did not consider flare positions discrepant unless reports in the CRPL series and the QB differed by at least four heliographic degrees in latitude, and six degrees in central meridian distance. However, all other entries were required to match exactly.

On the assumption that this additional number of small discrepancies in flare position is predominately in the CRPL series, the reliability of the flare data in the CRPL list becomes all the more questionable. The difference in the number of discrepancies between both publications is principally due to revisions that observatories made after reevaluation of their

* ITSA - Institute for Telecommunication Sciences and Aeronomy, ESSA, Boulder, Colorado

** IAU - International Astronomical Union

film records in preparation for publication of their flare lists in the QB. The necessity for these revisions demonstrates an inherent lack of discipline in the initial observing and reporting procedures. Laxity in observing and the ensuing formidable task of rechecking and editing flare reports are the underlying reasons that allow non-standardized reporting formats and observing practices to become prominent sources of error.

| Number of Erroneous Flare Reports (excluding sub-flares) in Flare Data (1955-1964) | | |
|---|-------------------------|----------------|
| Erroneous Entry | Discrepancies | |
| | CRPL-PART B (1955-1964) | QB (1955-1962) |
| Date | 8 | 1 |
| Station Identifier | 68 | 13 |
| Time | 2604 | 158 |
| Position | 570 | 219 |
| Importance | 335 | 10 |
| Areas | 1475 | 3128 |
| Total Discrepancies | 5060 | 3529 |
| Erroneous Reports | 4440 (12.5%) | 3506 (11.2%) |

Figure 1. Discrepancies and Erroneous Reports Found in the Flare Data on Basis of Consistency Checks and Comparison of Flare Reports in the CRPL-F, Part B Series and the Quarterly Bulletin (Fischer et al [1]).

II. REPORTING HABITS AND THE FLARE FORMAT

Figure 2 is an example of the flares which Krasnaya Pakhra (USSR) observed during July 1957 and submitted to the world data centers. The figure shows the type of flare information that is most commonly reported by all observatories. It also shows the general order in which the flare information appears in flare reports. The spectral measurements (columns 12 and 13) are frequently not reported. Discussion of these parameters will not be pursued further, although the following remarks are equally valid for these entries.

The order in which the flare parameters are reported varies among observatories. It often creates confusion and results in inadvertent errors in identifying columns of data, because all data columns are not always correctly and adequately labeled. Moreover, some observatories may not adhere consistently to one particular format arrangement. For example, Pirculi (USSR) during April 1960 reported seeing conditions between columns 1 and 2, while also reporting, in addition to heliographic latitude and central meridian distance, the redundant absolute longitude of flares between columns 6 and 7. Instead, column 11 was entirely deleted and only the measured area was reported. In January through March of the same year however, Pirculi used a similar format but without provisions to record seeing conditions. While there are numerous other examples, the combined effect of such non-standardized format

arrangement are runs of data in which similar looking numerical values of unrelated parameters are interchanged. At times, columns of data are unrelated to the flare observations. For example, Honolulu during September 3-28, 1959, reported data in the "time of measure" column which seemed to be irrelevant to the entire observation.

I.D.V. FLARE PATROL

Station *Krasnaya Pakhra*

Month *July*

VIZIR #82

Year *1957*

| Date | Time observed U. T. | | Time U. T. max. | Position | | Importance | Obs. Cond. | Time of Meas. U. T. | Meas. Area sq. deg. | Correct. Area sq. deg. | Max. width H & A | Max. Int. % | Remarks |
|------|---------------------|------|-----------------|----------|------------------|----------------|------------|---------------------|---------------------|------------------------|------------------|-------------|-----------|
| | Start. | End. | | Lat. | Cent. Mer. Dist. | | | | | | | | |
| 2 | 744 | 805 | 803 | -31 | -29 | I | 2 | 803 | 2,64 | 1,64 | | 0,84 | |
| | | 10 | | | | | | | | | | | |
| 2 | 822 | 826 | 824 | +10 | +30 | I ⁺ | 2 | 824 | 5,88 | 3,43 | | 0,77 | 5 |
| | 30 | 30 | 30 | | | | | 30 | | | | | |
| 2 | 829 | 830 | | -25 | +90 | I ⁺ | 2 | 830 | 1,18 | 6,02 | | 0,70 | 8 |
| | | 30 | | | | | | | | | | | |
| 2 | 839 | 929 | 918 | +09 | +31 | I ⁺ | 2 | 918 | 4,41 | 2,58 | | 1,05 | 5 |
| | | | | | | | | | | | | | |
| 9 | 935 | 940 | | +14 | +74 | I | 2 | 935 | 0,98 | 1,88 | | 0,70 | 4 |
| | 06 | 30 | | | | | | | | | | | |
| 9 | 912 | 935 | 918 | +06 | -69 | I | 2 | 918 | 1,08 | 1,50 | | 0,59 | |
| 10 | 950 | 1006 | | -12 | +1 | I ⁻ | 1 | 1055 | 1,18 | 0,61 | | 0,59 | |
| | | 30 | | | | | | 30 | | | | | |
| 15 | 708 | 716 | 710 | -32 | +12 | I | 2 | 710 | 1,08 | 0,57 | | 0,91 | |
| 16 | 734 | 810 | 757 | +33 | -84 | 2 | 2 | 757 | 1,37 | 7,50 | | 1,18 | |
| | | | 3 | | | | | 3 | | | | | |
| 16 | 836 | 851 | 842 | -34 | -31 | I ⁻ | 2 | 842 | 1,37 | 1,02 | | 0,77 | 5 |
| | 06 | 20 | | | | | | | | | | | |
| 17 | 636 | 713 | | +34 | -61 | 2 ⁺ | 2 | 636 | 6,86 | 4,09 | | 1,01 | 5 |
| 17 | 658 | 713 | 702 | -23 | -53 | I ⁺ | 2 | 702 | 2,35 | 2,21 | | 1,05 | 5 |
| | 45 | | 30 | | | | | 30 | | | | | |
| 17 | 702 | 717 | 711 | -34 | +35 | I ⁺ | 2 | 711 | 4,37 | 3,41 | | 0,70 | |
| | 30 | | | | | | | | | | | | |
| 17 | 833 | 833 | 834 | -38 | -22 | I ⁺ | 2 | 834 | 1,96 | 1,48 | | 1,15 | 4 |
| | 20 | 40 | 40 | | | | | 40 | | | | | |
| 17 | 1017 | 1026 | | -16 | +12 | I ⁻ | 2 | 1018 | 0,88 | 0,48 | | 0,54 | 5 |
| | 30 | | | | | | | | | | | | |
| 18 | 734 | 740 | 734 | -30 | -08 | I | 2 | 734 | 2,30 | 1,58 | | 0,80 | Start 175 |
| 19 | 821 | 839 | | -27 | -43 | I | 2 | 824 | 1,67 | 1,35 | | 0,70 | 5 |
| | | 40 | | | | | | | | | | | |
| 19 | 824 | 833 | 827 | -34 | +67 | I | 2 | 827 | 0,88 | 1,44 | | 0,84 | 4 |
| | | | 20 | | | | | 20 | | | | | |

Figure 2. Example of a Flare Record Submitted by Krasnaya Pakhra, USSR to World Data Center A, High Altitude Observatory, Boulder, Colorado.

The greatest number of errors resulting from interchanged columns of data have occurred in reports in which only the measured area or the corrected area were reported. Approximately one half of the discrepancies in the area entries in QB reports resulted from this type of error. All flare areas reported by the Sacramento Peak, Lockheed, and Climax observatories prior to November 1960 are measured areas and not corrected areas as published in the QB. In addition to the differences in the arrangement of reporting formats, there are other format details that constitute potential sources of errors. Principal among these is the order in which the time parameters of flares are arranged. In Figure 2 the order is start time, end time and time of maximum flare development. The format should reflect the chronological development of flares: Start time, time of maximum, and end time. Some support for the present arrangement may be found in the argument that the observer first "brackets" the time of flare maximum by determining the start and end time on the film before pinpointing the time of flare maximum. Nevertheless, a number of errors were found where the time of flare maximum or the time of measurement occurred after the end of a flare. One such case is the observation of July 10, 1957 in Figure 2. Reports from other observatories of the same flare suggest that the ~~end~~ time of the flare could be 1055 U.T. rather than 1006 U.T. and that these two times were interchanged.

Aside from inconsistencies in the format arrangement, a number of errors are related directly to the units in which flare areas are reported. The flare area is currently reported in any one of three units of measure (Figure 3). They are millionths of the solar disk, millionths of the solar hemisphere, and square heliographic degrees. (The last two units are defined at the center of the disk). The fundamental unit is millionths of the solar disk because it is the fraction of the area of the image of the solar disk on the photograph covered by the flare. The other units are redundant since they are derivatives of this fundamental measure. Common usage, however, has established the unit of millionths of the solar hemisphere and the unit of square degrees (recommended by the IAU) as the basic measure of the size of flares. As a result, conversion of millionths of the solar disk into these "more acceptable" units has contributed to errors in the area measurements and has caused confusion when the units in which the flare area was reported, were not explicitly stated.

An error of this type was made in the corrected flare areas in Figure 2. It will be noted that the measured area is almost always larger than the corrected area. The discrepancy appears to be an error in converting millionths of the solar disk into square degrees. Either the measured area is by a factor of two too large or the corrected area is too small by a factor of two. From the comparison of other reports of the same flare events, the corrected area appears to be erroneous; but the evidence is not conclusive, and both reported areas are suspect. It should also be noted that if only the corrected area had been reported (as often is the practice), this error would not have been discovered since the factor of two is easily absorbed in the wide range of numerical area values associated with each importance class. Errors of this type accounted for approximately 3/4 of all area discrepancies in the CRPL records and nearly all of the remaining area discrepancies in the records of the QB. It is therefore important to adopt only one unit of measure, preferably the fundamental unit of millionths of the solar disk, to eliminate conversion errors in future reports.

The last major source of errors are redundancies in the flare report. They are flare parameters which can be derived from other data in the report. The corrected area and the flare longitude fall in this category. The longitude of flares is reported by most Russian observatories in addition to central meridian distance. Knowing the heliographic coordinates of a flare's position, the longitude (L) can be conveniently recovered from the relation:

$$(1) \quad L = L_0 - 0.55t \pm \text{CMD}$$

where CMD is the distance of a flare from the sun's central meridian (east negative) in whole degrees, t is the start time of a flare in hours, and L_0 is the longitude of the prime meridian on that date. L_0 can be obtained from the American Ephemeris and Nautical Almanac for the appropriate year. The coefficient is based on a constant 27.27-day rotation period of the sun.

The most serious redundancy is the corrected area. Moreover, for reasons to be discussed in the next section, the corrected area is unreliable for flares that occur near the sun's limb. The immediate value of the corrected area to the observer lies in his ability to judge the importance class of a flare. For this purpose only a rough approximation of the true flare size is necessary and need not be reported. An estimate can be obtained directly from the photograph by means of an overlay on which small circles of unit area are calibrated

as a function of central distance. The McMath-Hulbert Observatory is currently using this method.

| AT CENTER OF DISK | | | |
|--------------------|--------------------------|----------------|------------------------------|
| Millionths of Disk | Millionths of Hemisphere | Square Degrees | Relation to Importance Scale |
| 200 | 100 | < 2.06 | Sub-flares |
| | | = 2.06 | Importance 1 |
| 500 | 250 | = 5.15 | |
| 1200 | 600 | = 12.4 | Importance 2 |
| 2400 | 1200 | = 24.7 | Importance 3 |
| | | > 24.7 | Importance 4 |

1 square degree = $\begin{cases} 97 \text{ millionths of the disk} \\ 48.5 \text{ millionths of hemisphere} \end{cases}$

1 degree heliographic = $\frac{1}{360}$ of solar circumference = 12,150 km

1 sq. degree = 1.476×10^8 sq. km of solar surface

Figure 3. Units of Measure Currently Used in Reporting Flare Area. (Recommendations of the Working Group for Commission 10 at the 12th General Assembly of the IAU, Hamburg, Germany).

From a statistical viewpoint, the time of measurement (column 9, Figure 2) is also of questionable value. Investigators of flare data generally assume that area measurements of flares are made at the time of flare maximum. This is frequently the case, and both time parameters are often identical. It has therefore become the practice in analysis of flare data to substitute the time of measurement for the time of flare maximum when the time of flare maximum is missing. This temptation is hard to resist particularly in those cases where the time of flare maximum is unknown and the start and end times are poorly defined. Furthermore, the distinction between the time of measurement and the time of flare maximum adds little to the assessment of all flares in those cases where a difference between these times is significant. In terms of reliability, simplicity, and clarity of the flare data, it seems therefore in the best interest of the user to eliminate the absolute flare longitude, as well as the corrected area and its time of measurement from the report format.

III. MANIPULATION OF FLARE DATA BY OBSERVERS

A major source of errors in the flare data are computations that the observer has to perform to convert the observation into the present format of the flare report. These computations involve specifically the determination of heliographic coordinates and the calculation of corrected area, as well as the conversion of units of measure which was discussed in the preceding section. The heliographic coordinates are determined by means of a Stonyhurst disk (a circular overlay of heliographic coordinates) which is centered on the enlarged image of

the sun and oriented with respect to the sun's apparent north point. The flare position can be read directly. Although the operation is fairly simple and can be quickly performed, there is considerable margin for error. The observers must choose one from among a set of six overlays corresponding to two months of the year; he must then orient the overlay right-side-up or up-side-down with respect to the north point depending on the correct month in question; and finally, he must insure that the circular overlay is accurately centered to prevent gross errors in the position of flares near the edge of the solar disk.

To prevent mistakes in manipulating the overlays, a comparably simple method is suggested which is similar to the one used in determining sunspot positions. The position of a flare would be determined and reported in terms of its distance from the center of the solar disk and a position angle measured clockwise (eastward) from the north point on the photograph (See Figure 5). The distance from the center is expressed in fractions of the radius of the solar disk image. Computer processing of the positional data at the world data centers, or at intermediate collecting agencies, can convert these measurements into conventional heliographic coordinates. According to Addey [2] the heliographic latitude (B) and the heliographic longitude (L) of a flare is given by:

$$(2) \sin B = \sin B_0 \cos D + \cos B_0 \sin D \cos Q$$

and

$$(3) \sin (L-L_0) = \sin Q \sin D \sec B$$

D is the distance of the flare from the center of the disk, and Q is found from the position angle of the flare by subtracting P, the position angle of the north end of the sun's axis. B_0 is the latitude of the earth, and L_0 is the longitude of the sun's prime meridian. The three quantities P, B_0 , and L_0 can be obtained from the American Ephemeris and Nautical Almanac.

Observers are also required to determine the corrected area of flares since flares appear as foreshortened structures in the chromosphere as a result of the curvature of the solar surface. To assess the true size of flares, the apparent or measured area (MA) of flares is corrected by means of the formula

$$(4) CA = MA \sec \theta$$

where θ is the heliocentric angle of the flare, and CA is the corrected flare area. This correction becomes infinite at the limb, and observatories have used different correction methods (some subjective) beyond certain distances from the center of the solar disk. The lack of knowledge of the exact form of these corrections and the distances beyond which they were applied, introduce uncertainties into the corrected flare area. For these reasons, it is also difficult to recover the measured flare area when only the corrected area is reported.

Figure 4 shows the mean correction that observatories have applied. The dashed curve represents the secant correction, and the solid curves are the mean corrections of five per cent of all observatories that consistently applied either high or low corrections over all central meridian distances. For example, the corrected area of a flare at 80° central meridian distance and near the solar equator can differ among observatories by as much as a factor of 1.7. This difference is much greater for flares at the limb and away from the solar equator. The practice of reporting corrected area is therefore a disservice to the user because it masks the uncertainties in the corrected area, and where only the corrected area is reported, it denies the user the opportunity to apply uniform corrections to all areas. The time and effort spent by observers in computing corrected area and heliographic coordinates could be used more productively in more careful observing and reporting of all flare parameters.

The suggested format improvements and measuring techniques can best be summarized in the form of the suggested flare report format in Figure 5. The information in the report is divided into three general categories: (1) Information associated with the observation (the date, the station, the seeing condition and possibly other entries such as the type of observation), (2) the basic flare report (where and when a flare occurred), and (3) additional measurements supplementing the basic report.

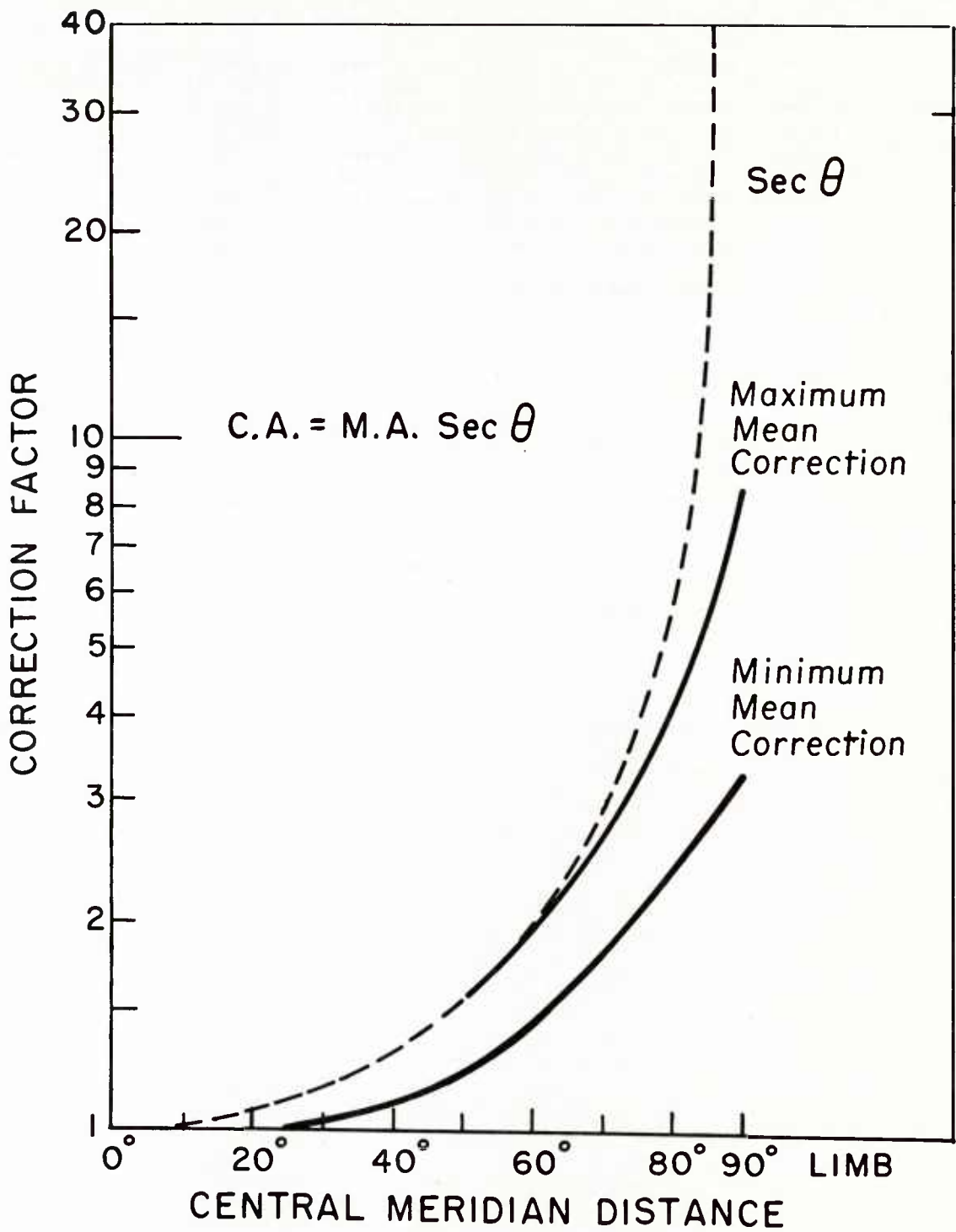


Figure 4. Curves Depicting the Geometrical (dashed) and Actual (solid) Corrections Applied by Observatories to Adjust for Foreshortening of Solar Flares.

| Associated Observational Information | | | Basic Flare Data | | | | | Supplemental Measurements | | | |
|--------------------------------------|------|------------------|------------------|----------------------------|----------|------------------------|--------------------|--|------------------------------|-------------|-------------------------|
| Station | Date | Seeing Condition | Observed Time at | | | Position Angle Degrees | Central Distance % | Observed at Time of Maximum Flare Brightness | | | |
| | | | Start U.T. | Max. Flare Brightness U.T. | End U.T. | | | Importance | Apparent Area 10^{-6} S.D. | Intensity % | H α Line Width Å |

Seeing Condition

Poor - 1
Fair - 2
Good - 3

Position Angle

Measured Clockwise
From Apparent North
Point of Disk;

Central Distance

Fraction in Percent
of the Radius of Solar
Disk from Apparent
Center:

Apparent Area

Flare Area in
Fraction of the Total
Area of the Disk $\times 10^6$

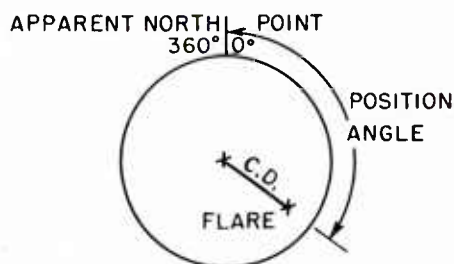


Figure 5. A Suggested Flare Report Format

This proposed format differs from the present one in several important aspects. The corrected area and the time of measurement are deleted in an effort to streamline the format and to prevent misinterpretation of entries. The columns of the end time and time of maximum development of flares are interchanged to follow the chronological development of flares. Finally, the flare position is reported as a distance and position angle relative to the center of the solar disk, and the apparent flare area is given in units of millionths of the solar disk. The principal advantage of this format is that it eliminates potential sources of error of the type discussed in the foregoing sections. Also, it reduces the work load of the observer and allows uniform application of corrections and conversions of all data since the flare parameters are reported in terms of their fundamental measurements. Implementation of such format, however, requires timely automatic or semi-automatic central computer processing so that the flare data is accessible to the user in conventional form.

IV. SUMMARY

Errors and discrepancies in flare reports published in the CRPL-F, Part B Series and the Quarterly Bulletin for the years 1955-1964 are due predominately to inconsistent observing and reporting practices. They are most evident in flare reports submitted by individual observatories to the world data centers and reflect a lack of discipline in data handling. This laxity is in part responsible for the large number of errors that have occurred as a result of inconsistent, frequently changing, and poorly arranged reporting formats; data redundancies in the reports; proliferation of units of measure; and unnecessary computations and manipulation of flare data by observers. A flare report format is suggested from which error sources of this type have been eliminated. In conjunction with computer processing, the format will minimize errors stemming from handling the data before it is published.

Awareness of deficiencies in the observing and reporting procedures is, however, not the whole solution toward improving the quality of the flare data. There still exist the

exceedingly difficult problem of describing the complex flare phenomenon by simple, objective means. Nevertheless, standardization of observing and reporting procedures is a first step toward reliable observations and one that can be realized with present resources.

REFERENCES

- [1] Fischer, H. J. E., and Jensen, D. C.: "Collected and Corrected Solar Flare Reports, 1955-1964," AFCRL Special Reports, No. 50, AFCRL-66-483, 21 pp., July 1966.
- [2] Addey, F.: "The Calculation of the Coordinates of Sunspots," British Astronomical Association Journal, Vol. 68, pp. 309-313, 1958.

A SOLAR FLARE VIDEOMETER

by

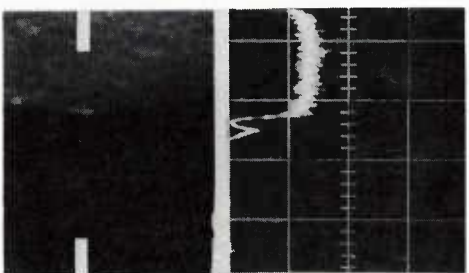
Paul E. Tallant
Sacramento Peak Observatory
Sunspot, New Mexico 88349

I. Introduction

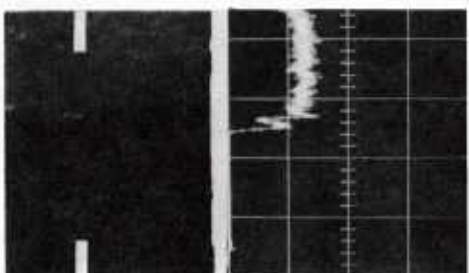
Measurement of flare area and intensity as functions of time have been used for a number of years to describe, in part, the temporal characteristics of a flare event. Richardson in 1939 measured the projected flare area from $H\alpha$ photographs and multiplied the resulting value by a visual estimate of the brightness to obtain an approximate integrated intensity. This parameter was obtained for several successive photographs of the flare event and thus an indication of the integrated intensity as a function of time was obtained. Giovanelli in 1940 made visual estimates of intensity during the progress of a flare. He compared the intensity of the flare image with that of an image of a headlight lamp filament attenuated by an optical wedge to match the flare intensity. Mohler in 1947 made intensity measurements of selected points in a flare from spectroheliograms made in the $CaIIK$ line and in 1949 Dodson made similar measurements from $H\alpha$ spectroheliograms. Others--Barton; Newton; Barton, Laurie, and Rhodes have measured the central intensity in $H\alpha$ as a function of time. These measurements usually were made on the brightest region of the flare. In 1952 Newkirk made isophotal contour maps of five frames of the $H\alpha$ image of the 22 July 1950 flare. This work was done by use of a direct recording microdensitometer. In 1953 Billings and Roberts, using an electronic contour densitometer, analyzed nine frames of the $H\alpha$ image of the 12 April 1950 flare. They measured the area contained within given contours, measured contour brightness as a function of the enclosed area, and obtained the integrated intensity by a measurement of the area under the brightness vs area curve. Dodson, Hedeman, and McMath in 1956 made a rather extensive analysis of the characteristics of the time behavior of flare intensity obtained from photometric measurements of $H\alpha$ spectroheliograms. These characteristics were compared with ionospheric effects observed during the course of the various flares. In 1960 Abramenko, Dubov, Ogir, Steshenko, Shaposhnikova, and Tsap described the results of photometric measurements of 14 flares which included measurements of the intensity and area as functions of time. This work was a continuation of an earlier one in 1959. This brief review is indeed not comprehensive but serves to indicate the interest over a number of years in photometric measurement of flares.

Throughout the literature one is impressed with the large amount of effort required to obtain even a rather meager photometric time history of a flare. This arises primarily from the methods that are imposed when one wishes to reduce a flare from film records. To measure area it is necessary to determine an isophotal contour and then measure the enclosed area. This either requires special instrumentation as used by Billings and Roberts or one may obtain this information from suitable processing of microdensitometer tracings. A localized measurement of intensity may be made in a straightforward manner with a densitometer. With this instrument the density of a small portion of the flare image can be measured for each frame and from this the intensity may be determined. To obtain a more complete history of the intensity behavior, these measurements are usually made for several different portions of the flare. Integrated intensity is perhaps the most difficult to obtain, since it is a function of both area and intensity. To accurately determine this parameter it is necessary to measure the area and obtain the intensity distribution within the measured area. In essence one needs to measure the volume of a solid, the base of which is bounded by a selected flare isophot and the height determined by the intensity distribution within the isophotal boundary. Since these measurements and associated computations are necessary for each film frame selected, it rapidly becomes evident that a nontrivial amount of effort is required.

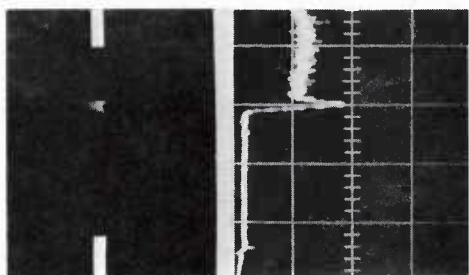
At Sacramento Peak we have a closed circuit television system that is used to display the $H\alpha$ images provided by the telescopes on the flare patrol spar. It was recognized by Dunn at Sacramento Peak that the information required to obtain flare area, peak intensity, and integrated intensity in real time was inherent in the video signal provided by the television



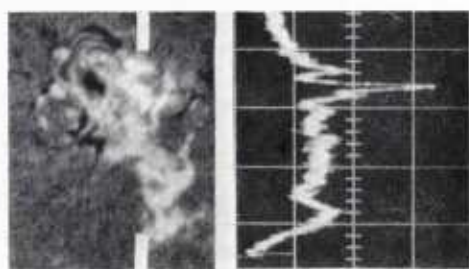
SURGE
MAR. 20, '66 UT 19:10



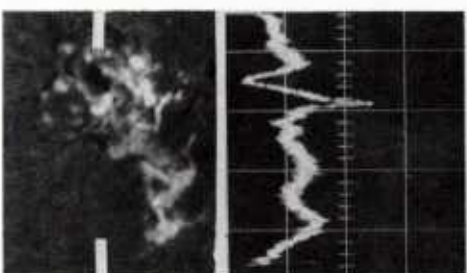
SURGE
MAR. 20, '66 UT 19:13



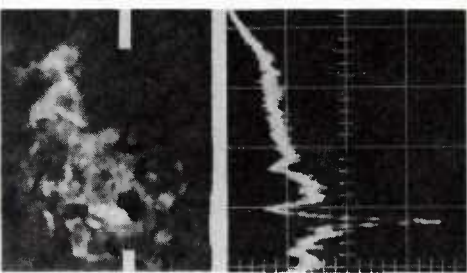
SURGE
MAR. 20, '66 UT 20:23



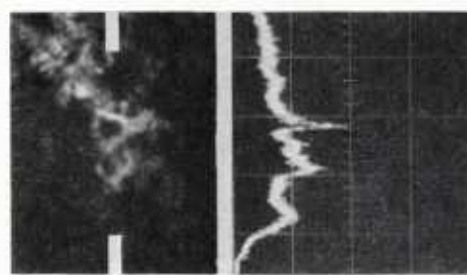
CLASS 1 FLARE
MAR. 20, '66 UT 18:53



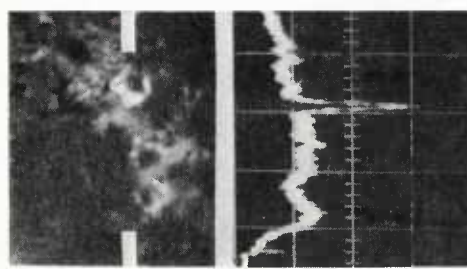
CLASS 1 FLARE
MAR. 20, '66 UT 18:59



CLASS 1 FLARE
MAR. 20, '66 UT 20:03



CLASS 0 FLARE
MAR. 21, '66 UT 14:23



CLASS 1 FLARE
MAR. 21, '66 UT 15:10

100^r
—

VIDEO WAVEFORMS OF FLARES AND SURGES

Taken with the Quad Telescope
Sacramento Peak Observatory

Figure 1.

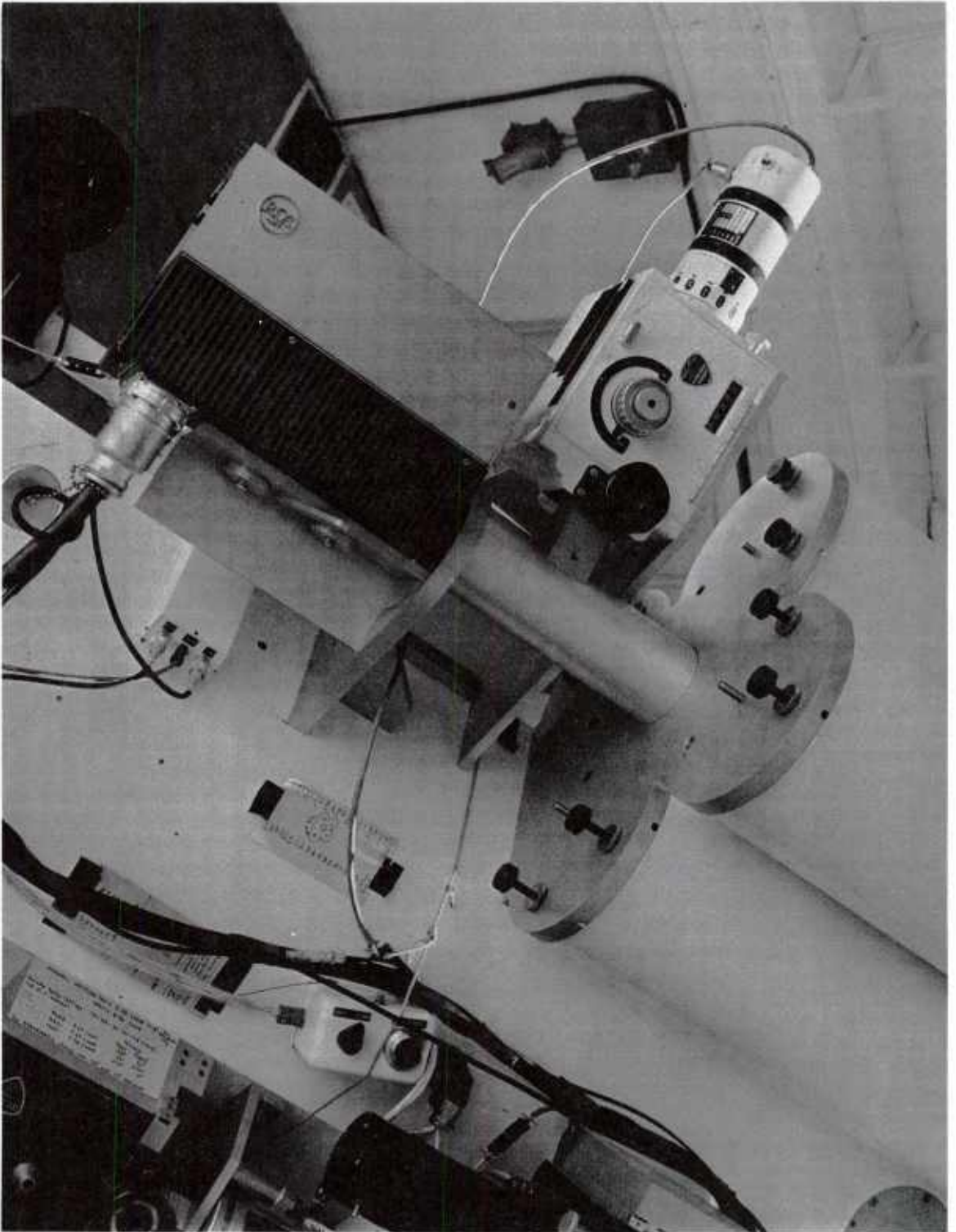
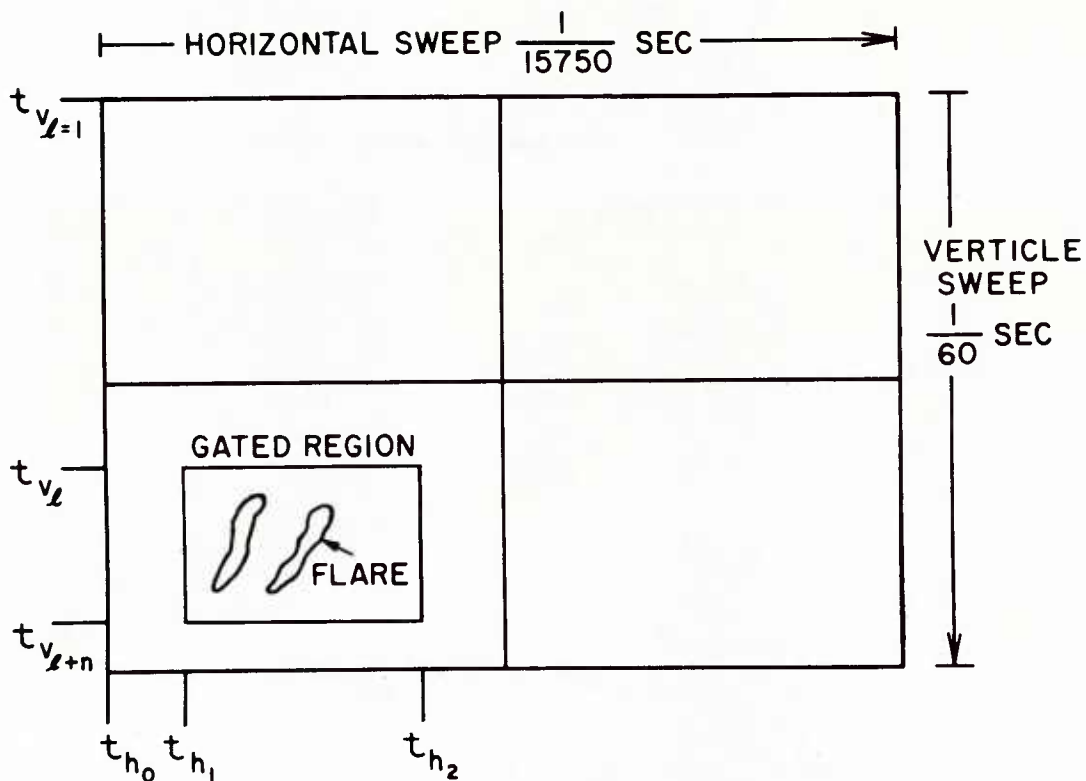


Figure 2
RCA TK-22 camera attached
to quad telescope



VIDEO FIELD TIME RELATIONSHIPS

Figure 3

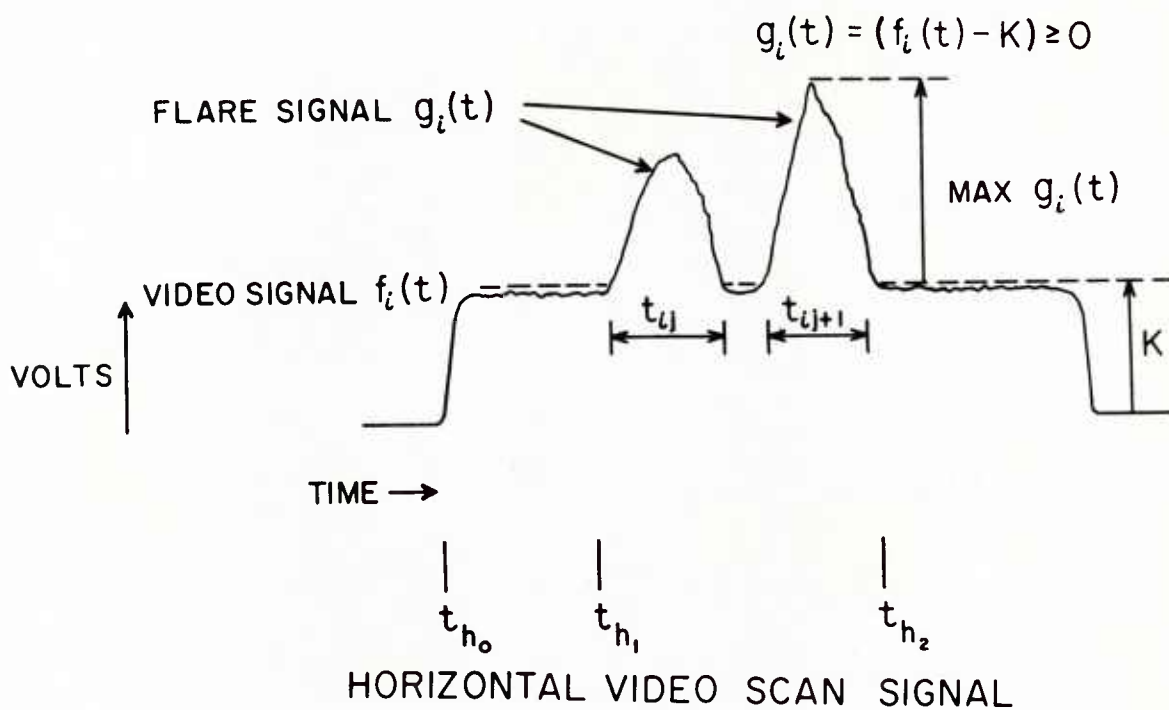


Figure 4

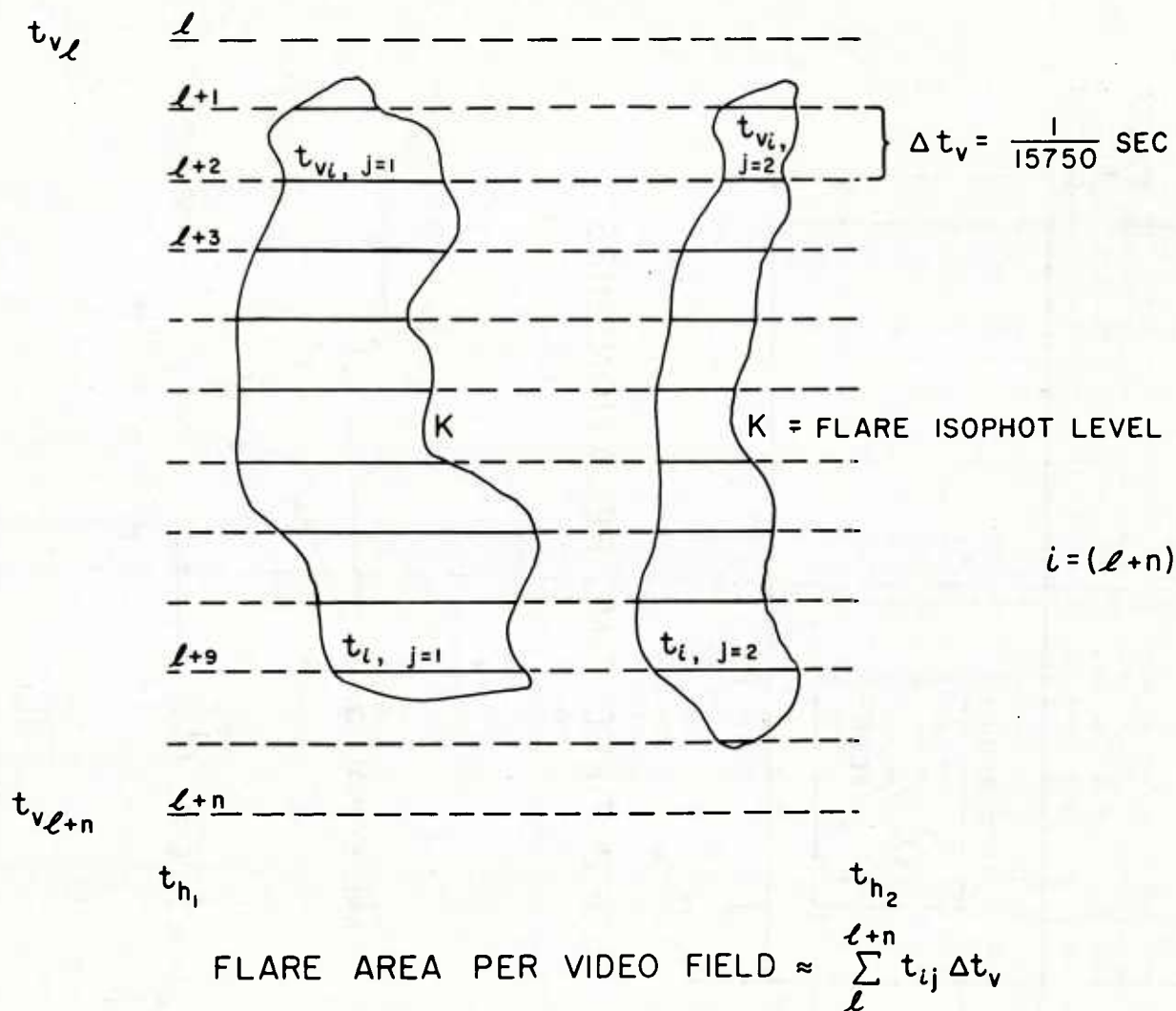


Figure 5

system. He observed the video output signal with a line selector to isolate a single scan. Figure 1 shows some of the results. The television camera response is shown for a selected scan across an H α image. The response is similar to that expected for a microdensitometer scan across the same part of the image. From this information it was evident that with suitable processing, flare area, peak intensity, and integrated intensity could simultaneously be obtained in real time from the video signal.

II. Videometer

Recently at Sacramento Peak an experimental electronic instrument has been developed to obtain these parameters. It is called a videometer for perhaps the obvious reason that it measures video signals. It functions in a manner to provide three dc signals, the magnitudes of which are proportional respectively to flare area, peak intensity, and integrated intensity as functions of time. The required video signals are obtained from an RCA TK-22 camera that views the H α image provided by the four image or quad telescope mounted on the flare patrol spar. This arrangement is shown in Figure 2.

A red sensitive vidicon is used in the camera and its target surface is scanned in the usual raster mode. Figure 3 shows the time relationships of the raster scan. The TK-22 system generates sixty video image fields per second. Each field consists of one vertical sweep across the vidicon target during which time the horizontal dimension is scanned 262.5 times. The vertical sweep requires 1/60 sec, while one horizontal scan requires 1/15750 sec. During the succeeding vertical sweep the horizontal scans occur between the previous ones and thus interlacing is achieved. As a consequence, there are 525 lines of unique video information per each two video fields or per frame.

An analog gate is used in the videometer to select a rectangular region within one of the images provided by the quad telescope. This is done to uniquely identify the solar region from which videometer observations are obtained. In Figure 3 the gate is open from $t_{v\ell}$ to $t_{v\ell+\eta}$, where $\ell = 1, 2, 3, \dots$ and $\eta = 0, 1, 2, \dots$. During this time the t_{h1} to t_{h2} portion of the ℓ to $\ell + \eta$ horizontal scans are used to provide flare information.

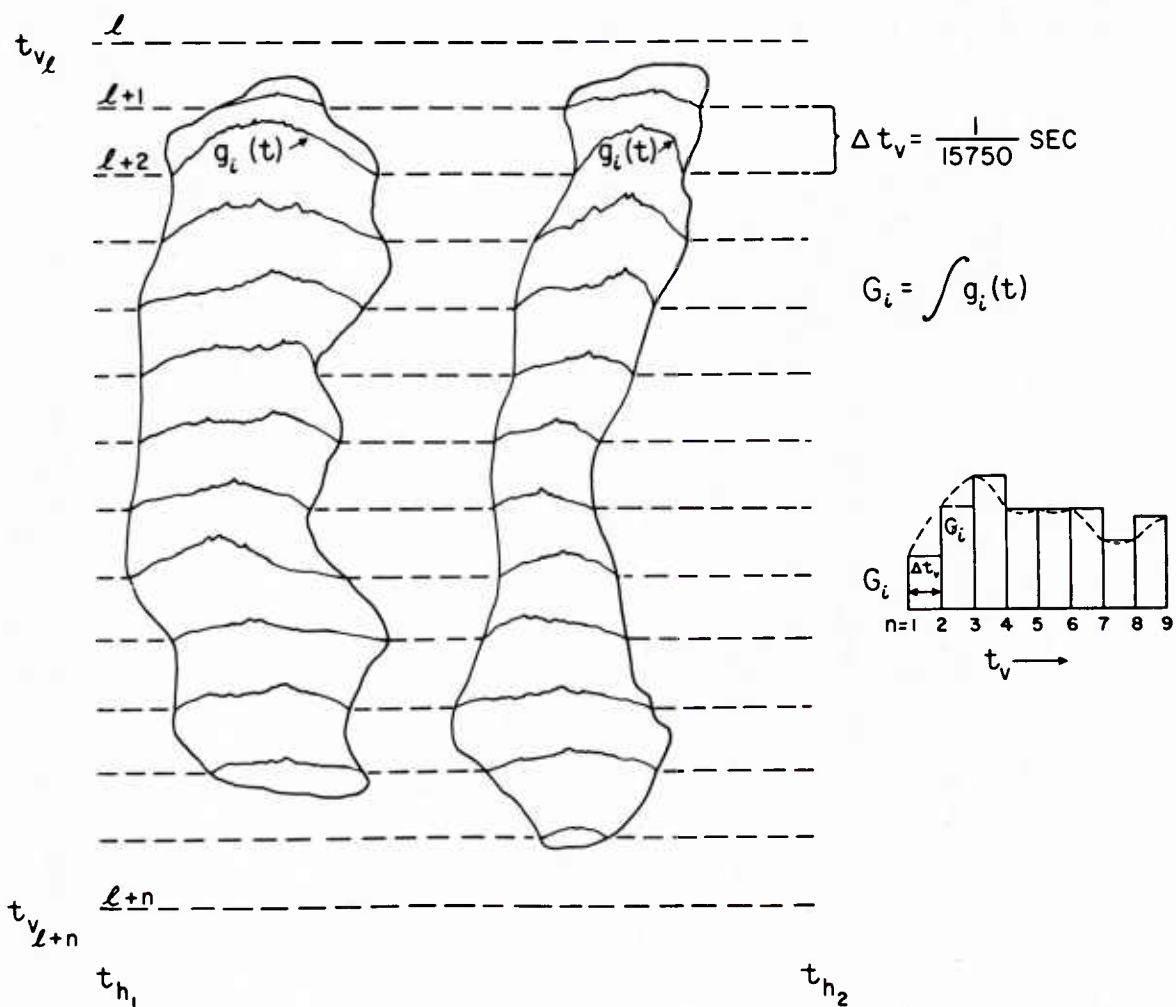
Figure 4 shows a representation of a horizontal scan signal. The signal produced by the electron beam scanning the vidicon target surface is called $f_i(t)$ where $i = (\ell + \eta)$ and designates the scan number. It commences at t_{h0} and continues across the flare image, which causes an increase in amplitude. The signal $f_i(t)$ is proportional to the H α intensity distribution across the scan line. Measurements are made on the signal $g_i(t)$ where $g_i(t) = [f_i(t) - k] \geq 0$. In order to measure only the signal resulting from a flare and not the surrounding plage, amplitude discrimination of adjustable magnitude k is used to eliminate the unwanted signal. This allows selection of the minimum isophotal contour from within which the flare parameters are obtained.

The three parameters, peak intensity, area and integrated intensity are obtained from the signal $g_i(t)$. The peak intensity is simply a measure of the signal maximum as a function time and is obtained by use of a conventional peak detector circuit. The area is measured ideally with a binary device that may have only states zero and one. The signal $g_i(t)$ is applied to this device and it changes its state from zero to one when $g_i(t)$ becomes greater than zero, and maintains the one state until $g_i(t) = 0$ again. This time is labeled t_{ij} where i designates the scan and j the number of the portion of the i -th scan during which $g_i(t)$ is greater than zero.

Figure 5 illustrates the manner in which flare area is measured. In this diagram the horizontal scans ℓ through $\ell + \eta$ are shown as dashed lines outside of the flare filaments and as solid within. The flare filaments are bounded by isophot k . This isophot represents an H α intensity sufficient to generate a video signal equal to the amplitude discrimination level k . The binary device is in state one for durations $t_{i,j=1}$ and $t_{i,j=2}$, for the $\ell + 2$ scan and similarly for all scans within the gated region. With this information the total area of the two flare filaments is approximated by

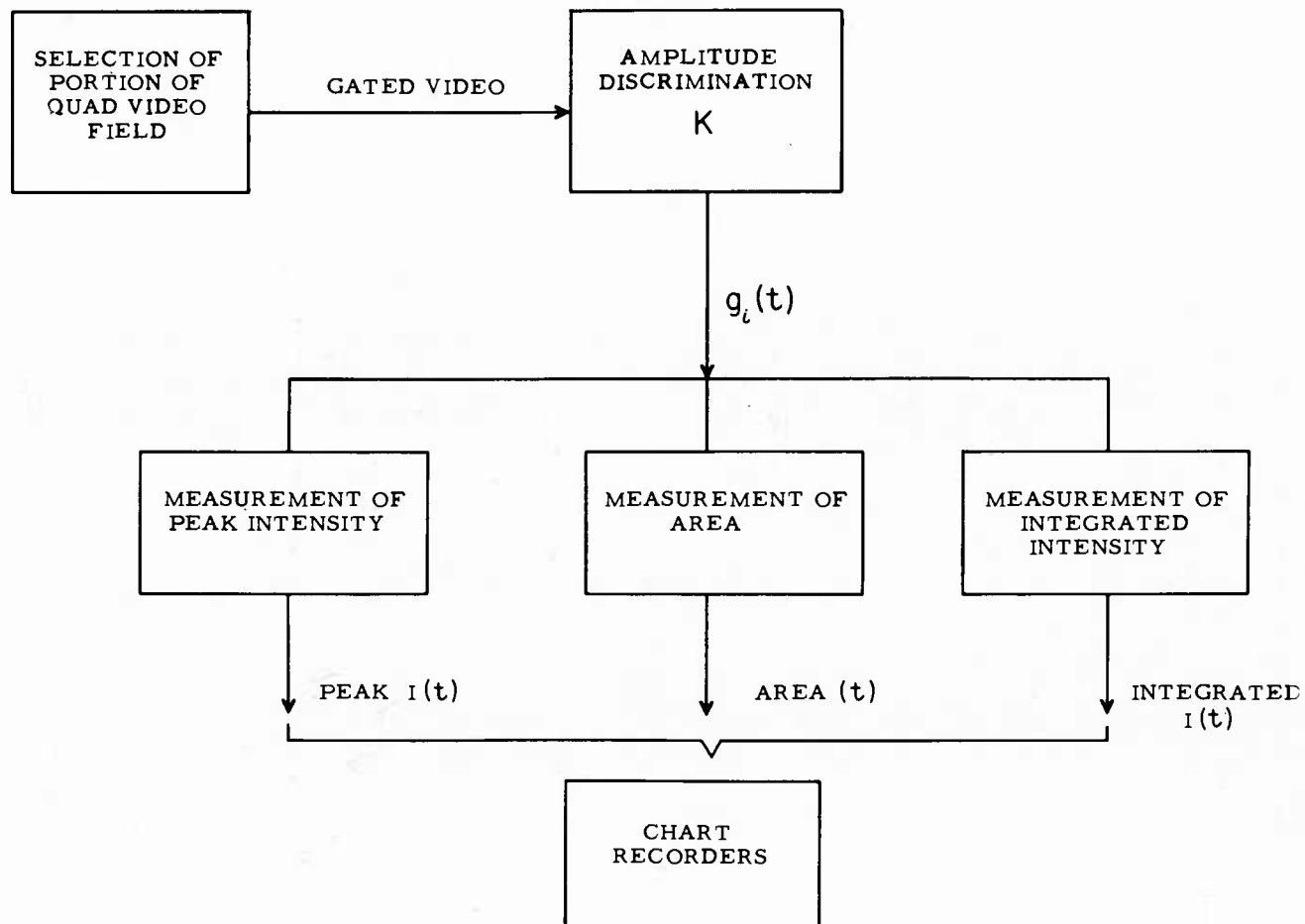
$$\sum_{\ell}^{\ell + \eta} t_{ij} \Delta t_v .$$

In the videometer the binary device is a high speed Schmidt trigger which produces a voltage pulse of constant height for the time that $g_i(t)$ is greater than zero. The output from the



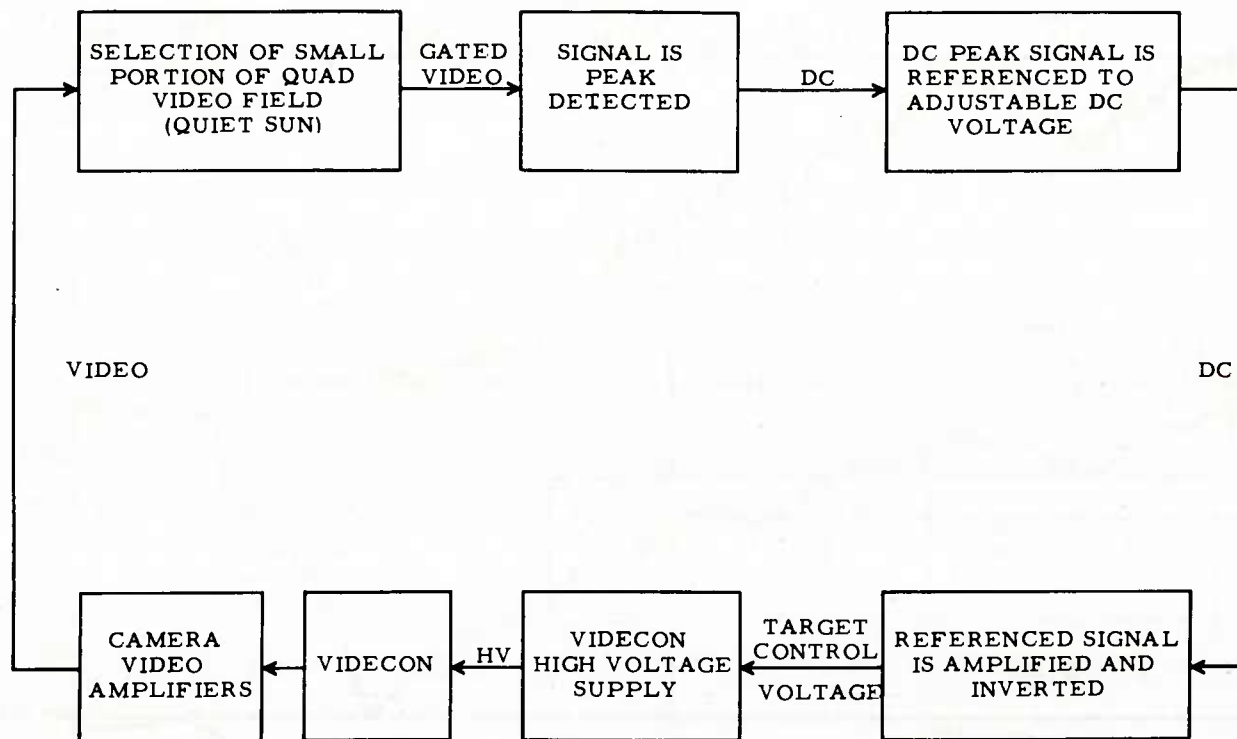
$$\text{INTEGRATED INTENSITY PER VIDEO FIELD} \approx \sum_{l}^{\ell+n} G_i \Delta t_v$$

Figure 6



VIDEOMETER FUNCTIONAL BLOCK DIAGRAM

Figure 7



VIDECON TARGET VOLTAGE CONTROL SCHEME

Figure 8

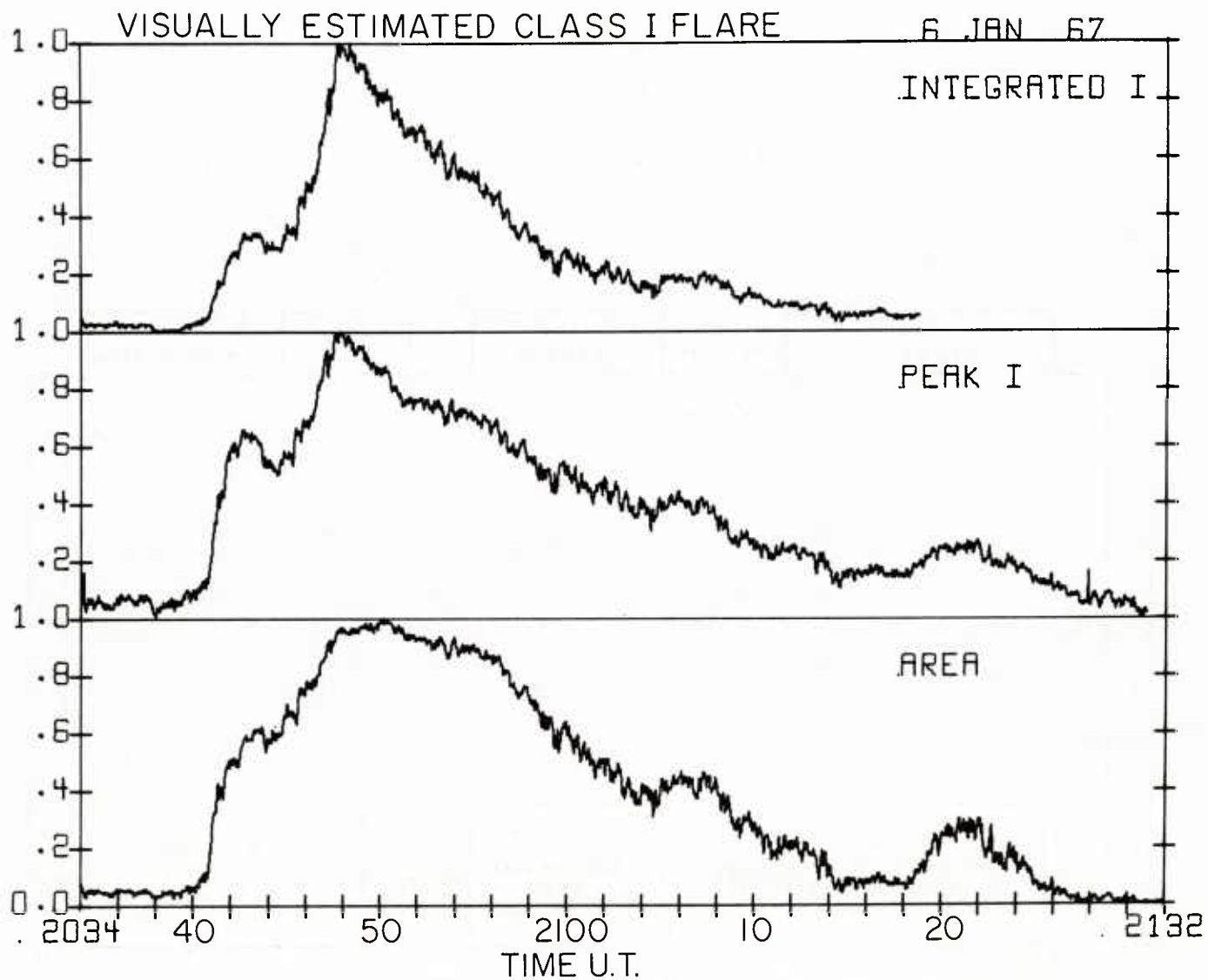


Figure 9

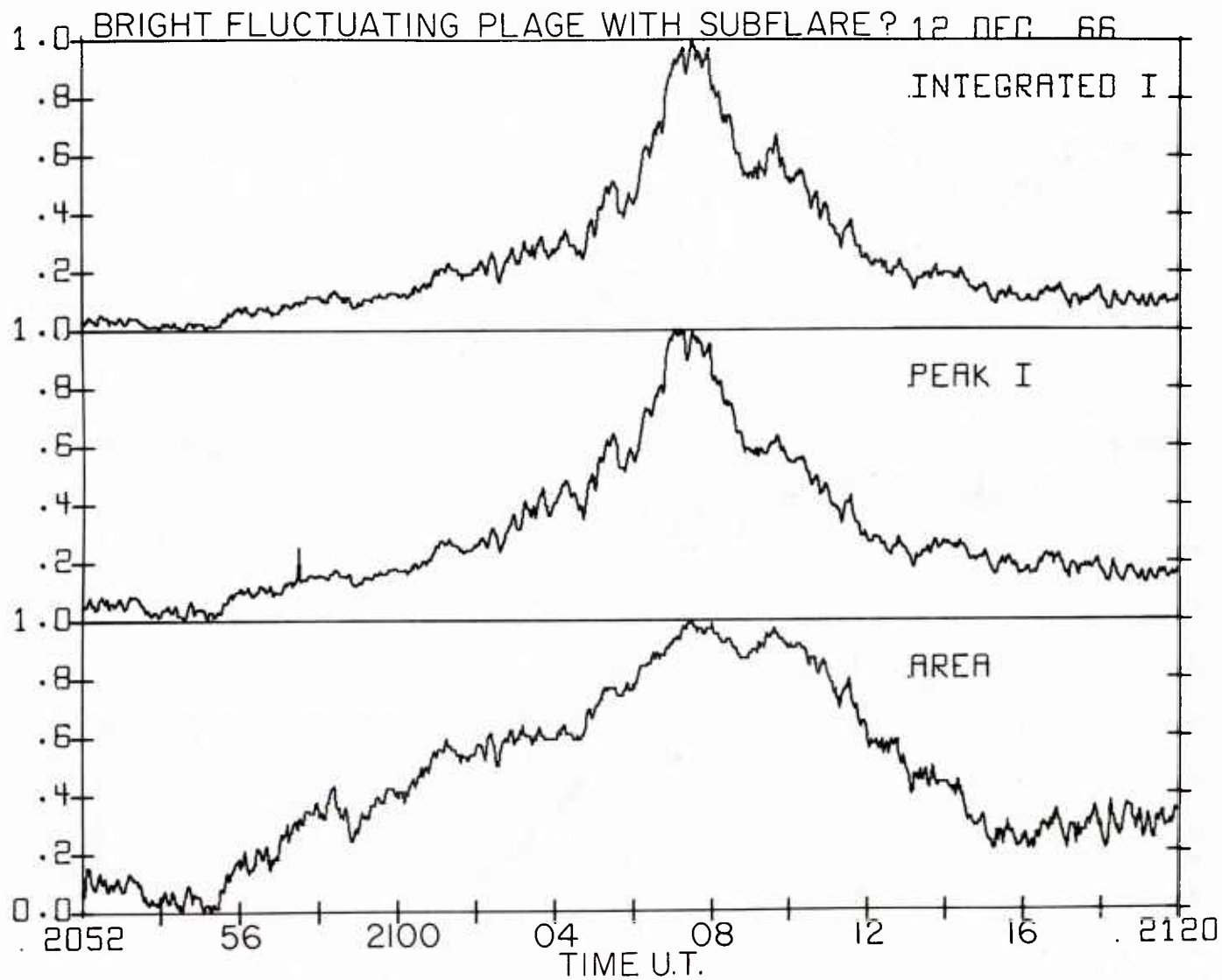


Figure 10

trigger is applied to a dc coupled operational amplifier with a one second time constant. The amplitude of the voltage output from the amplifier is then proportional to the flare area as a function of time.

The integrated intensity is obtained in a manner similar to that for the area except for the important difference that no binary device is used. The concept is illustrated in Figure 6. The integral of $g_i(t) = G_i$ is obtained for each scan i within the gated region. This integral is a measure of the integrated intensity across the scan i . An approximate value for the integrated intensity across all scans within the gated region is given by

$$\sum_{\ell}^{\ell + \eta} G_i \Delta t_v .$$

In practice, the signal $g_i(t)$ is applied to a dc coupled operational amplifier with a one second time constant. The amplifier output is proportional to the approximation of the integrated intensity of the flare as a function of time.

A summary of the basic functions performed by the videometer is shown in Figure 7. In concept the instrument is quite simple. A portion of the video field from the quad telescope is selected by use of some logic circuits and an analog gate. The gated video signal is applied to the amplitude discrimination circuit, the output of which is the signal $g_i(t)$. This signal is operated on by the measurement circuits to obtain the voltages which are proportional to the three desired flare parameters. Potentiometer type Honeywell recorders are used to provide a record of the outputs. In the near future it is planned to record the data digitally and thereby facilitate computer processing and analysis.

A problem that initially had to be solved for continuous use of the videometer throughout the day was correction of the diurnal solar intensity variation caused by atmospheric extinction. This effect is of course most noticeable during the early morning and late afternoon. With no correction the videometer would show a continual increase in peak intensity output during the morning and a decrease during the afternoon. The integrated intensity and the area outputs would also show similar changes. These variations would result from the change in the video signal level. To obtain the desired constant video signal level throughout the day, the vidicon target voltage is controlled with an electronic servo system which senses changes in the video level and adjusts the target voltage to compensate. The scheme used to accomplish this is shown in Figure 8. A small, undisturbed region of the sun is selected by logic and an analog gate and is peak detected. The dc voltage generated by peak detection is referenced to an adjustable dc voltage which provides the null reference for the servo. The resulting voltage is amplified and inverted and applied as a control voltage to the vidicon high voltage supply in the TK-22 camera. Variations in the target voltage result in corresponding changes in vidicon sensitivity. This, of course, is reflected in variations of the vidicon video output which are desired to correct the diurnal change in apparent solar intensity.

III. Observations

Some of the early flare observations made with the videometer are included in the following figures. The integrated intensity (I), peak intensity (I), and area are all given in units normalized relative to the respective maximum value recorded during the event. At present no absolute calibration is available. Plans for the immediate future, however, include the introduction of techniques that will allow calibration of the integrated I in ergs/second, the peak I in ergs/cm²/sec and the area in millionths of the disk.

Figure 9 shows a visually estimated class I flare which occurred on 6 January 1967. This flare had a rather steep initial rise to a local maximum in peak intensity and then exhibited some regression before attaining the maximum brightness. The area also showed an initial steep rise with a relatively small regression before attaining maximum. It may be noted that the area reached its maximum value about two minutes after the peak and integrated intensities had attained maximum.

Figures 10 and 11 show a bright fluctuating plage that was in the southern hemisphere. The question mark is attached to the title of Figure 10 since no observatory reported this

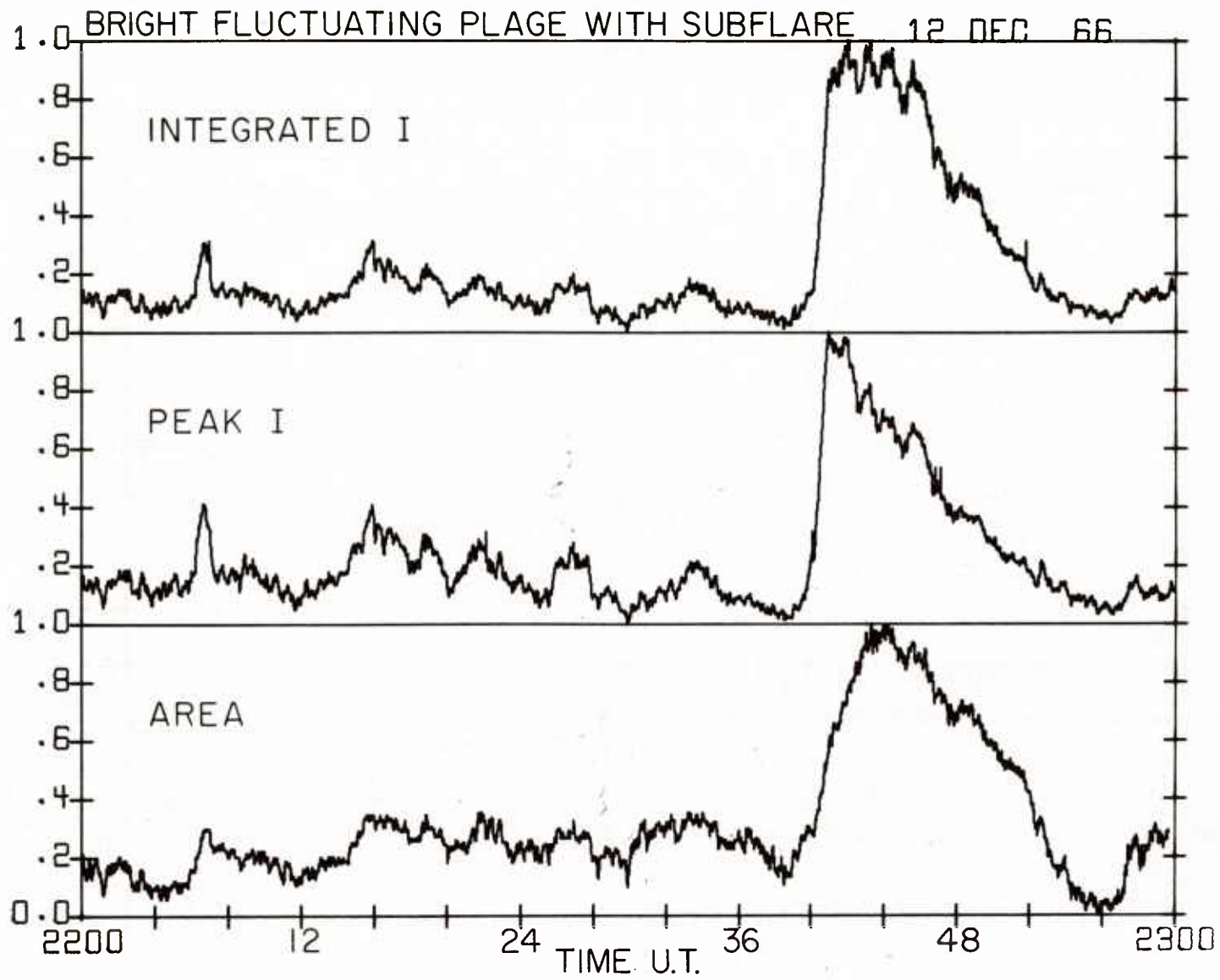


Figure 11

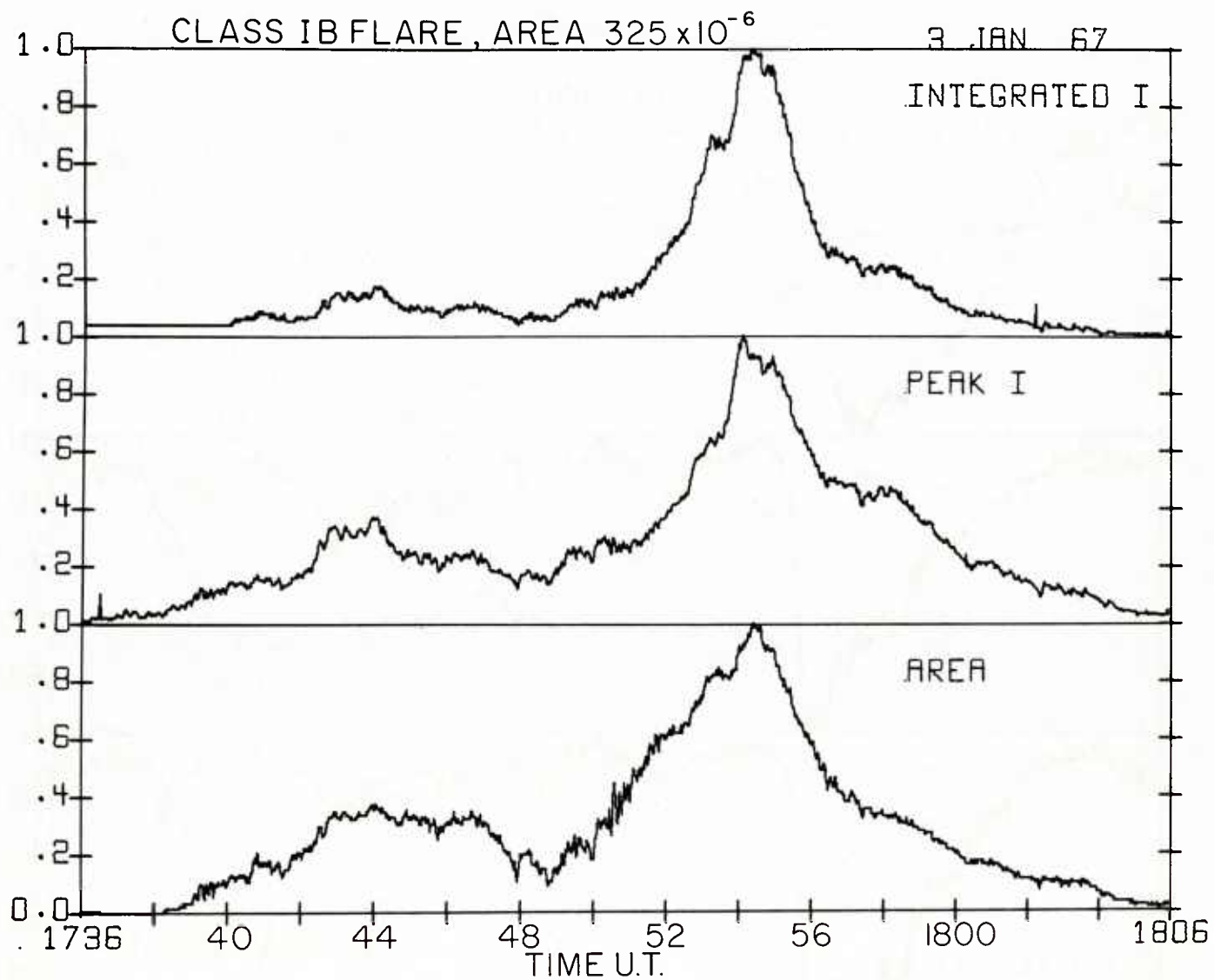


Figure 12

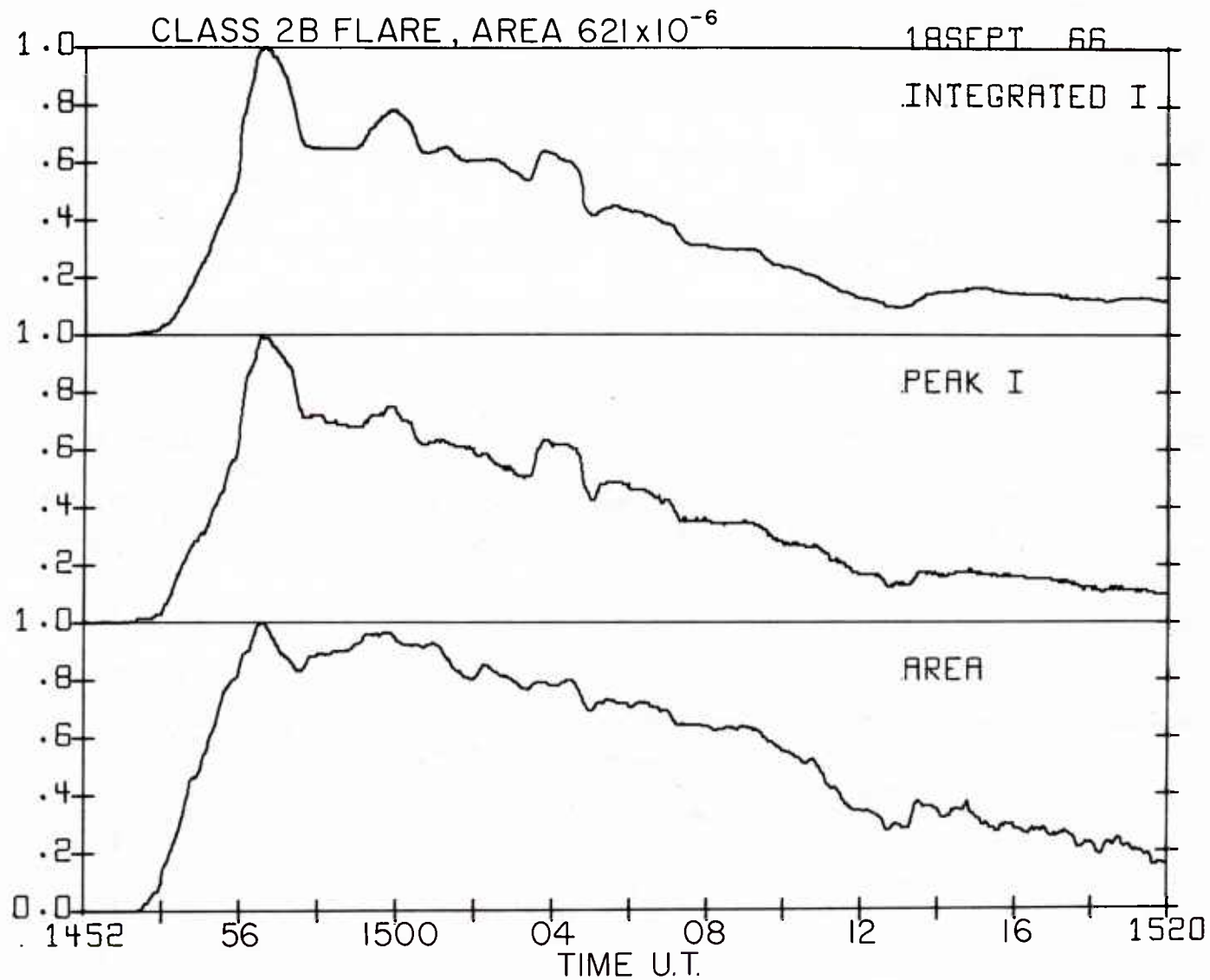


Figure 13

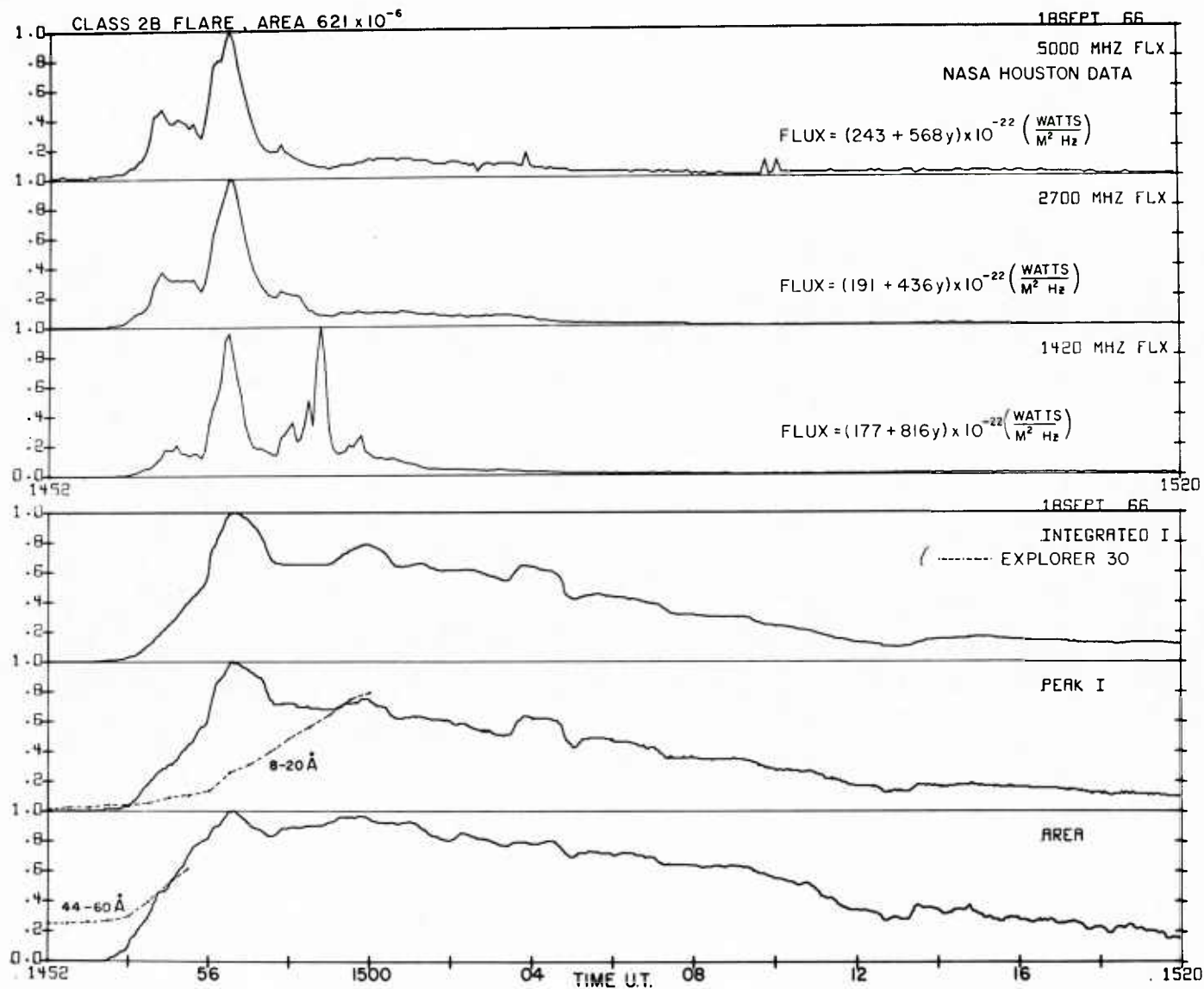


Figure 14

event as a subflare. One of its interesting features is the rather slow increase to maximum area and the fairly rapid increase to maximum peak and integrated intensities after previous slow growth. The close resemblance between the peak I and integrated I indicates that the observed intensity distribution was quite uniform, which perhaps is to be expected for a small chromospheric brightening. Figure 11 begins with the same plage forty minutes later. The normalized values for this figure cannot be directly compared with the previous one. However, the original records show that the maximum levels reached by the event shown in Figure 10 were about eight-tenths that shown in Figure 11. This is a rather interesting record of a fluctuating plage with some short duration brightenings. Also of interest is the decrease to nearly minimum level of the peak I and integrated I just prior to the fast rise to maximum. This event was reported as a subflare by Lockheed and was accompanied by a 0.5 Hz sudden frequency deviation on the 5 MHz transmission of WWVH.

The event shown in Figure 12 was accompanied by an intensity one plus type three radio burst beginning at 1745:40 and continuing until 1746:30. This burst covered the frequencies from 41 MHz to 22 MHz. This occurred during a precursor in H α and ended well before the main H α event. The event also had 10.7 centimeter maximums at 1759:24 and 1800. The 2.8 cm radiation peaked earlier at 1747:48. The area noted in the title is that determined from flare patrol film reduction at Sacramento Peak.

Figure 13 shows a class 2B flare that occurred on 18 September 1966. The area noted in the title is again that determined from film reduction at Sacramento Peak. The peak and integrated intensities show three rather well-defined time rates of increase with the steepest slope just prior to 1456 U.T. The area, however, with small variations, had a fairly uniform rate of increase to maximum and decreased to a local minimum at about the same rate. This decrease occurred while the peak and integrated intensities fell quite sharply. Possibly the most interesting H α features are the three peaks, each of about two minutes in duration, that occurred in the peak and integrated intensities. For this flare NASA Houston and ITSA at Boulder made available centimeter and X-ray data, respectively, which is compared with the videometer observations in Figure 14. The flux has been normalized relative to its maximum value and the scale factor is noted below the frequency designation. The variable y has the ordinate range of zero to one. The X-ray data is shown with the peak I and area. Because of the large negative aspect angle (-27°) of the satellite sensor, the absolute values of the flux are not very reliable. The values obtained, however, in ergs/cm²/sec are read directly from the ordinate. An interesting feature of the 8-20 Å data is that the flux continues to increase well after H α and centimeter maxima, except for the large second burst on 1420 MHz. These data also show an increase in radiation rate that is well correlated with the rapid rise to maximum in the H α and centimeter data. The 44-60 Å data show good correlation with the commencement in H α but instrument saturation occurred before a maximum time could be determined. This is also true for the 8-20 Å data. This flare was also quite productive in terms of meter radio bursts. An intensity one, type three burst from 320 to 180 MHz was observed from 1456 to 1457. This is the interval during which maxima occurred in the centimeter and H α data. An importance three, type two burst began at 1459:48 and continued until 1513. This burst covered the frequency range from 230 to 75 MHz.

IV. Summary

The technique used to obtain, from video information, the uncorrected area, peak intensity and integrated intensity of solar flares as functions of time has been described. Some of the first observations made with the videometer were included as illustrations of the potential of the technique. It is apparent that the observations, especially where radio and X-ray data are also available, beg analysis. However, such work is not included within the scope of this paper. It is also apparent that this technique will allow study of fine structure in flare growth and decay that has in the past been impeded by the great amount of effort required to do photometric reductions with the requisite high time resolution. Other intriguing possibilities arise: It should be possible to determine the power spectrum of individual fluctuating plages by Fourier analysis of the videometer output. Considerable refinement in statistical studies of the time correlation of H α maxima with radio, X-ray and geophysical indications are possible because of the inherent objectivity of the method. Flare classification based on total energy output within the effective line width of the telescope H α filter and appended by rise and decay time parameters also appears as a possibility. In the end, imaginative curiosity, effort, and time will reveal the usefulness of this technique.

REFERENCES

- Abramenko, S. I.; Dubov, E. E; Ogir, M. B; Steshenko, N. E.; Shaposhnikova, E. F.;
Tsap, T. T.: "Photometry of Solar Flares", Izvestia Krimskoi Ast. Obs., 23, 341, 1960.
- Barton, H.: "Correspondence: A Brilliant Solar Flare, 1948 May 21", Observatory, 68, 191,
1948.
- Barton, ; Laurie, ; Rhodes, : "Solar Flare 1951 May 18", Observatory, 71, 170,
1951.
- Billings, D. E. and Roberts, W. O.: "Isophotal Photometry of a Solar Flare", Ap. J., 118,
429, 1953.
- Dodson, H. W.: "Position and Development of the Solar Flares of May 8 and 10, 1949", Ap. J.,
110, 382, 1949.
- Dodson, H. W.; Hedeman, E. R.; and McMath, R. R.: "Photometry of Solar Flares", Ap. J.
Supplement No. 20, 2, 241, 1956.
- Dunn, R. B.: Private Communication.
- Giovanelli, R. G.: "Solar Eruptions", Ap. J., 91, 334, 1940.
- Mohler, O. C.: "Photometry of a Solar Flare", Pub. A.S.P., 59, 266, 1947.
- Newkirk, G. A.: "Photometry of a Solar Flare", Astr. J., 57, 21, 1952.
- Newton, H. W.: "Solar Notes", Observatory, 69, 235, 1949.
- Richardson, R. S.: "Intensity Changes in Bright Chromospheric Disturbances", Ap. J., 90,
368, 1939.
- Shaposhnikova, E. F. and Ogir, M. B.: "The Development of Chromospheric Flares According to
Observations made in 1957", Izvestia Krimskoi Ast. Obs., 21, 112, 1959.

ABSTRACT

An experimental electronic instrument designed to measure flare area, peak intensity and integrated intensity as functions of time is described from a functional standpoint. The instrument processes video signals obtained from a closed circuit television system used to view the H α solar image. Some early observations with the instrument are described and compared with radio and X-ray data.

THE USE OF GROUND LEVEL NEUTRON MONITORS IN A REAL TIME SOLAR PROTON MONITORING NETWORK

by

M. A. Shea
Air Force Cambridge Research Laboratories, Bedford, Mass.

ABSTRACT

During the past solar cycle, neutron monitors were a prime sensor for obtaining information relative to large solar particle events as these sensors recorded increases of the order of 100% during a sudden influx of solar-flare-associated protons with energies greater than 400 Mev. The data from these sensors were usually analyzed long after the event had occurred but the monitors were also utilized as a local alarm to initiate other experiments such as balloon launchings. It is currently planned to integrate several of these sensors into a monitoring network by the immediate transmission of the output data to a central collection agency and to use a computer to examine the data in real time to detect unusual deviations from the normal cosmic-ray intensity. Such a real time network should be capable of providing the first positive confirmation available from ground level sensors of the presence of high energy solar particles in the immediate vicinity of the earth. The concepts and plans for the implementation and operation of this type of monitoring network are presented.

I. INTRODUCTION

During the past solar cycle, neutron monitors were one of the principal sensors used to obtain information relative to high energy solar particle events. We are currently implementing a network of five neutron monitors, the data from which will be transmitted in real time as an aid in forecasting the space particle environment. In this paper the concept and operation of a neutron monitor is described, and the plans for utilizing this type of sensor to detect solar particle events are presented.

II. NEUTRON MONITOR DESCRIPTION

A neutron monitor is a 90,000 pound apparatus consisting of lead, polyethylene, and a few pounds of transistorized electronics. This description is appropriate to the newer IQSY NM-64 "super" neutron monitor designed by Dr. Hugh Carmichael of the Atomic Energy of Canada, Ltd. (Carmichael, 1964). These are very efficient, reliable, high counting rate instruments with automatic data systems designed for unattended operation. There are four of these super neutron monitors in the United States, about nine in Canada, one at Thule, Greenland and about a dozen in other countries.

In addition to the super monitors, there are many of the older IGY-type monitors, often called the Simpson monitors, in operation throughout the world. These instruments are considerably smaller weighing about 12,000 pounds of lead, paraffin and vacuum tubes (Simpson, 1955). Most of these smaller monitors are troublesome, temperamental, of an average age of about 10 years, and are in need of an extensive refurbishing job. In addition, the statistical accuracy of the data obtained from these monitors is of the order of 1%. Consequently, some difficulty is encountered in using these data in the analysis of small variations of the cosmic-ray intensity.

In brief, a neutron monitor is an instrument that indirectly monitors the flux of high energy particles capable of initiating nuclear cascades in the atmosphere (as shown in Figure 1) which are detectable at ground level. Local production of neutrons in a thin layer (~ 2 inches) of lead surrounding the monitor is used to enhance the counting rate, and a hydrogenous material, such as paraffin or polyethylene is used to thermalize the neutrons so that they may be detected by the BF_3 proportional counters at maximum efficiency. A pictorial diagram of a standard IGY neutron monitor is shown in Figure 2.

The neutron monitors are generally operated in independent sections (two sections for the IGY-type, three sections for the super monitor) as shown in Figure 3. The ratio between the counting rate of each section is used as an internal consistency check on the monitor

operation.

III. INTENSITY VARIATIONS

Variations in the measured cosmic-ray intensity can be divided into two general categories - those affecting the production of secondary particles in the atmosphere, and variations of the primary radiation above the atmosphere.

1. Variations in the Production of Secondary Particle

One of the principal factors affecting the neutron monitor counting rate is the atmospheric pressure with a typical change in the recorded intensity of 25% per inch of Hg. In contrast, the long-term change of the galactic background is about 25% during the solar cycle for stations at high latitudes; typical responses to high energy solar particle events are also of this same order of magnitude (2% - 250%). Since these variations occur simultaneously with changes in the primary intensity, it is imperative that the neutron monitor counting rate be accurately corrected for atmospheric pressure variations before utilizing these data for scientific studies, including even the high energy solar particle events. Most neutron monitor data are corrected for atmospheric pressure effects before being distributed to the scientific community or used for research.

2. Variations Affecting the Primary Radiation

Of particular interest are variations in the primary radiation, commonly called intensity-time variations. These can be divided into two major categories - long term variations extending over a period of several years, and short-term variations extending from a few hours to approximately 30 days.

The most significant long-term variation is the inverse correlation between solar activity and cosmic-ray intensity recorded at the earth. As shown in Figure 4, the relative cosmic-ray intensity recorded at Mt. Washington, N.H. decreased during the increasing phase of the last solar cycle until at solar maximum the intensity had decreased by 25% from the value recorded at solar minimum.

Short-term variations can be classified into three major groups; diurnal variations, sudden rapid decreases in intensity called Forbush events, and rapid increases from solar particle events.

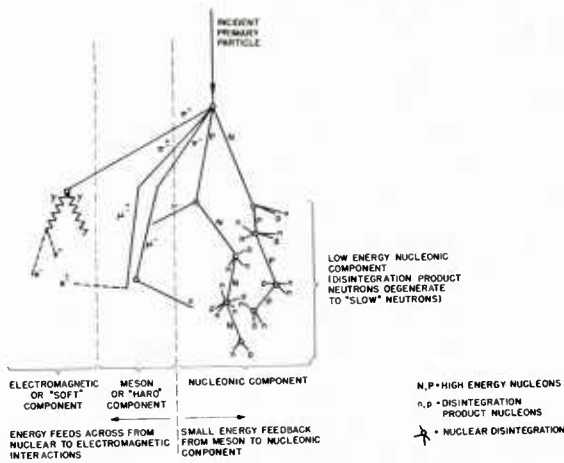


Fig. 1: Typical nuclear cascade produced in the atmosphere from a high energy primary particle.

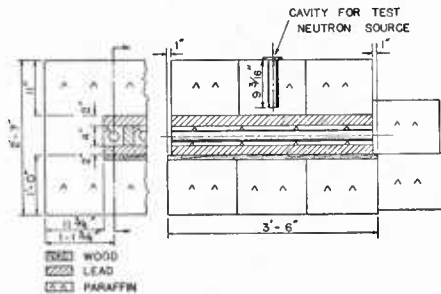


Fig. 2: IGY Standard neutron monitor design.

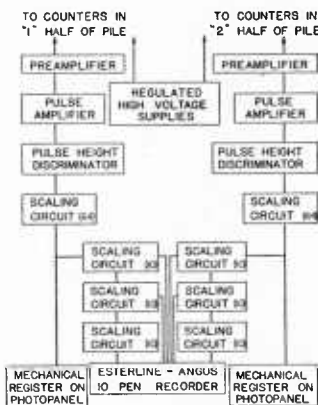


Fig. 3: Block diagram of electronic circuits for an IGY-type neutron monitor.

Diurnal variations are small changes, generally of the order of 1%, in the relative intensity observed at a specific station in the course of a day. An example of the diurnal variation recorded by four high latitude stations is shown in Figure 5.

Forbush events occur almost simultaneously with the initial phase of geomagnetic storms. As the earth is enveloped within a solar plasma cloud, the cosmic-ray intensity suddenly decreases by as much as 10 or 15 percent within a period of 4-10 hours. A currently accepted explanation assumes the solar plasma contains a "frozen" magnetic field which excludes many of the low energy galactic cosmic-ray particles normally incident on the top of the atmosphere. As the solar plasma continues to expand, its magnetic barrier becomes less effective and the relative cosmic-ray intensity gradually recovers. An example of a large Forbush decrease observed by the Mt. Washington, N.H. neutron monitor is shown in Figure 6. During this event, the onset of the geomagnetic storm was at 2318 UT on May 11, and the onset of the cosmic-ray decrease was at 0000 ± 15 min UT on May 12. This was a fairly rapid event with the recorded neutron monitor intensity decreasing by 14.8% within 7 hours.

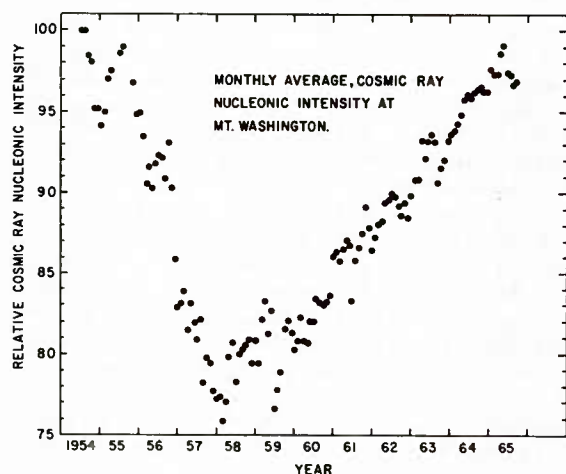


Fig. 4: Long-term Variation in the Nucleonic Intensity as recorded at Mt. Washington, N.H.

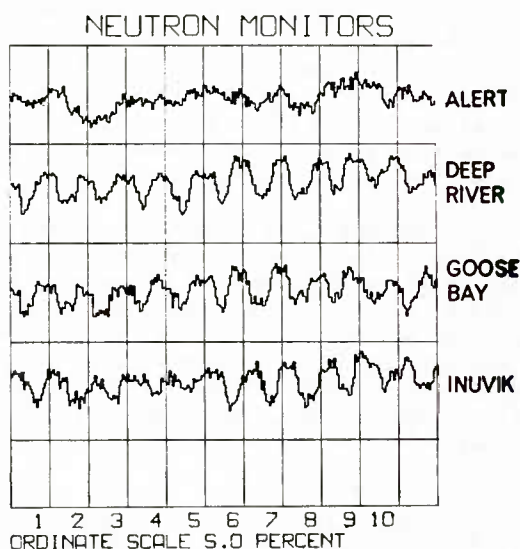


Fig. 5: Typical daily average in the nucleonic intensity as recorded at four high latitude locations in May 1966.

Of particular interest are sudden increases in the cosmic-ray intensity, such as the increases illustrated in Figure 7. During the last solar cycle there were nine large solar flares with which significant ground level cosmic-ray increases were associated. The largest of these events resulted in a 3000% intensity increase; the smaller events produced increases of the order of 10%. The characteristics of such an increase are a rapid rise in the cosmic-ray intensity until a maximum is reached followed by a much longer decay to normal intensity. The decay of the enhanced neutron monitor flux usually follows a $t^{-3/2}$ power law. The increase observed at various stations is extremely dependent upon latitude, indicative of a very steep spectrum for the incident solar particles.

IV. SOLAR PROTON EVENTS DETECTED BY NEUTRON MONITORS

In the following discussion it must be emphasized that ground level neutron monitors respond to particles with energies greater than 400 Mev; the smaller, lower energy solar proton events will not be detected by these sensors, but can be detected by riometer measurements.

1. Characteristics

High energy protons associated with large flares occurring west of the solar central meridian, usually have a shorter transit time than those particles associated with flares to the east of central meridian. Typical transit times range from 20 minutes to 4 hours. Typical rise times, from the onset of solar particle detection by neutron monitors to the maximum intensity, range from 10 minutes to 150 minutes.

High energy protons produced by large flares occurring between $\sim 30-90^\circ W$ are usually characterized by a fast rate of rise from the onset time to the maximum neutron monitor intensity. The radiation is

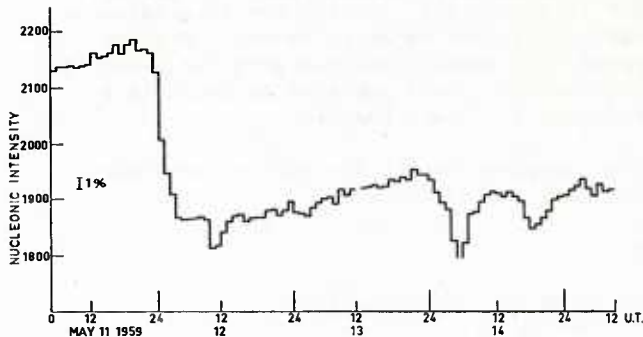


Fig. 6: Typical Forbush decrease as recorded by the Mt. Washington neutron monitor during May 1959.

usually anisotropic during the initial phase of these increases, but isotropy occurs within 1-2 hours. A typical neutron monitor response to a solar proton event from a 'west limb' flare is illustrated in Figure 8.

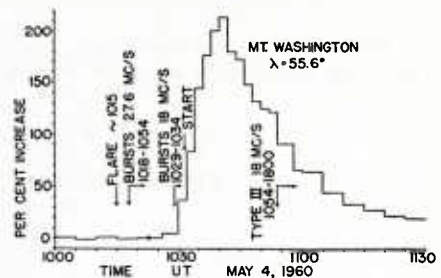


Fig. 8: Typical neutron monitor response to a high energy solar proton event from a 'west limb' flare.

High energy particle events associated with large flares occurring on the central part of the solar disk and on the eastern limb are characterized by a slow rate of rise from the onset time to the maximum intensity. This radiation is usually isotropic. An example of the ground level neutron monitor intensity increases to a solar proton event associated with a flare on the central part of the sun is shown by the slow intensity increase from 1330 to 1600 on Nov 12, 1960 as illustrated in Figure 9. Unfortunately, this was a very complex event with various associated geophysical phenomena resulting in the apparent 'double hump' of the intensity curve (Obayashi, 1961).

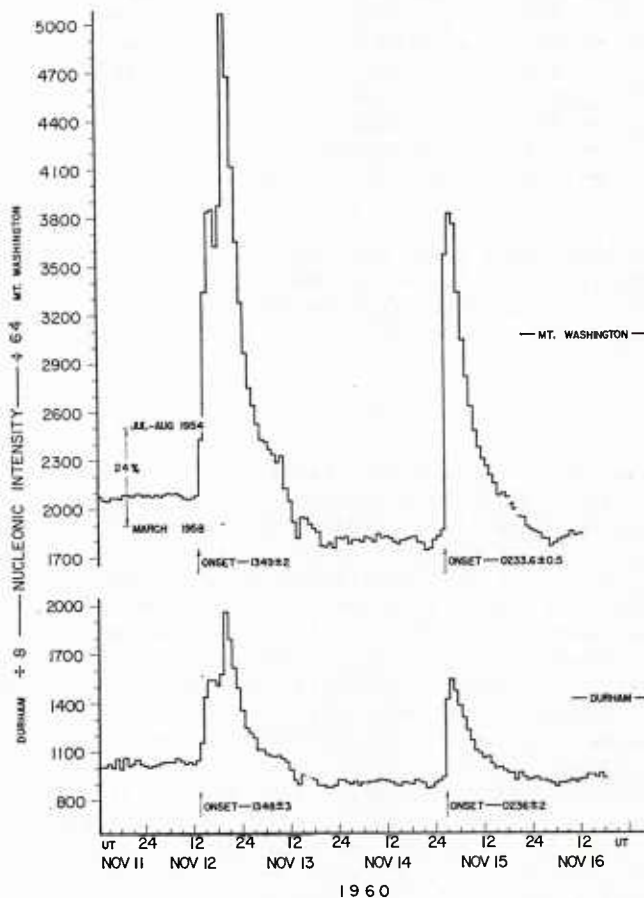


Fig. 7: Sudden increases in the nucleonic intensity as recorded by the Mt. Washington (elevation 6288 ft) and Durham, N.H. (elevation sea level) neutron monitors.

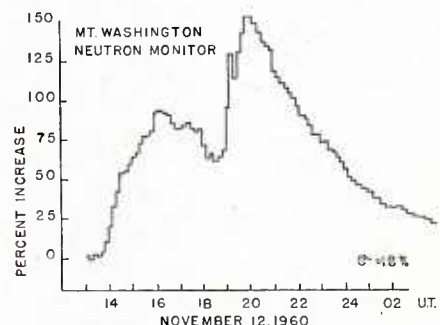


Fig. 9: The 10-minute average nucleonic intensity at Mt. Washington during the November 12, 1960 solar particle event.

Another typical characteristic of these solar proton events is the change in the slope of the rigidity spectrum. The normal galactic cosmic-ray integral spectrum approximates a $KP^{-1.5}$ power law where P is rigidity and K is a constant. During events detectable by neutron monitors, the spectral exponent increases to larger negative values. A solar flare particle spectrum of KP^{-6} is called a steep or soft spectrum with a very large population of low energy particles; a spectrum of KP^{-4} is called a hard spectrum as there is a larger number of high energy particles in proportion to the lower energies.

Table 1 lists nine major high energy solar particle events during the last solar cycle; related solar and neutron monitor intensity data are also given.

TABLE 1

Solar Flare and Related Cosmic-Ray Data for the Major Events
During the Past Solar Cycle

| Flare Data | | | Cosmic-Ray Neutron Monitor Data | | |
|------------|------------|------------|---------------------------------|---------------------------|---------------------------|
| Date | Location | Onset | Time of Onset | Time of Maximum Intensity | Magnitude of Increase (%) |
| 2/23/56 | 85°W, 25°N | 0331 | 0349 | 0410 | 3000 |
| 7/17/59 | 30°W, 17°N | 2118(7/16) | ~0200 | ~0800 | ~5 |
| 5/4/60 | 90°W, 10°N | ~1015 | 1031 | 1041 | 214 |
| 9/3/60 | 90°E, 17°N | 0040 | ~0500 | ~0700 | ~3 |
| 11/12/60 | 1°W, 27°N | ~1323 | 1349 | 1618 | 157 |
| 11/15/60 | 33°W, 26°N | 0207 | 0234 | 0256 | 134 |
| 11/20/60 | ~90°W | ~2023 | ~2115 | ~2200 | ~6 |
| 7/18/61 | 60°W, 7°S | 0929 | ~1030 | ~1100 | 18 |
| 7/20/61 | 90°W, 5°S | 1553 | ~1600 | ~1630 | 5 |

All times are in UT. The cosmic-ray data given are from the Mt. Washington neutron monitor with the exception of the Feb. 23, 1956 event, the information for which is given as recorded by the Chicago neutron monitor.

2. Time Sequence

Another important feature of the large solar particle events capable of being detected by neutron monitors is the relative consistency of the time sequence of the various associated geophysical phenomena. A typical time sequence is illustrated in the following example. First, assume a large proton producing flare has occurred on the visible solar disk. Approximately 8 minutes after its onset, this flare will be visible by solar observatories on the earth, and anywhere from 10 minutes to 4 hours later, an increase in the neutron monitor intensity will occur. This will be the first positive confirmation available from a ground based sensor that a solar particle event is in progress. In fact, such increases have been utilized as the alarm to initiate the launching of balloon experiments, such as was done both at Chicago and at Minneapolis during the last solar cycle. The low energy (50 Mev) particles usually detected by riometers, travel correspondingly slower than the high energy particles, and the arrival of a significant flux of these particles is generally about 4 hours after the onset of a neutron monitor increase. The relative time it takes for particles with various energies to travel from the sun to the earth is illustrated in Figure 10. Generally, the lower energy particles arrive during the decay of the neutron monitor event. The final event to be associated with the solar flare is the arrival of the solar plasma indicated by an increase in geomagnetic activity. This usually occurs anytime from 19 to 48 hours after the initial flare. A Forbush decrease often results from the envelopment of the earth by the solar plasma. Table 2 gives the time sequence of the geophysical effects associated with the November 15, 1960 solar particle event. The neutron monitor increase at Mt. Washington for this event is shown in Figure 11.

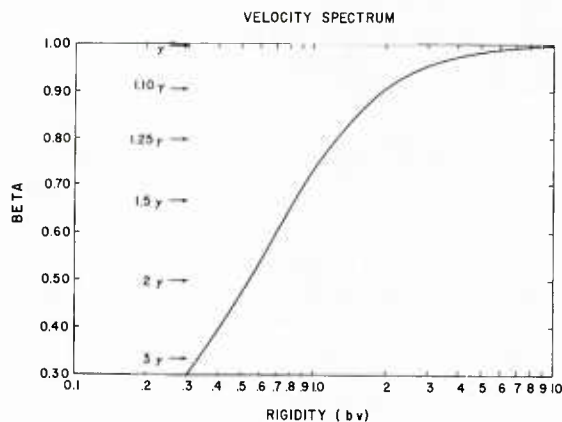


Fig. 10: The relative time (τ) it takes for particles of various rigidities to travel from the sun to the earth.

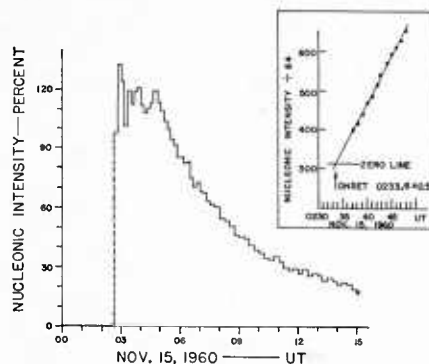


Fig. 11: The 10-minute average nucleonic intensity at Mt. Washington for the November 15, 1960 high energy solar particle event.

TABLE 2

Time-Sequence of Geophysical Events Associated with the November 15, 1960 High Energy Solar Particle Event

| <u>Time (UT)</u> | <u>Event</u> |
|------------------|--|
| 0207 | Class 3+ solar flare observed at 33°W, 26°N |
| 0220 | Sudden short wave fadeout observed |
| 0230 | Onset world-wide cosmic-ray neutron monitor intensity increase |
| 0500 | Start of riometer absorption at Kiruna, Sweden |
| 2155 | Sudden commencement geomagnetic storm |

V. PROPOSED REAL TIME NEUTRON MONITOR NETWORK

In order to utilize neutron monitors as solar particle indicators, five NM-64 neutron monitors are currently being integrated into a real time data acquisition network. These monitors are located at Thule, Greenland; Deep River, Ontario, Canada; Durham, New Hampshire; Swarthmore, Pennsylvania, and Dallas, Texas. The data from the Thule monitor will be transmitted to the Environmental Science Services Administration (ESSA) computer at Anchorage, Alaska, via a communication circuit across the DEW line. Data from the other four monitors will be transmitted on the AWS SOFNET teletype circuit to both the AWS and ESSA forecast facilities.

These five particular stations were selected on a basis of reliability, standardization, communications accessibility, and geophysical location. Of particular importance is the geomagnetic latitude, or more properly the cutoff rigidity, of these sensors. The cutoff rigidity (P_c) is defined as the lowest rigidity (momentum per unit charge) particle capable of transversing the geomagnetic field and arriving at a specific location on the earth's surface.

For example, all particles with rigidity greater than 1.02 bv are detectable at Deep River; but only particles with rigidities greater than 4.35 bv are detectable at Dallas. A solar particle event with a very steep spectrum may be detected at Deep River but not detected at Dallas. The relative percentage increase at each cutoff rigidity may be utilized to determine the slope of the high energy particle spectrum. An example of the relative increase observed by three European neutron monitors (Uppsala, $P_c = 1.43$ bv; Leeds, $P_c = 2.20$ bv; Zugspitze, $P_c = 4.24$ bv) during the November 12, 1969 solar proton event is shown in Figure 12.

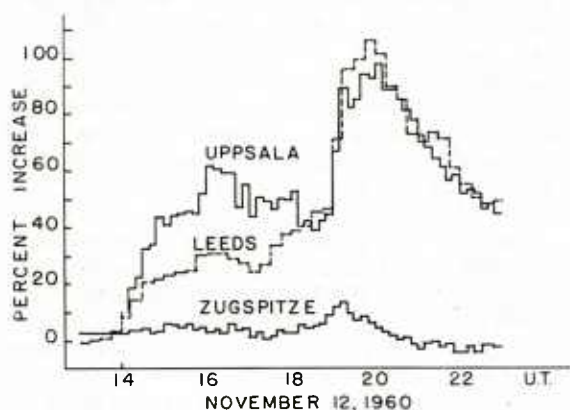


Fig. 12: Relative intensity increases recorded by three European neutron monitors during the November 12, 1960 high energy solar particle event.

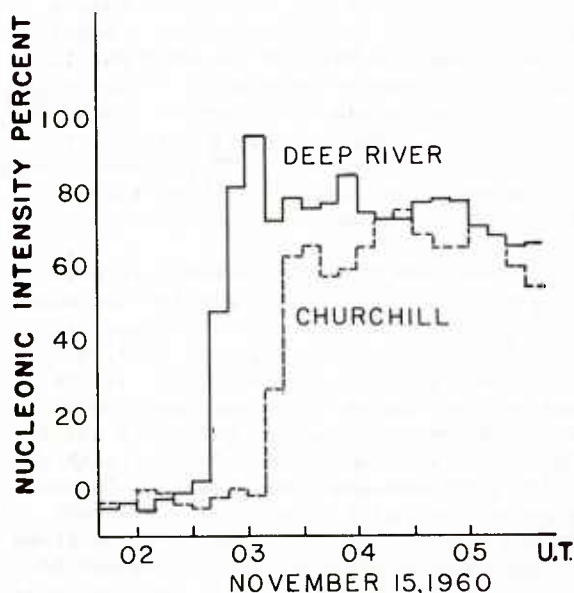


Fig. 13: Relative nucleonic intensity recorded by the Deep River and Churchill, Canada neutron monitors during the November 15, 1960 high energy solar particle event.

Another important consideration is the portion of the celestial sphere scanned by the various detectors. Cosmic-ray protons, being charged particles, are deflected as they traverse the earth's magnetic field. It is theoretically possible to determine the direction in space from which the particles have come before entry into the magnetosphere. By calculating the direction for particles of specific rigidities, one can determine the area in space scanned by each detector. These "asymptotic cones" (McCracken, 1962) are relatively small for high latitude locations, but they rapidly increase in extent as the station latitude decreases until a detector located in the mid and low latitudes essentially scans around the ecliptic plane.

The normal galactic cosmic radiation is essentially isotropic; consequently, neutron monitors are responding to the same primary intensity limited only by the earth's atmospheric effects and the magnetic cutoff rigidity at each location. On the other hand, the distribution of the high energy protons associated with solar flares is often highly anisotropic, and only the locations with asymptotic cones in the direction of the incident protons will record the initial increase of particles. Usually, after a period of time ranging anywhere from a few minutes to an hour, the increased particle intensity becomes isotropic and the remaining neutron monitors will detect the enhanced intensity appropriate to their relative cutoff rigidities. An excellent example of different increases observed by two stations located 1600 miles apart is shown in Figure 13; Deep River, Canada recorded a maximum intensity increase of 95% while Churchill, Canada observed only normal galactic intensity during the initial portion of this event.

In Figure 14 the asymptotic directions of the particles of different rigidities arriving at Deep River and Churchill have been plotted on a conformal projection of the globe on a plane. Inspection of this plot reveals that the asymptotic direction of 1.15 bv particles at Deep River is displaced 240° with respect to the station, and the large area of space scanned by the Deep River monitor is at once evident. The Churchill monitor would also scan a large area of space if particles from 1 bv down to the magnetic

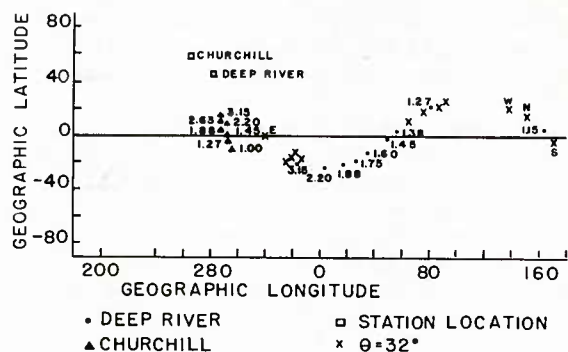


Fig. 14: Asymptotic directions for particles of discrete rigidities detectable at Deep River and Churchill, Canada.

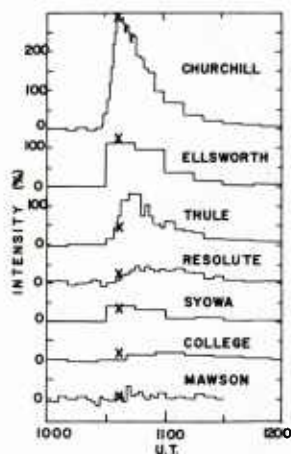


Fig. 15: Relative nucleonic intensity recorded by seven high latitude neutron monitors during the May 4, 1960 high energy solar particle event.

cutoff rigidity of 0.21 bv were detectable. However, the atmosphere absorbs particles with rigidities less than ~ 1 bv, so that the response of the high latitude stations is limited to particles of rigidities above this threshold, even though the magnetic cutoff rigidity may be lower. From this figure it is evident that for the observed effect, the incident particles must have initially arrived from a direction favorable to the Deep River monitor and not favorable to the Churchill detector. This would indicate an initial anisotropy in a direction defined by a geographic longitude of 75°E . Reference to Figure 13 indicates that both detectors were recording identical increases by 0400 indicative of the enhanced radiation being isotropic at that time.

Another excellent example of relative increases observed during a flare event is shown in Figure 15 where the intensity for seven high latitude stations is given for the May 4, 1960 event. The asymptotic cones for these stations are shown in Figure 16. A comparison of these two figures reveals that the most favorable viewing location was at a geographic longitude of $\sim 320^{\circ}\text{E}$.

The five neutron monitors that have been selected for this network will scan a relatively large section of the celestial sphere. However, because of the combination of their geographical position in North America and their cutoff rigidity, it is possible, but fairly unlikely, to have a small (10-20%), highly anisotropic event without noticeable enhancement of the neutron monitor intensity at any of these five locations. To decrease this possibility, additional monitors within a different range of geographical longitudes, such as in Europe, would have to be included.

Independent neutron monitor teletype-compatible data units to interface between the neutron monitor and the teletype circuit are being designed by Mr. John Steljes of the Atomic Energy of Canada, Ltd. at the Chalk River Nuclear Laboratories, Chalk River, Ontario, Canada. These data units have two independent accumulators, each of which will accumulate data for 10 minutes. When one accumulator is "full" (has collected data for 10 minutes), it is switched to the readout position and the second accumulator is switched to the counting position. The most recent 10 minute accumulation is always switched into the readout position, irregardless of whether a readout has occurred. When the data unit is interrogated by the circuit controller, it will reply with the data in the readout position, and will then give a "no-data" reply to

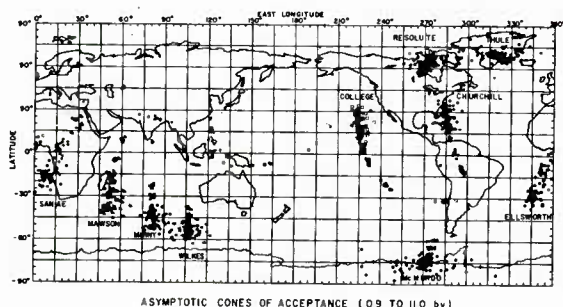


Fig. 16: Asymptotic cones of acceptance for several high latitude locations.

subsequent interrogations until the other accumulator has acquired 10 minutes of data and is switched into the readout position.

Included at all stations will be the 'alarm-over-ride' feature. When the counting rate rises above a preset level, the data unit will be capable of replying to interrogation every 10 minutes, irrespective of its quiet time readout sequence. When the neutron intensity drops below the preset level, the normal time sequence will be resumed. The alarm level being considered is 5% above the normal daily variation. Considering the accessibility of each station to solar protons, we have recommended the quiet time readout sequence given in Table 3.

TABLE 3
Recommended Quiet Time Readout Sequence

| <u>Location</u> | <u>Vertical Cutoff Rigidity (bv)</u> | <u>Time Sequence (min)</u> |
|--------------------------|--------------------------------------|----------------------------|
| Thule, Greenland | 0.00 | 10 |
| Deep River, Canada | 1.02 | 10 |
| Durham, New Hampshire | 1.41 | 20 |
| Swarthmore, Pennsylvania | 1.92 | 30 |
| Dallas, Texas | 4.35 | 60 |

The combined counting rate of all three sections will be quasi-corrected (about 1% accuracy) for atmospheric pressure by including a pressure-controlled variable dead-time feature in the data accumulators. This eliminates the necessity of utilizing a computer to pressure correct the intensity data as is done in normal scientific analysis.

The proposed message on the teletype circuit will consist of a special identification code which has been assigned as HNXX, the station identification given by four letters, the date-time group giving the day, hour and minute at the end of the accumulation interval, a two letter 'eyeball' code indicating whether the neutron intensity reflects a quiet time counting rate or an alarm condition, followed by the neutron counting rate.

The data received in Boulder, Colorado by the ESSA Forecast Center will be transferred to another circuit which will carry the data to the ESSA computer at Anchorage. This computer will examine the data, correlate it with the data obtained from other sensors available in the computer and report back any deviations from a normal expected quiet time counting rate.

VI. CURRENT STATUS

The current status of this network is the following: the prototype data unit which will interface between the neutron monitors and the teletype circuit is undergoing testing at the Atomic Energy of Canada, Ltd., Chalk River Laboratories, and a systems test of this unit with the actual teletype circuit is planned for the near future. Once the system test is successful, the existing teletype circuit will be extended to include the various neutron monitors. It is expected that the entire system will be in operation by January 1968.

REFERENCES

- (1) Carmichael, H., "Cosmic Rays," IQSY Instruction Manual No. 7, 1964.
- (2) McCracken, K.G., "The Cosmic-Ray Flare Effect, Some New Methods of Analysis," J. Geophys. Res., 67, 423-434, 1962.
- (3) Obayashi, T., "Resume of the Conference on the Solar-Terrestrial Events of November 1960". Arctic Institute of North America Research Paper No. 14. 1961.
- (4) Simpson, J.A., "Cosmic-Radiation Neutron Intensity Monitor," Annals of the IGY, IV, 351-373, 1957.

THE EFFECT OF PHYSICAL FORESHORTENING
ON SUNSPOT AREA MEASUREMENTS

by

Captain Ronald T. Podsiadlo
Detachment 54, 6th Weather Wing

SUMMARY

The daily positions and areas of sunspot groups have been measured for nearly a century at various observatories around the world. The standard correction applied to the measured (apparent) sunspot areas, to account for geometrical foreshortening, has been the secant of the central angle, i.e., the angular distance of the spot group from the center of the solar disk. This correction assumes that a sunspot is flat and lies on a smooth solar surface. However, it has been fairly well established that a sunspot is bowl-shaped, and the solar surface (photosphere) is coarse and irregular. These physical features cause the near edge of a sunspot (as viewed by a terrestrial observer) to be partially occulted when the spot is located towards the solar limb. As a result, the apparent area is less than it would be if the same spot were located at the center of the disk and viewed normal to the solar surface. This diminution of the apparent sunspot area is called physical foreshortening. The presence of this physical foreshortening effect has been known for many years, but no attempts have been made to adjust for it in actual sunspot area measurements.

Fifty years of sunspot data (Greenwich Photoheliographic Results, 1915-1964) were analyzed to determine (1) the extent of the effect of physical foreshortening, and (2) whether appropriate systematic corrections could be determined and applied to sunspot area measurements.

The frequency distribution of sunspot groups as a function of area (corrected for geometrical foreshortening) and Central Meridian Distance (CMD) was analyzed. In each of ten sunspot area ranges chosen, there was a systematic decrease in the number of groups with increasing CMD. The decrease was most marked for the smallest groups (areas less than 10 millionths). For example, there were two-thirds as many of these small groups in the interval 40° - 50° CMD as there were in the interval 0° - 10° CMD, and only one-tenth as many in the interval 70° - 80° CMD. For the largest groups (areas greater than 500 millionths) there were only three-fourths as many in the interval 70° - 80° CMD as there were from 0° - 10° CMD.

The rapid loss of the smaller spot groups with increasing CMD is likely caused by limitations in the resolving power of the observing telescopes and, to a lesser degree, by physical foreshortening. The larger groups are lost, i.e., their areas undercorrected, placing them in a lower area range, both by this same loss of the smaller spots in the groups, and by the physical foreshortening of the larger spots.

In order to recover this effective loss of sunspot area, physical foreshortening factors were empirically derived for each of the ten sunspot area ranges and for each 10° CMD interval. These factors were then applied to all the areas in the 50 year sunspot data sample. The revised frequency distribution was smoothed by this adjustment for physical foreshortening. That is, approximately the same number of groups fell into each 10° CMD interval for each area range, with the following exceptions; (1) For the interval 80° - 90° CMD, no suitable factors could be derived to obtain the desired smooth distribution. Near the limb, the attrition of groups in all area ranges is very severe, not only because of physical foreshortening, but also because portions of the larger groups are beyond the limb and therefore not visible. (2) Beyond 70° CMD, the number of groups in those area ranges less than 50 millionths was significantly less than desired in the revised distribution. From this result, it was reasoned that beyond 70° CMD many of those groups with areas less than 50 millionths simply are not visible, especially if they are comprised of a cluster of tiny spots.

The factors derived to obtain the smoothed frequency distribution were significant for all spot group sizes. The larger groups (greater than 200 millionths) were increased in area by 10% at 45° CMD and 20% at 75° CMD by the physical foreshortening correction. The smaller groups (less than 50 millionths) were increased in area by 50% or greater beyond 50° CMD.

Further study is underway to determine whether particular types of spot groups (eg., streams, singles, doubles, etc.) are more affected by physical foreshortening than others. If such is found to be the case, a different set of factors will be derived for each sunspot group type. When these factors are determined, they should be applied in real-time to routine sunspot area measurements as well as to historical sunspot data. The objective is to obtain a statistically more reliable data sample for research use, eg., the development of objective flare forecasting techniques.

NUMERICAL SIMULATION OF CUMULUS CONVECTION

F. W. Murray

The RAND Corporation, Santa Monica, California

Abstract

Atmospheric thermal convection, including condensation and evaporation, is modeled on the cumulus scale by numerically solving the equations of hydrodynamics and thermodynamics. Appropriate Boussinesq equations are derived for both axial and rectilinear symmetry. A mixed Eulerian-Lagrangian method is used. A specific example is discussed, and its computational results are compared with observations made from instrumented aircraft of the Naval Research Laboratory. It is concluded that the model is realistic in many respects, and that it could be a useful adjunct for research in cloud dynamics and cloud physics, particularly in the field of weather modification.

I. Introduction

Models of cumulus convection fall into two principal categories -- analytical and numerical. Analytical models may be as simple as the parcel or slice methods, or as complicated as the bubble model of Scorer and Ludlam [1953] or the spherical vortex of Levine [1959]. Typically they depend on dimensional analysis and invoke the principle of similarity. Numerical models, on the other hand, are merely applications of the equations of hydrodynamics and thermodynamics, solved numerically. This is the type of model discussed in the present paper.

II. The Model

The construction of dynamic models requires some consideration of matters of scale. Much of the basic work on the scale of meteorological phenomena has been done by Charney and Phillips, and Ogura and Phillips [1962] have extended the theory to the scale of cumulus convection. A table giving the dynamic properties of motions on various scales has been published by Ogura [1963]. It shows that the hydrostatic and geostrophic approximations are very good for the larger scales, but useless for the cumulus scale. Also, the Coriolis force is of no consequence on the cumulus scale, and acoustic waves should be filtered out. Ogura and Phillips developed a set of equations appropriate to these conditions, called the anelastic equations. For deep convection these equations take account of dynamic pressure, but since the relationship among pressure, temperature, and saturation mixing ratio is highly nonlinear, the general anelastic equations have been satisfactorily solved only for dry air. For shallow, moist convection, however, it is possible to use the hydrostatic approximation to compute the saturation mixing ratio only, and the anelastic equations then reduce to the Boussinesq equations. In the Boussinesq equations density varies only in the buoyancy term associated with vertical motion. Thus the atmosphere may be regarded as incompressible and a stream function may be defined. These considerations form the basis of the present model.

A cumulus cloud is a relatively small object in the meteorological context, and thus presumably would not make the same demands on a computer as a hemispheric numerical forecast or a general circulation model. That this is not the case, however, is shown by a table produced by the National Academy of Sciences [1966]. Because small-scale problems require greater resolution and shorter time steps than those of larger scale, the number of computations required is similar for all scales. Moreover, cumulus convection requires among the dependent variables three wind components and three phases of water substance -- more than are required by any other scale.

In order to make the problem feasible for solution on available computers, some compromises are necessary. In the present case, the following simplifications were adopted: (1) motion was confined to a vertical plane, eliminating one dimension; (2) symmetry was assumed, reducing the horizontal dimension by one-half; (3) the ice phase was excluded; and (4) a less-than-optimum resolution in space and time was accepted. These simplifications allow a single cell to be simulated on a 32,000-word machine. The model runs at approximately real time on an IBM 7094, and a little slower on an IBM 7044.

Two forms of symmetry -- rectilinear and axial -- have been used. The former, with motion in the x-z plane, simulates a roll cloud or a cloud street. The latter, with motion in the ρ -z plane (where ρ represents radial distance), simulates an isolated convective cell. The convergence of the coordinates in the axisymmetric formulation results in somewhat more vigorous circulation than in the rectilinear formulation, but with a relatively weaker compensating downdraft.

The wind components and meridional component of vorticity are given by

$$(1R) \quad u = - \frac{\partial \psi}{\partial z} \quad w = \frac{\partial \psi}{\partial x}$$

$$(2R) \quad \eta = - \left(\frac{\partial^2 \psi}{\partial x^2} + \frac{\partial^2 \psi}{\partial z^2} \right)$$

in the rectilinear formulation and by

$$(1A) \quad u = - \frac{1}{\rho} \frac{\partial \psi}{\partial z} \quad w = \frac{1}{\rho} \frac{\partial \psi}{\partial \rho}$$

$$(2A) \quad \eta = - \frac{1}{\rho^2} \left(- \frac{1}{\rho} \frac{\partial \psi}{\partial \rho} + \frac{\partial^2 \psi}{\partial \rho^2} + \frac{\partial^2 \psi}{\partial z^2} \right)$$

in the axisymmetric.

The corresponding prognostic equations are

$$(3R) \quad \frac{\partial \eta}{\partial t} = - \left(u \frac{\partial \eta}{\partial x} + w \frac{\partial \eta}{\partial z} \right) - \frac{\partial B}{\partial x} + v_M \left(\frac{\partial^2 \eta}{\partial x^2} + \frac{\partial^2 \eta}{\partial z^2} \right)$$

and

$$(3A) \quad \frac{\partial \eta}{\partial t} = - \left(u \frac{\partial \eta}{\partial \rho} + w \frac{\partial \eta}{\partial z} \right) - \frac{1}{\rho} \frac{\partial B}{\partial \rho} + v_M \left(\frac{3}{\rho} \frac{\partial \eta}{\partial \rho} + \frac{\partial^2 \eta}{\partial \rho^2} + \frac{\partial^2 \eta}{\partial z^2} \right)$$

where

$$B = g \left(\frac{T^*}{T^*} - r_\ell \right)$$

and g is the gravitational acceleration, T^* is the departure of virtual temperature from its basic value, $\overline{T^*}$ is mean virtual temperature, r_ℓ is the mixing ratio of liquid water to dry air, and v_M is the coefficient of eddy diffusion. New values of B may be determined at each time step by means of the Lagrangian equations

$$(4) \quad \frac{dr_\ell}{dt} = C + v_r \nabla^2 r_\ell$$

$$(5) \quad \frac{dr_v}{dt} = -C + v_r \nabla^2 r_v$$

$$(6) \quad \frac{dT}{dt} = - \frac{g}{c_p} w + \frac{LC}{c_p + c_{pv} r_v + c_w r_\ell} + v_T \nabla^2 T$$

where r_v is mixing ratio of water vapor, C is rate of condensation, g/c_p is the dry-adiabatic lapse rate, L is the latent heat of condensation, c_p , c_{pv} , and c_w are appropriate specific heats, and v_r and v_T are coefficients of eddy diffusion.

In practice Eqs. (3R) or (3A) are solved in the Eulerian manner for one time step, and ψ is found by relaxation of Eqs. (2R) or (2A), which yields the wind components through Eqs. (1R) or (1A). Then for each grid point we find an upstream point from which a parcel will move to the grid point during the time step. Values of all the variables at the upstream point for the initial time of the step are found by interpolation among the surrounding grid points. Next, Eqs. (4), (5), and (6) are solved in three steps: First, if the parcel is supersaturated, condensation occurs to the point of saturation; if it is subsaturated, evaporation occurs either to the point of saturation or until the liquid water is exhausted. Second, as the parcel moves downstream to the grid point, the rate of condensation (provided it is saturated) is given by an expression due to Berkofsky [1960]:

$$(7) \quad C = - \frac{1 - \frac{1}{\epsilon L} (c_p T - L r_s)}{L + \frac{c_p R T^2}{L r_s (\epsilon + r_s)}} g_w$$

where ϵ is the ratio of the molecular weight of water vapor to that of dry air and R is the gas constant for dry air. Third, after the parcel reaches its destination grid point it is again adjusted to equilibrium as in the first step, and the eddy diffusion is taken into account.

III. An Example

The model has been run with a number of different basic atmospheres and triggering perturbations. Most of the real cases have been from soundings over the Caribbean. One example, for which verifying observations made by instrumented aircraft of the Naval Research Laboratory are available, will be discussed briefly.

Observations were made at Roosevelt Roads, Puerto Rico, on the morning of 21 April 1965. A combination of the aircraft sounding in clear air and the San Juan RAOB defined the basic atmosphere, and the initial perturbation was based on temperature observations below the clouds. Condensation began after 9 minutes of simulated time, and subsequently the computed sounding rapidly became dry adiabatic below the condensation level and moist adiabatic within the cloud. At the top of the cloud a cold cap was formed by forced lifting and evaporation. In nature, turbulence on a scale too small for resolution by the grid probably acts to prevent formation of such a strongly superadiabatic lapse rate across the top of the cloud, but observations are not available to confirm or deny this.

A comparison of observations with computations is shown in Table 1. The four columns represent penetrations into four different clouds; they are compared with the computations for 20 and 25 minutes. In general, cloud bases and tops and liquid water content showed good agreement. Temperature departure was less satisfactory, partly because of the difficulty in establishing the observed basic temperature.

This case and others are discussed more fully in reports by Murray and Anderson [1965], Murray and Hollinden [1966], and Murray [1967].

IV. Conclusion

On the whole, results have been quite encouraging. It appears that this model can simulate many of the features of cumulus convection very well. This type of model can be a very powerful tool for the study of cumulus convection, but no routine operational use is envisaged. On the other hand, many applications can be devised. For example, its trajectory capabilities have been used to determine the most efficient level for cloud seeding under a variety of circumstances. Further use of the model in the study of cloud modification is seen. Although the model does not now incorporate the ice phase, the dynamic effects of seeding might be included in a parametric way. Some work has been done toward inclusion of the ice phase, and there is thought of including precipitation.

Table 1

Observed And Computed Values Of Cloud Properties

| Property | Cloud | | | | Notes |
|--|---------|---------|---------|---------|-------|
| | A | B | C | D | |
| Height of penetration (ft) | 6,600 | 7,100 | 7,350 | 7,700 | |
| Temperature departure (°C) | -0.6 | -1.0 | -1.2 | -2.2 | a |
| (Inside temperature minus outside temperature) | 1.8 | -1.1 | 0.0 | -1.0 | b |
| | 1.5 | 1.5 | 1.3 | 1.2 | c |
| Evaporator dew point (°C) | 13.3 | 13.5 | 12.8 | 10.6 | a |
| | 16.9 | 15.8 | 13.8 | 9.0 | b |
| | 16.5 | 16.0 | 15.8 | 15.5 | c |
| Liquid water content (g m^{-3}) | 2.0 | 2.3 | 2.3 | 1.2 | d |
| | 1.4 | 2.2 | 0.0 | 1.2 | e |
| | 2.1 | 2.1 | 1.5 | 0.6 | b |
| | 2.0 | 2.4 | 2.6 | 3.0 | c |
| Width of cloud (m) | 1,200 | 600 | 1,000 | 900 | a |
| | 1,070 | 1,040 | 430 | 120 | b |
| | 610 | 790 | 910 | 910 | c |
| Height of cloud base (ft) | 2,800 | 2,800 | 2,800 | 2,800 | a |
| | 3,200 | 3,200 | 3,200 | 3,200 | b |
| | 3,200 | 3,200 | 3,200 | 3,200 | c |
| Height of cloud top (ft) | ~10,000 | ~10,000 | ~10,000 | ~10,000 | a |
| | 7,900 | 7,900 | 7,900 | 7,900 | b |
| | 9,100 | 9,100 | 9,100 | 9,100 | c |

a Aircraft observation

b Computation at 20 minutes

c Computation at 25 minutes

d Observed by NRL total water instrument

e Observed by Johnson-Williams liquid water instrument

Research in atmospheric science is making increasing use of numerical modeling on all scales, from the planetary down to the microphysical. It is expected that this approach will be particularly valid on the scale of cumulus convection.

This work was supported by the Office of Naval Research under Contract No. N00014-6-67-C-0101. Material contained in this report is excerpted from RAND Memorandum RM-5316-NRL [Murray, 1967].

References

- Berkofsky, L.: "The Inclusion of Latent Heat of Condensation in a Numerical Forecasting Model," Cumulus Dynamics, C. E. Anderson (ed.), Pergamon Press, New York, pp. 85-102, 1960.
- Levine, J.: "Spherical Vortex Theory of Bubble-Like Motion in Cumulus Clouds," J. Meteorol., Vol. 16, pp. 653-662, 1959.
- Murray, F. W.: Numerical Simulation of Cumulus Convection, RM-5316-NRL, The RAND Corporation, 34 pp., 1967.

- Murray, F. W., and C. E. Anderson: Numerical Simulation of the Evolution of Cumulus Towers, Report SM-49230, Douglas Aircraft Company, Inc., 97 pp., 1965.
- Murray, F. W., and A. B. Hollinden: The Evolution of Cumulus Clouds: A Numerical Simulation and Its Comparison against Observations, Report SM-49372, Douglas Aircraft Company, Inc., 147 pp., 1966.
- National Academy of Sciences--National Research Council: Weather and Climate Modification Problems and Prospects, Volume II, Research and Development, Publ. No. 1350, p. 139, 1966.
- Ogura, Y.: "A Review of Numerical Modeling Research on Small-Scale Convection in the Atmosphere," Meteorol. Monographs, Vol. 5, No. 27, pp. 65-75, 1963.
- Ogura, Y., and N. A. Phillips: "Scale Analysis of Deep and Shallow Convection in the Atmosphere," J. Atmos. Sci., Vol. 19, pp. 173-179, 1962.
- Scorer, R. S., and F. H. Ludlam: "Bubble Theory of Penetrative Convection," Quart. J. Roy. Meteorol. Soc., Vol. 79, pp. 94-103, 1953.

FIELDS BY CORRELATION ASSEMBLY*

Maurice B. Danard, Manfred M. Holl and James R. Clark

Meteorology International Incorporated
Monterey, California

This is a numerical technique to produce meteorological or oceanographic fields. Associated distributions of reliability are concurrently produced. As used here, reliability is defined as $1/(2\sigma^2)$, where σ is the standard error.

As applied to 500 mb height, for example, the technique in its current version blends information on Z and ∇Z (from winds). Information on $\nabla^2 Z$ (e.g., from satellite data) could also be included. All data are combined in proportion to their reliabilities. Wind components are first geostrophically converted into height differences between adjacent grid points. These estimates are then assembled together with the first-guess gradients, each over a 5×5 set of grid points (omitting the corner ones) surrounding the wind report. Height estimates are next extrapolated to their nearest grid points using the analysed gradient fields. These modified estimates are then assembled together with the first-guess heights. The assembled height and gradient fields are then blended to form the final height and reliability fields. Provision is also made to check height and wind reports for detectable gross errors. Test results are shown.

The methods may be readily modified to apply to other geophysical fields. For example, two such versions currently being tested apply to sea-level pressure and sea-surface temperature.

*Progress-Report Paper. Contract No. N0022866C1325 for the U. S. Fleet Numerical Weather Facility.

ON THE APPLICATION OF SCALING THEORY AND ENERGETICS
TO THE THIRD WEATHER WING SIX-LEVEL MODEL

by

Major Harold B. Hart
Hq 3rd Weather Wing
Offutt AFB, Nebraska

ABSTRACT

A brief review of scaling theory for middle latitude macroscale flow together with energy balance considerations is presented. The 3WW Six-Level Model equations are then scaled and analyzed with respect to their consistency from the point of view of scale theory and energy balance.

SECTION A - INTRODUCTION

At the AWS Technique Development Conference held at Washington last year, Dr. Jule G. Charney emphasized the necessity of holding physical and mathematical restrictions firmly in mind when dealing with more sophisticated numerical prediction models. We need to account adequately for all large contributing factors first, before we concern ourselves with less important factors. Dr. Charney's work on the scale theory of atmospheric motion is quite useful in estimating the relative order of magnitudes of the various terms in the model equations.

In addition, we note that Dr. E.N. Lorenz has studied the energy balance of certain simplified models. Using his methods, one can ensure that failure to consider minor terms in the completely general model equations will not result in a destructive energy imbalance when the simplified model is run.

SECTION B - SCALING THEORY

Charney [1] defined the characteristic scale properties of macroscale motion in middle latitudes as follows. S , which represents the mean horizontal distance between points at which velocity components take extreme values, has an order of magnitude of 10^6 m. H , which represents the corresponding mean vertical distance, is of order 10^4 m. V , the mean magnitude of the horizontal wind, and C , the mean phase speed of the streamline pattern, are both of order 10 m/sec. It can be shown that W , the mean magnitude of the vertical velocity, depends on the size of the other scale parameters and is of order 10^{-2} m/sec.

$$(1) \quad K \equiv \frac{H}{\theta} \frac{\partial \theta}{\partial z} \sim 0.1$$

The static stability K is defined by equation (1), where θ is the potential temperature. Since θ increases by about 30° Kelvin from sea level to the tropopause in the atmosphere, K has the order of magnitude 0.1. Five other parameters which will be useful are the radius of the earth, a , which is of order 10^7 m, the gravitational acceleration g , which is of order 10 m/sec², f and j , the vertical and meridional components of the earth's vorticity, which both have 10^{-4} sec⁻¹ order of magnitudes, and β , the derivative of f in the meridional direction, which is of order 10^{-11} .

We can now apply these parameters to the evaluation of terms in the equations of motion and other equations. In order to evaluate the partial derivatives involved, we replace them by finite increments expressed in terms of the characteristic scale parameters. For example, the horizontal derivative of a horizontal velocity component u or v is evaluated as scale parameter V over scale parameter S . We find that this derivative has an order of magnitude of 10^{-5} . Similarly, the horizontal derivative of the vertical velocity is evaluated as W/S and is of order 10^{-8} . The vertical derivative of a horizontal velocity is evaluated as V/H with order 10^{-3} . Finally, the vertical derivative of the vertical velocity is evaluated as W/H with order of magnitude 10^{-6} .

We can estimate the space derivatives of pressure and density in a similar manner. However, by evaluating the logarithmic derivatives, one can avoid the introduction of separate characteristic values for pressure and density. We observe that fields of pressure and density have the same horizontal scale as the velocity field and that horizontal variations of pressure and density are of the same order or less than their mean values. In the vertical, however, variations through the scale distance H are

of the same order of magnitude as the mean value. Thus, the horizontal logarithmic derivatives are of order 10^{-6} or less, while the vertical logarithmic derivatives are of order 10^{-4} .

In order to evaluate time derivatives, we note that a system moving horizontally with speed C will move a distance ds in the time ds/C so that the local time variation may be evaluated as C times the space variation. The total time derivative may be evaluated by expanding into partial derivatives and then evaluating the individual terms. All terms are of order 10^{-5} except the vertical derivative, which is one order of magnitude lower. Thus, the total derivative may be taken to be of order V/S or 10^{-5} .

$$\begin{array}{lcl}
 \text{(2)} & \begin{array}{c} \textcircled{1} \\ \frac{du}{dt} \\ \frac{V^2}{S} \\ 10^{-4} \end{array} - \begin{array}{c} \textcircled{2} \\ \frac{uv \tan \phi}{a} \\ \frac{V^2}{a} \\ 10^{-5} \end{array} + \begin{array}{c} \textcircled{3} \\ \frac{uw}{a} \\ \frac{VW}{a} \\ 10^{-8} \end{array} - \begin{array}{c} \textcircled{4} \\ fV \\ 10^{-3} \end{array} + \begin{array}{c} \textcircled{5} \\ jW \\ 10^{-6} \end{array} = \begin{array}{c} \textcircled{6} \\ -\frac{1}{\rho} \frac{\partial p}{\partial x} \end{array} \\
 \text{(3)} & \begin{array}{c} \frac{dv}{dt} \\ \frac{V^2}{S} \\ 10^{-4} \end{array} + \begin{array}{c} \frac{u^2 \tan \phi}{a} \\ \frac{V^2}{a} \\ 10^{-5} \end{array} + \begin{array}{c} \frac{vw}{a} \\ \frac{VW}{a} \\ 10^{-8} \end{array} + \begin{array}{c} fV \\ 10^{-3} \end{array} = -\frac{1}{\rho} \frac{\partial p}{\partial y} \\
 \text{(4)} & \begin{array}{c} \frac{dw}{dt} \\ \frac{VW}{S} \\ 10^{-7} \end{array} - \begin{array}{c} \frac{u^2 + v^2}{a} \\ \frac{V^2}{a} \\ 10^{-5} \end{array} - \begin{array}{c} jU \\ jV \\ 10^{-3} \end{array} + \begin{array}{c} g \\ g \\ 10 \end{array} = -\frac{1}{\rho} \frac{\partial p}{\partial z}
 \end{array}$$

We may now consider the inviscid equations of motion and evaluate the terms as shown in equations (2), (3) and (4). Turning our attention first to equation (4), we note that the pressure gradient force term, term 6, must have the same order of magnitude as the largest term on the left hand side, which is term 4, the gravitational acceleration. Furthermore, if equation (4) is simplified to the hydrostatic equation by dropping terms 1, 2 and 3, this approximation should be accurate for macroscale flow to at least one-tenth of one percent.

Similarly, in the horizontal equations of motion (2) and (3), the pressure gradient term, term 6, must balance the largest term on the left hand side, term 4, the Coriolis force term. If all other terms were neglected, the result would be the equations of geostrophic flow. However, since term 1 is within one order of magnitude of the dominant terms, winds obtained by the geostrophic relation could be in error by as much as 10%. We can reduce the error to about 1% by retaining term 1 in addition to terms 4 and 6 in equations (2) and (3).

$$\begin{array}{lcl}
 \text{(5)} & \theta \equiv T \left(\frac{p}{p_0} \right)^k = \frac{p_0^k}{R} p^{1-k} \\
 \text{(6)} & \frac{\partial \ln \theta}{\partial z} = (1-k) \frac{\partial \ln p}{\partial z} - \frac{\partial \ln p}{\partial z} \\
 \text{(7)} & \frac{\partial \ln p}{\partial z} = \frac{1}{p} \frac{\partial p}{\partial z} \sim \frac{p f V}{p} \sim \frac{f V}{g} \frac{\partial \ln p}{\partial z} \sim \frac{f V}{g H} \sim 10^{-8} \\
 \text{(8)} & \left\{ \begin{array}{l} \frac{\partial p}{\partial z} = \rho f V \\ \frac{1}{\rho} \frac{\partial}{\partial z} \frac{\partial p}{\partial z} = -g \frac{\partial \ln p}{\partial z} = f \left(\frac{\partial V}{\partial z} + V \frac{\partial \ln p}{\partial z} \right) \\ \frac{\partial \ln p}{\partial z} \sim \frac{f V}{g H} \sim 10^{-8} \end{array} \right. \\
 \text{(9)} & W \sim \frac{\frac{\partial \ln \theta}{\partial t} + V \frac{\partial \ln \theta}{\partial z}}{\frac{\partial \ln \theta}{\partial z}} \sim \frac{\frac{f C V}{g H}}{\frac{K}{H}} \sim \frac{f C V}{g K} \sim 10^{-2}
 \end{array}$$

Use of the geostrophic approximation and the hydrostatic approximation also allows us to evaluate the logarithmic horizontal derivative of potential temperature, which is fundamental to the estimation of the vertical velocity using the adiabatic statement of the First Law of Thermodynamics. From the definition of potential temperature, equation (5), differentiating logarithmically in the horizontal, we obtain equation (6). From the geostrophic and hydrostatic approximations, we see in relation (7) that $\partial \ln p / \partial s$ is of order fV/gH or 10^{-8} . To obtain the required density derivative, one must differentiate the geostrophic relation in the vertical and combine with the hydrostatic equation as in relations (8). The density derivative is then seen to have the same order of magnitude, fV/gH or 10^{-8} . Since K , which represents R/C_p , is about 0.3, $\partial \ln \theta / \partial s$ must also have the order of magnitude fV/gH , while in the vertical, using the definition of static stability, $\partial \ln \theta / \partial z$ is of order K/H or 10^{-5} . Finally, by solving the adiabatic equation for the vertical velocity as in (9), we find that W is of order fCV/gK or 10^{-2} .

$$(10) \left\{ \begin{aligned} \frac{\omega}{p} &= \frac{d \ln p}{dt} = \frac{\partial \ln p}{\partial t} + V \frac{\partial \ln p}{\partial s} + w \frac{\partial \ln p}{\partial z} \\ &\quad \frac{fCV}{gH} \quad \frac{fCV}{gH} \quad \frac{fCV}{gHK} \\ &\quad 10^{-7} \quad 10^{-7} \quad 10^{-6} \end{aligned} \right.$$

$$\omega \sim w \frac{\partial p}{\partial z} \sim \rho g w \sim 10^{-2} W$$

$$(11) \quad \frac{\partial}{\partial p} \sim 10^2 \frac{\partial}{\partial z}$$

$$(12) \quad \sigma \equiv -\alpha \frac{\partial \ln \theta}{\partial p} \sim 10^2 \frac{K\alpha}{H}$$

$$(13) \quad \zeta \equiv \frac{\partial v}{\partial x} - \frac{\partial u}{\partial y} \sim \frac{V}{S} \sim 10^{-5}$$

$$(14) \quad \delta \equiv \frac{\partial u}{\partial x} + \frac{\partial v}{\partial y} = -\frac{\partial \omega}{\partial p} \sim \frac{W}{H} \sim 10^{-6}$$

We may now use these scaling evaluations to examine the Third Weather Wing Six-Level Model Equations. The latter equations are written in the x, y, p, t coordinate system in which omega, the total time derivative of pressure, is the vertical velocity component. The relation in orders of magnitude between omega and W is shown in equation (10), where the meter-ton-second system is used to evaluate density. We may also note that horizontal derivatives are evaluated in the same manner as for the x, y, z, t coordinate system, while vertical derivative evaluations may be performed using relation (11), in view of the fact that a scale height of 10^4 m corresponds to a pressure change on the order of 100 centibars. The stability parameter σ in the x, y, p, t system is related to the parameter K by relation (12), where α is the specific volume.

Finally, vorticity is evaluated in relation (13) as V/S or 10^{-5} , while horizontal divergence may be evaluated from the continuity equation as in (14). It has the order of magnitude of W/H or 10^{-6} .

SECTION C - ENERGY BALANCE

$$(15) \quad \frac{\partial \theta_1}{\partial t} = -J(\psi_2, \theta_1) - (\mathbf{V}_3 \cdot \nabla) \theta_1 - \omega_3 \frac{\partial \theta_1}{\partial p}$$

$$10^{-7} \theta_1 \quad 10^{-7} \theta_1 \quad 10^{-8} \theta_1 \quad 10^{-7} \theta_1$$

$$(16) \quad \frac{\partial \zeta_2}{\partial t} = -J(\psi_2, \zeta_2) - J(\psi_2, f) - \nabla \cdot f \mathbf{V}_3 - \mathbf{V}_3 \cdot \nabla \zeta_2$$

$$10^{-10} \quad 10^{-10} \quad 10^{-10} \quad 10^{-11}$$

$$- \zeta_2 \delta_3 - \omega_3 \frac{\partial \zeta_2}{\partial p} - \nabla \omega_3 \cdot \nabla \frac{\partial \psi_2}{\partial p} - J(\omega_3, \frac{\partial \chi_3}{\partial p})$$

$$10^{-11} \quad 10^{-11} \quad 10^{-11} \frac{\partial \psi_2}{\partial p} \quad 10^{-12} \frac{\partial \chi_3}{\partial p}$$

$$(17) \quad \frac{\partial \delta_3}{\partial t} = -\nabla^2 \Phi_1 + \nabla \cdot (f \nabla \psi_2) - J(f, \chi_3) - \nabla \cdot (\mathbf{V}_2 \cdot \nabla \mathbf{V}_2)$$

$$10^{-11} \quad 10^{-9} \quad 10^{-9} \quad 10^{-11} \quad 10^{-10}$$

$$- \nabla \cdot (\mathbf{V}_2 \cdot \nabla \mathbf{V}_3) - \nabla \cdot (\mathbf{V}_3 \cdot \nabla \mathbf{V}_2) - \nabla \omega_3 \cdot \frac{\partial \mathbf{V}_2}{\partial p} - \nabla \cdot (\mathbf{V}_3 \cdot \nabla \mathbf{V}_3) - \nabla \omega_3 \cdot \frac{\partial \mathbf{V}_3}{\partial p}$$

$$10^{-11} \quad 10^{-11} \quad 10^{-11} \quad 10^{-12} \quad 10^{-12}$$

Let us now turn to energy considerations. Lorenz [2] has elucidated the energy balance between total potential energy and the nondivergent kinetic energy and irrotational kinetic energy by displaying the nondivergent and irrotational wind components separately in the thermodynamic equation, the vorticity equation and the divergence equation as shown in equations (15), (16) and (17), where the terms have been scaled to show their orders of magnitude. In these equations, the subscript 1 identifies dependent variables which are related to the temperature, subscript 2 identifies variables related to the nondivergent wind and subscript 3 identifies variables related to the irrotational wind. ψ_2 is the nondivergent stream function and χ_3 is the velocity potential, while capital J indicates the horizontal Jacobian.

We note that terms on the right hand side of the thermodynamic equation (15) are divided into two classes, those having subscripts (1,2) and those having (1,3) subscripts. The former represents temperature advection by the nondivergent wind and the latter by the divergent wind. Terms of the vorticity equation fall into the five classes (2), (3), (2,2), (2,3) and (3,3). Finally, terms of the divergence equation reveal the six classes (1), (2), (3), (2,2), (2,3) and (3,3).

$$(18) \quad \frac{\partial}{\partial t} (P+I) = c_p \bar{p}_0^{-\kappa} \frac{\partial}{\partial t} \int \bar{p}^{\kappa} \theta_1 dM$$

$$(19) \quad \frac{\partial K_2}{\partial t} = \frac{1}{2} \frac{\partial}{\partial t} \int \nabla \psi_2 \cdot \nabla \psi_2 dM$$

$$(20) \quad \frac{\partial K_3}{\partial t} = \frac{1}{2} \frac{\partial}{\partial t} \int \nabla \chi_3 \cdot \nabla \chi_3 dM$$

These three equations may now be used to evaluate the classes of terms which occur in the expressions for the rates of change of total potential energy, nondivergent kinetic energy and irrotational kinetic energy which are given in equations (18), (19) and (20) in which dM represents a mass element. When these expressions are integrated over the entire atmosphere, many terms vanish. For equation (18), the non-vanishing terms are of class (1,3). For the nondivergent kinetic energy tendency, equation (19), the integrand may be transformed using Green's Theorem to $-\psi_2 \zeta_2$ and it is seen that the non-vanishing terms are of classes (2,3), (2,2,3) and (2,3,3). For the irrotational kinetic energy tendency, the integrand transforms to $-\chi_3 \delta_3$ and the non-vanishing terms are of classes (1,3), (2,3), (2,2,3) and (2,3,3). Now, since the equations (15), (16) and (17) are known to conserve total energy, the irrotational kinetic energy tendency term of class (1,3) must cancel the total potential energy tendency, which had non-vanishing terms of class (1,3) only. Similarly, the remaining terms of (20) must cancel the terms of the nondivergent kinetic energy tendency class by class.

In the case of a simplified model such as the Third Weather Wing Six-Level Model, care must be taken that terms are dropped in a consistent manner so that the energy balance expressed by the complete equations is not upset. A quasi-geostrophic model may be formed by retaining only the two largest terms in the divergence equation (17). These terms are of classes (1) and (2). The resulting irrotational kinetic energy tendency will therefore possess non-vanishing terms of classes (1,3) and (2,3). The class (1,3) terms will be cancelled by the (1,3) terms in the total potential energy expression using equation (15) unaltered. The vorticity equation must then be altered so that the nondivergent kinetic energy expression will provide non-vanishing terms of class (2,3) only to cancel the class (2,3) terms from the irrotational kinetic energy expression. This can be accomplished by dropping the terms of classes (2,3) and (3,3) from equation (16). It is apparent that these are the small terms, one or more orders of magnitude smaller than the dominant terms of order 10^{-10} .

In summary, the quasi-geostrophic set of equations may be obtained by simplifying both the vorticity and divergence equations down to their major terms by dropping all terms of lower orders of magnitude. However, in order to avoid disruption of the irrotational kinetic energy balance, all terms of the thermodynamic energy equation, including the small term representing temperature advection by the divergent wind, must be retained.

SECTION D - APPLICATIONS TO THE 3WW SIX-LEVEL MODEL

$$(21) \quad \underbrace{(\nabla^2 - \frac{\mu f_0}{\bar{p}})}_{10^{-10}} \frac{\partial \psi}{\partial t} = - \underbrace{J(\psi, \xi)}_{10^{-10}} - \underbrace{J(\psi, f)}_{10^{-10}} + \underbrace{f_0 \frac{\partial \omega}{\partial p}}_{10^{-10}}$$

$$(22) \quad \nabla^2 \frac{\partial \psi}{\partial t} = -J(\psi, \xi) - J(\psi, f) + f \frac{\partial \omega}{\partial p}$$

$$(23) \quad \frac{\partial \xi'_2}{\partial t} = -J(\psi_2, \xi'_2) - J(\psi'_2, \xi_2) - J(\psi'_2, f) - f \frac{\partial}{\partial p} \nabla \cdot \mathbf{V}_3$$

$$(24) \quad \int \frac{\partial \xi'_2}{\partial t} dM = \int \left[\nabla \cdot \left(f \frac{\partial \mathbf{V}_3}{\partial p} \right) - \frac{\partial \mathbf{V}_3}{\partial p} \cdot \nabla f \right] dM = - \int \frac{\partial \mathbf{V}_3}{\partial p} \cdot \nabla f dM$$

We will now compare the resulting set with the Six-Level Model, equation by equation. The Six-Level Model vorticity equation is shown as equation (21), while Lorenz's quasi-geostrophic vorticity equation is equation (22). The two equations are quite similar. The Helmholtz term in equation (21) is a very small artificial synoptic divergence devised by Cressman for the purpose of stabilizing the spurious ultra-long wave retrogression that had been observed. The other terms are identical except for the use of a standard Coriolis parameter f_0 in the last term. According to Wiin-Nielsen [3], it is necessary to use a constant Coriolis parameter in the quasi-geostrophic model in order to avoid a spurious source of globally averaged thermal vorticity. If one differentiates equation (22) with respect to pressure, the result is equation (23), where primes indicate vertical differentiation. When this equation is integrated over the entire atmosphere, all the Jacobians vanish and the equation may be written as in (24) with the aid of Gauss' Theorem. Since the integral on the right is not, in general, zero unless f is a constant, this justifies the use of f_0 for f where it appears in undifferentiated form in the vorticity equation. We may conclude that the Six-Level Model vorticity equation is consistent both from the point of view of scale theory and energy balance and would conserve both vorticity and thermal vorticity in a global integration.

$$(25) \quad \nabla^2 \psi = f^{-1} \nabla^2 \Phi - f^{-2} \nabla \Phi \cdot \nabla f$$

$$(26) \quad \nabla^2 \psi_2 = f^{-1} \nabla^2 \Phi_1 - f^{-1} \nabla \psi_2 \cdot \nabla f$$

$$(27) \quad \nabla \psi_2 = f^{-1} \nabla \Phi$$

$$(28) \quad \frac{\partial}{\partial t} \left(\frac{\partial \psi}{\partial p} \right) = -\overline{\nabla} \cdot \nabla \left(\frac{\partial \psi}{\partial p} \right) - \frac{\omega \sigma}{f_0}$$

$$(29) \quad \frac{\partial \theta_1}{\partial t} = -J(\psi_2, \theta_1) - (\mathbf{V}_3 \cdot \nabla) \theta_1 - \omega_3 \frac{\partial \theta_1}{\partial p}$$

Turning now to the Six-Level balance equation shown above as equation (25), we will compare this equation to Lorenz's balance equation shown in equation (26). They are identical except for the final term of (25) in which the geostrophic approximation (27) has been employed. Obviously, this substitution does not alter the order of magnitude of the final term. Nor has there been any alteration of the classes of terms appearing in the balance equation. We must conclude, therefore, that equation (25) is also consistent from scale and energy considerations.

Similarly, introduction of the geostrophic approximation into the adiabatic equation (28) does not alter the order of magnitude of its terms. Lorenz's adiabatic equation is shown in (29) for comparison. However, we must note that (28) is not consistent from the energetic point of view. The advecting wind $\overline{\nabla}$ is obtained solely from the nondivergent stream function in equation (25). The term involving advection by the divergent wind component visible in equation (29) has been omitted in (28). As Lorenz pointed out, it is not consistent to drop this small term because of the creation of an imbalance in the irrotational kinetic energy of the model. Thus, while the Six-Level Model is known to produce reasonably accurate short-range forecasts, this energetic inconsistency would probably be damaging for long range forecasts.

SECTION E - CONCLUSION

We conclude that the Third Weather Wing Six-Level Model is quite consistent with respect to the meteorological theory of macroscale motion. It retains only the dominant

terms of the complete equations. However, application of Lorenz's analysis reveals that there is an energy imbalance in the budget of irrotational kinetic energy which cannot be remedied without expanding the model to take into consideration the horizontal irrotational wind flow.

SECTION F - FINAL REMARKS

In closing, I might comment that during the past year, I have also examined more complicated sets of equations obtained by retaining terms one and two orders of magnitude smaller than the dominant terms in the complete inviscid adiabatic equations. These intermediate equations were also studied from the points of view of planetary scale and mesoscale motions in middle latitudes and macroscale flow in the tropics. The results have been published as Third Weather Wing Aerospace Sciences Technical Note 15, as a reference work and guide for future model development work. Copies of the paper are available for those who are interested at Hq, Third Weather Wing, Offutt AFB, Nebraska.

REFERENCES

- [1] Charney, J.G.: "On the scale of atmospheric motions", Geofys. Publikasjoner 17, 17 pp., (1948)
- [2] Lorenz, E.N.: "Energy and numerical weather prediction", Tellus 12, pp. 364-373, (1960)
- [3] Wiin-Nielsen, A.: "On certain integral constraints for the time integration of baroclinic models", Tellus 11, pp. 45-59, (1959)

OUTLINE OF PRIMITIVE EQUATION MODEL

T. N. Krishnamurti
Associate Professor
Department of Meteorology and Oceanography
Naval Postgraduate School
Monterey, California

I. Basic equations:

i) Equation of motion:

$$D \frac{DU}{Dt} = -\omega \frac{\partial U}{\partial p} + fV - mg \frac{\partial Z}{\partial x} - g \frac{\partial}{\partial p} \left\{ C_D \frac{p}{RT} U \sqrt{U^2 + V^2} \right\} \\ + k \frac{\partial^2 U}{\partial p^2} + \nu \nabla^2 U \quad \text{_____ (1)}$$

$$\frac{DV}{Dt} = -\omega \frac{\partial V}{\partial p} - fU - mg \frac{\partial Z}{\partial y} - g \frac{\partial}{\partial p} \left\{ C_D \frac{p}{RT} V \sqrt{U^2 + V^2} \right\} \\ + k \frac{\partial^2 V}{\partial p^2} + \nu \nabla^2 V \quad \text{_____ (2)}$$

$$\frac{RT}{p} = -g \frac{\partial Z}{\partial p} \quad \text{_____ (3)}$$

ii) Continuity equation:

$$\frac{\partial \omega}{\partial p} = -m \left(\frac{\partial U}{\partial x} + \frac{\partial V}{\partial y} \right) \quad \text{_____ (4)}$$

iii) First law of thermodynamics:

$$\frac{D\theta}{Dt} = -\omega \frac{\partial \theta}{\partial p} + \frac{1}{C_p} \left(\frac{p_0}{p} \right)^{R/C_p} \left[H_S + H_{L1} + H_{L2} \right] \\ + k \frac{\partial^2 \theta}{\partial p^2} + \nu \nabla^2 \theta \quad \text{_____ (5)}$$

iv) Moisture Conveyance equation:

$$\frac{Dq}{Dt} = -\omega \frac{\partial q}{\partial p} + E - \frac{1}{L} (H_{L1} + H_{L2}) + k \frac{\partial^2 q}{\partial p^2} \quad \text{_____ (6)}$$

v) Tendency equation:

$$\frac{DZ_{1000}}{Dt} = - \omega \frac{\partial Z_{1000}}{\partial p} + \left(U_{1000} \frac{\partial h}{\partial x} + V_{1000} \frac{\partial h}{\partial y} \right)_m + \nu \nabla^2 Z_{1000} \quad \text{_____ (7)}$$

II. Boundary Conditions:

i) $\omega = 0$ at $p = 0$

ii) $\frac{\partial}{\partial y} U = \frac{\partial \theta}{\partial y} = \frac{\partial Z}{\partial y} = \frac{\partial q}{\partial y} = 0$ at equator

iii) $V = 0$ at equator

iv) $U = V = 0$ at pole

v) θ at pole = $\frac{\sum \theta (\text{Pole} - \Delta y)}{N}$

same for Z , q and ω

III. Finite difference scheme:

Nonlinear computational stability is controlled through use of a quasilagrangian advective scheme. Krishnamurti (1962 JAM). A time step is selected small enough to avoid the linear computational instability. For a grid size of $2\frac{1}{2}$ degree latitude by $2\frac{1}{2}$ degree longitude in the middle latitudes over the computational region 20° to 60° N a time step of 10 minutes appears adequate.

IV. Horizontal and vertical mesh size:

$\Delta x = 2.5^\circ$ longitude 33 grid points along x axis

$\Delta y = 2.5^\circ$ latitude 19 grid points along y axis

$\Delta p = 200$ millibars 5 level in the vertical

U, V, Z appear at 1000, 800, 600, 400 and 200 mb.

θ, q, ω appear at 900, 700, 500, 300 mb.

ω also computer at $p = 1000$ mb from continuity equation.

No staggering of grid in the horizontal.

V. Initial state:

Geopotential height analysis at 1000, 850, 700, 500, 300 and 200 millibar surfaces are used to obtain Z field at 1000, 800, 600, 400 and 200 millibar surfaces. Specific humidity is analyzed at 1000, 850, 700 and 500 millibar surfaces, it is assumed zero at 300 millibar surface, values are interpolated at 900, 700 and the 500 millibar surfaces. θ is obtained from the hydrostatic equation.

U, V and ω are obtained by solving a non-linear diabatic balance model. Input for tropical calculation is based on wind analysis.

VI. Heating functions: H_S , H_{L1} and H_{L2}

H_S sensible heat transfer from water surface to atmosphere. Empirical transfer formulae are used.

$$H_{L1} = -L \omega \frac{\partial q_s}{\partial p} \quad \text{provided } \omega < 0 \quad \text{and} \quad \frac{q}{q_s} > 0.75$$

stable type of condensation heating

H_{L2} is a heating function for the conditionally unstable type of atmosphere. Cumulus scale is parameterised as a function of convergence of moisture of large scale flow. Heat is released over a small percent of the synoptic scale grid space.

VII. List of symbols:

$$\frac{D}{Dt} \equiv \frac{\partial}{\partial t} + m \left\{ U \frac{\partial}{\partial x} + V \frac{\partial}{\partial y} \right\} \quad \text{isobaric quasilagrangian operator}$$

m map-scale factor (Lambert conformal true at 30-60°)

U, V components of velocity

ω $\frac{dP}{dt}$ (vertical velocity)

C_D drag coefficient ($= 2.5 \times 10^{-3}$)
applies only at the 1000 millibar surface, $= 0$ elsewhere

k small scale vertical diffusion of heat, momentum, and moisture
 $\approx 10^6$ C.G.S. units

ν lateral diffusion coefficient

p_0 $p_0 = 1000$ millibars

∇^2 Laplacian operator in pressure frame

θ potential temperature

C_p specific heat at constant pressure

R gas constant

H heating function

T temperature

q specific humidity

q_s saturation specific humidity

h smoothed terrain height

L latent heat

E evaporation

N number of grid points along x axis

VIII. Computation time and computer:

The code is written in Fortran IV language for IBM 7094 and 360 system. It takes about 6 hours of computation time to make a 36 hour forecast. Initialisation program takes an additional 40 minutes.

MONITORING SOLAR COSMIC RAY EVENTS

by

G. W. Adams

Institute for Telecommunication Sciences and Aeronomy
Environmental Science Services Administration, Boulder, Colorado

A system of ground-based sensors coupled to a computer in Anchorage, Alaska, is being assembled as a real-time solar cosmic ray detection and monitoring system. This system is being funded by NASA-Houston and ESSA, with the cooperation of Air Weather Service for some phases of the program. The immediate need for this system is for the protection of men in space. Other uses include alerting scientific experimenters who need fast response times, as in rocket measurements, and as a warning of oncoming solar proton events for high-altitude polar-cap airline flights. Although a network of polar-orbiting satellites measuring solar proton influxes and telemetering the data in real time would be an optimum system, it is neither economically nor technically feasible for operation in 1967. The only system which will satisfy both requirements is a ground-station network.

There are several outputs desired from the system. Primarily, it is hoped to unambiguously identify solar proton events within thirty minutes of the start of the event. Ultimately it is hoped to obtain a complete description of each solar cosmic ray event, including the intensity and energy spectrum as a function of time throughout the event, the time and intensity of the maximum of the event, and the radiation dosage, both as a function of time and the time-integrated dosage.

Many of the ground-based sensors are also sensitive to other phenomena, such as auroras, solar x-ray events, and relativistic electron precipitation events. As a result, the system has considerable power as a basic research tool, and is being built so as to maintain a high degree of versatility and usefulness for research.

Physically, the system consists of the following sensors:

SENSOR

LOCATION (Geographic)

Riometers

| | |
|-------------------------|--------------------------|
| 1. Wildwood (Soldatna) | 151.2°W 60.4°N L=3.75 |
| 2. Anchorage | 149° 51'W 61° 14'N L=4.2 |
| 3. Sheep Mountain | 147.6°W 61.8°N L=4.5 |
| 4. Paxson | 145.7°W 63°N L=5.05 |
| 5. College (Pedro Dome) | 147° 49'W 64° 52'N L=5.5 |
| 6. Ft. Yukon | 145° 18'W 66° 34'N L=6.5 |
| 7. Barter Island | 143.8°W 70.1°N L=8.0 |
| 8. Barrow | 156° 20'W 71° 31'N L=8.0 |
| 9. Thule | 68° 50'W 76° 33'N L= >50 |

Forward Scatter

| | |
|--|---|
| 1. Barrow (trans.)→Anchorage (rec.) (23.185 mc/s) | Transmitter - 156° 45'W 71° 18'N Receiver - 149° 51'W 61° 14'N |
| 2. Annette (trans.)→College (rec.) (23.365 mc/s) | Transmitter - 131° 33'W 55° 04'N Receiver - 147° 20'W 64° 42'N |

VLF (Phase and Amplitude)

(Transmitter only - Receiver in Anchorage, Alaska)

| | |
|---|--------------------|
| 1. WWVL (19.0 & 20.0 kc/s) Ft. Collins, Colorado | 105° 03'W 40° 41'N |
| 2. NPM (26.1 kc/s) Hawaii | 158° 09'W 21° 25'N |

SENSORLOCATION (Geographic)VLF (Phase and Amplitude) (con't)

- | | |
|--|--------------------|
| 3. GBR (16.0 kc/s) GBZ (18.6 kc/s) Rugby, England | 1° 11'W 52° 22'N |
| 4. Nome-Barrow (100 kc/s) | 156° 20'W 71° 31'N |
| 5. NAA (17.8 kc/s) Cutler, Maine | 67° 17'W 44° 38'N |

HF (Transmitters) Received in Anchorage

- | | |
|----------------------------|--------------------|
| 1. Seattle (~5 + ~12 mc/s) | 122° 18'W 47° 36'N |
| 2. Adak (~5 + ~10 mc/s) | ~177°W 52°N |
| 3. Thule (~9 + ~12 mc/s) | 68° 50'W 76° 33'N |
| 4. WWV (5 + 10 mc/s) | 105° 03'W 40° 41'N |

Magnetometer

- | | |
|--|--------------------|
| 1. Anchorage, Alaska (3 components H, D, Z) | 149° 51'W 61° 14'N |
|--|--------------------|

Neutron Monitors

- | | |
|-----------------------------|-------------------|
| 1. Swarthmore, Pennsylvania | ~76.2°W 43°N |
| 2. Deep River, Ontario | ~76.3°W 45°N |
| 3. Durham, New Hampshire | ~71°W 43°N |
| 4. Thule, Greenland | 68° 50'W 76° 33'N |

In order to get direct information on the solar protons, rockets will be launched from Ft. Churchill, Canada. The data will be telemetered to the ground and the data transmitted via phone lines to the computer in Anchorage.

In summary, a complex system of ground stations plus real-time rocket flights is being assembled for the real-time detection and monitoring of solar cosmic ray events. The system will be operational in late 1967.

NOTE: The information contained in this summary should be considered tentative, as many changes and additions to the system are being made. When the system becomes reasonably fixed, a detailed report will be issued.

This material is not to be considered part of the scientific literature, and its citation, abstracting, or reprinting in the open literature is not authorized.

COMPUTER RAY TRACING TECHNIQUES TO DETERMINE THE EFFECT OF IONOSPHERIC TILTS ON MUF'S

Alfred F. Barghausen and James W. Finney

Institute for Telecommunication
Sciences and Aeronomy
Environmental Science
Services Administration
Boulder, Colorado

Abstract

This paper describes an application of a computer ray tracing program to the determination of the effect of ionospheric tilts on maximum usable frequencies (MUF's).

The assumption of spherical stratification of the F2 layer is invalid at certain times, particularly near sunrise and sunset, and near the magnetic equator. The effect of ionospheric tilts on radio propagation is described based on the results obtained using a ray tracing program.

Examples are shown of the influence of a tilted ionosphere on the maximum usable frequency (MUF), angles of take-off and angles of arrival for a 2000 km path. Calculations were made using realistic models of electron density distributions vs. height above the ground. Depending on the angle and location of the tilt along the great circle path, results indicate that the MUF can be increased or decreased, compared with the MUF for a concentric layer. The angles of take-off and arrival can differ by as much as 10°.

1. Introduction

Tracing of the path of the energy of high frequency radio waves in an anisotropic medium requires the integration of an expression that is very complicated if all the factors of a real situation are considered. In the past, the amount of calculation required for a numerical solution prohibited this approach, and any work done relied on simplifying approximations and determination of only one or two of the path variables. With the aid of high speed computers, however, it is now possible to derive full solutions for the ray paths through any ionosphere.

This paper illustrates the usefulness of a ray tracing program for determining the

influence of ionospheric tilts on the maximum usable frequency (MUF), angles of take-off, and angles of arrival.

Present computer techniques for the prediction of long-term and short-term maximum usable frequencies for point-to-point HF communication circuits assume parabolic models of the ionosphere based on vertical incidence ionosonde data with the application of the equivalent path concept and the secant law for a curved, concentric earth and ionosphere. The assumption of spherical stratification of the F2 layer is invalid at certain times, particularly near sunrise and sunset, and near the magnetic equator.

2. Ray Tracing Program

Evolving from a simple program applying Snell's Law to an ionosphere divided into small discrete slabs each with constant electron density, this ray tracing program (Finney, 1967) uses a detailed mathematical model that allows for the effect of nonuniformity in the electron distribution in the ionosphere.

The program traces the ray path in an inhomogeneous anisotropic medium (the ionosphere) by numerical integration of a set of differential equations due to Haselgrove (1954). The complex refractive index of the medium is calculated from the Appleton-Hartree equation including collision terms. Either the ordinary or the extraordinary rays may be traced.

The ray position is calculated at any point along the path in terms of (1) height above the earth's surface, (2) distance from transmitter to receiver, and (3) deviation from the great circle path, which accounts for the difference between the direction of travel for the wave normal and the ray in an anisotropic medium. A homing routine is used to vary the take-off angle to obtain a returned ray at the desired receiver location.

The ionosphere is described by tables of height profiles of the plasma frequency and collision frequency along the great circle path between transmitter and receiver. The profiles are usually obtained from true height reductions of vertical incidence ionograms and entered into the program as smooth discrete contours of constant plasma frequency.

3. Ionospheric Data and Sample Calculations

Figure 1 illustrates what one might expect under realistic conditions. It shows ionospheric plasma frequency contours obtained from a series of vertical incidence sounders along the 75th meridian (Wright, 1959). The range extends from 20°N to 30°S, and the geographic and geomagnetic equators are shown. The figure illustrates the great distortion of the ionosphere near the magnetic dip equator.

Also as shown in figure 1, at a 0° take-off angle, the ray (solid line) is reflected twice in the ionosphere without an intermediate ground reflection. The ray is propagated to a very long range with only two passes through the lower ionosphere absorbing region, thus high signal strengths would be expected. As seen here, the ray continues to miss the earth but proper tilts at the south end would return it to earth. The dashed ray, for a take-off angle of 5°, shows how the irregular ionosphere causes a wide difference between the take-off and arrival angles. The dotted ray indicates how reflections occur at a high take-off angle (42°) for one part of the ionosphere with subsequent penetration in an area of low critical frequencies. Note that between 12° S and 16°S the constant plasma frequency contour changes by approximately 100 km in height, which corresponds roughly to a 10° tilt.

Figure 2 (Davies, 1965) shows the same ionosphere, but we have increased the ray tracing frequency to 25 MHz to obtain a return for the case of two ionospheric reflections without an intermediate ground reflection. The take-off angle is 0° and the angle of arrival is 10° for a path which is approximately 6000 km in length (actually, using the usual method, for long term predictions we would have assumed a spherically stratified ionosphere, and the MUF's would have been less than 25 MHz for this particular case).

4. Ray Paths in the Presence of Ionospheric Tilts

An ionospheric tilt is defined as a change in height of constant plasma frequency contours with distance. To illustrate the effect of tilts on the propagated wave, we have assumed a path length of 2000 km and have neglected collisions and the earth's magnetic field in our calculations. Realistic (smoothed average true height reductions from vertical incidence ionograms) profiles of plasma frequency vs.

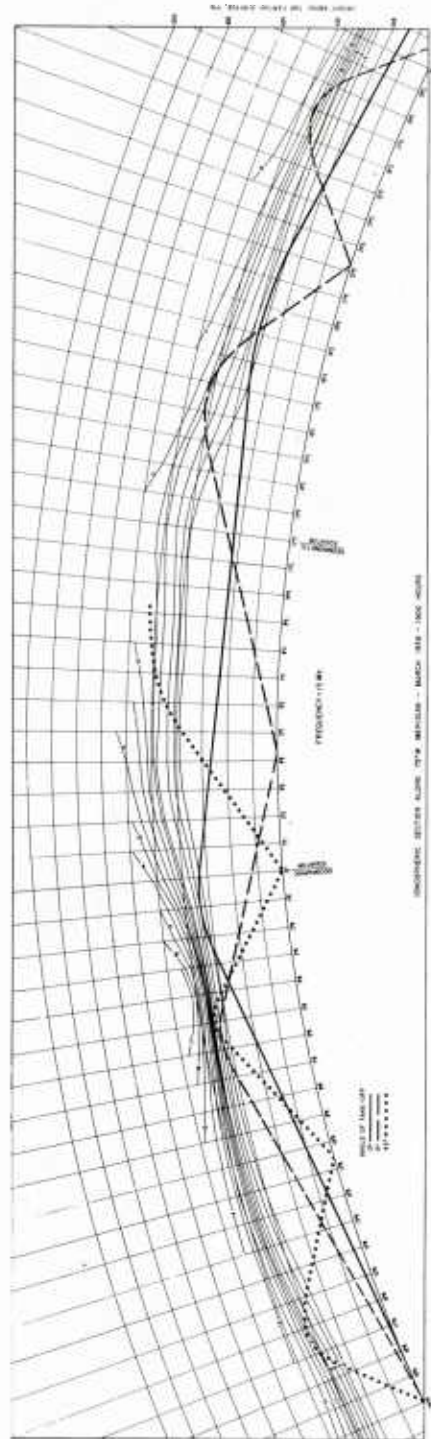


Figure 1 - Computer-raced ray paths as function of take-off angle at 15 MHz

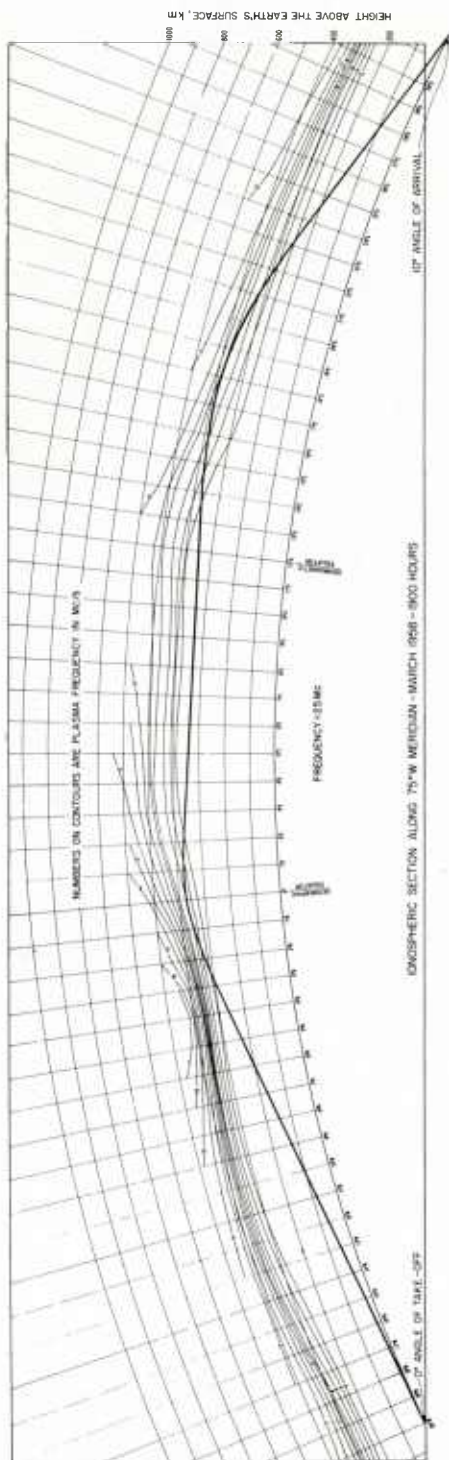


Figure 2 - Computer-traced ray path at 25 MHz for 0° take-off angle

height were used as program input. Tilts are introduced into the concentric layer ionospheric model by a smooth change in height of the constant plasma frequency contours over some arbitrary distance in the great circle plane between transmitter and receiver locations. If a concentric layer is assumed, the MUF for this 2000 km path is 12.5 MHz as calculated by the program with homing routine.

Figure 3 illustrates the resulting MUF ray paths for three different locations of a 5° ionospheric tilt. The 5° tilt was obtained by smoothly changing the height of the concentric layer 52 km over a distance of 600 km. The locations of the tilt were assumed to be (a) in the center of the path, 700-1300 km (dark solid lines), (b) close to the transmitter 450-1050 km (white solid lines), and (c) close to the receiver, 950-1550 km (dashed lines). The resulting ray paths are shown for each tilt location with their corresponding take-off angles, angles of arrival and calculated MUF's. Notice the comparatively greater penetration of the ray (dark solid line) into the ionosphere when the tilt is located close to the receiver. For this path highest transmission losses could result due to the combined effect of marked bending of the ray and greater distance of travel in the deviative absorption region of the ionosphere (Davies, 1965). Comparing the MUF's with that of a concentric ionosphere shows lower MUF's for tilt locations in the center of the path and close to the receiver, while the 5° tilt closest to the transmitter has the same MUF as that of a concentric ionosphere.

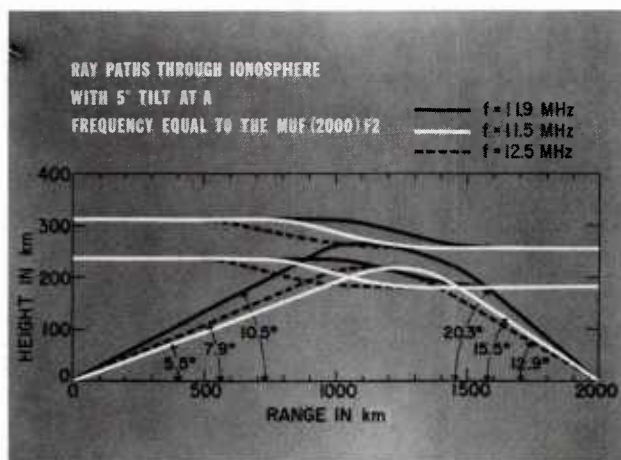


Figure 3 - Ray paths through the ionosphere with 5° tilt at a frequency equal to the MUF (2000)F2

The variations of ground range (distance) vs. take-off angle as a function of tilt location are illustrated in figure 4. The curves show the minimum take-off angle necessary to obtain the desired 2000 km ground range. As indicated the path centered tilt has the lowest take-off angle. For the tilt closest to the receiver, ionospheric penetration occurs at angles between 6° and 8° but the ray returns to the earth as the take-off angle is increased.

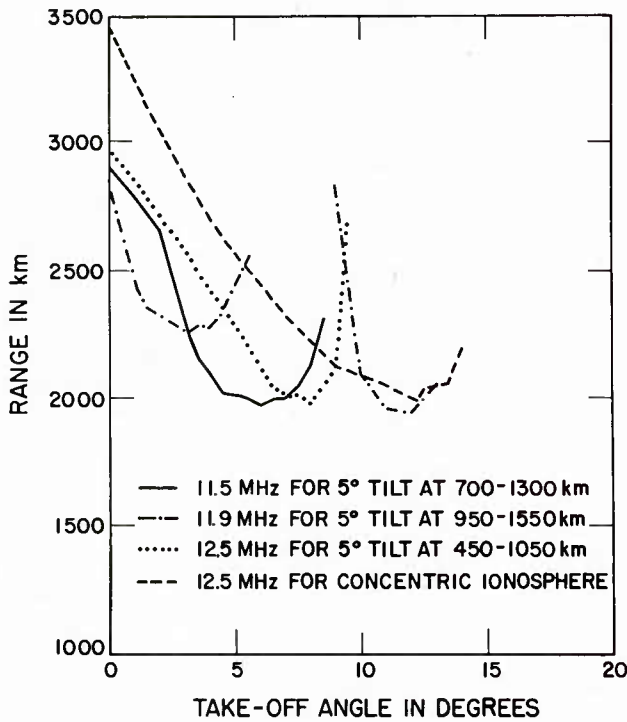


Figure 4 - Variation of range (distance) vs. take-off angle as a function of path location of a 5° tilt

As tilts on the order of 10° may be encountered (figure 1), we have examined the effect of a 10° tilt in the same manner as that of the 5° tilt, and the ray tracing results are shown in figure 5. Although the relative positions of all rays are the same, the path centered tilt has an angle of arrival which is approximately five times the take-off angle, compared with an angle of arrival only two times the take-off angle for the 5° tilt. The latter ratio remains approximately the same for all other tilt positions and tilt angles. The calculated MUF's show that when the 10° tilt is located close to the transmitter, the MUF (13.5 HFz) is higher than the concentric layer MUF (12.5 MHz). For all other tilt positions the tilt lowers the path

MUF. Again, for the tilt location closest to the receiver, the penetration into the ionosphere is greatest and higher transmission losses may be expected.

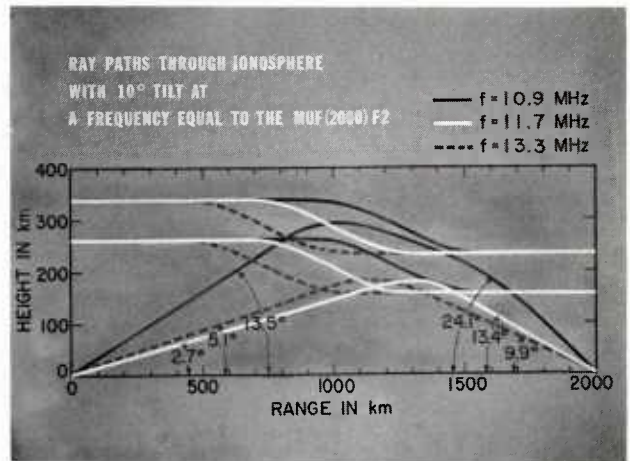


Figure 5- Ray paths through the ionosphere with 10° tilt at a frequency equal to the MUF (2000) F2

Figure 6 shows the variations of ground range vs. take-off angle as a function of the 10° tilt location. Again, for the tilt location closest to the receiver, ionospheric penetration occurs between angles of 3° and 13° ; but the ray is returned to the earth as the take-off angle is increased.

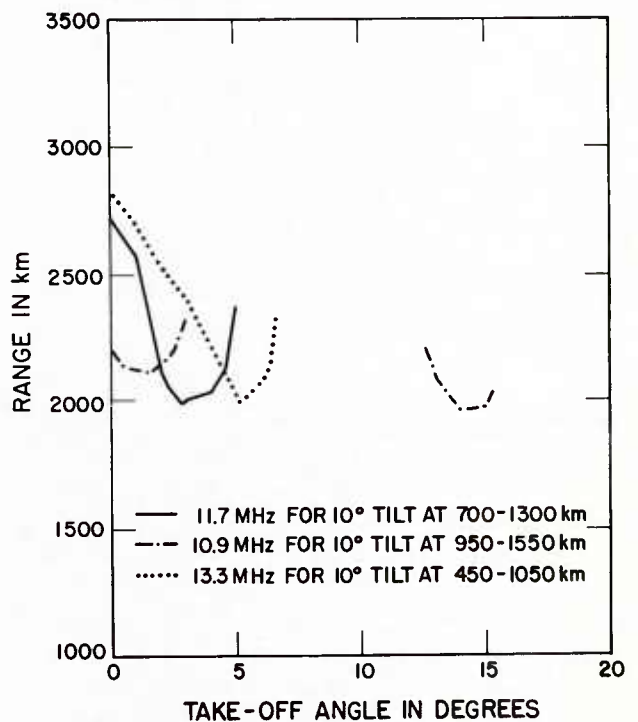


Figure 6 - Variation of range (distance) vs. take-off angle as a function of path location of a 10° tilt

Table I lists of some of the output parameters available from the ray tracing program and shows a comparison between these parameters for the concentric layer and the path-centered 5° tilt in opposite directions, i. e. , toward the receiver (tilt-down) as illustrated in figure 3, and toward the transmitter (tilt-up). The F2-MUF is the same for both tilt directions and lower than that for a concentric layer. Comparison between other parameters shows that the ray paths are reciprocal as would be expected. For example, the take-off angle for the tilt-up (5. 5°) is essentially the same as the angle of arrival for the tilt-down (6. 2°). Theoretically, they should be exactly the same; the extent to which they agree is an indication of the accuracy of the program.

| PARAMETER | TILT-DOWN | TILT-UP | CONCENTRIC |
|----------------------|-----------|---------|------------|
| Path Length | 2000km | 2000km | 2000km |
| F2-MUF | 11.5MHz | 11.6MHz | 12.5MHz |
| Take-off angle | 5.5° | 16.0° | 12.2° |
| Enters ionosphere | 1068km | 534km | 735km |
| Angle of Entry | 15.1° | 20.8° | 18.8° |
| Reflection range | 1223km | 803km | 1000km |
| Height of reflection | 217km | 222km | 245km |
| Exits ionosphere | 1452km | 968km | 1265km |
| Angle at exit | -20.4° | -15.5° | -18.8° |
| Angle of arrival | 15.5° | 6.2° | 12.2° |

Table I - Comparison between data from ray paths through the ionosphere with opposite 5° tilts and data from ray path through concentric layer

A similar tabulation is shown in Table II for the path centered 10° tilt in opposite directions. Here again comparison of the appropriate parameter values indicates that the ray paths are essentially reciprocal regardless of the tilt direction in the great circle plane between transmitter and receiver.

| PARAMETER | TILT-DOWN | TILT-UP | CONCENTRIC |
|----------------------|-----------|----------|------------|
| PATH LENGTH | 2000 km | 2000 km | 2000 km |
| F2-MUF | 11.7 MHz | 11.7 MHz | 12.5 MHz |
| TAKE-OFF ANGLE | 2.7° | 15.0° | 12.2° |
| ENTERS IONOSPHERE | 1173 km | 494 km | 735 km |
| ANGLE OF ENTRY | 13.2° | 19.4° | 18.8° |
| REFLECTION RANGE | 1293 km | 718 km | 1000 km |
| HEIGHT OF REFLECTION | 181 km | 188 km | 245 km |
| EXITS IONOSPHERE | 1459 km | 862 km | 1265 km |
| ANGLE OF EXIT | -18.2° | -13.6° | -18.8° |
| ANGLE OF ARRIVAL | 13.4° | 3.4° | 12.2° |

Table II - Comparison between data from ray paths through the ionosphere with opposite 10° tilts and data from ray path through concentric layer

By showing that an ionospheric tilt down close to the transmitter (or tilt-up near the receiver) will result in higher MUF's than that which would be predicted for a concentric layer, we have indicated the usefulness of a computer ray tracing program for determining the effect of ionospheric tilts on the MUF and the angles of take-off and arrival for a given communication path. It offers a rapid and efficient method for further study of this problem.

The program used here traces the ray in three dimensions; the ionospheric input data, however, vary only in two dimensions, i. e. , in height and ground range in a cross section along the path. Perpendicular to this plane the ionosphere is assumed not to vary. Some progress (Jones, 1966) is being made in extending this program to include those gradients transverse to the path in the ionosphere which would cause deviations from the great circle path, and thus obtain a complete three-dimensional ray tracing capability.

When sufficient information is available on the vertical ionization distribution, the ray tracing technique permits more accurate calculation of MUF than could be made by methods based on the assumption of concentric earth and ionosphere. Also, if lower layer ionization is included in the model of vertical ionization distribution, use of the ray tracing method permits the entire path calculation to be made in one operation, without requiring the separate calculations for the lower layers necessary when using older methods.

References

- Davies, Kenneth: Ionospheric radio propagation, U. S. Dept. of Commerce, National Bureau of Standards Monograph 80, Supt. of Documents, Government Printing Office, Wash., D. C. , 1965.
- Finney, J. W. : "A ray tracing program and its application to some ionospheric propagation problems," U. S. Dept. of Commerce, Radio Sci. (New Series) (submitted for publication), 1967.

- Jones, R. M. : "Three-dimensional ray tracing computer program. " ESSA Technical Report IER 17, 1966.
- Haselgrove, J. : "Ray theory and a new method for ray tracing. " Report of Conference on the Physics of the Ionosphere London Physical Society, 355-364, 1954.
- Wright, J. W. : "Note on quiet-day vertical cross sections of the ionosphere along 75° west geographic meridian, " J. Geophys. Res. , vol. 64, 1631-1634, 1959.

OBSERVATION AND MAPPING OF MUFs AND LARGE HORIZONTAL
VARIATIONS OF THE IONOSPHERE

L. A. Berry, R. D. Hunsucker, and L. H. Tveten
Institute for Telecommunication Sciences and Aeronomy
Environmental Science Services Administration
Boulder, Colorado

Abstract

A technique for measuring ionospheric parameters in real time over a wide area of the ionosphere has long been considered desirable. Possible techniques include orbiting sounder satellites, or a real-time-reporting grid of vertical and/or oblique sounders with interpolation. A third technique, a high-frequency ground backscatter radar, is discussed here.

In its simplest terms, a backscatter sounder is a pulse radar system operating in the HF band. The pulse energy is reflected from the ionosphere and hence is able to reach long ranges (~4000 km on one hop and more on subsequent hops). When the energy strikes the ground, irregularities scatter it; some energy is returned to the transmitter via the original path. This backscattered energy can be recorded and studied as a function of time, angle-of-arrival, and time delay.

The nature of the scatter returned depends on the characteristics of both the ground and the refracting ionosphere. To map the ionosphere, the ionospherically dependent characteristics of the scatter signal must be segregated and interpreted. The segregation is usually quite easy because the ground parameters affect only the magnitude of the scatter signal, although the sea surface does affect the signal spectrum. Quantitative interpretation of the data is more difficult.

The Institute for Telecommunication Sciences and Aeronomy has an experimental high-resolution, high-frequency ionospheric radar receiving system at Boulder, Colorado. It consists of two antenna arrays, their beam forming electronics, and associated data sampling and recording equipment. The array has a narrow beam in azimuth (1.5° to 3° , depending on frequency) which can be steered over a sector 40° to 90° wide (sector width depends on frequency). A vertical beam 3° to 6.5° can be steered from 0° elevation to 22° to 51° .

An example of the backscatter pictures provided by these scan beams is shown in figure 1. The pattern on the left is the azimuth and the one on the right is the corresponding elevation scan. The ordinate in both cases is group delay of the signal which is related to range. The lighter

patches show concentration of energy focused by the irregular ionosphere. The non-uniform scatter return over the different azimuths and ranges is shown by the azimuth scan presentation and the variation of elevation angle with delay is shown in the elevation scan presentation. As expected, the lower angles-of-elevation are associated with the longer delay times. Elevation-angle information is very important in assessing the modes of propagation for the backscatter signals.

Examples of interpretation and use of backscatter observations include:

- (1) Determination of the maximum usable frequency (MUF) around the backscatter sounder location. Variation of the skip distance with azimuth indicates tilts and distortions in the ionosphere.
- (2) A time series of records shows that the irregularities causing focusing of the energy move. If assumptions are made about the height of the irregularities, their velocity can be estimated.
- (3) Clouds of sporadic-E ionization can be identified and tracked.
- (4) By using all information available--time delay at the different azimuth and elevation angles for various frequencies--and by assuming the ionosphere has some particular profile (e.g., parabolic), the plasma frequency can be determined at various points in the volume monitored by the radar. Then three-dimensional numerical mapping techniques can be used to define the ionosphere throughout the volume.

These examples suggest that the major advantage of a high-frequency, ground backscatter radar is its ability to monitor a large sector of the ionosphere continuously from one central location. The major problem is the difficulty of interpreting the observations quantitatively. Progress is being made and research will continue in this area.

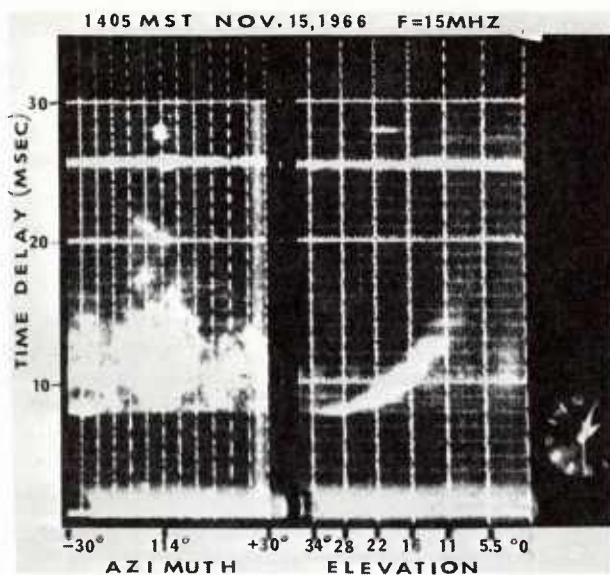


Figure 1. Sample elevation and azimuth scan record

THE IONIZATION IN POLAR LATITUDES

by

CHARLES F. POWER* and
CHARLES M. RUSH
University of California
U.S.A.

Introduction

The launch of the Alouette I satellite into a circular, polar orbit on September 29, 1962, marked the successful beginning of attempts to monitor, synoptically, the ionospheric electron density from the F_2 peak out to about 1000 km. To date, over two million sweep-frequency ionograms have been produced from the Alouette I soundings. Most of these measurements were made in rapid succession, one for each degree of latitude, from pole to pole. In this paper some of the results obtained from topside soundings taken at high geomagnetic latitudes during the first year of the experiment will be presented.

The results are based on the analyses of over 15,000 ionograms obtained during 302 transits of the satellite across the western hemisphere. Meridional cross-sections of the topside ionosphere were constructed from the height-versus-electron density profiles deduced from the ionograms. Cross-sections of a similar nature, but displaying constant plasma (1) frequency as a function of height and geographic latitude have been constructed by Nelms for about forty Alouette I transits during geomagnetically quiet periods covering several months of 1962-1963. Although it is considerably more difficult to construct cross-sections from the electron density profiles deduced from each ionogram, they are easily interpreted and may be more physically significant. Figure 1 is an example of one such cross-section, showing two characteristic features of such charts: the equatorial anomaly, centered over the magnetic equator, and the high-latitude enhancement in ionization, near the magnetic poles. We concentrate here on the latter.

The absence of read-out stations near the south pole precludes an investigation of this nature over that region. A poleward decrease in ionization is evident on the southern half of most cross-sections, to about 70° S dip latitude. As data is unavailable at higher latitudes, it is not known if enhancements in electron density, such as are indicated in Figure 1, occur regularly near the south pole.

Morphology

We have found a north polar enhancement to be a regular feature of the ionosphere throughout the year during all local times. It was identified on all but eight of the 302 cross-sections analyzed. The general features of electron density distribution near the polar maximum are apparent in Figure 1. There is usually a monotonic decrease in electron density with increasing dip latitude north of about 40° dip. This extends through all levels between the satellite and the F_2 peak. The decrease continues until the axis of the "trough" is reached at an average dip latitude of 71° N. The density then increases from this point poleward, and usually attains a maximum value at about 85° N. This maximum often exceeds the equatorial maximum in electron density at the same altitudes.

Although we are mainly concerned here with the nature of this polar maximum, it is convenient to refer to it in terms of the adjacent "trough". The "trough" in ionization at high dip latitudes was first identified by Muldrew⁽²⁾ from a study of the critical frequencies, fxF_2 , observed on Alouette I ionograms. Thomas et al.⁽³⁾ have also presented a preliminary study of this feature, emphasizing the adjacent polar maximum. The maximum is often poorly defined due to naturally occurring irregularities, difficulties in scaling the associated "spread" ionograms, and the absence of data beyond about 85° N dip latitude (the "turn-around" latitude of the Alouette I orbit). However, the axis of the trough, which is actually the leading edge of the enhanced region, is usually quite well defined. An example of one such case is illustrated in Figures 2 and 3.

*Presently at Headquarters, Air Weather Service, Scott Air Force Base, Illinois, U.S.A.

ELECTRON DENSITY CONTOURS
PASS 446
OCTOBER 31, 1962

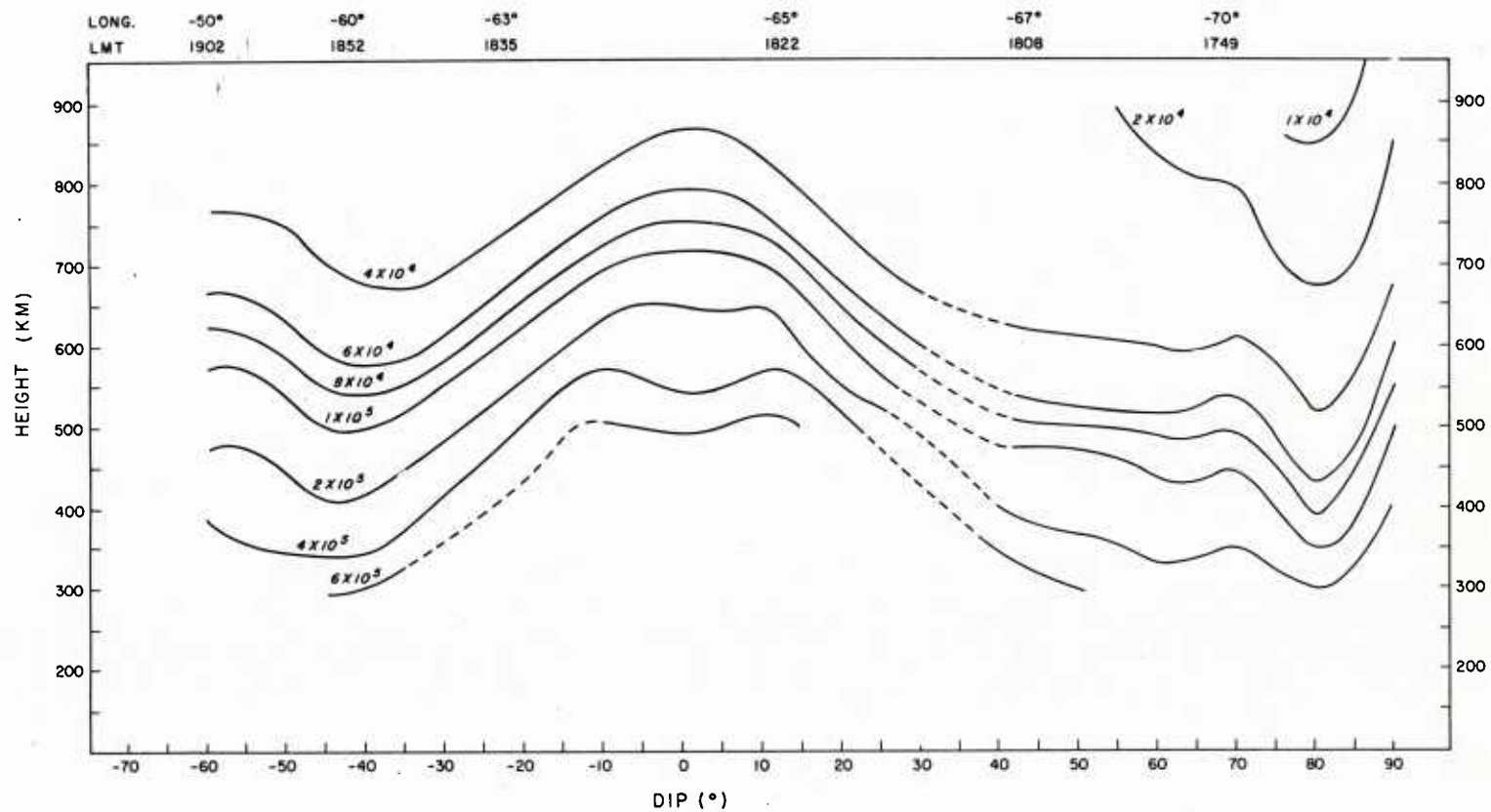


Figure 1. Latitudinal and vertical distributions of
Electron Density on October 31, 1962.

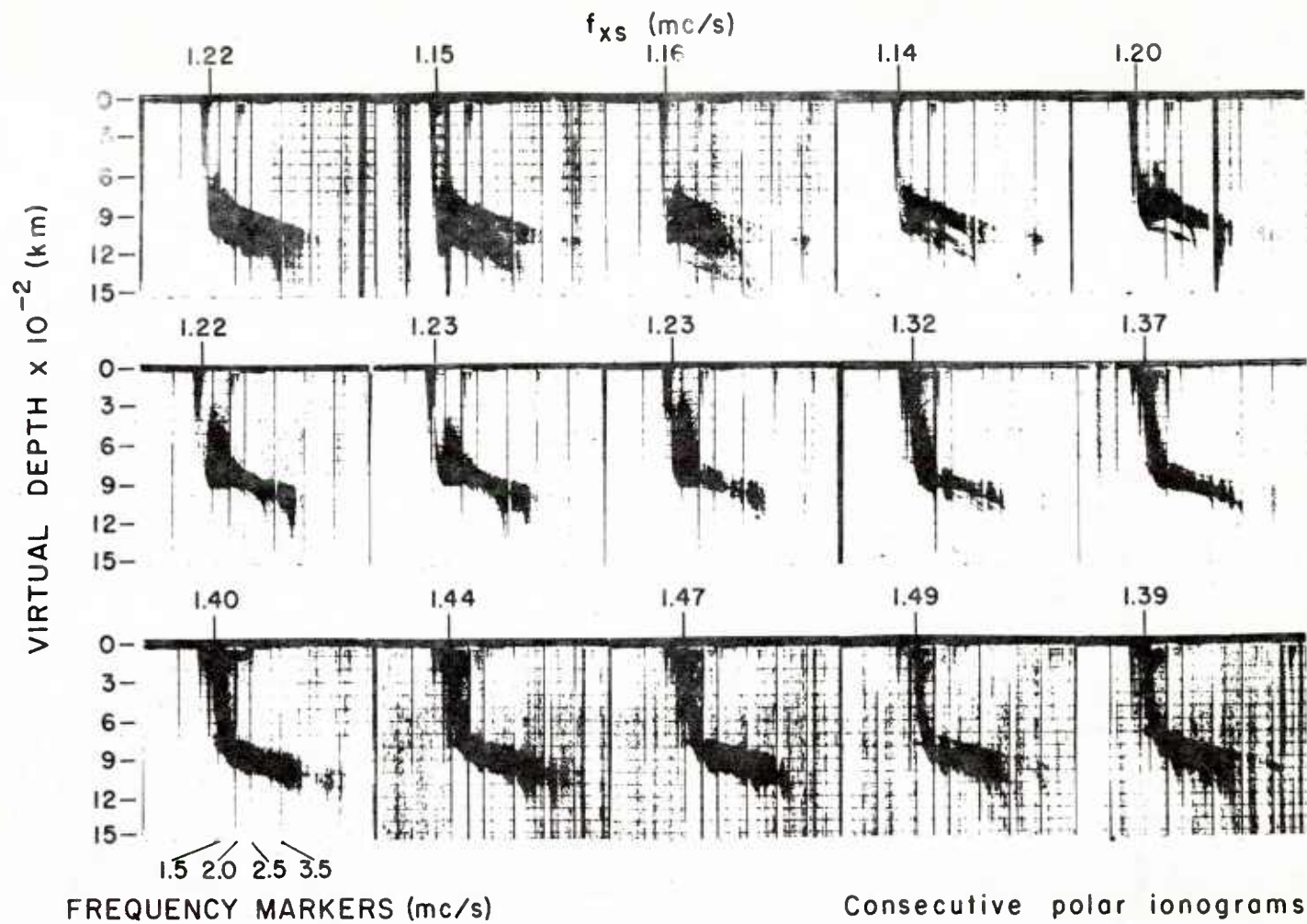


Figure 2. Consecutive Polar Ionograms on October 27, 1962

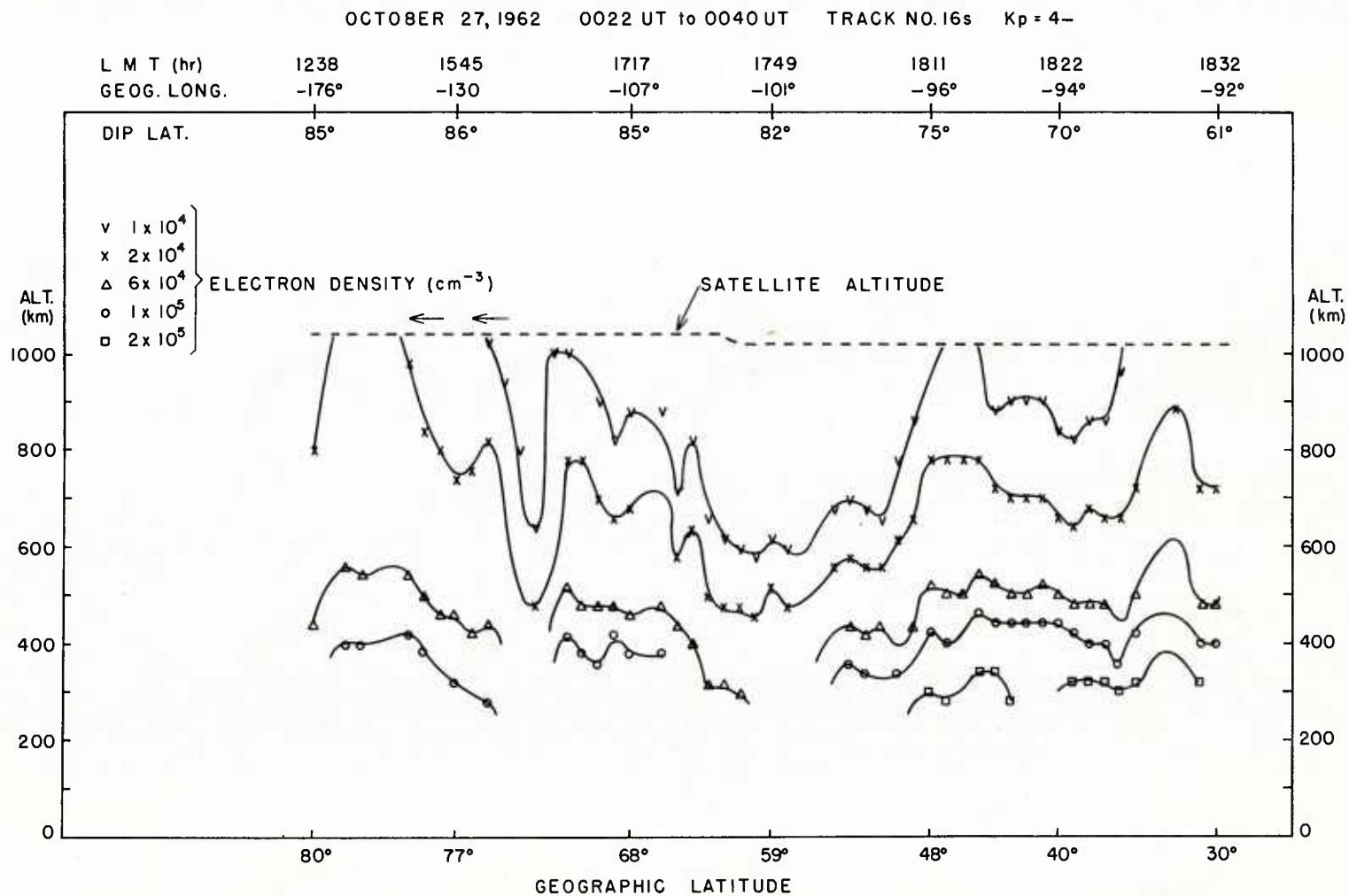


Figure 3. Latitudinal and vertical variations of electron density as determined from the ionograms of Fig 2.

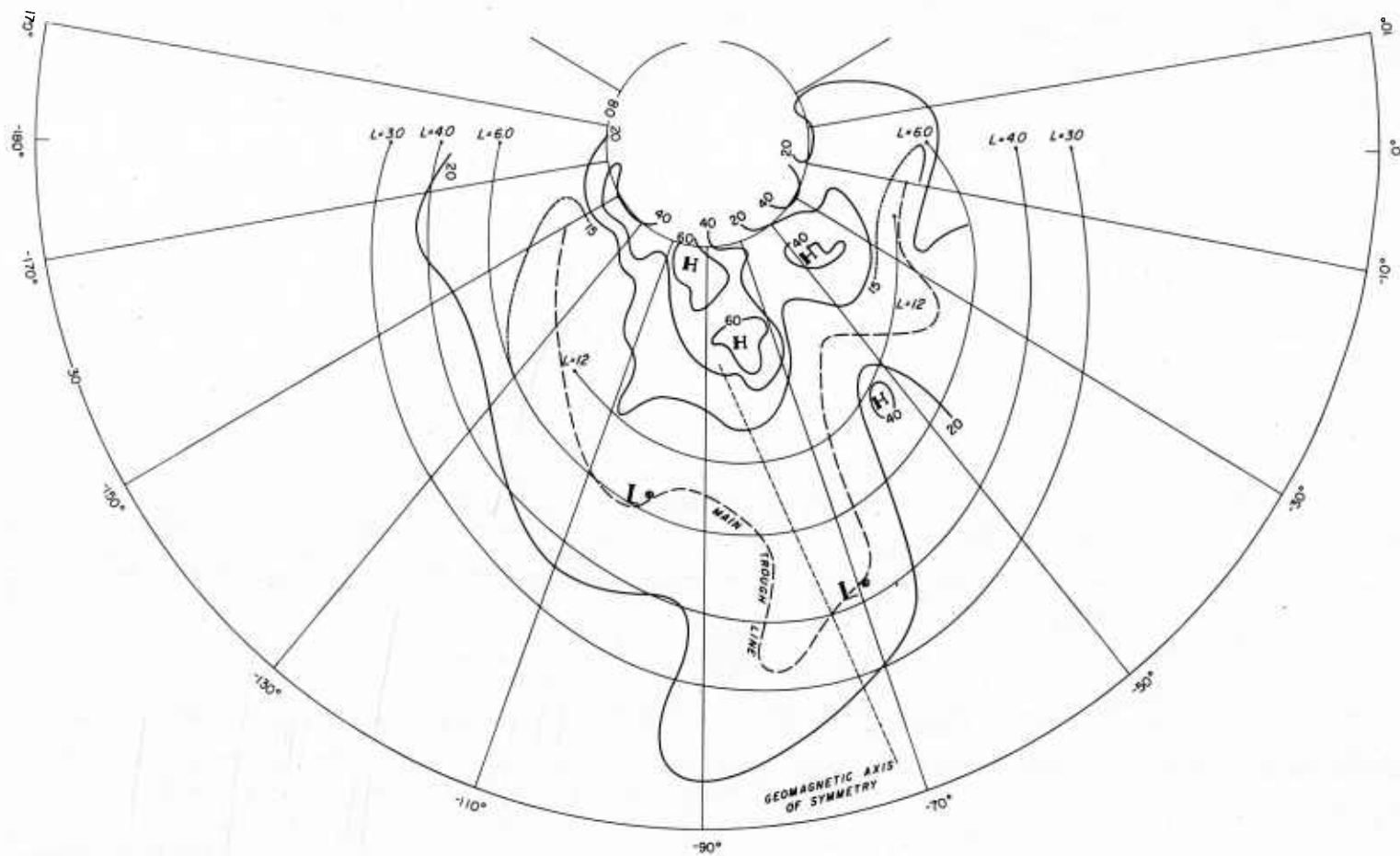


Figure 4. Horizontal cross section, at 700 km, of the polar ionospheric electron density ($\times 10^{-3} \text{ cm}^{-3}$) distribution on October 27, 1962.

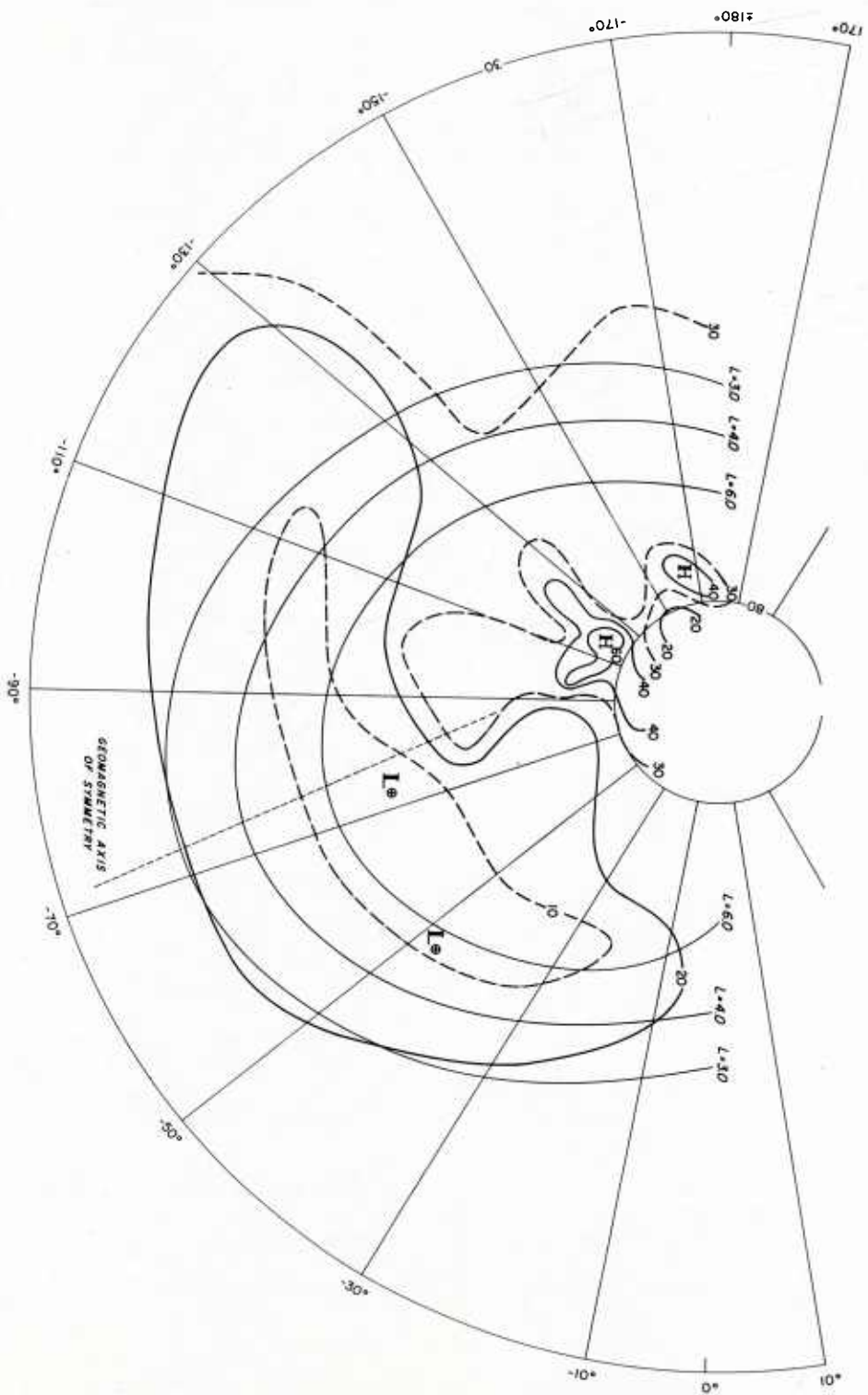


Figure 5. Horizontal cross section, at 700 km, of the polar ionospheric electron density ($\times 10^{-3} \text{ cm}^{-3}$) distribution on

April 4, 1963.

Figure 2 displays fifteen consecutive ionograms recorded at high latitudes on October 27, 1962. The virtual depth below the satellite is given in hundreds of kilometers to the left of each row of ionograms, corresponding to the faint horizontal markers on each record. The vertical lines are the frequency markers as indicated on the ionogram in the lower left hand corner. Scaling is made difficult because of the presence of considerable spread of the echoes and also because of the occasional occurrence of multiple reflections. Such features are typical of polar ionograms.

The frequencies at which the extraordinary wave traces have zero range are indicated along the tops of each ionogram, as determined from three independent readings. As the electron gyro-frequency varies only slightly over the range of interest, changes in these frequencies reflect real changes in electron density at the Alouette I orbit. An examination of the variation of this frequency from ionogram to ionogram indicates the irregular behavior of the ionospheric electron density near the dip-pole. The ionograms are separated in time by about 18 seconds or 100 km.

The first ionograms correspond to the primary minimum in electron density over the entire pass. A sharp increase in electron density on the poleward side of the "trough" is indicated by the jump in the zero range frequency from the 8th to 9th frame and a sharp decrease is indicated from frame 14 to frame 15.

A vertical cross-section through the polar ionosphere, constructed from the electron density profiles corresponding to 60 consecutive ionograms, including those shown in Figure 2, is shown in Figure 3. The electron density in the region from about 82° dip to about 73° dip latitude were deduced from the 15 ionograms of Figure 2. The first few frames correspond to the primary minimum. The abrupt changes mentioned occur between 77° and 76° dip and between 74° and 73° dip latitude.

The maxima and minima at orbital altitudes, expected on the basis of the changes in the zero range echoes seen on the ionograms are seen to extend through nearly all levels between the satellite and F_2 peak.

Cross-sections similar to this one were constructed for eight consecutive passes over polar regions on October 26-27, 1962. Taken together, these charts revealed the presence of some global-scale features of the topside ionosphere. In order to investigate these features at various levels, horizontal cross-sections at constant altitudes were prepared from all data profiles corresponding to the eight passes.

One such cross-section is shown in Figure 4 for the altitude 700 km. The data supports the location of a main trough at the position indicated by the dashed line. A region of electron density enhancement is centered near the magnetic pole and is bounded by the $L=12$ isoline, where L is McIlwain's parameter. An elongation of the trough occurs in the vicinity of the axis of symmetry of the ovals represented by the isolines of L . It is interesting to note that the central position of the main trough coincides approximately with the central position of the region of maximum auroral occurrence at about $L=8$.

Figure 5 shows a horizontal cross-section at 700 km, constructed in the same manner, from data obtained on April 4-5, 1963. The principle features are similar to those found six months earlier.

Variability

The following sections are devoted to the results of a study of solar-geomagnetic, seasonal, and diurnal effects on the position and structure of the enhanced region.

a. Solar-Geomagnetic. The main interest in the detailed study of the polar maximum lies in the possibility that this maximum is in some way the result of coupling between the magnetosphere and the polar ionosphere. Neither the preliminary study we have made nor similar studies so far reported, have enabled the precise nature of this coupling to be isolated.

However, on the assumption that the maximum may be governed by outer magnetospheric and interplanetary phenomena, it would appear reasonable to correlate its strength and location with parameters, such as K_p , which are grossly related to the strength of the solar wind and hence to the size of the magnetospheric cavity, etc. In the course of our investigation, relations were sought between the following parameters:

- a. trough axis position;
- b. amplitude of the polar enhancement;
- c. the solar-geophysical parameters K_p and 10.7 cm solar flux.

Any possible relations between these quantities were expected to depend on time and hence, longitude, and were therefore tested for different longitude sectors.

The results were disappointing in the sense that no clear-cut relations between any two of these could be substantiated on the basis of the data sample available for this study. It should be pointed out, however, that although no obvious relation between trough axis position and K_p was found in the gross sense, it was discovered that during sudden commencement storms, at least, the trough is displaced to the south of its average position.

b. Seasonal. The average positions of the low latitude boundary of the polar enhancement during the various seasons are summarized in Table I. Some care must be taken in considering these results for two reasons:

(1) The orbital plane of the Alouette I satellite precesses some two degrees per day with respect to the earth-sun line. Thus data is available for all local times once each season (90 days). Hence, each month of a particular season is represented by data collected during a different eight-hour period from the other two months. Some months have more data than others, which may cause any diurnal variation in the position of the trough to be reflected in the seasonal averages.

(2) The possible relations between trough axis position and K_p during sudden commencement storms may account partly for the fact that the average latitude of the trough is found significantly farther to the south during the seasons containing the months of November and December, 1962. This is because the sum of the K_p for this period was generally higher than that during any other two months of the year.

For these reasons it is felt that perhaps the most meaningful averages are those for the two six-month periods centered on the two solstices. The abundance of data for all local times should vitiate the effects listed above, while the symmetry with respect to the sun's declination is retained. These results suggest little dependence of the southern boundary of the enhancement of the solar declination.

c. Diurnal. The average position of the trough during various times of the day for the two six-month periods are summarized in Table II. Both sets of data show the trough occurring at higher latitudes on the day side of the earth. It is interesting to note that the variation of the trough position in each case is in the same direction and is of the same magnitude as the diurnal distortion of the field lines at about 1000 km due to the solar wind (4,5).

Data from the energetic particle detectors aboard the Alouette I, gathered during the same period, support a similar day-night variation of the high latitude boundary of trapped and precipitated electrons having energy above 40 KeV(6). The high latitude boundaries of the trapped 40 KeV electrons generally fall within a few degrees of the day and night positions of the trough given in Table II. However, the high latitude boundary of precipitated 40 KeV electrons lies well within the boundaries given in Table II. Further, McDiarmid et al.(7) and Frank(8) show an appreciable softening of the spectrum at these higher latitudes. If such softening does occur it may well be that the peak intensity of much lower energy trapped and precipitated electrons (1 eV) occurs at latitudes corresponding to peak polar electron density enhancements.

The average positions in the dawn-dusk sectors defy such easy comparisons, however. The elongation of the boundary in these directions is marked during the summer half of the year but is absent during the winter half. The average positions of the trough at dawn from October through March are higher than those at dusk from April through September. This is especially interesting in view of the findings of Frank (8), that the average intensities of 40 KeV electrons detected by the Explorer 14 in the magnetospheric tail were about ten times higher on the morning side during Winter, 1962, than on the evening side during Summer, 1963.

These same instruments detected a "catastrophic" two-order-of-magnitude decrease in the intensity of 40 KeV electrons at about L=5 on December 20, 1962. The electron density cross-sections constructed during this period show the positions of trough axes to

be much lower than average (35° to 45° dip).

CONCLUSIONS

Satellite sounders such as the Alouette I are seen to provide an excellent means of obtaining detailed synoptic information concerning vertical and meridional distributions of electron densities at F₂ altitudes and above. A typical pass across one hemisphere yields as much data from the F₂ region as a network of 150 or more bottomside sounders, spaced about one degree of latitude apart along a meridian, operating nearly simultaneously. Information concerning maximum usable frequencies, ionospheric tilts, and irregularities in electron density distribution can be readily determined for radio communication purposes, from cross-sectional "snapshots" of the ionosphere such as that shown in Figure 1.

The use of small samples of topside sounder data to specify the nature of "mean" seasonal or diurnal ionospheric configurations must be undertaken only with greatest care. If a large fraction of the data available is included in investigations of this type, the results should be correspondingly more significant.

Several comparisons have been made between ionospheric variations at high latitudes and variations in energetic particle distribution within the outer magnetosphere. These comparisons suggest the existence of significant ionospheric-magnetospheric coupling at high latitudes. The precise nature of the required coupling mechanism has not been isolated at this point. However, the impression was gained that the high-latitude ionosphere will have to be studied as a synoptic feature, at different elevations, ranging from the F₂ peak to very high levels in the magnetosphere, such as are accessible to the Alouette II satellite, launched during IQSY.

The present study is to be taken as a prelude to a more detailed investigation of this nature.

Acknowledgement: We are grateful to Professor S. V. Venkateswaran for many helpful suggestions and for uncounted hours of rewarding discussions on subjects covered in this paper. The data analyses for this investigation were carried out at the Department of Meteorology, University of California, Los Angeles, California, with financial support from the Naval Ordnance Test Station, Chinalake, California, and through a grant from NASA NsG 237-62.

TABLE I
Seasonal Variations of the
Average Positions of the Low-Latitude Boundary
of the Polar Enhancement

| | | | |
|--|--|----------------------------|-----------------------|
| Fall OND 69°N | Winter JFM 74°N | Spring AMJ 71°N | Summer JAS 73°N |
| Winter NDJF 69°N | Summer MJJA 71°N | Equinoctal SOMA 74°N | |
| Winter Half Oct '62 - Mar '63 71.0°N | Summer Half Apr '63 - Sep '63 71.5°N | | |

TABLE II

Diurnal Variations of the
Average Positions of the Low-Latitude Boundary
of the Polar Enhancement

October, 1962 - March, 1963

| Day 0800-1600L | Night 2000-0400L | Dawn 0400-0800L | Dusk 1600-2000L |
|-------------------|---------------------|--------------------|--------------------|
| 71°N | 69°N | 74°N | 69°N |

April, 1963 - September, 1963

| Day 0800-1600L | Night 2000-0400L | Dawn 0400-0800L | Dusk 1600-2000L |
|-------------------|---------------------|--------------------|--------------------|
| 74°N | 72°N | 65°N | 64°N |

REFERENCES

1. Nelms, G. L., Electron Density Profiles in Ionosphere and Exosphere, John Wiley & Sons, Inc., p 358, 1966.
2. Muldrew, D. B., Journal of Geophysical Research, Vol. 70, No. 4, p. 2635, June, 1965.
3. Thomas, J. O., et al., Electron Density Profiles in Ionosphere and Exosphere, John Wiley & Sons, Inc., p. 322, 1966.
4. Malville, J. M., Journal of Geophysical Research, Vol. 65, No. 9, p. 3008, September 1960.
5. Hones, E. W., Journal of Geophysical Research, Vol. 68, No. 5, p 1209, March, 1963.
6. Rose, D. C., Radiation Trapped in the Earth's Magnetic Field, Gordon and Breach, p. 192, 1966.
7. McDiarmid, F. B., et al., Canadian Journal of Physics, Vol. 41, p. 1332, 2064, 1963.
8. Frank, L. A., Journal of Geophysical Research, Vol. 70, No. 7, p. 1593, Apr, 1965.

THE COMPUTATION OF ATMOSPHERIC DENSITIES USING SPACE DEFENSE CENTER DATA

Captain Robert E. deMichaels

Chief, Automation Branch, Aerospace Sciences Division

4th Weather Wing, Ent AFB, Colorado 80912

ABSTRACT

This paper discusses the efforts of the 4th Weather Wing to compute atmospheric densities using Space Defense Center data. It covers the data which are available, our past efforts and our plans for further investigation.

A. SPACE DEFENSE CENTER DATA.

The Space Defense Center is a NORAD organization, located in the NORAD Cheyenne Mountain Complex, and operated by the 1st Aerospace Control Squadron of the 9th Aerospace Defense Division. Its mission is to catalog and predict positions for all man-made objects in space. The "raw data" or actual observations of these objects are provided to the Space Defense Center by the USAF Spacetrack System, which is operated by the 73d Aerospace Surveillance Wing of the 9th Aerospace Defense Division. The Spacetrack System consists of both direction and tracking radars and of Baker-Nunn electronically controlled telescopic cameras. All of the tracking done is of the "skin" type, that is, the object being tracked is in the passive mode.

How accurate are Spacetrack's observations? The "field-reduced" Baker-Nunn observations are accurate to within hundreds of meters, while the radar observations, which make up over 90% of the Spacetrack data, are accurate to within a few kilometers. In comparison, the "photo-reduced" Baker-Nunn observations used by Dr. Jacchia are accurate to within tens of meters.

The Space Defense Center furnishes two types of data to the 4th Weather Wing; observations and orbital elements. An observation consists of eight fields, namely:

1. Classification of the observation
2. Station which took the observation
3. Time of the observation
4. Elevation or declination of the object
5. Azimuth of the object
6. Range of the object
7. Type of observation
 - a. Azimuth, elevation
 - b. Range, azimuth, elevation
 - c. Right ascension, declination
8. Equinox indicator for the right ascension, declination type observations

Each orbital element set consists of six data cards containing a total of 45 separate fields. We reduce this six card set to a two card orbital element set. The actual content of the two card set depends upon which density determination program is being run. A typical set consists of such information as:

1. Time of the element set

2. Nighttime exospheric temperature
3. Area/mass ratio
4. Mean anomaly
5. Argument of perigee
6. Longitude of ascending node
7. Inclination angle
8. Eccentricity
9. Semi-major axis

B. SATELLITE ANALYSIS MONITOR.

A specific program the 4th Weather Wing uses in determining atmospheric densities is the Satellite Analysis Monitor Program (SAM). Our co-location with the Space Defense Center and the necessity of handling classified data made it more advantageous for us to run the program than for other agencies to do so.

This program was developed in 1964 by Branson and Foxworthy of the Cambridge Space Systems Group of the IBM Corporation, under a USAF contract with AFCRL. It was an attempt to automate methods and techniques developed by Dr. Jacchia of the Smithsonian Institution Astrophysical Observatory. By assuming the precision of the input observations to be that of "field-reduced" Baker-Nunn Camera plates, it was possible to neglect the high order effects on a satellite's motion, such as the sectorial and tesseral harmonics of the geopotential, the extraterrestrial gravitational effects, and the small, short, periodic perturbations due to the ellipticity of the equator, which Dr. Jacchia includes in his analyses. [1] We, in 4th Weather Wing, were interested in determining how well the program could derive densities from data much less accurate than Dr. Jacchia's "photo-reduced" Baker-Nunn plates.

"The SAM program computes atmospheric densities from satellite observations by: (1) obtaining orbital elements through differential orbital correction procedures; (2) representing satellite motion over extended time periods by least-squares fitting of orbital parameters using empirical expressions; (3) analyzing the residuals in the mean anomaly; (4) computing the rate of change of the anomalistic period; and (5) deriving atmospheric density by an integration of Sterne's equation. An array of 154 variable parameters is used to control the various sections of the program." [3]

The selection of which satellite to study is an extremely important step. Several restrictions are imposed upon this selection by the SAM program. First, the eccentricity of the orbit must be greater than .007 and the inclination of the orbit should not be close to 63° . The second restriction is that the perigee should be greater than 200 km but low enough that air drag and gravitation are the predominant forces acting on the satellite. A third factor of extreme importance is the geometry of the satellite since it determines the drag coefficient used in the program. In the case of nonspherical satellites, the stability of the object in orbit is also of prime importance. Because of the necessity to know such parameters as the geometry and the area/mass ratio, it is necessary to use only those satellites for which this information is readily available, namely either U.S. satellites or those of our allies. We have attempted to study three satellites to date, San Marco I, Injun 3 and Explorer 24.

San Marco I was launched on 15 December 1964 at an inclination of 37.8 degrees with an eccentricity of .045 and a perigee height of approximately 200 km. The satellite was nearly spherical and had an area/mass ratio of $0.03086 \text{ cm}^2/\text{g}$. A drag coefficient of 2.2 was used. Observations from 1 January through 13 September 1965 were obtained from the Space Defense Center. Except for placing the observations in chronological sequence, no editing was performed on the data prior to use in the SAM program. Radar observations outnumbered Baker-Nunn photographic observations by a 15 to 1 ratio, with 4 sensors contributing over 90% of the observations. The SAM program processed observations between 4 January and 23 June 1965, obtaining density values at half-day intervals. These values were compared to those published by Jacchia and Verniani in SAO Special Report 193. The SAM program derived densities, were

5 to 10 percent lower with differences of 10 to 25 percent during periods of geomagnetic enhancement. Major Eugene S. Harsh, who conducted this study, discussed his results in a paper presented at the joint AMS/AIAA Conference on Aerospace Meteorology in Los Angeles in March 1966. [3] Copies of this paper are available from 4th Weather Wing.

It is important to realize that these density values are averaged over both time and space. For example, a value obtained for a half-day interval would include effects of atmospheric drag over 8 orbits. The effect of drag along one orbit, a function of the eccentricity, is an average over at least 30° of arc, centered at perigee. [5]

Explorer 24, a 12 foot diameter balloon satellite, was launched on 21 November 1964 in an orbit having an inclination of 81.4° and a perigee height of approximately 550 km. Data were obtained from the Space Defense Center for the period September 1965 through May 1966. During this period, the eccentricity was approximately .117. The density values derived by SAM pointed out a problem inherent to the program. For a period of 16 days we computed negative densities. This is accounted for, at this perigee height, by radiation pressure, which is not considered in the SAM program. Jacchia and Slowey discussed radiation pressure and how they accounted for it using Explorer 19 and 24 data in SAO Special Report 207 [4]. No further work was done with the Explorer 24 density data since we could not correct for the radiation pressure effects in the SAM program.

Injun 3 was launched on 13 December 1962 with an inclination of 70.3° and a perigee height of 250 km. Observations were obtained for the period October 1965 through May 1966. At the beginning of this period the eccentricity was .132. Densities have been obtained at 24 hour intervals throughout this period, but no further analysis has been made of these data.

In each of these studies, data were obtained for a period of 6 or 7 months, well after the data had been catalogued by the Space Defense Center. In the future, we may be interested in real time density determination. How close is the Space Defense Center to meeting such a requirement? Today, there is a 27 hour delay in our obtaining observations. The Space Defense Center has set a goal of a 3 to 4 hour delay which they intend to reach in the near future. However, the use of the SAM program for real-time operations is not practical, since at least 50 days of data are necessary for a successful run.

C. NUMERICAL INTEGRATION PROCEDURE.

A new program, written by Bramson and Slowey of the Cambridge Advanced Space Systems Department of the IBM Corporation, has two advantages over the SAM program. NIP or Numerical Integration Procedure is designed to use observations covering a two or three day period for satellites having perigee heights less than 200 km. At present, there is considerable interest, Air Force wide, in obtaining density data between 150 and 200 km.

NIP uses the same observation data as SAM did. However, there are several changes in the orbital element input, the primary one being the inclusion of the nighttime exospheric temperature. NIP computes atmospheric densities from this input data by: "(1) converting the orbital elements to position and velocity; (2) using the numerical integration scheme to compute position and velocity at each of the observation times; (3) reconciling discrepancies between computed and observed position and velocity using standard differential correction techniques to correct seven quantities, the six components of position and velocity and the assumed atmospheric model; and (4) converting the corrected position and velocity back into orbital elements for output purposes. The corrected orbital elements from each observation also serve as the input elements for the next observation to be processed. An array of 77 input parameters is used to control the 41 routines which comprise this program." [2]

We received this program from AFCRL in late February 1967. To date, we have not had a successful run. We have tried the program several times on the San Marco I data originally obtained for the SAM program. The first few times, the program failed because we used data during a period when the perigee height was too high and the data were too sparse to allow the integration procedure to converge. We have since restricted our efforts to the last week of the satellite's lifetime, when observations were plentiful and expect to have a successful density determination from these data shortly.

Our future use of the NIP program will be a function of three factors. Primarily, it will be determined by AWS requirements for such data and by the ability of the Space Defense

Center to furnish the necessary observations. It will also depend upon the research efforts of Dr. Champion and Miss Almasian at AFCRL. It is our objective to supplement, not duplicate their work with this program. The third consideration is the importance of this work with respect to other 4th Weather Wing automation programs. Since we have only a two-man shop, careful consideration must be given before assigning a priority to each project.

REFERENCES

1. Bramson, A.S. and Foxworthy, V.L.: Atmospheric Density Determination Using the Satellite Analysis Monitor Program (SAM); Final Report AFCRL-65-25; December 1964 (available from DDC, AD-615 924)
2. Bramson, A.S. and Slowey, J.: Atmospheric Density Determination from Low Height Satellites; Scientific Report No. 3, AFCRL-66-809; November 1966 (available from DDC, AD-646 584) 50 pp
3. Harsh, E.S.: "Atmospheric Density Determination by the Satellite Analysis Monitor Program;" 4th Weather Wing Paper; March 1966, 28 pp
4. Jacchia, L.G. and Slowey, J.: "The Shape and Location of the Diurnal Bulge in the Upper Atmosphere;" Smithsonian Institution Astrophysical Observatory, Research in Space Science, Special Report No. 207; Cambridge, Massachusetts; April 1966
5. King Hele, D.G.: "Methods of Determining Air Density from Satellite Orbits;" Annales de Geophysique, Tome 22, #1; 1966 (available from DDC, AD-475 217)

AN INVESTIGATION OF ATMOSPHERIC DENSITY BETWEEN
ALTITUDES OF 180 KM AND 300 KM

Leonard L. DeVries, Lt Col, USAF
Air Weather Service (MAC)
United States Air Force

Summary

This report contains the results of a study of atmospheric density at altitudes from 180 to 300 km. Density data analyzed in this study were computed from observations of the decay rates of more than 40 satellites with perigee positions within this altitude range. Multiple regression equations were derived to specify the atmospheric density at 10-km intervals as a function of solar activity, time of day, time of year, and combinations of these variables. The step-by-step screening procedure was used to permit the selection of available variables which were most closely correlated with the density. This procedure also permitted the selection of significant parameters from a large number of potential parameters. Analyses of variance were conducted to determine how many terms to include in the regression equations. Density values depicted by these equations were then compared with density values calculated from satellite drag observations.

Nearly all that is known about atmospheric density and its variations at altitudes above about 170 km has been learned from observations of satellite decay since the orbit of the first artificial satellite on October 4, 1957. Sterne and King-Hele derived equations to compute atmospheric density from the orbital motion and characteristics of artificial satellites soon after such observations became available.

Atmospheric density data computed from the decay rate of the first artificial satellite showed that the density at an altitude of about 200 km was about eight times as large as had been previously estimated. Significant short- and long-term fluctuations in density soon became evident. Priester and Jacchia found that density variations were correlated with measurements of the solar radio flux at a wavelength of 10.7 cm. Measurements of the solar radio emission at a wavelength of 10.7 cm have been made since 1947 at the laboratories of the Canadian National Research Council at Ottawa. Jacchia also found that increases in density occurred during magnetic storms. Jacchia, May, and Paetzold found that these increases were proportional to the K_p and A_p magnetic indices. At each magnetic observing station a magnetic K-index is based on a curve generated by plotting the most disturbed component of the earth's magnetic field. The K_p -index and the daily planetary equivalent index, A_p , are daily measures of these disturbances for the entire earth.

It soon became apparent that a static model of the upper atmosphere could not represent its properties satisfactorily. Subsequent studies of the atmospheric density at altitudes above about 170 km have shown that its fluctuations are related to the following effects: a diurnal variation; a semiannual and an annual variation; variations resulting from changes in solar electromagnetic radiation, which are correlated with the solar decimetric radio flux; and variations caused by changes in solar corpuscular radiation, which are correlated with geomagnetic disturbances.

Several variable atmospheric density models have been derived since the first density data at high altitudes became available in 1957. The most widely-accepted density models presently available are the Jacchia Model and the Harris and Priester Model. The Jacchia Model is being considered by the Committee on Extension to the Standard Atmosphere (COESA) as the variable model to represent atmospheric properties between 120 and 700 km. The Harris and Priester Model has been proposed by the Committee on Space Research (COSPAR) to be the International Reference Atmosphere. Although both of these models permit the specification of density to altitudes as low as 120 km, the accuracy of the density depicted by these models below an altitude of about 230 km is questionable. There are two important reasons to question the accuracy of these models between altitudes of 120 and 230 km. First, few reliable density data in this altitude range were available when these models were derived. Second, constant boundary conditions at 120 km are assumed in these models. These assumed boundary conditions include temperature, density, mean molecular weight, and the number densities of N_2 , O_2 , O, and He. Harris and Priester estimate that a systematic uncertainty of a factor of two might still exist in some of the measured number densities.

Harris and Priester also estimate that the total ranges of uncertainty of density values due to systematic errors, after the short-term variations (27-day variations and corpuscular radiations effects associated with magnetic storms) have been accounted for, are ± 50 per cent at 120 km and are ± 25 per cent from 200 to 800 km during periods of low solar activity. The assumption of time-dependent boundary conditions at a chosen level may be satisfactory for density calculations designed primarily to agree with density observations well above that level. Such models do not give realistic density values at lower altitudes for a specific time of day, level of solar activity, or other values of specific variables.

One of the primary reasons for the previous lack of a satisfactory density model valid below an altitude of about 230 km has been a shortage of low-altitude density data. Nearly all satellites launched by the United States in low-altitude orbits have been classified Air Force missions, and precise orbital observations were not released. In July 1964, Small published a considerable amount of atmospheric density data deduced from the observations of 43 satellites orbited at altitudes between about 170 and 370 km during a time period of about five years. These data were made available because of the development of a technique for combining the satellite drag-free oblate-earth orbit solution with satellite decay measurements which have been accumulated during the past seven years by the Air Force Agency (SPADATS/SPACETRACK) charged with the responsibility of monitoring satellite positions for identification purposes.

Density equations derived in this report are based on calculated density values at or near the altitude at which they are valid. In addition, these equations are not restricted by the assumption of constant boundary conditions at a given level. Density data analyzed in this report were primarily those published by Small. Solar, geomagnetic, diurnal, and other parameters chosen to specify density were selected after a thorough review of density models which have been developed previously. Only those parameters which have been shown to be most closely associated with density from past studies were chosen for this study. Multiple regression equations were derived to permit a least-squares fit of values of these parameters to available density data. By a method of substitution, nonlinear terms were included in these equations. To avoid the selection of parameters which were most closely related with each other, the step-by-step screening procedure was used. This procedure orthogonalizes all remaining parameters with each parameter selected for the multiple regression equation. The multiple regression technique and associated screening procedure used in this report permitted the derivation of density equations based on a large number of potential parameters. Analyses of variance were conducted to assure that each parameter added to the multiple regression equations resulted in a significant reduction in unexplained variance. If this analysis indicated that a parameter by itself was not significant, an analysis of variance was conducted on the combination of this parameter with the one selected following it to determine if the combination of the two parameters in the equation resulted in a significant reduction in unexplained variance. About 25 per cent of the density values available for this study were withheld during the derivation of the density equations for a comparison of density values computed from these equations with density values calculated from observations of satellite drag. The accuracy of the density values depicted by these equations compares favorably with that demonstrated by previously developed density models.

(See AWS Technical Report 190 for the complete report.)

RECENT PROGRESS ON GENERAL CIRCULATION EXPERIMENTS AT NCAR

Warren M. Washington and Akira Kasahara

National Center for Atmospheric Research
Boulder, Colorado

I. Introduction

The purpose of this report is to review briefly progress made on general circulation experiments at the National Center for Atmospheric Research. Work on the formulation of a model began in the spring of 1964. We formulated a model which, basically, is similar to the one described by L. F. Richardson [1]. This model uses the height, z , as the vertical coordinate rather than the pressure p , which is more customary. The use of the z system allows for a straightforward approach to the incorporation of orography and boundary conditions at the surface of the earth.

We shall refer to a recent paper by A. Kasahara and W. M. Washington [2] which will be published soon. This article deals with the deviation of the basic model equations, explains the frictional and heating/cooling processes in the model, illustrates the energy conversion processes of this model, and lastly, gives a baroclinic stability analysis for our particular model.

A second article is now being written on the simulation of a mean January circulation. This article will show the numerical aspects of the model, the numerical treatment of frictional and heating/cooling terms, the heat balance, the evaluation of various energy conversion terms, a comparison with climatology, and finally, an evaluation of the angular momentum balance.

We shall show some synoptic features of the results so far obtained from the model. In this experiment we attempted to simulate a mean January circulation. Typical daily "weather" patterns are shown on different map projections produced by a cathode ray tube graphic display unit. A brief discussion of these patterns will be given.

II. The Basic Model Equations

The prognostic equations for the NCAR General Circulation Model are the two horizontal equations of motion and pressure tendency equation in spherical coordinates. We merely list the equations used. The equations of motion are:

$$\frac{\partial(\rho u)}{\partial t} = -\nabla \cdot (\rho u \mathbf{V}) - \frac{\partial}{\partial z} (\rho u w) - \frac{1}{a \cos \varphi} \frac{\partial p}{\partial \lambda}$$

(1)

$$+ (f + \frac{u}{a} \tan \varphi) \rho v + F_{\lambda} ,$$

$$\frac{\partial(\rho v)}{\partial t} = -\nabla \cdot (\rho v \mathbf{V}) - \frac{\partial}{\partial z} (\rho v w) - \frac{1}{a} \frac{\partial p}{\partial \varphi}$$

(2)

$$- (f + \frac{u}{a} \tan \varphi) \rho u + F_{\varphi} ,$$

where, for a scalar quantity A,

$$(3) \quad \nabla \cdot AV = \frac{1}{a \cos \varphi} \left[\frac{\partial(Au)}{\partial \lambda} + \frac{\partial}{\partial \varphi} (Av \cos \varphi) \right],$$

φ is latitude, λ is longitude, z is height, t is time, V is horizontal wind ($V = iu + jv$), w is vertical velocity, p is pressure, ρ is density, a is mean radius of the earth, Ω is angular velocity of the earth, $f = 2\Omega \sin \varphi$, F_λ and F_φ are the longitudinal and meridional components of the frictional force per unit volume.

The pressure tendency equation is

$$(4) \quad \frac{\partial p}{\partial t} = B + g\rho w - g \int_z^{z_T} \nabla \cdot (\rho V) dz$$

where $B = \partial p / \partial t$ evaluated at $z = z_T$ and g is the acceleration of gravity. In deriving (4) it was assumed that

$$(5) \quad w = 0 \quad \text{at} \quad z = z_T.$$

The diagnostic equations are also listed:

The equation of state:

$$(6) \quad \rho = pRT$$

where R is the gas constant for dry air and T is temperature.

The hydrostatic equation:

$$(7) \quad \frac{\partial p}{\partial z} = -g\rho$$

The vertical motion equation (Richardson's equation):

$$(8) \quad w = - \int_0^z \nabla \cdot V dz - \frac{1}{\gamma} \int_0^z \frac{1}{p} (B + J) dz + \frac{1}{C_p} \int_0^z \frac{Q}{T} dz$$

where we assumed that

$$(9) \quad w = 0 \quad \text{at} \quad z = 0,$$

$\gamma = C_p / C_v$, C_p and C_v are the specific heats, Q the rate of heating per unit mass, and

$$(10) \quad J = V \cdot \nabla p - g \int_z^{z_T} \nabla \cdot (\rho V) dz.$$

We can evaluate B by integrating (8) from the ground ($z = 0$ in the present case) to z_T where $w = 0$. This yields the following equation for B :

$$(11) \quad B = \frac{\frac{1}{\gamma} \int_0^{z_T} \frac{J}{p} dz - \frac{1}{C_p} \int_0^{z_T} \frac{Q}{T} dz + \int_0^{z_T} \nabla \cdot \mathbf{V} dz}{-\frac{1}{\gamma} \int_0^{z_T} \frac{dz}{p}} .$$

III. Frictional and Heating/Cooling Terms

We shall not derive the equations involved in frictional and heating/cooling terms since they are explained elsewhere [2]. However, the physical processes so far included in the present model will be outlined:

- A. Release of latent heat of condensation.
- B. Absorption of solar radiation by water vapor in the atmosphere.
- C. Long wave radiational cooling of the atmosphere.
- D. Horizontal and vertical diffusion of heat and momentum in the atmosphere and vertical transport of heat from the earth's surface.

IV. Computational Features

The finite difference method used to solve the prognostic equations is based upon a modification of the two-step Lax-Wendroff method discussed in [3] and [4]. The horizontal grid is made up of 5 degree longitude and latitude intersections over the entire globe. However, the grid is coarsened in the longitudinal direction near the poles in order to keep geographical distances from becoming too small. In the version of the model discussed here two layers of 6 km thickness were used. A time step of 5 minutes was chosen. This version runs approximately 30 times faster than real time on the CDC 6600 computer.

V. Preliminary Results

We mentioned in the Introduction that a complete description of the results is now being written. The preliminary results we wish to show here are from an experiment to simulate the circulation patterns of a mean January condition.

We began this experiment from an isothermal atmosphere of 250K with no motions initially. The sun's declination angle was set for January 15 and the distribution of surface temperature (which in this experiment is that of sea level due to the lack of orography) was prescribed for a January mean, as shown in Fig. 1. Within a few hours of commencing the experiment a Hadley-type circulation quickly started in both hemispheres with a small amount of longitudinal asymmetry due to the prescribed surface temperature distribution. The Hadley circulations are not an efficient method of transporting heat from the tropics to the polar regions so that the north-south temperature gradients increased with time in both hemispheres. When the temperature gradients had nearly reached the values observed in a mean January, weak baroclinic waves started to grow in both hemispheres. The Hadley circulation broke down into the characteristic three cell meridional structure found in the real atmosphere.

To demonstrate some of the synoptic features of the results we will show model "weather" patterns. Figs. 2 and 3 show surface pressure fields at days 78 and 80. The projection used in these figures is an orthographic view of the earth. This is the view of the earth from an infinitely long distance. We see in Fig. 2 that the low pressure center over central Canada has intensified and moved to a position west of Greenland after two days, as shown in Fig. 3. The low which was in the Gulf of Alaska on day 78 has also intensified and moved to west central Canada. The high pressure cell over the west coast of Canada on day 78 moves toward the southeast in two days. Likewise the high pressure cell over eastern Canada moves off the east. Fig. 4 shows the temperature field for day 80, where we note the

strong frontal packing of isotherms near the southeastern edge of Hudson's Bay. The frontal motion is more clearly depicted in the wind vector field shown on a polar projection in Fig. 5. Finally, to show the complete global circulation we show the surface distribution of pressure for day 80 on Fig. 6. We note the lows and highs are more intense in the northern hemisphere than in the southern hemisphere. The southern hemisphere appears to have a maximum baroclinic zone approximately 60°S where the weak waves in this zone are quite regular. This may be due to the fact that the surface temperature distribution in middle latitudes in the southern hemisphere has very little longitudinal variation.

VI. Future Improvements

We plan the following improvements in the model within the near future:

- A. The inclusion of orography.
- B. The calculation of surface temperature over continental areas.
- C. The incorporation of a more complete hydrological cycle.
- D. Extension of the model from the present two layers of 6 km each to six layers of 3 km each.

VII. References

- [1] Richardson, L.F.: Weather Prediction by Numerical Process, Cambridge University Press, 236 pp, 1922.
- [2] Kasahara, A. and Washington, W. M.: "NCAR Global General Circulation Model of the Atmosphere," Monthly Weather Review (to be published).
- [3] Houghton, D., Kasahara, A., and Washington, W.: "Long Term Integration of the Barotropic Equations by the Lax-Wendroff Method," Monthly Weather Review, vol. 94, pp. 141-150, March 1966.
- [4] Richtmyer, R.: "A Survey of Difference Methods for Non-Steady Fluid Dynamics," NCAR Technical Notes 63-2, National Center for Atmospheric Research, 25 pp., 1963.

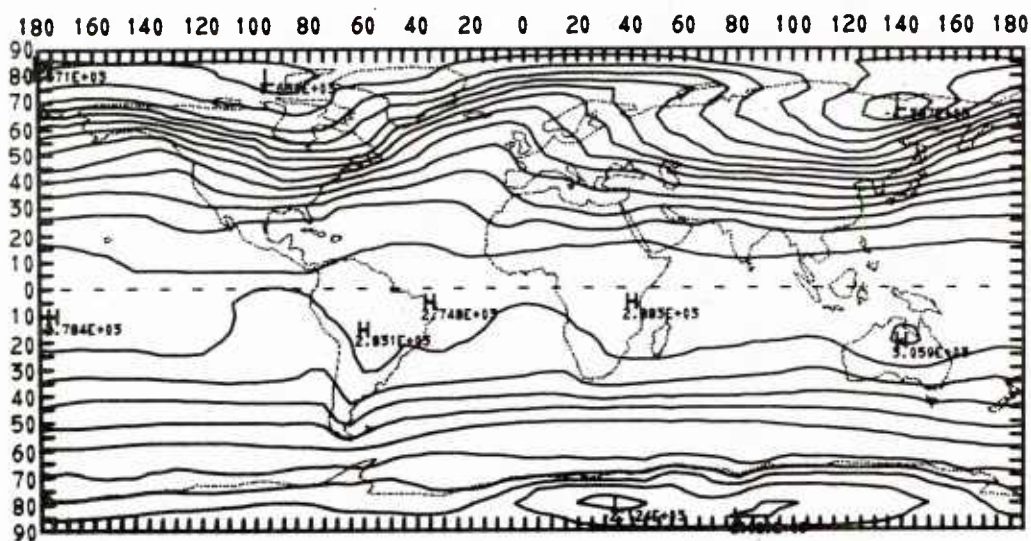


Figure 1. Distribution of January mean surface temperature. Contour interval is 5 C.

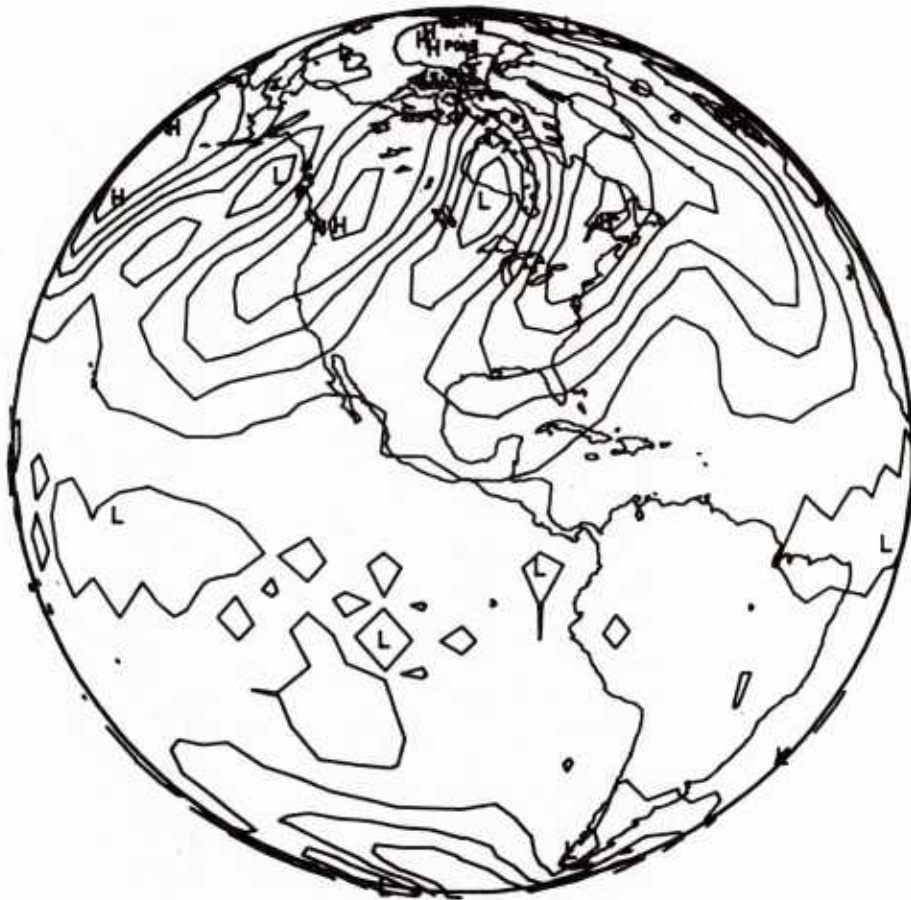


Figure 2. Surface pressure distribution on day 78. Contour interval is 5 mb.



Figure 3. Surface pressure distribution on day 80. Contour interval is 5 mb.

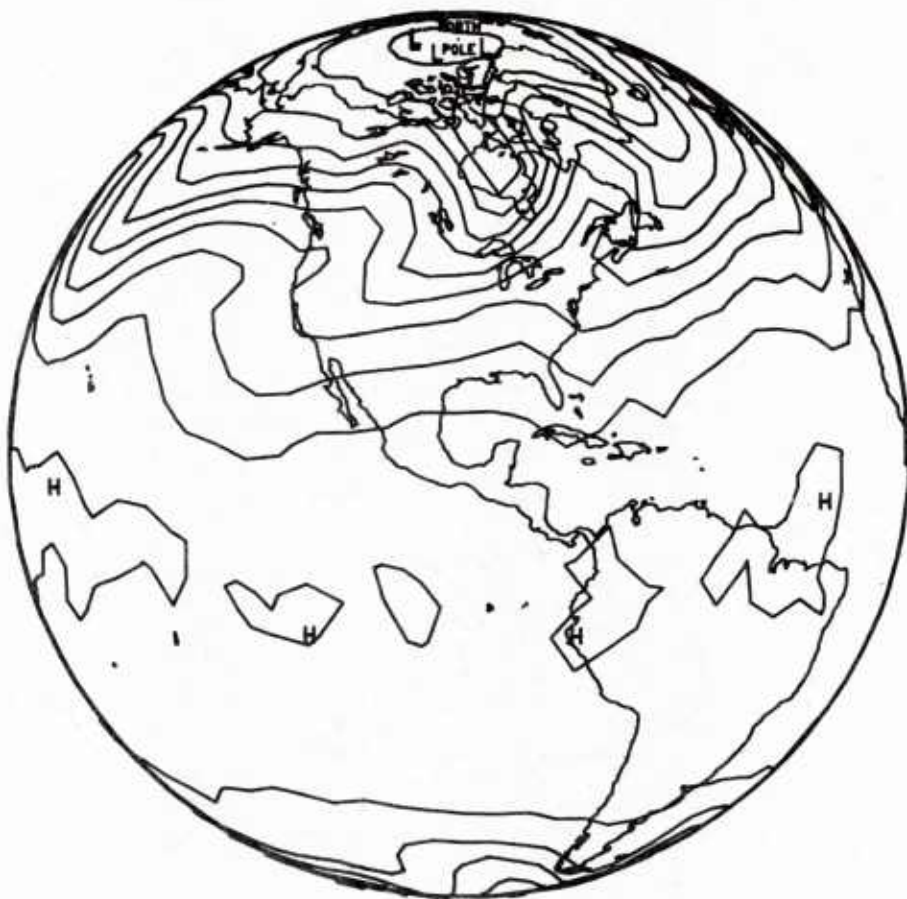


Figure 4. Temperature distribution at 3 km on day 80. Contour interval is 5 C.

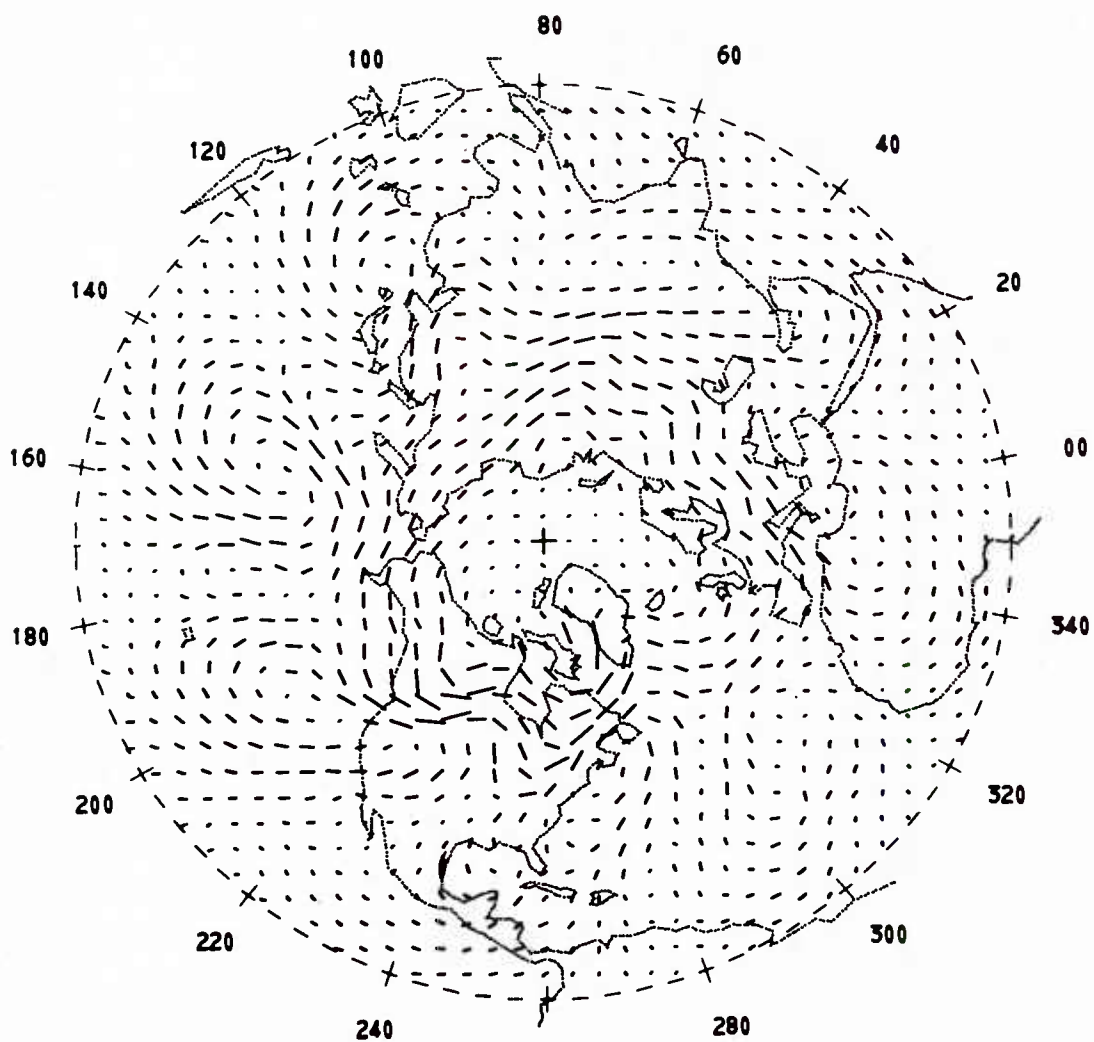


Figure 5. Horizontal wind vector distribution at 3 km on day 80.

GRID TELESCOPING IN NUMERICAL WEATHER PREDICTION

Geoffrey E. Hill

Air Force Cambridge Research Laboratories
Bedford, Massachusetts

Abstract

A method is devised whereby numerical forecasts cover the whole Northern Hemisphere, yet in certain regions the grid spacing is made as small as 40 km. The method involves solution of numerical equations on a grid of data points in the usual way. Then, results from that forecast are used for the boundary conditions of a more dense but smaller-size grid network placed within the original one. Successively smaller grids are introduced so that the final grid size is as small as desired. So far, results have been obtained from a barotropic model with a grid spacing reduced from 655 km to 82 km, and from a simple 2-level baroclinic model with a grid spacing reduced from 655 km to 164 km.

I. Introduction

In the present work a method is devised whereby numerical forecasts cover most of the Northern Hemisphere, yet the grid spacing in desired regions is made as small as 40 km. If such a grid spacing were used throughout the entire region over 150 thousand points per level would be required.

A method which we refer to as "grid telescoping" consists of the following: A numerical integration is first carried out for an octagonal hemispheric grid. Then, another grid, preferably of the same shape and number of points, but of half the gridpoint spacing, is placed within the original grid. Forecasts are made separately for each grid, except for the boundary of the second grid. When data is required there, it is obtained from the first grid.

Such a process is repeated by placing a third grid of appropriate size and dimensions on the second grid. Thus the forecast area of the third grid will be one sixteenth of the first grid.

To produce a forecast the time step is halved each time the grid spacing is halved. Data on the boundary points for the intermediate time step, $\tau + \frac{1}{2}$, is obtained by interpolation between time step τ and $\tau + 1$.

The method of grid telescoping makes feasible numerical forecasts on a much smaller size scale than presently available without greatly increasing computer storage or computation time. Also, the preparation of initial data for the method, though increased, remains feasible.

Grid telescoping may be applied to any model and ostensibly has its chief advantage in the forecast of small-scale cyclones, hurricanes, meso-scale features such as squall lines, and orographic effects not yet adequately treated.

II. Numerical Model

To test the merits of the idea outlined above we will develop a simple two-level model, construct a set of grids and numerically integrate the forecast equations for a particular case.

Here we will present only the finite-difference equations used and omit their derivation. The vorticity η is written

$$(1) \quad \eta = \frac{m^2}{d^2} \nabla^2 \psi + f$$

where m is the map factor, d is the grid spacing, ψ is the stream function, f is the coriolis parameter, and ∇^2 is the finite-difference Laplacian operator.

The barotropic vorticity equation (500 mb) is

$$(2) \quad \nabla^2 \frac{\partial \psi}{\partial t} + \frac{1}{4} \mathcal{J}(\psi, \eta) = 0$$

where \mathcal{J} is the finite-difference Jacobian operator.

The 500 mb temperature equation is

$$(3) \quad \frac{\partial T}{\partial t} + \frac{m^2}{4d^2} \mathcal{J}(\psi, T) + \sigma \omega = 0$$

where T is the temperature, σ is the static stability and $\omega \equiv dp/dt$.

The 500 mb ω equation is

$$(4) \quad \nabla^2 \sigma \omega + \frac{1}{4} \nabla^2 \frac{m^2}{d^2} \mathcal{J}(\psi, T) + \frac{f p}{4 R} \mathcal{J}\left(\frac{\partial \psi}{\partial p}, \eta\right) + \frac{f p}{4 R} \mathcal{J}\left(\psi, \frac{m^2}{d^2} \nabla^2 \frac{\partial \psi}{\partial p}\right) = 0$$

The balance equations are given in geostrophic form.

$$(5) \quad \nabla^2 \psi = \frac{g}{f} \nabla^2 z - \frac{g}{4 f^2} \nabla z \cdot \nabla f$$

$$\text{and } (6) \quad \nabla^2 Z = \frac{f}{g} \nabla^2 \psi + \frac{1}{4g} \nabla \psi \cdot \nabla f$$

where Z is the height of the pressure surface at which the equation is applied.

Differentiating with respect to p and using the hydrostatic relation we have

$$(7) \quad \nabla^2 \frac{\partial \psi}{\partial p} = -\frac{R}{f p} \nabla^2 T + \frac{R}{4 f^2 p} \nabla T \cdot \nabla f$$

where ∇ is the finite-difference grad operator. In this equation T and p may be taken at the 500 mb surface or an average between 500 and 1000 mb depending upon where $\partial \psi / \partial p$ is required. Finally, the 1000 mb temperature equation is

$$(8) \quad \frac{\partial T}{\partial t} + \frac{m^2}{4d^2} \mathcal{T}(\psi, T) = 0$$

In this equation ψ and T refer, of course, to the 1000 mb stream function and temperature.

Equations (1) through (8) form a complete system from which time changes of the dependent variables are found. Equations for ψ and T at 500 mb and T at 1000 mb are prognostic equations and the remaining are diagnostic.

The grid distance d and the time step δt are as follows:

| Grid | d | δt |
|------|--------|------------|
| 1 | 655 km | 1 hr |
| 2 | 328 | 1/2 " |
| 3 | 164 | 1/4 " |

III. Data and Results

Data is measured from the Hemispheric charts of 1200 Z, April 9, 1965. This data, i. e., 500 mb height, 500 mb temperature, and 1000 - 500 mb thickness are smoothed and adjusted so that two-grid interval variations are removed and the boundary values are constant. Also spurious vorticity concentrations are removed from low latitudes by the smoothing and adjusting. In Fig. 1 the initial 500 mb height in hundreds of meters is shown. We note especially the trough-ridge-trough pattern over North America, and lack of activity in low latitudes. In Fig. 2 which shows the absolute vorticity, we see the trough-ridge-trough pattern and presence of "spurious" centers in low latitudes. In Fig. 3 smoothing and adjusting are applied to the relative vorticity. The dominance of the trough-ridge-trough is now clear and there is little activity in low latitudes.

In Fig. 4 the initial 1000 mb height is shown. Also the next grid is included to show the area of interest. We note the center of East United States Coast low and cold

frontal trough extending inland and warm frontal trough in Western United States.

After 12 hours (Fig. 5) the positions of the centers have not changed greatly, although the Atlantic high and the Icelandic low show some movement. The cold frontal trough moved rapidly southward to a position through Florida and along the Gulf Coast. A 12-hour forecast starting from $\tau = 0$ and using the boundary conditions from the large grid is shown in Fig. 6. Changes in the positions of the centers are more clearly evident on this scale. The low off the east coast shows a definite eastward motion not clearly evident on the first grid. Also, the main frontal system can be located more accurately. The forecast is again made (Fig. 7) for 12 hours using the third grid (48 time steps, 15 min. each). Here the east coast low is on the edge of the grid. The frontal system in the United States is located with a refined accuracy.

IV. Conclusions

The process described here can be applied at least two more times, although this has not yet been tried. However, the computer program is general, so it is only a matter of changing a few control cards.

This is only a test model and the results of the forecasts are not so important as is the fact that the method is feasible when applied to a baroclinic vorticity model. Whether the same can be said for a primitive equation model remains to be seen.

Finally, the telescoping does not have to be geographically predetermined; the areas examined may be those of meteorological interest.

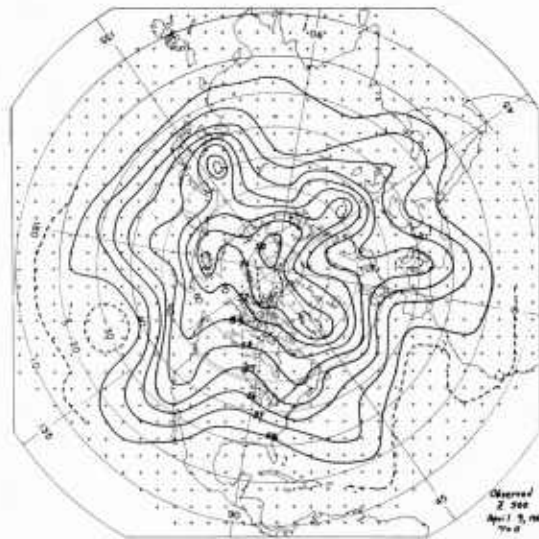


Fig. 1. Observed 500 mb height with boundary made constant.



Fig. 2. Absolute vorticity pattern from observed 500 mb.

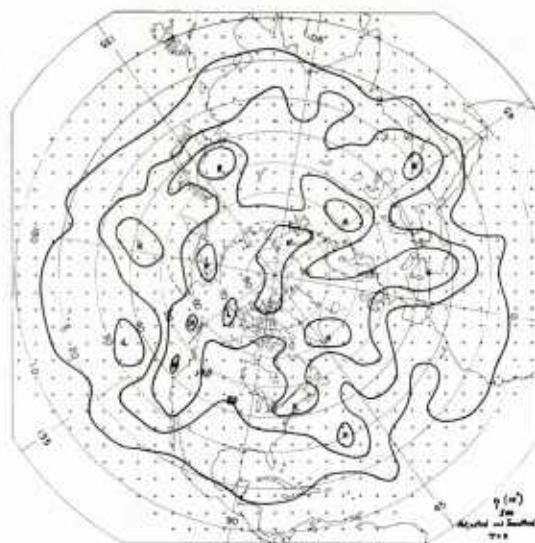


Fig. 3. Adjusted and smoothed absolute vorticity (adjusting and smoothing is on relative vorticity only and f is added).

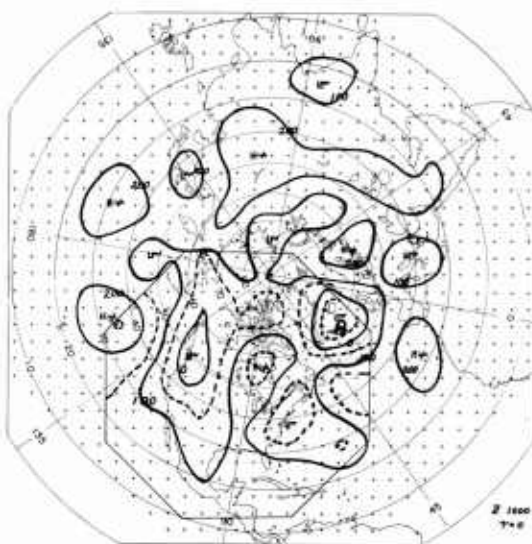


Fig. 4. 1000 mb height in meters at $\tau = 0$.



Fig. 5. Forecast 1000 mb height at $\tau = 12$.

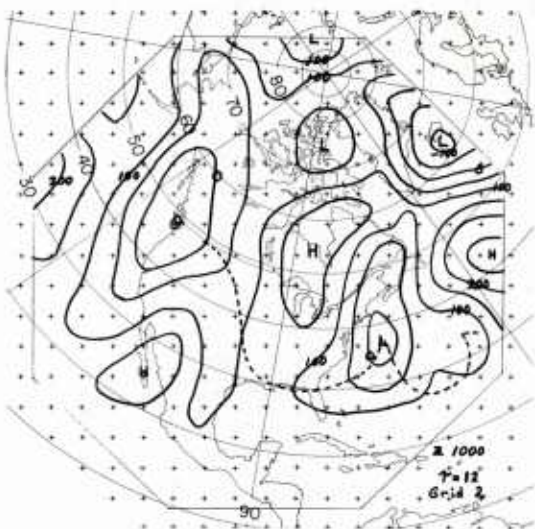


Fig. 6. Forecast 1000 mb height at $\Upsilon = 12$, grid 2.

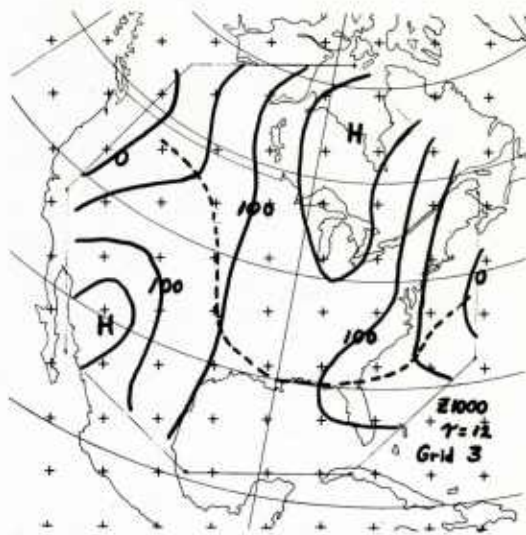


Fig. 7. Forecast 1000 mb height at $\Upsilon = 12$, grid 3.

OBJECTIVE IMPROVEMENT OF NUMERICAL PROGNOSSES

By H. B. Wobus and P. R. Lowe
U.S. Navy Weather Research Facility
U.S. Naval Air Station
Norfolk, Virginia 23511

(Abstract)

Forecasts or prognoses made by numerical or objective methods, however free of long term bias, may be subject to "temporary" periods of bias which are of somewhat longer duration than the time period of the actual forecasts. As example, local temperature forecasts, or the height of the 500 millibar surface at each of specific gridpoints in a region, may for the duration of some particular regime development show errors which indicate bias for periods ranging from a few days to a few weeks. One readily recognizes that not all Decembers are alike, or that for some April period the weather regime resembles winter while another resembles summer conditions. What we refer to as "regimes" give rise not only to differences in the weather, but also to differences in the way in which the weather "fools" prediction models by presenting situations systematically unexplained by the models.

A measure of errors recently made may be used as a parameter for prediction of the error to be expected in a new forecast, as it is made. A revised forecast then becomes possible: $F_{revised} = F_{unrevised} - EE$, where EE is the expected error that may be determined from the behavior of previous unrevised forecasts.

In application to 36-hour forecasts of several different parameters the following expressions have been found to give interesting results.

1. $EE = \bar{E}_{36}$
2. $EE = A \bar{E}_{36}$
3. $EE = A \bar{E}_{36} + B (E_{12} - \bar{E}_{12})$

The subscript denotes the period of forecast, E denotes the error of the most recently verified forecast, and \bar{E} represents the exponential mean (weighting factors decrease exponentially with age of error observed) of prior errors. Errors, means, and coefficients are treated separately for each gridpoint of area forecasts.

The first equation represents a direct, obvious approach. The second reflects the fact that successive values of the exponential mean are not perfect predictors for the immediately following forecast errors. In the third form, a second term is introduced to detect, on a more timely basis, the change in degree to which the weather regime "fools" the model. The error in the 12-hour forecast, made by the same model, is of some merit as a predictor of the error to be expected in the subsequent 36-hour forecast.

The coefficients A and B may be formally derived regression coefficients computed anew on each successive occasion; or they may be practical estimates of such coefficients derived by systematically adjusting previously used values each time a forecast is verified. In this second method, at each verification, each coefficient is adjusted slightly. If a smaller or larger value would have produced a better result on the situation just verified, the corresponding change is made.

Mean error and root-mean-square-error have been successfully reduced in several verification experiments: height of 500-millibar surface at gridpoints of numerical forecasts, gradients of heights on the same surface, and also local maximum temperature forecasts.

The potential of the scheme in other applications will depend upon the presence or absence of temporary periods of bias in the raw forecasts to which the method may be applied, and upon the ingenuity of the person devising appropriate expressions for the expected error EE .

THE APPLICATION OF NUMERICAL ANALYSIS OF BAROCLINICITY TO THE OBJECTIVE LOCATION OF FRONTAL ZONES

By Robert J. Renard
Department of Meteorology and Oceanography
Naval Postgraduate School
Monterey, California

I. Introduction:

For nearly two years the Navy's Fleet Numerical Weather Facility (FNWF) at Monterey, California has been producing, twice daily, Northern Hemisphere analyses and prognoses of baroclinic zones, for the purpose of objectivizing and standardizing the operational location of fronts. That such a need exists may be seen from Figure 1 showing surface frontal analyses from sixteen international and national analysis centers for 0000 GMT 5 March 1964. Even dense data areas like the United States bear witness to the inexactness of manually locating fronts, here by as much as five degrees latitude. Moreover, the quantitative criteria used for frontal placement and designation of intensity of the associated baroclinic zone are unknown to the user.

The model, currently used by the Navy to obtain a first approximation to frontal position and strength, [2] [4], is based on the widely held dynamic-synoptic concept of frontal zones, described in the Glossary of Meteorology, [3], as "the three dimensional zone or layer of large horizontal density gradient bounded by frontal surfaces across which the horizontal density gradient is discontinuous". Stated in another, but equivalent way, the FNWF model depicts frontal zones which are hyperbaroclinic regions whose boundaries, practically speaking, are quasi first order discontinuities in the thermal field.

II. Present Status of FNWF's Numerical Frontal Analysis Model:

In summarizing the essentials of FNWF's frontal analysis model, note Figure 2a, b and c which schematically depict one-dimensional profiles of parameters involved in the analysis. For simplicity, assume the profiles are oriented in the direction of the gradient of potential virtual temperature on an isobaric surface. Thus, Figure 2a represents a potential virtual temperature (θ^*) profile through a hyperbaroclinic zone. Figure 2b depicts a baroclinicity parameter in the form $|\nabla \theta^*|$. The point of maximum baroclinicity at "0" and locations of quasi-first order discontinuities in θ^* at 1 and 2 are to be noted. Shown in Figure 2c is $GG\theta^*$, the operational front-location parameter. As indicated on the figure, $GG\theta^*$ is essentially a second derivative taken in the direction of the gradient of θ^* and is proportional to the curvature of the basic θ^* profile. In this context the maximum positive and negative values of $GG\theta^*$ are at the quasi-discontinuity points in θ^* [2, 1] and, thus, are the warm- and cold-side boundaries of the hyperbaroclinic zone, respectively. Such points are also locations of maximum thermal wind shear and hence maximum thermal-shear vorticity. Zero points of $GG\theta^*$ lie at the points of maximum and minimum baroclinicity.

Figures 3a, b and c show small two-dimensional sections of objectively analyzed fields of 850 mb θ^* , $|\nabla \theta^*|$ and $GG\theta^*$ over a section of the North Atlantic area for 00Z 1 January 1965. The hyperbaroclinic frontal zones are bounded by the ridges and troughs in the $GG\theta^*$ field with the location of maximum baroclinicity ($\max |\nabla \theta^*|$) on or close to the "0" isoline of $GG\theta^*$ in the zone.

Figure 4 is a typical example of the hemispheric FNWF operational $GG\theta^*$ analysis; in this case 00Z 6 March 1966. In the current model, potential virtual temperature takes the form of the mean value in the layer 1000/700 mb. Only positive isolines are portrayed. This is sufficient for the field meteorologist who is directed to use the centrum of the major elongated closed isolines as first guess on front location while employing the orientation,



Figure 1. Surface fronts at 0000GMT, 5 March 1964. Positions from analyses made by sixteen foreign, national and military analysis and forecast centers [4] .

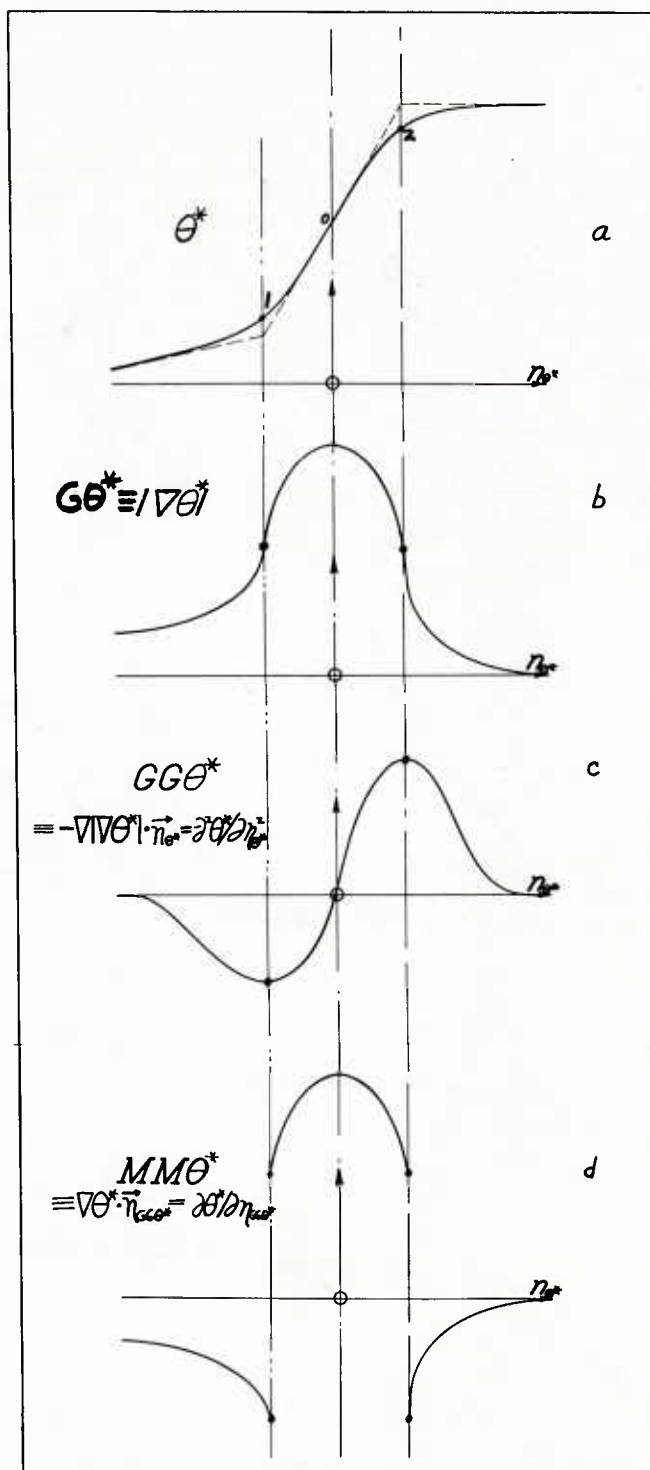


Figure 2. Schematic profiles of potential virtual temperature, θ^* , and its derivatives. Locations 1 and 2 represent quasi first-order discontinuity points, idealized by dashed lines. 2a. Profile of θ^* . 2b. Profile of $|\nabla\theta^*|$, derived from 2a. 2c. Profile of $GG\theta^*$, derived from 2a and 2b. 2d. Profile of $MM\theta^*$, derived from 2b and 2c. [After 2]

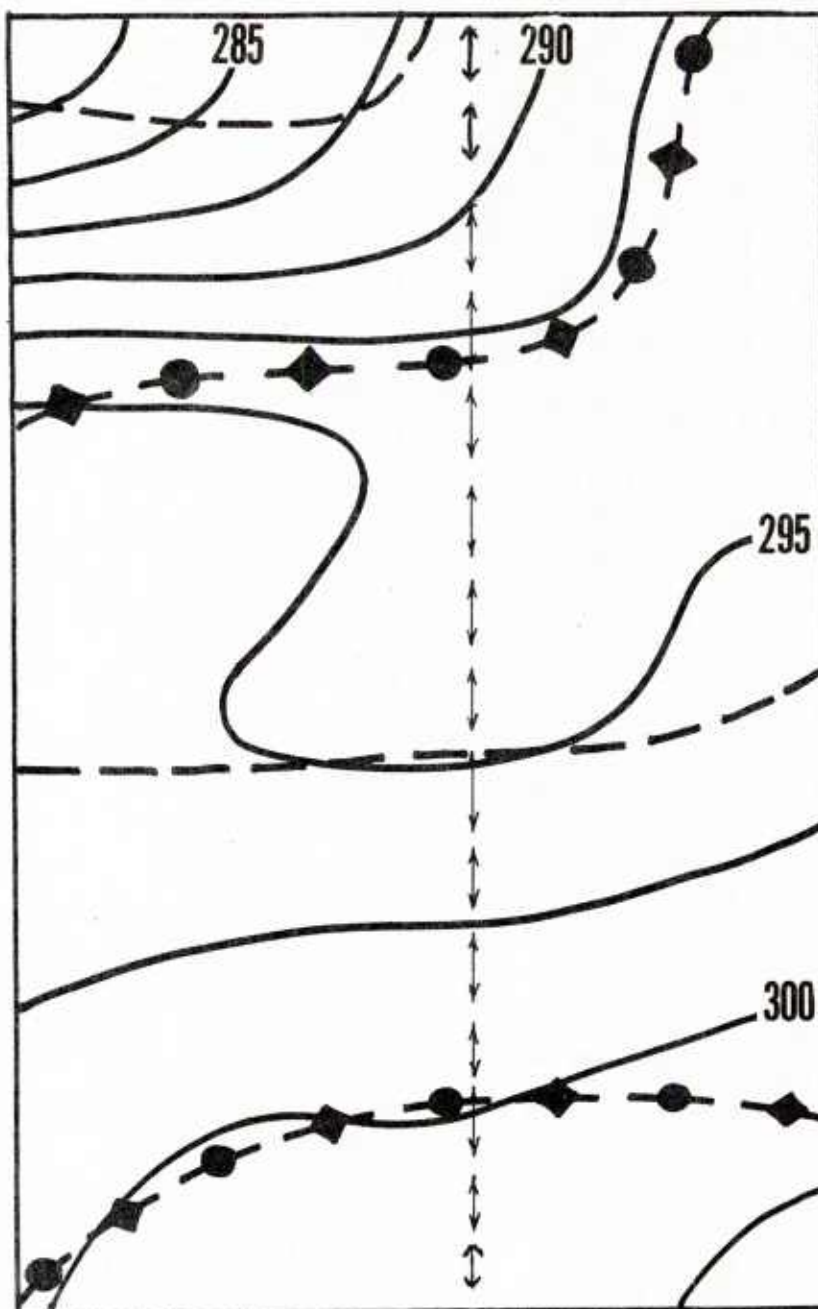


Figure 3a. Field of θ^* ($^{\circ}\text{C}$) for a $(21^{\circ}\text{lat})^2$ midlatitude section of the North Atlantic area at 850 mb 0000GMT 1 January 1965. Dashed lines: GG θ^* troughs; dashed lines with superposed symbols: GG θ^* ridges (fronts). \longleftrightarrow arbitrarily located position on abscissa [after 4] .

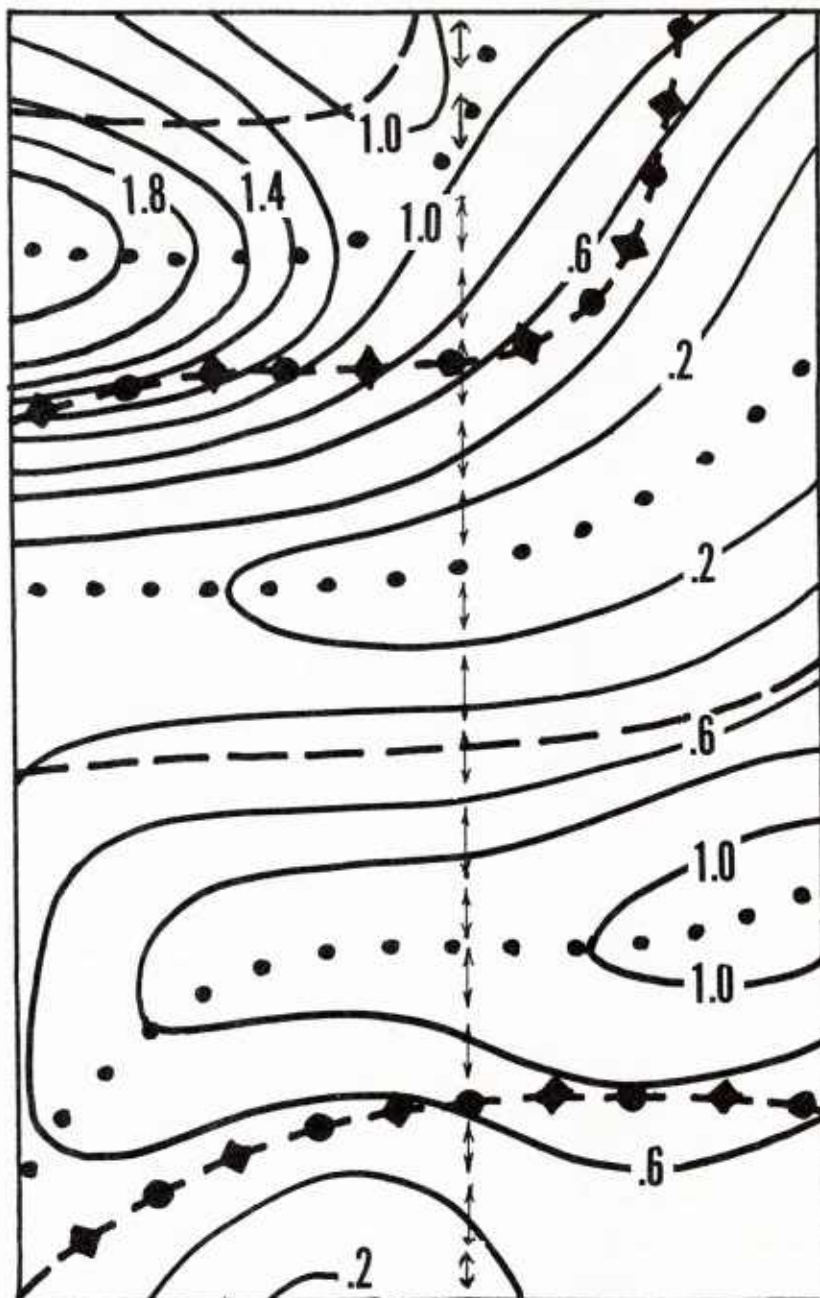


Figure 3b. Field of $|\nabla\theta^*|$ (C/100 km), as calculated from Figure 3a. Dotted lines: ridges and troughs in $|\nabla\theta^*|$ field. Other lines and symbols as in Figure 3a [after 4] .

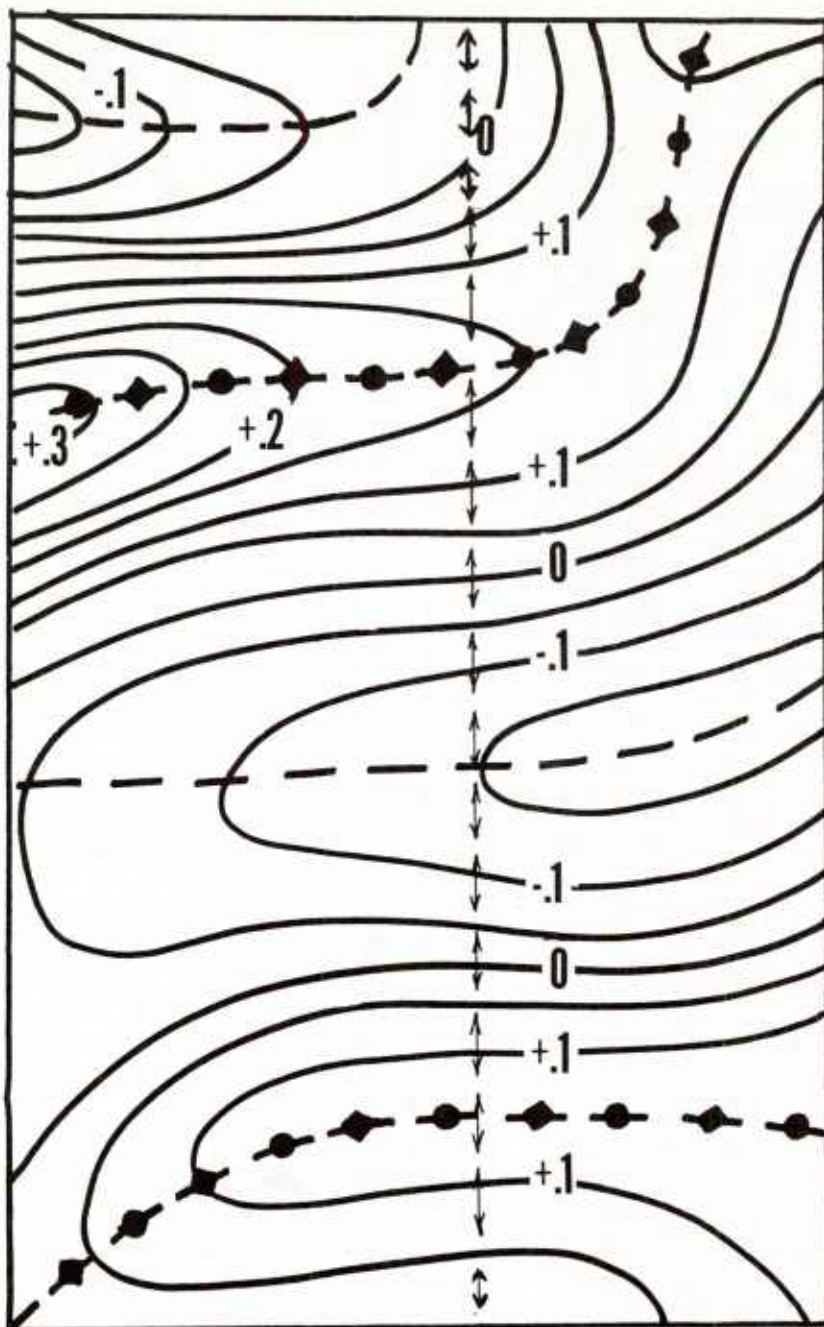


Figure 3c. $GG\theta^*$ ($C/(100 \text{ km})^2$), as calculated from Figure 3a and b. Other lines as in Figure 3a [After 4].

pattern and magnitude of $GG\theta^*$ lines to assist in designating type, stage of development and intensity of conventional fronts, respectively. The magnitude of $GG\theta^*$, which has a high positive correlation with baroclinicity (i.e. $|\nabla \theta^*|$) serves as a numerical indicator of frontal intensity. In Figure 4 the most intense front is over Eastern Siberia and has a $GG\theta^*$ magnitude in excess of 60 units.

Conclusive evidence of frontal type (warm, cold, stationary, occluded) and stage of development requires the $GG\theta^*$ analysis to be viewed in coincidence with the surface or 1000-mb pressure pattern. Minor axes or bulges such as found over eastern Canada (A), and the central Pacific (B) are frequently symptomatic of occluded structure (Figure 4).

Small $GG\theta^*$ zones, as noted in northeastern Canada (C) and eastern Asia (D), depend on the noise level (i.e. smallest $GG\theta^*$ value plotted) and smoothing. It has been found desirable to maintain a low noise level in order to allow depiction of the extensive weak baroclinic zones over eastern ocean areas as seen in the eastern Pacific and Atlantic in Figure 4.

III. Verification Statistics on Numerical Frontal Analysis:

With regard to verification of numerical frontal analysis, an absolute standard to which frontal positions and intensities may be related is non-existent. However, as with all numerical operational products, a comparison to similar analyses, performed manually, must be made. Several such evaluations have been made in the past two years and Table 1 shows a recapitulation of one of the more extensive ones.

The test covered a late summer period of sixteen observation times from 23 August to 6 September 1965 and related over a quarter of a million miles of FNWF numerically analyzed and NMC manually analyzed fronts. The results, as seen in the table, are similar to other tests on winter data. The more obvious conclusions may be stated as follows:

- a. The two independent frontal analyses have the closest relation over dense data land and ocean areas, such as the United States and the Atlantic, while the relation is poorest over the Pacific and North African areas. The 1.2° latitude difference for Asia is considered anomalously good and not representative of that area.
- b. Numerical fronts associated with intense baroclinic zones north of 30°N , over east continents and west oceans, compare most favorably with NMC positions.
- c. Only two-thirds of the NMC fronts could be associated with FNWF fronts. The remainder (34%), not appearing on the FNWF analyses, are mostly due to manually analyzed occlusions and weak fronts in east ocean areas, both categories of the same nature.
- d. A similar percentage of significant FNWF fronts (72%) could be associated with NMC fronts. The remainder, (28%), represents baroclinic zones over North Africa, and thermal-low and mountainous areas in general. This figure is a measure of the greater number of numerically analyzed fronts compared to the hand analyzed warm, cold and stationary fronts.

Upon comparison to the Canadian model of frontal analysis one finds the large number of FNWF baroclinic zones reasonable since the Canadian concept features the TROWAL rather than the occlusion and a three-front rather than a (usually) two-front model [1]. But the deficiency of not portraying occlusions or very weak fronts is considered a more serious problem than the excess of baroclinic zones, at least in relation to the frontal concepts apparently widely held by the American operational meteorologist. Thus, a modification to the current $GG\theta^*$ model is being developed by FNWF.

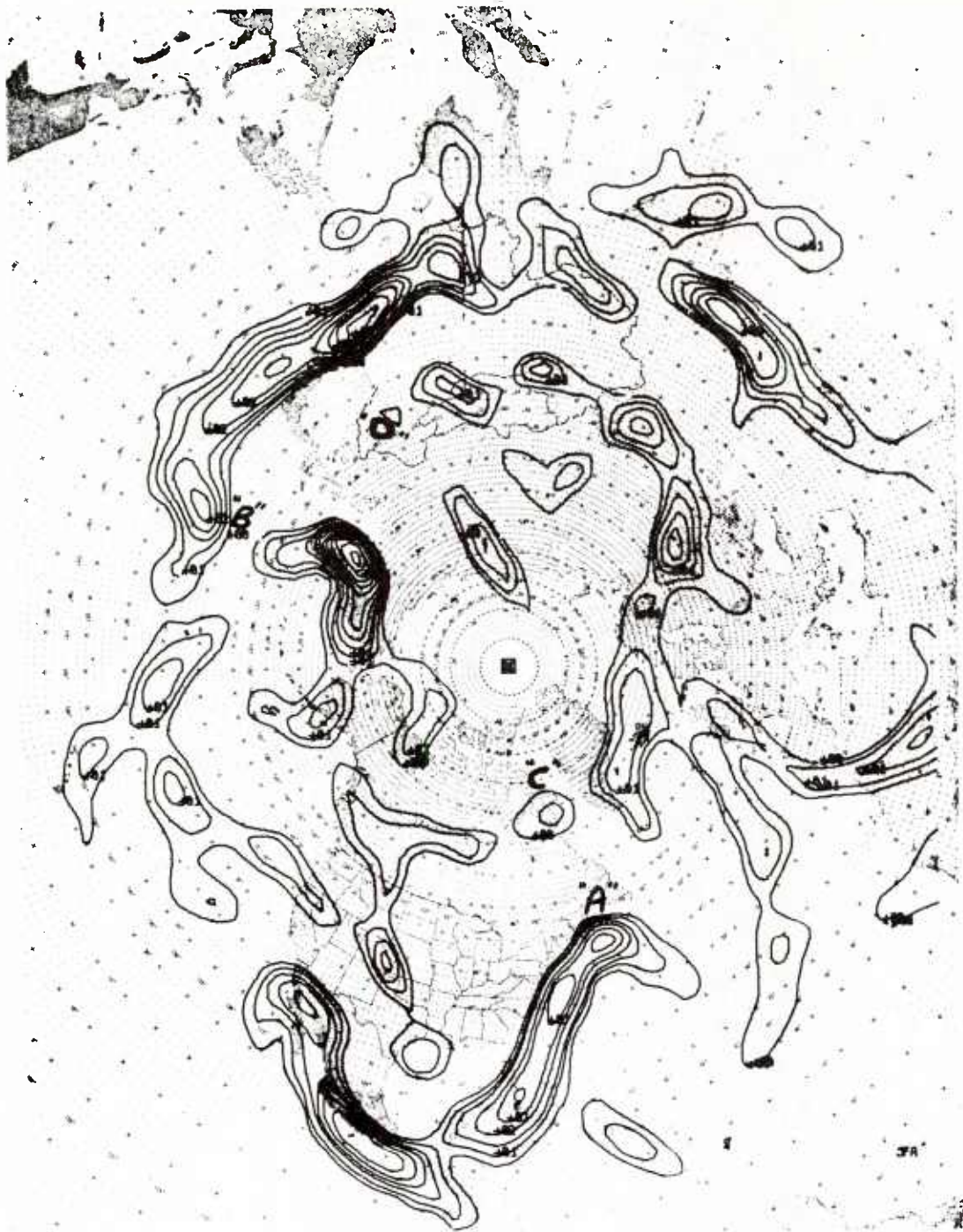


Figure 4. Operational FNWF 1000 mb frontal analysis for 0000GMT 6 March 1966. (1000/700 mb model). Isolines: $GG\theta^*$ ($C/(100 \text{ km})^2$) at interval of 5×10^{-2} , starting with "5" line.

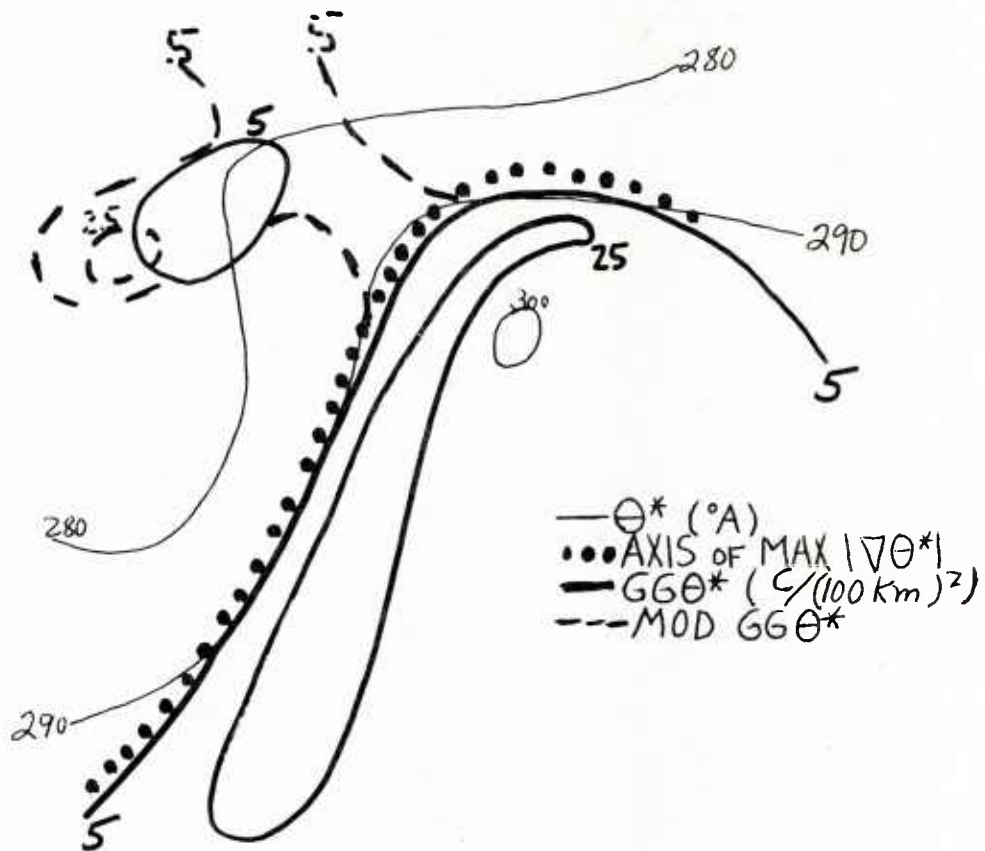


Figure 5. Modification to the front location parameter, $GG\Theta^*$, by selective addition of curvature term, $GK\Theta^*$, for section of eastern United States, 1000 mb 0000GMT 6 March 1966. $Mod GG\Theta^* = GG\Theta^* + GK\Theta^*$, where $GG\Theta^* < 0$, $GK\Theta^* > 0$, $|GG\Theta^*| < |GK\Theta^*|$

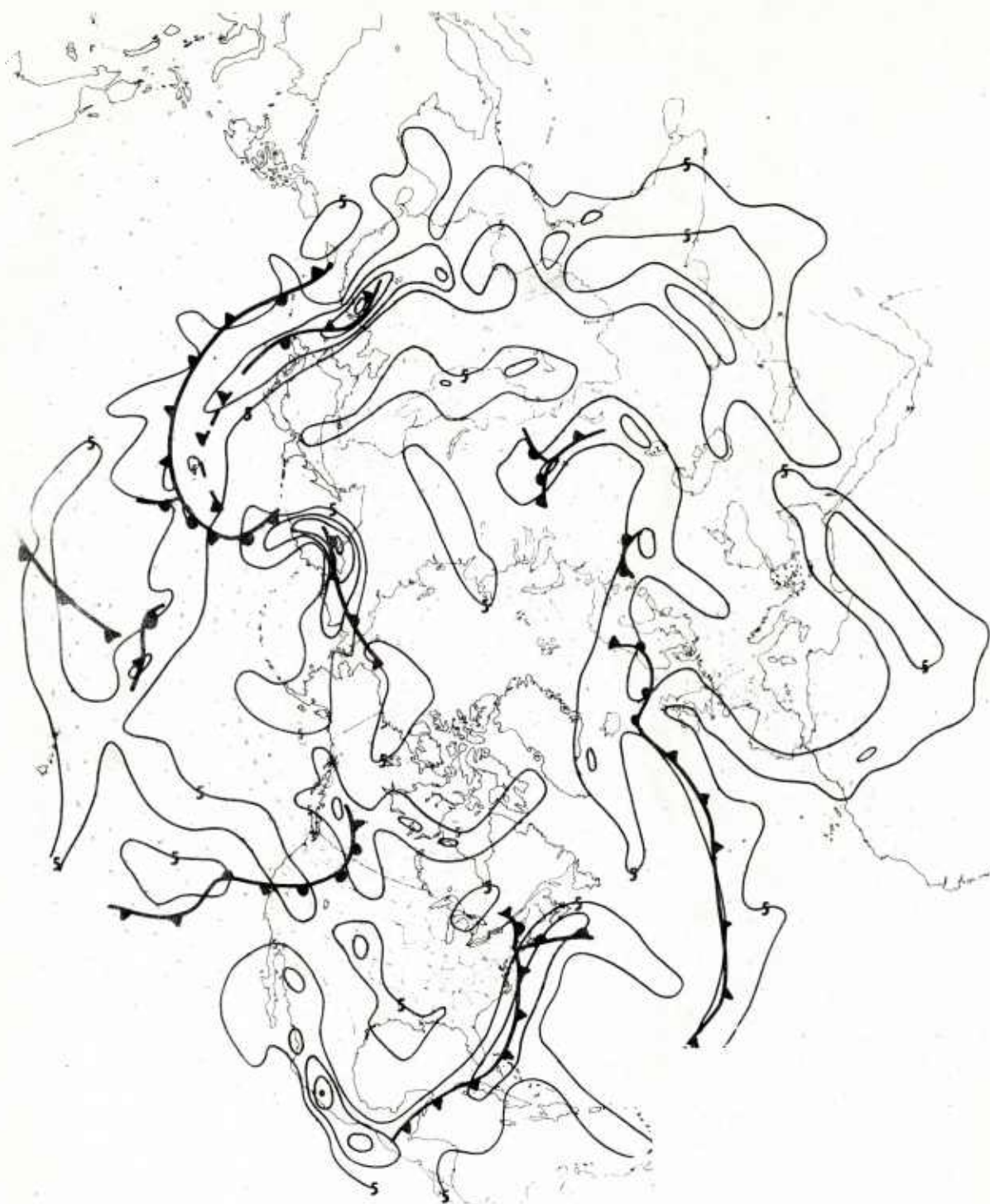



Figure 6. 1000 mb $GG\theta^*$, 0000GMT 6 March 1966 (update) (from 1000/700 mb model). Units: $10^{-2} \text{ C}/(100 \text{ km})^2$; interval: 20;  NMC fronts with conventional symbols.

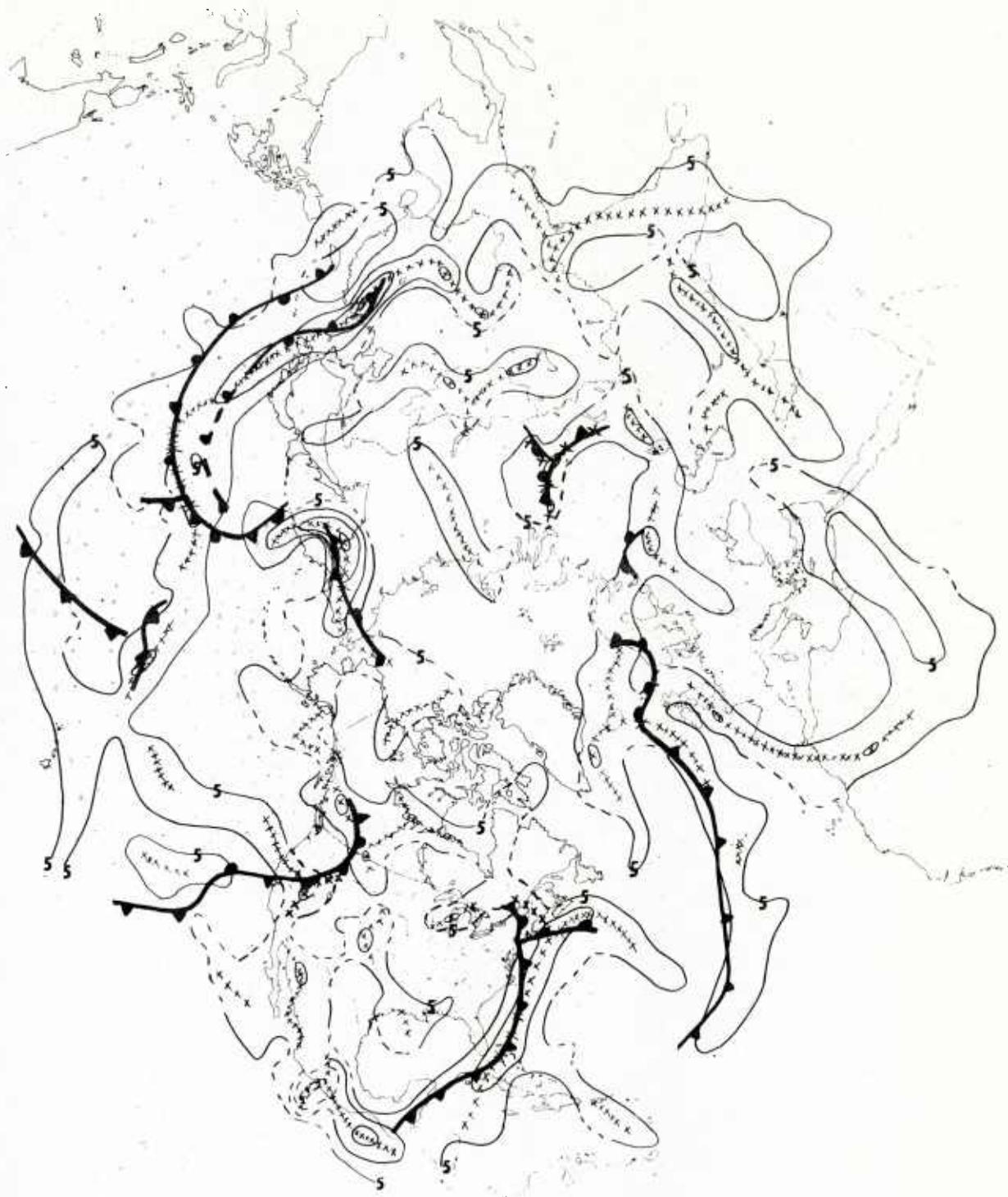


Figure 7. Mod $GG\theta^*$, as defined in Figure 5, with legend as in Figure 6. XXX = numerical fronts where Mod $GG\theta^* \geq 15$ units.

IV. Modification to $GG\theta^*$ to Enhance Analysis of Occlusions:

The modification, currently being tested at FNWF, adjusts the $GG\theta^*$ field by selectively, but objectively, adding to it a thermal-curvature term ($GK\theta^*$) in the form as shown in the following expression [2]:

$$\begin{aligned} -\nabla^2\theta^* &= -\nabla|\nabla\theta^*| \cdot \vec{\eta}_{\theta^*} - |\nabla\theta^*| \nabla \cdot \vec{\eta}_{\theta^*} \\ (1) \qquad &= GG\theta^* + GK\theta^* \\ &= \text{shear term} + \text{curvature term} \end{aligned}$$

where $\vec{\eta}_{\theta^*}$ represents a unit vector in the direction of $\nabla\theta^*$

Since the sole purpose of this adjunct is to aid in the analysis of the occluded structure, the curvature component of the Laplacian of θ^* is added to $GG\theta^*$ only where the latter field and isotherm curvature are both negative. Specifically, the area of thermal ridging between the cold side of maximum baroclinicity and the warm side of minimum baroclinicity is such an area. The next figure (Figure 5) shows an actual case of this modification.

To exemplify the modification on a hemispheric basis note Figure 6 which again shows the $GG\theta^*$ analysis for 00GMT 6 March 1966, in this case derived from the so-called updated FNWF fields, which characteristically include 10-20% more data than the operational version. The NMC fronts are superimposed to indicate the variant relation of manually and numerically analyzed fronts.

Figure 7, in the same format as Figure 6, shows the modified frontal field (Mod $GG\theta^*$) combining shear and curvature effects. Dashed isolines indicate where the modified field differs from $GG\theta^*$. Significantly strong numerical fronts (greater than 15 units of Mod $GG\theta^*$) are shown by XXXX and manually analyzed NMC fronts by usual symbols. With reference to Figure 6, note the changes in orientation and structure of certain baroclinic boundaries that are associated with occlusions, as for example the extreme eastern and western sections of northern United States as well as northern Russia. Unfortunately, the curvature modification is not all good. Note the mountainous subtropical area of North America, frequently associated with low tropospheric thermal ridges. Here, an already troublesome area, due to topography problems, suffers further from the curvature modification. Overall, the major objection to the "Laplacian" adjustment is that the curvature-vorticity term is not directly related to baroclinicity and hence fictitious temperature gradients are implied.

V. Other Problems And Their Suggested Solutions:

Several other major problems are associated with the numerical frontal analysis model. For instance, what level and temperature parameter yields the best representation of surface fronts, using the "GG" approach? Many levels and layers, geometric and isobaric, and various temperatures and deviations and/or anomalies of temperature were tested. The results showed that the present model, using mean θ^* in the 1000/700 mb layer is the most well behaved considering topography variations, the grossness of the operational grid-size used (381 km at 60N) at FNWF, inhomogeneity of data density and low values of baroclinicity over east ocean areas near the surface.

For instance, one particular problem concerns the resolution of the fields of baroclinicity. It has been established that the consideration of mandatory level data only, with the use of the quartic interpolation polynomial for computing derivatives on the present FNWF mesh, does not allow accuracy of frontal analysis to exceed the limits shown previously. However, there are solutions to this problem, at least one of which is being presently pursued at Monterey [5]. In this approach a further resolution of the baroclinicity field ($G\theta$) is introduced in

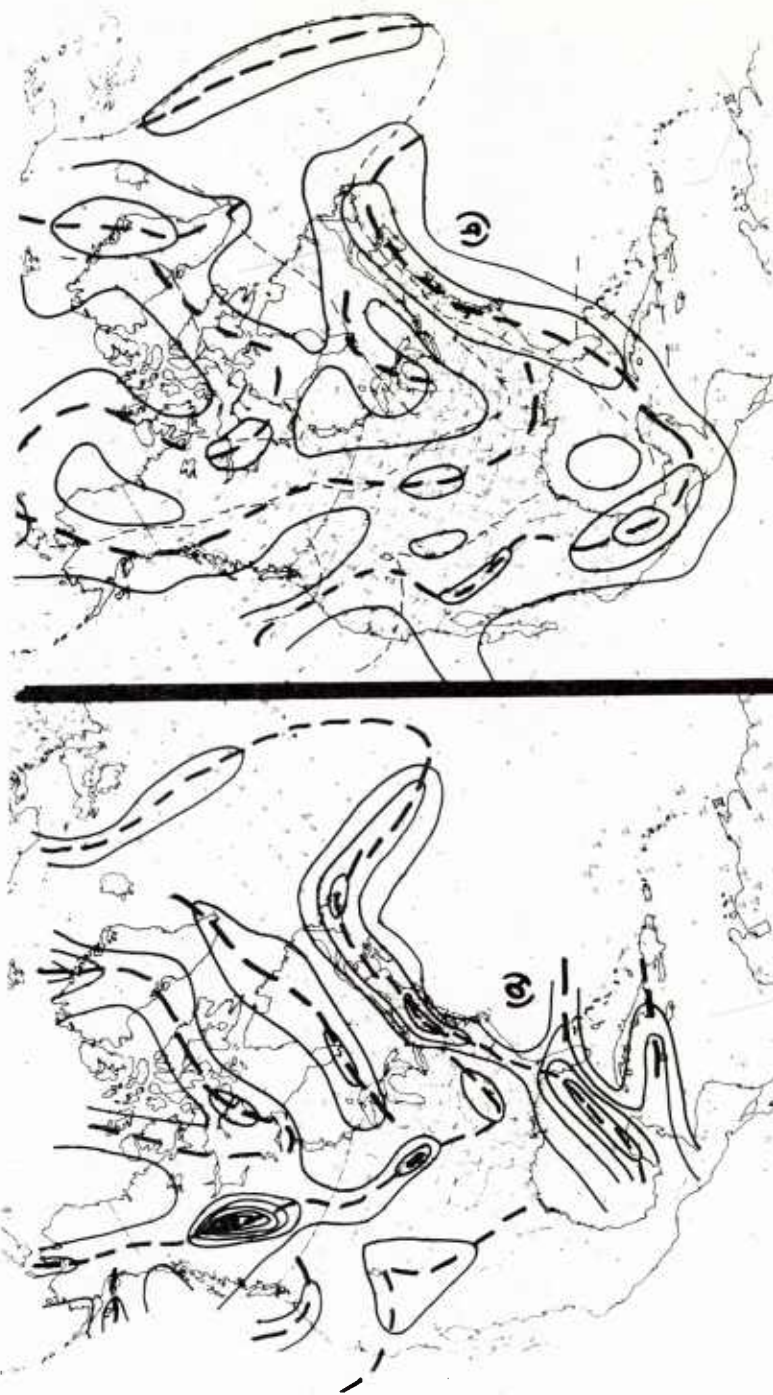


Figure 8a. $G\theta'$, 850 mb 0000GMT 6 March 1966, --- ridge. 8b. $G\theta^*$, same date; --- $G\theta'$ ridge; — $G\theta^*$ ridge. Units: C/100 km; interval: 1 C, starting with "1" line.

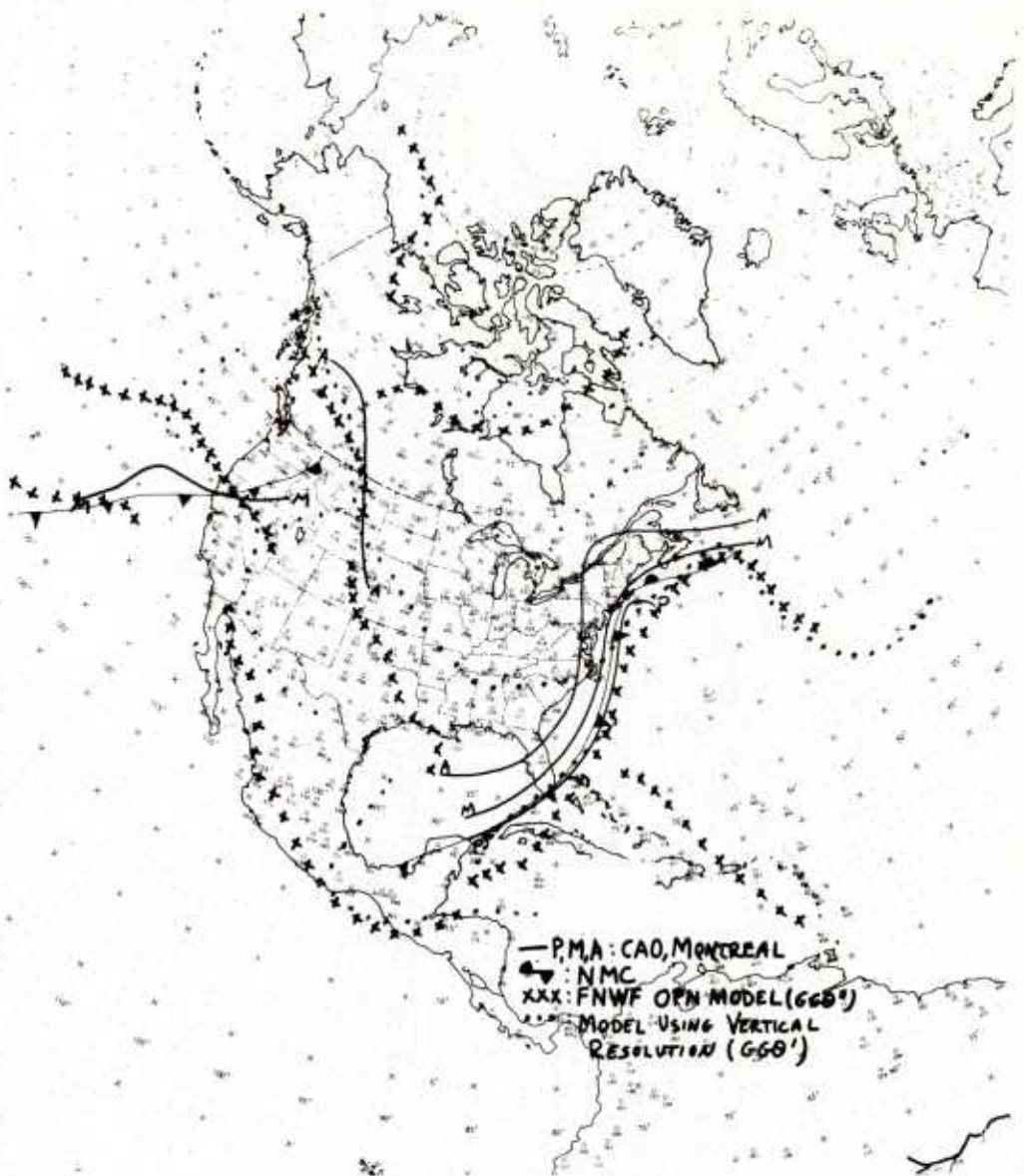


Figure 9. Comparison of 850 mb 0000GMT 6 March 1966 frontal positions analyzed manually by NMC, Washington D.C., and the Central Analysis Office, Montreal, Canada (P = polar, M = maritime, A = artic); and numerically by FNWF (GG0') and using vertical resolution (GG0').

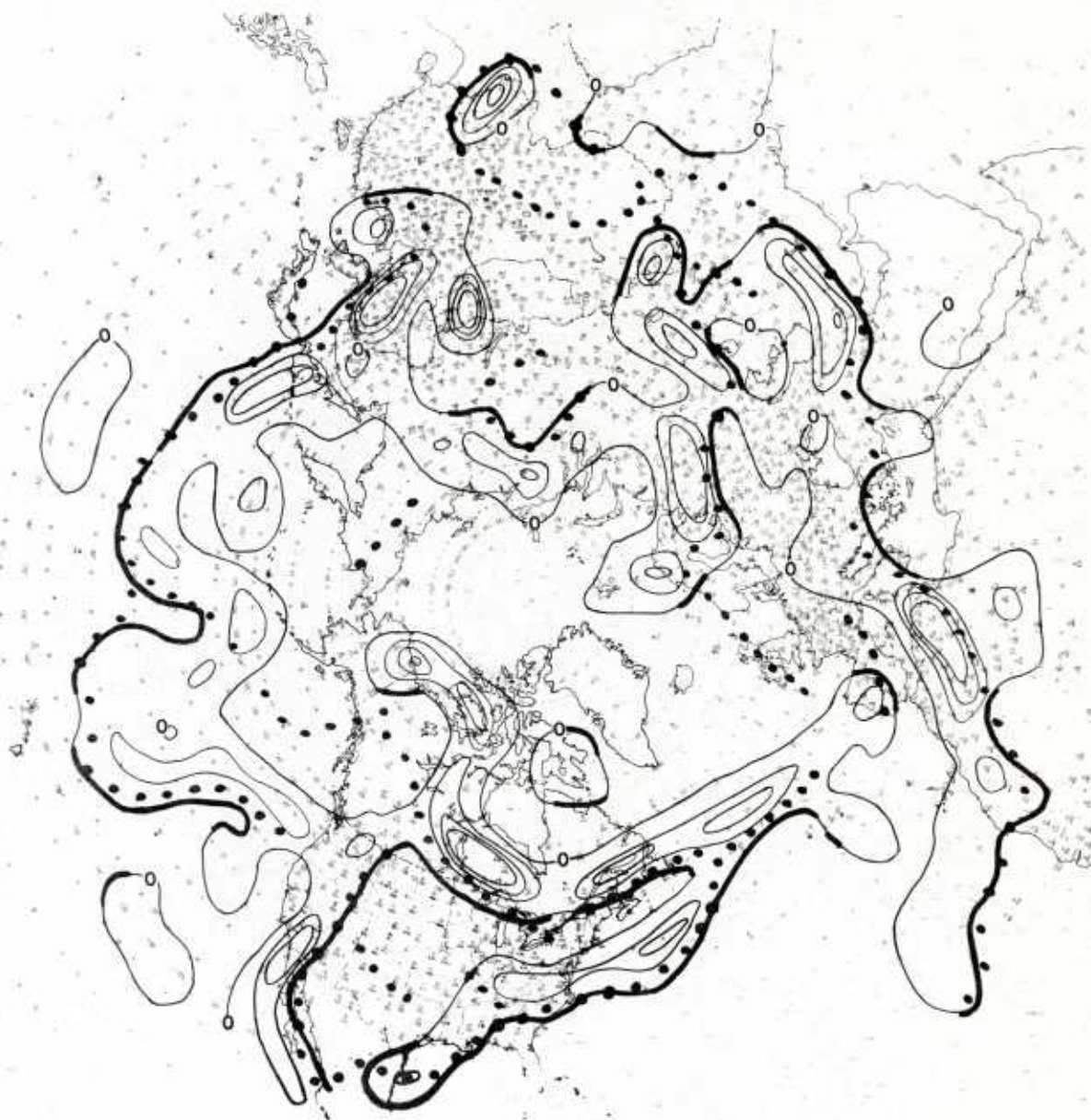


Figure 10. $MM\theta^*$ 1000 mb 1200GMT 12 August 1965. Thin lines: $MM\theta^*$; units $10^{-1} \text{ } ^\circ\text{C}/100 \text{ km}$; isolines: 0,10,15,20,30. Heavy lines: $MI\theta^*$. Dotted lines: $GG\theta^*$ ridges. [2]

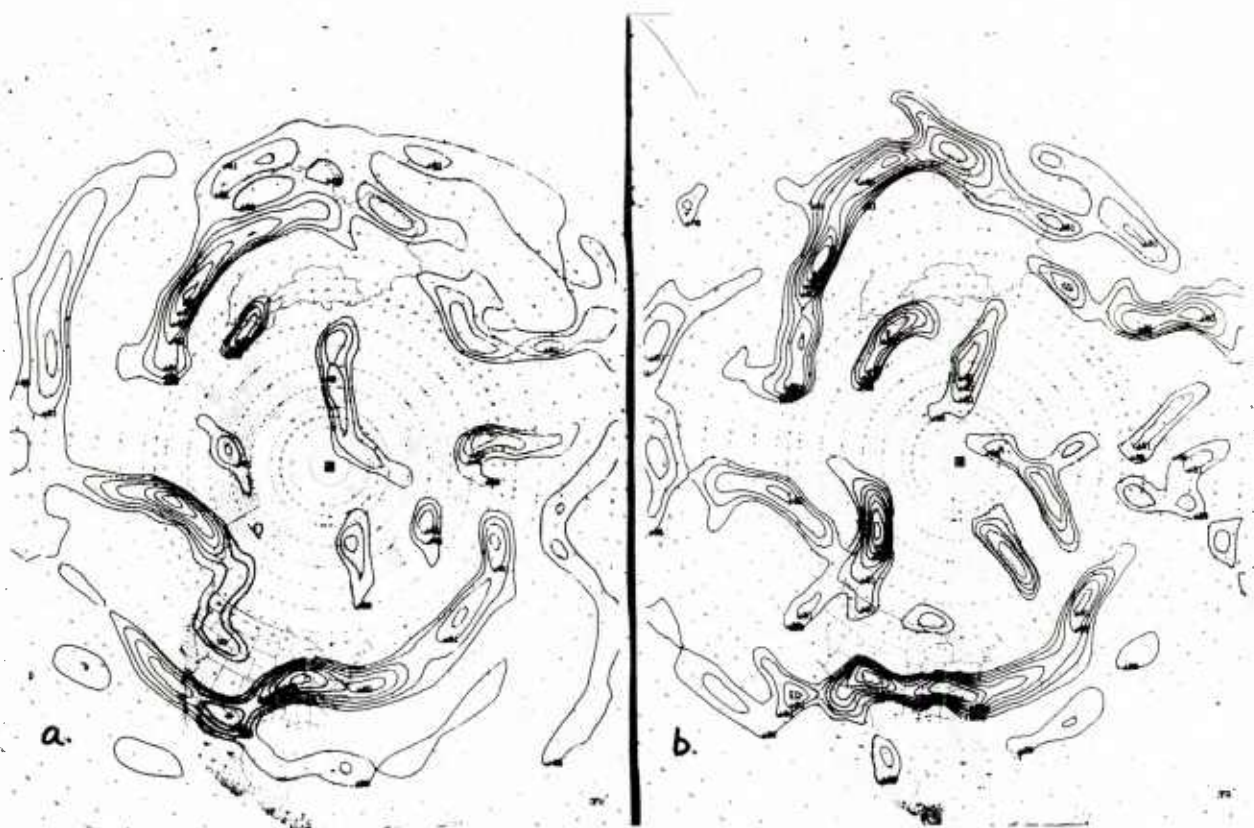


Figure 11a. 36 hour 1000 mb frontal prognosis from 1200GMT 3 March 1967. 11b. 1000 mb frontal analysis for 0000GMT 5 March 1967.

terms of the vertical resolution inherent in soundings containing significant levels. Here, $|\nabla \theta|$ is computed from the product of the vertical gradient of potential temperature, $\partial\theta/\partial p$, and the slope of the isentropic surface, $\delta p/\delta \eta$. The stability parameter is computed in such a way as to capture the full detail of the significant-level data, while the slope term is obtained from FNWF's numerically-produced and processed mandatory level data. The gradient, computed in this way, is referred to as $G\theta'$ here.

Frontal phenomena on the $G\theta'$ analysis are focused into narrower, more intense baroclinic zones than on the FNWF $G\theta^*$. As an example, Figure 8 shows the two gradient fields for 00GMT 6 March 1966 at 850 mb. Increased detail and magnitude and change in structure and position of baroclinicity is to be noted in the $G\theta'$ relative to the $G\theta^*$ field. The comparison of NMC, Canadian, $G\theta^*$ and $G\theta'$ frontal positions on Figure 9 indicates the relation of the various numerically and manually derived solutions.

Another problem has to do with the pictorial presentation of the frontal analysis. The operational user traditionally demands a "line" representation but the present mode of operational presentation (Figure 4) has much in its favor since the structure of baroclinic zones, with a suitable analysis interval, is such as to allow accurate placement of the front while retention of field values of $G\theta^*$ gives a measure of frontal intensity. Also, the present model allows a two-dimensional measurement of the baroclinic-zone extent as well as location of the axis of maximum gradient. Notwithstanding these advantages of the present mode of depiction some work has been done on numerical specification of the "front" rather than the "zone".

Referring back to Figure 2, again note the profiles of θ^* , $|\nabla \theta^*|$ and $G\theta^*$ and now the $MM\theta^*$ profile, whose symbolic definition is indicated thereon. The purpose of this further differentiation of the temperature field is to locate maxima and minima in the $G\theta^*$ field. Such axes of maxima and minima are denoted by zero $MM\theta^*$. The magnitude of $MM\theta^*$, except at "1" and "2", reflects the magnitude of $\nabla \theta^*$.

A hemispheric operational analysis of $MM\theta^*$ for 1000 mb 12Z 20 August 1965 shows its properties (Figure 10). The $ML\theta^*$ lines represent isolines along which $MM\theta^* = 0$ and where $G\theta^*$ is greater than an arbitrarily set critical "noise" value of $.05 \text{ C}/(100 \text{ km})^2$. Noncoincidence of $G\theta^*$ ridge and zero $MM\theta^*$ is to be noted. Much of this incompatibility is caused by practical problems involved with the third derivative and the asymmetrical nature of baroclinic zones. Active research in this area has not been continued at FNWF.

However, the Canadians at the Central Analysis Office (CAO), Montreal, Canada, have pursued this aspect. Under William Creswick an approach similar to that at FNWF has been applied to the wet bulb potential temperature (θ_w) and extended to result in objectively placing frontal contours at 850, 700 and 500 mb. In their case the counterpart to FNWF's $MM\theta^*$ may be symbolized as:

$$MM\theta_w = - \nabla(GG\theta_w) \cdot \vec{\eta}_\theta \text{ where } \vec{\eta}_\theta \text{ is a unit vector along the gradient of } \theta_w$$

Moreover, an objective adjunct is used to correct for errors in placing the front due to the finite differencing scheme used. In addition positioning is improved for the upper level fronts by incorporating parameters involving the use of the GG operator on thickness and gradient of geostrophic wind.

EVALUATION OF FRONTAL ANALYSIS

F. N. W. F (Numerical) 1000 Mb vs. NMC (Manual)

SFC. Fronts

(16 OBSN. times: 23 AUG.—06 SEP. 65)

Frontal Distance Sampled: 259,000 N.mi.

% F.N.W.F Fronts having a NMC counterpart: 72%

% NMC Fronts having a F.N.W.F counterpart: 66%

| Sector | F.N.W.F Frontal distance (N. miles) | Ave. distance separating NMC & F.N.W.F Fronts (°Lat.) |
|------------------|---|--|
| North America | 49,250 | 1.6 |
| Atlantic | 46,900 | 1.4 |
| Pacific | 46,300 | 2.1 |
| Eur. — N. Africa | 26,000 | 1.8 |
| Asia | 18,000 | 1.2 |
| Overall Ave. | | 1.7 |

Table 1. Relation of numerically analyzed FNWF and manually analyzed NMC fronts for sixteen observation times, 23 August to 6 September 1965.

EVALUATION OF FRONTAL PROGNOSIS

F.N.W.F (Numerical) 36hour vs NMC (Manual) 30hour

SFC. Fronts

(16 OBSN. times: 23 AUG.— 06 SEP. 65)

Frontal Distance Sampled: F.N.W.F— 295,500 N.mi.
NMC — 191,500 N.mi.

— (+) = Prog on Cold (Warm) side of the analysis

| F.N.W.F | | NMC | |
|---------------|----------------------|---------------|----------------------|
| Distribution% | Ave. Deviation(°lat) | Distribution% | Ave. Deviation(°lat) |
| 46 | — 3.0 | 48 | — 2.5 |
| 40 | + 3.0 | 38 | + 2.8 |
| 14 | ± 0.0 | 14 | ± 0.0 |
| | Ave.maq.2.6 | | Ave.maq.2.3 |

F.N.W.F

Frontal Distance Sampled: 99,000 N.mi.

— (+) Prog slow (fast)

| Distribution% | Ave. Deviation(° lat) |
|---------------|-----------------------|
| 51 | — 3.0 |
| 37 | + 2.7 |
| 12 | ± 0.0 |
| | Ave.maq.2.5 |

Table 2. Relation of numerically prognosticated FNWF and manually prognosticated NMC fronts for sixteen observation times, 23 August to 6 September 1965.

VI. Prognosis of Numerical Fronts:

The FNWF forecast model is used to generate prognostic temperature fields which, in turn, may be used to diagnose the baroclinicity. Operational 36-hour 1000-mb GGθ* prognoses are made twice daily. The period used for comparison of FNWF and NMC analyses was also used to compare the prognostic frontal positions of FNWF and NMC. As Table 2 shows, the 30-hour NMC and 36-hour FNWF forecasts compare very well; the differences in the average errors (2.3° lat for NMC; 2.6° lat for FNWF) are academic, when taking forecast interval into account. Further, both NMC and FNWF tend to move fronts too slow during this 1965 period with a modal value of $.5^{\circ}$ lat/36 hours in the case of FNWF. There is loss in structural detail in forecasted frontal positions from both units. Figure 11 shows a recent typical example of a 36-hour prog verifying at 00GMT 5 March 1967.

VII. Conclusions:

It has been demonstrated, quantitatively and qualitatively, that frontal-zone location and intensity may be handled objectively by numerical techniques, [2, 4, 5], thereby progressively removing one of the last few major manual operations in synoptic scale analysis and prognosis.

Recent inquiries to Navy field units, as centrals, facilities, etc., indicate the GGθ* analyses and forecasts are serving an important and provocative role as first approximators to location and intensity of fronts, especially cold fronts. The product tends to be of least use in sparse data sub-tropical areas where satellite pictures (especially APT) are much more informative as to operationally significant weather.

To completely capitalize on the developments summarized in this paper, a new approach to "frontal analysis" is appropriate. It is no longer desirable, nor was it ever necessary, to force a "front" to be representative of temperature and weather phenomena. The advent of weather satellite observations, indicating details of cloud patterns symptomatic of frontal cyclone structure, now makes feasible a more exacting approach to operational weather analysis. Let fronts be, clear and pure, temperature and density phenomena, as dynamically defined, and utilize the symbolic notation associated with weather satellite observations to represent cloud and precipitation processes. Undoubtedly there are usable relations and a high degree of coincidence between features of thermal and moisture systems. Perhaps such an approach will manifest itself as an improvement in forecasting all operationally important weather elements, associated or not with frontal phenomena.

VIII. Acknowledgments:

The research summarized in this paper has been supported by the Navy Weather Research Facility, Norfolk, Virginia, Fleet Numerical Weather Facility (FNWF), Monterey, California and Office of Naval Research. As indicated by the references, close working coordination has been maintained with Mr. Leo Clarke, FNWF, who also programmed most of the basic equations used in the present FNWF frontal analysis model. Many students in the Department of Meteorology and Oceanography, Naval Postgraduate School, Monterey, California also assisted in various phases of this research.

IX. References:

- [1] Anderson, R., B. W. Boville and D. E. McClellan:
"An Operational Frontal Contour - Analysis Model".
Quarterly Journal of the Royal Meteorological Society, 81, 588-99, 1955.
- [2] Clarke, L. C., and R. J. Renard:
"The U. S. Navy Numerical Frontal Analysis Scheme: Further Development and a Limited Evaluation".
Journal of Applied Meteorology, 5, 764-77, 1966.
- [3] Huschke, R. E., Editor:
Glossary of Meteorology, American Meteorological Society, Boston, Mass., 638 pages, 1959.
- [4] Renard, R. J., and L. C. Clarke:
"Experiments in Numerical Objective Frontal Analysis".
Monthly Weather Review, 93, 547-56, 1965
- [5] Renard, R. J.:
"Further Experiments in Numerical Analysis of Baroclinicity".
Research Progress Report #1, Department of Meteorology and Oceanography,
Naval Postgraduate School, Monterey, California, 31 pages, January 1967

ABSTRACT

THE APPLICATION OF NUMERICAL ANALYSIS OF BAROCLINICITY TO THE
OBJECTIVE LOCATION OF FRONTAL ZONES

By Robert J. Renard
Department of Meteorology and Oceanography
Naval Postgraduate School
Monterey, California

The status of the Navy's numerical frontal analysis and prognosis scheme is reviewed and updated. The substance of the operational program, as used at Fleet Numerical Weather Facility (FNWF), Monterey, California, and innovations to the program, presently in a research phase, are outlined. Statistical relationships of FNWF and NMC frontal analyses and prognoses are presented. Some reference to recent work of the Canadians in this area is also made.

NUMERICAL MODELING EFFORTS AT 3d WEATHER WING

by

Lt Colonel Herbert Edson
Hq 3d Weather Wing
Offutt Air Force Base, Nebraska

(SUMMARY)

The functions of the 3d Weather Wing Aerospace Sciences Division, Development Branch can best be described as the development of techniques and mathematical models for the numerical prediction of fields of motion, state parameters and cloudiness on a hemispheric or global basis, or on a scale appropriate to data density and user requirements. Over the past years we have developed a number of models of this type. We have previously reported on the development and progress of the Six-Level Baroclinic Height Model (2) and the CPS-Trajectory Cloud Model (1) which provide operational forecasts of wind, temperature, moisture, stability and other pertinent meteorological parameters at the Air Force Global Weather Central (GWC), Offutt Air Force Base, Nebraska. We have continued to improve the various products derived from these models. Recently, however, we have tried to critically evaluate our accomplishments and determine where we may logically progress in the modeling field.

One conclusion we have reached is that although our models and numerical techniques have shown improvement, there appears to be a gap between the apparent skill of these models as reflected by our verification statistics and their functional value as reflected by their use in providing meaningful weather predictors and tools to the field. For example, our Six-Level and Trajectory Models were designed to produce hemispheric grid forecasts of winds and clouds. While these forecasts have been turned out with reasonable accuracy - and we have some users who are specifically interested in them - we find that many forecasters have greater need for numerical products which provide more direct support to operationally oriented problems such as terminal weather, route weather, severe weather, delineation of bases and tops of clouds, ceilings, precipitation, icing, and turbulence.

It logically follows that greater emphasis must be placed in our development efforts on the operational application of numerical forecasting techniques and models. This does not imply that modeling efforts should be curtailed, but does raise the pertinent question as to what intelligence we need from our dynamic models in order to produce meaningful forecasts of sensible weather. Along these lines, we have explored the premise that while our present numerical models obviously require considerable refinements which are dependent upon a greater understanding of the atmospheric processes, we nevertheless have not fully exploited the potential that exists within the present state of the art to provide useful weather forecasting tools and techniques. With this in mind, over the past year we have placed emphasis on the following specific projects; development of a fine mesh boundary layer model (see paper by Captain Paul Janota in this Technical Report), refinement of upper level wind forecasts, particularly in the vicinity of the jet stream; and investigations of the functional potential of the CPS-Trajectory Cloud Model.

The CPS-Trajectory Model, in addition to producing cloud forecasts, is capable of providing forecasts of moisture, and temperature at each GWC grid point from the 850-mb level to the 300-mb level. This information has been employed internally in the program for the specification of cloudiness and has not been distributed to the field. It is the type of intelligence, however, which we feel would be extremely useful, particularly on a fine mesh grid and in conjunction with our development of a boundary layer model. In the past, we have verified temperature and moisture forecasts at grid points with minimum reference to vertical consistency. Recently we have taken a more functional look at these forecast soundings by comparing them both objectively and subjectively against actual 12, 24, 36 and 48-hour verifying station RAOBS. Results are particularly encouraging. They are discussed and illustrated in detail in 3d Weather Wing Aerospace Sciences Technical Note 16.

Another important area of investigation within the framework of current models has been the development of a technique to forecast bases and tops of clouds. Our approach here has been to place into an automated program the intelligence provided by the trajectory program plus the decision making rationale of the experienced forecaster. The individual forecaster takes the initial cloud situation as he sees it from surface observations, airways reports, soundings, radar reports, and satellite data and adds to this his concept of advection and

dynamic changes. We have attempted to program this method. We have developed a detailed 12-layer moisture-cloud analysis by interrogating every bit of automated data available for a "cloud" or "no cloud" decision. This information is then translated with trajectories at four levels from the CPS-Trajectory Model and modified with forecast cloud amounts and vertical velocities. Initial results are again encouraging. The technique will be reported on in detail at a later date.

We have also begun an integrated effort on the part of our Development Branch to convert existing automated meteorological techniques - analysis, nephanalysis, and the prediction of winds, temperatures, moisture and clouds - to a fine mesh grid. This presents complicated problems in terms of computer limitations, data requirements essential for greater resolution, and the danger of computational "blow up" resulting from the introduction of spurious features in our physical equations. Nevertheless we must solve these problems if we are to reach our ultimate goal and bridge the gap between generalized modeling and detailed, sensible weather products and forecast tools.

REFERENCES

- (1) Edson, H., et al., "Numerical Cloud Prediction," AWSTR 188, pp 91-97, Nov 1966
- (2) O'Neil, H.M., "The Air Weather Service Six-Level Model," AWSTR 188, pp 37-42, Nov 1966

TECHNIQUES FOR PREDICTION OF SOLAR FLARES AND ENERGETIC PARTICLE EVENTS

The following presentation was given by Major Donald T. Sherry, OIC, Solar Forecast Center, NORAD Cheyenne Mountain Complex, on 5 April 1967 to the Joint Technical Exchange Conference, Naval and Air Weather Services, Monterey, California. These new techniques are published in 4WMM 105-1, "Forecasting Solar Activity and Geophysical Responses," dated 30 December 1966. Figure 1, Activity Level Designator Chart, was reaccomplished in January 1967 by TSgt Richard B. Agee. Figure 2, Pre-flare Evaluation, was prepared by Major Sherry. Figure 3, Post-flare Evaluation was prepared by Major Jack L. Buckingham.

I. Forecasting Solar Flares

The Activity Level Designator Chart is designed to give the forecaster the percentage probability for an importance Two or greater Solar Flare within 24 hours for a selected region.

A study of 103 active region was completed using data from Sept 1965 through Jan 1967. Solar Forecast Center records were the primary source of data. Each region was studied daily as it traversed the disk regardless of the activity level. (Regions were studied from 60° E to 60° W only, to minimize errors resulting from foreshortening.) Daily tabulations were made on calcium plage area, plage brightness, total sunspot area, sunspot Brunner classification, sunspot magnetic classification, 9.1 cm radio brightness temperature, and past flare production of a given region. Major flare occurrence was correlated with each of these parameters with a resultant percentage.

The Activity Level Designator Chart is divided into six sections, labeled A through F. Significant known parameters, which are flare related are contained in these sections and each considered as an independent precursor for a major flare. The chart was prepared from objective percentages where possible, however, it was necessary to obtain percentages somewhat subjectively for some parameters due to lack of data. Each parameter was weighted and assigned index numbers across the top of each section. The index numbers, when totaled, correspond to a percentage probability for a major flare within 24 hours.

To use the chart:

1. Enter section (A-F) with plage area, 9.1 cm radio temp, etc, at the left side of the chart.
2. Move horizontally to the appropriate position on the bar or line graph.
3. Read index number at the top of each section and place in index box at right of chart. (Additional indices are contained in section A and B at right edge of graph.)

Use section F1 for eastlimb regions and F2 for disk regions.

The index figures in parenthesis indicate the highest possible number for each section.

If a region contains more than one spot group select the most significant group for sections C and D.

Plage and sunspot area figures are X (10^{-6} Hemisphere) and radio brightness figures are X (10^3 °K).

If one or more sections are missing use the formula: $\% = \frac{\text{Index}}{(\text{Max Index})}$. Where:

Index = sum of all available index figures, and (Max Index) = sum of max index figures for sections used.

Once a flare probability, P_i , has been assigned to each of the N regions on the disk, the total flare probability for 24 hours, P_t , is computed by:

$$P_t = 1 - \prod_{i=1}^N (1 - P_i)$$

This formula may also be used for long range forecasts where:

P_t = total flare probability for period of forecast.

P_i = one-day flare probability for each day of the forecast period.

N = number of days.

II. Forecasting Energetic particle Events

1 Pre-flare Evaluation

Figure 2 is the worksheet used to evaluate solar regions prior to the occurrence of a proton flare. The forecast is an alert which states that a proton event is considered likely if a major flare occurs that has the favorable optical and/or radio indicators of a proton flare. Ten parameters are listed in the worksheet for which statistics are available to correlate with proton producing regions. Each predictor is considered to be independent of the others. Other parameters are also considered (filament configuration, spot history, longitude and previous flare activity). An index of less than 2.5 is considered to be entirely unfavorable while an index of 4.0 or greater is most favorable for each predictor listed. An average index is computed for each solar region considered significant. A region index greater than 3.9 with 70% favorable predictors is used as a guide to forecast an alert of solar protons if a major flare occurs. This criteria includes 75% of the sixty PCA events included in this study.

2. Post-flare evaluation

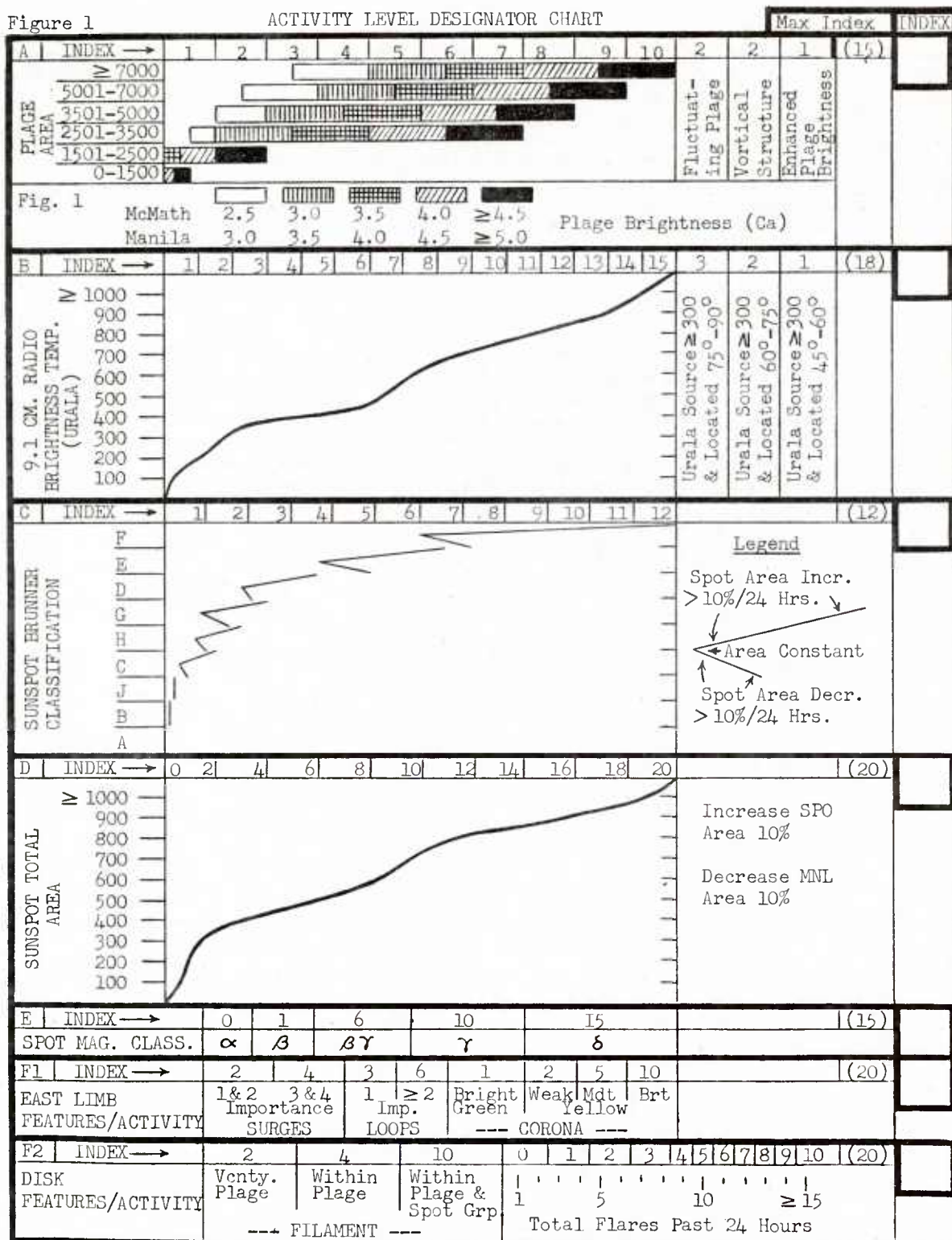
Figure 3 is the exact statistical percentage probability of detectable protons at the earth's surface for each parameter listed. Some of the parameters are not independent of each other. The forecaster must select the parameter(s) available to him at the time he prepares his forecast. He has approximately 20 minutes after the beginning of a flare to disseminate proton event forecast. This forecast is made only when the probability is at least 30%. As an example, parameters 3 and 4 each give a minimum probability for protons of 30% after the occurrence of a reliable type IV radio burst associated with a large flare. Parameters 1, 2 and 12 can be considered as being independent, placing each percentage (P_i) into the formula

$$P_t = 1 - \prod_{i=1}^N (1 - P_i)$$

for the final percentage P_t .

Figure 1

ACTIVITY LEVEL DESIGNATOR CHART



NOTE: Use either F1 or F2 but not both.

If data for one or more sections are missing

use the following formula: $\% = \frac{\sum \text{INDEX}}{\sum (\text{Max Index})}$

Max Total → (100)

 $\% \text{ PROBABILITY IMP.}$
 $\geq 2 \text{ FLARE/24 HOURS}$

[illegible]

Figure 2

| | | PCA EVALUATION AFTER FLARE OF IMPORTANCE ≥ 2 | | | | | | | | | | | | REFERENCE | |
|----|---|---|---|----|------------------|----|---|---------|-------------|---------|--|---------|--------------|-----------|--|
| | | 0% | 5 | 10 | 15 | 20 | 30 | 40 | 50 | 60 | 70 | 80 | 90 | 100 | |
| 1 | Flare Importance | Imp 2 <1% | | | | | Imp 3 | | | | | Imp 4 | | | Jonah, Dodson-Prince, Hedeman, 1965 Smith & Smith, 1963 |
| 2 | Preflare Index | <2.5 | | | 2.5-2.9 | | | 3.0-3.9 | | | 4.0-4.9 | | 5.0 | | SFC Unpublished Forecast Study |
| 3 | Flare Importance and Type IV | Imp 1 | | | | | Imp 2 | | Imp 3 | | | Imp 4 | | | SFC Unpublished Forecast Study |
| 4 | Location of Flare with Type IV | | | | | | 90E-30E | 30E-0M | 0M-20W | | | | | | SFC Unpublished Forecast Study |
| 5 | Flare and 10 cm Burst ≥ 500 | 10 cm max precedes H_{α} max | | | | | 10 cm burst only | | | | 10 cm max follows H_{α} max | | | | Dodson and Hedeman, 1964 |
| or | Flare, 10 cm Burst ≥ 500 and Type IV | 10 cm max precedes H_{α} max, no Type IV | | | | | 10 cm max precedes H_{α} max & Type IV | | | | 10 cm max follows H_{α} max & Type IV | | | | Dodson and Hedeman, 1964 |
| 6 | Broad cm, Type II, IV & Disk Position | | | | | | | | Eastern Hem | | Western Hem | | | | Harvey, 1965 |
| 7 | Broad cm, no II, and Disk Position | | | | | | Eastern Hem | | Western Hem | | | | | | Harvey, 1965 |
| 8 | Loops | | | | E Limb | | | W Limb | | Ern Hem | | Wrn Hem | | | Bruzek, 1964 |
| 9 | Flare Filament | | | | V or Y | | Parallel | | | | | | | | Warwick, 1965 |
| 10 | Umbra Covered | | | | | | | | | | | | | | Dodson and Hedeman, 1964 |
| 11 | White Light Flare | | | | | | | | | | | | Disk or Limb | | Bruzek, 1964 |
| 12 | Region Previously Produced Protons | | | | Current Rotation | | Current & Previous Rotation | | | | | | | | SFC Unpublished Forecast Study |

Figure 3

APPLICATION OF MILLIMETER WAVE RADIO MAPPING TO FLARE PREDICTION

WILLIAM O. BANKS, Major, USAF
SOFNET-6, Detachment 7, 4 Weather Wing
Los Angeles Air Force Station, California

ABSTRACT

Radio waves of millimeter wave lengths reach us from the sun's lower chromosphere. These radio frequencies can be used to map temperatures at about the same altitude on the sun as seen when viewed optically with a hydrogen-alpha filter.

The Space Radio Facility in Los Angeles provides a mapping capability at 3 millimeters. An SDS-920 computer drives a 15 foot parabolic antenna which feeds a 94 Gigahertz radiometer. The sun's disk is sampled in the pattern of a 19 by 19 matrix and then broadcast on the SOFNET teletype twice daily.

Although the routine mapping is only a few months old, the daily isotherms show great potential as a solar flare predictor. The occurrence of significant flares seems to depend more on a tight gradient than how hot the spot.

I INTRODUCTION

Flares are a chromospheric phenomenon. The Space Radio Facility in El Segundo provides a means of measuring the chromospheric temperatures at flare altitudes.

The Space Radio Facility has a 15 foot parabolic antenna which feeds a 94 Gigahertz (3.2mm) radiometer. The antenna has a beamwidth of 3 minutes of arc and is driven by an SDS 920 computer.

II MAPPING THE SUN

Since the radio signal (or noise) of a source depends on its temperature, it is possible to scan across the solar disk and make a synoptic temperature map. The antenna scans across the disk in 19 rows. Each row is 99 sec of arc below the previous row. Within each row the antenna stops at 19 points, also 99 sec of arc apart. At each point the radiometer samples the temperature about 10 times before moving to the next point. Thus a 19 by 19 matrix produces a synoptic temperature map of the solar disk.

The computer not only prints out the 19 by 19 matrix but it also cuts the tape for teletype transmissions. The teletype

print out is in a form such that when a Stonyhurst overlay with grid points is superimposed an analysis can easily be made. Analysis is usually made by drawing isotherms in 2% increments.

III THE FORECAST

After the map is made and analyzed, a 24 hour forecast is made for occurrence of major flares (class 2 or greater). This forecast, like the temperature map, is relayed throughout SOFNET by teletype.

In making the forecast each region of the sun which shows a temperature enhancement of 4% or more is considered. If a region meets certain enhancement and gradient criteria as set down by TSgt John Higman, a "yes" forecast is made for that region.

It was discovered by TSgt John Higman that if a hot region of at least 8% enhancement over the quiet sun had an associated temperature gradient of 0.48 % per degree of solar great circle, the region would remain above these enhancement and gradient thresholds until a major flare occurred.

IV DISCUSSION

The operation here is only a few months old. Since we have been making a teletype forecast for less than two months verification statistics are limited. The record which we have is filled with interruptions due to weather, maintenance and preemption by Aerospace Corp research programs. Because of a low priority, maps are never made at the same time of day.

Until more is known about how and why the temperature appear to drop off near the limb, only the analysis within 0.7 radii of the disk center is used for the forecast.

Although the flare forecast is for a 24 hour period, only about half of the "yes" forecasts verify within that time because the sun does not operate on a 24 hour diurnal oscillation like the earth's atmosphere does. Since teletype forecasts have been made for less than two months verification is limited. Of the "yes" forecasts about half verified within 24 hours, most verified within 36 hours and in about three cases no major flare was observed. In no case did a region within our 24 hour purview flare without our having forecast it.

V SUMMARY

The 3mm high resolution radio telescope provides a means of mapping the temperature field in the same region of the cromosphere that flares are optically observed with a hydrogen alpha telescope.

A remarkable feature is the high degree of accuracy with which such a map can be used to forecast major solar flares. A longer and more continuous record is urgently needed.

SHORT-TERM PREDICTION OF F2-LAYER MAXIMUM USABLE FREQUENCIES FROM LOCAL MAGNETIC ACTIVITY

R. M. Davis, Jr.

Institute for Telecommunication
Sciences and Aeronomy
Environmental Science
Services Administration
Boulder, Colorado

This paper describes and evaluates a method of predicting the maximum usable frequency (MUF) that can be supported by the F2 layer of the ionosphere in a given location at a given time. The information used is a measured value of the K-index in that location, and the prediction is made in terms of the percentage ratio ("percentage-MUF") that the predicted MUF bears to the monthly median MUF, available on a regular basis from various agencies such as ITSA. The prediction is designed to cover a three hour local-time period, which may begin from 0 to 12 hours after the prediction is made, at the option of the user.

The method is based on computing the linear regression of the percentage-MUF on the appropriate K-index for general conditions of location and time. The computations provide values of the regression constants P_0 and b in the regression relation

$$P = P_0 + b K,$$

where P is the computed percentage-MUF, P_0 is the percentage-MUF for a K-figure of 0, and b is the regression coefficient (the slope of the regression line).

The regression constants were computed at 20 ionosonde stations, located for the most part in the Western Hemisphere. The index of magnetic activity used in the calculations is the local K-index from the magnetic observatory nearest the ionosonde. Each computation applied to one of the eight local-time intervals, one of three seasons, and one of three levels of solar activity: high, medium and low. Regression constants were also developed for each of four time relationships between the MUF-prediction period and the period covered by the K-index. These relationships are illustrated in figure 1.

An example of the results is seen in figure 2, where the diurnal variation of the computed correlation coefficient is shown for the K/12A time relationship in three seasons and seven geomagnetic latitude ranges.

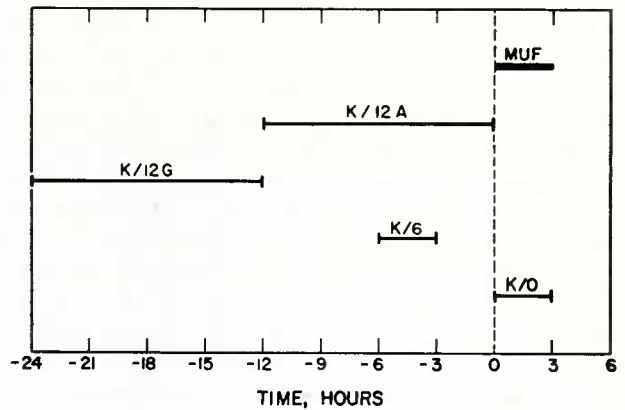


Figure 1 - Time relationship of predicted-MUF period and magnetic activity interval

The shaded areas represent negative correlation coefficients. Data from two to four ionosondes are incorporated in each zone. As figure 2 shows, the correlation coefficient r is close to -0.6 throughout the day in summer in the auroral zone (60° - 67° geomagnetic latitude) and slightly lower at higher latitudes. Below 35° geomagnetic latitude, r becomes very small turning positive within 15° of the magnetic equator. The contrast between the summer and winter patterns of r is easily noted: in winter, early morning values of r become positive in the 60° - 67° range and also in the 35° - 49° range.

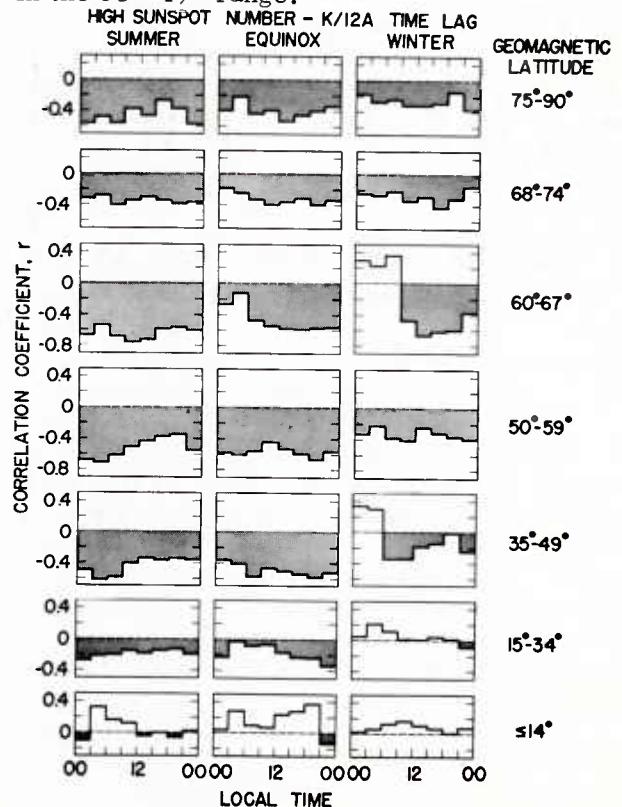


Figure 2 - Diurnal variation of the correlation coefficient of percentage-MUF with K-index

The variation with geomagnetic latitude of the regression constants P_0 and b is shown in figure 3, which contains data for the summer season, high sunspot number, and the K/6 time relationship. The left-hand panels pertain to night hours 00-03 LT, the right-hand panels to the 12-15 LT period. Computations for the individual stations, instead of latitude ranges, are given. The vertical bars represent 95% confidence intervals about the true values of P_0 and b . This figure clearly indicates the progression of P_0 from higher values toward 100 and the progression of b from lower values toward 0 as the geomagnetic latitude changes from 90° to 0°.

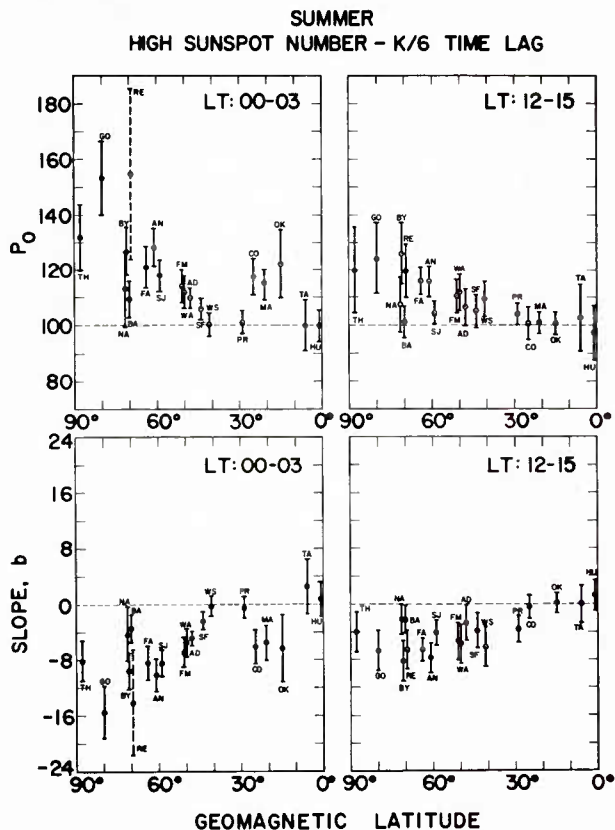


Figure 3 - Constants of regression of percentage-MUF on K-index

Where a statistical test indicated that values of r over several local time periods, or in adjoining geomagnetic latitude zones, belong to the same population, the results of this study were compressed into more compact form. The values of r were converted to values of z , a variable approximately normally distributed, before computer

processing ($r = \tanh z$). The condensed results for the K/12A time lag and high solar activity are shown in figure 4,

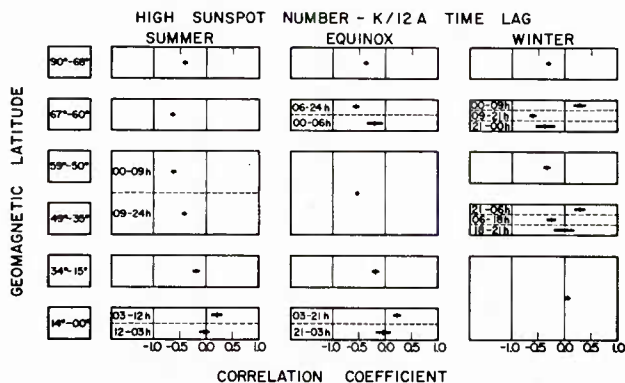


Figure 4 - Combined correlation coefficients of percentage-MUF on K-index, with 95% confidence intervals, for three seasons

where the horizontal bar for each combination of latitude zone and season represents the extent of the 95% confidence interval about the computed mean value of r . The local time period used is shown in each box, unless the entire 00-24 period was used, in which case the box is left blank. Here again, the strongest correlation between percentage-MUF and magnetic activity index is found in the auroral zone in summer. In summer and at equinox, the correlations remain quite high down to 35° latitude, while in winter they are generally weaker, except in the 60°-67° zone during daytime hours.

A measure of the usefulness of the method may be gained by converting values of r to values of the available reduction in the root-mean-square error provided by the predictions. If s_p is the rms deviation from the regression line, and s_o is the standard deviation of the daily values of percentage-MUF, then $s_p / s_o = (1 - r^2)^{1/2}$. If s_p / s_o is expressed in percent and subtracted from 100%, the result is the percentage error reduction. The formula indicates that a correlation coefficient of 0.7 gives an expected reduction in rms error of 29%; correlations of 0.4 or less give reductions of only 8% or less. Having decided on some minimum acceptable error reduction, the user can determine when this reduction is realizable by referring to figure 4.

In figure 5, the condensed values of r are compared for high, medium, and low sunspot numbers. The weakening of the correlations from 35° to 67° geomagnetic latitude is very noticeable as solar activity changes from high to low.

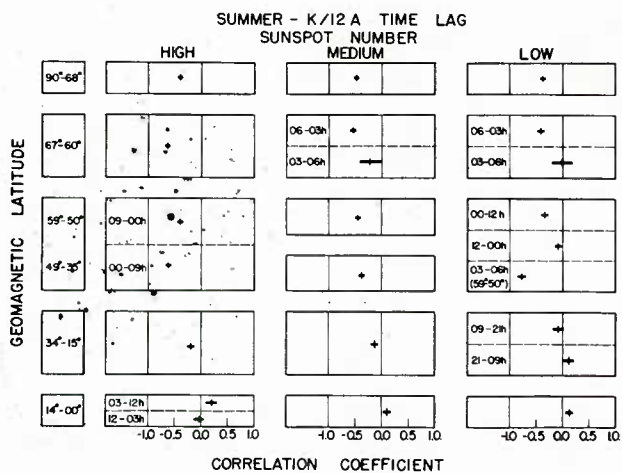


Figure 5 - Combined correlation coefficients of percentage-MUF on K-index for three levels of solar activity

The results presented above have been examined to determine the magnitude of predicted departures from the median percentage-MUF for the various space and time conditions, for a relatively high degree of magnetic activity. The level of magnetic activity selected is the K-index exceeded 10% of the time. In calculating this estimate and its 95% confidence limits for the K/6 time relationship, it was found that the largest departure, i.e., $27\% \pm 5\%$, occurs in the auroral zone at 1800 and 0000 hours.

The several variations of the relationship between F2-layer ionization and magnetic activity with space and time parameters found in this study have been compared with published results of related work. (See references.) Good agreement with the published results is found, even when the earlier work is confined to relationships derived exclusively for periods of recognized magnetic activity. Agreement is noted with regard to the change in the relationship with geomagnetic latitude, the seasonal phenomenon of positive correlations at high and medium latitudes during winter nighttime, and the effect of solar activity on the strength of the correlation.

In conclusion, the results of the present study provide a means of predicting imminent F2-layer maximum usable frequencies, insofar as they depend on the activity of the earth's magnetic field. In practice, such predictions are generally not useful at geomagnetic latitudes lower than 35° . Stronger correlations might be expected if additional independent variables were used in the correlation analysis, e.g., 10-cm solar flux.

The value of the technique would depend on the magnitude of the user's predicted departures from normal and the precision with which he could predict them. As to magnitude, departures of $-25\% \pm 5\%$ are typical in the auroral zone, and departures of $-10\% \pm 4\%$ are common at middle latitudes. The precision of the predictions varies with location and time, as indicated by the computed mean rms error reduction of $23\% \pm 3\%$ in the auroral zone, compared with a reduction of $8\% \pm 2\%$ at medium latitudes.

Finally, the relationships developed here with data for all days included in the analysis correspond closely with variations for storm days reported in the literature.

References

- Appleton, E. V., and W. R. Piggott: "The morphology of storms in the F2 layer of the ionosphere," JATP, Vol. 2, 236, 1952.
- Berkner, L. V., and S. L. Seaton: "Systematic ionospheric changes associated with geomagnetic activity," Terr. Mag. Atmos. Elec., Vol. 45, 419, 1940.
- King, J. W., and C. Graham: "The relationship between foF2 and magnetic phenomena," JATP, Vol. 24, 107, 1962.
- Martyn, D. F.: "The morphology of the ionospheric variations associated with magnetic disturbances, I. Variations at moderately low latitudes," Proc. Roy. Soc., London, A, Vol. 218, 1, 1953.
- Matsushita, S.: "A study of the morphology of ionospheric storms," JGR, Vol 64, 305, 1959.
- Nagata, T. and T. Oguti: "Ionospheric storms in the auroral zone," Rep. Ionos. Res. Japan, Vol. 7, 21, 1953.
- Sato, Teruo: "Disturbances in the ionospheric F2 region associated with geomagnetic storms, II. Middle latitudes," J. Geomag. and Geoelec., Vol. 9, 1, 1957.
- Sinno, K.: "Studies on the disturbances in F2 layer associated with geomagnetic disturbances," Rep. Ionos. Res. Japan, Vol. 9, 166, 1955.

SHORT-TERM FORECASTING OF IONOSPHERIC PROPAGATION FOR
DCA TRUNKS IN SOUTHEAST ASIA

Ralph J. Slutz, T. N. Gautier, and M. Leftin

Institute for Telecommunication Sciences and Aeronomy*
Environmental Science Services Administration
Boulder, Colorado

Short-term forecasts of maximum usable frequency for high frequency trunks of the Defense Communications System in the Southeast Asia area are issued hourly by ESSA's Institute for Telecommunication Sciences and Aeronomy in Boulder, Colorado. The forecasts are based on values of the 3000 km MUF scaled hourly from ionograms at Okinawa, Taipei, Manila, and Bangkok, and telegraphed immediately to Boulder via DCS common user circuits. At Boulder these values are translated by means of a small computer into trunk MUF forecasts for a time three hours later than the observations, and then telegraphed to DCS trunk terminals at Tokyo, Okinawa, Taipei, Clark Air Base and San Miguel Naval Base in the Philippines, Bangkok, Saigon, and other points as required. Similar forecasts are also issued for air-to-ground HF communication in the vicinity of Clark Air Base, and for ship-to-shore paths terminating at San Miguel.

The forecasts are currently based solely on ionospheric persistence, both in time and space, as determined by regression analysis.

Each user of the forecasts is furnished with a set of curves for each trunk representing possible diurnal variations of the MUF. The hourly forecast message, then, simply designates the curve which represents the current forecast trend. Expressed in this way the forecasts, though based on three-hour persistence, may be applied immediately upon receipt by the user anytime up to about three and one-half hours after the time at which the observations were made. Typically, the user receives the forecast 2 to 2 1/2 hours after the observation time.

- - - - -
* Formerly the Central Radio Propagation Laboratory of the
National Bureau of Standards.

REAL-TIME SPECIFICATION OF THE PLANETARY GEOMAGNETIC
INDEX, a_p ; PRELIMINARY REPORT

by

William F. Johnson, Capt, USAF
Hq Air Weather Service

The AWS has recently completed the installation of a magnetometer network. This network furnishes real-time observations of the variations of the earth's magnetic field. This network is composed of magnetometers measuring the H and Z components of the geomagnetic field at Thule AB, Greenland ($+88.0^\circ$, 5.7°), Eielson AFB, Alaska ($+64.6^\circ$, 257.4°), Melville AFS, Labrador ($+64.6^\circ$, 11.9°), and Loring AFB, Maine ($+58.4^\circ$, 1.6°). In addition three-hourly K values are furnished on a real-time basis from a magnetometer installation at Ft. Belvoir, Virginia ($+49.7^\circ$, 349.9°). This network observes geomagnetic variations in the polar cap (Thule AB), the auroral zone (Eielson AFB and Melville AFS), and mid-latitudes (Loring AFB and Ft. Belvoir.)

The three-hourly planetary magnetic range index, a_p , is used in several models of the upper atmosphere along with other factors to specify density/temperature. In aerospace operations a real-time knowledge of upper atmospheric densities is needed but the current value of a_p is not available until one to two months after the fact. A study was made to see if data from the magnetometer network could be used to indicate the current value of a_p .

Historical geomagnetic data from Thule Village, Greenland; College, Alaska; and Fredericksburg, Va. were used in this study to discover their relationship with a_p . For real-time use the data from Thule AB, Eielson AFB, and Ft. Belvoir will be substituted. The data for the period September 1955 to July 1964 were used in a screening-regression technique to specify a_p . Ninety-six regression equations were developed, one for each three hour period of the day and a complete set for each month of the year. The latest eight a_K values from Fredericksburg, College, and Thule as well as the latest eight average a_{KS} of the three stations were used to specify the current a_p . The resulting regression equations correlate highly with a_p yielding a correlation coefficient of 0.95 or better in almost all cases. The correlation is highest during the months of higher geomagnetic activity (March, April, September, and October) and lowest during months of quiet geomagnetic conditions (Dec, Jan, Jun, and Jul). The study revealed that during particular times of the day and year the geomagnetic variations at College and Thule precede the variations in a_p by as much as six hours.

A test of the equations was made on data from the three historical stations for the period July 1964 and June 1965. The RMS error of the a_p specified by the equations was well within the limits expected from the screening-regression analysis. Preliminary results from a second test of the equations using the real-time data available from Thule AB, Eielson AFB, and Ft. Belvoir indicate that the regression equations for specifying a_p are indeed valid and perhaps work even better with the magnetic ranges furnished by the magnetometer network.

Further work remains before this study can be considered complete. It is planned to incorporate the data from the Loring AFB magnetometers into the regression equations. This will be done by redeveloping the equations as before with the addition of a_k values from the historical station at Agincourt, Ontario. Other averages of a_k values of the four stations will also be tested.

PREDICTION OF HURRICANE MOVEMENT

Banner I. Miller and R. Cecil Gentry
National Hurricane Research Laboratory
Environmental Science Services Administration
Miami, Florida

ABSTRACT

During the past ten years several statistical and dynamical methods for forecasting the motion of tropical cyclones have been developed. Many of these have been tested at the National Hurricane Center. These tests have shown that forecasts prepared by a statistical method developed at the National Hurricane Research Laboratory verify significantly better than forecasts prepared by other objective techniques. Current efforts at the National Hurricane Research Laboratory directed toward the improvement of the statistical methods and to develop an improved dynamical model for hurricane prediction are discussed. Initial data requirements for both models are reviewed. There are reasons to believe that a similar statistical forecasting technique can be developed for the Pacific. Efficient utilization of such a tool, however, would probably be dependent on development of operational objective analysis procedures for the Pacific on such a time scale that the hurricane forecasts could be made within 2 to 4 hours after the data were observed.

1. Introduction.

When the National Hurricane Research Laboratory was established in 1956, one of the main objectives was to develop forecast techniques which would help to improve the Hurricane Warning Service. Another similar objective was the evaluation of forecast procedures developed by other investigators. This has resulted in a continuing program of hurricane forecast verification, including the verification of the official Weather Bureau predictions. The official hurricane forecasts have shown a significant improvement in accuracy during the past 10 years. During the same period, the objective forecast techniques have also improved.

2. Statistical techniques for forecasting hurricane movement.

Ideally the prediction of hurricane motion should be based on forecasts of the field of motion over a large area surrounding the vortex, as for example by numerical prediction on a hemispheric basis. However, the prediction of circulation patterns at low latitudes over oceanic regions, which is necessary for numerical prediction of hurricane movement, has thus far proved to be a difficult task. Recognizing these problems many investigators have chosen to bypass the explicit prediction of circulation patterns. Instead, they have chosen to develop forecast techniques which make use of the current circulation patterns, auto-correlation functions, and features of the immediate past, which are known to be related to the subsequent track of the tropical cyclone. This line of approach (essentially statistical and climatological) has the advantage of being able to produce results for immediate use, whereas the more desirable (from a physical standpoint) dynamical approach takes longer and may have to await vastly improved data networks in tropical regions. Also, at present the forecasts of hurricane motion based on statistical methods verify significantly better than those produced by dynamical means, although it is to be expected that eventually the numerical forecasts will become superior, as prediction models and data networks improve.

During the past ten years, a number of objective methods for forecasting hurricane motion have been developed. Most of these have been evaluated at the National Hurricane Center. A few of these have now progressed to the point where they are at least as good as the forecasts prepared by experienced forecasters. A summary of the characteristics of these methods is shown in Table I.

The first of the objective systems for hurricane forecasting was developed by Riehl et al [13]. They postulated that the hurricane would move with the speed of the vertically integrated flow surrounding the vortex, and used the 500-mb chart to represent the vertical mean. The geostrophic wind components computed from the 500-mb heights around the periphery

| Forecast Method | Data Levels | Predictors | Grid Size | Forecast Periods |
|-----------------|-----------------------------------|--|-----------------------------|------------------------|
| RIEHL-HAGGARD | 500 M.B. | U, V | 10-17.5° LAT. 15° LONG. | 24 HOURS |
| MILLER-MOORE | 700 M.B. | $U, V, P_x, P_y, H_x, \partial H_x / \partial t$ | 10-17.5° LAT. 15° LONG. | 24 HOURS |
| T-59 | SEA LEVEL | P_0, P_x, P_y | 30° LAT. 60° LONG. | 24 HOURS |
| T-60 | SEA LEVEL 500 M.B. | P_0, Z_x, U, V, P_x, P_y | 2100 N.M. X 4200 N.M. | 12, 24, 36 HOURS |
| NHC-64 | SEA LEVEL 700 M.B. 500 M.B. | $U, V, P_0, H_x, Z_x, P_x, P_y, \partial Z_x / \partial t, \Delta Z_x$ | 2100 N.M. X 4200 N.M. | 12, 24 36, 48 HOURS |

TABLE 1.—Characteristics of objective forecast systems

screening-multiple linear regression statistical methods, developed by Miller [9, 10], to the problem of hurricane forecasting. These methods have become powerful tools in the development of statistical forecast systems, and they have since been refined and extended to numerous related problems. In the first hurricane forecast method developed by Travelers [17], a small set of predictors was selected from an initial set which included 91 sea level pressures and the past motion of the cyclone. The sea level pressures were read from a grid formed by the intersection of the latitude and longitude lines at five degree intervals. The grid was centered at the five degree intersection nearest the hurricane center. A revised method [20] was developed in 1960 in cooperation with the National Hurricane Research Laboratory. An equal area grid, with grid length 300 nautical miles, centered on the surface position of the cyclone was adopted. The grid moves with the cyclone.

After several years of operational testing of these four techniques, it was apparent that all of them possessed varying degrees of forecast skill. However, if forecasts were prepared by several different methods the forecaster was frequently confronted with a wide divergence in the forecast tracks, and this usually caused the forecaster to give little or no weight to any of the objective systems. To lessen this difficulty as much as possible, the National Hurricane Research Laboratory has developed a set of prediction equations which seems to incorporate many of the best features of the earlier objective methods for hurricane forecasting.

The NHC-64 is the latest in the series of methods derived by the screening regression technique. It was developed at the National Hurricane Research Laboratory in Miami, using the development data from the T-60, plus three additional years of data. Another level (700 mb) was added. The equations have been described in another paper [11] and will not be repeated here. The predictors from which the selections were made included the following.

- a. Sea level pressures (mb) ----- P_i
- b. 700-mb heights (meters) ----- H_i
- c. 500-mb heights (meters) ----- Z_i
- d. 1000-700 mb thicknesses (meters) ----- DH_i
- e. 700-500 mb thicknesses (meters) ----- TH_i
- f. 500-mb height changes (meters) ----- DZ
- g. Geostrophic wind components at three levels -- SY_5, T_3, S_{57}, SX_7
- h. The past 12-hour movement of the cyclone center (nautical miles) ----- P_x, P_y (westward and northward positive)

Equations were derived for forecast periods up to 72 hours. For the first 48 hours, the forecast is prepared in four 12-hour steps. The 48-72 portion is made in only one step. Positions at intermediate times along the track are obtained by adding the forecast displacements. Forecasts could have been prepared in one time step, i.e. 0-12 hours, 0-24 hours, and 0-48 hours. Equations to do this were actually derived, but no real differences between these and the equations to make the forecasts in 12-hour steps could be detected.

of a small grid centered on the surface position of the cyclone were used as predictors. Miller and Moore [8] subsequently applied a Riehl-Haggard type grid [13] to the 700-mb chart and derived a set of prediction equations which used the geostrophic wind components and the past movement of the cyclone center as predictors. An unpublished modification of the Miller-Moore method incorporated heights and height changes of the 700-mb surface as predictors. Arakawa [11] has developed similar methods for use in the Pacific area.

In 1959, Veigas, Miller, and Howe [19] of the Travelers Research Center applied the

Hence, the latter were adopted for operational use since they had the advantage of showing intermediate positions along the track.

The physical interpretation of the results of the screening process is not always clear cut, although if a selected predictor continues to contribute significantly to forecast accuracy, there must obviously be some physical explanation for that fact, however obscure it may be. Meteorological variables are highly correlated both in space and time, and these correlations make it difficult to determine whether a selected predictor is physically significant for its own sake or because both the predictor and the predictand are correlated with some unidentified factor. However, a brief discussion of the forecast equations may be of some benefit to the forecaster who must make the decision as to the accuracy of a particular forecast which he may encounter operationally.

Figures 1-5 show the locations of the sea level pressures, 700-mb heights, 500-mb heights, 24-hour height changes at the 500-mb surface, and the thickness values which were selected as predictors. These locations are in addition to the ones used to define the steering components at the 700- and 500-mb levels, since the interpretation of the forecast value of these components (SY₅, T₃, S₅₇, and SX₇) is relatively simple.

The letters N and W, together with a sign and a number have been entered on figures 1-5. The letter indicates the forecast equation in which each predictor appears, i.e. N means that the predictor appears in an equation used to forecast north-south movement and the W in an equation to forecast east-west movement. The sign designates the sign of the coefficient of each predictor. The number denotes the equation in which the predictor appears. A "2" indicates that the predictor appears in the 0-12 hour prediction equation, a "4" in the 12-24 hour equation, a "6" in the 24-36 hour equation, and an "8" in the 36-48 hour equation. Predictors which appear in the north zone equations are underlined. Looking at figure 1, one sees that in general above-normal pressures to the east and below-normal pressures to the north of the center are associated with northward motion of the hurricane. Similarly, above-normal pressures to the north are associated with westward motion. There is also a tendency for gradients to be defined in a crude way even though the screening program used did not specifically select predictors in pairs. For example, in the north-south equation for a 12-hour forecast (South Zone) P₆₉ (to the east of the center) appears with a plus sign, while P₅₂ to the

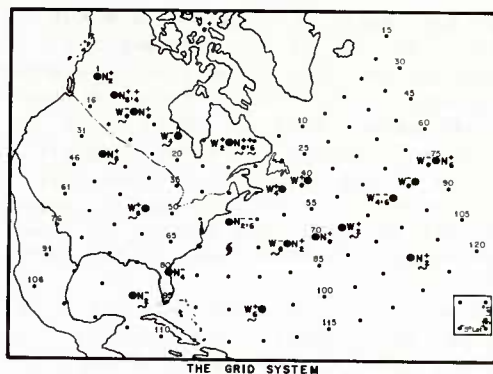


FIGURE 1.—Sea level pressures used as predictors

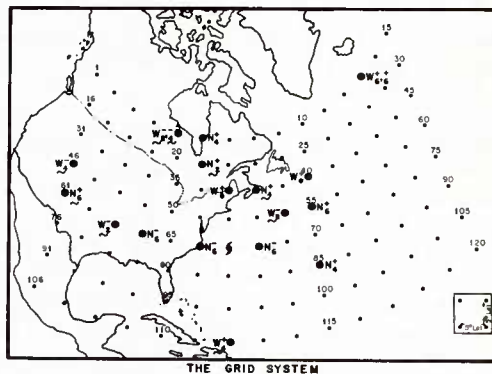


FIGURE 2.—700-mb heights selected as predictors

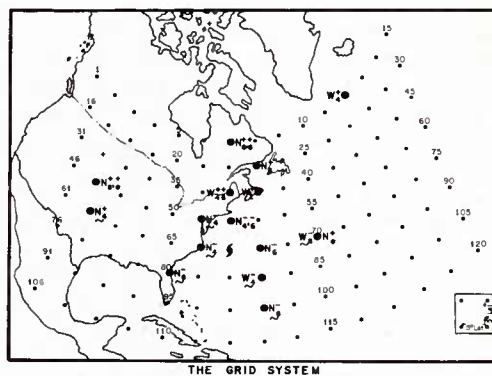


FIGURE 3.—500-mb heights selected as predictors

north of the center appears with a minus sign. Less obvious is the tendency for northward motion to be associated with above-normal pressures over the extreme northwest part of the grid. This may imply (in a statistical-climatological sense) that if an anticyclone at sea level is situated over that portion of the grid, a trough is probably located near the longitude of the hurricane which is about 1500-1800 n.m. to the east.

A similar pattern seems to exist at both 700 and 500 mb (figures 2 and 3). The heights ten degrees north of the center at both 700 and 500 mb are particularly important in forecasting east-west motion. For example, in the 12-24 hour longitude forecast (South Zone) Z_{37} was the first predictor selected, and contributed 67.3% to the reduction in the variance. In the 36-48 hour forecast of east-west movement (North Zone) H_{37} was the first predictor selected and made a 39.3% contribution to the reduction in variance.

The selection of 500-mb height changes (figure 4) reflect well known empirical rules for forecasting acceleration of hurricanes. Falls to the west of the center are associated with northward acceleration, while rises to the west are associated with deceleration. Rises to the north or northeast are associated with slowing down or turning westward, while falls to the north may result in acceleration or recurvature. Below-normal thickness values (figure 5) to the north are related to eastward movement, while above-normal values are related to westward motion. Above-normal values to the south or east are associated with northward displacement.

The past 12-hour movement of the hurricane center was among the original set of possible predictors screened. For periods beyond 24 hours in the south zone, the past motion makes no substantial contribution to the forecast. In the north zone the past motion is unimportant after the first 12 hours. Thus, the NHC-64 equations are not heavily dependent upon persistence for their forecast skill. That deceleration and changes in direction (even though climatologically improbable) may be forecast by these equations are indicated by a forecast made for Hurricane Betsy (1965) as shown in figure 6.

3. The accuracy of hurricane forecasts.

The performance of the objective and official hurricane forecasts were published last year by Tracy [17]. For some of these techniques which are still in use, we have been able to add data through the 1966 hurricane season. Forecasts have been verified by geographical areas, as shown in figure 7. These data are for the official weather bureau forecasts which verify 28 hours

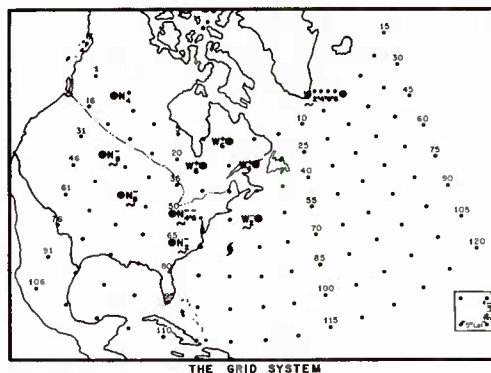


FIGURE 4.—500-mb height changes selected as predictors

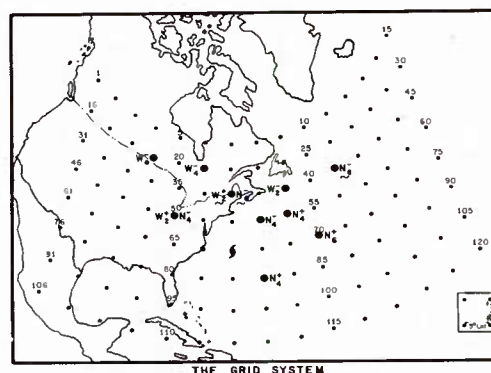


FIGURE 5.—Thicknesses selected as predictors

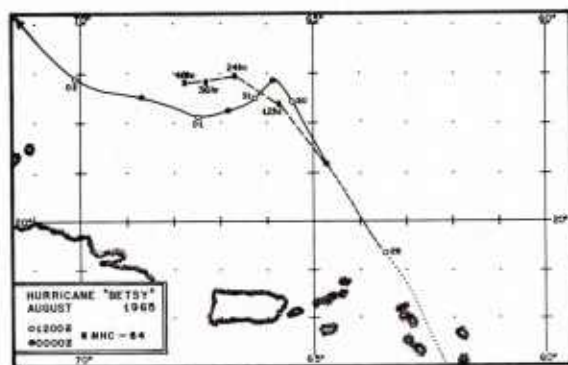


FIGURE 6.—A forecast prepared by NHC-64, Betsy, 1965

after the latest synoptic data time. The number of forecasts (for the years 1959-1966) and the mean vector error are shown. Area "B" has the smallest mean errors, 116 nautical miles for 585 cases. This superior performance in area "B" is due partly to better initial data and partly to less variability in the hurricane tracks within that area.

Figure 8 shows the average errors for a 24-hour forecast for several objective systems in area "B". These data are not homogeneous, and it is not possible to obtain a meaningful homogeneous sample since some of the earlier forecast techniques are no longer used at the National Hurricane Center. The periods of record, the number of forecasts, and the average errors are shown. This diagram may indicate a gradual improvement in the accuracy of the objective systems. The two with the smallest average errors were developed at NHRL. Incidentally, the NHC-64 technique did not do well in forecasting the erratic behaviour of Inez as it moved across the Gulf of Mexico. This is reflected in the increase in the vector errors for the NHC-64 system for 1966 over the previous years.

It has been possible to prepare a homogeneous sample for comparison of the NWP and the NHC-64 hurricane forecasts, as shown in figure 9. This sample is for the years 1964-1966, and the statistical forecasts demonstrated a clear superiority over the dynamical forecasts. In area "B" the average 24-hour errors were 95 and 120 n.m. for 72 forecasts. For 48-hour forecasts the errors were 197 and 274 n.m. for 67 forecasts. In the other areas, both techniques result in larger errors, but the advantage of the statistical forecasts is maintained.

An examination of the errors in the official weather bureau hurricane forecasts since 1954 has revealed a significant improvement in forecast accuracy. This is shown by figure 10. In figure 10a (which is for area "B") the dashed line shows the average 24-hour errors by years. There is considerable year-to-year variability, but in general the maxima and minima show a decrease with time. The trend is more clearly demonstrated by the solid line which is a three year overlapping average. The blocks are the average errors for a five year period (1954-1958), and two four year periods (1959-1962 and 1963-1966). No verification data were available prior to 1954. The first five years (1954-1958) were taken as the base years for comparative purposes. In 1959 the National Hurricane Research Laboratory moved to Miami and a closer co-operation between forecasters and researchers was initiated. This included daily map discussions during the hurricane season and the use of research people to assist the forecasters by making objective forecast computations

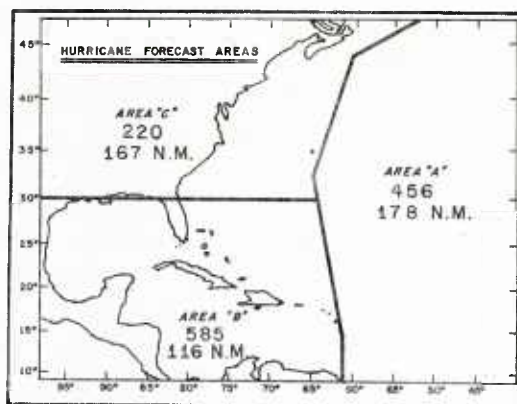


FIGURE 7.—Eight year average of official 24-hour forecast errors, by areas

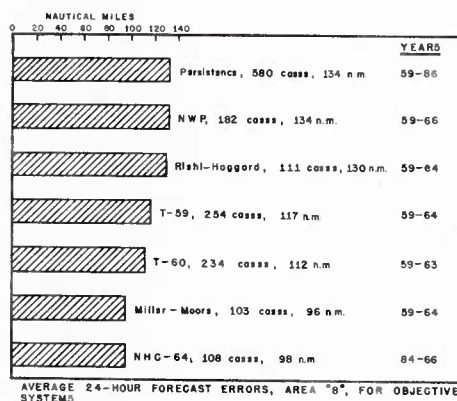


FIGURE 8.—Average of objective 24-hour forecast errors, Area "B"

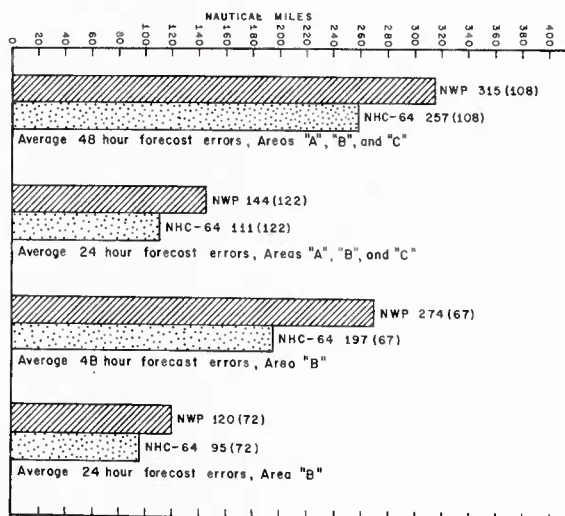


FIGURE 9.—Three year comparison of forecast errors for Area "B", NWP and NHC-64 24- and 48-hour forecasts

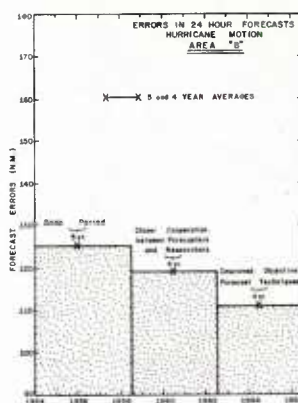
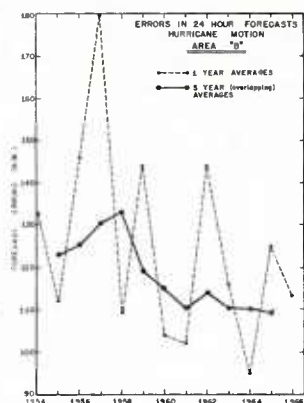


TABLE 10a.—Average forecast errors for area "B" for a 13-year period. Dashed line is yearly average. Solid line is three year overlapping average. Blocks indicate 5, and 4-year averages.

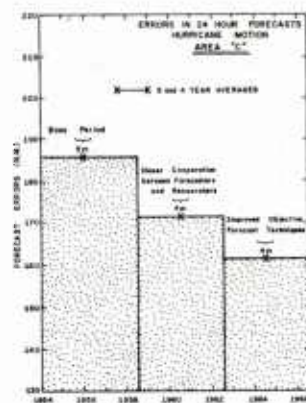
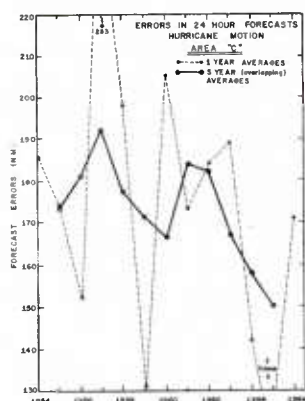


TABLE 10b.—Same as for figure 10a, except for area "C"

whenever a hurricane was in progress. The following four year period (1959-1962) saw a reduction in the average forecast errors. By 1963 and 1964 the improved objective forecast techniques developed at NHRL were in operational use. This period shows another decrease in forecast errors. This trend has been found to be statistically significant at the 5% level. No one can really say just what caused the improvement in the forecast, but it is probably due to increased experience on the part of the hurricane forecasters, closer cooperation between forecast and research personnel, and the development of improved objective forecast techniques.

Figure 10b shows a similar trend for area "C". The percentage improvement is about the same as for area "B".

4. Development of statistical forecast methods for the Pacific area.

The statistical forecast equations (which have proved to be the best objective technique in the Atlantic) have been tested on a number of typhoons in the Western Pacific. The equations lose much of the predictive value when used in the Pacific. This is not surprising, since statistical systems must necessarily contain a large amount of the climatology of the area in which they are developed. However, there is no reason why a similar set of equations could not be developed and usefully applied in the Pacific. The NHRL would be happy to assist in the development of such a system.

In the Atlantic area the statistical forecasts are prepared at the National Meteorological Center from the preliminary objective analyses, and are usually available to the

forecaster within 2 to 2½ hours after data time. This rapid preparation of the forecasts is necessary if one is to obtain the maximum usefulness from the objective forecasts, i.e. the forecaster should have the objective forecast before he has to issue his warnings. It is probable that the success of a statistical forecast system in the Pacific would depend upon the production of a rapid objective analysis upon which the forecasts could be based.

5. Forecast research at the National Hurricane Research Laboratory.

a. Improved statistical forecast models.

Thus far most of the efforts at NHRL to improve forecast models have been devoted to the development of statistical prediction methods. This approach was adopted because it was felt that results could be obtained sooner by statistical rather than dynamical methods. This belief has been justified by the development of the NHC-64 equations, since these forecasts are now prepared operationally at NMC.

The statistical equations did not perform well, however, in forecasting the erratic behaviour of Inez last year. The errors have been analyzed and the equations are being revised. Some new data have been added to the developmental sample. It is anticipated that new and improved equations will be ready for operational testing this year.

b. Numerical prediction.

During the past ten years there have been numerous attempts to develop dynamical models for hurricane prediction. Some of the more important are those developed by Saski [14], Kasahara [5, 6], Birchfield [2, 3], Morikawa [12], Kasahara and Platzman [7], Vanderman [18], Terauchi [16], and Jones [4]. These include the barotropic, equivalent barotropic, baroclinic models. All are essentially steering current models. The operational model now in use at Suitland is the barotropic. Some excellent forecasts have been produced by this model, but the over-all results have been disappointing.

This raises the question as to why the statistical forecasts have been somewhat better than the dynamical for the past two years, since input data for both came from the NMC analyses. It is apparent that the dynamical model is more sensitive to initial data errors than the statistical model. However, this is probably not the complete reason for the better performance of the statistical model, and one is forced to conclude that the dynamical model needs to be improved.

People at NHRL feel that (even though some initial advantage has gone to the statistical model) eventually the dynamical forecasts must be superior, simply because the latter are based on physical principles. Accordingly most of our efforts on forecast development are now going into numerical prediction. The modifications now being worked on include

1. Primitive equation model.
2. Diabatic and viscous.
3. Fine grid surrounding vortex.
4. Multi-level.

c. Improvement in initial data.

For any of the models to show much improvement over those of the past, we desperately need more and better data. How can the initial data be improved? The most obvious way is to collect more data inside the fine grid around the vortex by use of aircraft. Consider the data required to prepare the NHC-64 statistical forecasts as an example.

The relative importance of the various grid point data required to prepare the NHC-64 forecasts has been determined. Figure 11 shows the results of this analysis. Note the shaded area where data are of the most importance. On this has been superimposed a proposed flight path, with recommended points for dropsonde and other observations. These flights should be at the 500-mb level. An additional flight at or near 250-mb level would provide enough information to permit reasonable interpolation to obtain the data needed at other levels in a multi-level model.



FIGURE 11.—Areas near hurricane where peripheral reconnaissance needed for hurricane prediction.

6. Summary.

Several objective systems for forecasting the movement of hurricanes have been developed during the past 10 years. Many of these have been evaluated at the NHC in Miami. Two have given consistently better results than the others. The last of these to be developed uses data at three levels and prepares forecasts up to 72 hours. This model has been adopted for operational use and the forecasts are prepared at NMC from the objective analyses. After three years of operational testing, the NHC-64 statistical model has maintained superior performance over other objective systems, including the operational barotropic model and makes just as good forecasts on the average as those prepared subjectively.

The official hurricane forecasts issued by the weather bureau have shown a significant improvement during the past ten years. This is thought to be partly due to increased skill on the part of the hurricane forecasters, closer cooperation between the forecast and research personnel, and the development of better objective forecast methods. It is hoped that with improved objective forecasts to aid them this year that the forecasters will be able to show further improvement.

REFERENCES

1. H. Arakawa "Studies on Statistical Prediction of Typhoons," National Hurricane Research Project Report No. 61, U. S. Weather Bureau, Washington, D. C., 1963, 15 pp.
2. Gene E. Birchfield, 1960: "Numerical Prediction of Hurricane Movement with the Use of Fine Grid," Jour. Meteor., 17, pp. 406-414.
3. Gene E. Birchfield, 1961: "Numerical Prediction of Hurricane Movement with the Equivalent Barotropic Model," Jour. Meteor., 18, pp. 402-409.
4. R. W. Jones, 1961: "The Tracking of Hurricane Audrey (1957) by Numerical Prediction," Jour. Meteor., 18, pp. 127-128.
5. A. Kasahara, 1957: "The Numerical Prediction of Hurricane Movement with a Two-level Baroclinic Model," Jour. Meteor., 14, pp. 386-402.
6. A. Kasahara, 1960: "The Numerical Prediction of Hurricane Movement with a Two-level Baroclinic Model," Jour. Meteor., 17, pp. 357-370.
7. A. Kasahara and G. W. Platzman, 1963: "Interaction of a Hurricane with the Steering Flow and Its Effect Upon the Hurricane Trajectory," Tellus, 15, pp. 321-335.
8. B. I. Miller and P. L. Moore, 1960: "A Comparison of Hurricane Steering Levels," Bulletin, American Meteorological Society, vol. 41, pp. 59-63.
9. B. I. Miller, 1958a: "Statistics and Predictability of Weather," Studies in Statistical Weather Prediction, Final Report, AF19(604)-1590, The Travelers Weather Research Center, Inc., Hartford, Conn., pp. 137-153.
10. B. I. Miller, 1958b: "The Screening Procedure," Studies in Statistical Weather Prediction, Final Report, AF19(604)-1590, The Travelers Weather Research Center, Inc., Hartford, Conn., pp. 86-96.
11. B. I. Miller and P. P. Chase, 1966: "The Prediction of Hurricane Motion by Statistical Methods," Monthly Weather Review, 94, pp. 399-406.

12. G. K. Morikawa, 1962: "On the Prediction of Hurricane Tracks Using a Geostrophic Point Vortex," Proceedings of the International Symposium on Numerical Weather Prediction in Tokyo, Met. Soc. of Japan, Tokyo, pp. 349-360.
13. H. Riehl, W. H. Haggard, and R. W. Sanborn, 1956: "On the Prediction of 24-Hour Hurricane Motion," Journal of Meteorology, vol. 13, pp. 415-420.
14. Y. Sasaki, 1955: "Barotropic Forecasting for the Displacement of Typhoons," Jour. Met. Soc. Japan, 33, pp. 1-8.
15. A. L. Sugg, 1967: "Economic Aspects of Hurricanes," Monthly Weather Review, vol. 95, pp. 143-146.
16. E. Terauchi, 1963: "An Outline of Numerical Prediction for Typhoon or Hurricane Tracks," Proceedings of the Inter-regional Seminar on Tropical Cyclones in Tokyo 18-31 January 1962, Met. Soc. of Japan, Tokyo, pp. 215-227.
17. J. D. Tracy, 1966: "The Accuracy of Hurricane Forecasts," Monthly Weather Review, vol. 94, pp. 407-418.
18. L. W. Vanderman, 1962: "An Improved NWP Model for Forecasting the Paths of Tropical Cyclones," Monthly Weather Review, vol. 90, pp. 19-22.
19. K. W. Veigas, R. G. Miller, and G. M. Howe, 1959: "Probabilistic Prediction of Hurricane Movements by Synoptic Climatology," Occasional Papers in Meteorology, No. 2, The Travelers Weather Research Center, Inc., Hartford, Connecticut, 54 pp.
20. K. W. Veigas, 1961: "Prediction of Twelve, Twenty-four, and Thirty-six Hour Displacement of Hurricanes by Statistical Methods," Final Report Contract No. Cwb. 9807, The Travelers Weather Research Center, Inc., Hartford, Connecticut, 36 pp.
21. K. W. Veigas, 1962: "Development of Prediction Equations for Hurricane Movement," Final Report Contract No. Cwb 10170, The Travelers Weather Research Center, Inc., Hartford, Connecticut, 59 pp.

THE ONSET OF WIDESPREAD RAIN DURING THE SOUTHEAST ASIA SUMMER MONSOON

Walter C. Conover
Atmospheric Sciences Laboratory, U. S. Army Electronics Command
Fort Monmouth, New Jersey

This presentation summarizes a study done under contract by Joseph Pellisier (then of Colorado State University) for the Atmospheric Sciences Laboratory, USAECOM, Fort Monmouth, N. J. This study is reported in contract report, "Forecasting the Onset of Widespread Rain During the Southeast Asia Summer Monsoon," by Joseph Pellisier, Report 2245/1, Department of Atmospheric Science, Colorado State University, July 1966, Contract No. DA28-043 AMC-01303(E), DDC AD No. 487-282.

A. Monsoon Precipitation

The purpose of this study was to develop an objective method for forecasting the onsets of precipitation episodes during the summer monsoon season in Southeast Asia. Note that "onset of precipitation" for this report means a significant increase in the spread of precipitation over the area of interest; "onset" does not denote the commencement of rain at any particular station.

Except for the case of a tropical storm passing over an area, rain patterns do not in general progress into an area, but rather they occur "spontaneously" over the area. However, it has been observed that eastward propagating 500 mb troughs in the mid-latitude westerlies are strongly correlated with rain episodes in Southeast Asia. One can hypothesize that northerly winds to the rear of a trough set up a zone of convergence where they meet the equatorial monsoon westerlies. The clockwise curving flow behind the trough establishes a belt of easterlies not previously present. The reaction of these easterlies produces an area of high cyclonic vorticity intensifying the equatorial extent of the trough with a resultant increase in precipitation.

B. Forecast Procedure

A simple objective forecast method that follows the stated hypothesis uses the definitions and conditions listed here.

C. Definitions

1. Rain index: the number, or percentage, of stations in the area of interest which report a minimum of 10 mm of rain within the 24-hour period 0000Z to 0000Z.

2. Trough: its position, intensity (determined by measurement of winds at five degrees longitude either side of the trough line at 40°N), and rate of movement are obtained from the 500-mb chart.

3. Onset day: a day in which the rain index exceeds a value which is expected no more than 20 percent of the time.

4. Forecast day: a day in which the rain index is less than the onset day value.

D. Conditions

1) A forecast day exists, 2) an eastward propagating trough passes 105 E at 40N, and 3) the intensity of the trough exceeds a shear of 20 knots.

E. Forecast Verification

A forecast verification scheme was devised to record a percentage "hit" or "miss" ('h' or 'm') according to whether the rain index value did or did not exceed the 80 percent level within 72 hours after an onset was forecast. Also, an 'h*' or 'm*' is recorded according to the 24-hour accuracy of a no-onset forecast.

The forecast method was tested on a 1961-1962 series of observations taken in South-east Asia, with results as follows:

| | |
|---------------------------------|-----|
| $h/(h + m)$ | 43% |
| $h^*/(h^* + m^*)$ | 90% |
| $(h + h^*)/(h + h^* + m + m^*)$ | 80% |

F. Conclusions

1. Most rain episodes in Southeast Asia, which are not obvious results of tropical storms, can be linked to troughs in the westerlies.

2. The forecast method described over-forecasts: most onsets are forecast, but many onset forecasts do not verify. This is the reason for the 43% figure above. One explanation for this is that the 80% frequency level is not always attained. Improved verification figures were attained when lower frequency levels were used. Another reason for the low verification figure is that the troughs have rather erratic behavior after passing 105° E, whereas the forecasts are based on linear extrapolation.

3. When trough intensity reaches a shear of 20 knots, the subsequent magnitude and duration of areal precipitation is uncorrelated to trough intensity.

4. Using this forecasting method, few military operations will be scheduled that would be affected by unexpectedly adverse weather; relatively more operations might be cancelled because of a forecast that fails to verify.

THE RELATIONSHIP BETWEEN DAILY AND ANNUAL RAINFALL IN THAILAND

Ruth L. Wexler
US Army Natick Laboratories
Natick, Massachusetts

Abstract

The probable spectra of precipitation rates over brief periods of time may be critical in the design of Army materiel. Generally, such information is not available. To meet the problem, empirical methods have been relied on for the derivation of daily, hourly, or instantaneous precipitation rates from ordinary climatic data. The basis of these methods rests on the fact that for many regions of the world the mass distribution of rain tends to follow a predictable pattern. Whether this is so throughout the monsoon climate has been a question. Consequently, from daily rainfall observations in Thailand for a number of stations, the respective annual rainfall mass distributions have been determined. Preliminary results indicate that these distributions are similar to those found elsewhere. Therefore, a universal rainfall distribution curve may be employed for estimates of daily (hourly) intensities, as is demonstrated. Prediction equations and nomograms are provided. Estimates are compared with observations. The required parameters are the total amount of annual precipitation and the corresponding number of rain days per year. While the study is concerned mainly with the relationship between the daily and annual rainfall, hourly intensities are considered briefly.

I. Introduction

Rainfall mass distribution, when expressed as cumulative percent amount versus cumulative percent frequency, has been found to be similar for a number of widely dispersed stations in North and Central America [1]. The mean curve for these stations is given in a Texas A & M report [1] and is reproduced here as Figure 1. The amount may be the total precipitation for the year or month, while the frequency may be hours or days* of rain per year or month. Approximately the same curve has been found characteristic of annual rainfall in other areas, particularly throughout Argentina [2, 3, 7]. This rainfall distribution curve appears to be valid for a range of climates, regardless of surrounding topography or magnitude of annual rainfall. It is seen that 10% of the total rain occurs in 50% of the time, whereas 50% of the total occurs in less than 15% of the time. In order to employ this curve as a forecast tool for daily intensities, the required parameters are P, the annual precipitation, and D, the number of rain days per year.

Other investigators have utilized the ratio P/D to obtain hourly frequencies directly [4, 5].

This study is concerned with two aspects of the mass rainfall distribution curve. The first concern is the applicability of the curve to the monsoonal rainfall of Thailand. A series of annual rainfall distribution curves, based on daily rainfall observations at selected stations, have been developed for comparison with the rainfall distribution curve in Figure 1. The second concern is with the practicality of using this "universal" curve, or similar curves, for estimating probable expectancy of daily or hourly rainfall intensities.

II. General Precipitation Regime in Thailand

Many earlier reports have thoroughly treated the climate and topography of Thailand [6, 7, 8, 9, 10].

* For North and Central America, a day (hour) of rain is defined as a day (hour) with measurable rain $\geq .01$ inch. For Thailand, 0.1 mm is the lower limit.

While local precipitation is affected by landforms (Fig. 2), the overall rain is controlled by large-scale circulation patterns, namely, the reversal of the monsoon winds. The southern section of the country is first subject to the Southwest Monsoon in mid-May, at which time the Inter-Tropical Convergence Zone begins its passage northward, reaching its most northerly position usually in September [10]. Recent synoptic studies indicate that tropical cyclones appear to be influential in "triggering" off the onset of the monsoon over Southeast Asia [11]. The moist southerly and southwesterly winds prevail from mid-May to October; the dry northeast winds, or the Northeast Monsoon, from November to February. During the Southwest Monsoon, practically all of Thailand receives some rain, whereas during the Northeast Monsoon, most of the country experiences a relatively long drought. In the dry season, only the Isthmus of Kra may depend on rain, particularly its east coast which generally has heavy rain.

III. Observations of Daily Rainfall in Thailand

1. Extreme rainfall regimes

Two stations with very different rainfall regimes were chosen for initial study. The choice depended both on the amount of rain and the number of rain days per year. Their locations are shown in Figure 2.

The first, Kantharalak, a relatively dry inland station at the southern edge of the Korat Plateau, is apparently in a rain shadow caused by hills immediately to its south. The second, Ban Nong Prue, situated closer to the Gulf of Thailand, is a rather wet station facing the moist Southwest Monsoon. This station is subject to orographic rain due to hills to the east.

Daily rainfall observations for Kantharalak for the calendar year 1964 are given in Table 1. The annual total was 319 mm, occurring on 29 days. The monsoon nature of the rain is seen in the table, with most of the annual amount in the month of May.

Daily rainfall observations for Ban Nong Prue, also for 1964, are given in Table 2, which shows two peak months, May and August. The total annual amount was 3085 mm, nearly ten times that of Kantharalak. Rain occurred on 183 days, or six times as many as at Kantharalak.

Figure 3 consists of percent frequency histograms of daily rainfall for the two stations. The abscissa represents classes of rainfall in uneven intervals, from 0.1-1.0 mm/day up to >120 mm/day. At the dry station, Kantharalak, rainfall intensities < 1.0 mm/day were not observed, while at Ban Nong Prue such light rain accounted for more than 15% of the rain days. It is noted that the highest frequencies, 38% (11 days) for Kantharalak, and 17% (31 days) for Ban Nong Prue, were of the same class, namely 4-8 mm/day. Only 1 day at Kantharalak and 28 days at Ban Nong Prue were greater than 40 mm. The maximum daily rainfall for Kantharalak was 57 mm, while that for Ban Nong Prue was 146 mm.

Figure 4 gives curves of cumulative percent frequency versus cumulative percent amount for both stations for comparison with the curve in Figure 1. The latter curve would nearly superimpose that for Ban Nong Prue, while the curve for Kantharalak is not very different.

At first it might be assumed that the Ban Nong Prue curve depicts a wet monsoon station, while the Kantharalak curve depicts a dry station. Yet Figure 1 also serves such desert stations as Yuma, Arizona [1]. Moreover, another station, Ban Thung Pene, which is very close in location to Ban Nong Prue, has a curve nearly the same as that for Kantharalak. Ban Thung Pene has a slightly higher annual rainfall than Ban Nong Prue but fewer days of rain. The question of distribution characteristics will be considered more completely in part 3 of this section.

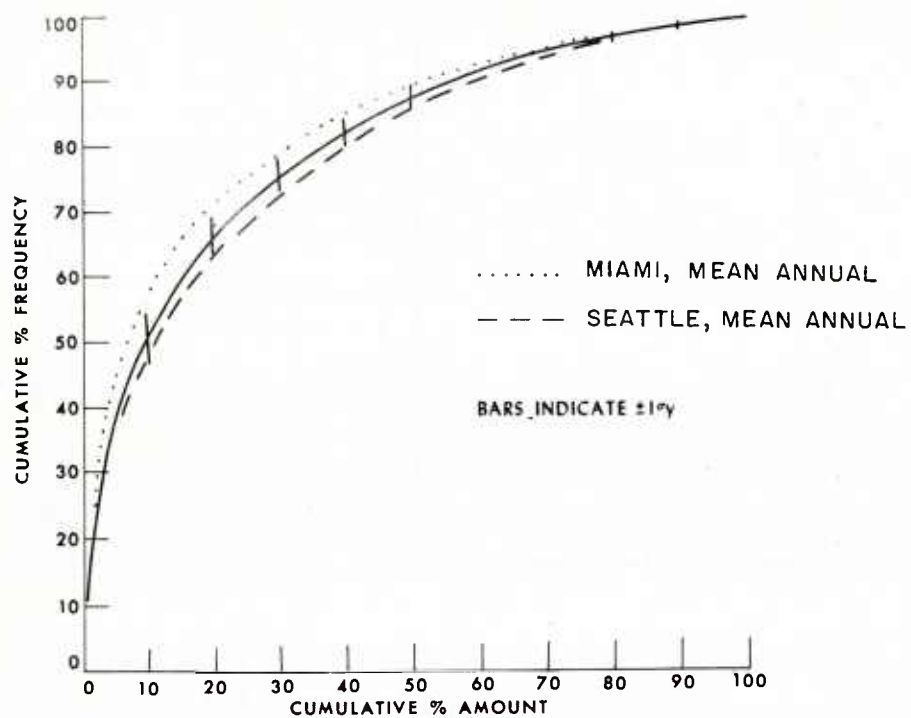


Figure 1 Mean Rainfall Distribution Curve for North and Central America (Solid line). This figure is from a Texas A & M report [1]

Figure 2 Map of Thailand

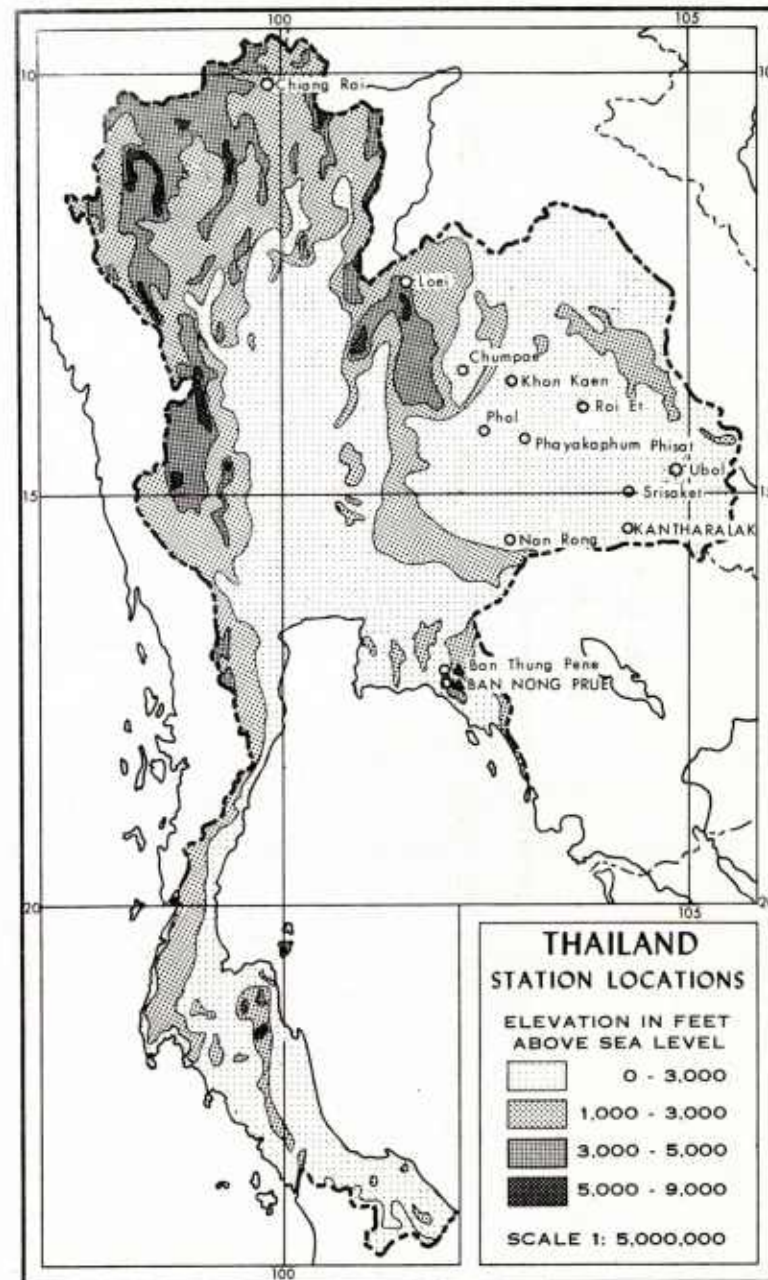


TABLE 1 *

KANTHARALAK

Daily Precipitation in Millimeters for Calendar Year 1964

| <u>Days</u> | <u>Jan</u> | <u>Fed</u> | <u>Mar</u> | <u>Apr</u> | <u>May</u> | <u>June</u> | <u>July</u> | <u>Aug</u> | <u>Sep</u> | <u>Oct</u> | <u>Nov</u> | <u>Dec</u> |
|-------------|------------|------------|------------|------------|------------|-------------|-------------|------------|------------|------------|------------|------------|
| 1 | | | | | 33.1 | | | | | | | |
| 2 | | | | | 56.8 | | | | | 4.0 | | |
| 3 | | | | | | | | | | | | |
| 4 | | | | | | 4.3 | | | | | | 4.5 |
| 5 | | | | | | 4.1 | | | | | | |
| 6 | | | | | | | | | | | | |
| 7 | | | | | | | | | | | | |
| 8 | | | | | 1.8 | | | | | | | |
| 9 | | | | | 13.3 | | 2.9 | | | | | |
| 10 | | | | | | | | | | | | |
| 11 | | | | | | | 9.4 | | | | | |
| 12 | | | | | | 5.7 | | | | | | |
| 13 | | | | | | 5.3 | | | | | | |
| 14 | | | | | | | | | | | | |
| 15 | | | | | 4.2 | | | | | | | |
| 16 | | | | | | | | | | | | |
| 17 | | | | | | | | | | | | |
| 18 | | | | | 18.8 | | | | | | | |
| 19 | | | | | 1.2 | | | | | | | |
| 20 | | | | | 7.5 | 5.3 | | | | | | |
| 21 | | | | | 20.7 | | | | | | | |
| 22 | | | | | 18.3 | | | | 14.2 | | | |
| 23 | | | | | | 9.2 | | | | | | |
| 24 | | | | | | | | | 7.1 | | | |
| 25 | | | | | 5.3 | 10.0 | | | 2.5 | | | |
| 26 | | | | | 30.9 | 2.1 | | | 3.7 | | | |
| 27 | | | | | | 12.9 | | | | | | |
| 28 | | | | | | | | | | | | |
| 29 | | | | | | | | | | | | |
| 30 | | | | | | | | | | | | |
| 31 | | | | | | | | | | | | |
| Total | 0.0 | 0.0 | 0.0 | 0.0 | 211.9 | 58.9 | 12.3 | 0.0 | 27.5 | 4.0 | 0.0 | 4.5 |

Annual Precipitation: 319.1 mm

* Hydrologic Data Book 1964 [12]

TABLE 2 *

BAN NONG PRUE

Daily Precipitation in Millimeters for Calendar Year 1964

| <u>Days</u> | <u>Jan</u> | <u>Feb</u> | <u>Mar</u> | <u>Apr</u> | <u>May</u> | <u>June</u> | <u>July</u> | <u>Aug</u> | <u>Sep</u> | <u>Oct</u> | <u>Nov</u> | <u>Dec</u> |
|-------------|------------|------------|------------|------------|------------|-------------|-------------|------------|------------|------------|------------|------------|
| 1 | | | | | | T | | 10.7 | 43.3 | 63.3 | | |
| 2 | | | | | | 8.2 | 18.9 | 13.3 | 0.2 | 41.2 | 9.3 | |
| 3 | | | | | 0.4 | 23.6 | 10.0 | 16.2 | | 24.3 | 3.5 | |
| 4 | | | | | 29.8 | | 48.0 | 5.9 | | 86.8 | 0.4 | |
| 5 | | | | | 0.4 | 1.6 | 22.8 | 12.3 | | 0.6 | | |
| 6 | | | | | 4.5 | 9.5 | | 5.4 | 3.0 | 0.2 | | |
| 7 | | | | | 53.9 | 31.7 | | 0.6 | | 0.3 | 6.1 | |
| 8 | | 4.4 | | | 6.3 | 1.7 | | 2.9 | | 3.5 | | |
| 9 | | | 41.6 | | 2.6 | 6.5 | 17.7 | 58.7 | | 34.3 | | |
| 10 | | | 64.2 | | | 13.0 | | 49.6 | 1.9 | 0.3 | 0.7 | |
| 11 | | 14.6 | 24.4 | | | 0.6 | | 89.3 | 29.0 | 26.4 | 1.4 | |
| 12 | | | | | 7.9 | 1.7 | 0.9 | 3.4 | 9.3 | 8.2 | 0.5 | |
| 13 | | | | 39.6 | 0.5 | | | 0.9 | 29.8 | 5.9 | | |
| 14 | | | | 6.0 | 14.8 | 8.9 | 7.0 | 24.7 | 3.3 | 8.7 | | |
| 15 | | | | 0.9 | 0.1 | 9.0 | 34.8 | 31.0 | 60.1 | 30.3 | | 0.4 |
| 16 | | | | 0.7 | | 0.3 | | 9.1 | 8.9 | 3.9 | | |
| 17 | | | | | 0.7 | 10.3 | 8.4 | 12.7 | 6.4 | | 9.5 | |
| 18 | | | | 0.8 | | 2.4 | 24.4 | 54.9 | 13.8 | | 1.4 | |
| 19 | | 3.5 | | 39.6 | 0.3 | | | 0.8 | 46.5 | | 4.9 | |
| 20 | 0.3 | 7.0 | | | 2.5 | | | 32.2 | 8.7 | | 6.8 | |
| 21 | | 16.2 | | 3.6 | 29.3 | 19.7 | 6.1 | 18.7 | 6.5 | | | |
| 22 | | | | | 5.9 | 73.2 | 3.9 | 4.9 | 19.2 | 3.1 | | |
| 23 | | | | 6.1 | 2.8 | 23.0 | | 42.7 | 8.0 | 12.2 | | |
| 24 | | | | | 4.2 | 27.2 | 16.6 | 42.2 | 21.3 | | | |
| 25 | | | | 6.7 | 146.2 | 8.3 | 6.1 | 1.2 | 3.4 | 41.6 | | |
| 26 | 75.0 | | | 2.3 | 91.0 | 68.1 | | 26.8 | 1.3 | 15.5 | | |
| 27 | | | | 8.4 | 69.3 | 21.4 | 1.2 | 83.0 | 1.8 | 0.6 | | |
| 28 | | | | | 5.9 | 2.3 | 0.5 | 8.1 | 28.1 | | | |
| 29 | 6.8 | | | 4.1 | 16.2 | 7.4 | 4.8 | 14.2 | 10.3 | 1.6 | | |
| 30 | | | | 3.8 | 8.9 | 6.3 | 6.4 | 6.5 | 45.1 | | | |
| 31 | | | | | 1.5 | | 20.2 | 0.9 | | 3.1 | | |
| <hr/> | | | | | | | | | | | | |
| Total | 82.1 | 45.7 | 130.2 | 122.6 | 505.9 | 385.9 | 258.7 | 683.8 | 409.2 | 415.9 | 44.5 | 0.4 |

Annual Precipitation: 3084.9 mm

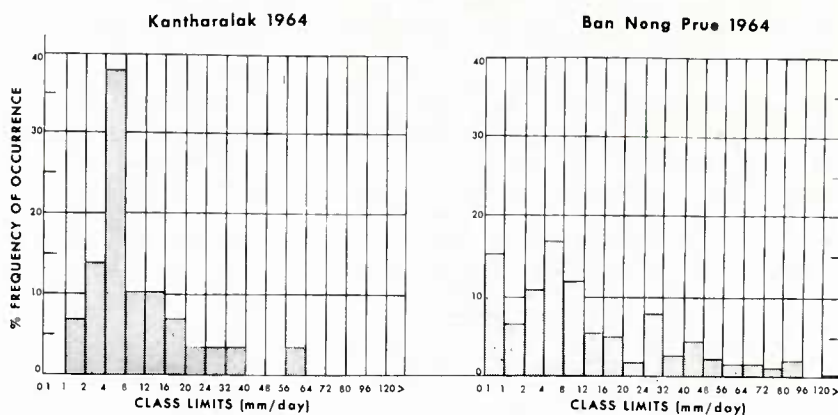


Figure 3 Percent Frequency Histograms of Daily Rainfall. The abscissae give classes of rainfall in unequal intervals, from 0.1-1.0 mm/day to > 120 mm

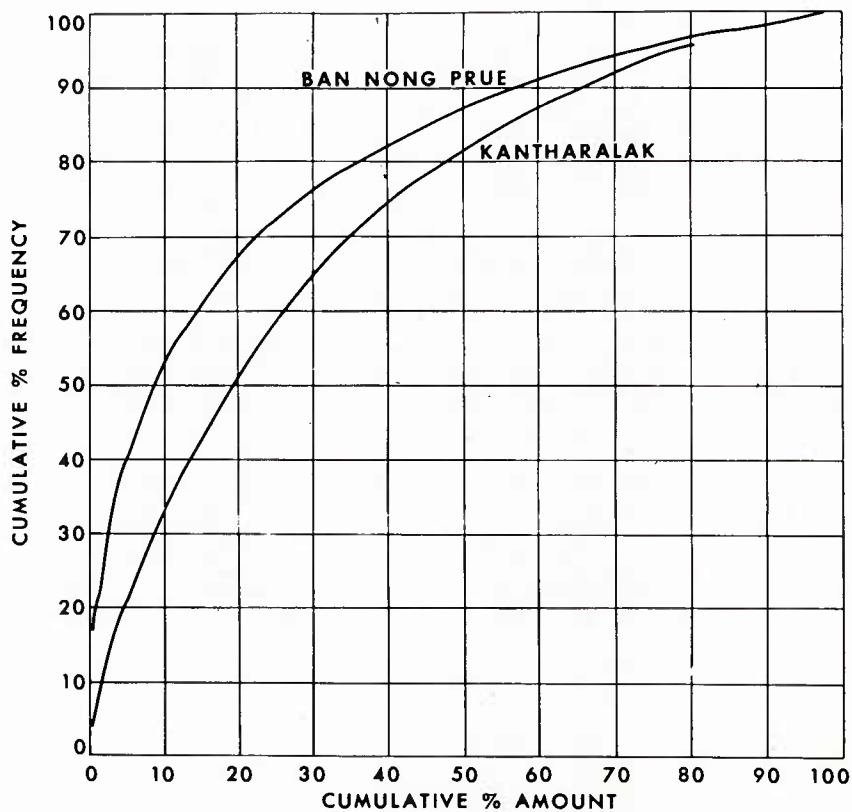


Figure 4 Annual Rainfall Curves for Ban Nong Prue and Kantharalak

2. Other stations

Except for Chiangrai in the northwestern highlands, and Loei in the northern highlands, most of the other stations are located in the Korat Plateau, where agricultural planning is beset with difficulties due to the unreliability of the rainfall. Station locations are shown in Figure 2.

In all, frequency counts of daily rainfall intensities were made for 13 stations, for the single years 1962-1964 [12, 13, 14]. For the individual station-years, a total of 29 cumulative percent frequency versus cumulative percent amount curves were drawn, represented by the six "types" in Figure 5. The system of typing was purely arbitrary, merely to facilitate the comparison of stations or to determine the annual variation at a single station. Curves #3 and #5 are interpolated, although #5 is nearly coincident with that for Srisaket 1963, while the other curves are "natural" distributions. Despite the fact that the stations selected had combinations of rain amounts and days in intervals between the initial extremes (Kantharalak and Ban Nong Prue), the resultant curves were not completely contained within the envelope provided by types #2 and #4: Type #2 (Fig. 1) has been substituted for Ban Nong Prue. Table 3, which gives observed and predicted values of daily intensities for a number of stations, also gives distribution types. A double number means the curve crosses over from one type to another, the first number referring to the upper 50 percentile. Of the 29 cases, over three-fifths were types #1 to #3, or an average of type #2; the rest approximated type #4, except for one of type #6.

On the basis of these observations, it was concluded that if daily observations were lacking, the universal distribution curve (type #2) could be employed for retrieving or estimating frequencies of daily rainfall intensities. For the Korat Plateau, the employment of this curve would tend to give a slight overestimate of intensities above the 50 percentile and an underestimate below.

3. Significance of distribution type

Whether the distribution types are specific for the stations or merely fluctuations of general rainfall sampling has not been firmly established. An argument in favor of the latter possibility is that the family of curves in Figure 5 is similar to other sets of rainfall distributions for various time intervals and conditions, based on data from either discrete or continuous rainfall, or from simulated storms [15, 16, 17]. While there was marked variation in distribution type at certain stations, as Phol and Srisaket, others as Loei had a curve each year that departed little from curve #2. However, the persistence of distribution types #4 to #6 at certain stations, as Srisaket and Chumpae, does seem to indicate a strong terrain effect evidenced by the unavailability of moisture for "light" precipitation. No matter what the annual rainfall, if no days of rain are observed with less than 5.0 mm, or even less than 1.0 mm, and the total number of rain days per year is about 50 or less, then the chances are high that the distribution type will be #4. In such cases, the corresponding P/D's are also relatively high, ranging from 18.0 to 38.0 mm/day (Table 3). Such "dry" stations are subject to intense daily rain, which is a function of P/D (Section IV).

It is apparent that the fewer the days of rain, the greater will be the burden on the single day of maximum to measure up to percent amount required to maintain the type #2 distribution. Except for Ban Thung Pene in 1964, nearly all stations with ≥ 100 days of rain had distribution types #1-#3, while most with < 60 days had types #4-#6. Consequently, the predictions in Table 3 would have been improved if a type #4 curve had been employed instead for all stations with < 60 days of rain per year.

TABLE 3: OBSERVED AND ESTIMATED* DAILY RAINFALL, THAILAND, 1962-1964

| STATION | Yr | Annual Rain (mm) P | Number Rain Days Per.Yr. D | Annual Average Daily Rain (mm/day) P/D | Type** Curve | Daily Rainfall (mm) at Indicated Percentile | | | | Number of Days (Frequency) of Indicated Intensity | | | | Maximum Daily Rainfall (mm) | |
|----------------|----|-----------------------|-------------------------------|---|-----------------|--|------|------|-------|--|-----|------|-----|-----------------------------|-------|
| | | | | | | 50% | | 90% | | 6mm | | 12mm | | | |
| | | | | | | OBS | EST | OBS | EST | OBS | EST | OBS | EST | OBS | EST |
| BAN NONG PRUE | 64 | 3085 | 183 | 21.1 | 2 | 8.0 | 8.5 | 47.0 | 55.0 | 108 | 109 | 70 | 78 | 142.2 | 148.0 |
| BAN THUNG PENE | 64 | 3387 | 145 | 24.2 | 4 | 9.1 | 9.7 | 57.0 | 63.0 | 127 | 92 | 93 | 66 | 140.6 | 196.2 |
| CHIANG RAE | 62 | 1219 | 121 | 10.1 | 2-1 | 4.2 | 4.0 | 26.0 | 26.2 | 56 | 51 | 36 | 32 | 85.5 | 85.5 |
| CHUMPAE | 64 | 1040 | 54 | 19.3 | 4 | 13.0 | 7.7 | 49.0 | 50.2 | 38 | 31 | 29 | 22 | 84.8 | 131.0 |
| KANTHARALK | 64 | 319 | 29 | 11.0 | 4 | 7.0 | 4.4 | 24.1 | 28.6 | 18 | 13 | 9 | 8 | 56.8 | 67.0 |
| KHON KAEN | 62 | 1232 | 103 | 12.0 | 1-2 | 5.0 | 4.8 | 26.1 | 31.2 | 52 | 47 | 35 | 31 | 112.9 | 96.0 |
| LOEI | 64 | 1259 | 141 | 8.9 | 2 | 3.2 | 3.6 | 23.9 | 23.0 | 57 | 55 | 35 | 33 | 102.3 | 75.5 |
| LOEI | 63 | 1129 | 147 | 7.7 | 2-1 | 2.9 | 3.1 | 22.0 | 20.0 | 56 | 53 | 34 | 29 | 81.3 | 63.2 |
| LOEI | 62 | 1007 | 126 | 8.0 | 2 | 3.2 | 3.2 | 19.2 | 20.8 | 53 | 46 | 28 | 26 | 60.7 | 65.5 |
| NANG RONG | 64 | 973 | 82 | 11.8 | 2 | 5.0 | 4.7 | 38.4 | 30.8 | 40 | 37 | 25 | 25 | 90.0 | 92.4 |
| P. PHISAI | 62 | 1615 | 75 | 21.5 | 2 | 11.2 | 8.6 | 47.0 | 55.8 | 49 | 45 | 37 | 32 | 208.2 | 161.5 |
| PHOL | 64 | 988 | 36 | 27.5 | 5-4 | 23.0 | 11.0 | 46.0 | 71.6 | 31 | 25 | 25 | 17 | 223.6 | 171.0 |
| PHOL | 62 | 1632 | 77 | 21.2 | 3-2 | 9.1 | 8.5 | 59.0 | 53.0 | 51 | 39 | 34 | 35 | 157.2 | 163.0 |
| ROI ET | 63 | 1697 | 111 | 15.3 | 1 | 4.8 | 4.6 | 32.0 | 29.8 | 53 | 50 | 33 | 33 | 140.2 | 124.0 |
| SRISAKET | 64 | 840 | 30 | 28.2 | 6 | 23.0 | 11.3 | 42.7 | 73.2 | 29 | 21 | 27 | 15 | 102.1 | 168.0 |
| SRISAKET | 63 | 1481 | 54 | 27.5 | 5 | 21.0 | 11.0 | 63.0 | 71.6 | 51 | 36 | 42 | 21 | 80.5 | 181.0 |
| SRISAKET | 62 | 1921 | 50 | 38.4 | 4-5 | 24.0 | 15.4 | 80.0 | 100.0 | 49 | 37 | 42 | 28 | 200.0 | 252.0 |
| UBOL | 62 | 2040 | 129 | 15.9 | 2 | 7.0 | 6.4 | 45.0 | 41.2 | 71 | 66 | 49 | 57 | 112.4 | 143.0 |

* Based on Curve # 2

** See Fig. 5

IV. Estimation of daily rainfall occurrence from annual data

1. Daily rainfall at any given percentile

Any selected daily rainfall, equal to or less than the maximum, represents a value attained at a specific percentile, y , for a given total annual precipitation, P , and number of rain days, D . Now if the annual distribution is represented by curve #2, then y may be readily determined, as follows

$$(1) x = \exp (A y)$$

$$(2) s_y = dx/dy = A \exp (A y)$$

$$(3) I_y = s_y (P/D)$$

$$(4) y = \ln (s_y / A) / A$$

where x = cumulative percent amount annual rain

y = cumulative percent frequency (rain days only)

I_y = daily intensity at the y^{th} percentile

$s_y = dx/dy$ = inverse of slope at y

$A = .04545$

To obtain y for other rainfall distributions, either different constants or other equations* might be employed in place of (1) and (2). Otherwise, s_y 's may be read directly from the curves as those in Figure 5. Table 4 contains such s_y values for curves #1-#6 for selected y 's.

Figure 6 is a nomogram for estimating y' , or $(100-y)$, the percent of rain days/year that a given daily rainfall, I_y , would be equalled or exceeded, given P and D . (Figures 6-10 are based on curve # 2). y' The actual frequency in number of days per year = $d = (y' D/100)$.

Figure 7 is a graph of s_y versus y or y' . It provides an alternate (simpler) method for deriving d from s_y for any daily intensity. In table 3 is given a comparison of estimated and observed d for I_y of 6mm/day and 12mm/day, respectively.

Estimates of I_y for the 50 and 95 frequency percentiles for annual average rainfall data (4-23 years) for Thailand are given in Figure 8. In this figure also are values of d , the number of days exceeding I_y , that is D_{50} and D_{95} , for I_{50} and I_{95} , respectively.

2. Maximum and extreme daily rainfall

A complete explanation for obtaining maximum or extreme rainfall for a known period has been given in an earlier report [1]. Briefly, if the percent frequency equivalent to one day of rain, that is $(100/D)$, is set equal to y' , the corresponding x' , or $(100-x)$ may be read from the appropriate curve in Figure 5. For a given total number of rain days per year, the maximum daily rainfall, $M = x' (P/100)$.

* Other equations for (1) from reference [1]

a) $x = y \exp B (y - 100)$

b) $x = A y \exp (B y)$

Figure 9 is a graph for estimating M in terms of x' or percent annual precipitation. In Table 3 are comparisons of estimated and observed values of M for a number of stations. For the single year 1962, for about 50 stations in Thailand (some of which are included in Table 3), three-quarters of the estimated maxima were within 20% of the observed maxima [19]. Figure 10 gives estimates of \bar{M} for Thailand for average annual rainfall of various lengths of time. (M is actually an average of the N -highest days, not necessarily distributed evenly over the N -years). The results are roughly similar to average maxima obtained for an unknown period.

It has been noted that despite the amount of annual rainfall, the daily maximum seems to reach a limiting value of about 1000 mm, or 40 inches [1]. Attempts to correlate maximum daily rainfall with total annual rainfall for 45 stations in Thailand in 1964 met with little success. From Figure 9, it is evident that the maximum daily rainfall per year, M is proportional to P/D , or

$$(5) M \approx k (P/D) \\ \text{where } k \approx (100-x) / (100-y) \approx x' / (100/D)$$

$$k \approx 8, \text{ for curve \#2, if } D > 50 \\ k \approx 5, \text{ for curve \#4, if } D > 20$$

Equation (5) may serve as an order-of-magnitude approximation for maximum daily rainfall.

V. Estimation of hourly intensities (clock hourly rainfall)

Since it has been shown previously [1] that the mass distribution of hourly rainfall (Fig. 1) is similar to that for daily rainfall, the prediction nomograms, Figures 6 and 7, may also be used for hourly rainfall, provided the ratio of hours to days, or H/D , is known. From data of days and hours of rain per year for a number of stations over the world [21], H/D was found to average 4.4. For 24 stations in Indonesia, an average $H/D = 3.5$, whereas for Jakarta alone, $H/D = 2.4$ [18]. For most stations, $H/D = 4.0$ would give a rough approximation of the relationship between hours and days, while $H/D = 2.0$ would perhaps be more reasonable for those tropical stations with exclusively convective showers. In Figure 6, the daily rainfall amounts were divided by 4.0 to give the scale for hourly intensities on the right. In order to employ equation (3), substitute $4.0 i_y$ for I_y , where i_y = hourly intensity at the y^{th} percentile. For tropical stations with only convective showers, multiply the right scale by 2, and use $2.0 i_y$ instead of I_y in equation (3).

The above procedure for obtaining hourly frequencies for a given P/D implies a constant H/D , regardless of the cumulative percent amount of annual rain, a situation which may not always hold true. At some stations, as Pensacola, Florida, H/D is relatively high for "light" rain. A comparison of daily and hourly distributions for single stations in Southeast Asia is yet to be made. However, hourly frequencies have been estimated for Saigon and Bangkok [20]. Methods which relate hourly frequencies to P/D for sets of hourly intensities [5] evidently incorporate a variable H/D . These methods give similar frequencies to those obtained here for hourly precipitation rates of $\geq .06$ inches if $H/D=5$, whereas for higher intensities, as $\geq .18$ inches, H/D seems to be < 4 .

In order to produce a more realistic scale for hourly intensities in Figure 6, it is necessary therefore, to determine the nature of the change in H/D with cumulative amount of rain.

VI. Summary

On the basis of daily rainfall observations in Thailand, it has been shown that the mass distribution of annual rainfall, when plotted as cumulative percent frequency versus cumulative percent amount, is similar to that found elsewhere. When short-term precipitation data are not available, a universal rainfall distribution curve may be employed

TABLE 4

S_y 's FOR CURVES #1-#6, FOR FREQUENCY PERCENTILES INDICATED

| Curve Type # | 50% | 75% | 90% | 95% |
|--------------|-----|-----|-----|-----|
| 1 | 0.3 | 1.1 | 3.0 | 4.0 |
| 2 | 0.4 | 1.3 | 2.6 | 4.0 |
| 3 | 0.5 | 1.4 | 2.4 | 3.5 |
| 4 | 0.7 | 1.3 | 2.3 | 3.2 |
| 5 | 0.7 | 1.2 | 1.9 | 2.6 |
| 6 | 0.9 | 1.1 | 1.7 | 2.2 |

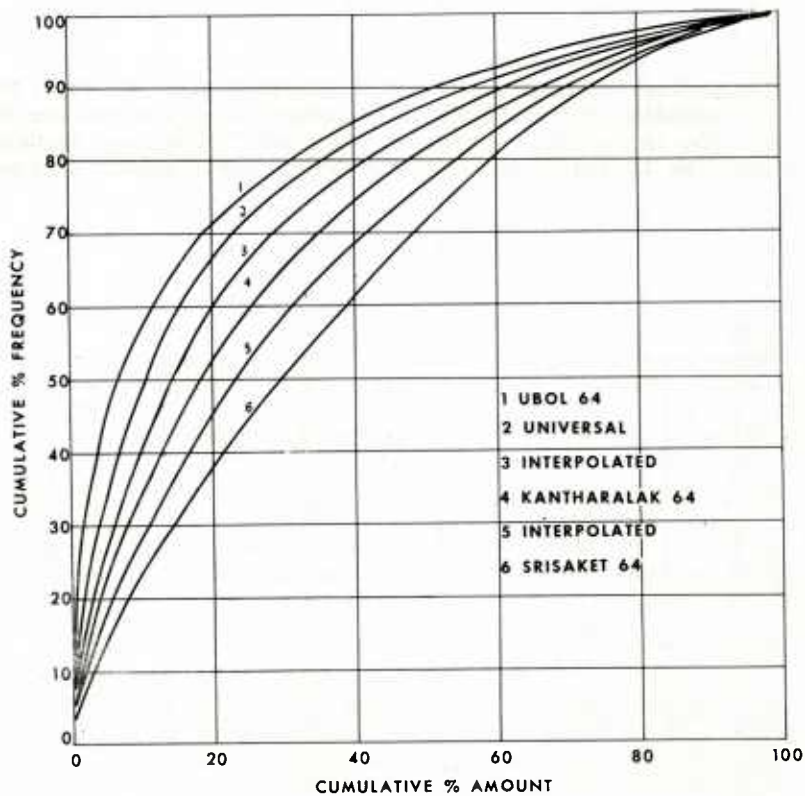


Figure 5 A Set of Rainfall Curves Representative of a Variety of Stations in Thailand

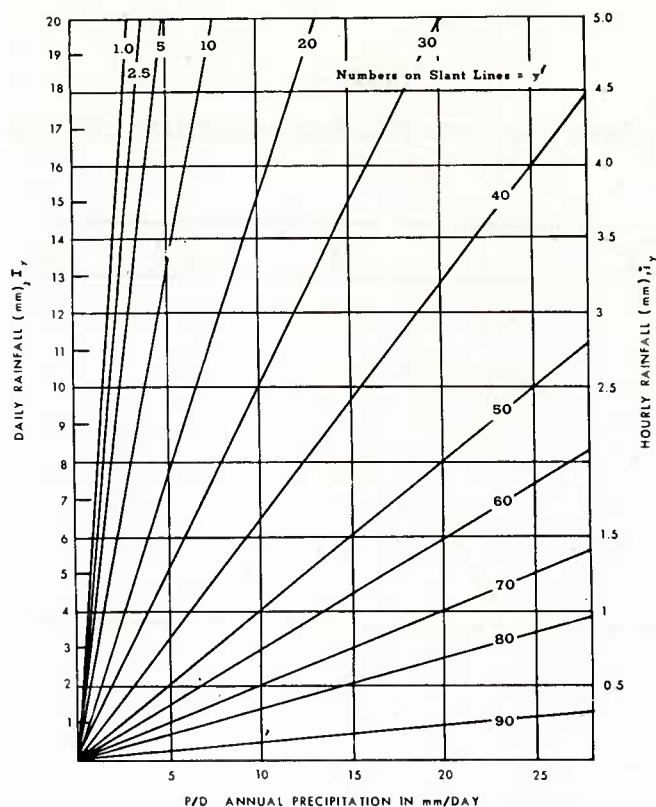


Figure 6 Nomogram for Estimating the Percent (y') of Total Rain Days per Year, with Intensities Equal to or Exceeding any Selected Daily Intensity, I_y , given the Annual Average Daily Intensity, P/D , in mm/day. (based on curve #2). (The same nomogram may be used for hourly intensities if H/D is about 4, and hourly distribution is similar to curve #2)

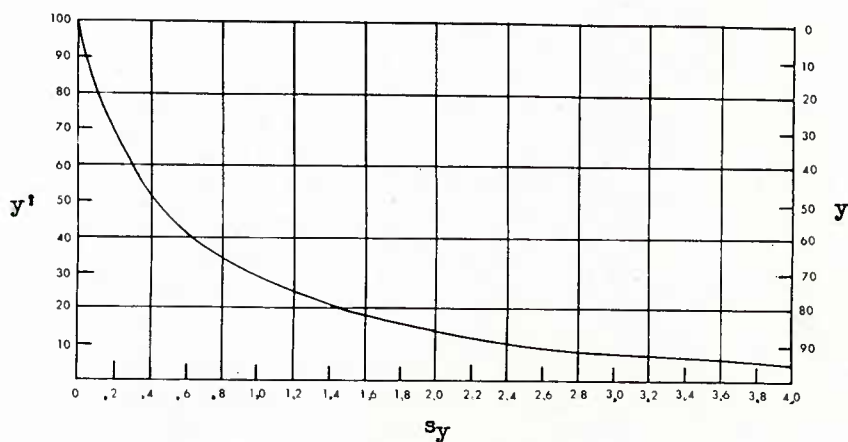


Figure 7 s_y versus y or y' (Based on curve #2)

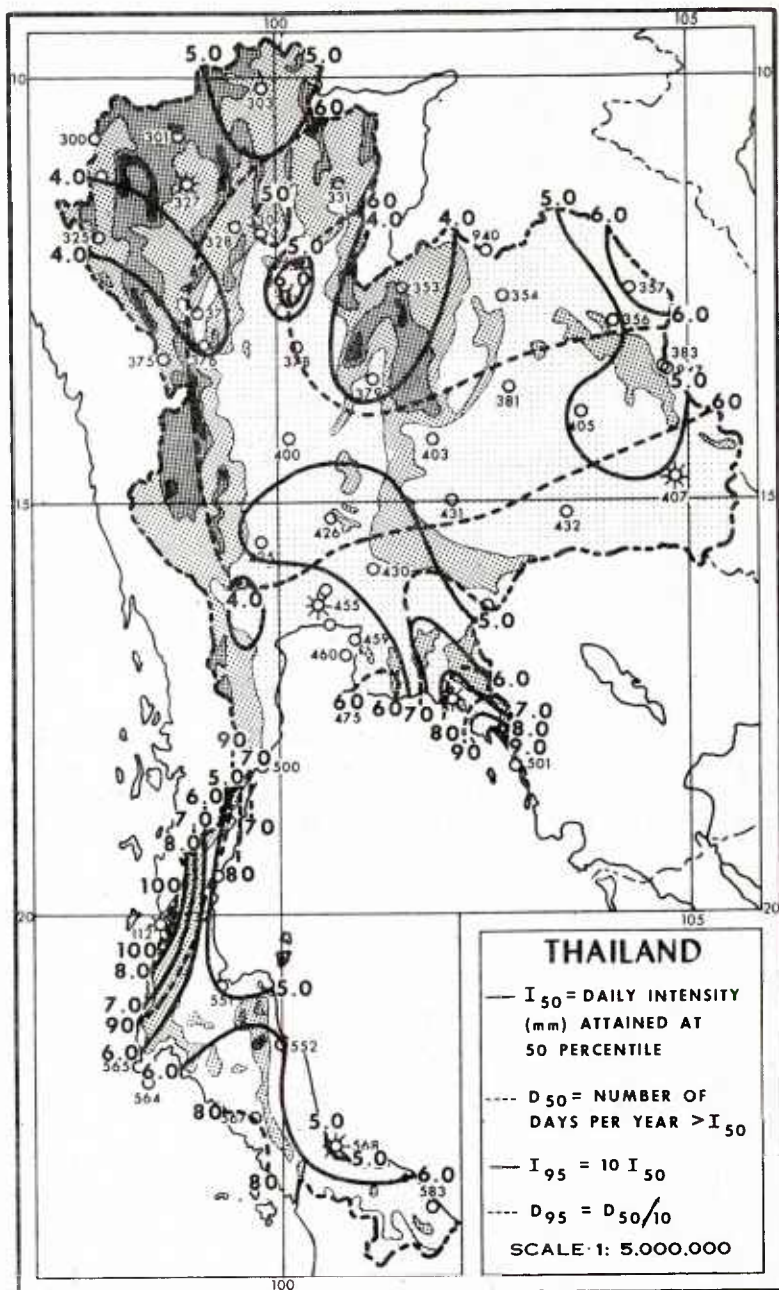


Figure 8 Estimate of Daily Rainfall Attained at the 50 and 95 Frequency Percentiles (rain days) and Number of Days on which Intensities Equal or Exceed Intensity Indicated. To obtain I_{95} multiply I_{50} by 10. To obtain D_{95} divide D_{50} by 10. (Based on curve #2)

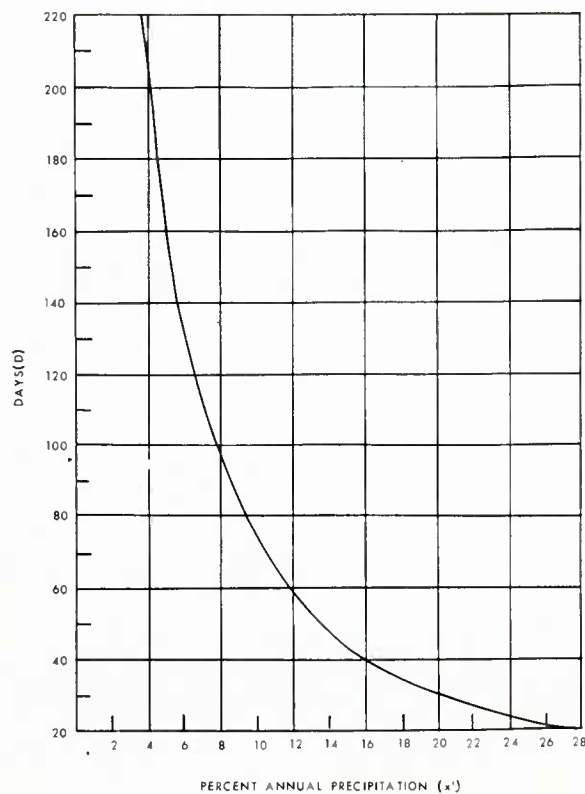


Figure 9 Graph for Estimating Maximum Daily Rainfall/Year in Terms of Percent Annual Rainfall, Given Days of Rain per Year (Based on curve # 2)

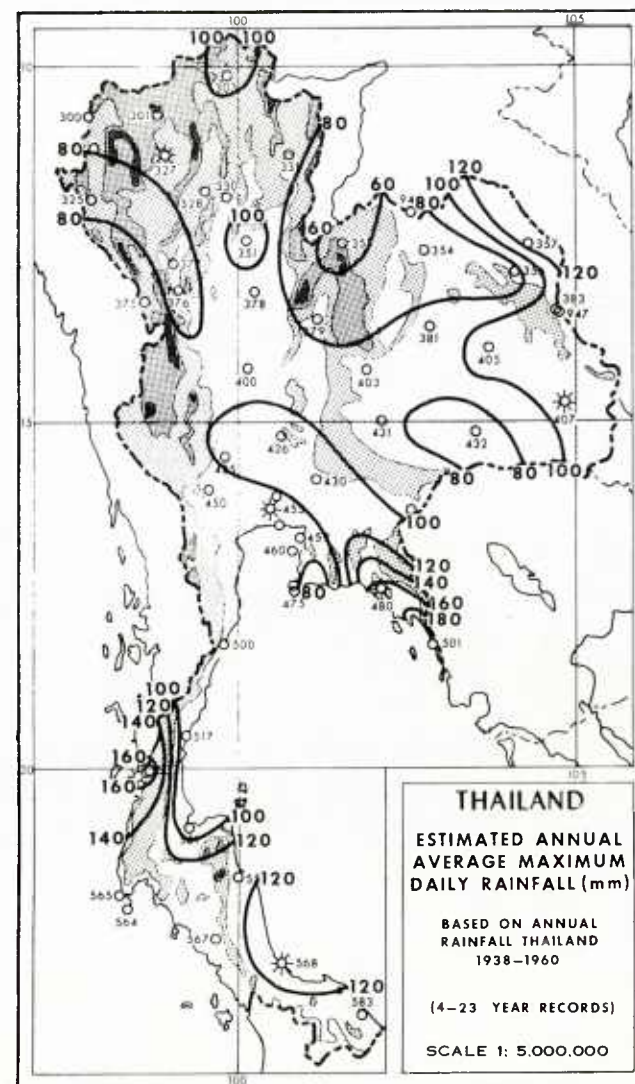


Figure 10 Estimates of Average Maximum Daily Rainfall (Based on curve # 2)

with annual data for the estimation of daily or hourly rainfall. For extremely dry stations, an alternate curve is suggested. The techniques offered here for the estimation of short-term precipitation are somewhat more flexible than those given previously. A wide variety of climates may be accommodated. Frequencies may be readily obtained for a considerable range of daily or hourly intensities. While the hourly estimates are somewhat speculative for Southeast Asia, they might be improved by the determination, for representative cases, of the variation of H/D with the cumulative amount of annual rainfall.

References and Bibliography

1. Griffiths, J. F., and Henry, W. K., and Martin, L. A.: Research on tropical rainfall patterns and associated meso-scale systems; Contact DA-36-039 SC 89202, Texas A & M University, College Station, May 1964.
2. Reihl, H.: Tropical Meteorology, 392 pp, McGraw-Hill, N. Y., 1954.
3. Olascoaga, M. J.: "Some aspects of Argentine Rainfall", Tellus, 2, 1950.
4. Russak, S. E., and Easley, J. W.: "A practical method for estimating rainfall frequencies directly from climatic data", Bulletin AMS, Vol. 39, pp 469-472, 1958.
5. Cole, A. E., and Donaldson, R. J.: "Precipitation", Handbook of Geophysics and Space Environments, Chapter 5-1, AFCL, 1965.
6. Wiley, S. C., Robison, W. C., Dodd, A. V., and Falkowski, S. J.: Environment of Southeast Asia; Environmental Protection Division, Natick QMR&D Laboratory; Report 219; 45 pp; August 1953.
7. Thompson, W. F.: Canal Zone Analogs II: Analogs of Canal Zone Climate in India and Southeast Asia; Environmental Protection Research Division, HQ QMR&E Command, U.S. Army; Technical Report EP-91; 24 pp; Natick, Mass.; June 1958.
8. Chambers, J. V.: An Environmental Comparison of Southeast Asia and the Island of Hawaii; Environmental Protection Research Division, HQ QMR&E Command, U.S. Army; Research Study Report RER-38; 33 pp; Natick, Mass.; January 1961.
9. Staff, Earth Sciences Division: Notes on Some Environmental Conditions Affecting Military Logistics in Thailand; HQ QMR&E Command, U.S. Army; Special Report S-1; 41 pp; Natick, Mass.; June 1962.
10. Sternstein, L.: The Rainfall of Thailand; Indiana University Foundation Research Division, Contract No. DA19-129-QM-1582; 149pp.; Bloomington, Ind.; 1962.
11. Riehl, H.: Southeast Asia Monsoon Study, Contract No. DA 28-043-AMC-01303 (E), Dept. of Atmospheric Science, Colorado State University, December 1965.
12. National Energy Authority, Thailand: Hydrologic Data Book 1964
13. National Energy Authority, Thailand: Hydrologic Data Book 1963
14. National Energy Authority, Thailand: Hydrologic Data Book 1962
15. Shands, A. L., and Brancato, G. N.: Applied Meteorology: Mass Curves of Rainfall, United States Weather Bureau Hydrometeorological Section Technical Paper No. 4, 56 pp, March 1948.
16. United States Weather Bureau Technical Paper No. 29-part 1- The Ohio Valley, Rainfall-Intensity-Frequency Regimes, 44 pp, June 1957.
17. United States Weather Bureau Technical Paper No. 29-part 2- Southeastern Section United States, Rainfall-Intensity-Frequency-Regimes, 51 pp, 1958.

18. Mohr, E. C. J., and Van Baren, F. A.: Tropical Soils, Interscience Publishers Ltd., London, 498 pp, 1954.
19. Monthly Meteorological Bulletin, Vol. 27, Parts 1-12, 1962, Office of the Prime Minister, Meteorological Department, Thailand.
20. Environmental Technical Applications Center, USAF, Report No. 5503: Precipitation Rate Relationships, 18 pp, June 1966.
21. Climatic Center, United States Air Force, Report No. 4100: Precipitation Attenuation at 8 Kmc - Final Estimates, 18 pp, February 1962.
22. Meteorological Station Records, Chanthaburi, Thailand.

THE TROPICAL ANALYSIS AND FORECAST OPERATIONS AT FWC, PEARL HARBOR

By
Major John G. Joern

I. ABSTRACT

An automated tropical analysis and forecast over the Pacific has been produced operationally in Hawaii since 1964. (Bedient and Vederman (1)). The original models were run at the Kunia Forecast Center on an IBM 704 and later converted to a CDC 1604 system. Data input was provided by manually produced punched cards and output distributed via teletype in the form of gridded winds and temperatures, and route wind factors and flight plans. No attempt was made by the center to manually modify the output. In 1965 the operation was moved to Fleet Weather Central, Pearl Harbor in cooperation with the Navy and Weather Bureau. The programs were converted to a CDC 3100 system and became operational in May, 1966, at which time the operation at Kunia ceased. Several important modifications to the programs and operations were initiated at FWC, Pearl. The grid area was extended to 90°W and 75°E longitude. The latitude strip from 37°N to 24°S remained the same as the Kunia model. An analysis and forecast are produced for six levels from 700 mb to 200 mb every six hours but the products are being distributed by teletype only at 12 hour intervals. The intermediate products are used in-house and by the USWB, Honolulu. Data input was modified to include paper tape from teletype repeaters, magnetic tape from autocollector circuits, and high speed data relay from Guam and Monterey.

Perhaps the most significant change in operations was the establishment of Quality Control Monitor teams. Personnel assigned to the teams are professional meteorologists trained in tropical analysis and forecasting. A team is on duty for each computer run. Its responsibility includes insuring maximum data input, error checking, a complete hand streamlining of each level of output, and preparation of correction messages. Their input to the machine is by punched card. The teams provide valuable feed-back to the Meteorological Systems Analysts and programmers assigned the task of improving the models as well as insuring high quality of the output products. One basic change to the original analysis model was incorporated after several months of operation at FWC. The original analysis scheme provided for computation of a stream-function between analysis scans with subsequent feed-back and a final stream function calculation to insure non-divergence. The

method used was found to be responsible for large wind errors, especially in data-sparse areas, near the boundaries, and in areas where erroneous data was not caught by either the program or the monitor team. Since the analysis is not used by a forecast scheme that requires non-divergence, the stream function calculations were abandoned and the scan radii tightened in an effort to represent the observed wind field more accurately. The monitor teams found this to be a distinct improvement since the effect of erroneous data became more obvious and fewer grid winds had to be corrected because there was no smoothing effect of the stream function to spread the error to surrounding grid points.

The forecast scheme used is patterned after Lavoie and Weideranders (2) and is described by Bedient and Vederman (1). Operational experience to date indicates the 24 hour forecast verifies slightly better than persistence. A barotropic forecast model is currently being tested at FWC and a continuing climatological update program has been initiated.

The output format of both the analysis and forecast is the teletype "paper doll" gridded winds and temperatures on 1/20M scale prepared in six strips. These are transmitted to detachments throughout the Pacific and Southeast Asia. For in-house and local use on the island of Oahu, the gridded winds are plotted in wind-barb format on a Calcomp plotter for easy hand analysis. This is the major tool used by the monitor teams and USWB forecasters at Honolulu International Airport in preparation of flight folders. Route zonal wind factors and temperatures are also computed for all major Pacific flight routes. These are provided to the forecaster at Hickam and serve as a supplement to the MAC flight plan product.

There are two programs in the final stages of development at FWC, Pearl. A surface analysis over the same grid as described above is scheduled for operations during the third quarter of 1967. Also, a fine-mesh 850 mb analysis over Southeast Asia is in the final stages of testing. Decisions on the output format and distribution of these products have not yet been made.

A presentation of five papers describing operations and developmental programs of the tropical team at FWC, Pearl is scheduled for

the National AMS meeting at Monterey, California in October - November 1967. Specific details of the operations and new techniques will be described and published as indicated by authors.

REFERENCES

- [1] Bedient, H. A., and Vederman, J.:
"Computer Analysis and Forecasting in

the Tropics", Monthly Weather Review,
Vol. 92, No. 12, Oct. 1964, pp. 565 -
577.

- [2] Lavoie, R. L., and Weideranders, C. J.:
"Objective Wind Forecasting over the
Tropical Pacific", University of Hawaii
Institute of Geophysics, Meteorology
Division, Scientific Report No. 1,
Contract No. AF 19(604)-7229, AFCRL-
TN-60-832, Dec. 1960.

DIURNAL STUDIES OF TIROS VII 8-12μ "WINDOW"
RADIATION OVER INDONESIA AND MALAYSIA†

by

Earl S. Merritt

Allied Research Associates, Inc.

Virginia Road, Concord, Massachusetts

ABSTRACT

TIROS VII 8-12μ "window" investigations of the diurnal variation in cloudiness over Indonesia and Malaysia during June-September 1963. This study revealed a pronounced semi-diurnal cloud cycle with maxima at 0600L and 1800L and minima at 1200L and 2200L over land areas. Ocean areas revealed a similar cycle but the amplitude of the variation was much smaller than that over the land.

I - Introduction

The Indonesian region (shown in Fig. 1) is well known for its extensive cloudiness. During much of the year transient disturbances, moving along the ITCZ/ETZ, influence the production of these clouds. During the period from late June through to late September, however, most of the cloudiness appears to be related to the land and sea wind regimes, and to heating of the land surface. A study of the area, using TIROS IV, was prepared by Saha [3]. His study, for April and May concluded:

"...However, in the light of evidence furnished by the TIROS radiation data, we may conclude that, given a synoptic situation in the equatorial trough zone, we may expect to see cloud towers growing preferentially over large land masses and islands within this zone; particularly in such areas where there are mountain ranges normal to the prevailing wind and relatively little or moderate vertical cloud growth over the wide ocean areas, except, perhaps when the latter areas are disturbed by an activation of the equatorial trough or by such synoptic disturbances as depressions or tropical storms."

This result is very similar to an earlier statement by Palmer et al., [2]:

"About mid-day, even though there may be little cloud over the sea, large cumulus will have built up to a height varying between 8,000 and 15,000 feet above the mountain crest, depending on the latitude of the island and its position with respect to the semi-permanent oceanic highs. Already rain will be falling on the windward side of the mountain chain, and, as the afternoon progresses, the cumulus will spread horizontally along the chain and over the leeward slopes. At the same time the tops will grow into the higher atmosphere. Depending upon the latitude, time of the year, and other factors which need not be elaborated here, the tops, reaching their maximum development towards the middle of the afternoon, may grow to as little as 16,000 feet or to as much as 45,000 feet. If cumulonimbus is produced by this process, it may be accompanied by thunder and lightning, and, towards the latter part of the afternoon, will give rise to a great variety of clouds, such as altostratus, altocumulus, stratocumulus and various types of cirrus. From time to time, incipient cumulonimbus cells may become detached from the peaks and drift over the leeward side of the island; if this occurs, sporadic and isolated thunderstorms will briefly strike stations situated on the leeward plain and may even affect the neighboring sea downwind. By 7:00 or 8:00 P.M., the lower portions of the orographic cumulus, or cumulonimbus, will have vanished. Patches of cloud at the

†

The studies reported on here were supported by the National Aeronautics and Space Administration, Laboratory for Atmospheric and Biological Sciences, Goddard Space Flight Center, under Contract No. NAS 5-10151.

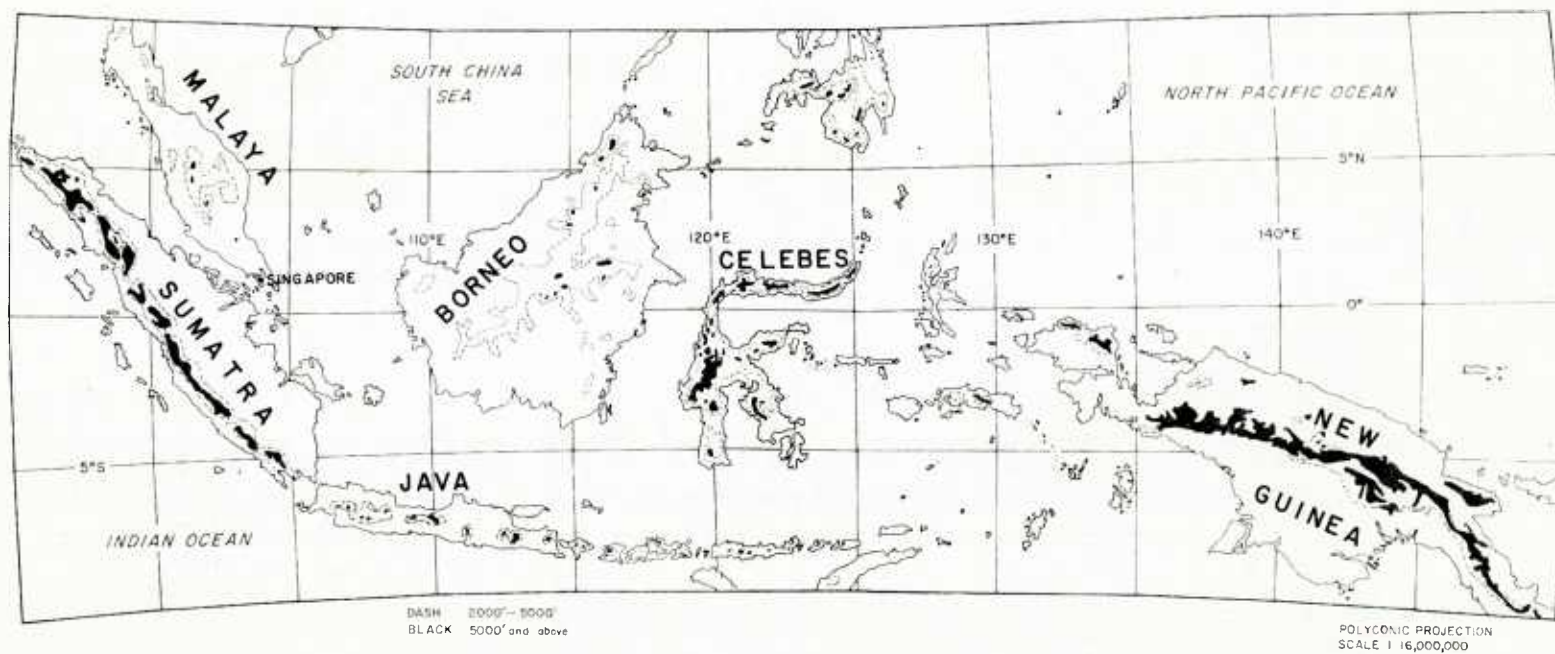


FIGURE 1. MAP SHOWING INDONESIA, MALAYSIAN AREA OF INTEREST

altocumulus and cirrus level, however, may persist. At the same time, or a little later, cumulus will be observed forming in a line parallel with the coast, usually on the leeward side. By about midnight, this oceanic cumulus will be quite evident to an observer on the leeward shore, and its dimensions and structure can be easily explored by aircraft on a moonlit night. If the diurnal cycle of convection is extreme, the oceanic cumulus will continue to grow during the night, reaching maximum dimensions just before dawn. Therefore, an aircraft taking off before dawn from a leeward airfield may find itself involved with a nocturnal thunderstorm off-shore at a distance between five and twenty-five miles, depending upon the terrain, season, etc. The mountain peaks may be quite clear of cloud at this time. Isolated cumulus or cumulonimbus accompanied by showers, may drift toward the land from the pre-existing line, so that a leeward station may have a secondary maximum of showers between 6:00 and 9:00 A.M. local time. By 10:00 A.M., the off-shore cloud will usually completely disappear and the first orographic cumulus will begin to build up on the peaks; then the cycle is repeated with varying intensity, depending on the synoptic situation. During the whole of this cycle, the cloud over the open sea may show very little variation."

Studies by LaSeur and Garstang [1] over a much smaller island, Barbados (West Indies), show a semi-diurnal variation in cloud amount, but greatly influenced by the synoptic situation.

As discussed below, the TIROS VII analyses show a semi-diurnal cycle, similar to that described by LaSeur and Garstang [1].

1.1 Philosophy of Approach

The approach employed was to analyze all useful TIROS VII observations over the area for a four month period, June-September 1963. The regression of the nodes of the TIROS VII orbit provides a slow progression of the local time of observation. Selection of those analyses from which the diurnal cycle can be derived has been accomplished subjectively, with reference to appropriate climatologies of the region.

Selection of the period June-September 1963 was determined by the requirement to define a diurnal cycle of free and forced tropical island convective cloudiness, i.e., the convective cloudiness produced through solar heating of the land surface or by the influence of the island boundary on the ambient wind, not that due to variation in the velocity field associated with major transient disturbances. The period selected is reasonably free of transient disturbances, since the ITCZ/ETZ is normally displaced well to the north of 10N.

II - Data Processing and Analysis

2.1 Data Processing

The data used in the analyses were selected from the TIROS VII Radiation Data Catalog and User's Manual, Vol. 1, for 19 June-30 September 1963 [6]. Case selection was guided by review of the available TIROS VI and VII photographs, and inferences from synoptic analyses of the area. The cases selected for use were chosen as periods free of transient cloud influences. However, some cases of minor transient influences may have been inadvertently included.

The majority of the analyses were prepared from single open mode data, with closed and alternating mode data used, when necessary, to assure complete coverage. Orbits for which data were computer mapped and manually analyzed are summarized in Table 1.

2.2 Analysis Procedures

The orbits listed in Table 1 were processed on an IBM 7094, and printouts prepared on an IBM 1460. Program control was accomplished through the NASA Mercator Mapping Program (MSC-2) (Staff Members, GSFC, 1962 [5]) using a scale of 1:2,500,000. Nadir angles were limited to less than 60°. No correction was made for limb darkening. Consideration was given, however, to correlations due to overall sensor degradation, and to floor-wall asymmetries. Data listings were used, to a limited extent, to assure proper data spot locations and reasonable swath lengths, (for discussion see Sherr [4]).

Table 1
List of TIROS VII 8-12 μ Analyses

| | Sumatra Malaysia Java | Borneo Celebes | New Guinea |
|-----|------------------------------|-----------------------------------|---------------------------------|
| LST | | | |
| 24 | | 181 | 1289 |
| 23 | | 802 | 151 |
| 22 | <u>240</u> , 802, 831 | <u>239</u> , <u>254</u> | 224, 282 |
| 21 | 313, 846 | 312, 1436 | <u>238</u> , <u>311</u> |
| 20 | 342, 875, 919 | 341, <u>904</u> , 1480 | |
| 19 | 948, 963, <u>1481</u> | | |
| 18 | <u>459</u> , 977, | <u>444</u> , 458 | |
| 17 | | 502, 517 | 501, <u>516</u> |
| 16 | 532, 1094 | 531, 560, 561 | |
| 15 | 029, 605, <u>1123</u> , 1138 | <u>575</u> , 1152 | <u>530</u> , 559, <u>574</u> |
| 14 | 634, <u>1211</u> | 662, 1196, <u>1225</u> | 603, 632 |
| 13 | <u>1284</u> | 706 | |
| 12 | 175, 751, <u>1269</u> | 735, <u>736</u> , 765, 1266, 1298 | 705 |
| 11 | 780 | 779, 794 | 749, <u>793</u> |
| 10 | 277, 309, <u>853</u> | 808 | <u>837</u> |
| 09 | 306, <u>882</u> | <u>838</u> | <u>851</u> , 895, |
| 08 | 911 | 881, 896, <u>1473</u> | <u>939</u> , 968 |
| 07 | 940 | 910, 925, <u>954</u> , 969 | <u>909</u> |
| 06 | <u>452</u> , <u>984</u> | <u>437</u> , 983 | <u>953</u> |
| 05 | | | |
| 04 | 569, <u>1101</u> | 554, <u>1101</u> , 1159 | 005, <u>1099</u> |
| 03 | 1130 | 006, 035, <u>1188</u> | <u>034</u> , 1143 |
| 02 | 627, 1203, 1918, <u>1291</u> | 1246 | |
| 01 | | <u>729</u> | <u>1216</u> , 1245, <u>1304</u> |
| 00 | <u>744</u> , <u>1276</u> | 152 | |

III - Diurnal Temperature Variation

3.1 Procedure

In order to obtain a quantitative presentation of the diurnal TIROS VII 8-12 μ "window" temperature cycle, averages were obtained from the analyses (not presented) composited at two hour intervals. These averages were obtained for each island, and for selected ocean areas. Figure 2 shows these areas.

The procedures followed in each case were: (1) divide the area into small subsections of approximately equal size, (2) obtain an estimate of the average TIROS VII "window" temperatures in each subsection, and (3) average the estimates from each subsection to obtain a mean. Additional mean values were obtained from processed analyses not included in the composite analysis.

3.2 Examples

Figure 3 presents the curves [†] of diurnal 8-12 μ "window" temperature variations for some of the areas in Figure 2, and for an overall mean of the entire analysis area. Notice the general tendency for a semi-diurnal variation, with temperature minima (cloudiness maxima) at 0200-0800 LMT (Local Mean Time) and 1600-2000 LMT, and temperature maxima (cloud minima) at 1200-1400 LMT and 2200-2400 LMT. It is obvious that random selection of analyses has introduced non-representative, noisy data into the sample. In spite of these non-representative data, significant similarities exist among the various island and ocean areas. Figure 4 presents three-hourly running means for an island (Sumatra), the ocean and an overall mean. These indicate the overall pattern quite dramatically.

IV - Land Area Versus Oceans

Comparison of the variations in "window" temperatures over an ocean area (Fig. 3E; area E in Fig. 2)[‡] and an adjacent land area such as Sumatra (Fig. 3A; area A in Fig. 2) dramatically reveals the land control of free and mechanically forced convection within the analysis area. Averaged "window" temperature differences of nearly 30°K exist during the 1600 LMT minimum, in spite of the oscillations in the curves. Figure 4 reveals the differences in a more dramatic manner.

V - Summary Discussion of Possible Causes of the Observed Cycle

The causes of diurnal variations in cloudiness and precipitation, over small islands and the open sea, were discussed by LaSeur and Garstang [1] as follows:

"A complex relationship apparently exists between the synoptic scale system and land effects . . . A tentative suggestion seems to be that the obstacle effect plays a major role in the production of cloud and precipitation. This and other interactions may explain why studies based upon observations taken on land have not shown a semi-diurnal or even diurnal cycle, while, from time to time, studies made over the oceans or atolls have demonstrated the existence of such cycles...

[†] Uncorrected for floor/wall differences, and sun phase related response variations. Analysis of the sun phase variation has indicated that these variations do not influence the overall appearance of the curves.

[‡] A difference in response between floor and wall sensors (observed by NASA, GSFC; TIROS VII Radiation Data Catalog and User's Manual, Vol. III; and by Mr. Krishna Rao of the National Environmental Satellite Center of ESSA) has been noted. Studies had indicated that, from day of launch, wall measurements were 3-5°K higher than similar floor measurements. Floor measurements over the Indonesian area occur between 0600 LMT and 1800 LMT, and wall measurements between 1800 LMT and 0600 LMT. Thus the ocean area diurnal curve can be used as a coarse check on this value. After correction for (1) symmetrical degradation and (2) the apparent sun phase related response variations, the mean wall sensor measurements appear to be no more than 1°K higher than the floor measurements. Possible sources of error in this estimate are (1) the influence of diurnal cloud variations, i.e., the 2200 LMT temperature maxima feature in all diurnal curves; and (2) the limitation of the data record length.

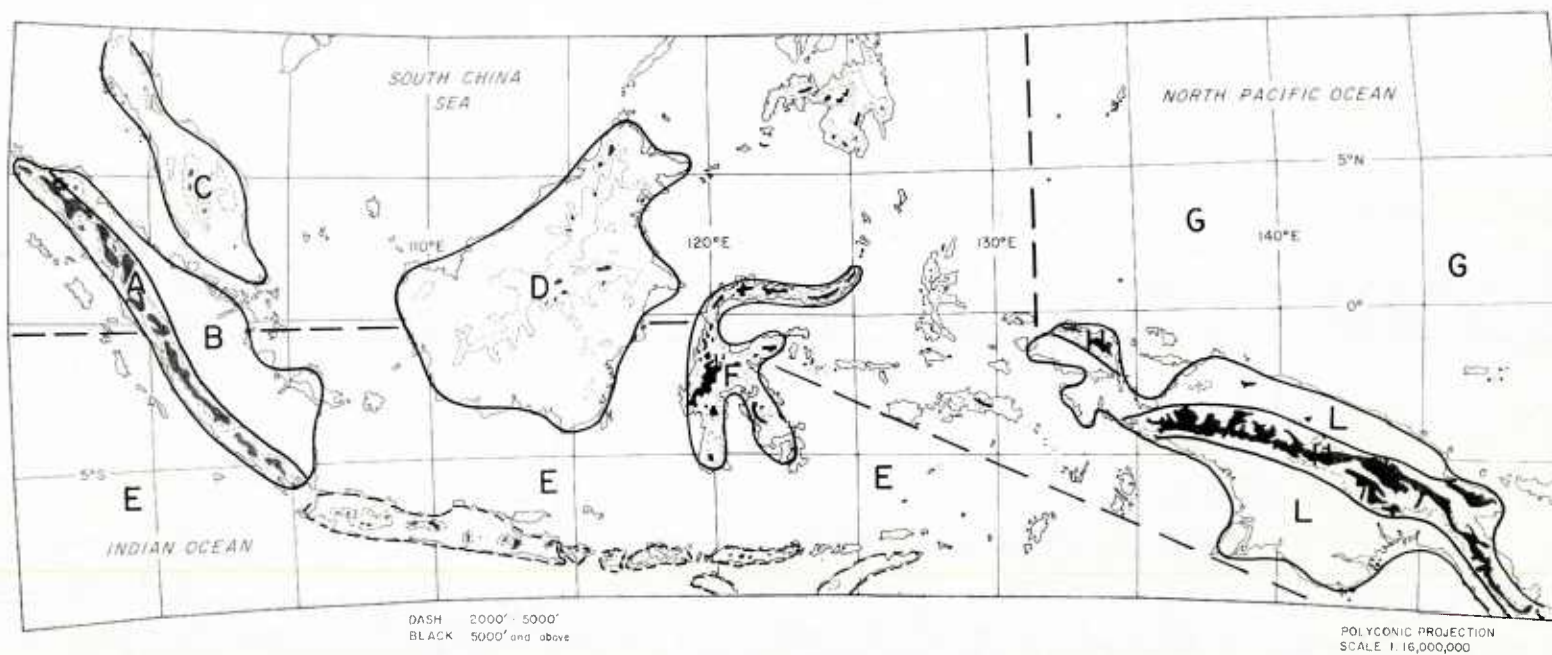


FIGURE 2 AREAS USED FOR PREPARATION OF DIURNAL TEMP. VARIATIONS - (REF. FIGS. 3 and 4)

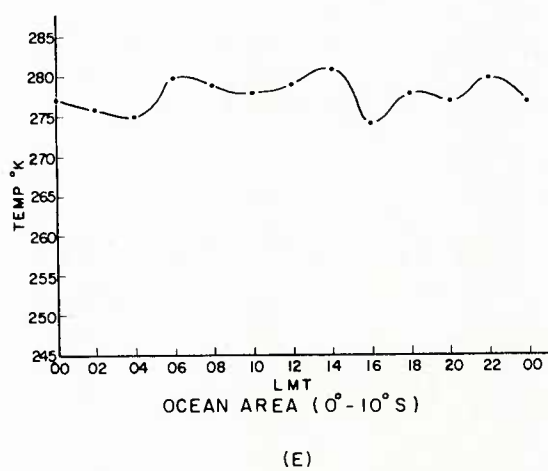
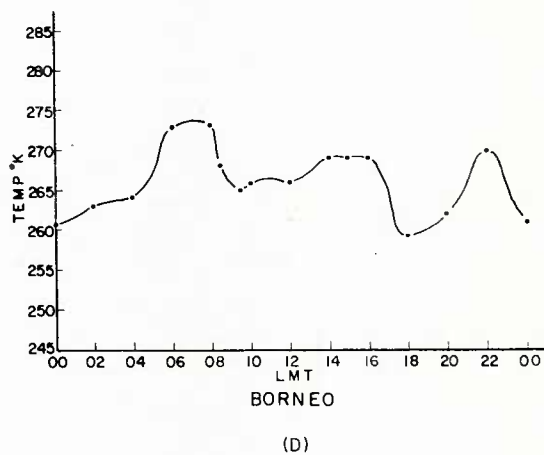
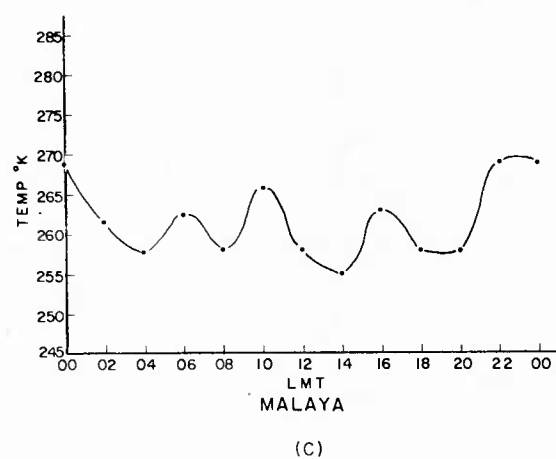
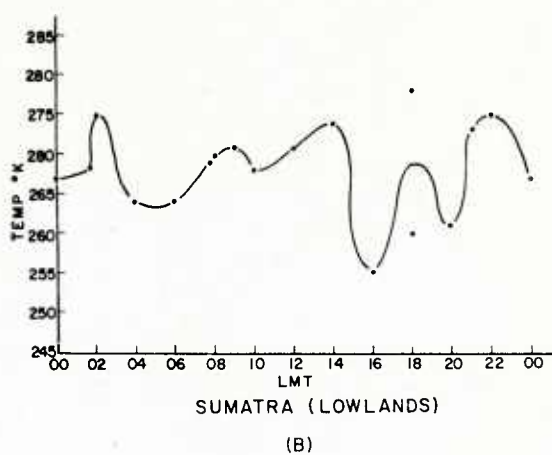
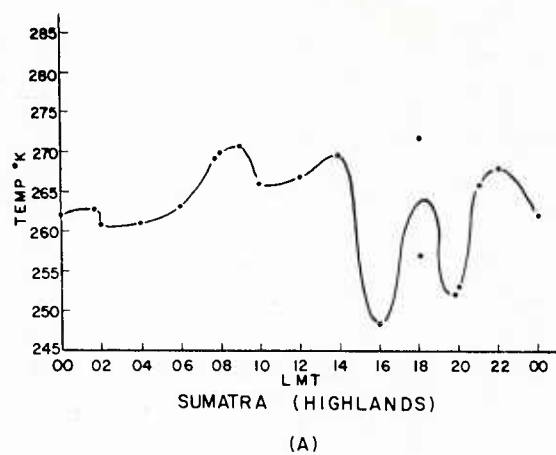


FIGURE 3 DIURNAL VARIATION OF TIROS VII 8-12 μ AVERAGED TEMPERATURES

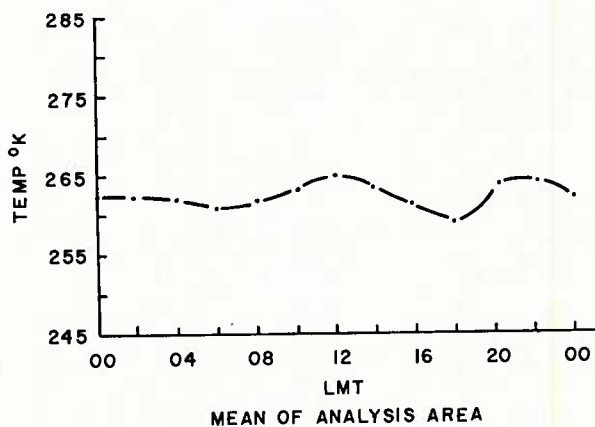
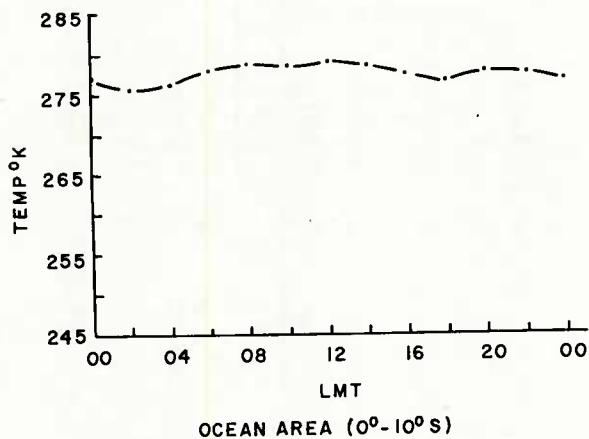
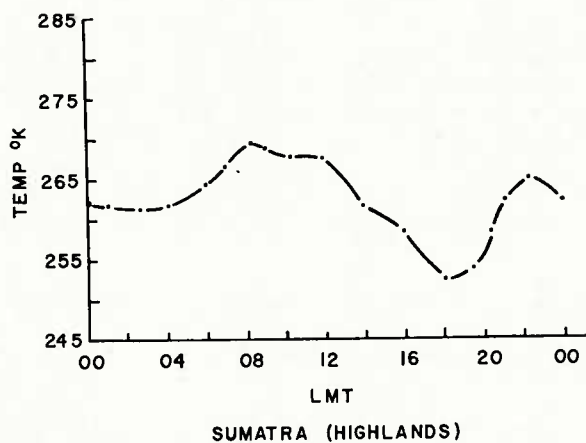


FIGURE 4 THREE-HOURLY OVERLAPPING AVERAGE TIROS VII 8-12 μ TEMPERATURES

" . . . there seems to be at least three mechanisms involved in producing the observed distributions of precipitation and cloudiness over the open ocean. A diurnal cycle can be produced by at least two mechanisms:

- "i. solar radiation: the effect may be to inhibit cloud growth over the ocean during the day (through absorption of solar energy by water vapor). . . and to enhance cloud growth at night through cooling . . .
 - "ii. sensible heat transport: while this is related to radiation, it depends largely upon the out-of-phase relationship between air and sea surface temperature. It is also related to any diurnal variation in the wind speed as will be described in the next paragraph.
- "The semi-diurnal cycle appears to depend upon at least one recognizable mechanism:
- "iii. the atmospheric tide: this mechanism, which is directly related to the semi-diurnal pressure oscillation, is called upon to produce a response in the wind field which produces the required divergence to create a semi-diurnal cycle in precipitation."

The TIROS VII 8-12 μ "window" curves presented in Figures 3 and 4 can be explained in terms of the LaSeur and Garstang mechanisms. Variations in the area northeast of New Guinea, however, would appear to fall outside these explanations unless the atmospheric tide mechanism can be assumed to produce large enough variations in the velocity field to influence dynamically forced cloudiness areas. This speculation deserves further study.

References

1. LaSeur, N., and M. Garstang: Tropical Convective and Synoptic Scale Weather Systems and Their Statistical Contribution to Tropical Meteorology, Final Report, Grant Nos. DA-SIG-36-039-62-G23 and DA ARO 49-92-63-G23, Florida State University 1964.
2. Palmer, C.E., C. Wise, L. Stimpson, G. Duncan: The Practical Aspect of Tropical Meteorology, Air Weather Service Manual 105-48, Vol. I, 1955.
3. Saha, K.R.: A Contribution to the Study of Convection Patterns in the Equatorial Trough Aone Using TIROS IV Radiation Data, Technical Report No. 74, Dept. of Atmospheric Science, Fort Collins, Colorado, 1966.
4. Sherr, P.E.: "Some Problems in Using TIROS Radiation Data as Filed on Final Meteorological Radiation Tapes," Proc. 4th Symposium on Remote Sensing of Environment, University of Michigan, Institute of Science and Technology, 1966.
5. Staff Members, Goddard Space Flight Center: TIROS III Radiation User's Catalog, National Aeronautics and Space Administration, Greenbelt, Maryland, 1962.
6. Staff Members, Aeronomy and Meteorology Division: TIROS VII Radiation Data Catalog and User's Manual, Vol. 1, NASA, GSFC, Greenbelt, Maryland, 1965.

SHORT RANGE, SUBSYNOPTIC SURFACE WEATHER PREDICTION

Harry R. Glahn and Dale A. Lowry

ESSA, Weather Bureau, Techniques Development Laboratory
Silver Spring, Maryland

ABSTRACT

An on-going program within the Techniques Development Laboratory of the Weather Bureau to develop an operating system for making objective forecasts of weather variables on a space scale of approximately 50 miles and a time scale of 1 hour up to about 18 hours is described. The system will consist of a combination of numerical (dynamic) and statistical models. Precipitation and cloudiness forecasts for the "Today" period, 7:00 A.M. to 7:00 P.M., over the eastern United States are receiving primary emphasis. Intermediate products are hourly sea level pressure forecasts valid between 7:00 A.M. and 7:00 P.M.; it appears these forecasts are superior to the sea-level pressure guidance forecasts presently available within NMC.

In this paper we will describe an on-going program within the Techniques Development Laboratory of the Weather Bureau to develop an operating system for making objective forecasts of weather variables on a space scale of approximately 50 miles and a time scale of 1 hour up to about 18 hours. Our primary interest is in precipitation forecasting as indicated in Table 1. Other variables of interest are also shown. Since numerical models do not forecast some of the variables directly and do not produce probability forecasts which the Weather Bureau is emphasizing, we chose to use a combination of numerical and statistical techniques.

VARIABLES TO BE PREDICTED

PRIMARY

1. Precipitation
 - a. Probability of occurrence at a particular time
 - b. Probability of occurrence over a specified period
 - c. Estimate of beginning and ending times
 - d. Estimate of amount over a specified period
 - e. Forecast of type - - liquid or frozen.
2. Cloud Amount.

SECONDARY

1. Sea level pressure pattern
2. Surface winds
3. Surface temperature
4. Surface relative humidity
5. Ceiling
6. Visibility.

Table 1. Weather variables for which objective forecast techniques will be devised.

In order to make the problem of manageable size, we are concentrating on the "Today" period of forecast, 7:00 A.M. to 7:00 P.M., for the eastern part of the United States. A forecast for this period is issued by local offices about 4:30 - 5:00 A.M. and guidance must arrive there by about 4:00 A.M. We are using 0800 GMT (3:00 A.M. EST) hourly data as input, but if this technique were implemented we might have to use 0700 GMT data in order to meet communication schedules.

A 39 x 40 grid shown in Fig. 1 is used which has a grid length of $1/4$ that used at NMC. This grid length is about 50 miles and is not much different from the average spacing of hourly reporting stations in the eastern and central United States.

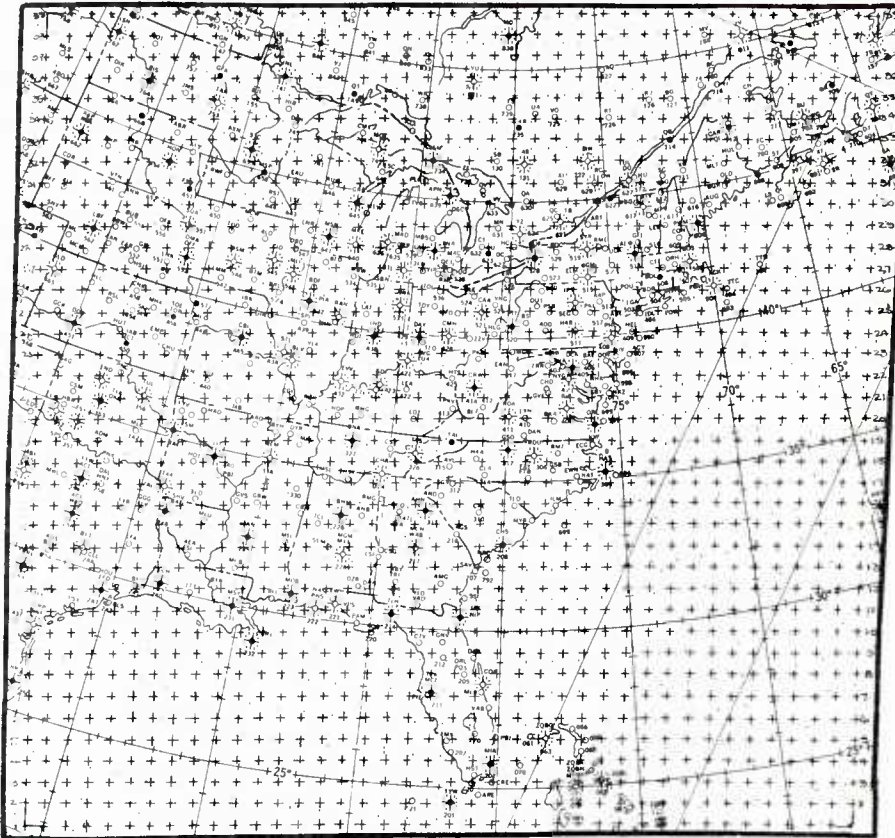


Fig. 1. The 39 x 40 grid used in the study.

We are using at the present time a 1000 mb. prediction model much like that developed by Reed* and used at NMC for several years. Computations are done in a Lagrangian framework. The prediction equation is shown below:

$$(1) \quad Z_{\cdot}^{fd} = Z_{\cdot}^{iu} + .55 (Z_{\cdot}^{fd} - Z_5^{iu}) + (G^d - G^u) - (M^d - M^u)$$

Where Z_{\cdot} = 1000 mb height
 Z_5 = 500 mb height
 G = Latitude term
 M = Terrain term
 fd = Forecast value at downstream point
 iu = Initial value at upstream point.

* Reed, R. J.: "Experiments in 1000 mb Prognosis." NMC Tech. Memo No. 26, 36 pp, 1963.

The only change we have made in the model as originally formulated was in the use of a smoothed rather than an unsmoothed 500 mb advecting wind. We smooth the 500 mb height field by setting the height at each grid point equal to the average of the 25 NMC grid points centered at that grid point. Then 55% of the geostrophic wind computed from this smoothed field is used as the advecting wind. By using the smoothed wind, the blowup of the highs has been greatly reduced and the shape of the "teardrop high" has been improved. This simple change resulted in an improvement of 12% in S1* scores for 15 test cases of 12-hour forecasts made in 1966. It is not known how this change would affect longer, say 36-hour, forecasts.

The precipitation model is very similar to the SLYH** model developed by Sanders, LaRue, Younkin, and Hovermale and used for a time at NMC. The prediction equation is

$$(2) \quad S_d^{fd} = S_d^{iu} - 2(h_5^{iu} - h_5^{fd}) + (PMA^u - PMA^d)$$

Where S_d = Saturation deficit
 h_5 = 1000 - 500 mb thickness
PMA = Terrain term
fd = Forecast value at downstream point
iu = Initial value at upstream point.

The advecting wind is a combination of the 500 mb and 1000 mb winds; we are currently using 33% of the 500 mb smoothed geostrophic wind plus 50% of the smoothed 1000 mb geostrophic wind. The moisture variable is the saturation deficit defined as

$$(3) \quad S_d = h_5 - S_T$$

Where S_T = Saturation thickness.

For our purposes, saturation thickness is defined as that thickness between 1000 and 500 mbs for which precipitation will occur for a given amount of moisture between those levels.

We estimate the saturation thickness at 0800 GMT from 0800 GMT surface observations. Regression equations have been determined for each month which specify saturation thickness as a function of surface dew point, sky condition, weather, and station elevation.*** This regression estimate is overridden for stations where precipitation is occurring and the regression estimate indicates otherwise and also for stations where precipitation is not occurring and the regression estimate indicates otherwise. This specification of integrated moisture from surface observations is, of course, a crucial point in our procedure. With the overriding feature we feel we can do better than we could by using only the moisture computed from 0000 GMT soundings.

The input needed for the sea level pressure model is 0800 GMT sea level pressure reports, 500 mb forecast heights (which we get from the NMC PE model) and a smooth terrain field. The input needed for the precipitation model is 0800 GMT saturation thickness, 1000 mb forecast heights (from the sea level pressure model), 500 mb forecast heights, and a smooth terrain field.

* Teweles, S., Jr, and H. B. Wobus: "Verification of Prognostic Charts." Bulletin of the AMS, vol. 35, No. 10, pp 455-463, Dec. 1954.

** Younkin, R. J., J. A. LaRue, and F. Sanders: "The Objective Prediction of Clouds and Precipitation Using Vertically Integrated Moisture and Adiabatic Motions." Journal of Applied Meteorology, vol. 4, No. 1, pp 3-17, Feb. 1965.

*** Lowry, D. A., and H. R. Glahn: "Integrated Moisture - Surface Variable Relationships." Abstract in Bulletin of the AMS, vol. 48, No. 3, p. 205, March, 1967.

The time scale of our forecasts is shown in Fig. 2. Hourly data cutoff time is 0835 GMT, and the forecast can be produced by 0900 GMT for the period 1200 to 2400 GMT.

TIME SCALE FOR COMPUTER PREDICTION

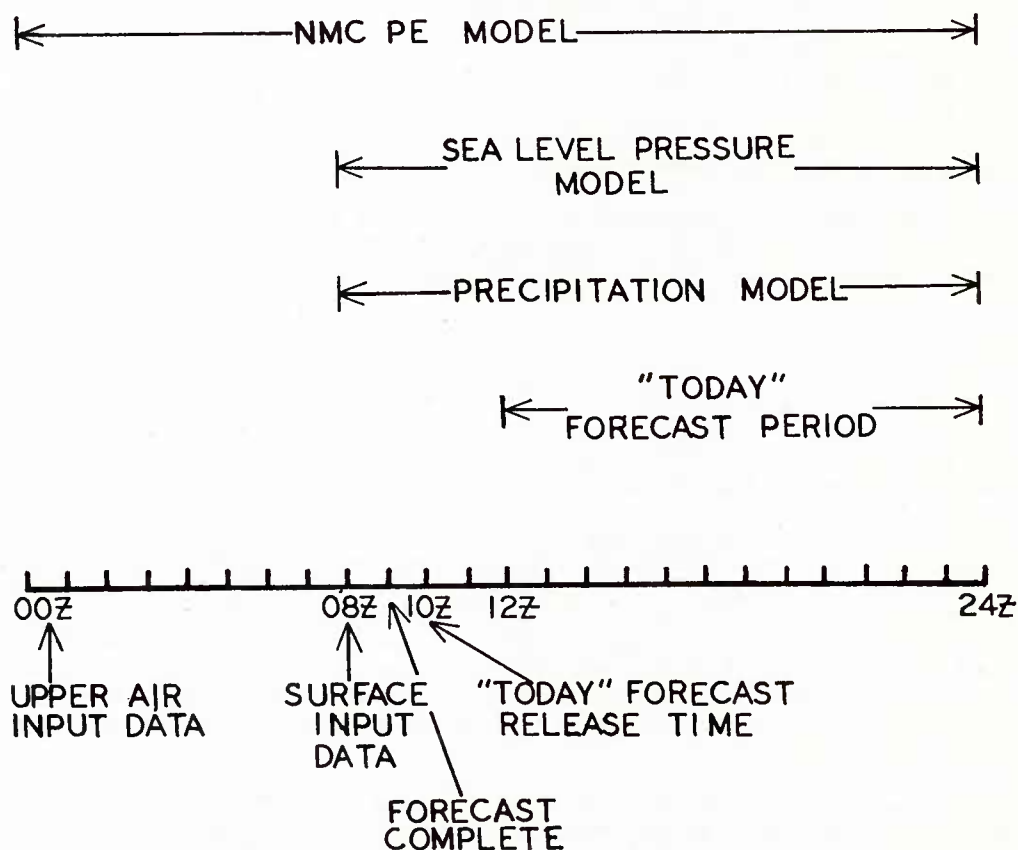


Fig. 2. Time scale for computer prediction of weather on a sub-synoptic scale.

Our models produce hourly forecasts of sea level pressure, 1000 mb geostrophic winds, and saturation deficit. We also have available 0800 GMT data and the NMC PE model output. Many of these variables are saved on magnetic tape for statistical analysis as indicated in Table 2. We are receiving from the National Weather Records Center in Asheville, North Carolina observations to be used as predictand data; the variables are weather, sky condition, 6-hourly precipitation amounts, ceiling, visibility, surface wind, surface temperature, surface dew point, and daily maximum temperature. Once we have finalized our numerical models, we will gradually acquire a data sample and will develop statistical relationships, probably by regression techniques, between the predictands and predictors.

VARIABLES SAVED ON MAGNETIC TAPE

| <u>VARIABLE</u> | <u>TIME (GMT)</u> | <u>SOURCE</u> |
|---|-------------------|---------------|
| Surface dew point | 08 | OBS |
| Weather (coded) | 08 | OBS |
| Height of lowest clouds | 08 | OBS |
| Surface temperature | 08 | OBS |
| Ceiling | 08 | OBS |
| Visibility | 08 | OBS |
| 500 mb height | 08-24 | PE |
| 500 mb geostrophic U-wind component | 08-24 | PE |
| 500 mb geostrophic V-wind component | 08-24 | PE |
| 1000 mb W-wind | 09-24 | PE |
| 850 mb W-wind | 09-24 | PE |
| 500 mb W-wind | 09-24 | PE |
| Sea level pressure | 08-24 | TDL |
| 1000 mb geostrophic U-wind component | 08-24 | TDL |
| 1000 mb geostrophic V-wind component | 08-24 | TDL |
| Upslope component of 1000 mb geostrophic wind | 08-24 | TDL |
| Saturation deficit | 08-24 | TDL |

Table 2. The variables saved on magnetic tape for statistical analysis.

The present status of our program is:

1. Automatic hourly data decoding, error checking, and analysis programs are completed.
2. The sea level pressure model is completed.
3. The precipitation model is nearly completed.
4. Beginning the first of March, 1967 the entire package including ADP and numerical predictions is being run twice a week. The program runs on the CDC 6600 in about 6 minutes.
5. Comparative verification of NMC Primitive Equation and TDL sea level pressure forecasts is complete for 17 cases. These are "independent" cases in the sense that the model was not adjusted during the period of test - - all development was accomplished prior to the test period.

Forecasts for 1200 GMT are 4-hour forecasts for our model and 12-hour forecasts for the PE model; also forecasts for 2400 GMT are 16-hour forecasts for our model and 24-hour forecasts for the PE model. These products are the latest that would be available to the forecaster at about 4:00 A.M. The verification statistics over the area roughly east of the Mississippi River, which is the region not usually affected by the boundaries in our model, are shown in Table 3.

SEA LEVEL PRESSURE VERIFICATION

| DATE | VALID 1200 GMT | | | | | | VALID 2400 GMT | | | | | |
|---------|----------------|-----|-----|-----|-----|-----|----------------|-----|-----|-----|-----|-----|
| | RMSE | | MAE | | SI | | RMSE | | MAE | | SI | |
| | TDL | NMC | TDL | NMC | TDL | NMC | TDL | NMC | TDL | NMC | TDL | NMC |
| 1967 | | | | | | | | | | | | |
| MARCH 1 | 1.5 | 2.7 | 1.1 | 2.4 | 29 | 52 | 5.4 | 5.9 | 4.6 | 4.8 | 51 | 73 |
| 7 | 1.7 | 3.2 | 1.3 | 2.5 | 22 | 49 | 4.3 | 4.6 | 3.6 | 3.4 | 76 | 59 |
| 10 | 1.3 | 4.2 | 1.1 | 3.7 | 23 | 50 | 1.9 | 3.8 | 1.6 | 3.6 | 30 | 24 |
| 14 | 1.4 | 2.8 | 1.1 | 2.4 | 30 | 47 | 2.8 | 4.5 | 1.9 | 4.0 | 42 | 46 |
| 21 | 1.6 | 3.1 | 1.3 | 2.5 | 30 | 51 | 3.8 | 5.0 | 3.0 | 3.9 | 55 | 69 |
| 24 | 2.3 | 5.1 | 1.9 | 4.8 | 34 | 50 | 3.1 | 7.2 | 2.4 | 6.7 | 45 | 53 |
| 29 | 1.8 | 2.2 | 1.6 | 1.7 | 30 | 57 | 1.9 | 2.2 | 1.5 | 1.8 | 41 | 50 |
| 31 | 2.1 | 3.5 | 1.7 | 2.9 | 18 | 30 | 2.4 | 2.9 | 2.0 | 2.2 | 37 | 41 |
| APRIL 4 | 2.6 | 3.9 | 2.4 | 3.6 | 28 | 48 | 3.7 | 4.5 | 2.9 | 4.1 | 58 | 38 |
| 13 | 1.4 | 3.4 | 1.2 | 3.0 | 18 | 31 | 2.1 | 3.0 | 1.5 | 2.4 | 33 | 29 |
| 14 | 1.2 | 2.3 | 0.9 | 2.2 | 19 | 16 | 2.5 | 3.9 | 2.0 | 3.4 | 35 | 43 |
| 18 | 3.2 | 3.7 | 2.9 | 3.3 | 28 | 35 | 4.7 | 6.2 | 3.8 | 5.7 | 49 | 44 |
| 21 | 2.4 | 5.2 | 2.1 | 5.0 | 26 | 31 | 2.5 | 5.6 | 2.2 | 5.2 | 30 | 34 |
| 25 | 1.9 | 4.8 | 1.6 | 4.6 | 23 | 32 | 3.4 | 6.0 | 2.9 | 5.3 | 50 | 47 |
| MAY 2 | 1.5 | 2.1 | 1.2 | 1.7 | 21 | 38 | 2.8 | 2.7 | 2.4 | 2.2 | 40 | 54 |
| 10 | 1.6 | 2.5 | 1.4 | 2.2 | 23 | 36 | 2.1 | 2.3 | 1.4 | 2.0 | 35 | 38 |
| 12 | 2.8 | 4.7 | 2.6 | 4.4 | 27 | 41 | 4.7 | 5.6 | 4.4 | 5.1 | 48 | 49 |
| AVERAGE | 1.9 | 3.5 | 1.6 | 3.1 | 25 | 41 | 3.2 | 4.5 | 2.6 | 3.9 | 44 | 47 |

Table 3. Root mean square error, mean absolute error, and SI scores for currently available guidance and TDL experimental model. RMSE and MAE values are in millibars. Low scores are desirable in all categories.

It can be seen that the TDL model has significantly better average verification scores in all categories at 1200 GMT. A paired t-test on 2400 GMT results indicates significance at the 0.1% level for both RMSE and MAE. The improvement in SI scores shown by the TDL model did not indicate statistical significance.

In summary, we feel we can improve the guidance to forecasters who issue the "Today" forecast in the early morning. This improvement would be due to:

1. More recent data (by 7 or 8 hours)
2. More detailed analysis over the relatively dense data regions of the eastern and central U. S.
3. Inclusion of observed weather in the saturation deficit analysis
4. Statistical analysis of actual model output to produce forecasts of the variables in which the forecaster is interested and in the terms in which he needs them, such as the probability of precipitation.

FLOW CHARACTERISTICS AND MATHEMATICAL MODELING OF CANOPY REGIMES

RONALD M. CIONCO

Atmospheric Sciences Laboratory, Research Division, Fort Huachuca, Arizona

SUMMARY*

For the purpose of this research, the canopy domain is defined as that volume spanning the region from the top of the vegetation down to the ground surface. Our model, therefore, considers more than the crown region itself. If there is significant air spacing in this domain, the model will account for this as well. This research effort has been restricted to the study of the turbulent transfer of momentum when both temperature and water vapor are uniformly distributed with height. That is, this is the neutral thermal case with the further restriction to consider the steady state condition with no advection. The objective of this simplified modeling approach is to express the aerodynamics roughness effects of the surface boundary layer in terms of the height, density, and drag characteristics of vegetation canopies.

The basic statement of the turbulent transfer of momentum within vegetative canopies is:

$$\frac{\partial \tau}{\partial z} = S u^2 \quad (1)$$

or:

$$\frac{\partial}{\partial z} \left[L \frac{\partial u}{\partial z} \right]^2 = \frac{1}{2} \rho C_D' A^2 L u^2 \quad (2)$$

where τ is the shearing stress, z is the vertical space coordinate, U is the mean wind speed and S is similar to Prandtl's skin friction term described by ρ - the air density, C_D - the drag coefficient of leaves and stalks, A - the effective aerodynamic surface area of the vegetation per unit volume, and L - the mixing length. The significant properties of this simplified model are that the mixing length and the intensity of turbulence are essentially constant with height and the wind speed is an exponential function of height.

The resultant equation is:

$$u = u_H \text{EXP} \left[a \left(\frac{z}{H} - 1 \right) \right] \quad (3)$$

where H is the height of the canopy and a is an attenuation coefficient. The model is relatively successful provided the canopy elements are horizontally and vertically uniform and not too tall or dense. For example, the model does a reasonable job for mature corn crops, rice paddies, mature wheat fields and sunflowers. Several artificial and field simulated canopies also conform to the model. Specific examples are wind tunnel experiments using flexible strip-elements and rigid peg-elements as well as controlled field experiments using "Xmas trees" and bushel baskets as roughness elements. Figure 1 depicts this orderly agreement on the basis of comparable unit canopies.

Closer inspection of the profiles indicates there is an apparent relationship not obvious from equation 3. There is an apparent grouping of canopy types according to the effects of density arrays and flexibility of various elements upon the wind flow. The natural corn and wheat canopies are similar to the artificial flexible wind tunnel canopy - they each represent elements that are semi-rigid in a dense array. The other profiles of "Xmas trees", bushel baskets and the wind tunnel peg canopy represent the opposite case of a sparse array of rigid elements. This density - flexibility effects are masked by the attenuation coefficient of equation 3.

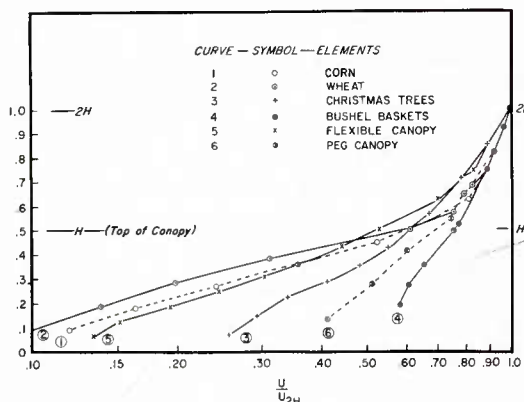


Figure 1

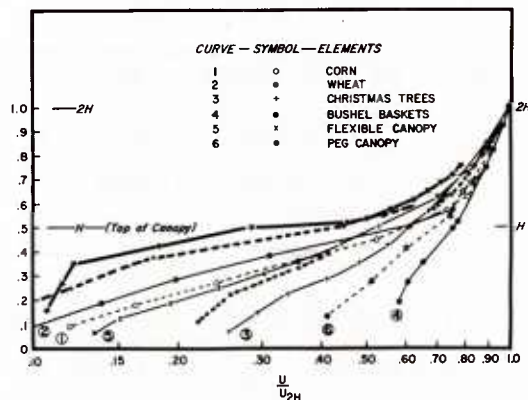


Figure 2

Considering profiles representative of more complex canopies overlayed on Figure 1, Figure 2 shows that the agreement is not violated. The star-continuous line (heavy) profile represents a Japanese Larch forest canopy. The long-dashed (heavy) profile is from a soybean canopy and the short-dashed (heavy) profile represents a sunflower canopy. The more ideal-type sunflower profile conforms nicely. It is not as rigid as the wooden pegs or as flexible as wheat or corn. The larch and soybean data represent probably the most dense type of vegetative canopies. In spite of their more complex structure, they conform to the density-flexibility-flow relation more because of their relatively high leaf area rather than their ability to streamline with the flow.

A more detailed analysis of the density-flexibility-flow relationship is in order, however the available data does not permit this. A series of very elaborate field experiments or well designed wind tunnel simulations could resolve this problem.

* A complete report will be published by Atmospheric Sciences Research Division, Fort Huachuca, Arizona. Publication date has not been scheduled.

AN EMPIRICAL STUDY OF LOW-LEVEL SOUNDING PREDICTION

Carl W. Kreitzberg
Air Force Cambridge Research Laboratories

Abstract

A pilot study has been performed to assess the variability and predictability of low-level soundings (0.5 to 2.0 km) for time scales of 1.5 and 3 hours and a space scale of 100 km. The data used were from AFCRL's Project Stormy Spring mesoscale rawinsonde network for a 27-hour period during passage of an occlusion of moderate intensity. Parameters examined include: temperature and lapse rate; wind direction, speed, shear and geostrophic and ageostrophic components; humidity; geopotential height; and static energy ($c_p T + gz + Lm$). The ratios of signal (variability) to noise (rawinsonde measurement errors) vary from 2 to 15 depending on the parameter.

Trend prediction is of little value, except for height prediction, which means that the changes are the result of systems having a small wavelength. Horizontal advection does have predictive value, however. Using a higher "steering level" at about 700 mb yields a substantial improvement for advection of low-level gradients over the results obtained from advection with the wind at the level of the gradients.

Wind shear change has a high signal to noise ratio but it is not well predicted by trend or advection. These shears are largely made up of ageostrophic components and the ageostrophic wind profiles change systematically as the storm passes over the network. Calculation of the momentum balance terms reveals that net accelerations and eddy viscous forces have magnitudes comparable to the ageostrophic accelerations.

I. Introduction

This investigation utilizes data from a mesoscale rawinsonde network to examine the layer in the atmosphere (0.5 to 2.0 km) that is too high for tower observations and too low to be considered as the "free atmosphere." The time and space variability in this region on scales of 1.5 and 3 hours and 100 km is examined along with the effectiveness of trend forecasting and horizontal advection forecasting. The advection technique requires a spacial network of observations while single-station serial ascents permit trend forecasts. This study indicates the resolving power of a mesoscale network of soundings using standard rawinsonde equipment and balloon ascent rates.

No attempt is made to include the effects of eddy fluxes explicitly in the forecasts; rather this study indicates how well or bad off one is in making short term sounding predictions without explicit consideration of eddy fluxes. In essence, then, this is a pilot study to evaluate the magnitude of the sounding prediction problem by considering observational accuracy, atmospheric variability and the effectiveness of individual simple prediction schemes.

Perhaps the most important of the low-level data are the wind profiles. If trajectories are to be used in the prediction of low-level cloudiness, fog, or contamination, accurate specification of the hodograph between the surface and 850 mb will be necessary. Any simple dynamic model will only be able to predict conditions at the surface and 850 mb or so, and a good parametric interpolation scheme will be required to obtain trajectories between these levels (Janota, 1967).

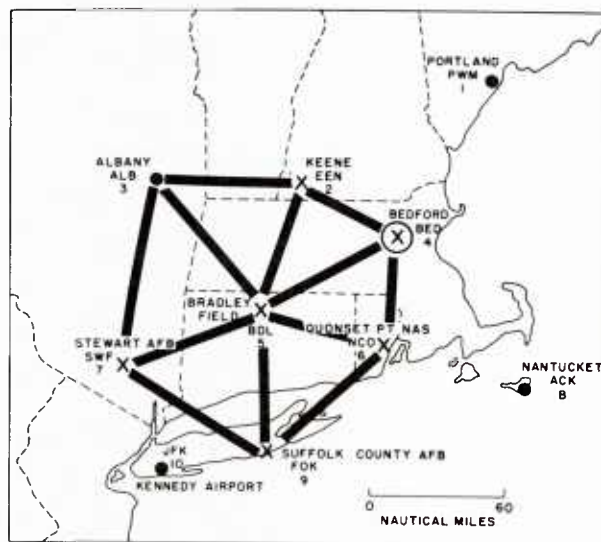
Since the initial attempts in this study at predicting low-level shear were not successful, the wind and wind shear were decomposed into the geostrophic (\vec{V}_g) and ageostrophic ($\vec{V}_{ag} = \vec{V} - \vec{V}_g$) components. Most of the wind shear arises from the ageostrophic component. Hodographs of this ageostrophic wind are shown at 1.5 hour intervals and show a systematic progression throughout the storm. The ageostrophic wind enters the momentum equations (equations of motion) as a force to be balanced by the eddy viscous force and/or the inertial force. All terms in the momentum equation are computed and their relative magnitudes are examined along with their computational accuracy.

This study is based primarily on rawinsonde data collected from the special network shown in Fig. 1. This network was part of AFCRL's Project Stormy Spring which included making a variety of mesoscale observations during five storms in March and April 1965. Only one storm, the moderately intense occlusion of 15-16 April 1965, is considered in this pilot study. However, all soundings from all storms have been converted to punched cards and processed by computer in great detail (Kreitzberg and Brockman, 1966). The resulting data have been made available through the Environmental Technical Applications Center or the National Weather Records Center, Asheville, N. C.

The soundings used in this study were taken at 1.5 hour intervals from EEN, BED, BDL and NCO in Fig. 1. One sounding out of 76 was missing and linear time interpolation was used to reconstruct a bogus sounding. Soundings released offtime were modified using three-point time interpolation to obtain on-time values. All winds used to compute means and shears were essentially 2-minute or 0.3 km averages themselves.

The changes in subsequent 1.5 hour and 3 hour periods will be predicted for the following parameters in the following layers:

- 950 - 900 mb \approx 0.5 to 1.0 km
- 900 - 850 mb \approx 1.0 to 1.5 km
- 850 - 800 mb \approx 1.5 to 2.0 km
- TCL ($^{\circ}$ C) mean temperature in the layer
- ALR ($^{\circ}$ C/km) lapse rate from base to top of the 50-mb layer
- RHIL (%) mean relative humidity w.r.t. ice in the layer
- HTB (m) geopotential height at the base of the layer
- SIGSL (j/gm) mean static energy in the layer: the sum of enthalpy $c_p T$, geopotential gz , and latent heat Lm forms of energy
- DIREL (deg) mean wind direction in the layer
- $\partial D/\partial z$ (deg/km) wind direction change from base to top of the 50-mb layer
- SPDL (m/s) mean wind speed in the layer
- $\partial S/\partial z$ (m/s/km) wind speed change from base to top of the 50-mb layer



- (X) HANSCOM FIELD, BEDFORD: AFCRL RAWINSONDES AT 90 MINUTE INTERVALS INCLUDING SOME OZONESONDES.
- X AIR WEATHER SERVICE: MOBILE RAWINSONDES AT 90 MINUTE INTERVALS.
- WEATHER BUREAU RAWINSONDES AT 3 HOUR INTERVALS.

FIGURE 1. RAWINSONDE NETWORK FOR PROJECT STORMY SPRING.

The prediction techniques that are examined are designed to predict changes in a sounding to be expected in the subsequent 1.5 to 3 hour period. The effectiveness of a prediction scheme is measured by the percent reduction of the standard error of estimate of the prediction equation $S_{y,x}$ over the standard deviation of the predictand S_y . The prediction equation for Y with the predictor X is of the form

$$Y = a + b X$$

and the percent improvement is

$$\text{IMP (\%)} = 100 \times (S_y - S_{y,x}) / S_y.$$

For small improvement scores, a score based on percent reduction of variance would give "values" about twice as large but the percent reduction in standard deviation is felt to be more meaningful.

II. Observational Accuracy

When interpreting measured variability and prediction verifications, one should keep in mind the limitations imposed by observational accuracy. Estimates of this accuracy will be made in this section and their reasonableness will be substantiated in some respects by the prediction statistics. In particular, the observational errors (listed in Table 1) must be less than the RMS errors of the best prediction scheme.

Table 1. Estimates of RMS errors in measuring changes in various parameters ΔA and the corresponding errors in derived quantities

| | | | |
|----------------------------------|--------------|--------------------------------|-------------------------------------|
| ΔTCL | : 0.4°C | V_g | : 3 m/s |
| ΔALR | : 1.5°C/km | $\partial V_g / \partial z$ | : 1.5 m/s/km |
| $\Delta RHIL$ | : 7% | V_{ag} | : 3.1 m/s |
| ΔHTB | : 3 m | $\partial V_{ag} / \partial z$ | : 1.8 m/s/km |
| $\Delta SIGSL$ | : .7 j/gm | VORT | : $1 \times 10^{-5} \text{ s}^{-1}$ |
| $\Delta Dirl$ | : 1.5 deg | DIV | : $1 \times 10^{-5} \text{ s}^{-1}$ |
| $\Delta \partial D / \partial z$ | : 3 deg/km | ω (800 mb) | : $1.1 \times 10^{-3} \text{ mb/s}$ |
| ΔSPD_L | : .7 m/s | w (800 mb) | : 1.1 cm/s |
| $\Delta \partial S / \partial z$ | : 1.4 m/s/km | | |

The root-mean-square (RMS) differences between simultaneous rawinsonde observations inferred from Hodge and Harmantas (1965) are 0.51°C for temperature, 8% for relative humidity and 3.1 m for 850-mb heights. It is reasonable to assume that 50-mb mean temperature changes can be measured with an RMS error of 0.4°C. Assuming that temperature change from level to level for the same sounding can be measured with an accuracy of 0.38°C yields a lapse rate error estimate of about 20% less than the best standard error of estimate obtained from a prediction scheme. Thus our lapse rate error may be an over-estimate.

A 3 m error in measuring the height difference will yield a 3 m/s error in measuring the geostrophic wind V_g from height changes over 100 km. This error is rather large but the magnitudes of even the ageostrophic winds are large enough to be significant. The shear of the geostrophic wind can be measured quite accurately because it depends solely on the accuracy of measuring the layer-mean horizontal temperature gradient.

The wind errors are strongly dependent on the averaging interval used to compute the winds and on the elevation angle. Of course, the wind direction accuracy depends on the wind speed. The error estimates for wind and wind shear are for the mean conditions encountered at low levels for 2-minute mean winds.

Table 1 lists the RMS errors in measuring changes in different parameters and the implications of these errors in calculating geostrophic wind, ageostrophic wind, vorticity VORT and divergence DIV from gradients measured over 100 km. The effect of the DIV errors alone on calculating vertical velocity at 800 mb in pressure coordinates $\omega = Dp/Dt$ and height coordinates $w = Dz/Dt$ are listed assuming integration of the continuity equation upward from 950 mb. All shear and lapse rate errors assume that changes are measured over a layer 0.5 km thick.

From the error estimates in Table 1, the error in computing rates of change and gradients can be calculated by considering the interval over which the change is measured. For example the RMS errors in measuring the local temperature change $\partial T/\partial t$ is $0.4/1.5 = .27^\circ\text{C/hr}$ for $\Delta t = 1.5$ hour and $0.4/3 = .13^\circ\text{C/hr}$ for $\Delta t = 3$ hr.

The appropriate RMS errors will be compared with observed variability in the next section to compute the signal to noise ratio. For example, the RMS value of the observed $\partial T/\partial t$ is 0.77°C/hr for $\Delta t = 1.5$ hour so that $\text{SIGNAL/NOISE} = 0.77/.27 = 2.9$.

III. Variability in time and space; signal to noise ratios.

The observed time and space variability has been analyzed in terms of RMS values of changes over intervals of 1.5 hr, 3 hr and 100 km with the results expressed in units of per hour and per 100 kms. The sample includes data from four sites, EEN, BED, BDL and NCO (See Fig. 1) and the three layers 950-900 mb, 900-850 mb and 850-800 mb. The results are listed in Table 2 along with the signal to noise ratios as defined in the preceding section.

Table 2. Observed time and space RMS variability in units of change per hr or per 100 km along with signal to noise ratios.

| Parameter (A) | $\Delta t = 1.5$ km | | $\Delta t = 3$ hr | | $\Delta s = 100$ km | |
|-------------------------|--------------------------------|------------------------|--------------------------------|------------------------|----------------------------|------------------------|
| | RMS ($\Delta A/\Delta t$) | <u>SIGNAL</u> NOISE | RMS ($\Delta A/\Delta t$) | <u>SIGNAL</u> NOISE | RMS $\Delta A/\Delta s$ | <u>SIGNAL</u> NOISE |
| TCL | .77 | 2.9 | .56 | 3.7 | 1.62 | 4.1 |
| ALR | 1.6 | 1.6 | 1.0 | 2.0 | 2.8 | 1.9 |
| RHIL | 9.0 | 1.8 | 5.5 | 2.2 | 13.4 | 1.9 |
| HTB | 7.5 | 3.8 | 6.6 | 6.6 | 15.5 | 5.1 |
| SIGSL | 1.47 | 2.9 | .96 | 3.8 | 3.07 | 4.4 |
| DIRL | 10.2 | 5.1 | 7.4 | 7.4 | 18.5 | 6.2 |
| $\partial D/\partial z$ | 20.9 | 10.5 | 12.9 | 12.9 | 25.5 | 8.5 |
| SPDL | 2.5 | 5.0 | 2.0 | 8.0 | 5.2 | 7.4 |
| $\partial S/\partial z$ | 3.9 | 4.3 | 2.4 | 4.8 | 5.1 | 3.6 |

This sample was gathered over a 27 hour period extending from 18 hours before to 9 hours after passage of the occlusion in a mature storm of moderate intensity. These statistics show that rawinsonde errors are substantially less than atmospheric variability on scales of 1.5 hr and 100 km.

The smallest signal to noise ratio is with lapse rate. If lapse rate were to be computed over a layer much thinner than 0.5 km the noise might exceed the signal. The variability of relative humidity with respect to ice is small in this sample so that even with the low error estimate, the signal to noise ratio is small. It will be difficult for the prediction techniques to produce a standard error of estimate of lapse rate and humidity much below the RMS values.

The variability of wind and wind shear is large relative to the observational accuracy. The temperature, static energy and geopotential height variability is large enough that substantial improvement is possible if an adequate prediction technique can be found.

IV. Prediction of Sounding Changes

A number of predictors were tested individually in linear regression equations to specify changes in a sounding in the following 1.5 hr or 3 hr. The predictors will be described and then the results will be summarized for all the predictors tested. The predictands are the changes in the 9 parameters listed in the first section.

The predictors include:

Trends: the preceding 1.5-hour change is used to predict the subsequent 1.5-hour change and the preceding 3-hour change is used to predict the subsequent 3-hour change at the same site.

Upwind trends: the preceding trends from BDL (Upwd Tnd) are used to predict subsequent changes at BED which is 1.29 km downstream in relation to the motion of the storm as a whole (Fig. 1). The single-site trend prediction extrapolates a trend while this technique advects a trend at a fixed rate.

Advective change: data from BED, BDL and NCO (Fig. 1) are used to compute the horizontal gradient ∇A which is then dotted with the mean wind from the three sites to yield the advective change - $\vec{V} \cdot \nabla A \equiv ADA$. The ADA is used to predict subsequent time changes at the downwind site, BED.

System advection*: this technique differs from "advective change" in that the advective wind comes from a higher layer in order to simulate a "steering level" wind. The regression analysis will yield the optimum proportion of the steering level wind speed. Steering winds tested were means for layers 800-750 mb, 700-650 mb, 600-550 mb and 500-450 mb. The predictors are designated ADA8, ADA7, ADA6 and ADA5 respectively.

Differential advection for prediction of lapse rate and shear. The vertical change of horizontal advection (ADADIF) is used to predict the subsequent time change of the vertical gradient of A.

*Testing of this technique was suggested by Col. Donald E. Martin.

The distinction between advection and differential advection for predicting time changes of vertical gradients can be seen from the following equations:

$$\frac{\partial T}{\partial t} = -\vec{V} \cdot \nabla T - w(\Gamma - \gamma) \quad (1) \quad (2) \quad (3)$$

$$\frac{\partial}{\partial t} \left(\frac{\partial T}{\partial z} \right) = -\vec{V} \cdot \nabla \frac{\partial T}{\partial z} - \frac{\partial \vec{V}}{\partial z} \cdot \nabla T - \frac{\partial}{\partial z} [w(\Gamma - \gamma)] \quad (4) \quad (5) \quad (6) \quad (7)$$

$$\text{or} \quad \frac{\partial}{\partial t} \left(\frac{\partial T}{\partial z} \right) = \frac{\partial}{\partial z} (-\vec{V} \cdot \nabla T) - \frac{\partial}{\partial z} [w(\Gamma - \gamma)] \quad (4) \quad (8) \quad (7)$$

Terms (3) and (7) are due to vertical motion and are not explicitly included in this study. The advective change technique uses term (2) as a predictor of term (1) and term (5) as a predictor of term (4). The differential advection technique uses term (8) which is the sum of terms (5) and (6) to predict term (4). The term (6) which is included in the differential advection scheme is due to the differential advection which is zero in a geostrophic model but not in the real atmosphere.

Another prediction technique which might be successful but which has not been tested is the prediction of the change in trend by advection of trend. This method corresponds to advection of the isallobaric field to predict pressure changes. The inherent weakness of this method lies in its use of second-order changes, the space change of the trend, in the predictor. Since second-order changes are that much more sensitive to observational errors, this method could be expected to work only where the signal to noise ratios are large.

The percent reductions in standard deviation achieved by using the various predictors individually are listed in Table 3. The futility of single-station forecasting (based solely on data from the site itself) is shown by the failure of trend forecasts to achieve even significant correlations except for HTB and SPDL. At these low levels, HTB changes are nearly equivalent to surface pressure changes which are known to be persistent. The lack of persistence in the trends of the other parameters indicates that the changes over 1.5 and 3-hr periods are caused primarily by mesoscale systems without continuity (at a site) over longer time periods. This is a remarkable conclusion which would lead one to fear that these short term changes and the mesoscale systems they imply are too short in wavelength to be predictable. Fortunately, the positive results obtained using advection predictors show that the mesoscale systems can be defined in space and advected downwind in a reasonable manner.

Table 3. Percent reduction in standard error of estimate of 1.5 and 3 hour time changes achieved by linear regression with various predictors. The N's indicate no significant positive correlation at the 95% level. The $s_{y.x}$ values are for regressions yielding the underlined percent reduction values. The Error s_y are in units of change per hour as are $s_{y.x}$.

| Parameter | TCL | | ALR | | RHIL | | HTB | | SIGSL | | DIRL | | $\partial D/\partial z$ | | SPDL | | $\partial S/\partial z$ | |
|-----------------------|-----------|-----------|-----------|-----------|-----------|-----------|-----------|-----------|-----------|-----------|-----------|-----------|-------------------------|-----------|-----------|-----------|-------------------------|-----------|
| $\Delta t(\text{hr})$ | 1.5 | 3 | 1.5 | 3 | 1.5 | 3 | 1.5 | 3 | 1.5 | 3 | 1.5 | 3 | 1.5 | 3 | 1.5 | 3 | 1.5 | 3 |
| Predictor | | | | | | | | | | | | | | | | | | |
| Trend | N | N | N | N | N | N | 22 | 22 | N | N | N | N | N | N | 6 | 4 | N | N |
| Upwd Tnd | 26 | 7 | N | N | 16 | N | 14 | 6 | 6 | N | 43 | 40 | N | 9 | 14 | 28 | N | N |
| ADA | 16 | 15 | 8 | 7 | N | N | N | N | 27 | 24 | 40 | 46 | 6 | 16 | 14 | 12 | N | 7 |
| ADA8 | <u>27</u> | <u>27</u> | <u>12</u> | <u>12</u> | 7 | N | 15 | 9 | 33 | 33 | <u>41</u> | <u>47</u> | <u>15</u> | <u>27</u> | <u>30</u> | <u>38</u> | 6 | 8 |
| ADA7 | 22 | 25 | 10 | 20 | <u>25</u> | 30 | 34 | 41 | <u>33</u> | <u>33</u> | 37 | 39 | 13 | 24 | 19 | 26 | <u>10</u> | <u>14</u> |
| ADA6 | 12 | 13 | 8 | 18 | 23 | <u>36</u> | <u>39</u> | <u>47</u> | <u>33</u> | <u>22</u> | 34 | 40 | 7 | 17 | 9 | 12 | 6 | 10 |
| ADA5 | 10 | 10 | 7 | 15 | 17 | 33 | 35 | 42 | 17 | 12 | 30 | 37 | 5 | 14 | 7 | 12 | 5 | 10 |
| ADADIF | | | <u>11</u> | <u>24</u> | | | | | | | | | N | 15 | | | 9 | 9 |
| $s_{y.x}$ | .57 | .43 | 1.3 | .79 | 5.5 | 3.4 | 4.0 | 3.0 | .99 | .67 | 6.5 | 4.2 | 17. | 9.8 | 1.9 | 1.4 | 3.6 | 2.3 |
| Error s_y | .27 | .13 | 1.0 | .50 | 4.7 | 2.3 | 2.0 | 1.0 | .47 | .23 | 1.0 | 0.5 | 2.0 | 1.0 | .47 | .23 | .93 | .47 |

Upwind trends (Upwd Tnd) do contain significant information on changes to be expected in many parameters at a downwind site. Substantial success is obtained in predicting wind direction changes while some success is achieved in the prediction of temperature, humidity and wind speed.

The advective change predictor, $ADA = -\vec{V} \cdot \nabla A$ is reasonably successful in anticipating changes at the downwind corner of the triangular array of three sites. The notable exceptions are with HTB and RHIL. The failure of HTB contours at low levels to be advected with winds at the same level is to be expected. Cross-contour flow toward lower geopotential is routinely found ahead of a trough due to friction. Thus, the lower heights are moving into the area having positive height advection. On the other hand, it is difficult to understand why humidity changes are not predictable from consideration of $-\vec{V} \cdot \nabla RHIL$. One is tempted to use the small RHIL signal to noise ratio to rationalize this result but the success achieved by steering the low-level moisture field with the 700-650-mb wind negates this hypothesis.

The use of "steering level" winds to advect gradients measured at low levels is rather successful and this success has a fundamental implication. The implication is that a significant part of the low-level sounding changes are associated with mesoscale systems (too short in wavelength to be detected in the preceding trend at the site) which propagate in the direction of the flow at some higher level. The percentages in Table 3 indicates that the optimum steering level for the majority of the parameters is about 700 mb. This 700-mb steering level is often quoted to explain the propagation of radar echoes which are themselves imbedded in this flow to some extent. The fact that the lower-level humidity field is coupled with the 700-mb flow may reflect the addition of low-level humidity by evaporation of precipitation falling from higher levels. However, the coupling of all the other parameters to the 700-mb flow implies the propagation of mesoscale systems as a whole through the lower levels in response to the flow at higher levels.

The optimum steering level does vary somewhat depending on the parameter being predicted. For example, the wind is best steered by the 800-750 mb flow while the geopotential is best steered by the 600-550 mb flow. In any case, this limited sample is inadequate to determine exactly the best steering level for a particular parameter.

The best percent reduction for each parameter achieved using any of the advection predictors is underlined in Table 3. For the regression yielding the underlined percentage, the standard error of estimate $s_{y,x}$ has been listed in the table in units of change per hour. The error estimates in Table 1, converted to units of change per hour, are listed in Table 3 as Error s_y for comparison with $s_{y,x}$.

It can be seen that little further improvement can be made in the prediction of lapse rate and humidity unless the error estimates can be revised downward. This conclusion as well as many of the statistical results in this paper apply to a limited sample from this single storm so indiscriminate generalizations are not warranted. Nevertheless this storm is of a variety frequently encountered in extratropical regions, namely an occlusion of moderate intensity.

The differential advection predictor ADADIF, applicable to vertical gradient predictions only, is generally more effective than the advective change predictor ADA. Thus, explicit inclusion of the differential advection term $\partial \vec{V} / \partial z \cdot \nabla A$ does help somewhat.

The conclusion that most changes can best be predicted by advection with a steering level flow means that an observational network designed to predict low-level sounding changes should include provisions for measuring winds above the levels for which predictions are to be made.

V. Ageostrophic Wind Profiles

It has been seen in previous sections that wind shear has both a large signal to noise ratio and a small amount of predictability. Since strong wind shears are important to aircraft operations and the wind profile is important to trajectory calculations and cloud dynamics, the nature of these shears will be examined further.

During the 27-hour period, which included the passage of an occlusion of moderate intensity, the RMS values of surface wind \bar{V}_{sfc} , geostrophic wind \bar{V}_{gSFC} and ageostrophic wind \bar{V}_{agSFC} were 4.3, 20.3 and 17.1 m/s respectively. Thus, substantial shears would be expected in the boundary layer as the wind attempts to adjust to geostrophic or gradient balance at some gradient wind level. The RMS vector shears in the layers SFC-950 mb, 950-900 mb and 900-850 mb are (in m/s):

$$\Delta V(S95) = 9.6; \quad \Delta V(9590) = 5.2; \quad \Delta V(9085) = 5.1$$

$$\Delta V_g(S95) = 6.9; \quad \Delta V_g(9590) = 3.1; \quad \Delta V_g(9085) = 3.8$$

$$\Delta V_{ag}(S95) = 10.8; \quad \Delta V_{ag}(9590) = 5.1; \quad \Delta V_{ag}(9085) = 4.7.$$

Therefore, the wind shears and the ageostrophic wind shears are large while the geostrophic wind shears are smaller but not negligible; specifically, $RMS(\Delta V_g) = 0.66RMS(\Delta V_{ag})$.

One might expect that the wind shear in the lowest layer $\Delta V(S95)$ would be well related to the magnitude of the surface ageostrophic wind V_{agSFC} . For this sample,*

$$\Delta V(S95) = 4.56 + (.29 \pm .09) V_{agSFC}; \quad S_y = 3.44; \quad S_{y,x} = 2.75 \text{ (m/s)}.$$

where S_y is the standard deviation of the predictand and $S_{y,x}$ is its standard error of estimate using the regression equation. A substantial portion of the wind shear remains "unexplained."

Even if a dynamic model predicts the surface pressure and the thermal field so that the V_g hodograph is known, one must predict the V_{ag} hodograph in order to arrive at the V hodograph. The surface winds in this sample were not too large and the regression of surface wind speed V_s on surface geostrophic wind speed V_{gs} yields (in m/s):

$$V_s = 1.05 + (.15 \pm .03) V_{gs}; \quad S_y = 1.73; \quad S_{y,x} = 1.17 \text{ (m/s)}.$$

Thus, the main prediction problem to be considered here is not the prediction of surface wind or the geostrophic wind profile, but rather the ageostrophic wind profile.

The first and perhaps the crucial question is do the ageostrophic wind hodographs up to 2 km change with time in a systematic manner. If the changes are systematic ("well behaved"), then one can hope to predict them. Such ageostrophic wind hodographs are shown in Fig. 2 for 19 sequential ascent times at 1.5-hour intervals. The plotted points are for SFC, 950 mb, 900 mb and 850 mb with the arrowhead at the 850-mb point. These hodographs were computed from mean winds and geopotential gradients for an area of about 100 km on a side (enclosed by EEN, BED, NCO and BDL in Fig. 1).

The magnitude of the ageostrophic wind and shear is illustrated in Fig. 2. Notice also that where surface ageostrophic winds are large, ascents 10-17 for example, there is a rapid decrease of ageostrophic wind with height to a gradient wind level near 850 mb. Where surface ageostrophic winds are small, ascents 18-24 for example, the gradient wind level as defined by the level of minimum ageostrophic wind is somewhat variable.

* The term $\pm .09$ is the 95% confidence interval for the regression coefficient .29.

In the conventional Ekman spiral theory, the surface wind is zero and the geostrophic wind does not vary with height; hence, $\vec{V}(z)$ is $(\vec{V}_{ag}(z) - \vec{V}_{agSFC})$. In practice, particularly in frontal situations, these model conditions do not exist but a spacial network of rawinsondes permits $(\vec{V}_{ag}(z) - \vec{V}_{agSFC})$ to be determined and its hodograph bears a striking resemblance to the Ekman spiral. These hodographs are merely those in Fig. 2 with \vec{V}_{agSFC} subtracted out and they are shown in Fig. 3.

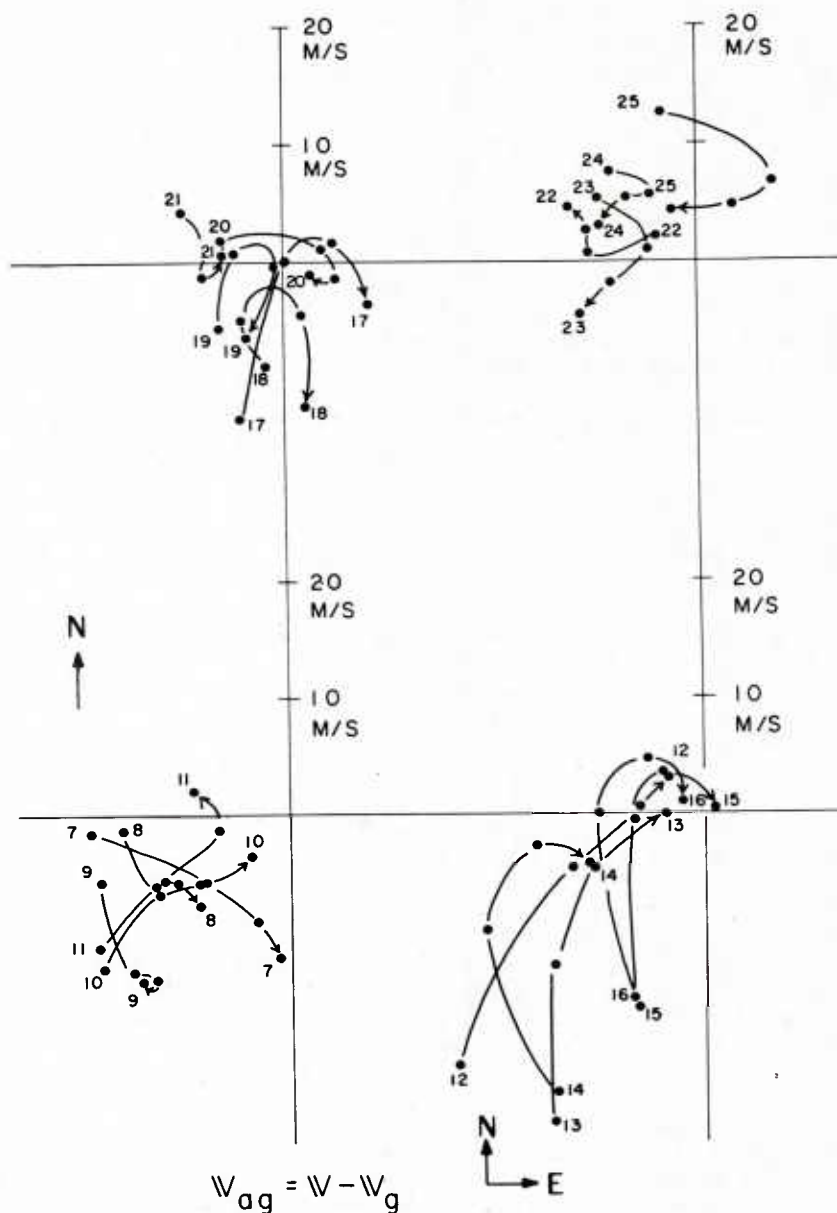
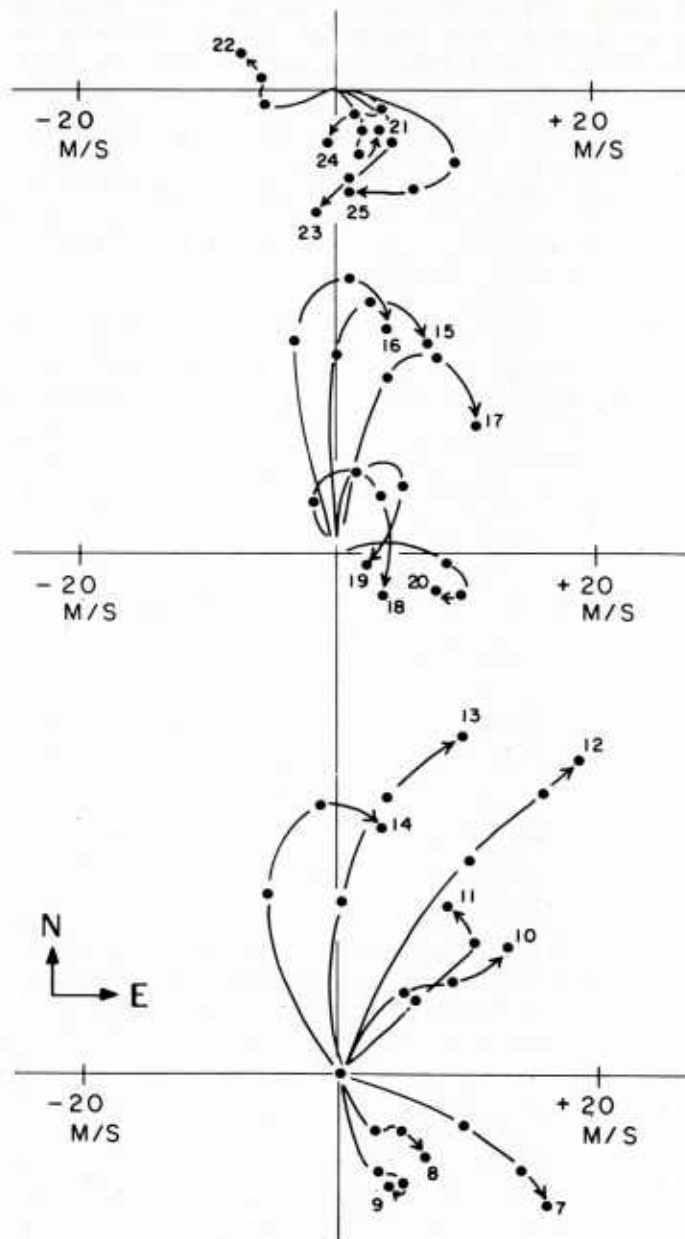


Figure 2. Hodographs of the ageostrophic wind for 19 sequential times at 1.5-hr intervals.



$$W_{ag} - W_{ag \text{ SFC}} = (W - W_{SFC}) - (W_g - W_{g \text{ SFC}})$$

Figure 3. Hodographs as in Fig. 2 but with the surface ageostrophic wind subtracted out.

Notice the continuity of the hodographs in Fig. 3 over the 1.5-hr time intervals between ascents. The exception to this continuity is between ascents 9 and 10. This change was caused by an otherwise unimpressive change in the horizontal temperature gradient from the surface to 0.5 km. The most impressive feature in Fig. 3 is the systematic progression of the profiles from medium linear shears for ascents 7 to 11, to larger and progressively more spiral curves during ascents 12 to 17 and finally to the small tight spirals in ascents 18 to 25.

The large ageostrophic winds and the large shears with ascents 12 to 14 occurred in conjunction with an intense low-level jet on the leading boundary of the storm. Extreme winds, wind shears and probably turbulence were observed in the lowest 1.0 km. Winds of 40 m/s were observed at as low as 600 meters at FOK where surface winds were generally 15-18 knots with some gusts. This situation would be hazardous, particularly to helicopters or VTOL aircraft. Wind shears above 1 km were negligible.

Figs. 2 and 3 suggest that the change in \vec{V}_{ag} from SFC to 950 mb is proportional to \vec{V}_{agSFC} and similarly for the change in \vec{V}_{ag} from 950 mb to 900 mb. For this sample of 19 profiles a linear regression analysis does yield statistically significant correlations with

$$\left| \vec{V}_{ag}(950) - \vec{V}_{ag}(SFC) \right| = 2.93 + (0.44 \pm 0.11) \left| \vec{V}_{agSFC} \right| \quad (\text{m/s})$$

$$s_y = 4.74 ; \quad s_{y,x} = 3.44 ; \quad \text{IMP} = 27\%$$

and

$$\left| \vec{V}_{ag}(900) - \vec{V}_{ag}(950) \right| = 1.11 + (0.23 \pm 0.04) \left| \vec{V}_{agSFC} \right| \quad (\text{m/s})$$

$$s_y = 2.18 ; \quad s_{y,x} = 1.40 ; \quad \text{IMP} = 36\%$$

The standard error of estimate of 1.40 m/s for the change of ageostrophic wind from 950 to 900 mb corresponds to about 2.8 m/s/km error in $\partial \vec{V}_{ag} / \partial z$. This forecast error compares favorably with the estimate of 1.8 m/s/km for the RMS error of measuring $\partial \vec{V}_{ag} / \partial z$.

Unfortunately, the wind change from 950 to 900 mb was not significantly correlated to \vec{V}_{agSFC} so that one must consider the change of \vec{V}_g as well as the change of \vec{V}_{ag} as inferred from \vec{V}_{agSFC} in order to predict the change of \vec{V} from 950 to 900 mb.

Let us now consider the relative magnitudes of the terms in the momentum equation to see which terms must be considered in modeling the wind profile. In particular, we have seen that $\partial \vec{V}_g / \partial z$ is smaller than but not negligible in comparison to $\partial \vec{V}_{ag} / \partial z$. We would like to know also if the acceleration $D\vec{V}/Dt$ is negligible in comparison to $f \vec{V}_{ag}$ and the convergence of eddy momentum flux.

VI. Low-level Momentum Balance

The ageostrophic wind calculations indicate that large forces exist in the low-level flow which must be balanced by eddy viscous and/or inertial forces. The momentum equations in practical units at 43°N are

$$(1) \quad \frac{Du}{Dt} \left(\frac{\text{m/s}}{\text{hr}} \right) = .36 v_{ag} \text{ (m/s)} + FR_x \left(\frac{\text{m/s}}{\text{hr}} \right)$$

$$(2) \quad \frac{Dv}{Dt} \left(\frac{\text{m/s}}{\text{hr}} \right) = .36 u_{ag} \text{ (m/s)} + FR_y \left(\frac{\text{m/s}}{\text{hr}} \right)$$

where u , u_{ag} and v , v_{ag} are wind and ageostrophic wind components in the north x and east y directions respectively. The viscous accelerations in the two directions are FR_x and FR_y and represent the effects of eddy momentum convergence.

The total (material) derivatives in the two directions can be expanded into

$$(3) \frac{Du}{Dt} \left(\frac{m/s}{hr} \right) = \frac{\partial u}{\partial t} \left(\frac{m/s}{hr} \right) + .036 \left(u \frac{\partial u}{\partial x} + v \frac{\partial u}{\partial y} \right) \frac{(m/s)^2}{(100KM)} + .18 \omega \frac{\partial u}{\partial p} \frac{(10^{-3}mb)(m/s)}{(200 mb)}$$

$$(4) \frac{Dv}{Dt} \left(\frac{m/s}{hr} \right) = \frac{\partial v}{\partial t} \left(\frac{m/s}{hr} \right) + .036 \left(u \frac{\partial v}{\partial x} + v \frac{\partial v}{\partial y} \right) \frac{(m/s)^2}{(100km)} + .18 \omega \frac{\partial v}{\partial p} \frac{(10^{-3}mb)(m/s)}{(200 mb)}$$

where $\omega = Dp/Dt$ is the vertical velocity in pressure coordinates. The terms on the right side of equations 3 and 4 have been calculated from the soundings at EEN, BED, BDL and NCO in Fig. 1. This area is roughly 100 km on a side and values are computed each 1.5 hour. The local changes $\partial u/\partial t$ are computed from centered differences over a total of 3 hours. To date, calculations have used 100-mb mean values centered at 900 mb, 800 mb, - - - 200 mb. The vertical velocity, ω is calculated kinematically with reasonably good results in the lower troposphere. A crude lower boundary condition of $\omega = 0$ at 950 mb has been used.

Values of u_{ag} , v_{ag} are computed for the same area and equations 1 and 2 are used to compute FR_x and FR_y . The results for the 900-mb and 800-mb levels have been examined to determine the mean and RMS values of each term for 17 observation times throughout the storm. The results from this analysis are listed in Table 4 along with estimates of the RMS errors in calculating each term at a single time. The error estimates are compatible with the observational errors in Table 1 and the RMS magnitudes of the terms in Table 4.

Table 4. Statistics on each term in the momentum equations.
Mean and RMS values are in units of m/s/hr.

| | $\frac{\partial u}{\partial t}$ | $u \frac{\partial u}{\partial x}$ | $v \frac{\partial u}{\partial y}$ | $\omega \frac{\partial u}{\partial p}$ | $\frac{Du}{Dt}$ | $f v_{ag}$ | FR_x | | $\frac{\partial v}{\partial t}$ | $u \frac{\partial v}{\partial x}$ | $v \frac{\partial v}{\partial y}$ | $\omega \frac{\partial v}{\partial p}$ | $\frac{Dv}{Dt}$ | $f u_{ag}$ | FR_y |
|--------------|---------------------------------|-----------------------------------|-----------------------------------|--|-----------------|------------|--------|--|---------------------------------|-----------------------------------|-----------------------------------|--|-----------------|------------|--------|
| MEAN: 900 MB | 0.22 | 0.36 | -1.9 | 0 | -1.4 | -1.0 | -.36 | | -.48 | 1.1 | -1.9 | 0 | -1.3 | -1.9 | -3.2 |
| 800 MB | 0.13 | 0.66 | -1.1 | .04 | -.22 | -1.5 | 1.3 | | -.34 | .49 | -.46 | -.09 | -.40 | -2.3 | -2.8 |
| RMS: 900 MB | 0.9 | 0.7 | 2.7 | 0 | 1.9 | 2.1 | 2.5 | | 2.4 | 2.2 | 2.6 | 0 | 2.6 | 2.8 | 4.5 |
| 800 MB | 1.6 | 1.6 | 1.4 | 0.2 | 1.8 | 2.6 | 3.1 | | 2.2 | 1.8 | 1.0 | 0.3 | 2.0 | 3.0 | 3.7 |
| RMS ERROR | 0.2 | .2 | .4 | .1 | .5 | 1.1 | 1.2 | | 0.2 | .4 | .3 | .1 | .5 | 1.1 | 1.2 |
| % ERROR | 16 | 18 | 18 | 47 | 30 | 48 | 43 | | 9 | 18 | 18 | 47 | 22 | 38 | 29 |

The momentum budget statistics in Table 4 show that the inertial, ageostrophic and viscous accelerations are all of comparable magnitude. The only negligible term is the vertical advection of momentum. The viscous drag decreases with height in the mean and is an accelerating factor at 800 mb for the u-component.

Table 4 shows that the RMS values of Du/Dt and Dv/Dt are slightly smaller than but not negligible in comparison to the ageostrophic and viscous terms. The question then arises as to whether the accelerations may be centrifugal in nature so that the acceleration in the direction of flow might be negligible. Calculations of RMS values of $\frac{\vec{V} \cdot \frac{D\vec{V}}{Dt}}{|\vec{V}|}$ give 2.9 and 1.9 m/s/hr for the 900 and 800-mb levels respectively. Thus, this component of the

acceleration is also of the same order as the ageostrophic and viscous terms in the momentum equation.

The percent errors are large for the vertical advection of momentum but, since this term contributes little, this error is not important and reasonably good estimates of acceleration, Du/Dt and Dv/Dt are obtained. The errors in ageostrophic acceleration are substantial which leads to comparable errors in the viscous terms.

In view of the errors in calculating the ageostrophic and the viscous terms, three-point equally-weighted time averages should be computed before examining the momentum balance at any particular time. Using such a procedure, the magnitude of the RMS errors would be about 58% of the values in Table 4. The momentum balance would then apply to a mean over 100 km, 100 mb and 3 hours. Thus the high frequency (essentially independent) measurements permit reasonably reliable momentum budget calculations for systems on the scale resolved by 3-hourly means.

VII. Summary and Conclusions

This pilot study is restricted to statistical analyses of data from a single storm which is of a common variety, an occlusion of moderate intensity. The variability in soundings from 0.5 to 2.0 km over time intervals of 1.5 and 3 hours is substantially larger than the errors in measuring such changes with rawinsondes. The smallest signal to noise ratios are encountered in measuring time changes in lapse rate and humidity.

The trend in the previous 1.5 hr and 3 hr interval is not correlated with the trend in the following interval of equal duration except for geopotential height and, to a small extent, wind speed. Thus the changes measured by the serial ascents are not associated with systems of wavelengths long in comparison to the 1.5 and 3 hour prediction scale. The use of single-station serial ascents to anticipate future mesoscale events at the same site would be ineffective. However, it is found that the trend at an "upwind" site is useful to predict future changes at a downwind site.

Given only a three-site rawinsonde network in a triangular array, it is possible to compute horizontal gradients and construct advection predictors by advection with winds at the same level or at a higher "steering level." The advection predictors are generally correlated with changes at the downwind corner of the triangle in the subsequent 1.5 and 3-hour period. The best results for predicting changes in the 0.5 to 2.0 km layer are obtained from advecting with winds at about the 3 km layer.

These results indicate that the changes which are uncorrelated from one 1.5 or 3-hr period to the next are in part associated with mesoscale systems which propagate in the direction of the 700-mb flow. Thus, observational networks designed to predict changes in the lower layers should contain provisions for measuring winds up to substantially higher levels.

The importance of low-level wind profiles coupled with the high signal to noise ratio and low predictability of wind shear achieved with trend and advection techniques led to the examination of the geostrophic and ageostrophic components of the hodographs. In this sample, which includes passage of a moderate baroclinic occlusion, the geostrophic wind shears in the layer 0.5 to 2.0 km are about 66% as large as the ageostrophic shears; thus both must be predicted in order to predict the wind shear.

The magnitudes of the ageostrophic winds and their shears are large in comparison to errors inherent in their measurement. The ageostrophic wind hodographs are found to change rather systematically with time throughout the storm which gives hope for their predictability. About 30% of the standard deviation (51% of the variance) of the ageostrophic wind shear in the SFC to 950-mb and 950-900-mb layers is "explained" by regression with the magnitude of \bar{V}_{agSFC} .

Calculation of the individual terms in the momentum balance equation reveals that the net acceleration term, the eddy viscous term and the ageostrophic acceleration terms are all of comparable magnitude and must be considered when explaining the wind profiles in the 0.5 to 2.0 km layer. The inaccuracy of measuring the terms requires that means be computed for a 3-hr period, which includes 3 sounding times, before reliable data can be obtained. The source of most of the inaccuracy in evaluating the momentum equation arises in measuring the geostrophic wind.

The importance of these conclusions does not lie in the operational usefulness of the particular regression forecast equations. Operational forecast relations can be formulated only when an operational network with operational requirements has been established. Furthermore, the improvement in such a thing as a 1.5-hour temperature change predictions from a $s_y = 0.77^\circ\text{C/hr}$ to $s_{x,y} = 0.57^\circ\text{C/hr}$ may not be operationally significant. A more important result is that observational accuracy and atmospheric behavior will permit small temperature changes to be predicted at all using horizontal gradients inferred from but three sites. The conclusions that consecutive trends are not correlated and that such a parameter as low-level wind shear change is better advected with the 700-mb flow reveal important information about the systems responsible for the mesoscale changes. Specifically, the meso-systems must be short in wavelength and dynamically coupled with the flow aloft.

This pilot study should be expanded to include more cases, such as the other four Stormy Spring cases. Also such a statistical study is supplementary to and not a substitution for explicit synoptic-type analysis and dynamical analysis.

References

- Hodge, M. W., C. Harmantas: "Compatibility of United States Radiosondes." Mon. Wea. Rev. 93: 253-266 (1965).
- Janota, Paul: A low level circulation model for diagnostic and prognostic applications. Proceedings of the Joint Technical Exchange Conference, April 4-7, 1967, Monterey, Calif. (1967).
- Kreitzberg, C. W., W. E. Brockman: Computer Processing of Mesoscale Rawinsonde Data from Project Stormy Spring, AFCRL-66-97 Special Reports, No. 41, 35 pp (1966).

A LOW LEVEL CIRCULATION MODEL
FOR
DIAGNOSTIC AND PROGNOSTIC APPLICATIONS

by
Major R.A. Derrickson and Captain P. Janota
Headquarters 3d Weather Wing
Offutt AFB, Nebraska

The following material summarizes the paper given by Captain Janota at the Joint Technical Exchange Conference, Monterey, 4-7 April 1967 and abstracts a Third Weather Wing Technical Note now in preparation.

Our goal is to improve the specification of winds and weather in the troposphere below 850mb. The latter region is called the boundary layer in this report. Our Boundary Layer Model (BLAMO for short) is designed to be run in conjunction with the comprehensive fine-mesh forecast effort now underway at 3WW.* It is primarily a diagnostic tool for specifying the three wind components on a surface defined as a constant pressure increment above the terrain. At present, this increment is 50mb (or about 1500ft). BLAMO is to be added to the 850mb forecast fields of a free-atmosphere model; hence, it may also be considered a forecast tool. Once wind components have been specified at regular intervals, we integrate a moisture tendency equation using all available soundings and surface synoptic reports as input data.**

At any time period, the first step is the forecast of mean static stability by a successive approximations method which includes parameterized diabatic effects. A temperature field is then built down from 850mb and used to determine surface pressure from the hydrostatic equation and geostrophic wind from the thermal wind equation. We specify the vertical motion (ω) by combining a parabolic fit from the driving forecast model with a terrain term derived in BLAMO. The latter component is damped with height as a function of the static stability. Divergence is then computed analytically by differentiating ω in pressure. The velocity potential is recovered by relaxation of a Poisson's equation with divergence as the forcing function, differentiation of the potential field gives the divergent part of the wind and this component is added to the previously derived geostrophic field.

A correction to the non-divergent wind is derived by solving a perturbation form of the steady state vorticity equation with the previously derived divergence as the source term. One of the effects of this term is the intensification of the lee-side trough; we also expect that it will produce a super-geostrophic acceleration of southerly flow over the Great Plains. In order to provide for the effect of friction, we require that frictional dissipation balance the energy supplied by cross-isobar flow. Correction equations for the layer-mean wind in the first 50mb are derived from this energy constraint and involve surface roughness, static stability and geostrophic speed.

Results from a series of 12-hr progs (using only one 12 hour time step in the stability forecast routine) on a small grid in the eastern U.S. have encouraged us to enlarge our grid to include that part of the U.S. and Canada east of the Rockies. Input data will include: fine-mesh analyses of height and temperature at 850mb and fine-mesh prog fields from both the filtered dynamic model and the trajectory cloud model. Forecast output will be: horizontal and vertical wind components, sea-level pressure, mean static stability and moisture. Full scale tests of the complete package will begin in early July 1967.

* The fine-mesh grid is one half the NMC grid spacing or about 200km. The project at 3WW combines: surface and upper-air analyses developed by Capt. R. Fleming of Det. 1, 3WW; a capped version of the 3WW 6-level model developed by Lt. Col. J.G. Howcroft of the 1210th Weather Squadron; and a fine-mesh version of the CPS-Trajectory Cloud Model. The latter two models are described in Technical Report 188 published by Air Weather Service (MAC), Nov 1966.

** The moisture parameter used is condensation pressure spread (CPS), a variable which is described in 3d Weather Wing Technical Note 13 by Lt. Col. H. Edson, USAF.

ON THE NUMERICAL FORECASTING OF
PRECIPITATION AND CLOUDS'

By

Leo C. Clarke

Fleet Numerical Weather Facility
Monterey, California

A hemispheric forecast scheme for precipitation and clouds based on the approach of Sanders (1963), and the theoretical development of Younkin, Larue, Sanders (1965) is presented wherein the vertically integrated precipitable water from the surface to 300 mb is the principal moisture parameter. The observed and forecast vertical distribution of moisture is characterized by a parameter K, which is a function of the surface dewpoint and the precipitable water. The same principle is applied to the saturated atmosphere. The parameter K is heavily smoothed and is assumed to persist for the duration of the forecast period as a "grosswettenlagen" moisture typing. The calculated precipitable water values and the desired column mean relative humidities using mandatory level information only show good correlation to observed values. A simple bilinear wind profile is assumed in order to utilize the output of the FNWF two level forecast model. A space variable moisture steering wind is then obtained from the wind and moisture profiles. Values obtained agree well with observed values.

Vertical motions are obtained from the thermodynamic equation for a two level model using the independently forecast 1000 and 500 mb geopotential fields. These vertical motions are adjusted to allow the pseudo-release of latent heat following the method of Harley (1966).

The moisture forecast equation is integrated in hourly steps to 48 hours. Every 12 hours, the input parameters of the forecast equation are recalculated using the forecast data and precipitation for the past 12 hours is obtained. The amount of evaporation is also calculated and is

considered in calculating the precipitation. The forecast is restarted every 12 hours so that the progressive modification of air masses by evaporation and precipitation is taken into account.

The total cloud cover is related to the column mean relative humidity through an empirical relationship obtained from satellite nephanalyses. Forecast surface and upper air dewpoints are obtained from the forecast precipitable water and conserved moisture parameter K. Layer cloudiness is calculated from these values.

A SYSTEMATIC APPROACH TO WEATHER PRESENTATION

By Clement J. Todd and Steven H. Cohen

U.S. Navy Weather Research Facility
U.S. Naval Air Station
Norfolk, Virginia 23511

We are convinced that, if the data is presented properly, people have the capacity to understand all of the information necessary within a given system. On the other hand, improper presentations can saturate human capacity while conveying little information.

Two related problems being investigated at NWRF are:

1. determining what people must know about the weather in order to optimize operations.
2. retrieving the maximum amount of information from our present weather service.

We know many of the shortcomings of our present system, and we have a number of ideas how these problems might be corrected. However, the problem is so important to the Navy that we must take advantage of the best professional advice in order to couple our meteorological and operational understanding with human factors and display engineering. We would like to introduce some of the concepts we are exploring at the present time.

We have come to recognize two distinct users. First is the ultimate user, defined as he who plans and carries out military operations. This category includes aviators, squadron and group commanders, ship captains, task level commanders, etc., up to the Chief of Naval Operations. If these professional military men are fully aware of the present and future state of the environment throughout the course of their operations, they can then use the information to the best advantage.

Because weather is exceedingly complex, many operational groups receive close support from professional meteorologists (our second category). These men assemble information forwarded from weather centrals and facilities, and apply a physical interpretation before making their presentation to the ultimate user. Thus the total presentation system must satisfy the needs of both the ultimate (operational) and intermediate (meteorologist) user. Basic developments are presently being undergone, while other more sophisticated changes must evolve over various periods of time.

First and simplest, we can improve the use of the teletype. Through this medium we communicate weather information to virtually all of the Navy's ships as well as shore installations. This means that a smaller unit, not having the immediate access to a meteorologist, must rely almost completely upon information via teletype. By simple teletype graphics and use of computers, we have shown that the utility of the messages can be improved notably. For example, a ship's CO can see the state of the environment at his location without recourse to complicated interpretation.

Although this type of presentation is lavish in the use of valuable communication time, the expenditure is more than justified by the increased service to a large number of users. Actually a large effort is being made in this area to design computer-produced presentations which conserve communications and at the same time, increase comprehensibility. This will, therefore, increase the utilization of weather information.

Secondly, the present mapping system may be subject to criticism. Our concept is that the operational meteorologist must understand the weather as a three-dimensional, moving system in order to judge the motions and changes. The meteorologist, however, is given a force field map from which he must derive the desired quantities.

This problem can be eliminated through the use of computer transformations. The derived maps would most likely be in the form of six-hour horizontal and vertical vectors and vertical temperature and moisture structure. From these, the operational meteorologist can tie horizontal and vertical advection as well as vertical stability structure into his forecast-time scale.

Thirdly, although the meteorologist is, in reality, working with a four-dimensional field, most graphic information is being relayed to him in two-dimensional slices; thus it is extremely difficult to piece together a complete physical picture of the environment. There are

a number of ways, however, that the present state of the art may be used to display a three-dimensional swath of the atmosphere. For instance, we can build three-dimensional models by using transparent weather maps; or we can animate our systems, thereby creating a third dimension through the use of time. Most important, we feel that we can now do these transformations simply and rapidly enough so that they can be accomplished without increasing the burden on the meteorologist.

Fourthly, we have had operational satellite information with us long enough to be disappointed at the rate in which we are incorporating it into our weather forecasts. There are many difficulties and frustrations, but we are on the verge of the synchronous satellite era and in this we have the opportunity to make great strides in our short tactical forecasts by assuring that the information is comprehensible. Our suggestion is that the satellite pictures should be animated and conventional data superimposed in a compatible form.

Our human factors collaborators say that some of those concepts sound like good ideas and may even be right, but we had better test them. They tell us that time after time careful analysis and testing have shown that it is possible to make substantial improvements on the way people do things. They assure us that there is every indication that weather presentation is such a field.

Our aim is to tackle this problem uninhibited by tradition, but we will take advantage of every aspect of the present weather systems that is now available. From this without increasing the burden on personnel we will evolve a system that lets the user take maximum advantage of what is available through an optimum presentation.

TELEPLOT

by

Mr. J. W. Nickerson
U.S. Navy Weather Research Facility
NAS Norfolk, Va. 23511

ABSTRACT

The Navy employs a number of different communication systems for transmitting intelligence from data sources to operational units. The TELEPLOT procedure described herein constitutes a method by which computer products and other graphical intelligence can readily be made available to ships and small facilities which have only teletypewriter equipment. These data are received in a plotted form directly from the teletypewriter, and are therefore almost immediately usable for briefing purposes.

INTRODUCTION

1. Background.

TELEPLOT is a method of transmitting intelligence via teletype so that the data are provided in a pre-plotted, and in some cases pre-analyzed, form. Since the teletypewriter does the plotting, the method was named TELEPLOT (TELEtypewriter PLOTting). The principle of this method is not new or untried. The Weather Bureau had a rudimentary system in the early 1900's which was crowded off the combined collection and distribution networks. Now that the distribution networks are a separate system, another look at the advantages of this method seems in order. The author successfully used a manual version of the TELEPLOT method between the Naval Weather Service Office at NAS Jacksonville, Florida and an aircraft carrier at sea in 1962.

2. Recent Developments.

In May 1966 a computer program was developed at the Navy Weather Research Facility for rearranging synoptic weather data as received in an incoming teletype tape from its standard message form into a plotted form, in which reporting stations are positioned according to their relative geographical locations. The resultant TELEPLOT tape produces a pre-plotted regional surface weather chart, see figure 3.

With the aid of a digitizer, Fleet Weather Facility, Norfolk began using this method operationally in July 1966 to issue high seas and wind warnings in TELEPLOT form. Subsequently, sonic layer depth, sea-surface temperature and surface pressure charts were made available in pre-analyzed form under the name of RATTGRAPHICS. Comments from fleet users on the utility of this TELEPLOT/RATTGRAPHIC method indicate that it is easily understood and utilized in daily operations.

TELEPLOT

1. Methods.

TELEPLOT is the name for the plotted data that comes from the teletypewriter at the receiving ship or facility. There are several methods of putting the data on the teletype tape for transmission. In the manual method, the data is put in a tape cutting teletypewriter and an appropriate code digit is typed for each isopleth as it comes into the typing position. A faster method is to follow each isopleth with a digitizer. The digitizer magnetic tape is then transformed into a teletype tape by a computer. The fastest method for complex phenomena is by programming a computer to automatically produce a TELEPLOT teletypewriter tape from the incoming observational data. A grid to grid method, though not a true TELEPLOT, can be used when only CW is available for transmitting data.

2. Manual Method.

The manual method would normally be used for relatively simple situations, situations of

a non-recurring nature, or by ships of facilities which do not have access to a digitizer and computer. An example of this type situation is a moving forecast area which is positioned over a ship or task force.

| | | | | |
|---------------------|---------------------|-------|-----------|-----------|
| L_o | $ddffW_1$ | L_o | $ddffW_1$ | L_o/L_a |
| $d_w d_w P_w H_w V$ | $d_w d_w P_w H_w V$ | L_a | | |
| $ddffW_1$ | $ddffW_1$ | | | |
| $d_w d_w P_w H_w V$ | $d_w d_w P_w H_w V$ | | | |
| | | | | |
| | | | | |

The letters represent standard World Meteorological Organization Codes, WMO Fascicule 9, Volume B. The above grid size could easily be varied to accommodate a variety of situations. Fronts could be positioned by the letters C for cold front and W for warm front, as appropriate. Other manual TELEPLOT formats are available for sea and surf presentations, underwater demolition team reports of beach gradient, water depths, natural and man-made obstructions, minefield locations, and charts depicting refractive index and sea ice patterns.

3. Digitizer Method.

This method is best used for data that can be isoplethed by single lines, such as sea-surface temperature, sonic layer depth, pressure patterns, sea height, wind speed areas, climatological data, etc. The degree of character or feature definition is inversely proportional to the TELEPLOT scale. Figure 1 is a TELEPLOT of the sea-surface temperature for the North Atlantic. Figure 2 is a TELEPLOT of the same data for the Virginia Capes Operating Area.

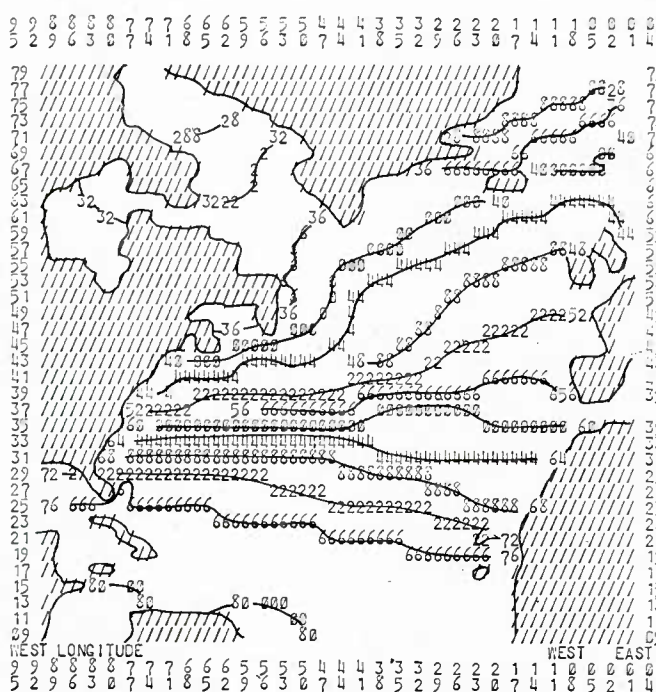


Figure 1. Sea-surface temperature TELEPLOT, North Atlantic in April. Land areas depicted by slants. SST in degrees Fahrenheit.

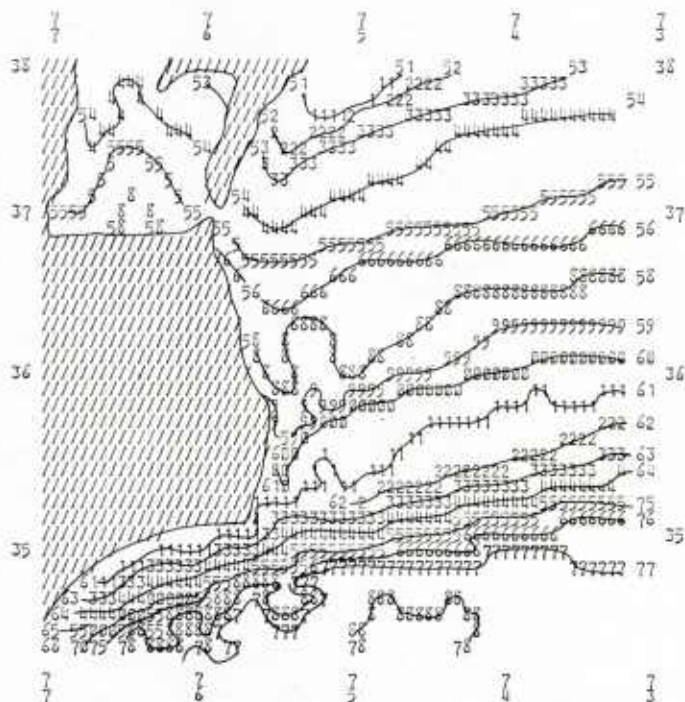


Figure 2. Sea-surface temperature TELEPLOT, Virginia Capes Operating Area in April. Land areas depicted by slants. SST in degrees Fahrenheit.

4. Computer Method.

More complex derivations, extrapolations and rearrangements of environmental data can be produced for distribution through computer programming, and with a significant reduction in

the time from observation to briefing. Figure 3 is a TELEPLOT of a regional synoptic surface weather chart. Longitude is printed along the top and bottom border, latitude along the left border. The format for land station observations is in the upper left corner, and that for ship station observations is in the lower right. The geographical features of the weather chart would be printed on a plastic overlay, upon which the analysis would be performed. Other computer produced TELEPLOTS include various ASW parameters, approach/landing conditions, horizontal weather depiction, vertical weather cross-section, coastal weather cross-sections and upper air data.

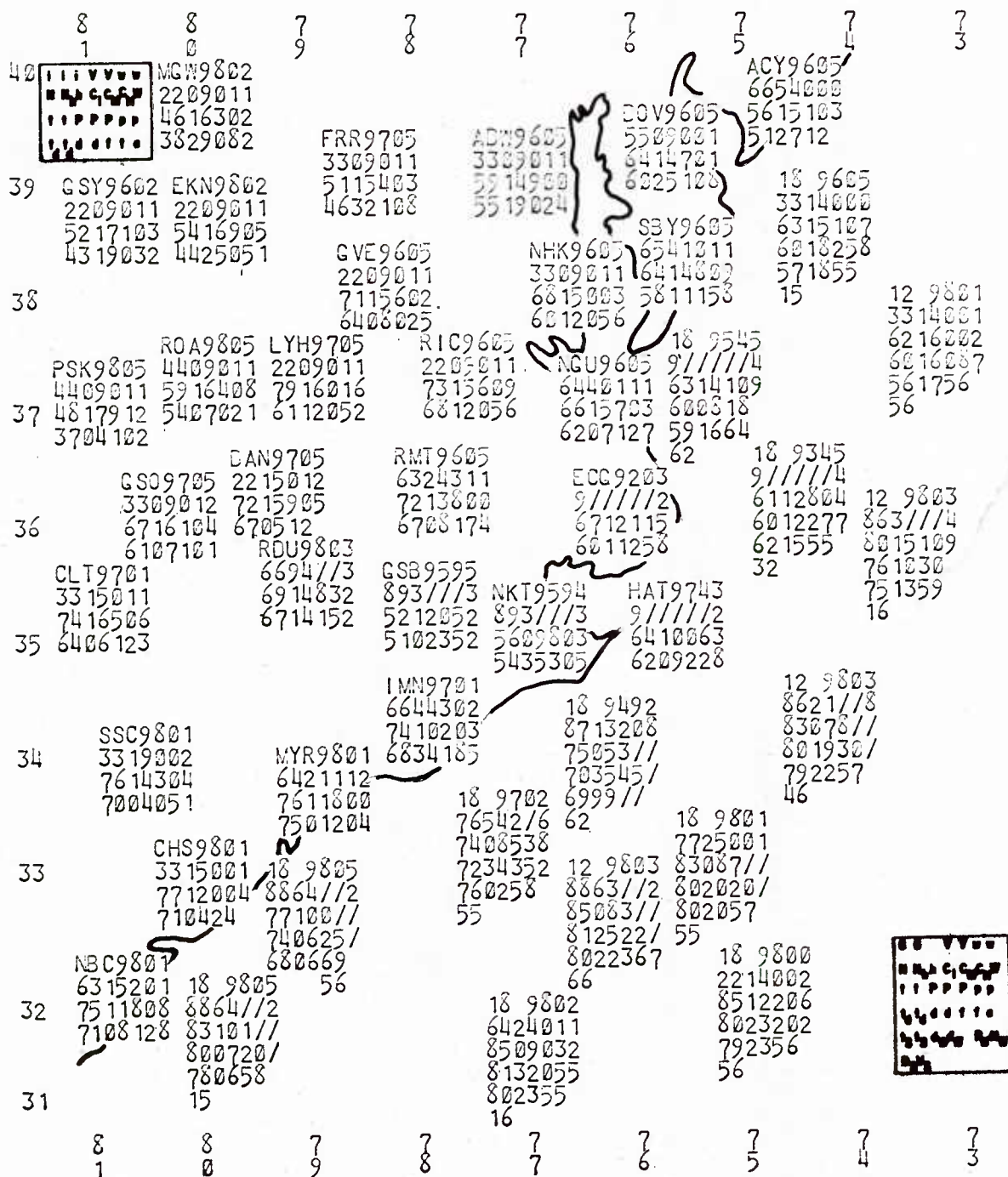


Figure 3. Surface Weather TELEPLOT. The land area outline would be on the plastic overlay.

5. Grid to Grid Method.

This method could be used by aircraft, ships or facilities which have only CW or voice communications. Since both the sender and receiver must use the same grid and format, a TELEPLOT Code and Format Manual would be required. For example, the radar scope presentation of a tropical cyclone as seen by a Navy typhoon/hurricane hunter aircraft could be transformed into a pseudo iso-echo representation for transmission. A Polaroid photograph of the radar scope is gridded to conform to the teletypewriter spacing, and then each space is assigned a brightness number (visual estimate). A brightness scale has arbitrarily been chosen in which the brightness of the echo increases from 1 to 9. The message is prepared by designating the brightness value for the appropriate line and row number as follows:

HURRICANE ELLA CENTERED 15.2 N 43.7 W
TELEPLOT GRID A LINE II ROW 21

L2 R20 2233443321 R29 L3 R17 1123335777776542222 R35 L4 R14 334543332267888766554222
R38 L5 R11 24456541 R19 R25 678885 R30 R34 54433211 R41 L6 R10 23457653 R17 R26 883
R30 R36 332211 R42 L7 R8 255577632 R16, etc.

Figure 4 is the data as plotted on grid A by the receiver. Connecting the brightness numbers with faired lines provides the recipient with a pseudo iso-echo picture of that which is observed by the typhoon/hurricane hunter aircraft. The receiving facility could then quickly prepare a TELEPLOT for transmission to threatened ships and facilities (This example has been expanded to show the detail available, but operational messages could obviously be much shorter). The advent of radio teletype equipment and single side band communications in Navy reconnaissance aircraft will greatly facilitate the preparation and transmission of such radar scope photographs as the hurricane or typhoon warning centers may require.

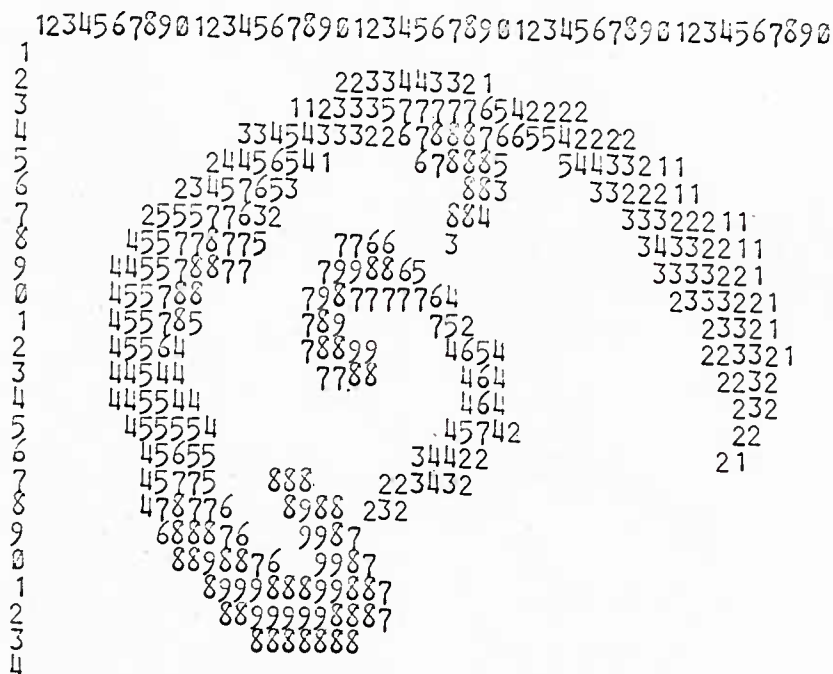
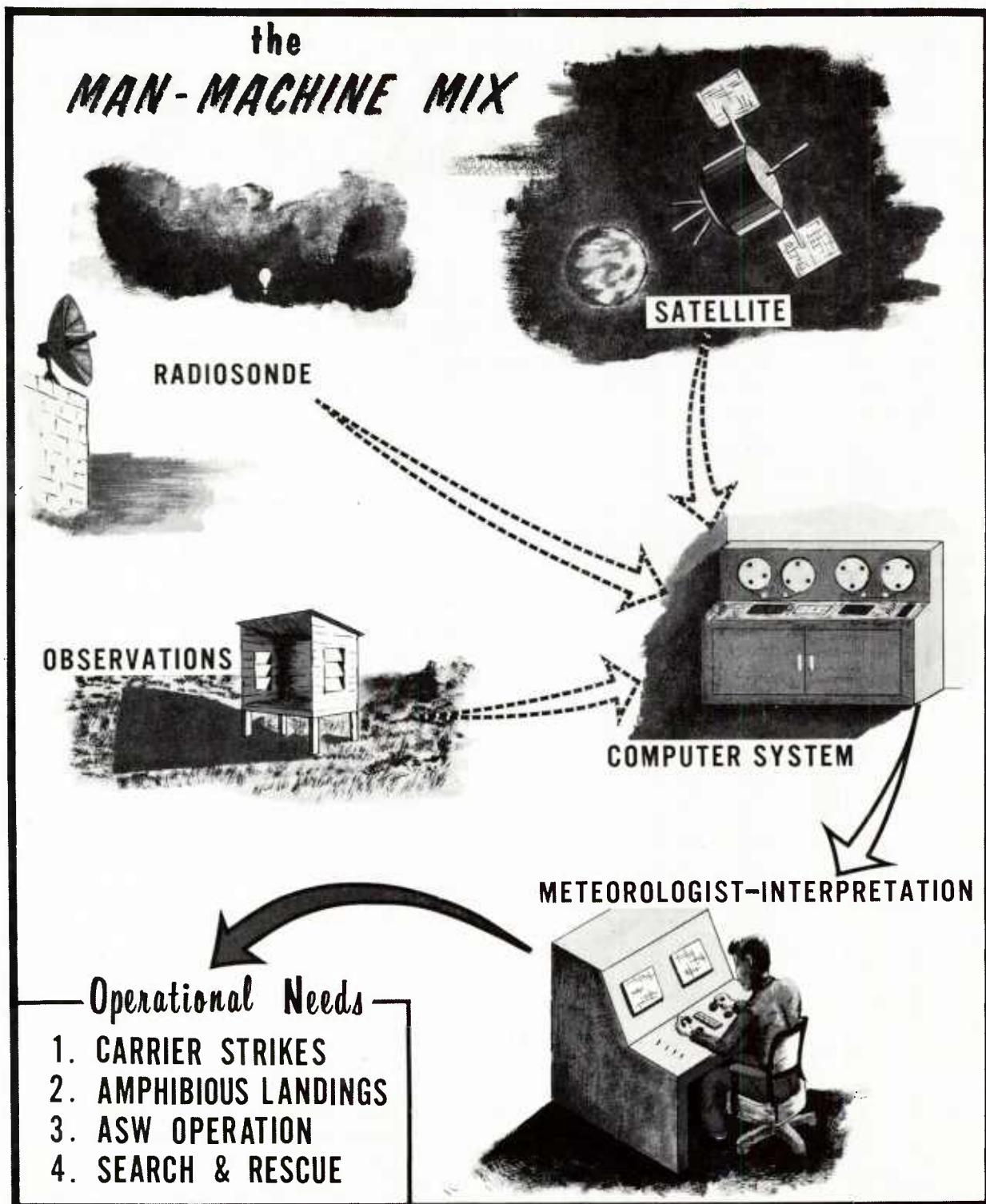


Figure 4. Typhoon/Hurricane TELEPLOT. Radar echo brightness estimated by the observer in the typhoon/hurricane hunter aircraft on an increasing scale from 1 to 9.

6. Summary and Conclusions.

Two notable advances in the environmental and communications fields have made the TELEPLOT method attractive as a means of transmitting intelligence. Computers have extended our ability to use the data available, make extrapolations to fill data voids, and produce derivations beyond the capacity of manual methods. The collection and distribution functions of the communications networks have been separated, allowing the capabilities of the communications systems to be more fully realized. The TELEPLOT method takes advantage of both of these changes, and allows complex computer products to reach the user on ships and facilities through the medium of the teletypewriter.



SURFACE OBSERVATIONS OF SNOW AND ICE FOR CORRELATION
WITH REMOTELY COLLECTED DATA

by

Michael Bilello

U. S. Army Cold Regions Research and Engineering Laboratory
Hanover, New Hampshire

ABSTRACT

The seasonal extension of the earth's snow and ice cover is easily determined by aircraft and satellite reconnaissance. However, determination of the depth and physical properties of snow and the thickness of ice on lakes, rivers and along coastlines by these remote sensors is presently at an early stage of development. Correlations of the remote sensing data and actual surface conditions could well be accomplished through use of the observations being received from a network of snow and ice stations throughout North America. This network, comprising over 100 stations, is being conducted by USA CRREL in cooperation with other government agencies, including the Air Weather Service, and provides the most extensive and reliable data accumulation for such correlation studies.

SURFACE OBSERVATIONS OF SNOW AND ICE FOR CORRELATION WITH REMOTELY COLLECTED DATA

by

Michael Bilello

U. S. Army Cold Regions Research and Engineering Laboratory
Hanover, New Hampshire

A. Introduction

Examination of photographs received from meteorological satellites has confirmed man's ability to utilize this new method to survey the extent of the snow and ice cover in the cold regions of the world.

Fritz [1963] states that, "Satellites can see white snow fields against darker backgrounds. Moreover, a snow field can be distinguished from clouds, which also appear white in satellite pictures, when pictures are taken on successive days. The cloud patterns change from day to day, but the snow fields generally remain unaltered over a period of a few days." D. Q. Wark, et al. [1962] report that from TIROS II photographs "many details of the ice can be distinguished, such as type of ice, amount, and presence of leads and cracks." They further state that although some clouds of a certain type and amount resemble ice, there is usually enough difference in appearance to allow identification by an experienced interpreter.

Snow and ice reconnaissance from satellites continues to improve since the sensors are now earth-oriented and the vehicles are in quasi-polar orbits. The equipment on board is also improving and with time will be able to take on new and more sophisticated chores such as recording the depth and density of a snow cover and the thickness of ice on lakes, rivers, and oceans.

When this new era arrives it would be beneficial to be able to compare the data collected from these sensors with concurrent ground measurements for verification purposes. An extensive snow property and ice thickness observing network which has been established in North America could provide such information. Discussion of this network and a summary of the to-date analysis of the data is the subject of this paper.

B. Snow and Ice Observing Networks*

To satisfy a need for information on the thickness of sea, lake and river ice, and the properties of the snow cover, a number of snow and ice observing stations were established in North America starting in 1946. This network extends from the west coast of Alaska to the east coast of Canada, and from just below 83°N. latitude to as far south as the Great Lakes (Fig. 1 and 2). The data obtained at these widely distributed stations are valuable to commercial fishermen, loggers, aircraft pilots, government agencies, and the military. The military uses of the data are in connection with, for example, the winter movement of troops and vehicles, the landing of aircraft on ice and the operations of ice breakers and other ships through ice. The data have also proved useful for long-range analyses of climatic and environmental regimes in the Arctic and Subarctic.

The first five stations in the network were established in the Canadian Archipelago Islands between 1946 and 1950 as a joint venture of the Canadian Department of Transport's Meteorological Division and the United States Weather Bureau. Subsequently, through the cooperation of the USAF Air Weather Service, USARAL (U. S. Army Alaska), the Soil Conservation Service, and the Alaska Regional Office - ESSA, the network gradually expanded to the south and westward. Most of the observations are being made by military and civilian personnel associated with these agencies. Many measurements in Alaska are being made by Eskimos, native Indians, school teachers, clergymen, homesteaders, and lodge-keepers.

* A portion of the discussion in this and the following section was taken from a brief report given by the author at the 15th Meeting of the U.S. Army Meteorological R and D Coordination Committee, Nov. 1966, Hanover, N. H.

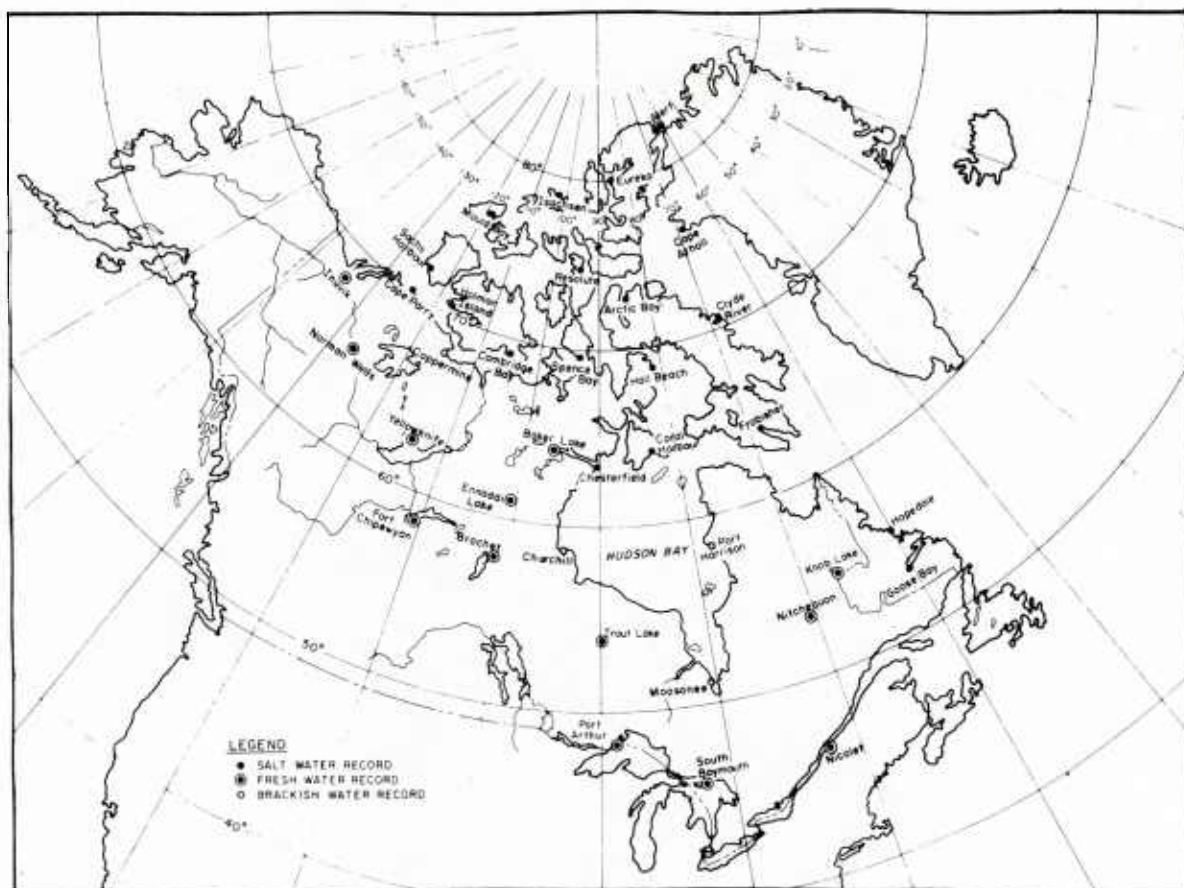


Figure 1. Map of Canadian stations.

C. Type of Observations and Equipment

1. Snow observations

The snow observations, which are made in accordance with standard procedures described in USA CRREL Instruction Manual No. 1 [USA CRREL, 1962], provide data on certain properties of each layer of snow in a vertical profile. The different layers of snow could be visually delineated by structural differences, such as size and shape of the snow grains, or textural variations identifying periods of major snow accumulation. The properties measured weekly are density, temperature, hardness and crystal size.

The original snow-measuring equipment for these stations was provided by the National Research Council of Canada. USA CRREL later designed its own snow kit (Fig. 3). The USA CRREL equipment differs only slightly from that in the Canadian kit and consists of:

1. A set of snow sampling tubes to measure density in g/cm^3 .
2. A balance for weighing snow samples.
3. Two hardness gages, with disks, of from 1 to 100,000 g/cm^2 capacities.
4. A set of thermometers to measure snow temperature in different layers.
5. A graduated plate with etched concentric 1-mm spaced rings for measuring grain size, and a hand lens for determining snow crystal type.

2. Ice observation

During the first years of operation, ice thickness was measured through holes chiseled in the ice. When the ice was too thick for chiseling, the upper part was blasted with dynamite. To facilitate the ice thickness observation and to improve the accuracy of measurement, USA CRREL developed a hand-operated ice auger (Fig. 4), and, in April 1956, distributed one to each station. With this auger, a 1 or 1½ inch diameter hole can be bored through 7 feet of ice in about 15 minutes.

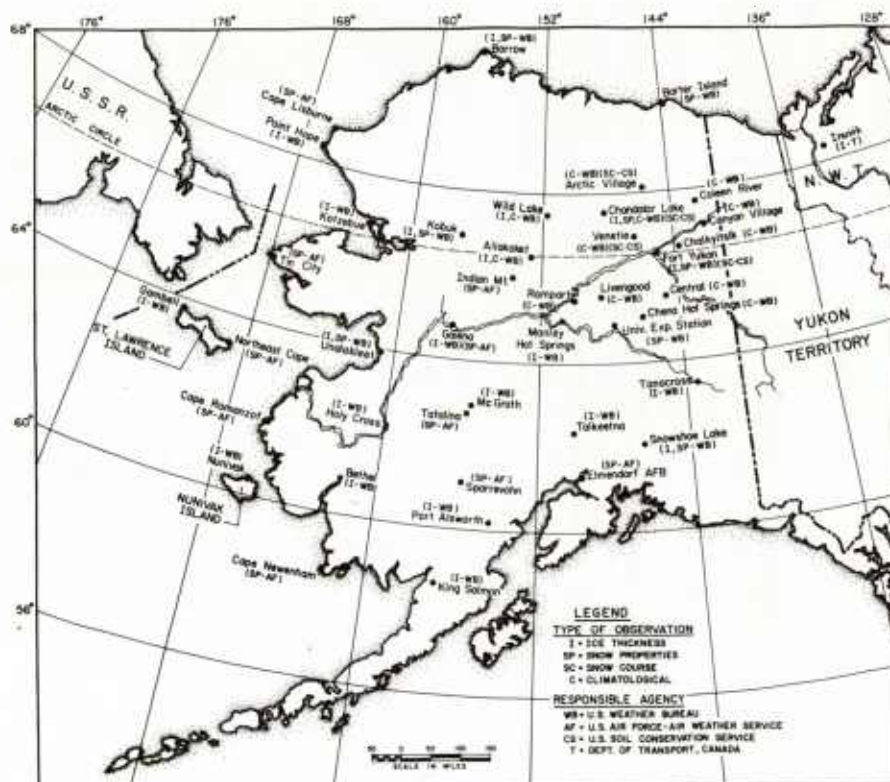


Figure 2. Map of Alaskan stations.

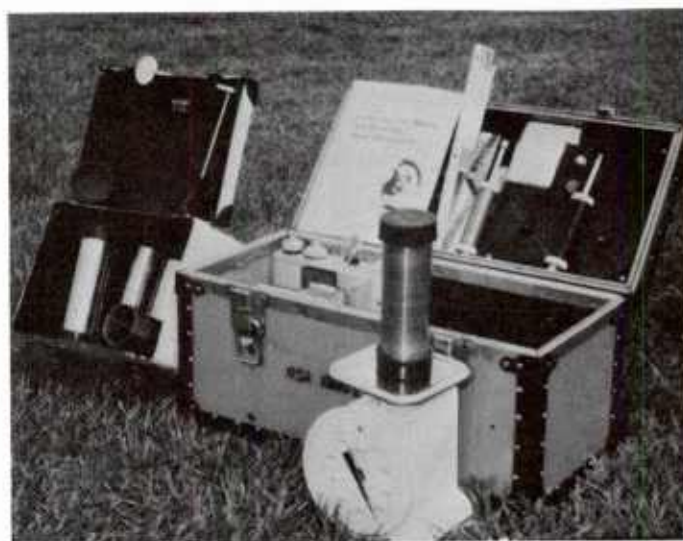


Figure 3. Snow observation equipment.

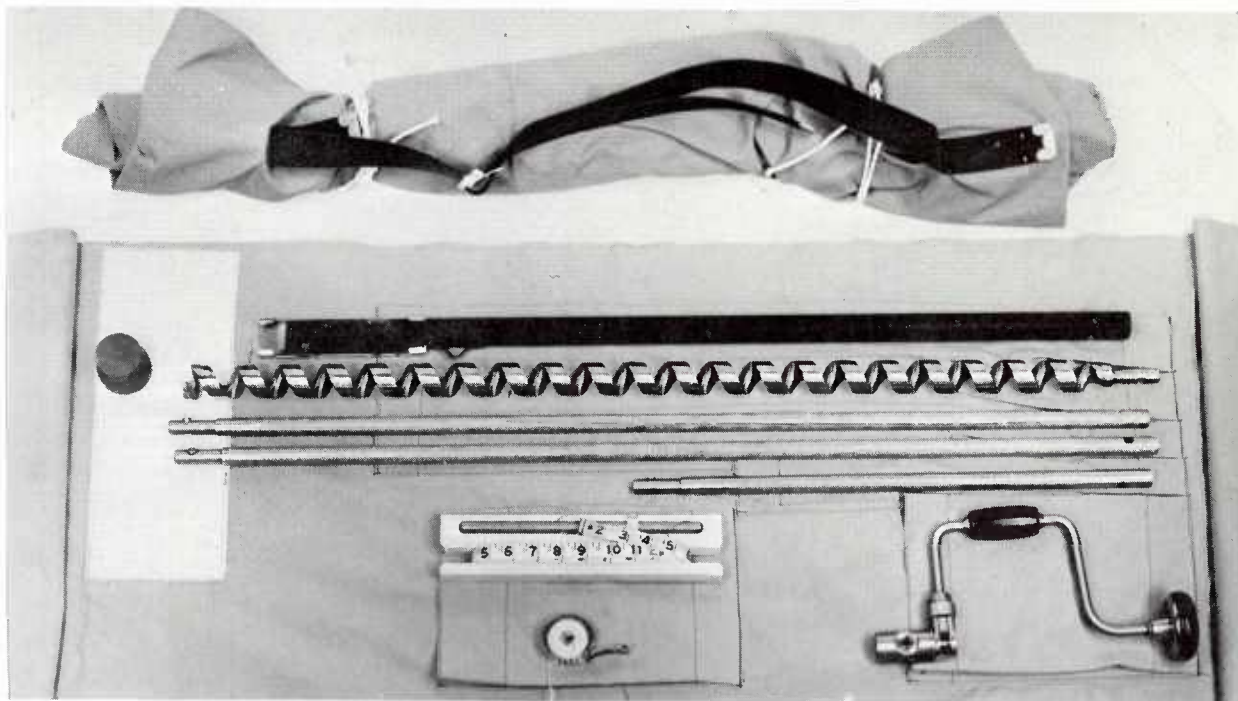


Figure 4. Ice thickness measuring kit.

To measure ice thickness, a measuring tape with a short pivotable rod attached to its end is lowered into the augered hole. When the rod is below the ice, it swings to a horizontal position. The tape is then lifted until the rod contacts the undersurface of the ice. The thickness of the ice is then recorded. A separate wire attached to the end of the rod is used to return it to the vertical position so that the rod and tape can be withdrawn from the hole.

The ice thickness observations are made once each week in bodies of water close to the station. The snow depth on the ice as well as ice surface conditions, e.g., occurrence of cracks, leads and dates of first-ice, freeze-over and break-up are also recorded.

Most observers in the network mentioned above auger only one hole at each site each week. Personnel associated with the U. S. Department of the Interior, Geological Survey, Water Resources Division in Alaska periodically make measurements of flow beneath the river ice in Alaska during the winter. Information on the thickness of the ice is thus obtained every several feet or several yards across the river. These data have been furnished to USA CRREL for publication and are reported in Part III of a series of special reports on ice thickness observations in the North American Arctic and Subarctic [USA CRREL, 1961, 1964 and 1966].

D. Results of Data Analysis

1. Snow cover properties

An analysis of snow-cover density, temperature, and hardness data showed the snow in the Canadian Archipelago to be colder, denser and harder than in the interior of Alaska [USA SIPRE, 1957]. The average snow cover temperature from November through March at the Alaskan stations was 4°C to 9°C higher than the average air temperature whereas it was 4.5°C higher than the air at the Canadian Archipelago stations. Investigation of snow-cover hardness revealed regional variations similar to that for density. The range in snow cover density for interior Alaskan stations is approximately 0.13 to 0.20 g/cm³ in November and 0.23 to 0.27 g/cm³ in March. The densities along the north coast of Alaska and the northern islands of Canada range from approximately 0.30 to 0.36 g/cm³ in November, and from 0.33 to 0.39 g/cm³ in March.

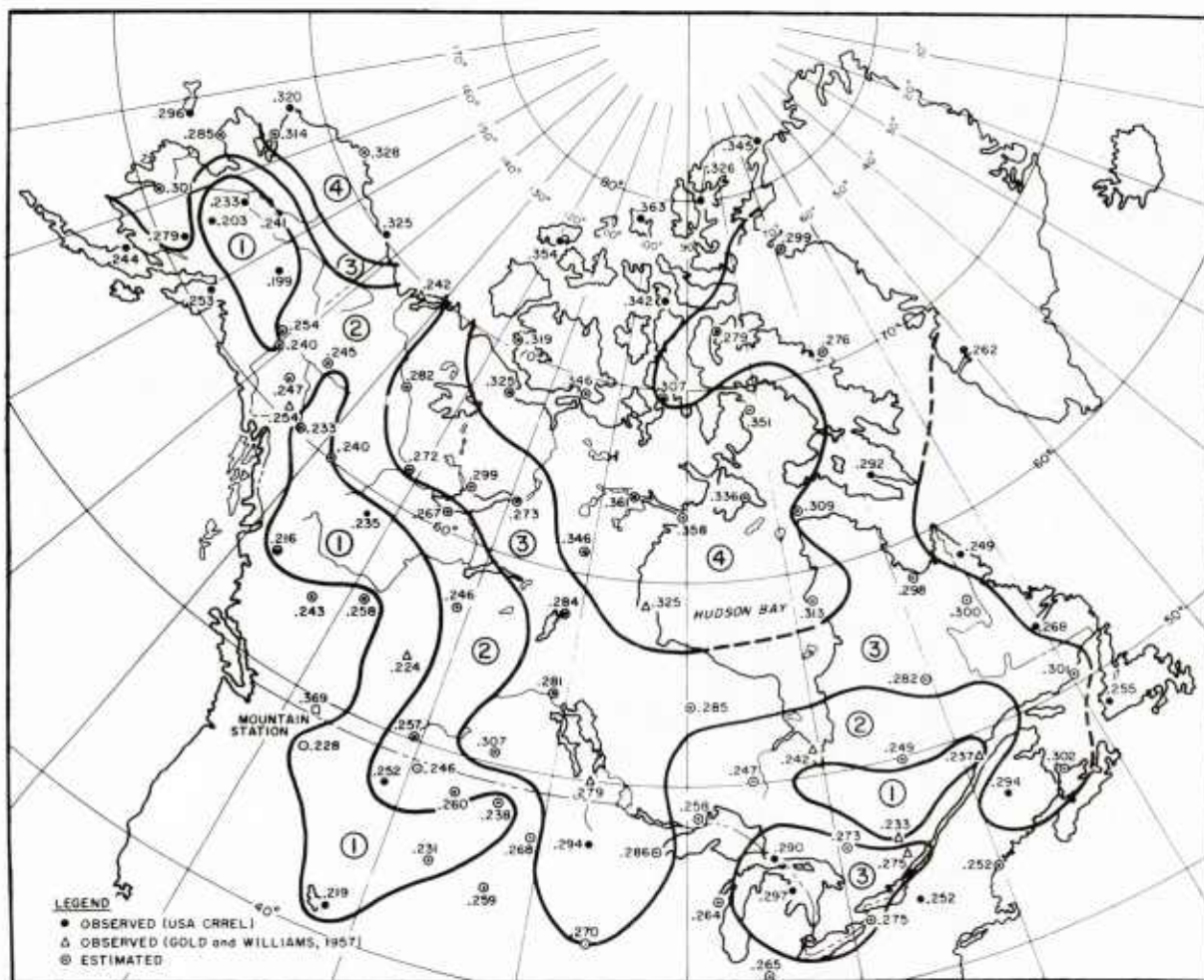


Figure 5. Average seasonal snow-cover densities. Categories 1-4 are separated at densities of 0.24, 0.27 and 0.31 g/cm³.

A subsequent study associated regional variations in snow density with observed temperatures and wind speeds [Bilello, 1966]. A multiple regression analysis made on the relationship provided the following equation:

$$\rho = 0.152 - 0.0031 T + 0.019 W$$

where:

ρ = average seasonal* snow-cover density (g/cm³)
 T = average seasonal air temperature (°C) and
 W = average seasonal wind speed (m/sec).

The correlation coefficient and the standard error of estimate for this multiple relationship was 0.84 and 0.025 g/cm³ respectively.

An average snow density map of North America (Fig. 5) was drawn using: 1) the observed densities from the stations in the USA CRREL network, 2) 10 stations operated by the Canadian National Research Council, Division of Building Research [Gold and Williams, 1957], and 3) estimated densities for 61 other locations. The continent was divided into areas based on four categories:

- Category 1 - Inland stations reporting light winds
- Category 2 - Stations generally reporting moderate winds
- Category 3 - Inland and coastal locations with stronger winds
- Category 4 - Cold and windy stations in the Arctic and Subarctic.

* The term "seasonal" refers to November through March inclusive, unless the average air temperature for the month is above freezing.

Naturally, the local topography and vegetation create differences in the density from point to point within a categorically defined region. Deviations from the average value for each region can also be expected from month to month and year to year. Standard deviations from the average values ranged from .033 to .102 g/cm³.

2. Ice thicknesses

Chronological listings of fast-ice measurements observed on lakes and rivers and along the coast in North America are given in USA CRREL Special Report 43 [op. cit.]. To indicate the magnitude and distribution of ice thickness, isoline maps of maximum observed ice thicknesses are also presented for each year starting with the winter of 1956-57.

Sufficient information on maximum annual ice in the North American Arctic and Subarctic had accumulated to permit an analysis on: 1) the least ice thickness observed at the time of maximum thickness (Fig. 6), and 2) the greatest ice thickness observed at the time of maximum thickness (Fig. 7). Records of the maximum ice thickness attained during each season were utilized in this analysis. The lowest value and the highest value observed during the period of record were used to draw the isolines in Figures 6 and 7 respectively. The period of record used varied from 3 to more than 10 years. Some of the information used in Figures 6 and 7 was obtained from the Canadian Department of Transport Circular 3195, Ice 4 [1959].

From Figure 5, we note that in Canada the least ice thickness observed at the time of maximum thickness ranged from less than 20 cm in the vicinity of Nova Scotia to near 200 cm in the north central region. In Alaska, excluding the Aleutian chain and the southeast panhandle regions, the value ranged from near 60 cm in the southern part of the state to 170 cm on the west coast. From Figure 7, we find that the greatest ice thickness observed in Canada ranged from 30 cm near Nova Scotia to over 260 cm in parts of the Arctic.

A preliminary summary of the year-to-year variations in maximum ice for 25 stations in the network showed an average deviation of 11.6%. Except for an isolated case, the highest and lowest deviations were 27% and 2% respectively.

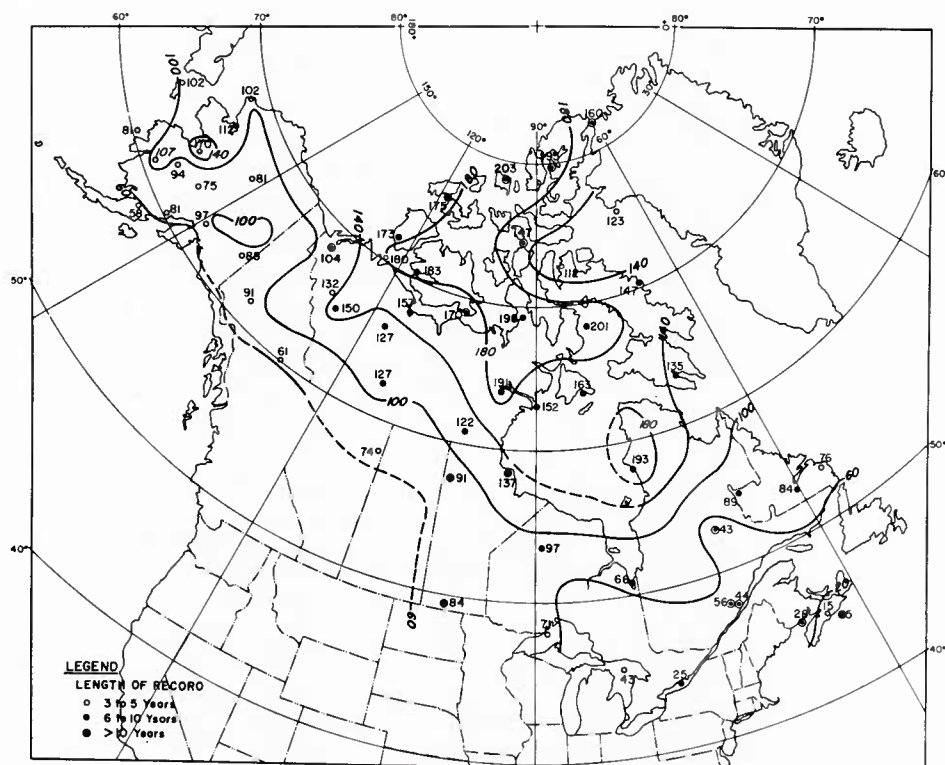


Figure 6. Least ice thickness observed at the time of maximum thickness for the years of record in cm.

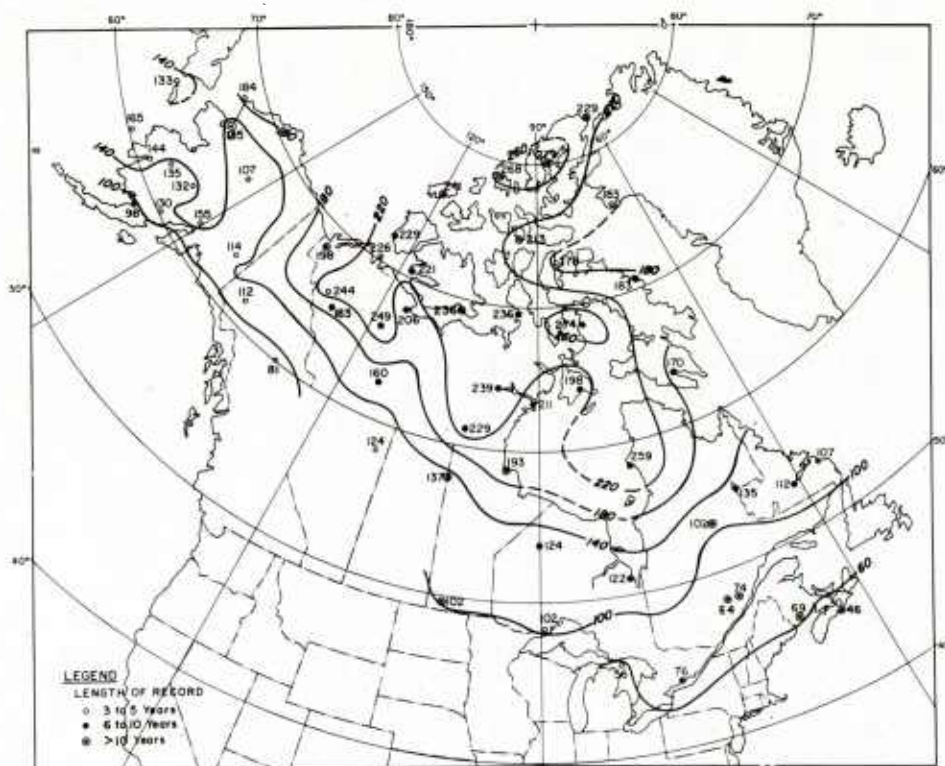


Figure 7. Greatest ice thickness observed at the time of maximum thickness for the years of record in cm.

In addition to yearly differences, areal variations in maximum ice thickness were considered. Except for two particular sites near Churchill, Canada, the average areal deviation in maximum ice thickness at the stations was 10.7%. The greatest deviation was 20%, the least 3%. The difference in snow depth on the ice at the two sites near Churchill resulted in a deviation in maximum ice thickness of 68%.

In some instances, extreme variability in ice thickness is apparently due to ice rafting. Ice rafting in oceans is usually a result of action by winds, tides and currents. On lakes and rivers thawing conditions and changes in water level cause the ice to break up and raft. For example, seven out of eight river sites in Alaska reported variations exceeding 50% during November and December 1956. Meteorological records show that the southern valleys and the Yukon basin of Alaska experienced freezing temperature during the first half of November 1956 and above freezing temperatures with some rain during the last half of the month [U. S. Department of Commerce, 1956].

E. Discussion

The main purpose of this report was to describe a network of stations in North America where observations on the properties of snow and thickness of ice are being made. Results of studies using the data collected from these stations show that despite areal and yearly variations definite patterns in the magnitudes of the values emerge when plotted on small scale maps.

Aerial infrared and passive micro-wave systems are being studied for separating clouds from snow covered terrain and penetrating clouds to obtain snow and ice data. The Nimbus II High Resolution Infrared Radiometer pictures, taken at midnight, showed the Gulf Stream in the Atlantic Ocean by differentiating colder and warmer surface water temperatures [Americal Meteorological Society, 1966]. A method of determining the temperatures of rivers through the use of narrow-angle radiation measuring devices installed in satellites has also been investigated [Dmitriev and Evnevich, 1966]. Estimates of the heights of drifted snow accumulations and rafted ice can be determined by photogrammetric methods.

Development of advanced equipment to measure snow-cover depths and ice thickness from aircraft or from space is currently under contract by several agencies including the U. S. Army and ESSA. Remote sensors that will provide information on the physical properties of the snow cover and conditions of the ice on earth will very likely be developed in the near future [see Carter, 1967].

Another approach would be to install equipment such as snow pillows and nuclear devices within remote snow packs to measure the density. The equipment would contain a telemetering device to periodically send its information to satellites which, in turn, would relay the data to a central station on command. The same procedures could be used to obtain ice thickness measurements in isolated regions. However, there are some problems associated with this plan, principally the installation, care and reliability of the sensors and the inclusion of the power pack and the antenna assembly necessary for transmission.

These are but a few of the ground-space systems for measuring surface snow and ice conditions which undoubtedly will be tested in the future. When one of the systems proves promising, observations by man on the ground could be used to verify its worth.

F. References

American Meteorological Society: "Cover Photograph", Bulletin, Vol. 47; No. 9; September, 1966.

Bilello, M.A. and Bates, R.E.: "Ice Thickness Observations, North American Arctic and Subarctic, 1958-1964", USA CRREL Special Report 43, Parts I, II and III; 1961, 1964, and 1966.

Bilello, M.A.: "Relationships Between Climate and Regional Variations in Snow-Cover Density in North America", International Conference on Low Temperature Science, Hokkaido, Japan; 15 p; 1966.

Carter, L.J.: "Post-Apollo: NASA's Plans Get Boost from LBJ and PSAC," Science, Vol. 155; No. 3766; p. 1084-1087; March 1967.

Department of Transport (Canada): "Maximum Winter Ice Thicknesses in Rivers and Lakes in Canada", Meteorological Branch, CIR-3195, Ice 4; 1959.

Dmitriev, A.A. and Evnevich, T.V.: "A Modeling Approach to the Problem of Determining the Temperature of Rivers from Satellites", Atmospheric and Oceanic Physics; Vol. 2; No. 8; p. 897-899; 1966.

Fritz, S.: "Snow Surveys from Satellite Pictures", Rocket and Satellite Meteorology; North Holland Publishing Co., Amsterdam; p. 419-421; 1963.

Gold, L.W. and Williams, G.P.: "Some Results of the Snow Survey of Canada", Division of Building Research, National Research Council, Canada; Research Paper No. 38; 15 p; 1957.

U. S. Army Cold Regions Research and Engineering Laboratory (USA CRREL): "Instructions for Making and Recording Snow Observations", Instruction Manual 1; 10 p; 1962.

U. S. Army Snow, Ice and Permafrost Research Establishment (USA SIPRE, now USA CRREL): "A Survey of Arctic Snow-Cover Properties as Related to Climatic Conditions", USA SIPRE Research Report 39, 9 p; 1957.

U. S. Department of Commerce: "Climatological Data, Alaska", Monthly Records (November), U. S. Weather Bureau, 1956.

Wark, D.Q.; Popham, R.W.; Dotson, W.A. and Colow, K.S.: "Ice Observations by the Tiros II Satellite and by Aircraft", Arctic; Vol. 15 (1); p. 9-26; 1962.

APPLICATION OF RADIO AND OPTICAL PATH LENGTH MEASUREMENTS TO STUDIES OF LOW-LEVEL TURBULENCE

B. R. Bean and C. B. Emmanuel
Environmental Science Services Administration
Institute for Telecommunication Sciences and Aeronomy
Boulder, Colorado

Abstract

It is our purpose to bring to the meteorologist's attention the potential use of radio and optical distance measurements as indicators of average humidity and temperature variations over distances of up to several tens of kilometers. The time variability of humidity and temperature are also indicated by those of the radio and optical path lengths.

By measuring the radio path length, L_r , over a geometric distance S in the fashion described by Thompson et al [1960] one obtains an integrated value of the radio refractive index, n_r . That is

$$L_r = \int_0^S n_r ds. \quad (1)$$

For the radio refractive index, one has

$$n_r = 1 + k_1 \rho + k_2 \frac{\rho_w}{T} \quad (2)$$

where ρ is the dry air density ($g \cdot m^{-3}$), ρ_w is the water vapor density ($g \cdot m^{-3}$) and T is the temperature ($^{\circ}K$). The constants k_1 and k_2 are known to a precision exceeding that of the normal field measurement of ρ_w and T [Bean and Dutton, 1966]. Examination of observations obtained in Colorado and Florida has shown that variations in L_r are well correlated with those of ρ_w . Examples of this correlation derived from observations supplied by the authors' colleague, Dr. M. C. Thompson, are:

| S(km) | Correlation Coefficient |
|-------|-------------------------|
| 0.7 | 0.675 |
| 3.2 | 0.794 |
| 7.7 | 0.721 |
| 15.2 | 0.917 |
| 15.5 | 0.775 |
| 17.1 | 0.820 |

These correlations were derived by comparing the variations of L_r with those of ρ_w determined as the average of the values at both ends of the radio path.

The optical path length may also be determined. For this case, the optical refractive index, n , is given to a first approximation by

$$n_o = 1 + k_1 \rho. \quad (3)$$

[Owens, 1967, has recently given a thorough review of the constants in the equation for the optical refractive index.] Variations of the optical path length would be expected to be correlated principally with those of temperature.

Examples of these correlations were obtained during a recent field program where the authors were studying evaporation from Lake Hefner in Oklahoma City during August of 1966.

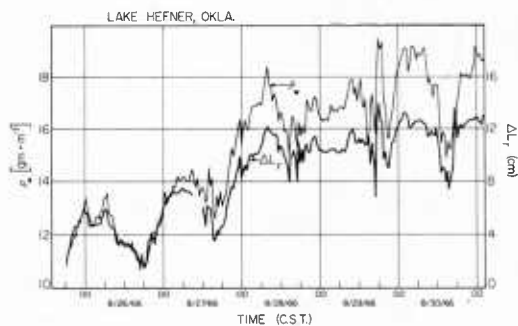


Fig. 1. A comparison of the radio path length fluctuations, ΔL_r , with variations in the water vapor density, ρ_w .

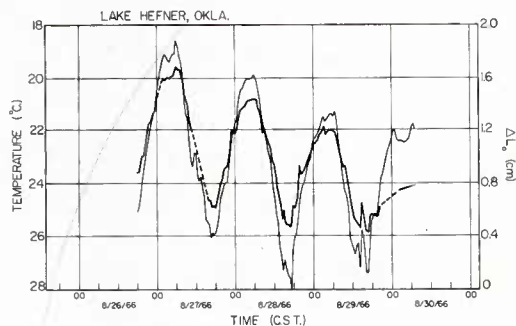


Fig. 2. A comparison of the optical path length fluctuations, ΔL_o , (heavy line) with temperature.

Figure 1 compares variations of $L_r, \Delta L_r$, with those of ρ_w determined at the midpoint of the 1.64 km path while figure 2 compares variations of $L_o, \Delta L_o$, with those of temperature. [The optical data were kindly supplied by the authors' colleague Dr. J. Owens.] Good agreement was obtained in each case. One may also use the radio and optical measurements combined with temperature at midpath to estimate ρ_w from the expression

$$T(L_R - L_O). \quad (4)$$

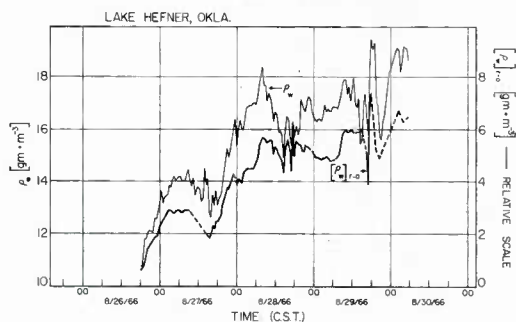


Fig. 3. A comparison of ρ_w as calculated from (4) with water vapor density obtained from psychrometric observations.

The results are shown on figure 3. The agreement also appears to be good in this case. A more quantitative measure of the agreement between these data was obtained by calculation of the correlation coefficient:

| Variables | Correlation coefficient |
|----------------------------|-------------------------|
| L_o vs T | - 0.915 |
| L_o vs ρ | 0.923 |
| L_r vs ρ_w | 0.922 |
| $T(L_r - L_o)$ vs ρ_w | 0.953 |

These initial results offer encouragement that the method may be eventually useful for measurement of average humidity and temperature over distances of interest to studies of meso-scale phenomena.

The application of such techniques to studies of turbulent micropulsations of humidity is illustrated on figures 4 and 5 where the spectral density of ρ_w and radio phase (or L_r) are compared for midday and night conditions. An additional comparison is made for these times as to the effect of evaporation-suppressing monomolecular film. It is seen that there is general agreement between the various spectra in that the presence of the film reduces the spectral amplitudes of both radio phase and ρ_w .

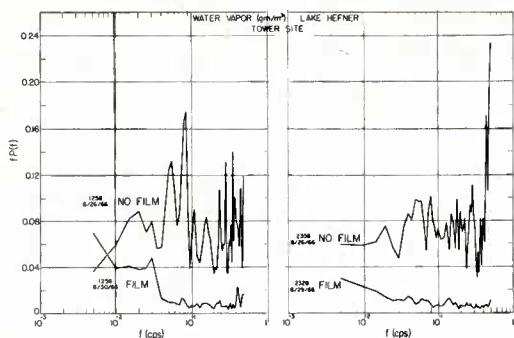


Fig. 4. Spectral variation of water vapor density as observed with tower-mounted barium fluoride elements at Lake Hefner, Oklahoma.

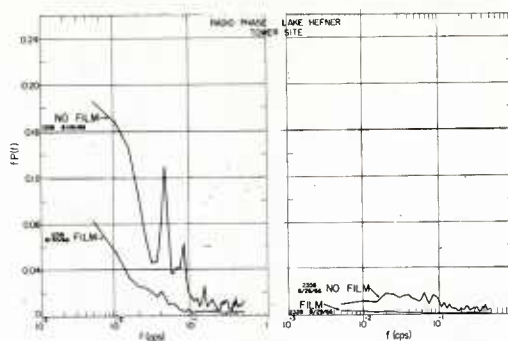


Fig. 5. Spectral variation of radio phase as observed for the same time as that of ρ_w of figure 4.

The analysis of the Lake Hefner data continues and is expected to be reported in detail at the forthcoming AGARD/EPC Conference in Ankara, Turkey, October 9-12, 1967.

References

- Bean, B. R., and E. J. Dutton (1966), Radio Meteorology, NBS Monograph 92.
- Owens, J. C. (1967), Optical refractive index of air: Dependence on pressure, temperature, and composition, *Applied Optics*, 6, No. 1.
- Thompson, M. C., Jr., H. B. Janes, and A. W. Kirkpatrick (1960), An analysis of time variations in tropospheric refractive index and apparent radio path length, *J. Geophys. Res.* 65, No. 1.